

University of Warwick institutional repository: <http://go.warwick.ac.uk/wrap>

**A Thesis Submitted for the Degree of PhD at the University of Warwick**

<http://go.warwick.ac.uk/wrap/67281>

This thesis is made available online and is protected by original copyright.

Please scroll down to view the document itself.

Please refer to the repository record for this item for information to help you to cite it. Our policy information is available from the repository home page.

*Particle Encapsulation and Modification to  
Afford Hierarchical Composite Materials*

By  
Holly McKenzie

A Thesis Submitted in Fulfilment of the Requirements for  
the Degree of  
Doctor of Philosophy

University of Warwick

September 2014

# Contents

---

|   |              |
|---|--------------|
| <b>Figures.....</b>   | <b>i</b>     |
| <b>Tables .....</b>   | <b>xvi</b>   |
| <b>Acknowledgements.....</b>  | <b>xx</b>    |
| <b>Declaration .....</b>  | <b>xxi</b>   |
| <b>Abstract.....</b>  | <b>xxii</b>  |
| <b>Abbreviations .....</b>  | <b>xxiii</b> |
| <b>Chapter 1: Introduction.....</b>   | <b>1</b>     |
| 1.1. Heterogeneous Polymerization Techniques.....   | 1            |
| 1.1.1. Emulsion polymerization.....   | 2            |
| 1.1.2. Miniemulsion polymerization.....   | 7            |
| 1.1.3. Suspension polymerization.....   | 8            |
| 1.1.4. Dispersion polymerization.....   | 9            |
| 1.1.5. Precipitation .....  | 10           |
| 1.1.6. Pickering emulsion polymerization .....  | 11           |
| 1.2. Film Formation.....  | 14           |
| 1.3. Stabilization of Colloids .....  | 16           |
| 1.3.1. Electrostatic stabilization .....  | 17           |
| 1.3.2. Steric stabilization .....   | 18           |
| 1.4. RAFT Polymerization.....   | 19           |
| 1.5. Scope and Outline of Thesis .....  | 21           |
| 1.6. References .....   | 23           |
| <b>Chapter 2: Particle Encapsulation by Starved-Feed Emulsion<br/>Polymerization.....</b> | <b>28</b>    |
| 2.1. Abstract.....  | 28           |
| 2.2. Introduction.....  | 29           |
| 2.2.1. Layer-by-layer deposition of oppositely charged electrolytes                       | 30           |
| 2.2.2. Heterocoagulation of oppositely charged particles.....                             | 31           |
| 2.2.3. Particle encapsulation by emulsion polymerization.....                             | 32           |
| 2.2.4. Particle encapsulation by miniemulsion polymerization .....                        | 33           |
| 2.2.5. Particle encapsulation by dispersion polymerization.....                           | 35           |
| 2.2.6. Particle encapsulation by precipitation polymerization.....                        | 36           |
| 2.2.7. Particle encapsulation by emulsion polymerization using<br>macro-RAFT agents ..... | 37           |

|  |    |
|--|----|
| 2.3. Results and Discussion.....   | 39 |
| 2.3.1. Characterization of calcium carbonate particles .....   | 39 |
| 2.3.2. Encapsulation of calcium carbonate particles .....  | 46 |
| 2.3.3. Control of shell thickness.....   | 59 |
| 2.3.4. CaCO <sub>3</sub> as a sacrificial template for nano-rattles.....                                 | 65 |
| 2.4. Conclusion .....  | 77 |
| 2.5. Experimental .....  | 78 |
| 2.5.1. Materials.....  | 78 |
| 2.5.2. Equipment .....   | 78 |
| 2.5.3. Encapsulation of calcium carbonate with polymer primer .....                                      | 79 |
| 2.5.4. Etching of calcium carbonate core to yield hollow particles (HM-207).....                         | 80 |
| 2.5.5. Shell Growth (HM-208) .....   | 80 |
| 2.5.6. Water solubility of DEGDA (HM-209) .....  | 80 |
| 2.5.7. Synthesis of amorphous calcium carbonate particles (HM-210) .....                                 | 81 |
| 2.5.8. Synthesis of amorphous calcium carbonate particles containing silica nanoparticles (HM-211) ..... | 82 |
| 2.5.9. Encapsulation of amorphous calcium carbonate particles .....                                      | 82 |
| 2.5.10. Hollow particles template on amorphous calcium carbonate .....                                   | 83 |
| 2.6. References .....  | 84 |

## **Chapter 3: Composite Particle Surface Modification.....89**

|  |     |
|--|-----|
| 3.1. Abstract.....   | 89  |
| 3.2. Introduction .....  | 90  |
| 3.2.1. Click chemistry .....   | 90  |
| 3.2.2. Particle modification.....  | 95  |
| 3.3. Results and Discussion.....   | 100 |
| 3.3.1. Encapsulation of calcium carbonate particles with multi-acrylate monomers to afford pendant vinyl groups.....                             | 100 |
| 3.3.2. Thiol-Michael addition to pendant vinyl groups .....  | 111 |
| 3.3.3. Synthesis and thiol Michael addition of $\omega$ -thiol functionalized poly(styrene) to composite particles.....                          | 121 |
| 3.4. Conclusions .....   | 132 |
| 3.5. Experimental .....  | 133 |
| 3.5.1. Materials.....  | 133 |
| 3.5.2. Equipment .....   | 133 |
| 3.5.3. Calcium carbonate encapsulated in a polymeric shell with pendant vinyl groups .....   | 134 |
| 3.5.4. Hollow particles .....  | 137 |
| 3.5.5. Quantifying pendant vinyl groups on encapsulated particles .....  | 139 |
| 3.5.6. Typical method for thiol Michael addition of 2-mercapto ethanol to pendant vinyl groups on encapsulated CaCO <sub>3</sub> particles ..... | 141 |



|  |     |
|--|-----|
| 3.5.7. Typical method for thiol Michael addition of dodecanethiol to pendant vinyl groups on encapsulated $\text{CaCO}_3$ .....                                  | 144 |
| 3.5.8. Synthesis of RAFT agent (propanoic acid)-2-yl butyl trithiocarbonate (PABTC) (HM-320) .....   | 145 |
| 3.5.9. RAFT polymerization of styrene using PABTC .....  | 147 |
| 3.5.10. Aminolysis of RAFT functionalized poly(styrene) (HM-323) .....   | 148 |
| 3.5.11. Reduction of disulfides with DTT (HM-324) .....  | 149 |
| 3.5.12. Method for thiol Michael addition of $\omega$ -thiol functionalized poly(styrene) to pendant vinyl groups on encapsulated $\text{CaCO}_3$ (HM-325) ..... | 149 |
| 3.6. References .....  | 151 |

## **Chapter 4: pH Responsive Microgel Particles..... 156**

|   |     |
|---|-----|
| 4.1. Abstract.....  | 156 |
| 4.2. Introduction .....   | 157 |
| 4.3. Results and Discussion .....   | 163 |
| 4.3.1. Particle synthesis.....  | 163 |
| 4.3.2. Responsive behaviour .....   | 170 |
| 4.3.3. Pickering emulsions .....  | 185 |
| 4.4. Conclusions .....  | 194 |
| 4.5. Experimental .....   | 195 |
| 4.5.1. Materials.....   | 195 |
| 4.5.2. Equipment .....  | 195 |
| 4.5.3. Microgel synthesis .....   | 196 |
| 4.5.4. Gels .....   | 197 |
| 4.5.5. Microgel Pickering emulsions (HM-412) .....                                      | 199 |
| 4.5.6. Monoliths prepared from concentrated microgel Pickering emulsions (HM-413) ..... | 199 |
| 4.5.7. Microgel Pickering emulsion polymerizations (HM-414) .....                       | 200 |
| 4.6. References .....   | 201 |

## **Chapter 5: Hybrid Multi-Layered Particles..... 204**

|   |     |
|---|-----|
| 5.1. Abstract.....  | 204 |
| 5.2. Introduction .....   | 205 |
| 5.2.1. Clay armoured particles .....  | 205 |
| 5.2.2. Multi-layered particles.....   | 208 |
| 5.2.3. Encapsulation of clay particles .....  | 212 |
| 5.2.4. Laponite clay .....  | 215 |
| 5.3. Results and Discussion .....   | 218 |
| 5.3.1. Synthesis of armoured and multi-layered particles.....                             | 218 |
| 5.3.2. Thermal and mechanical testing of films prepared from multi-layered particles..... | 244 |
| 5.4. Conclusions .....  | 263 |

|   |            |
|---|------------|
| 5.5. Experimental .....   | 264        |
| 5.5.1. Materials.....   | 264        |
| 5.5.2. Equipment .....  | 264        |
| 5.5.3. Particle synthesis.....  | 265        |
| 5.6. References .....   | 269        |
| <b>Chapter 6: Conclusions and Outlook.....</b>                            | <b>275</b> |
| <b>Appendix I: Characterization of Colloids.....</b>                      | <b>277</b> |
| I.1. Gravimetry.....  | 277        |
| I.2. Electrophoretic Light Scattering.....                                | 277        |
| I.3. Particle Size Measurements .....                                     | 279        |
| I.3.1. Dynamic light scattering.....                                      | 279        |
| I.3.2. Laser diffraction.....   | 280        |
| I.4. Electron Microscopy.....   | 281        |
| I.4.1. Scanning electron microscopy.....                                  | 281        |
| I.4.2. Transmission electron microscopy .....                             | 281        |
| I.5. Rheology .....   | 282        |
| <b>Appendix II: Complement to Chapter 2.....</b>                          | <b>286</b> |
| II.1. Raw Zeta Potential Data .....                                       | 286        |
| II.2. Repeated Conversion Plots for CaCO <sub>3</sub> Encapsulation ..... | 290        |
| II.3. EDAX Analysis of Calcium Carbonate-Silica Composite Particles.....  | 291        |
| <b>Appendix III: Complement to Chapter 3 .....</b>                        | <b>292</b> |
| III.1. Additional Images of Composite Particles.....                      | 292        |
| III.2. Zeta Potential Data.....   | 293        |
| <b>Appendix IV: Complement to Chapter 4 .....</b>                         | <b>296</b> |
| IV.1. Pycnometry Data.....  | 296        |
| IV.2. Rheology of Gels .....  | 297        |
| <b>Appendix V: Complement to Chapter 5 .....</b>                          | <b>298</b> |
| V.1. Additional SEM Images .....  | 298        |
| V.2. Temperature Sweep Plots .....  | 299        |
| V.3. Additional DSC Data .....  | 302        |
| V.4. TGA vs. Heatflow Plots .....   | 304        |

# Figures

---

|  |    |
|--|----|
| <b>Figure 1.1</b> Illustration of particle size ranges achievable by various heterogeneous polymerization techniques. ....   | 1  |
| <b>Figure 1.2</b> Scheme of the three intervals in emulsion polymerization. <sup>8</sup> .....   | 3  |
| <b>Figure 1.3</b> Scheme of kinetic processes taking place in a typical emulsion polymerization. <sup>16</sup> .....   | 5  |
| <b>Figure 1.4</b> Scheme illustrating (a) Smith-Ewart case 2, (b) Smith Ewart case 1 and (c) Smith-Ewart case 3. ....  | 6  |
| <b>Figure 1.5</b> Schematic of the effect of sonication on droplet size. <sup>19</sup> .....   | 7  |
| <b>Figure 1.6</b> Photomicrographs illustrating Ostwald ripening of a 1,2-dichloroethane emulsion by a double exposure on the same frame; time from the start of experiment: 0 s (image shifted on the left) and 300 s (shifted to the right). <sup>23</sup> .....   | 8  |
| <b>Figure 1.7</b> Scheme of proposed particle formation mechanism in dispersion polymerization: (A) a homogeneous mixture of monomer, stabilizer, initiator and solvent, (B) primary particles generated through precipitation of polymer chains equal or longer than the critical chain length, (C) formation of mature particles through aggregation of unstable primary particles, (D) no new particles formed, particles are the locus of polymerization, (E) only mature particles observed at the end of the reaction. <sup>37</sup> ..... | 10 |
| <b>Figure 1.8</b> Schematic representation of a sphere of radius $r$ at the interface of $\phi_1$ and $\phi_2$ at a distance of $Z$ from the centre, $C$ . $\gamma_{P-1}$ , $\gamma_{P-2}$ and $\gamma_{1-2}$ are the surface/interfacial tensions between the particle and $\phi_1$ , the particle and $\phi_2$ and the two phases respectively and $\theta$ is the three phase angle. ....   | 11 |
| <b>Figure 1.9</b> Potential energy profile of a solid particle leaving the $\phi_1/\phi_2$ interface and moving into either $\phi_1$ ( $\tilde{E}_1$ ) or $\phi_2$ ( $\tilde{E}_2$ ). Where $\tilde{z}_{\min}$ is the vertical coordinate of the centre of the particle, $C$ . ....  | 13 |
| <b>Figure 1.10</b> Particles prepared utilizing Pickering stabilization: (left) Laponite armoured poly(Sty-co-BA) prepared by Pickering emulsion polymerization, <sup>49</sup> (middle) responsive capsule prepared by cross-linking a microgel stabilized Pickering emulsion of a sacrificial solvent (propyl acetate) <sup>57</sup> and (right) silica armoured poly(MMA) particles prepared by Pickering emulsion polymerization and said particles after encapsulation in (1b) poly(acrylonitrile) and (1c) poly(BA). <sup>54</sup> ...      | 14 |
| <b>Figure 1.11</b> Schematic of water-borne polymer film formation from colloidal particle latexes, where 1 is water evaporation, 2 is particle deformation and 3 is polymer inter-diffusion. ....   | 16 |
| <b>Figure 1.12</b> Scheme representing the total potential energy ( $\text{—}$ ) from adding the van der Waals attraction potential ( $V_a$ ) and the electrostatic and Born repulsion potentials ( $V_r$ ) as a function of distance between two spherical particles.....   | 18 |
| <b>Figure 1.13</b> Structural features of thiocarbonylthio RAFT agent and the intermediate formed on radical addition. Recreated from <sup>79</sup> .....  | 19 |
| <b>Figure 1.14</b> Mechanism of RAFT polymerization. ....  | 20 |
| <b>Figure 1.15</b> Types of RAFT agent and monomers they are suitable to polymerize. ....  | 20 |

|   |    |
|---|----|
| <b>Figure 1.16</b> Selection guidelines of RAFT agents for various monomers. For Z, from left to right; addition rates decrease and fragmentation rates increase. For R, from left to right; fragmentation rates decrease. Dashed lines illustrate partial control (i.e. control of molecular weight but not dispersity or retardation for VAc). <sup>80</sup> .....  | 21 |
| <b>Figure 2.1</b> TFFDSEM (thin-film freeze-drying scanning electron microscope) images of various anionic small polymer latexes of different sizes adsorbed onto larger particles. Poly(vinyl chloride) latex of (a) 116 nm, and polystyrene particles (b) 180 nm, (c) 320 nm and (d) 696 nm assembled onto a large cationic polystyrene latex of 2170 nm by heterocoagulation in 0.5 mM KCl background electrolyte. <sup>15</sup> ... | 31 |
| <b>Figure 2.2</b> (1) Phthalocyanine blue, (2) azo pigment yellow and (3) quinacridone pigment violet. ....   | 34 |
| <b>Figure 2.3</b> Cryo-TEM images of silica particles encapsulated in poly(MMA- <i>co</i> -BA) with (a) 3.5, (b and c) 20 wt.% silica content. <sup>37</sup> .....  | 35 |
| <b>Figure 2.4</b> TEM image of encapsulated silica particles of sizes (a) 72, (b) 120, (c) 352 and (d) 629 nm in diameter in poly(styrene). <sup>40</sup> .....   | 36 |
| <b>Figure 2.5</b> SEM images of (a) bare Lycopodium spores, (b) and (c) spores selectively decorated with poly(DVB) (scale bar: 10µm). <sup>45</sup> .....  | 36 |
| <b>Figure 2.6</b> Schematic representation of pigment dispersion and encapsulation by emulsion polymerization using a macro-RAFT agent. <sup>47</sup> .....   | 37 |
| <b>Figure 2.7</b> TEM images of particles encapsulated by emulsion polymerization using macro-RAFT agents; (a) titanium dioxide, <sup>47</sup> (b) phthalocyanine blue, <sup>47</sup> (c) gibbsite platelets <sup>51</sup> and (d) cerium oxide. <sup>52</sup> .....  | 38 |
| <b>Figure 2.8</b> TEM images of calcium carbonate (SOCAL P3) (scale bar: 200 nm). ...   | 39 |
| <b>Figure 2.9</b> SEM images of calcium carbonate (SOCAL P3) (scale bar: 200 nm). ...   | 40 |
| <b>Figure 2.10</b> X-ray diffraction spectra of SOCAL P3, the ■ represents the diffraction pattern of calcite and the ■ represent the diffraction of the aluminium holder, demonstrating that SOCAL P3 precipitated calcite. ....   | 41 |
| <b>Figure 2.11</b> Crystal structure of calcite. <sup>56</sup> .....  | 41 |
| <b>Figure 2.12</b> BET transform plot of calcium carbonate (SOCAL P3) obtained by nitrogen porosimetry; quantity of gas adsorbed as a function of relative pressure. SOCAL P3 has a BET surface area of $8.92 \pm 0.05 \text{ m}^2 \text{ g}^{-1}$ and a <i>C</i> value of 336. ....  | 42 |
| <b>Figure 2.13</b> Nitrogen adsorption isotherm of calcium carbonate (SOCAL P3); it has a type II isotherm meaning that is essentially non-porous. ....   | 43 |
| <b>Figure 2.14</b> Zeta potential of calcium carbonate (SOCAL P3) as a function of salt (NaCl) concentration. The zeta potentials were measured at pH 9.33, and an average of 6 measurements were recorded. ....  | 44 |
| <b>Figure 2.15</b> Zeta potential as a function of pH of calcium carbonate (SOCAL P3). An average of 6 measurements were recorded. ....   | 46 |
| <b>Figure 2.16</b> Di(ethylene glycol) diacrylate. ....   | 46 |
| <b>Figure 2.17</b> Water solubility of DEGDA in D <sub>2</sub> O at varying temperatures, measured by <sup>1</sup> H NMR. ....  | 47 |

|   |    |
|---|----|
| <b>Figure 2.18</b> TEM images of DEGDA polymerized in the presence of calcium carbonate. (a) poly(DEGDA) is unstable and coagulates, (b) calcium carbonate remains uncoated (HM-201) (scale bar: 100 nm). .....   | 48 |
| <b>Figure 2.19</b> Scheme depicting the adsorption of deprotonated methacrylic acid onto the positively charged surface of the calcium carbonate particles, where R is the poly(MAA-co-DEGDA) chains/particles. ....  | 49 |
| <b>Figure 2.20</b> TEM images of a 14:86 wt.% mixture of MAA and DEGDA polymerized in the presence of calcium carbonate (HM-202). The wettability of the polymer to the calcium carbonate surface has improved though dewetting is still observable (scale bar: 100 nm). ....   | 50 |
| <b>Figure 2.21</b> Overall monomer conversion $X_m$ vs. time of encapsulation of calcium carbonate (HM-204). Feed 1 represents the feed of MAA and DEGDA mixture and feed 2 represents the DEGDA feed. Monomer was fed at a rate of $0.5 \text{ mL h}^{-1}$ . ....  | 51 |
| <b>Figure 2.22</b> Zeta potential of calcium carbonate (SOCAL P3) (■) and calcium carbonate encapsulated in poly(MAA-co-DEGDA) (HM-203) (●) as a function of salt (NaCl) concentration. Zeta potential measurements were performed at pH 9.3 and an average of 6 measurements were recorded. ....   | 52 |
| <b>Figure 2.23</b> TEM image of bare and encapsulated calcium carbonate. (a) Bare calcium carbonate particles. (b), (c) and (d) Calcium carbonate encapsulated in poly(MAA-co-DEGDA) (HM-203). (Images (a) (b) and (c) scale bar: 200 nm, image (d) scale bar: 100 nm). ....  | 53 |
| <b>Figure 2.24</b> TEM images of (a) calcium carbonate encapsulated in poly(MAA-co-DEGDA), (b) an increased magnification of image (a) (HM-203), (c) bare calcium carbonate and (d) an increased magnification of image (c) illustrating the bumpy surface of the encapsulated calcium carbonate compared to the relatively smooth surface of the bare calcium carbonate (scale bar: 100 nm). ....                                    | 54 |
| <b>Figure 2.25</b> SEM images of (a) bare calcium carbonate, (b) and (c) calcium carbonate encapsulated in poly(MAA-co-DEGDA) (HM-206) (scale bar (a): 500 nm, scale bar (b) and (c): 200 nm). ....   | 55 |
| <b>Figure 2.26</b> SEM images of calcium carbonate encapsulated in poly(MAA-co-DEGDA) (HM-206) (a) broad overview of particles, showing small fragmented calcium carbonate particles and (b) small calcium carbonate fragment coated in a polymeric shell (scale bar (a): $2 \mu\text{m}$ , scale bar (b): 100 nm) .....  | 56 |
| <b>Figure 2.27</b> Cryo-TEM images of calcium carbonate encapsulated in poly(MAA-co-DEGDA), with the calcium carbonate etched out with HCl (HM-207) (scale bar: 200 nm). ....   | 57 |
| <b>Figure 2.28</b> STEM images of (a) calcium carbonate encapsulated in poly (MAA-co-DEGDA) (scale bar: 20 nm) where (b) is the corresponding EDX linescans (— calcium, — oxygen and — carbon). The black line across particles indicates place of linescan (HM-205). ....  | 58 |
| <b>Figure 2.29</b> Overall monomer conversion; $X_m$ vs. time of encapsulation of calcium carbonate (HM-208). Feed 1 represents the feed of methacrylic acid and di(ethylene glycol) diacrylate mixture, feed 2 represents the di(ethylene glycol) diacrylate feed and feed 3 represents the MMA feed. In the first two feeds were fed at a rate of $0.5 \text{ mL h}^{-1}$ and MMA was fed at a rate of $1 \text{ mL h}^{-1}$ . .... | 60 |

|   |    |
|---|----|
| <b>Figure 2.30</b> Zeta potential of calcium carbonate (SOCAL P3) (■), calcium carbonate encapsulated in poly(MAA-co-DEGDA) (HM-203) (●) and calcium carbonate encapsulated in poly(MAA-co-DEGDA) primer with poly(MMA) shell extension (▲) (HM-208) as a function of salt (NaCl) concentration. Zeta potential measurements were performed at pH 9.3 and an average of 6 measurements were recorded..... | 61 |
| <b>Figure 2.31</b> Particle size analysis by laser diffraction of bare calcium carbonate (—), and encapsulated calcium carbonate; at 2 mL (—), 3 mL (—), 4 mL (—), 5 mL (—) and 6 mL (—) methyl methacrylate (HM-208).....  | 62 |
| <b>Figure 2.32</b> (a) TEM image of calcium carbonate encapsulated in initial poly(MAA-co-DEGDA) (M-203), and (b), (c) and (d) corresponding cryo-TEM image of said encapsulated particles with shell extended with poly(MMA) (HM-208) (scale bar: 200 nm).....   | 63 |
| <b>Figure 2.33</b> TEM images of calcium carbonate encapsulated in initial poly(MAA-co-DEGDA) followed by shell extension with poly(MMA) (HM-208) (scale bar: 200 nm).....  | 63 |
| <b>Figure 2.34</b> (a) SEM image of calcium carbonate encapsulated in initial poly(MAA-co-DEGDA) (HM-206), and (b) and (c) the corresponding SEM image of said encapsulated particles with shell extended with poly(MMA) (HM-208) (scale bar: 200 nm).....  | 64 |
| <b>Figure 2.35</b> SEM images of amorphous calcium carbonate particles; (a) whole particles and (b) broken particle (HM-210) (scale bar: 1 μm).....   | 66 |
| <b>Figure 2.36</b> SEM images of amorphous calcium carbonate particles formed in the presence of silica particles (Ludox); (a) whole particles and (b) broken particle (HM-211) (scale bar: 1 μm).....  | 67 |
| <b>Figure 2.37</b> EDAX spectrum of (a) amorphous calcium carbonate (HM-210) and (b) amorphous calcium carbonate formed in the presence of silica particles (Ludox) (HM-211). An average of 8 samples were taken.....   | 68 |
| <b>Figure 2.38</b> TGA of amorphous calcium carbonate (HM-210) (—) and amorphous calcium carbonate formed in the presence of silica (Ludox) (HM-211) (—).....   | 69 |
| <b>Figure 2.39</b> Scheme illustrating the area (yellow outline) from which EDAX data is gained.....  | 69 |
| <b>Figure 2.40</b> Zeta potential as a function of pH of amorphous calcium carbonate particles (HM-210) (■) and amorphous calcium carbonate particles formed in the presence of silica nanoparticles (HM-211) (●). An average of 6 measurements were recorded.....  | 70 |
| <b>Figure 2.41</b> SEM images of silica after the CaCO <sub>3</sub> has been etched out using acetic acid ((a) scale bar: 200nm, (b) scale bar: 100 nm).....  | 71 |
| <b>Figure 2.42</b> SEM images of (a) amorphous calcium carbonate particle (HM-210), (b) and (c) amorphous calcium carbonate encapsulated in poly(DEGDA-co-MAA) (HM-212) (scale bar: 1 μm).....  | 72 |
| <b>Figure 2.43</b> SEM images of amorphous calcium carbonate encapsulated in poly(DEGDA-co-MAA) after 3 days in aqueous conditions ((a) scale bar: 10 μm. (b-   |    |

|   |     |
|---|-----|
| c) scale bar: 2 $\mu\text{m}$ ). It appears as though the calcium carbonate has been etched from the core and re-precipitated outside the polymer shell.....  | 74  |
| <b>Figure 2.44</b> SEM images of (a) amorphous calcium carbonate particle formed in the presence of silica (HM-211), (b) and (c) amorphous calcium carbonate formed in the presences of silica encapsulated in poly(DEGDA- <i>co</i> -MAA) (HM-213) (scale bar: 1 $\mu\text{m}$ ). .....  | 75  |
| <b>Figure 2.45</b> SEM image of hollow poly(DEGDA- <i>co</i> -MAA) templated on amorphous calcium carbonate particles (HM-214) (scale bar: 1 $\mu\text{m}$ ). .....   | 76  |
| <b>Figure 2.46</b> SEM image of hollow poly(DEGDA- <i>co</i> -MAA) templated on amorphous calcium carbonate particles formed in the presence of silica (HM-215) (scale bar: 1 $\mu\text{m}$ ). .....  | 76  |
| <b>Figure 2.47</b> Di(ethylene glycol) diacrylate (DEGDA).....  | 81  |
| <b>Figure 3.1</b> Radical thiol-ene mechanism.....  | 91  |
| <b>Figure 3.2</b> Base catalysed thiol-Michael addition mechanism.....  | 92  |
| <b>Figure 3.3</b> Nucleophile catalyzed thiol-Michael addition mechanism.....   | 94  |
| <b>Figure 3.4</b> (a) TEM image of composite multimodal composite poly(divinylbenzene)-inorganic latex particles prepared by co-encapsulation of $\text{MnFe}_2\text{O}_4$ and Au nanoparticles and (b) photograph of composite latex particles redispersed in THF; (left) before and (right) after attachment of PEG. <sup>44</sup> .....                                    | 96  |
| <b>Figure 3.5</b> (1) 3-mercaptopropionic acid methyl ester, (2) 3-mercaptopropanesulfonic acid sodium salt and (3) glutathione.....  | 96  |
| <b>Figure 3.6</b> Preparation of (PVP/PMA <sub>Thiol</sub> /PVP/PMA <sub>Ene</sub> )-coated particles, (1-2) PEGylation and stabilization using thiol-ene chemistry, (3) removal of silica core and (4) removal of PVP. <sup>50</sup> .....   | 98  |
| <b>Figure 3.7</b> Overall synthetic approach for the surface modification of $\text{TiO}_2$ nanoparticles. <sup>53</sup> .....  | 99  |
| <b>Figure 3.8</b> Multiple acrylate containing monomers; (1) di(ethylene glycol) diacrylate (DEGDA), (2) pentaerythritol triacrylate (PETA), (3) dipentaerythritol penta-/hexa-acrylate (DPEPHA).....   | 100 |
| <b>Figure 3.9</b> TEM image of poly(DEGDA)-C particles (HM-301) (scale bar: 100nm). .....   | 102 |
| <b>Figure 3.10</b> TEM images of poly(PETA)-C particles (HM-302) (scale bar: 100 nm). .....   | 103 |
| <b>Figure 3.11</b> TEM images of poly(DPEPHA)-C particles (HM-303) (scale bar: 100 nm). .....   | 103 |
| <b>Figure 3.12</b> FTIR spectra of bare $\text{CaCO}_3$ particles (—), poly(DEGDA)-C particles (HM-301) (—), poly(PETA)-C particles (HM-302) (—) and poly(DPEPHA)-C particles (HM-303) (—). Very weak vinyl –CH stretches at 809 and 984 $\text{cm}^{-1}$ are observed in the cases for the poly(PETA)-C and poly(DPEPHA)-C particles (illustrated by the black boxes). ..... | 104 |
| <b>Figure 3.13</b> Raman spectra of bare $\text{CaCO}_3$ particles (—), poly(DEGDA)-C (HM-301) (—), poly(PETA)-C (HM-302) (—) and poly(DPEPHA)-C particles (HM-303) (—). The presence of C=C double bonds in HM-302 and HM-303 are observed with  |     |



1637  $\text{cm}^{-1}$  indicating C=C stretch and vinyl C-H stretches at 1409, 3040, 3075 and 3109  $\text{cm}^{-1}$  (illustrated by the black boxes). No vinyl groups were observed for the poly(DEGDA)-C particles. .... 105

**Figure 3.14** Mechanism of alkene bromination. .... 106

**Figure 3.15** FTIR spectra of hollowed poly(PETA)-C particles (HM-305) (—) and said particles after bromination (HM-308) (—). After the bromination the vinyl –CH shift at 808  $\text{cm}^{-1}$  is lost (illustrated by the black boxes)..... 109

**Figure 3.16** Raman spectra of hollowed poly(PETA)-C particles (HM-305) (—) and said particles after bromination (HM-308) (—). After the bromination the vinyl C-H shifts at 733, 1380, 1408 and 3036  $\text{cm}^{-1}$  and vinyl C=C shift at 1634  $\text{cm}^{-1}$  are lost and a C-Br shift at 758  $\text{cm}^{-1}$  is gained (illustrated by the black boxes). .... 109

**Figure 3.17** FTIR spectra of hollowed poly(DPEPHA)-C particles (HM-306) (—) and said particles after bromination (HM-309) (—). After the bromination the vinyl shift at 1634  $\text{cm}^{-1}$  and vinyl –CH shift at 808  $\text{cm}^{-1}$  is lost (illustrated by the black boxes). .... 110

**Figure 3.18** Raman spectra of hollowed poly(DPEPHA)-C particles (HM-306) (—) and said particles after bromination (HM-309) (—). After the bromination the vinyl C-H shifts at 733, 1380, 1408 and 3036  $\text{cm}^{-1}$  and vinyl C=C shifts at 1634  $\text{cm}^{-1}$  are lost, C-BR shifts at 635 and 758  $\text{cm}^{-1}$  are gained, (illustrated by the black boxes). 110

**Figure 3.19** Scheme depicting the looping of DEGDA, where R is the rest of the DEGDA unit. .... 111

**Figure 3.20** FTIR spectra of poly(PETA)-C particles (HM-302) (—) and said particles after the thiol Michael addition with 2-mecapto ethanol (HM-310) (—). Very weak vinyl –CH stretches at 809 and 984  $\text{cm}^{-1}$  are lost and thioether stretch at 667  $\text{cm}^{-1}$  gained after the Michael addition. .... 112

**Figure 3.21** Raman spectra of poly(PETA)-C particles (HM-302) (—) and said particles after the thiol Michael addition with 2-mecapto ethanol (HM-310) (—). After the thiol Michael addition the vinyl C-H shifts at 1409, 3075, 3109  $\text{cm}^{-1}$  and vinyl C=C shifts at 1637  $\text{cm}^{-1}$  are lost (illustrated by the black boxes). .... 113

**Figure 3.22** FTIR spectra of poly(DPEPHA)-C particles (HM-303) (—) and said particles after the thiol Michael addition with 2-mecapto ethanol (HM-311) (—). Vinyl –CH stretches at 809 and 984  $\text{cm}^{-1}$  are lost after the Michael addition. . 113

**Figure 3.23** Raman spectra of poly(DPEPHA)-C particles (HM-303) (—) and said particles after the thiol Michael addition with 2-mecapto ethanol (HM-311) (—). After the thiol Michael addition the vinyl C-H shifts at 1409, 3040, 2075 and 3109  $\text{cm}^{-1}$  and vinyl C=C shifts 1637  $\text{cm}^{-1}$  are lost (illustrated by the black boxes). ..... 114

**Figure 3.24** FTIR spectra of hollowed poly(PETA)-C particles (HM-305) (—) and said particles after the thiol Michael addition with 2-mecapto ethanol (HM-312) (—). After the thiol Michael addition, the vinyl –CH shift at 808  $\text{cm}^{-1}$  is lost..... 115

**Figure 3.25** Raman spectra of hollowed poly(PETA)-C particles (HM-305) (—) and said particles after the thiol Michael addition with 2-mecapto ethanol (HM-312) (—). After the thiol Michael addition the vinyl C-H shifts at 733, 1380, 1408 and 3036  $\text{cm}^{-1}$  and vinyl C=C shift at 1634  $\text{cm}^{-1}$  are lost, C-S shifts at 646 and 748 are gained, (illustrated by the black boxes). .... 115



- Figure 3.26** FTIR spectra of hollowed poly(DPEPHA)-C particles (HM-306) (—) and said particles after the thiol Michael addition with 2-mecapto ethanol (HM-313) (—). After the thiol Michael addition the vinyl C=C shift at  $1634\text{ cm}^{-1}$  and the vinyl –CH shift at  $987$  and  $808\text{ cm}^{-1}$  are lost..... 116
- Figure 3.27** Raman spectra of hollowed particles of poly(DPEPHA)-C particles (HM-306) (—) and said particles after the thiol Michael addition with 2-mecapto ethanol (HM-313) (—). After the thiol Michael addition the vinyl C-H shifts at  $733$ ,  $1380$ ,  $1408$ , and  $2036\text{ cm}^{-1}$  and vinyl C=C shift at  $1634\text{ cm}^{-1}$  are lost, C-S shifts at  $651$ , and  $758\text{ cm}^{-1}$  are gained, (illustrated by the black boxes)..... 116
- Figure 3.28** FTIR spectra of poly(PETA)-C particles (HM-302) (—) and said particles after the thiol Michael addition with dodecanethiol in acetone (HM-316) (—). Vinyl –CH stretches at  $809$  and  $984\text{ cm}^{-1}$  are lost and thioether stretch at  $667\text{ cm}^{-1}$  gained after the Michael addition. .... 118
- Figure 3.29** Raman spectra of poly(PETA)-C particles (HM-302) (—) and said particles after the thiol Michael addition with dodecane thiol in acetone (HM-316) (—). After the thiol Michael addition the vinyl shifts at  $1409$ ,  $1637$ ,  $3040$ ,  $3075$  and  $3109\text{ cm}^{-1}$  are lost (illustrated by the black boxes). .... 119
- Figure 3.30** FTIR spectra of poly(DPEPHA)-C particles (HM-303) (—) and said particles after the thiol Michael addition with dodecane thiol in acetone (HM-317) (—). Vinyl –CH stretches at  $809$  and  $984\text{ cm}^{-1}$  are lost after the Michael addition (illustrated by the black boxes). .... 119
- Figure 3.31** Raman Spectra of poly(DPEPHA)-C particles (HM-303) (—) and said particles after the thiol Michael addition with dodecanethiol in acetone (HM-317) (—). After the thiol Michael addition the vinyl shifts at  $1409$ ,  $1637$ ,  $3040$ ,  $3075$  and  $3109\text{ cm}^{-1}$  are lost (illustrated by the black boxes). .... 120
- Figure 3.32** RAFT agent (Propanoic acid)-2-yl butyl trithiocarbonate (PABTC).. 121
- Figure 3.33** Mechanism of RAFT agent synthesis..... 122
- Figure 3.34** Overall monomer conversion,  $X_m$ , (■) and  $\ln([M]_0/[M])$  (●) versus time for the RAFT polymerization of styrene where the expected molecular weight at 60 % monomer conversion is  $10,000\text{ g mol}^{-1}$  (HM-321).  $R^2$  for the linear fit of the  $\ln([M]_0/[M])$  plot is 0.9979..... 122
- Figure 3.35**  $M_n$  versus conversion for poly(styrene) synthesized using PABTC RAFT agent with a target molecular weight at 60 % conversion of  $10,000\text{ g mol}^{-1}$  (HM-321); (■)  $M_n$  and (■) PDI, where for  $M_n$   $R^2=0.995$ . .... 123
- Figure 3.36** Molecular weight distributions of poly(styrene) synthesized using PABTC RAFT agent with a target molecular weight at 60 % conversion of  $10,000\text{ g mol}^{-1}$  (HM-321). Samples taken at 2 (—), 3 (—), 5 (—), 6 (—), 7 (—), 8 (—), 9 (—), 10 (—), 11 (—), 12 (—), 13 (—), 14 (—), 15 (—), 16 (—) and 17 (—) hours, before this samples could not be accurately analyzed by SEC. As conversion increases so does molecular weight, whilst dispersity decreases..... 124
- Figure 3.37** Mechanism of aminolysis of the trithiocarbonate to achieve thiol  $\omega$ -end functionalized poly(styrene)..... 125
- Figure 3.38**  $^1\text{H}$  NMR (a)  $\omega$ -RAFT functionalized poly(styrene) and (b)  $\omega$ -thiol functionalized poly(styrene) yielded after aminolysis. .... 126

- Figure 3.39** SEC of (a) RAFT-functionalized poly(styrene) (HM-322) and (b) poly(styrene) after aminolysis of trithiocarbonate group and reduction with DTT (HM-324). RI (—) and UV ( $\lambda = 309$  nm) detector response (—) vs. retention time. After aminolysis the UV trace disappears, suggesting that the trithiocarbonate group has been cleaved. .... 127
- Figure 3.40** SEC chromatogram of poly(styrene) after aminolysis of trithiocarbonate group (HM-323) (—), deconvolution (Gaussian fit) of bimodal plot (—) and the sum of the deconvoluted plots (—). .... 127
- Figure 3.41** Reaction scheme of disulfide reduction by DTT.<sup>73</sup> .... 128
- Figure 3.42 (a) poly(styrene) after aminolysis of trithiocarbonate group (HM-323) and (b) after reduction of disulfide bonds with DTT (HM-324); SEC chromatogram (—), deconvolution (Gaussian fit) of bimodal plot (—) and the sum of the deconvoluted plots (—). .... 128
- Figure 3.43** FTIR spectra of poly(PETA)-C particles (HM-302) (—) and said particles after the thiol Michael addition with poly(styrene)-SH (HM-325) (—). Very weak vinyl  $\text{—CH}$  stretch at  $984\text{ cm}^{-1}$  is lost, however the very weak vinyl  $\text{—CH}$  stretch at  $809\text{ cm}^{-1}$  remains and aromatic C-H stretch from styrene at  $698\text{ cm}^{-1}$  is gained after the Michael addition. .... 130
- Figure 3.44** Raman spectra of poly(PETA)-C particles (HM-302) (—) and said particles after the thiol Michael addition with poly(styrene)-SH in acetone (HM-316) (—). After the thiol Michael addition the vinyl shifts at  $1409$ ,  $1637$ ,  $3040$ ,  $3075$  and  $3109\text{ cm}^{-1}$  diminish and aromatic C-H shifts at  $837$  and  $1000\text{ cm}^{-1}$  appear (illustrated by the black boxes); indicating that some polystyrene chains have “clicked” to the particles. .... 131
- Figure 4.1** Illustration of a microgel particle in a (a) poor and (b) good solvent.<sup>15</sup> 157
- Figure 4.2** Scheme of controlled aggregation and colloidal gelation of microgel particles, to prepare doubly cross-linked gels.<sup>25</sup> .... 159
- Figure 4.3** (a) Optical micrographs illustrating temperature dependent stability of poly(NIPAAm-*co*-MAA) microgel stabilized emulsion at pH 6.1 and 9.4 (scale bar:  $20\text{ }\mu\text{m}$ ). (b) Illustration of temperature and pH dependent stability of poly(NIPAAm-*co*-MAA) microgel stabilized emulsion.<sup>36</sup> .... 161
- Figure 4.4** Overall monomer conversion,  $X_m$ , versus time for poly(DEGDA) particles (HM-401) (■) and poly(DEGDA-*co*-MAA) (HM-402) (●). Monomer was fed at a rate of  $0.5\text{ mL h}^{-1}$ . .... 165
- Figure 4.5** (a) Average particle diameter,  $d_z$  and  $d_z^3$ , and (b) dispersity,  $D_I$ , versus monomer fed into the reaction (mL), of poly(DEGDA) (HM-401) (■), poly(DEGDA-*co*-MAA) (HM-402) (●), poly(PETA-*co*-DEGDA-*co*-MAA) (HM-403) (▲) and poly(DPEPHA-*co*-DEGDA-*co*-MAA) (HM-404) (▼). DLS measurements were performed at pH 5.5. .... 166
- Figure 4.6**  $d_z^3$  versus monomer fed into the reaction (mL) of poly(DEGDA) (HM-401) (■), poly(DEGDA-*co*-MAA) (HM-402) (●), poly(PETA-*co*-DEGDA-*co*-MAA) (HM-403) (▲) and poly(DPEPHA-*co*-DEGDA-*co*-MAA) (HM-404) (▼). Linear fit of  $d_z^3$ ;  $R^2 = 0.994$  for poly(DEGDA),  $R^2 = 0.993$  for poly(DEGDA-*co*-MAA),  $R^2 = 0.992$  for poly(PETA-*co*-DEGDA-*co*-MAA) and  $R^2 = 0.992$  for

|  |     |
|--|-----|
| poly(DPEPHA- <i>co</i> -DEGDA- <i>co</i> -MAA). DLS measurements were performed at pH 5.5.....   | 167 |
| <b>Figure 4.7</b> SEM images of poly(DEGDA) particles (HM-401) (scale bar: 200 nm). .....  | 168 |
| <b>Figure 4.8</b> SEM images of poly(DEGDA- <i>co</i> -MAA) particles (HM-402) (scale bar: 100 nm). .....  | 168 |
| <b>Figure 4.9</b> SEM images of poly(PETA- <i>co</i> -DEGDA- <i>co</i> -MAA) (HM-403) (scale bar: 100 nm). .....   | 169 |
| <b>Figure 4.10</b> SEM images of poly(DPEPHA- <i>co</i> -DEGDA- <i>co</i> -MAA) particles (HM-404) (scale bar: 100 nm). .....  | 169 |
| <b>Figure 4.11</b> Images of (a) poly(DEGDA) (HM-401), (b) poly(MAA- <i>co</i> -DEGDA) (HM-402), (c) poly(PETA- <i>co</i> -MAA- <i>co</i> -DEGDA) (HM-403) and (d) poly(DPEPHA- <i>co</i> -MAA- <i>co</i> -DEGDA) (HM-404) at pH's from left to right: 2, 3, 4, 5, 6, 7, 7.5, 8, 8.5 and 9. ....                     | 171 |
| <b>Figure 4.12</b> (a) Average particle diameter, $d_z$ , and (b) dispersity, $D_I$ , versus pH of poly(DEGDA) (HM-401) (■), poly(DEGDA- <i>co</i> -MAA) (HM-402) (●), poly(PETA- <i>co</i> -DEGDA- <i>co</i> -MAA) (HM-403) (▲), poly(DPEPHA- <i>co</i> -DEGDA- <i>co</i> -MAA) (HM-404) (▼). ....                  | 173 |
| <b>Figure 4.13</b> (a) Average particle diameter, $d_z$ , and (b) dispersity, $D_I$ , versus temperature of poly(DEGDA) (HM-401) (■), poly(DEGDA- <i>co</i> -MAA) (HM-402) (●), poly(PETA- <i>co</i> -DEGDA- <i>co</i> -MAA) (HM-403) (▲), poly(DPEPHA- <i>co</i> -DEGDA- <i>co</i> -MAA) (HM-404) (▼) at pH 8. .... | 175 |
| <b>Figure 4.14</b> (a) Average particle diameter, $d_z$ , and (b) dispersity, $D_I$ , versus temperature of (1) poly(DEGDA- <i>co</i> -MAA) (HM-402) and (2) poly(DPEPHA- <i>co</i> -DEGDA- <i>co</i> -MAA) (HM-404) at pH values 4 (■), 6 (●) and 8 (▲). ....   | 176 |
| <b>Figure 4.15</b> Shear viscosity vs. shear rate of 1 wt.% poly(MAA- <i>co</i> -DEGDA) latex at pH values 4 (—), 6 (—), 8 (—) and 10 (—). Three cycles of 0-1000-0 s <sup>-1</sup> were performed. ....   | 177 |
| <b>Figure 4.16</b> Log plot of shear viscosity vs. shear rate of 1 wt.% poly(MAA- <i>co</i> -DEGDA) latex at pH values 4 (■), 6 (●), 8 (▲) and 10 (▼). ....  | 178 |
| <b>Figure 4.17</b> Scheme illustrating the relationship between shear stress and shear rate for Newtonian and non-Newtonian liquids. ....  | 179 |
| <b>Figure 4.18</b> Shear stress vs. shear rate of 1 wt.% poly(MAA- <i>co</i> -DEGDA) latex at pH values 4 (■), 6 (●), 8 (▲) and 10 (▼). The plot indicates that the latexes are dilatant. ....   | 179 |
| <b>Figure 4.19</b> Image of poly(DEGDA- <i>co</i> -MAA) particles dispersed in water adjusted to pH 13 (prior to addition of particles) at 2.5, 4, 5, 6, 7.5 and 10 wt.% solids (HM-407). From 5 wt.% solids the solution gels. ....   | 180 |
| <b>Figure 4.20</b> Amplitude sweep of 5 (■), 6 (●), 7.5 (▲) and 10 (▼) wt.% microgels. ....  | 181 |
| <b>Figure 4.21</b> Frequency sweeps of (a) 5, (b) 6, (c) 7.5 and (d) 10 wt.% poly(DEGDA- <i>co</i> -MAA) microgels; storage modulus, $G'$ , (■), loss modulus, $G''$ , (●) and phase angle, $\delta$ , (▲). ....   | 183 |

|  |     |
|--|-----|
| <b>Figure 4.22</b> Image of poly(DEGDA- <i>co</i> -MAA) particles dispersed in water adjusted to pH 13 (prior to addition of particles) showing repeatable destruction and reformation of the gel by adjusting the pH; (a) 5, 6, 7.5 and 10 wt.% solids after addition of 20 $\mu$ L 1M HCl, gel is lost; (b) 5, 6, 7.5 and 10 wt.% solids after addition of 30 $\mu$ L 1M NaOH, gel reforms for 7.5 and 10 wt.% solids only; (c) 7.5 and 10 wt.% solids after addition of 20 $\mu$ L 1M HCl, gel is lost; (d) 7.5 and 10 wt.% solids after addition of 30 $\mu$ L 1M NaOH, gel reforms for 10 wt.% solids only; (e) 10 wt.% solids after addition of 10 $\mu$ L 1M HCl, gel is lost; (f) 10 wt.% solids after addition of 50 $\mu$ L 1M HCl, gel is lost. Acid and base were added 10 $\mu$ L at a time until change was observed. .... | 184 |
| <b>Figure 4.23</b> Image of dodecane emulsions stabilized by poly(DEGDA- <i>co</i> -MAA) microgels. From left to right: pH; 4, 6, 8 and 10. At pH 8 and 10 the Pickering emulsions were stable, however, at pH 4 and 6 they were unstable. ....  | 185 |
| <b>Figure 4.24</b> Optical microscope image of dodecane emulsions stabilized by poly(DEGDA- <i>co</i> -MAA) microgels at (a) pH 4, (b) pH 6, (c) pH 8 and (d) pH 10 ((a-b) scale bar: 50 $\mu$ m. (c-d) scale bar: 20 $\mu$ m). At low pH (pH 4 and 6) flocculation occurs, at high pH (pH8 and 10) particles are well dispersed. ....   | 186 |
| <b>Figure 4.25</b> Laser scattering of dodecane emulsions stabilized by poly(DEGDA- <i>co</i> -MAA) microgels at pH 4 (—), pH 6 (—), pH 8 (—) and pH 10 (—). ....  | 186 |
| <b>Figure 4.26</b> Images of responsive Pickering emulsion (a) emulsion formed with poly(DEGDA- <i>co</i> -MAA) particles at pH 4, (b) adjusted to pH 10. ....   | 187 |
| <b>Figure 4.27</b> Optical microscope image of dodecane emulsion (a) formed with poly(DEGDA- <i>co</i> -MAA) particles at pH 4, (b) adjusted to pH 10. ((a) scale bar: 50 $\mu$ m. (b) scale bar: 20 $\mu$ m). ....  | 187 |
| <b>Figure 4.28</b> Laser scattering of responsive Pickering emulsion of dodecane emulsion formed with poly(DEGDA- <i>co</i> -MAA) particles at pH 4 (—) and adjusted to pH 10 (—). ....  | 188 |
| <b>Figure 4.29</b> Images of responsive Pickering emulsion of dodecane (a) emulsion formed with poly(DEGDA- <i>co</i> -MAA) particles at pH 10, (b) adjusted to pH 4 and (c) adjusted back to pH 10. ....  | 189 |
| <b>Figure 4.30</b> Optical microscope images of dodecane emulsion (a) formed with poly(DEGDA- <i>co</i> -MAA) particles at pH 10, (b) adjusted to pH 4 and (c) adjusted back to pH 10 ((a and c) scale bar (a): 20 $\mu$ m. (b) scale bar: 50 $\mu$ m). ....   | 189 |
| <b>Figure 4.31</b> Laser scattering of responsive Pickering emulsion of dodecane emulsion formed with poly(DEGDA- <i>co</i> -MAA) particles at pH 10 (—), adjusted to pH 4 (—) and adjusted back to pH 10 (—). ....  | 190 |
| <b>Figure 4.32</b> Image of HIPE prepared from concentrated Pickering stabilized emulsions. ....   | 191 |
| <b>Figure 4.33</b> (a) and (b) monolith of poly(DEGDA- <i>co</i> -MAA) stabilized dodecane concentrated emulsion gel and (c) collapse of monolith after addition of base (scale bar: 2 mm). ....   | 191 |
| <b>Figure 4.34</b> Optical microscope image of hollow poly(methyl methacrylate) stabilized with poly(DEGDA- <i>co</i> -MAA) (HM-414) (scale bar: 20 $\mu$ m). ....   | 192 |

|  |     |
|--|-----|
| <b>Figure 4.35</b> SEM image of hollow poly poly(methyl methacrylate) prepared from microgel Pickering emulsion polymerization with a non-solvent (dodecane), illustrating cavity (HM-414) (scale bar: 1 $\mu\text{m}$ ). .....  | 192 |
| <b>Figure 4.36</b> SEM images of hollow poly(methyl methacrylate) prepared from microgel Pickering emulsion polymerization with a non-solvent (dodecane) (HM-414) ((a) scale bar: 10 $\mu\text{m}$ . (b) scale bar: 1 $\mu\text{m}$ ). .....   | 193 |
| <b>Figure 5.1</b> (a) TEM image of silica armoured poly(MMA) prepared by emulsion polymerization. <sup>13</sup> (b) SEM image of $\text{TiO}_2$ -stabilized poly(styrene) with hollow core prepared by miniemulsion polymerization with a sacrificial solvent (scale bar: 10 $\mu\text{m}$ ). <sup>18</sup> (c) TEM image of $\text{Fe}_2\text{O}_3$ /poly(styrene) particles prepared by miniemulsion polymerization (scale bar: 50 nm). <sup>24</sup> (d) TEM image of GO/poly(styrene) particles prepared by miniemulsion polymerization (scale bar: 100 nm). <sup>28</sup> ..... | 206 |
| <b>Figure 5.2</b> (a) Cryo-TEM image of Laponite armoured poly(Sty-co-BA) particles (scale bar: 100 nm). <sup>43</sup> (b) Cryo-TEM of a monolayer film of poly(Sty-co-BA) latex particles armoured with Laponite clay, illustrating the honey-comb structure of Laponite (dark lines) produced on film formation (scale bar: 500 nm). <sup>45</sup> .....   | 207 |
| <b>Figure 5.3</b> SEM images of multi-layered particle with silica outer shell, (b) cross-section of multi-layered particle and (c) microcapsular structure after removal of organic inner-shell by calcinations. <sup>49</sup> .....  | 208 |
| <b>Figure 5.4</b> Laser confocal fluorescent microscopy image of CdS-polymer nanocomposites, illustrating the periodic array of the metal inner-shell, where the spacing is controlled by the thickness of the polymer shell (scale bar: 2 $\mu\text{m}$ ). <sup>53</sup> .....  | 210 |
| <b>Figure 5.5</b> TEM images of (a) $\text{Fe}_2\text{O}_3$ nanoparticles, (b) $\text{Fe}_2\text{O}_3$ stabilized MPTMS and (c) multi-layered particles with a poly(MMA) shell. <sup>56</sup> .....  | 211 |
| <b>Figure 5.6</b> TEM images of (a) silica armoured poly(MMA) latex, (b) hairy outer-layer of poly(acrylonitrile) and (c) a soft shell of poly(BA) (scale bar: 100 nm). <sup>57</sup> .....  | 212 |
| <b>Figure 5.7</b> (1) MPTMS, (2) MPDES, (3) KRTTS and (4) isopropyl triacryl titanate. ....  | 214 |
| <b>Figure 5.8</b> Cryo-TEM image of poly(MMA) particles containing (a) Laponite (scale bar: 50 nm) and (b) montmorillonite (scale bar: 100 nm). <sup>61</sup> .....  | 215 |
| <b>Figure 5.9</b> (Left) Single Laponite particle, (right) structure of Laponite. <sup>62</sup> .....  | 216 |
| <b>Figure 5.10</b> Tetrasodium pyrophosphate; used to edge modify Laponite clay discs to aid dispersion. ....  | 216 |
| <b>Figure 5.11</b> Overall monomer conversion, $X_m$ , versus time of Laponite armoured poly(Sty-co-BA) particles (HM-502). .....  | 219 |
| <b>Figure 5.12</b> (a) Average particle diameter, $d_z$ (■) and $d_z^3$ (●), and (b) dispersity, $D_i$ , versus monomer conversion, $X_m$ , of Laponite armoured poly(Sty-co-BA) particles (HM-502). $R^2$ for linear fit of $d_z^3$ is 0.998. ....  | 220 |
| <b>Figure 5.13</b> Cryo-TEM images of Laponite armoured poly(Sty-co-BA) particles (HM-502) (scale bar: 50 nm). ....  | 221 |
| <b>Figure 5.14</b> Cryo-TEM images of poly(Sty-co-BA) particles (HM-501) (scale bar: 100 nm). ....   | 222 |
| <b>Figure 5.15</b> Scheme illustrating multi-layered particle morphology. ....   | 224 |



|   |     |
|---|-----|
| <b>Figure 5.16</b> 3-(trimethoxysilyl) propyl methacrylate (MPTMS). .....   | 225 |
| <b>Figure 5.17</b> Scheme illustrating the reaction of MPTMS and Laponite in water and potential to react with more than one Laponite disc. ....  | 226 |
| <b>Figure 5.18</b> Scheme depicting effect of MPTMS on particle morphology of Laponite armoured poly(Sty- <i>co</i> -BA) particles. ....  | 227 |
| <b>Figure 5.19</b> Overall monomer conversion, $X_m$ , versus time for Laponite armoured poly(Sty- <i>co</i> -BA) particles (HM-502) (■) and the same polymerization reaction with MPTMS (0.1 g) added at $t_6$ (HM-503) (●). The dashed line indicates the time at which 0.1 g MPTMS was added to the reaction. ....   | 228 |
| <b>Figure 5.20</b> (a) Average particle diameter, $d_z$ (■) and $d_z^3$ (●), and (b) dispersity, $D_I$ , versus monomer conversion, $X_m$ , of Laponite armoured poly(Sty- <i>co</i> -BA) where of MPTMS has been added at $t_6$ (HM-503). The dashed line indicates the time at which 0.1 g MPTMS was shot added to the reaction. $R^2$ for linear fit of $d_z^3$ is 0.996. ....   | 229 |
| <b>Figure 5.21</b> Cryo-TEM images of Laponite armoured poly(Sty- <i>co</i> -BA) where MPTMS is added at $t_6$ (scale bar: 50 nm) (BL-067). It appears as though particles have core-shell morphology with a double layer of Laponite in the “shell”. ....  | 231 |
| <b>Figure 5.22</b> Overall monomer conversion, $X_m$ , versus time for Laponite armoured poly(Sty- <i>co</i> -BA) (HM-502) (■) and the same polymerization reaction with MPTMS (0.1 g) added at $t_6$ (HM-503) (●) and with the MPTMS added at $t_0$ (HM-504) (▼). ....   | 232 |
| <b>Figure 5.23</b> (a) Average particle diameter, $d_z$ (■) and $d_z^3$ (●), and (b) dispersity, $D_I$ , versus monomer conversion, $X_m$ , of Laponite armoured poly(Sty- <i>co</i> -BA) particles where MPTMS is added at $t_0$ (HM-504). $R^2$ for linear fit of $d_z^3$ is 0.986. ....  | 234 |
| <b>Figure 5.24</b> Cryo-TEM images of Laponite armoured poly(styrene- <i>co</i> - <i>n</i> -butyl acrylate) with MPTMS added at $t_0$ (scale bar a-c: 100 nm; scale bar d: 50 nm) (BL-050). Dumbbell shaped particles are highlighted by the red arrows. ....   | 236 |
| <b>Figure 5.25</b> Scheme depicting steps to form multi-layered particles. ....   | 237 |
| <b>Figure 5.26</b> Overall monomer conversion, $X_m$ , versus time for Laponite armoured poly(Sty- <i>co</i> -BA) (HM-502) (■), the same polymerization reaction but where MPTMS (0.1 g) was added at $t_6$ (HM-503) (●) and the multi-layered particles (HM-505) (▲). The dashed line at 360 minutes indicates the shot addition of 0.1 g MPTMS, the dashed line at 420 minutes indicates the beginning of encapsulating feed of styrene and <i>n</i> -butyl acrylate and the dashed line at 900 minutes indicates the end of the monomer feed. The blue line (—) represents the 0 % conversion line during the monomer feed. Monomer was fed at a rate of 2.5 mL h <sup>-1</sup> . .... | 238 |
| <b>Figure 5.27</b> Overall monomer conversion, $X_m$ , versus monomer fed into the reaction mixture for multi-layered particles; where monomer was fed at 2.5 mL h <sup>-1</sup> (HM-505) (▲) and 1.5 mL h <sup>-1</sup> (HM-507) (◆). HM-507 coagulated after 9 mL of monomer was fed in. ....   | 238 |
| <b>Figure 5.28</b> (a) Average particle diameter, $d_z$ , and (b) dispersity, $D_I$ , versus monomer conversion, $X_m$ , of multi-layered particles (HM-505). The dashed line at 360 minutes indicates the shot addition of 0.1 g MPTMS, the dashed line at 420 minutes indicates the beginning of encapsulating feed of styrene and <i>n</i> -butyl acrylate and the dashed line at 900 minutes indicates the end of the monomer feed. Monomer   |     |

was fed at a rate of 2.5 mL h<sup>-1</sup>. On feeding monomer particle size increases with little change to the dispersity.....239

**Figure 5.29** Average particle diameter,  $d_z$  (■) and  $d_z^3$  versus monomer conversion,  $X_m$ , of multi-layered particles before the monomer feed (HM-505).  $R^2$  for linear fit of  $d_z^3$  is 0.994. ....240

**Figure 5.30** Average particle diameter,  $d_z$  (■) and  $d_z^3$  versus monomer fed in to the reaction (mL) of multi-layered particles during the monomer feed (HM-505).  $R^2$  for linear fit of  $d_z^3$  is 0.998.....241

**Figure 5.31** SEM image of multi-layered particle (HM-505) (scale: 100 nm). .....243

**Figure 5.32** Thin films of (a) poly(styrene-*co*-*n*-butyl acrylate) (HM-501), (b) Laponite armoured particles (HM-502), (c) Laponite core-shell particles (HM-503) and (d) multi-layered particles of 1% cross-linked Laponite armoured poly(styrene-*co*-*n*-butyl acrylate) multi-layered particles (HM-505). Films were prepared by casting 10.0 g of 10 wt.% latexes in a polypropylene pot.....245

**Figure 5.33** Stress-strain curve of films formed from poly(styrene-*co*-*n*-butyl acrylate) particles (HM-501) (—), Laponite armoured particles (HM-502) (—), Laponite core-shell particles (HM-503) (—) and multi-layered particles (HM-505) (—).....246

**Figure 5.34** Schematic representation of the multilayer particles and the respective structure of the film they form. (a) poly(Sty-*co*-BA) latex, (b) Laponite armoured poly(Sty-*co*-BA) latex, (c) cross-linked Laponite armoured poly(Sty-*co*-BA) latex and (d) multi-layered particles of encapsulated cross-linked Laponite armoured poly(Sty-*co*-BA) latex.....249

**Figure 5.35** Storage modulus versus temperature of films formed from poly(styrene-*co*-*n*-butyl acrylate) particles (HM-501) (—), Laponite armoured particles (HM-502) (—), Laponite core-shell particles (HM-503) (—) and multi-layered particles (HM-505) (—). ....251

**Figure 5.36** Loss Modulus versus temperature of films formed from poly(styrene-*co*-*n*-butyl acrylate) particles (HM-501) (—), Laponite armoured particles (HM-502) (—), Laponite core-shell particles (HM-503) (—) and multi-layered particles (HM-505) (—). ....252

**Figure 5.37** Tan  $\delta$  versus temperature of films formed from poly(styrene-*co*-*n*-butyl acrylate) particles (HM-501) (—), Laponite armoured particles (HM-502) (—), Laponite core-shell particles (HM-503) (—) and multi-layered particles (HM-505) (—).....254

**Figure 5.38** TGA of films formed from poly(styrene-*co*-*n*-butyl acrylate) particles (HM-501) (—), Laponite armoured particles (HM-502) (—), Laponite core-shell particles (HM-503) (—), multi-layered particles (HM-505) (—) and Laponite XLS (—).....256

**Figure 5.39** Scheme illustrating the effect of morphology on thermal stability of polymer. ....260

**Figure 5.40** SEM images of films of (a) Laponite armoured particles (HM-502), (b) Laponite core-shell particles (HM-503) and (c) multi-layered particles (HM-505) after being heated to 500 °C for two hours. ....261

|   |     |
|---|-----|
| <b>Figure 5.41</b> TGA of films formed from Laponite armoured particles (HM-502) (—), Laponite core-shell particles (HM-503) (—) and multi-layered particles (HM-505) (—). Samples were heated to 500 °C at a rate of 10 °C min <sup>-1</sup> , after which the 500 °C temperature was maintained for two hours. The dashed line represents the start of the 500 °C isothermal..... | 262 |
| <b>Figure I.1</b> Schematic representation of the slipping plane and the corresponding zeta potential.....  | 278 |
| <b>Figure I.2</b> Scheme representing typical intensity fluctuations for large and small particles.....   | 280 |
| <b>Figure I.3</b> Graph of the correlation function as a function of time for small or large particles in dynamic light scattering measurements.....  | 280 |
| <b>Figure I.4</b> Scheme of shear stress vs. shear rate, illustrating changes in plot for Newtonian and non-Newtonian materials.....  | 283 |
| <b>Figure I.5</b> Scheme illustrating the appearance of a yield stress and zero shear viscosity on a log plot of viscosity vs. shear rate.....  | 283 |
| <b>Figure I.6</b> Scheme indicating relationship between applied stress and measure strain for viscoelastic materials.....  | 284 |
| <b>Figure I.7</b> Illustration of the phase angle as a result the lag between applied and measured sinusoidal signals.....  | 284 |
| <b>Figure I.8</b> Illustration of the phase angle of purely elastic and purely viscous materials.....   | 285 |
| <b>Figure I.9</b> Illustration of plots produced from a frequency sweep for viscoelastic solids, viscoelastic liquids and gels.....   | 285 |
| <b>Figure II.1</b> Overall monomer conversion, $X_m$ , versus time for the encapsulation of calcium carbonate (HM-4-120, repeat of HM-3-014). Feed 1; MAA and DEGDA mixture. Feed 2; DEGDA. Monomer was fed at a rate of 0.5 mL h <sup>-1</sup> .....   | 290 |
| <b>Figure II.2</b> Overall monomer conversion; $X_m$ vs. time of encapsulation of calcium carbonate (HM-4-136, repeat of HM-3-006). Feed 1; MAA and DEGDA mixture. Feed 2; DEGDA. Feed 3; MMA feed. Fhe first two feeds were fed at a rate of 0.5 mL h <sup>-1</sup> and MMA was fed at a rate of 1 mL h <sup>-1</sup> .....  | 290 |
| <b>Figure III.1</b> SEM images of (a) poly(DEGDA)-C particles (HM-301), (b) poly(PETA)-C and (c) poly(DPEPHA)-C particles ((a) scale bar: 200 nm. (b-c) scale bar: 100 nm).....   | 292 |
| <b>Figure III.2</b> Cryo-TEM images of (a) hollowed poly(DEGDA)-C particles (HM-304) and (b) hollowed poly(DPEPHA)-C particles (scale bar: 200 nm).....   | 292 |
| <b>Figure III.3</b> Graph of zeta potential of bare CaCO <sub>3</sub> particles (Socal P3) (■), poly(DEGDA)-C particles (HM-301) (●), poly(PETA)-C particles (▲) (HM-302) and poly(DPEPHA)-C particles (▼) (HM-303) as a function of salt (NaCl) concentration. Zeta potential measurements were performed at pH 9.3 and an average of 6 measurements was recorded.....             | 293 |
| <b>Figure IV.1</b> Frequency sweeps of (a) 5, (b) 6, (c) 7.5 and (d) 10 wt.% poly(DEGDA-co-MAA) microgels; storage modulus, $G'$ , (■), loss modulus, $G''$ , (■) and phase angle, $\delta$ , (■). Each frequency sweep was repeated for three different microgels  |     |



represented by a different shaped symbol; HM-409 (■), HM-410 (●) and HM-411 (▲). .....297

**Figure V.1** Additional SEM images of 1 % cross-linked Laponite Pickering poly(styrene-*co*-*n*-butyl acrylate) encapsulated in film poly(styrene-*co*-*n*-butyl acrylate) (HM-504) (scale: 100 nm). Where a and b are different particles and 1 denotes the original SEM image and 2 and 3 are the image with increased contrast to elucidate the film formed polymer shell. The apparent hole in the images is from sublimed polymer as a result of high magnification (required to accurately focus the image). .....298

**Figure V.2** Storage modulus vs. temperature for (a) poly(Sty-*co*-BA) (HM-501), (b) Laponite armoured poly(Sty-*co*-BA) (HM-502), (c) Laponite core-shell (HM-503) and (d) multi-layered particles (HM-505), conducted at frequencies of 1 Hz (—) and 10 Hz (—). .....299

**Figure V.3** Loss modulus vs. temperature for (a) poly(Sty-*co*-BA) (HM-501), (b) Laponite armoured poly(Sty-*co*-BA) (HM-502), (c) Laponite core-shell (HM-503) and (d) multi-layered particles (HM-505), conducted at frequencies of 1 Hz (—) and 10 Hz (—). .....300

**Figure V.4** Tan $\delta$  vs. temperature for (a) poly(Sty-*co*-BA) (HM-501), (b) Laponite armoured poly(Sty-*co*-BA) (HM-502), (c) Laponite core-shell (HM-503) and (d) multi-layered particles (HM-505), conducted at frequencies of 1 Hz (—) and 10 Hz (—). .....301

**Figure V.5** DSC of poly(styrene-*co*-*n*-butyl acrylate) film (HM-4-085) (—), 1% Laponite Pickering poly(styrene-*co*-*n*-butyl acrylate) film (HM-4-074) (—), 1% cross-linked Laponite Pickering poly(styrene-*co*-*n*-butyl acrylate) (—) and 1 % cross-linked Laponite Pickering poly(styrene-*co*-*n*-butyl acrylate)encapsulated in film poly(styrene-*co*-*n*-butyl acrylate) (HM-4-095) (—). .....302

**Figure V.6** TGA of (a) poly(Sty-*co*-BA) film (HM-501), Laponite armoured poly(Sty-*co*-BA) film (HM-502), (c) Laponite core-shell particles (HM-503), (d) multi-layered particles (HM-505) and (e) Laponite XLS; mass loss (—) and heatflow (—). .....304

# Tables

---

|   |     |
|---|-----|
| <b>Table 2.1</b> Table showing SiO <sub>2</sub> content determined by EDAX and TGA for amorphous calcium carbonate-silica particles. ....   | 69  |
| <b>Table 2.2</b> Table of repeated reactions of the encapsulation of calcium carbonate in poly(DEGDA- <i>co</i> -MAA). ....   | 80  |
| <b>Table 2.3</b> Table of <sup>1</sup> H NMR data for the solubility of DEGDA in D <sub>2</sub> O .....   | 81  |
| <b>Table 2.4</b> Encapsulated amorphous calcium carbonate particles within a polymeric shell monomer fed amounts fed into a mixture of 5.0 g calcium carbonate and 25.0 g water. Monomer feeds 1 and 2 were both 0.5 mL and fed at 0.5 mL h <sup>-1</sup> .....   | 83  |
| <b>Table 3.1</b> Encapsulated calcium carbonate particles within a polymeric shell with various multiple acrylate containing monomers, monomer feed amounts fed into a mixture of 10.0 g calcium carbonate and 50.0 g water. Monomer feeds 1 and 2 were both 0.5 mL and fed at 0.5 mL h <sup>-1</sup> ..... | 101 |
| <b>Table 3.2</b> Table listing composite particles synthesized and their abbreviations....  | 101 |
| <b>Table 3.3</b> Table of multi-acrylate monomer and multi-acrylate monomer vinyl groups present in the composite particles, where MA <sub>x</sub> is the multi-acrylate in question. ....  | 107 |
| <b>Table 3.4</b> Table of Bromine Index values and the % of vinyl groups remaining from the addition of multi-acrylate, where monomer vinyl groups is the total possible mmol of vinyl groups in the specific monomer in 100 g of particles. ....   | 108 |
| <b>Table 3.5</b> Table of Bromine Index values and the % of vinyl groups remaining after thiol-ene Michael of 2-mercapto ethanol. BI of 0 for both particles indicates that the all vinyl groups are consumed in the thiol-ene Michael addition. ....   | 117 |
| <b>Table 3.6</b> Table of Bromine Index values and the % of vinyl groups remaining after thiol-ene Michael addition of 1-dodecane thiol. BI of 0 for both particles indicates that the all vinyl groups are consumed in the thiol-ene Michael addition. ....  | 120 |
| <b>Table 3.7</b> Table of monomer conversion (measured by <sup>1</sup> H NMR) and molecular weights (measured by THF SEC) for poly(styrene) synthesized by RAFT polymerization. ....  | 124 |
| <b>Table 3.8</b> Table of molecular weights and % of coupled polymer chains for poly(styrene) after aminolysis of trithiocarbonate group (HM-323). Where reported M <sub>n</sub> and M <sub>w</sub> are of the system. ....   | 128 |
| <b>Table 3.9</b> Table of molecular weights and % of coupled polymer chains for poly(styrene) after aminolysis of trithiocarbonate group (HM-323) and after reduction of disulfide bonds with DTT (HM-324). Where reported M <sub>n</sub> and M <sub>w</sub> are of the system.....                         | 128 |
| <b>Table 3.10</b> Table of Bromine Index of poly(PETA)-C particles and poly(PETA)-C particles after thiol Michael addition with poly(styrene)-SH. ....  | 131 |
| <b>Table 3.11</b> Encapsulated calcium carbonate particles within a polymeric shell with various multiple acrylate containing monomers, monomer fed amounts fed into a mixture of 10.0 g calcium carbonate and 50.0 g water. Monomer feeds 1 and 2 were both 0.5 mL and fed at 0.5 mL h <sup>-1</sup> ..... | 135 |

|   |     |
|---|-----|
| <b>Table 3.12</b> Table of average titration volumes and corresponding Bromine Index for composite particles. $V_1$ and $V_2$ denote the volume of $\text{Na}_2\text{S}_2\text{O}_3$ titrated in the blank and sample solution respectively. ....   | 140 |
| <b>Table 3.13</b> Table of average titration volumes and corresponding Bromine Index for composite particles after thiol Michael addition of 2-mercapto ethanol. $V_1$ and $V_2$ denote the volume of $\text{Na}_2\text{S}_2\text{O}_3$ titrated in the blank and sample solution respectively. ....  | 143 |
| <b>Table 3.14</b> Table of average titration volumes and corresponding Bromine Index for composite particles after thiol Michael addition of 1-dodecane thiol. $V_1$ and $V_2$ denote the volume of $\text{Na}_2\text{S}_2\text{O}_3$ titrated in the blank and sample solution respectively. ....    | 145 |
| <b>Table 3.15</b> Table of polymerization of styrene using PABTC RAFT agent. The number in the brackets denotes the molecular weight aim at 60 % monomer conversion. ....   | 147 |
| <b>Table 3.16</b> Table of average titration volumes and corresponding Bromine Index for poly(PETA)-C particles after thiol Michael addition of poly(styrene)-SH. $V_1$ and $V_2$ denote the volume of $\text{Na}_2\text{S}_2\text{O}_3$ titrated in the blank and sample solution respectively. .... | 150 |
| <b>Table 4.1</b> Table of monomer quantities in starved-fed emulsion polymerization...  | 164 |
| <b>Table 4.2</b> Methacrylic acid content (mol%) in microgels. ....   | 164 |
| <b>Table 4.3</b> Table of % change in particle hydrodynamic diameter with respect to pH. ....   | 173 |
| <b>Table 4.4</b> Particle size measurements of microgels in water (at pH 5.5) and after swelling in THF. ....   | 174 |
| <b>Table 4.5</b> Wt.% of poly(DEGDA- <i>co</i> -MAA) microgels in preparation of gels (HM-407). ....  | 180 |
| <b>Table 4.6</b> Table of quantities of 1 M HCl and 1 M NaOH added in reversible gel experiment. HCl and NaOH were added 10 $\mu\text{L}$ at a time until a response was observed. ....   | 184 |
| <b>Table 4.7</b> Table of monomer quantities for microgel synthesis. ....   | 197 |
| <b>Table 4.8</b> Table of reagent quantities for microgel gels; reversible gel experiment (HM-407). ....  | 198 |
| <b>Table 4.9</b> Table of quantities of 1 M HCl and 1 M NaOH added in reversible gel experiment. HCl and NaOH were added 10 $\mu\text{L}$ at a time until a response was observed. ....   | 198 |
| <b>Table 4.10</b> Table of reagent quantities for microgel gels for rheological experiments. ....   | 199 |
| <b>Table 5.1</b> Table listing all particles synthesized and their abbreviations. ....  | 244 |
| <b>Table 5.2</b> Table of characteristic properties from Stress-Strain DMTA plots, at 25 $^{\circ}\text{C}$ . ....  | 248 |
| <b>Table 5.3</b> Table of the $T_g$ measured by DMTA, where the $T_g$ is taken as the onset and the maximum of the $\tan \delta$ versus temperature plot (Figure 5.37). ....  | 254 |

|  |     |
|--|-----|
| <b>Table 5.4</b> Table of $T_g$ of the polymer films measured by DSC. ....   | 255 |
| <b>Table 5.5</b> Table showing final monomer conversion and composition of polymer films. ....   | 257 |
| <b>Table 5.6</b> Table showing the theoretical mass loss, calculated from relative masses, of the films broken down into its substituents; % mass loss of film due to complete polymer calcination and % mass loss of film due to Laponite clay..... | 258 |
| <b>Table 5.7</b> Table comparing theoretical and experimental mass loss (%) of films when heated to 1000 °C at a rate of 10 °C min <sup>-1</sup> , where experimental mass loss is measured by TGA. ....   | 258 |
| <b>Table 5.8</b> Table illustrating temperature at points of mass loss and percentage of mass lost at said temperature.....  | 258 |
| <b>Table 5.9</b> Table comparing final mass (%) when sample is heated to 1000 °C and after a two hour isothermal at 500 °C. Char remaining is the difference between mass remaining at 1000 °C and 500 °C. ....                                      | 262 |
| <b>Table 5.10</b> Table of reagent quantities. ....  | 266 |
| <b>Table 5.11</b> Table showing conversion particle size and dispersity of particles. ....   | 266 |
| <b>Table 5.12</b> Table of reagent quantities. ....  | 267 |
| <b>Table 5.13</b> Table showing monomer conversion, particle size and dispersity of particles. ....  | 267 |
| <b>Table 5.14</b> Table of encapsulation of Laponite stabilized poly(styrene- <i>co</i> - <i>n</i> -butyl acrylate) latex before encapsulating feed. ....  | 268 |
| <b>Table 5.15</b> Table of encapsulation of Laponite stabilized (styrene- <i>co</i> - <i>n</i> -butyl acrylate) latex. Amounts of monomer stated are those from the feed. ....   | 268 |
| <b>Table II.1</b> Raw data for zeta potential measurements as a function of [NaCl] for calcium carbonate (SOCAL P3) (Figure 2.14). ....  | 286 |
| <b>Table II.2</b> Raw data for zeta potential measurements as a function of pH for calcium carbonate (SOCAL P3) (Figure 2.15). ....  | 287 |
| <b>Table II.3</b> Raw data for zeta potential measurements as a function of [NaCl] for calcium carbonate particles encapsulated in a poly(MAA- <i>co</i> -DEGDA) shell (Figure 2.22). ....   | 288 |
| <b>Table II.4</b> Raw data for zeta potential measurements as a function of [NaCl] for calcium carbonate encapsulated in poly(MAA- <i>co</i> -DEGDA) primer followed by a poly(MMA) shell (HM-4-136) (Figure 2.30). ....                             | 288 |
| <b>Table II.5</b> Raw data for zeta potential measurements as a function of pH for amorphous calcium carbonate (Figure 2.40).....  | 289 |
| <b>Table II.6</b> Raw data for zeta potential measurements as a function of pH for amorphous calcium carbonate-silica composite particles (Figure 2.40). ....  | 289 |
| <b>Table II.7</b> Table of wt.% of silica in amorphous CaCO <sub>3</sub> particles formed in the presence of Ludox calculated from EDAX measurements. ....   | 291 |
| <b>Table III.1</b> Raw data for zeta potential measurements as a function of [NaCl] for calcium carbonate (SOCAL P3).....  | 293 |

|   |     |
|---|-----|
| <b>Table III.2</b> Raw data for zeta potential measurements as a function of [NaCl] for calcium carbonate encapsulated in poly(MAA- <i>co</i> -DEGDA). .....                    | 294 |
| <b>Table III.3</b> Raw data for zeta potential measurements as a function of [NaCl] for calcium carbonate encapsulated in poly(MAA- <i>co</i> -DEGDA- <i>co</i> -PETA). .....   | 294 |
| <b>Table III.4</b> Raw data for zeta potential measurements as a function of [NaCl] for calcium carbonate encapsulated in poly(MAA- <i>co</i> -DEGDA- <i>co</i> -DPEPHA). ..... | 295 |
| <b>Table IV.1</b> Pycnometry of poly(DEGDA- <i>co</i> -MAA); sample weight was 0.3226 g and experiment was performed at 28.6 °C. ....   | 296 |
| <b>Table V.1</b> Table of T <sub>g</sub> of the polymer films measured by DSC. ....   | 303 |

# Acknowledgements

---

I would like to thank the entire Bon group, both past and present whom I have had the pleasure to work with; namely Yunhua, Nick, Rong, Gabit, Rob (Imperial), Joe, Ross. Special thanks go to Rob (non-imperial) and Cathy for all their help (particularly in the last month) and moral support provided through sweets and cakes. Special thanks also go to Tom, Adam who I have really missed this past year. I also want to thank Jamie for all the much needed distractions.

I would especially like to thanks my supervisor Prof. Stefan Bon for his help, support and friendship throughout my time at Warwick. I greatly appreciate all the opportunities that he has afforded me.

Much of this work would not have been possible without the help of various university staff including Ian Portman, Ben Douglas, Ivan Prokes, Steve York and Richard Beanland. I would also like to thank Nick Barker for providing me the opportunity to take part in the Outreach programme, I have loved every day that I took part. I would also like to thank my industrial sponsor Sappi for their financial support of my project.

I'm very grateful to my family for always being there and supporting me. Finally I would like to thank Danny for putting up with my seemingly never ending education, for moving around the country for me, patiently pretending to be interested in colloids and for taking complete care of me while I wrote my thesis.

# Declaration

---

I hereby declare that this thesis consists of my own work, with the exception of the collaborative work listed below:

- Chapter 2 – Porosimetry measurements were performed by Adam Morgan. EDX analysis on STEM was performed with the aid of Richard Beanland. Cryo-TEM was performed by Ian Portman. Powder X-ray diffraction was performed by Craig Hiley.
- Chapter 3 - Cryo-TEM was performed by Ian Portman. Raman spectroscopy was performed with the aid of Ben Douglas.
- Chapter 4 – Rheology was performed by Ross Jagers. Yunhua Chen prepared the gels from the highly concentrated Pickering emulsions. Rob Young performed pynometry.
- Chapter 5 – Synthesis of composite particles (labelled BL-) was carried out by Brooke Longbottom under my supervisions. Cryo-TEM was performed by Ian Portman.

All work contained herein was conducted in the Department of Chemistry at the University of Warwick, between October 2010 and October 2014. No material contained in this thesis has been submitted for any other degree, or at any other institution.

Signed \_\_\_\_\_ Date \_\_\_\_\_

**Holly McKenzie**

# Abstract

---

Within this thesis we explore the synthesis and modification of hierarchical composite particles and responsive microgels. Initially in **Chapter 2** we describe the encapsulation of calcium carbonate particles within a polymeric shell, wherein the inorganic core is kinetically trapped within a cross-linked polymer network. Once primed in this shell we illustrate control of polymer shell thickness through a secondary polymerization. We also begin to investigate the possibility of preparing nano-rattles, using the calcium carbonate core as a sacrificial template. In **Chapter 3** we expand on the work presented in Chapter 2, by incorporating pendant vinyl groups into the polymer shell of the composite particles from which we use thiol-ene Michael addition to modify their surface. In **Chapter 4** perform the encapsulating polymerization from Chapter 2 and 3, but in the absence of the calcium carbonate core. The stable particles formed were found to be pH responsive microgel particles. We illustrate the gelling behaviour of these particles and use as Pickering stabilizers for oil-in-water emulsions which show reversible flocculation on adjustment of the pH. In investigating these microgel particles we also begin to elucidate unanswered questions from Chapters 2 and 3. Finally in **Chapter 5** we go back to encapsulation, this time to synthesize multi-layered particles by encapsulation of Laponite armoured soft latexes. We infer how alterations to particle morphology affect the bulk properties of polymer films by mechanical and thermal analysis.



# Abbreviations

---

|                 |  |
|-----------------|--|
| APS             | Ammonium persulfate  |
| BA              | n-Butyl acrylate   |
| BMA             | Butyl methacrylate   |
| BDDA            | Butanediol diacrylate                                      |
| BI              | Bromine Index (mg / 100 g)                                 |
| BN              | Bromine Number (g / 100 g)                                 |
| $C$             | BET constant   |
| CPS             | Disc centrifuge particle sizing                            |
| $\delta$        | Phase angle  |
| DEGDA           | Di(ethylene glycol) diacrylate                             |
| $D_1$           | Dispersity   |
| DLS             | Dynamic light scattering                                   |
| DMTA            | Dynamic mechanical thermal analysis, also described as DMA |
| DPEPHA          | Dipentaerythritol penta-/hexa-acrylate                     |
| DTT             | Dithiothreitol   |
| DVB             | Divinylbenzene   |
| $d_z$           | Average particle hydrodynamic diameter (nm)                |
| $\varepsilon$   | Strain   |
| $\varepsilon_0$ | Strain at maximum stress                                   |
| $E$             | Complex modulus  |

|            |                                      |
|------------|--------------------------------------|
| $E'$       | Storage modulus                      |
| $E''$      | Loss Modulus                         |
| EA         | Ethyl acrylate                       |
| EGDMA      | Ethylene glycol diacrylate           |
| EDX        | Energy dispersive X-ray analysis     |
| FEG        | Field emission gun                   |
| FTIR       | Fourier transform infrared           |
| $G'$       | Storage modulus (shear)              |
| $G''$      | Loss modulus (shear)                 |
| HIPE       | High internal phase emulsion         |
| IEP        | Isoelectric point                    |
| $l$        | Length                               |
| $\Delta l$ | Change in length                     |
| LVR        | Linear viscoelastic region           |
| MAA        | Methacrylic acid                     |
| MFFT       | Minimum film formation temperature   |
| MMA        | Methyl methacrylate                  |
| $M_n$      | Number average molecular weight      |
| $M_p$      | Peak molecular weight                |
| MPTMS      | 3-Methacryloxypropyltrimethoxysilane |
| $M_w$      | Weight average molecular weight      |

|                |  |
|----------------|--|
| $N$            | Number of particles ( $\text{dm}^{-3}$ )   |
| $\bar{n}$      | Average number of radicals per particle  |
| NIPAAm         | N-Isopropyl acrylamide   |
| $P$            | Absolute pressure of bulk gas above sample   |
| $P_0$          | Saturation pressure of the adsorptive  |
| PABTC          | (Propanoic acid)-2-yl butyl trithiocarbonate   |
| PDI            | Polydispersity index   |
| PETA           | Pentaerythritol triacrylate  |
| Poly(DEGDA)-C  | Calcium carbonate particles encapsulated in poly(MAA- <i>co</i> -DEGDA)                    |
| Poly(DPEPHA)-C | Calcium carbonate particles encapsulated in poly(MAA- <i>co</i> -DEGDA- <i>co</i> -DPEPHA) |
| Poly(PETA)-C   | Calcium carbonate particles encapsulated in poly(MAA- <i>co</i> -DEGDA- <i>co</i> -PETA)   |
| PVA            | Polyvinyl alcohol  |
| PZC            | Point of zero-charge   |
| RAFT           | Reversible addition-fragmentation chain transfer   |
| $R_c$          | Overall rate of capture of oligoradicals by particles ( $\text{dm}^{-3} \text{s}^{-1}$ )   |
| $R_f$          | Overall rate of coagulation ( $\text{dm}^{-3} \text{s}^{-1}$ )                             |
| $R_i$          | Rate of initiation ( $\text{mol dm}^{-3} \text{s}^{-1}$ )                                  |
| $R_p$          | Rate of propagation ( $\text{mol dm}^{-3} \text{s}^{-1}$ )                                 |

|            |  |
|------------|--|
| RPM        | Rotations per minute   |
| $\sigma$   | Stress   |
| $\sigma_0$ | Maximum stress   |
| SEM        | Scanning electron microscopy   |
| STEM       | Scanning transmission electron microscopy  |
| Sty        | Styrene  |
| $t$        | Time   |
| TEM        | Transmission electron microscopy   |
| $T_g$      | Glass transition temperature   |
| TGA        | Thermal gravimetric analysis   |
| THF        | Tetrahydrofuran  |
| UTS        | Ultimate tensile strength  |
| VA-088     | 1,1'-Azobis(cyclohexanecarbonitrile)   |
| $V_m$      | Volume of gas adsorbed when the entire surface is covered with a monomolecular layer |
| $X_m$      | Monomer conversion   |
| $Z_{ave}$  | Intensity average diameter   |

# Chapter 1: Introduction

In this body of work we investigate encapsulation of sub-micron particles, synthesis of microgels and particle surface modification with thiol  $\omega$ -functionalized polymers. In order to discuss these particles we must understand heterogeneous polymerization techniques, particle stability and RAFT polymerization.

## 1.1. Heterogeneous Polymerization Techniques

Radical heterogeneous polymerization techniques can be divided into several categories, each exhibiting different features including type of particle nucleation, size range of respective particles (Figure 1.1) and types of monomers used.<sup>1</sup>

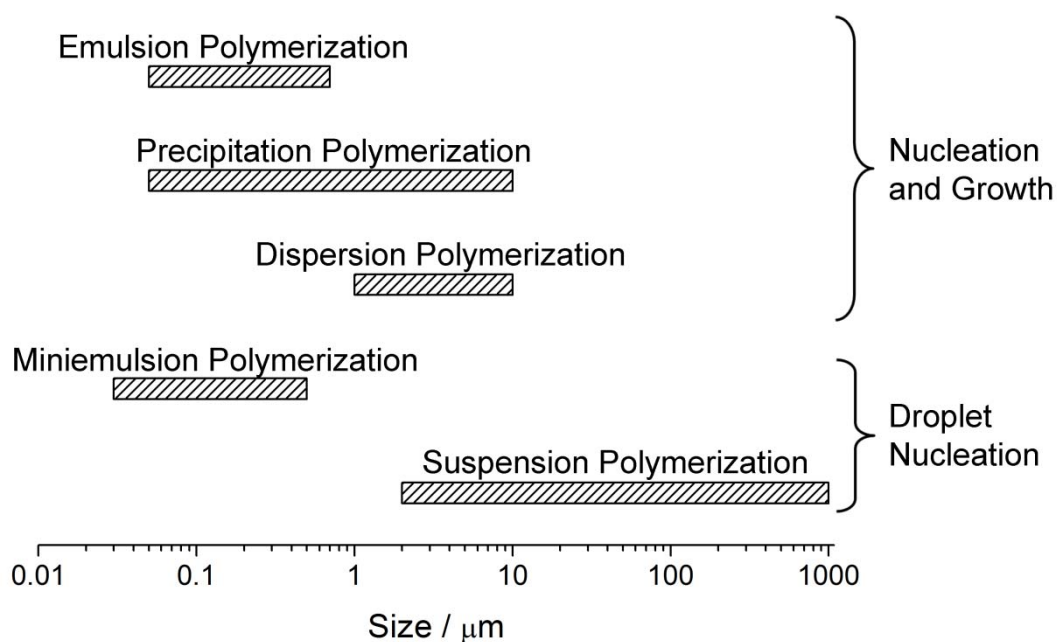


**Figure 1.1** Illustration of particle size ranges achievable by various heterogeneous polymerization techniques.

These heterogeneous polymerization methods are often more complicated than their homogeneous counterparts, as multi-phase polymerization kinetics and the kinetics of particle nucleation and growth must be considered.

### **1.1.1. Emulsion polymerization**

Emulsion polymerization is a heterogeneous polymerization method where particles of 50-600 nm in diameter are formed. The term emulsion polymerization is in fact a misnomer; polymerization does not occur in monomer droplets as the name suggests, but in monomer swollen particles. Emulsion polymerization is split into three intervals describing the main characteristics (Figure 1.2).<sup>2-7</sup> Interval I; the nucleation period describes the formation of all particles, assuming secondary nucleation (the formation of a secondary crop of particles) does not occur. In this interval particle number and particle size is increasing and monomer droplets are present. The nucleation stage is typically short and occurs in 0-10 % conversion, short nucleation periods yield a monomodal size distribution. Initiation occurs in the aqueous phase where the water soluble initiator species undergoes homolysis and reacts with the finitely water-soluble monomer; this oligomer propagates until it reaches a critical chain length ( $j_{cr}$ ), at this point particle nucleation proceeds in one of two ways, through micellar or homogeneous nucleation.

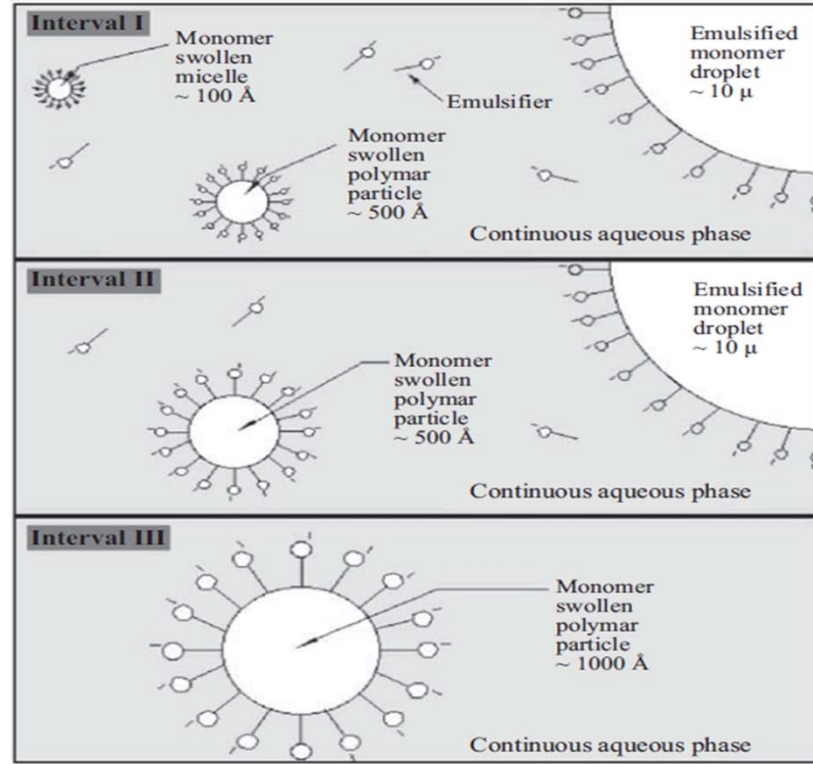


**Figure 1.2** Scheme of the three intervals in emulsion polymerization.<sup>8</sup>

#### 1.1.1.1. Homogeneous nucleation

Once the oligoradicals have reached  $j_{cr}$  in the aqueous phase, the hydrophobic attributes outweigh the hydrophilic, and the polymer collapses to form a primary particle. Once a sufficient number of particles exist, capture of surface active oligoradicals (z-mers) occurs and overtakes new particle formation. Brownian motion, the random movement of particles, leads to particle collision; if the surface charge, obtained from ionic initiator species or surfactant, is not great enough these collisions result in the particles coagulating and fusing together. This coagulation occurs until enough particles have fused to result in a high enough surface charge density to warrant stable particles.<sup>9-11</sup> This was first described in the Fitch-Tsai theory:

$$\frac{\delta N}{\delta t} = bR_{iw} - R_c - R_f \quad (1.1)$$

where  $N$  is the number of particles  $\text{dm}^{-3}$ ,  $b$  is the compensation of radical loss,  $R_{\text{iw}}$  is the rate of appearance of primary radicals,  $R_c$  is the rate of radical capture and  $R_f$  is the rate of particle coagulation.<sup>12</sup>

#### 1.1.1.2. Micellar nucleation<sup>13</sup>

Where there is surfactant present at a concentration greater than the critical micelle concentration (CMC), micellar nucleation occurs. Surface active oligoradicals, formed in the aqueous phase, enter monomer swollen micelles to produce primary particles. At a constant rate of initiation it was found that the concentration of surfactant affects the number of particles with a dependence on monomer hydrophobicity. This led to the theory of particle formation based on radical capture by surfactant micelles described by the Smith-Ewart-Roe equation:

$$N = K \left( \frac{bR_i}{\mu} \right)^{0.4} \times (\alpha_s S)^{0.6} \quad (1.2)$$

where  $N$  is the number of particles,  $K$  is a constant with the value of 0.53 for purely micellar capture and 0.37 if capture by new particles is taken into account,  $\mu$  is the rate of particle volume growth which is assumed to be constant,  $\alpha_s$  is the area covered by the surfactant molecule and  $S$  is the total number of surfactant molecules.<sup>14, 15</sup> In this case coagulation was not considered due to the high concentration of surfactant. Roe showed that this also applied for systems without micelles. They suggested that particle nucleation stops once the polymer-water interfacial area stabilized by surfactant equals the area which can be covered by the amount of surfactant.



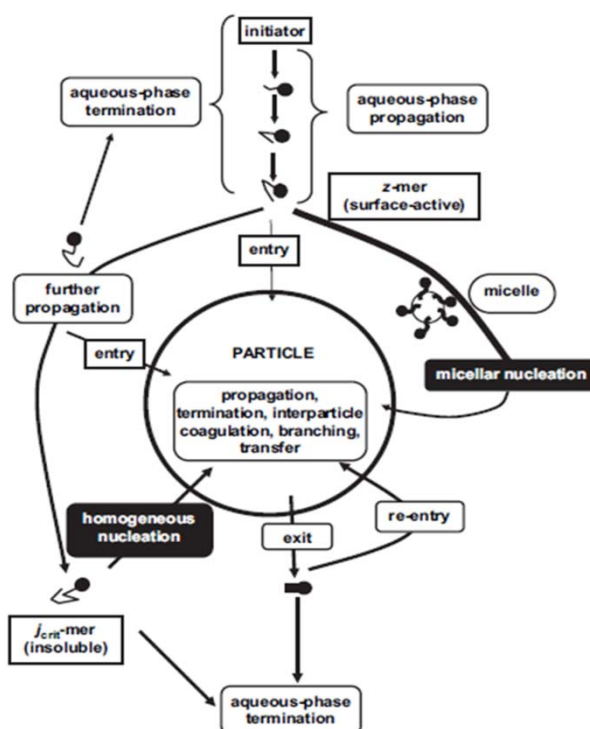


**Figure 1.3** Scheme of kinetic processes taking place in a typical emulsion polymerization.<sup>16</sup>

Once particles have formed, reversible entry of z-mers occurs until they reach  $j_{cr}$ , at which point they are irreversibly trapped (Figure 1.3). Entry into monomer droplets, and thus monomer droplet nucleation, is unlikely due to their comparatively small surface area. Interval I ends and interval II begins when particle nucleation has stopped; the number of particles are now approximately constant. The particles swell with monomer, which has diffused from the still present reservoirs of monomer droplets. During this stage the rate of polymerization is considered constant, due to a constant concentration of monomer with respect to polymer in the particles. Particle size is increasing throughout this interval.

In Interval I and II the small latex particles cannot accommodate more than one radical, on entry of a second radical instantaneous termination occurs resulting in no radicals in the particle, hence zero-one kinetics is observed. In this case (Smith-Ewart case 2, Figure 1.4 a) the average number of radicals per particle ( $\bar{n}$ ) is considered to be  $\frac{1}{2}$ . If there is significant chain transfer to small molecules the

resulting radical, typically smaller than  $j_{cr}$ , can exit the particle further reducing the probability of the presence of a radical in the particle, in this case (Smith-Ewart case 1, Figure 1.4 b)  $\bar{n} < \frac{1}{2}$ .<sup>14</sup> Interval III begins when there are no monomer droplets remaining, all monomer is now found in the polymer particles; monomer concentration in the particles is now decreasing and correspondingly the viscosity within the particles is increasing. This increased viscosity slows the rate of termination; more than one radical can be present in a particle at one time,  $\bar{n} \gg \frac{1}{2}$  (Smith-Ewart case 3, Figure 1.4 c), the kinetics at this stage resembles that of solution polymerization. Due to the reduced termination, an increased rate in reaction is observed, a phenomena known as the Trommsdorff-Norrish or gel effect.

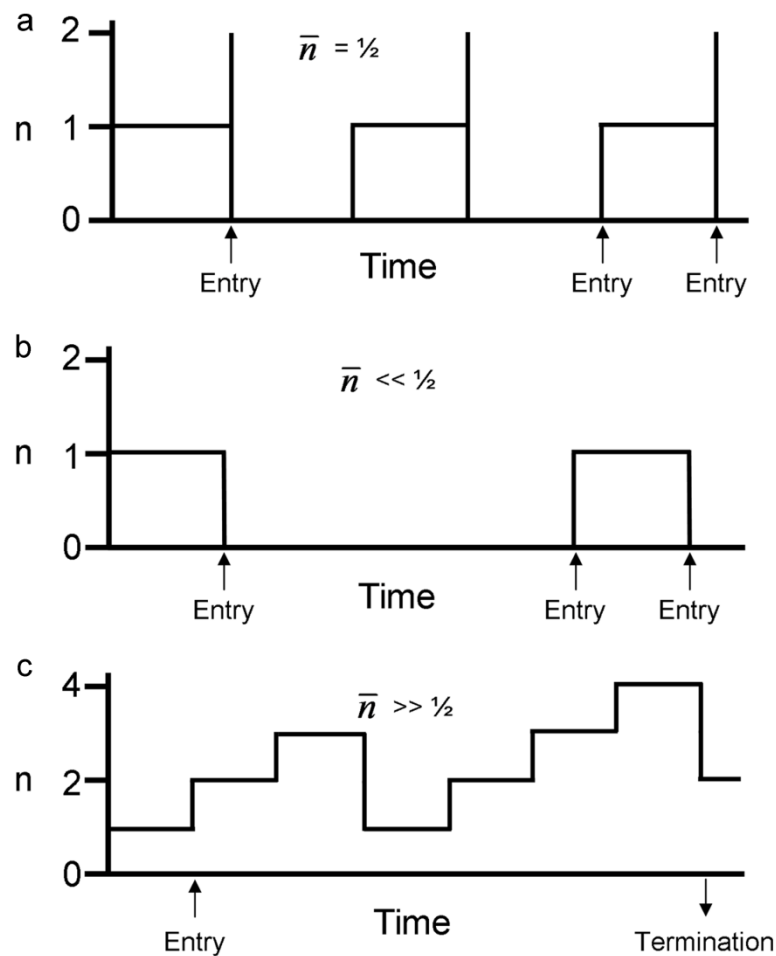


**Figure 1.4** Scheme illustrating (a) Smith-Ewart case 2, (b) Smith Ewart case 1 and (c) Smith-Ewart case 3.

Rate of polymerization is faster for emulsion polymerization than for the corresponding bulk polymerization due to the compartmentalization effect, as radicals are isolated in separate particles. Compartmentalization yields fast polymerization rates and high molecular weights.<sup>16</sup>

### 1.1.2. Miniemulsion polymerization

Miniemulsion polymerization is effectively the polymerization of small monomer emulsion droplets; it was first reported by Ugelstad when investigating the possibility of initiating polymerization within monomer droplets.<sup>17, 18</sup> Droplet nucleation with a water soluble initiator was achieved by significantly increasing monomer droplet surface area; reducing droplet size using surfactants thus allowed for radical capture. As polymerization occurs in the monomer droplets there are no reservoirs of monomer as in emulsion polymerization, as a result of this interval II effectively does not exist in miniemulsion polymerization.

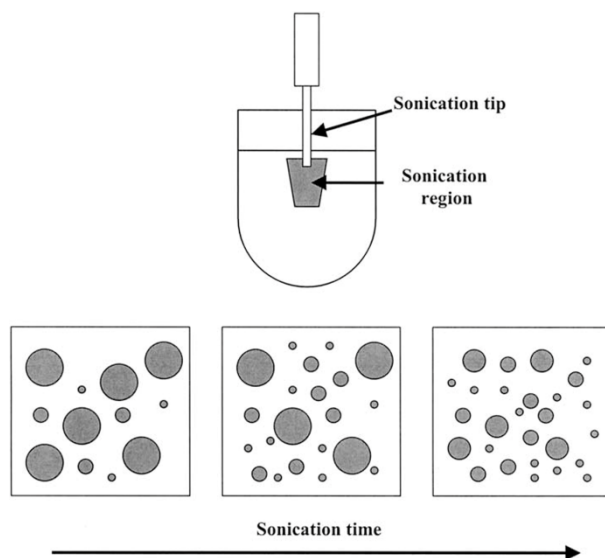


**Figure 1.5** Schematic of the effect of sonication on droplet size.<sup>19</sup>

Early work demonstrated the significance of emulsification methods and surfactants in forming stable droplets; to achieve small enough droplets high shear, typically from a mechanical homogenizer or sonicator (Figure 1.5), along with

surfactants is required.<sup>20</sup> Co-surfactants or hydrophobes, such as hexadecane, have an important role in miniemulsion polymerization; being more hydrophobic than the monomer the co-surfactant becomes irreversibly trapped in the monomer droplet due to hydrophobic interactions, thus preventing Ostwald ripening of the monomer droplets (Figure 1.6).<sup>21, 22</sup>

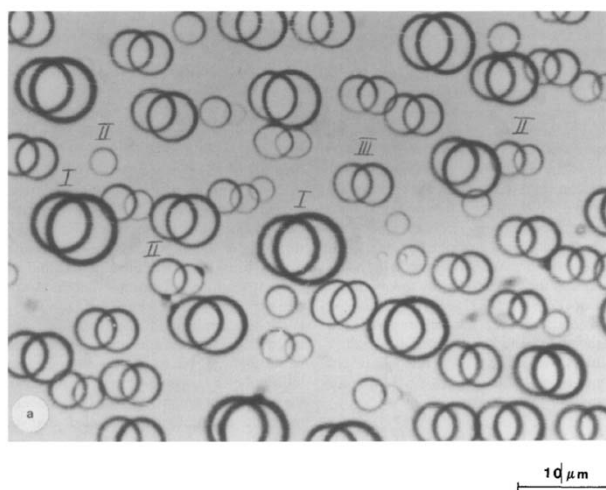


**Figure 1.6** Photomicrographs illustrating Ostwald ripening of a 1,2-dichloroethane emulsion by a double exposure on the same frame; time from the start of experiment: 0 s (image shifted on the left) and 300 s (shifted to the right).<sup>23</sup>

A significant difference between miniemulsion and emulsion polymerization is that particle nucleation occurs in the very small monomer droplets, resulting in the polymer particles often being a 1:1 copy of the initial monomer droplets.<sup>24</sup> However, it must be noted that radical capture is slow and not all droplets are necessarily nucleated, complicating the reaction kinetics.<sup>25, 26</sup> The use of hydrophobes has contributed to faster rates of polymerization and an increase in the number of final particles in miniemulsion polymerizations, with the final system being representative of the initial miniemulsion.<sup>27-29</sup>

### 1.1.3. Suspension polymerization

Suspension is possibly the simplest of the heterogeneous polymerization methods; similar to an emulsion polymerization in that the monomer is insoluble in

the continuous phase and surfactant is present, it differs in that the initiator is oil-soluble and thus polymerization takes place in the pre-existing monomer droplets. As initiation occurs in the monomer droplets, the mechanism of particle nucleation is termed droplet nucleation. As the monomer droplets are large, the resulting polymer particles formed are greater than 1  $\mu\text{m}$  and particle size distribution is broad. Particle size can be controlled to a small degree by the rate of stirring and surfactant concentration.<sup>30, 31</sup> The kinetics of polymerization is thought to be similar to that of bulk polymerizations, with the monomer droplets behaving as micro-reactors.<sup>32, 33</sup>

#### **1.1.4. Dispersion polymerization**

Dispersion polymerization can be described as an initially homogeneous mixture of monomer, initiator and stabilizer often in an organic solvent. Upon initiation, polymerization occurs in the continuous phase until the polymer chain reaches a critical chain length and precipitates out of solution to form a particle. Particle formation is very rapid and typically all particles are formed under 1 % conversion (Figure 1.7). The primary particle adsorbs stabilizer from the continuous phase and coagulates until a stable particle is formed. Once formed, the insoluble particle swells with its own monomer and the particle now becomes the locus of polymerization.<sup>34-36</sup> The coagulation of young, small, unstable particles in dispersion polymerizations was studied by DLS at the formation stage for the case of methyl methacrylate in methanol; rapid aggregation of small unstable particles, in the size region of 15-20 nm, to form larger stable particles was found.<sup>37</sup> Particles are typically large and in the range of 1-15  $\mu\text{m}$  in diameter.

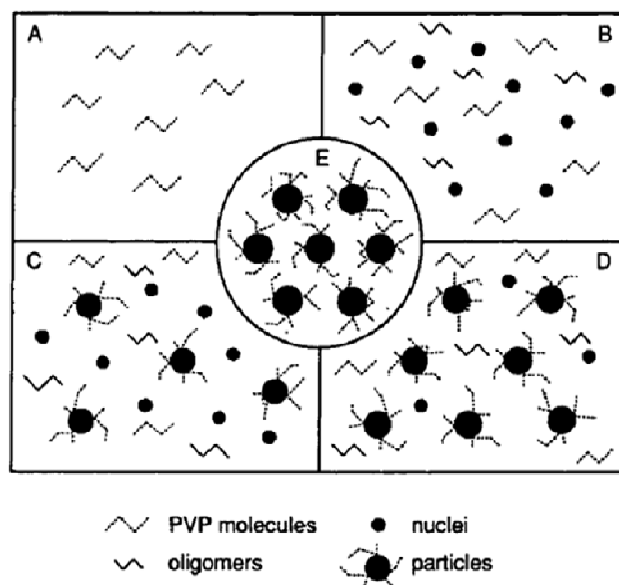


**Figure 1.7** Scheme of proposed particle formation mechanism in dispersion polymerization: (A) a homogeneous mixture of monomer, stabilizer, initiator and solvent, (B) primary particles generated through precipitation of polymer chains equal or longer than the critical chain length, (C) formation of mature particles through aggregation of unstable primary particles, (D) no new particles formed, particles are the locus of polymerization, (E) only mature particles observed at the end of the reaction.<sup>37</sup>

### 1.1.5. Precipitation

Precipitation polymerization is similar to dispersion polymerization in that the monomer and initiator are soluble in the continuous phase and the polymer is not soluble in the continuous phase. It differs in that the formed polymer does not swell with its monomer either due to unfavourable interactions (described as enthalpic precipitation; an example of which is the polymerization of acrylonitrile in water) or due to heavy cross-linking which prevents mixing (described as entropic precipitation; an example of which is the polymerization of divinylbenzene in acetonitrile).<sup>38</sup> The polymer precipitates out of the continuous phase and since it cannot swell with monomer the locus of polymerization is at the particle-continuous phase interface. The polymerization kinetics can be understood in terms of emulsion polymerization.<sup>38, 39</sup> Particle sizes are typically in the order of a few microns, and can be produced without the need of surfactant.

### 1.1.6. Pickering emulsion polymerization

The stabilization of biphasic interfaces by solid particles was first mentioned by Ramsden in 1903 and then shortly after by Pickering, after whom the phenomena has since been named, in 1907.<sup>40, 41</sup> Both had independently found that solid particulates could stabilize emulsions in the absence of soluble surfactants and even displayed superior properties; unlike with soluble surfactants, de-emulsification was not observed with solid particulates. It was later suggested by Finkle that the solid particulates are partially wettable by both the phases involved.<sup>42</sup>

Pieranski described how the solid particles acted like a surfactant using a 2-D model of the interactions of a polystyrene sphere of uniform surface tension trapped at an air/water interface, in the absence of any imposed external force.<sup>43</sup> It was found that the cause of particle adhesion to the interface was due to energy minimization, as a result of the removal of an area of the water-air interface. Pieranski observed that the polystyrene spheres at the water-air interface seemed to be trapped in a surface energy well greater than  $k_B T$ .

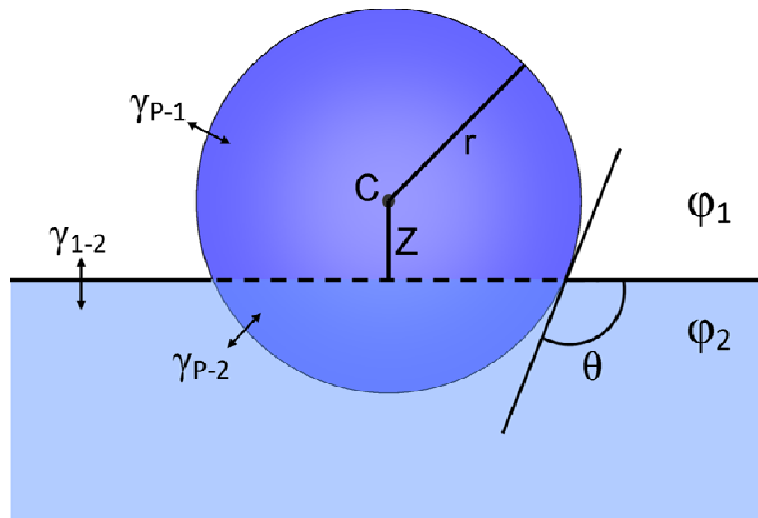


**Figure 1.8** Schematic representation of a sphere of radius  $r$  at the interface of  $\phi_1$  and  $\phi_2$  at a distance of  $Z$  from the centre,  $C$ .  $\gamma_{P-1}$ ,  $\gamma_{P-2}$  and  $\gamma_{1-2}$  are the surface/interfacial tensions between the particle and  $\phi_1$ , the particle and  $\phi_2$  and the two phases respectively and  $\theta$  is the three phase angle.

There are three contributions to the surface energy; the energy of the particle/ $\phi_1$  interface, the energy of the particle/ $\phi_2$  interface and the negative energy of the missing  $\phi_1/\phi_2$  interface (shown in Figure 1.8 and equations (1.3), (1.4) and (1.5) respectively).

$$E_{P-1} = \gamma_{P-1} \cdot 2\pi r^2(1 + \tilde{z}) \quad (1.3)$$

$$E_{P-2} = \gamma_{P-2} \cdot 2\pi r^2(1 - \tilde{z}) \quad (1.4)$$

$$E_{1-2} = -\gamma_{1-2} \cdot \pi r^2(1 - \tilde{z}^2) \quad (1.5)$$

Where  $\gamma$ 's are the corresponding surface tensions and  $\tilde{z} = Z/r$ . The total energy,  $E$ , in other words the summation of equations (1.3), (1.4) and (1.5), is scaled by  $E_{unit}$  (equation (1.6)) to give  $\tilde{E}$  (equation (1.7)).

$$E_{unit} = \pi r^2 \gamma_{1-2} \quad (1.6)$$

$$\tilde{E} = \frac{E}{E_{unit}} \quad (1.7)$$

$\tilde{E}$  can be rewritten to give the following quadratic function:

$$\tilde{E} = \tilde{z}^2 + 2(a - b)\tilde{z} + 2a + 2b - 1 \quad (1.8)$$

Where  $a = \gamma_{P-1}/\gamma_{1-2}$  and  $b = \gamma_{P-2}/\gamma_{1-2}$ . From this a parabola of energy profile versus particle displacement ( $z$ ) from the interface can be plotted where the minimum,  $\tilde{E}_{min}$ , at a particular  $z$  value can be used to calculate the energy barrier for the particle to escape into either phase 1 or 2 (Figure 1.9 and equations (1.9) and (1.10)).



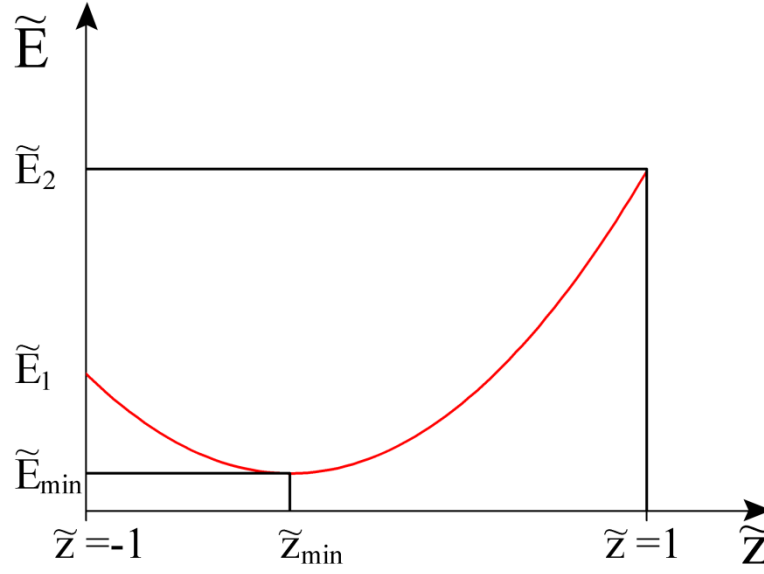


**Figure 1.9** Potential energy profile of a solid particle leaving the  $\phi_1/\phi_2$  interface and moving into either  $\phi_1$  ( $\tilde{E}_1$ ) or  $\phi_2$  ( $\tilde{E}_2$ ). Where  $\tilde{z}_{min}$  is the vertical coordinate of the centre of the particle, C.

$$\Delta\tilde{E}_1 = \tilde{E}_1 - \tilde{E}_{min} \quad (1.9)$$

$$\Delta\tilde{E}_2 = \tilde{E}_2 - \tilde{E}_{min} \quad (1.10)$$

Where  $\Delta\tilde{E}_1$  and  $\Delta\tilde{E}_2$  are the energies required to move the particle from the interface and into phase 1 and 2 respectively. In the case of a polystyrene sphere of a given size at the water/air interface, the energy required to remove it is of the order of  $10^6 k_B T$ .

Using Young's equation for equilibrium at the three phase contact line (equation (1.11)) it has been possible to calculate the energy required to remove the particle from the interface.

$$\gamma_{p-1} - \gamma_{p-2} = \gamma_{1-2} \cos\theta \quad (1.11)$$

Where  $\theta$  is the three phase contact angle which describes where the particle sits at the interface. The energy to remove the particle from the interface is given by:

$$E = \pi r^2 \gamma_{1-2} (1 \pm \cos\theta)^2 \quad (1.12)$$

Where the sign in the bracket is negative if  $\theta < 90^\circ$  and the particle is removed into  $\phi_2$  and positive if  $\theta > 90^\circ$  and the particle is removed into  $\phi_1$ .<sup>44-48</sup> The

three phase contact angle also provides information similar to that of the hydrophilic-lipophilic balance (HLB) for soluble surfactants in that it can be used to determine the type of solid stabilized emulsion gained (such as oil/water or water/oil). For  $\theta < 90^\circ$  solids stabilized oil-in-water emulsions may form and for  $\theta > 90^\circ$  solids stabilized water-in-oil emulsions may form. It is important to note that here oil may be replaced by air to produce the corresponding solids stabilized foam or aerosol. Pickering stabilization has proven to be a useful tool in the preparation of hierarchical colloidal structures (Figure 1.10), such as armoured polymer particles,<sup>49-52</sup> responsive microgel capsules<sup>53</sup> and multi-layered particles.<sup>54-56</sup>

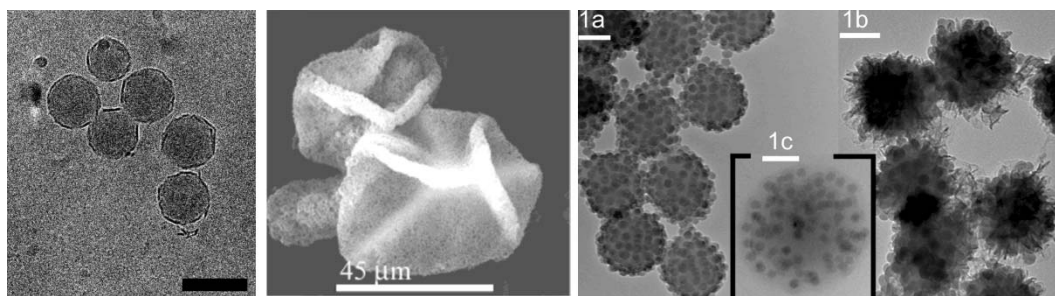


**Figure 1.10** Particles prepared utilizing Pickering stabilization: (left) Laponite armoured poly(Sty-*co*-BA) prepared by Pickering emulsion polymerization,<sup>49</sup> (middle) responsive capsule prepared by cross-linking a microgel stabilized Pickering emulsion of a sacrificial solvent (propyl acetate)<sup>57</sup> and (right) silica armoured poly(MMA) particles prepared by Pickering emulsion polymerization and said particles after encapsulation in (1b) poly(acrylonitrile) and (1c) poly(BA).<sup>54</sup>

## 1.2. Film Formation

Film formation of “soft” polymer colloids is of great importance for the coatings and adhesive industries as there is an environmental drive to greatly reduce volatile organic content (VOC) by using water-borne systems.<sup>58-60</sup> The ultimate aim is to produce homogeneous films; if weak points are present (i.e. the film is not homogeneous) the overall barrier properties of the film are reduced, resulting in a film which is vulnerable to chemical breakdown.

One consideration in film formation is the minimum film formation temperature (MFFT); the MFFT is related to the  $T_g$  of the latex polymer and crudely

determines the deformability of particles during the drying process. If film formation is conducted above the MFFT then transparent, homogenous films can be formed, if below the MFFT the films are likely to be cracked or turbid (this can be overcome by the addition of coalescing agent such as volatile organic solvents). Water from the continuous phase can have a plastifying effect, lowering the MFFT to below the  $T_g$  of the dry polymer.<sup>61</sup> The film formation from water-borne latexes consists of three stages (Figure 1.11).

Stage 1 is water evaporation; as the water evaporates the particle concentration increases and the particles become close in proximity. Water evaporation occurs largely from the edges of the dispersion creating a transition zone separating the dry regions from the wet. The water evaporates at a constant rate as it takes place preferentially at the dry/wet boundary.

Stage 2 is particle deformation; spherical particles are deformed into polyhedral cells, if deformation is isotropic then the cells are formed in to a face-centred cubic or hexagonally close packed array. In some cases particle deformation can precede contact, in these cases the capillary and osmotic pressures overcome the internal stresses in the latex causing the deformation.<sup>61, 62</sup> In either case void-free transparent films can be formed. If the particles are hard rather than soft, particle deformation does not occur and colloidal crystals are formed, which often display excellent optical properties due to Bragg diffraction if monodisperse and below an micron in size.<sup>63, 64</sup>

Stage 3 is polymer inter-diffusion; this is the final stage of film formation, polymer chains diffuse between the particle boundaries, resulting in a homogenous film.<sup>65</sup> To achieve a homogenous film the inter-diffusion distance of the polymer chains should be comparable to the radius of gyration of the latex particle.<sup>66</sup> It should

be noted that in cases where surfactants have been used, the surfactant may remain at the original particle boundary even after polymer inter-diffusion, resulting in interstitial weak points in the film.<sup>67</sup>

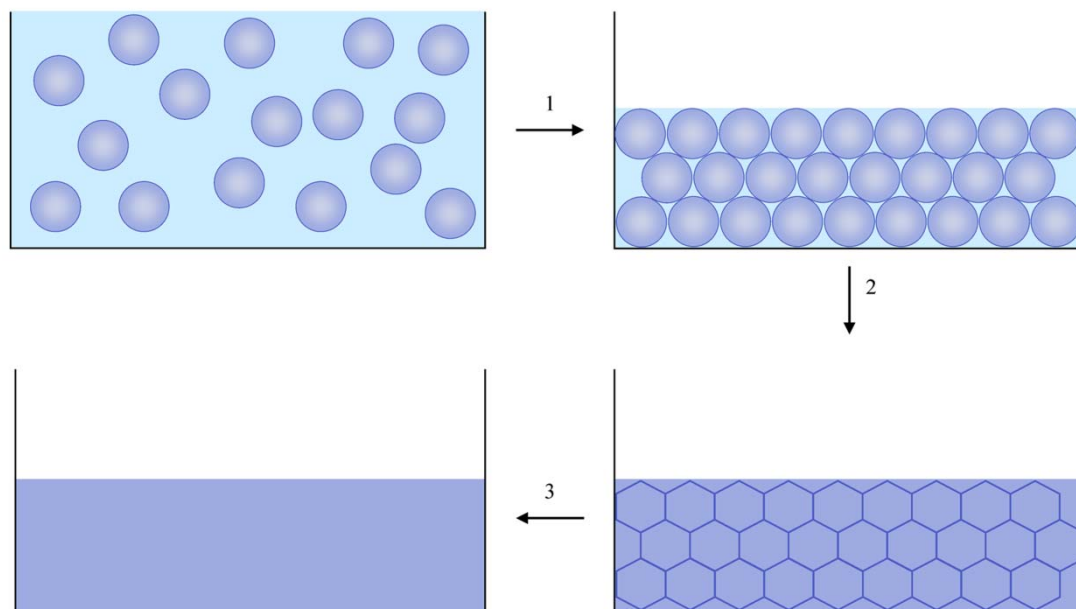


**Figure 1.11** Schematic of water-borne polymer film formation from colloidal particle latexes, where 1 is water evaporation, 2 is particle deformation and 3 is polymer inter-diffusion.

### 1.3. Stabilization of Colloids

Colloids can be divided into two categories, lyophilic and lyophobic, where lyo denotes the continuous phase the colloids exist in. Lyophilic colloids, such as microgels, are thermodynamically stable and thus there is no driving force for aggregation. On the other hand lyophobic colloids, such as poly(styrene) in water, are thermodynamically unstable, though they can be made metastable for long periods of time by erecting an energy barrier of sufficient height to prevent aggregation. Aggregation occurs from a combination of particle-particle collisions driven by Brownian motion (also known as thermal motion) and attractive (van der Waals) forces between the particles. Here we discuss how lyophobic colloids can be made metastable through electrostatic and steric stabilization.

### 1.3.1. Electrostatic stabilization

Particles can be stabilized by introducing a surface charge from bound ionic groups such as sulphate groups from an initiator or adsorbed ionic surfactants. The surface charge can be anionic or cationic, for simplicity we shall use anionic charge in this discussion, though cationic charge works in the same manner. The stabilization is more complex, however, than the simple repulsion of similarly charged species. An electrical double layer surrounds the particles, with an equal number of counter-ions (e.g.  $\text{Na}^+$ ,  $\text{K}^+$  or  $\text{NH}_4^+$ ) located in the vicinity of the surface ions and a diffuse layer of moving ions outside that layer.

A model to characterize the repulsive free energy between electrostatically stabilized lyophobic particles was developed by two groups independently Derjaguin and Landau<sup>68</sup> and, Verwey and Overbeek;<sup>69-71</sup> the theory was named after each by taking their last initial to give “DLVO”. DLVO theory combines van der Waals attractions and double layer repulsion. When two charged particles approach each other as a result of Brownian motion, their diffuse electrical layers overlap resulting in a higher ionic concentration between the particles than elsewhere. As a result, the free energy of the system is increased, either in terms of electrochemical potential or the increase in osmotic pressure bringing in solvent, leading to the particles being pushed apart. Figure 1.12 illustrates the combination of the van der Waals attraction with the electric double layer and Born repulsion potentials as a function of distance between the two particles. Two minima are present and  $V_{\text{max}}$  is the energy barrier; the primary minimum is a result of van der Waals attraction, which is very strong at short distances and Born repulsion, this minima is so deep that the reverse process of separating the particles is considered to be infinite. In some cases a shallow secondary minimum is present, it describing reversible flocculation.

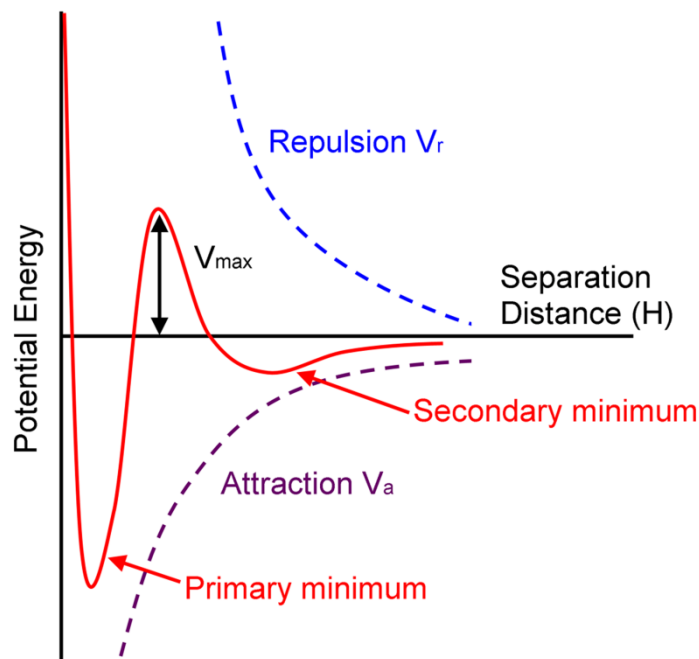


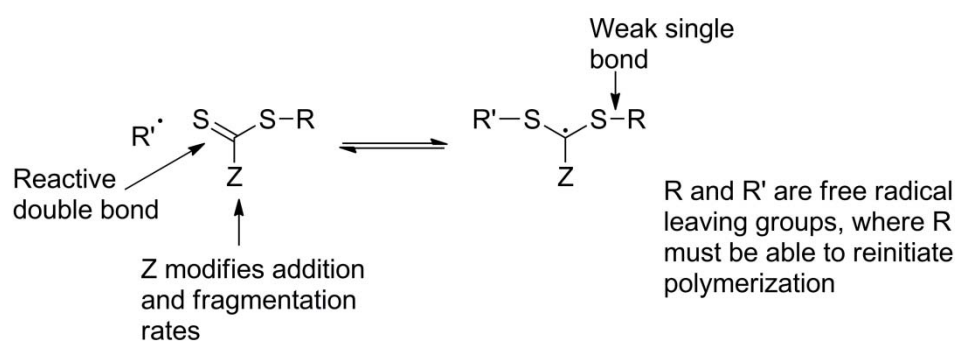
**Figure 1.12** Scheme representing the total potential energy (—) from adding the van der Waals attraction potential ( $V_a$ ) and the electrostatic and Born repulsion potentials ( $V_r$ ) as a function of distance between two spherical particles.

### 1.3.2. Steric stabilization

Steric stabilization of carbon black particles was first reported by van der Waarden<sup>72</sup> in 1950, and was later fully established for colloidal systems by Napper.<sup>73-77</sup> Steric stabilization is often achieved by the adsorption of non-ionic, normally hydrophilic or amphiphilic macromolecules, to the particle surface. Interaction only occurs when the outermost segment of the adsorbed layers begin to overlap. As the particles are brought closer together, the concentration of polymer units increases, resulting in entropic compression of polymer chains and an increase in osmotic pressure which drive particle separation. Steric stabilization of colloids is commonly used in industry, where the polymeric stabilizer acts as an anti-caking/suspending agent and can, in some instances, provide favourable properties on film formation. It is an effective stabilization mechanism for non-aqueous systems or in aqueous systems where the electric double layer is suppressed.

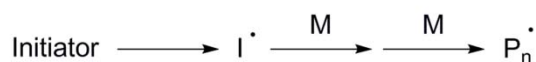
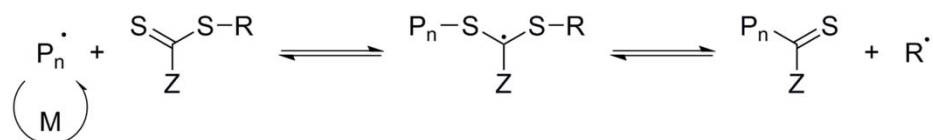
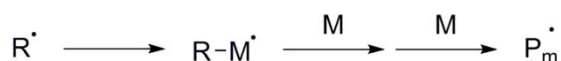
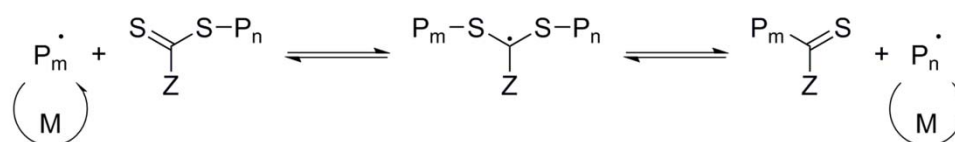
## 1.4. RAFT Polymerization

Reversible addition-fragmentation chain transfer (RAFT) polymerization was first reported by Moad and co-workers in 1998.<sup>78</sup> RAFT polymerization uses a thiocarbonylthio chain transfer agent of the formula  $\text{RSC}(\text{Z})=\text{S}$  to facilitate the polymerization, where  $\text{C}=\text{S}$  is a reactive double bond, R is a leaving group that can reinitiate polymerization and Z alters the electronics of the RAFT agent (Figure 1.13). The Z group can be chosen to activate or deactivate the  $\text{C}=\text{S}$  bond of the RAFT agent and modify the stability of the intermediate radicals.

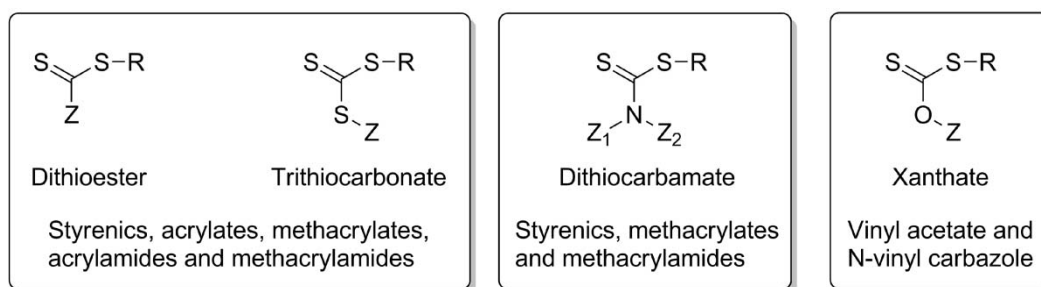


**Figure 1.13** Structural features of thiocarbonylthio RAFT agent and the intermediate formed on radical addition. Recreated from <sup>79</sup>.

The mechanism of RAFT is thought to proceed as follows (Figure 1.14).<sup>80</sup> A radical formed from an initiator species reacts with monomer to yield a propagating radical  $\text{P}_n\cdot$ ; addition of  $\text{P}_n\cdot$  to the thiocarbonylthio compound ( $\text{RSC}(\text{Z})=\text{S}$ ) creates an intermediate species  $\text{P}_n\text{SC}^\bullet(\text{Z})\text{SR}$ . Fragmentation of the intermediate provides a new polymeric thiocarbonylthio compound ( $\text{P}_n\text{SC}(\text{Z})=\text{S}$ ) and a new radical  $\text{R}^\cdot$ ; reaction of  $\text{R}^\cdot$  with monomer forms a new propagating radical  $\text{P}_m\cdot$ . Rapid equilibrium of propagating radicals  $\text{P}_n\cdot$  and  $\text{P}_m\cdot$  and dormant thiocarbonylthio compounds provides equal opportunity for all chains to grow, yielding narrow dispersity polymers. On completion of the polymerization most of the chains retain their thiocarbonylthio end group, which often be modified to yield  $\omega$ -functionalized polymers.<sup>81, 82</sup>

**Initiation****Reversible chain transfer/propagation****Reinitiation****Chain equilibration/propagation****Termination****Figure 1.14** Mechanism of RAFT polymerization.

RAFT agents can be tuned to polymerize a variety of monomers. There are four main types of RAFT agents: dithioesters, trithiocarbonate, dithiocarbamates and xanthates (Figure 1.15). Each type of RAFT agent is used for polymerizing different monomers due to differing Z groups. The choice of RAFT agents based on experimental data has been summarized within review articles.<sup>79, 80, 83</sup>

**Figure 1.15** Types of RAFT agent and monomers they are suitable to polymerize.



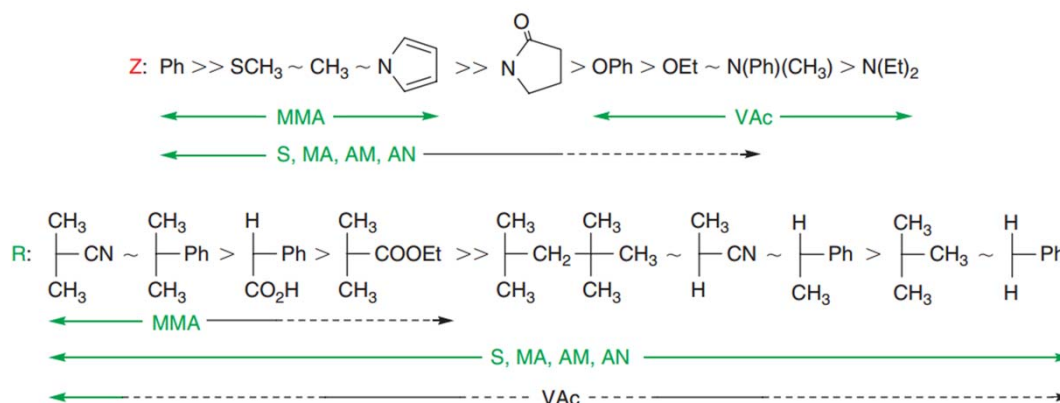


**Figure 1.16** Selection guidelines of RAFT agents for various monomers. For Z, from left to right; addition rates decrease and fragmentation rates increase. For R, from left to right; fragmentation rates decrease. Dashed lines illustrate partial control (i.e. control of molecular weight but not dispersity or retardation for VAc).<sup>80</sup>

## 1.5. Scope and Outline of Thesis

In **chapter 2** we discuss the encapsulation of sub-micron calcium carbonate particles by starved-feed emulsion polymerization. We approach particle encapsulation in two steps; (1) formation of an initial cross-linked shell to kinetically trap the core and (2) shell thickness. We further demonstrate the potential to use calcium carbonate as a sacrificial template for micron-sized rattle-like structures.

In **chapter 3** we synthesize encapsulated sub-micron calcium carbonate particles with pendant vinyl groups from which we discuss modification by thiol-ene Michael addition. On demonstration of Michael addition we synthesize poly(styrene) by RAFT polymerization to yield thiol  $\omega$ -functionalized polymers which can be clicked to these particles to illustrate the ability to tune surface properties.

In **chapter 4** we prepare microgels from the monomers used in Chapter 2 and 3 in the absence of the calcium carbonate core. We discuss their responsive behaviour and ability to form gels and act as responsive Pickering stabilizers. We also use these microgels as models to further investigate the encapsulation method described in Chapter 2 and issues arisen concerning pendant vinyl groups in Chapter 3.

In **Chapter 5**, continuing with the encapsulation theme, we discuss the synthesis of multi-layered particles templated on Laponite armoured soft particles. We investigate how the film properties are affected by the morphology of these sub-micron particles.

## 1.6. References

1. Arshady, R. *Colloid. Polym. Sci.* **1992**, 270, 717-732.
2. Gardon, J. L. *J. Polym. Sci. A1* **1968**, 6, 623-641.
3. Gardon, J. L. *J. Polym. Sci. A1* **1968**, 6, 643-664.
4. Gardon, J. L. *J. Polym. Sci. A1* **1968**, 6, 665-685.
5. Gardon, J. L. *J. Polym. Sci. A1* **1968**, 6, 687-710.
6. Gardon, J. L. *J. Polym. Sci. A1* **1968**, 6, 2853-2857.
7. Gardon, J. L. *J. Polym. Sci. A1* **1968**, 6, 2859-2879.
8. Schork, F. J.; Luo, Y.; Smulders, W.; Russum, J.; Butté, A.; Fontenot, K. Miniemulsion Polymerization. *Advances in Polymer Science* Polymer Particles. Springer Berlin Heidelberg, 2005, 129-255.
9. Hansen, F. K.; Ugelstad, J. *J. Polym. Sci. Polym. Chem. Ed.* **1978**, 16, 1953-1979.
10. Hansen, F. K.; Ugelstad, J. *J. Polym. Sci. Polym. Chem. Ed.* **1979**, 17, 3033-3045.
11. Hansen, F. K.; Ugelstad, J. *J. Polym. Sci. Polym. Chem. Ed.* **1979**, 17, 3047-3067.
12. Fitch, R. M. *Brit. Poly. J.* **1973**, 5, 467-483.
13. Harkins, W. D. *J. Am. Chem. Soc.* **1947**, 69, 1428-1444.
14. Smith, W. V.; Ewart, R. H. *J. Chem. Phys.* **1948**, 16, 592-599.
15. Roe, C. P. *Ind. Eng. Chem.* **1968**, 60, 20-33.
16. Thickett, S. C.; Gilbert, R. G. *Polymer* **2007**, 48, 6965-6991.
17. Ugelstad, J.; El-Aasser, M. S.; Vanderhoff, J. W. *J. Polym. Sci. B. Polym. Lett. Ed.* **1973**, 11, 503-513.
18. Hansen, F. K.; Ugelstad, J. *J. Polym. Sci. Polym. Chem. Ed.* **1979**, 17, 3069-3082.
19. Asua, J. M. *Prog. Polym. Sci.* **2002**, 27, 1283-1346.
20. Ugelstad, J.; Hansen, F. K.; Lange, S. *Makromol. Chem.* **1974**, 175, 507-521.

21. Delgado, J.; El-Aasser, M. S.; Silebi, C. A.; Vanderhoff, J. W. *J. Polym. Sci., Part A: Polym. Chem.* **1989**, 27, 193-202.
22. Chern, C. S.; Chen, T. J. *Colloids. Surf. A* **1998**, 138, 65-74.
23. Kabalnov, A. S.; Pertzov, A. V.; Shchukin, E. D. *J. Colloid Interface Sci.* **1987**, 118, 590-597.
24. Landfester, K.; Bechthold, N.; Förster, S.; Antonietti, M. *Macromol. Rapid Commun.* **1999**, 20, 81-84.
25. Choi, Y. T.; El-Aasser, M. S.; Sudol, E. D.; Vanderhoff, J. W. *J. Polym. Sci. Polym. Chem. Ed.* **1985**, 23, 2973-2987.
26. Chamberlain, B. J.; Napper, D. H.; Gilbert, R. G. *J. Chem. Soc., Faraday Trans.* **1982**, 78, 591-606.
27. Miller, C. M.; Sudol, E. D.; Silebi, C. A.; El-Aasser, M. S. *Macromolecules* **1995**, 28, 2754-2764.
28. Miller, C. M.; Sudol, E. D.; Silebi, C. A.; El-Aasser, M. S. *Macromolecules* **1995**, 28, 2765-2771.
29. Miller, C. M.; Sudol, E. D.; Silebi, C. A.; El-Aasser, M. S. *Macromolecules* **1995**, 28, 2772-2780.
30. Tanaka, M.; Hosogai, K. *J. Appl. Polym. Sci.* **1990**, 39, 955-966.
31. Vivaldo-Lima, E.; Wood, P. E.; Hamielec, A. E.; Penlidis, A. *Ind. Eng. Chem. Res.* **1997**, 36, 939-965.
32. Trommsdorff, V. E.; Köhle, H.; Lagally, P. *Makromol. Chem.* **1948**, 1, 169-198.
33. Hohenstein, W. P.; Mark, H. *J. Polym. Sci.* **1946**, 1, 127-145.
34. Tseng, C. M.; Lu, Y. Y.; El-Aasser, M. S.; Vanderhoff, J. W. *J. Polym. Sci., Part A: Polym. Chem.* **1986**, 24, 2995-3007.
35. Barrett, K. E. J.; Thomas, H. R. *J. Polym. Sci. A1* **1969**, 7, 2621-2650.
36. Barrett, K. E. J. *Brit. Poly. J.* **1973**, 5, 259-271.
37. Shen, S.; Sudol, E. D.; El-Aasser, M. S. *J. Polym. Sci., Part A: Polym. Chem.* **1994**, 32, 1087-1100.
38. Downey, J. S.; Frank, R. S.; Li, W.-H.; Stöver, H. D. H. *Macromolecules* **1999**, 32, 2838-2844.
39. Taylor, P. *Adv. Colloid Interface Sci.* **1998**, 75, 107-163.

40. Ramsden, W. *Proc. R. Soc. Lond.* **1903**, 72, 156-164.
41. Pickering, S. U. *J. Chem. Soc., Trans.* **1907**, 91, 2001-2021.
42. Finkle, P.; Draper, H. D.; Hildebrand, J. H. *J. Am. Chem. Soc.* **1923**, 45, 2780-2788.
43. Pieranski, P. *Phys. Rev. Lett.* **1980**, 45, 569-572.
44. Clint, J. H.; Taylor, S. E. *Colloids Surfaces* **1992**, 65, 61-67.
45. Binks, B. P.; Clint, J. H. *Langmuir* **2002**, 18, 1270-1273.
46. Binks, B. P. *Curr. Opin. Colloids Interface Sci.* **2002**, 7, 21-41.
47. Xu, H.; Melle, S.; Golemanov, K.; Fuller, G. *Langmuir* **2005**, 21, 10016-10020.
48. Levine, S.; Bowen, B. D.; Partridge, S. J. *Colloids Surfaces* **1989**, 38, 325-343.
49. Teixeira, R. F. A.; McKenzie, H. S.; Boyd, A. A.; Bon, S. A. F. *Macromolecules* **2011**, 44, 7415-7422.
50. Bon, S. A. F.; Colver, P. J. *Langmuir* **2007**, 23, 8316-8322.
51. Bourgeat-Lami, E.; Lansalot, M. *Organic/Inorganic Composite Latexes: The Marriage of Emulsion Polymerization and Inorganic Chemistry Hybrid Latex Particles* Springer Berlin / Heidelberg, 2011, 53-123.
52. Colard, C. A. L.; Teixeira, R. F. A.; Bon, S. A. F. *Langmuir* **2010**, 26, 7915-7921.
53. Croll, L. M.; Stöver, H. D. H. *Langmuir* **2003**, 19, 10077-10080.
54. Colver, P. J.; Colard, C. A. L.; Bon, S. A. F. *J. Am. Chem. Soc.* **2008**, 130, 16850-16851.
55. Li, J.; Hitchcock, A. P.; Stöver, H. D. H. *Langmuir* **2010**, 26, 17926-17935.
56. Li, J.; Stöver, H. D. H. *Langmuir* **2010**, 26, 15554-15560.
57. Croll, L. M.; Stöver, H. D. H.; Hitchcock, A. P. *Macromolecules* **2005**, 38, 2903-2910.
58. Weiss, K. D. *Prog. Polym. Sci.* **1997**, 22, 203-245.
59. Jotischky, H. *Surf. Coating Int. B: Coating Trans.* **2001**, 84, 11-20.

60. Wang, T.; Lei, C. H.; Dalton, A. B.; Creton, C.; Lin, Y.; Fernando, K. A. S.; Sun, Y. P.; Manea, M.; Asua, J. M.; Keddie, J. L. *Adv. Mater.* **2006**, 18, 2730-2734.
61. Winnik, M. A. *Curr. Opin. Colloids Interface Sci.* **1997**, 2, 192-199.
62. Tirumkudulu, M. S.; Russel, W. B. *Langmuir* **2004**, 20, 2947-2961.
63. Velev, O. D.; Lenhoff, A. M.; Kaler, E. W. *Science* **2000**, 287, 2240-2243.
64. Pusey, P. N.; van Megen, W. *Nature* **1986**, 320, 340-342.
65. Steward, P. A.; Hearn, J.; Wilkinson, M. C. *Adv. Colloid Interface Sci.* **2000**, 86, 195-267.
66. Mohammadi, N.; Klein, A.; Sperling, L. H. *Macromolecules* **1993**, 26, 1019-1026.
67. Chevalier, Y.; Pichot, C.; Graillat, C.; Joanicot, M.; Wong, K.; Maquet, J.; Lindner, P.; Cabane, B. *Colloid. Polym. Sci.* **1992**, 270, 806-821.
68. Deryagin, B.; Landau, L. *Acta Physicochimica U.R.S.S* **1941**, 14, 633-662.
69. Verwey, E. J. W. *J. Phys. Chem.* **1947**, 51, 631-636.
70. Overbeek, J. T. G. *J. Colloid Interface Sci.* **1977**, 58, 408-422.
71. Verwey, E. J. W.; Overbeek, J. T. G. *Theory of the Stability of Lyophobic Colloids* Elsevier Pub. Co., New York, 1948.
72. van der Waarden, M. *J. Colloid Sci.* **1950**, 5, 317-325.
73. Napper, D. H. *J. Colloid Interface Sci.* **1969**, 29, 168-170.
74. Napper, D. H. *J. Colloid Interface Sci.* **1970**, 32, 106-114.
75. Napper, D. H. *J. Colloid Interface Sci.* **1970**, 33, 384-392.
76. Napper, D. H.; Netschey, A. *J. Colloid Interface Sci.* **1971**, 37, 528-535.
77. Napper, D. H. *J. Colloid Interface Sci.* **1977**, 58, 390-407.
78. Chiefari, J.; Chong, Y. K. B.; Ercole, F.; Krstina, J.; Jeffery, J.; Le, T. P. T.; Mayadunne, R. T. A.; Meijs, G. F.; Moad, C. L.; Moad, G.; Rizzardo, E.; Thang, S. H. *Macromolecules* **1998**, 31, 5559-5562.
79. Moad, G.; Rizzardo, E.; Thang, S. H. *Aust. J. Chem.* **2009**, 62, 1402-1472.
80. Moad, G.; Rizzardo, E.; Thang, S. H. *Aust. J. Chem.* **2005**, 58, 379-410.

81. Willcock, H.; O'Reilly, R. K. *Polym. Chem.* **2010**, 1, 149-157.
82. Moad, G.; Rizzardo, E.; Thang, S. H. *Polym. Int.* **2011**, 60, 9-25.
83. Moad, G.; Rizzardo, E.; Thang, S. H. *Aust. J. Chem.* **2006**, 59, 669-692.

# Chapter 2: Particle Encapsulation by Starved-Feed Emulsion Polymerization

---

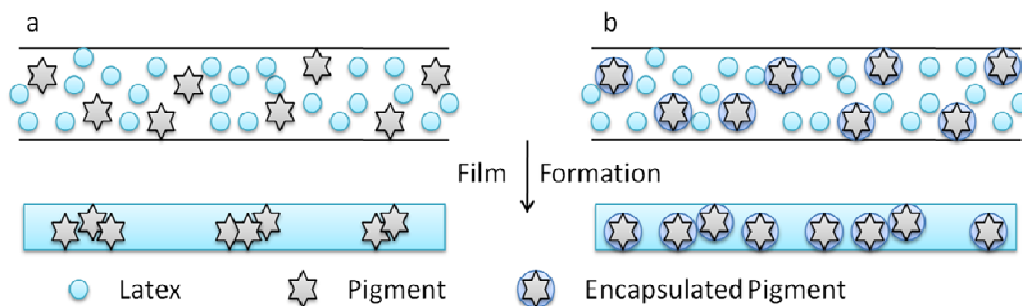
## 2.1. Abstract

We demonstrate a versatile method to encapsulate calcium carbonate particles with a shell of polymer by means of a conventional free radical emulsion polymerization process. Our strategy relies on the encapsulation of the pigment particles with a thin primer layer of cross-linked poly(acrylate). Starved-fed addition and emulsion polymerization of di(ethylene glycol) diacrylate and methacrylic acid, allows the uniform decoration of the pigment particles with the polymer primer shell. We demonstrate efficient encapsulation of calcium carbonate, from which we produce hollow particles. The thickness of the polymer shell can easily be controlled, which we demonstrate with sequential seeded polymerization of methyl methacrylate under starved fed conditions.



## 2.2. Introduction

When small pigment particles are dispersed into a polymer matrix to form a nanocomposite material, synergistic properties are often achieved. For these combined properties in materials the encapsulation of particles has been of great interest, particularly in the coatings industry. Waterborne coatings have multiple constituents, the most important being the binder (soft latex particles) and the pigment. Typical inorganic pigments include titanium dioxide and calcium carbonate, organic pigments such as phthalocyanine blue and carbon black are also used. In the area of waterborne decorative coatings pigments are required to achieve high opacity and hiding power in order to conceal the underlying surface. An even distribution of pigment particles throughout the polymer latex based film is desired to maximize scattering efficacy. A considerable problem, however, is that particles such as titanium dioxide and calcium carbonate tend to aggregate upon film formation. One underlying reason is the high Hamaker constant resulting in a strong attractive interaction between the colloids.<sup>1</sup> The clustering of pigment dramatically reduces the quality of the coating, with detrimental effects on mechanical robustness, water uptake resistance, an increase in film roughness and marked reduction in opacity as a result of pigment clusters similar light scattering ability to one pigment particle.<sup>2, 3</sup> One method to overcome agglomeration of pigments is to coat individual particles with a shell of polymer, providing a steric spatial exclusion zone (Scheme 2.1). This prevents the particles from forming “tight” clusters, whilst concurrently providing the ability to tune the compatibility/wettability with the polymer matrix. Encapsulating pigment particles in a water based systems remains a challenge.<sup>4-7</sup> Herein we describe the numerous strategies which have been employed.



**Scheme 2.1** Illustration of (a) the clustering of pigment particles on film formation and (b) the prevention of pigment clustering on film formation by the spatial exclusion zone provided by polymer shell around the pigment.

### 2.2.1. Layer-by-layer deposition of oppositely charged electrolytes

One approach to encapsulate particles in a polymer shell demonstrated by Caruso *et al.* is the sequential layer-by-layer (LbL) deposition of oppositely charged polyelectrolytes, such as negatively charged poly(styrene sulfonate) and positively charged poly(allylamine hydrochloride).<sup>8, 9</sup> A thin polymer shell is slowly built up around the particles and is stable enough to form hollow structures; this method has been used to encapsulate sacrificial calcium carbonate particles for drug delivery applications.<sup>10-13</sup> The requirement of several cleaning cycles between each deposition step makes this a laborious technique. Caruso and co-workers modified this approach to eliminate the cleaning cycles, by using electrophoretic polymer assembly; immobilised particles in an electrophoretic cell were coated by sequential addition of polyelectrolytes.<sup>14</sup> In sequential steps anionic polyelectrolytes flow from wells adjacent to the cathode to the anode and cationic polyelectrolytes flow from wells adjacent to the anode to the cathode. Immobilization of the particles removes the necessity of centrifugation cycles, though heating is required to recover the particles. Although efficient in that the method of LbL coats all particles, the drawbacks include; dilute concentrations, the slow increase in polymer shell thickness intrinsic to the LbL approach, and the laborious cleaning cycles required.

### 2.2.2. Heterocoagulation of oppositely charged particles

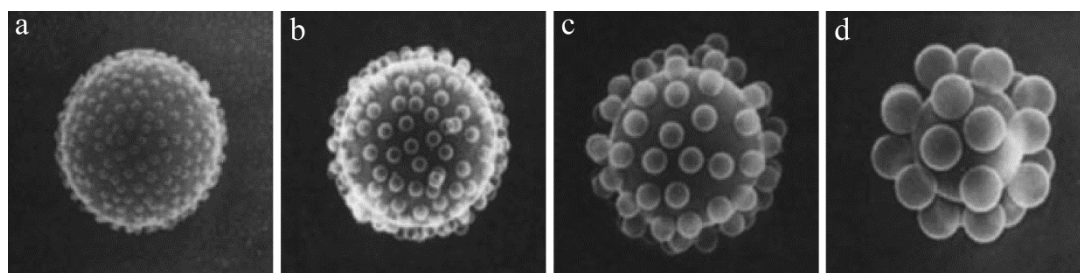


**Figure 2.1** TFFDSEM (thin-film freeze-drying scanning electron microscope) images of various anionic small polymer latexes of different sizes adsorbed onto larger particles. Poly(vinyl chloride) latex of (a) 116 nm, and polystyrene particles (b) 180 nm, (c) 320 nm and (d) 696 nm assembled onto a large cationic polystyrene latex of 2170 nm by heterocoagulation in 0.5 mM KCl background electrolyte.<sup>15</sup>

Similar to the layer-by-layer approach, heterocoagulation of oppositely charged particles can be used to achieve hierarchical structures. Typically, smaller particles are adsorbed onto larger particles to create a raspberry like morphology. Hogg, Healy and Fuerstenau developed the HHF theory<sup>16</sup> that describes the interaction of two particles of different sizes; this was later found to provide good results for systems of dissimilar particles with particles of opposite charges and the same charge.<sup>17</sup> Vincent and co-workers produced raspberry-like structures with beautiful symmetry by heterocoagulating small anionic latex particles onto larger cationic latex particles (Figure 2.1).<sup>15, 18</sup> Particle encapsulation can be achieved through the heterocoagulation of latex particles onto inorganic particles; this has been demonstrated for the encapsulation of silica<sup>19, 20</sup> and gibbsite clay.<sup>21</sup> Controlled heterocoagulation provides a simple and thorough encapsulation method, however low concentrations must be used, cleaning cycles by centrifugation are required to remove excess non-coagulated latex particles and there is little control over shell thickness as it is dependent on the latex size.

### 2.2.3. Particle encapsulation by emulsion polymerization

A more efficient process would be to encapsulate by an *in situ* approach such as emulsion polymerization; this allows for higher solids content than the LbL and heterocoagulation techniques and it is easier to scale. Conceptually this method seems straightforward, in practice however, it is more complex. Haga *et al.* demonstrated, in the encapsulation of titanium dioxide particles, that initiator, pigment surface, monomer concentrations and pH have a profound influence on the encapsulation process, thus rendering it a sensitive method.<sup>22</sup>

Maintaining particle dispersion throughout the polymerization is also a problem; the use of surfactants to disperse particles and prime their surface to enhance affinity for polymer deposition is common.<sup>23</sup> Templeton-Knight and co-workers combined non-ionic surfactants with agitation provided by a sonic bath to encapsulate titanium dioxide particles in poly(methyl methacrylate-*co*-methacrylic acid-*co*-ethylene glycol dimethacrylate).<sup>24</sup> A thin polymeric shell was produced, though TEM analysis suggests that particle dispersion remained an issue. However, these additives often lead to deteriorative properties in the final nanocomposite material, for example through surfactant migration. One strategy that restricts the latter is the use of polymerizable surfactants; use of surfmers to achieve encapsulation has been illustrated by Tian and co-workers in the encapsulation phthalocyanine blue.<sup>25, 26</sup> Closely related and achieving similar results is the adsorption of initiator molecules (coined inisurfs) onto the surface of the target pigment particles to aid the build-up of a polymer shell, illustrated by Bourgeat-Lami and co-workers in the encapsulation of silica nanoparticles.<sup>27, 28</sup> An alternative approach is to adjust the wettability of the pigment surface to promote polymer deposition by pre-modifying its surface. Dos Santos and co-workers encapsulated

titanium dioxide particles by emulsion polymerization of methyl methacrylate by initially chemically modifying the surface of the titanium dioxide particles hydrophobically with a stearate functionalised titanate.<sup>29</sup> However, encapsulation efficiency defined as amount of pigment encapsulated was found to be below 10 %. Similar results were achieved by Wang *et al.* by adsorbing monomer functionalized titanates to titanium dioxide particles prior to encapsulation.<sup>30</sup> Strategies using surfactants and dispersants are of great concern due to reduced efficiency; the term efficiency means covering all pigment particles with a shell of polymer, and preventing the occurrence of secondary nucleation, that is the formation of ordinary polymer latex particles alongside the encapsulated pigments.

#### **2.2.4. Particle encapsulation by miniemulsion polymerization**

Miniemulsion polymerization has also proven a popular tool in encapsulation of particles. Bourgeat-Lami and co-workers demonstrated that encapsulation of the hydrophobic pigments such as phthalocyanine blue (Figure 2.2 1), are relatively simple by miniemulsion polymerization; the hydrophobic nature of the pigment drives the particle into the monomer droplets which, upon initiation, are polymerized.<sup>31, 32</sup> However, monomer compatibility with the particle was an issue; encapsulation in styrene was successful, whereas attempts to encapsulate phthalocyanine blue in methyl methacrylate, butyl acrylate and vinyl acetate polymers proved fruitless. Landfester *et al.* further illustrated the effectiveness of miniemulsion polymerization as a tool to encapsulate hydrophobic pigments, demonstrated in the encapsulation of azo pigment yellow and quinacridone pigment violet (Figure 2.2 2 and 3 respectively) in poly(styrene).

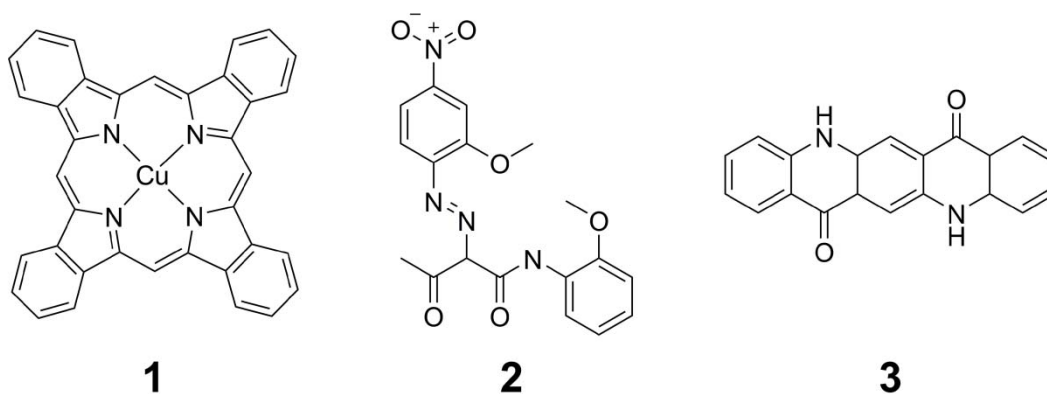


**Figure 2.2** (1) Phthalocyanine blue, (2) azo pigment yellow and (3) quinacridone pigment violet.

Contrastingly, encapsulation of hydrophilic particles by miniemulsion polymerization has proven to be more difficult; surface modification prior to polymerization is required. El-Aasser *et al.* encapsulated titanium dioxide particles in poly(styrene) by modifying the titania surface with hydrophobic amine functionalized polymers.<sup>33-36</sup> Encapsulation efficiency was found to be strongly dependent on the concentration of the stabilizer and on TiO<sub>2</sub> particle size; higher concentrations of stabilizer and smaller particle sizes (below 50 nm) lead to higher encapsulation content of titanium dioxide particles. Where larger titania particles or lower concentrations of stabilizer were used, bare titanium dioxide particles were found. Bourgeat-Lami and co-workers showed that surface modification of silica particles with monomer functionalized silanes yielded encapsulated particles on miniemulsion polymerization of methyl methacrylate, however TEM analysis highlighted that many secondary particles without a silica core were also produced (Figure 2.3).<sup>37</sup> Encapsulation of calcium carbonate particles modified by stearic acid by Antonietti and co-workers, again illustrated the requirement to hydrophobically modify the surface of the inorganic particle, however once again empty polymer particles were also formed.<sup>38</sup> Encapsulation by miniemulsion polymerization suffers

from similar problems to emulsion polymerization; not all pigment particles have a shell of polymer, and secondary nucleation is common.

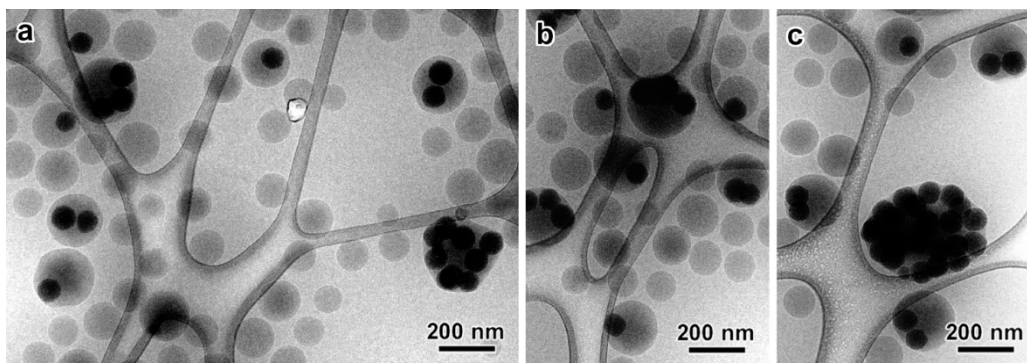


**Figure 2.3** Cryo-TEM images of silica particles encapsulated in poly(MMA-*co*-BA) with (a) 3.5, (b) and (c) 20 wt.% silica content.<sup>37</sup>

### 2.2.5. Particle encapsulation by dispersion polymerization

Particle encapsulation has also been achieved by dispersion polymerization. Bourgeat-Lami *et al.* demonstrated encapsulation of silica beads by dispersion polymerization of styrene in an ethanol-water (95:5 wt.%) medium.<sup>39</sup> The silica was modified with a monomer functionalized silane to promote encapsulation over surface stabilization. Bourgeat-Lami and co-workers also found that particle size effected the encapsulation; for the encapsulation of silica in poly(styrene), silica particles smaller than 200 nm in diameter yielded multiple encapsulations, whereas above 200 nm polymer particles containing 1 or 0 silica particles were found.<sup>40</sup> An and co-workers encapsulated titanium dioxide particles in a poly(styrene-*co*-divinylbenzene) by dispersion polymerization in a methanol medium containing PVP, however, low wt.% (1-2 %) of titanium dioxide were required for a successful encapsulation, rendering this method unfeasible for scaling up.<sup>41, 42</sup> Huang and co-workers demonstrated the encapsulation of calcium carbonate nano-particles by the dispersion polymerization of styrene maleic anhydride in a methanol-water mixture; incorporation of maleic anhydride increased encapsulation of the particles through interactions of C=O groups of maleic anhydride on the CaCO<sub>3</sub> surface.<sup>43</sup> Dispersion



polymerizations typically produce particles greater than a micron,<sup>44</sup> therefore it is an unsuitable method for the encapsulation of single particles in the sub-micron region.

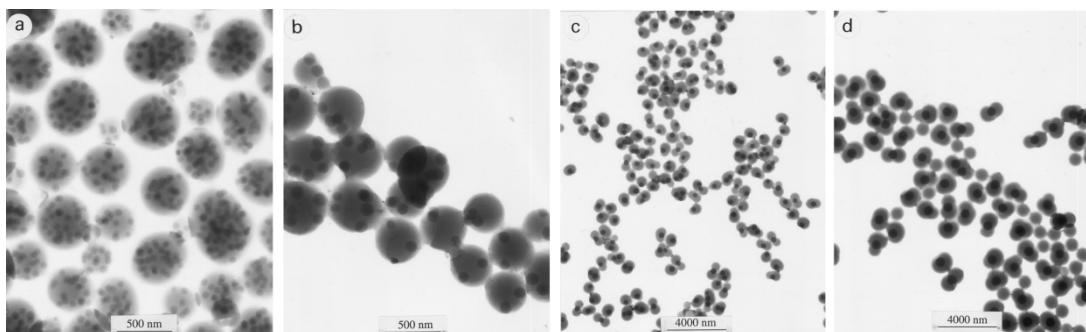


**Figure 2.4** TEM image of encapsulated silica particles of sizes (a) 72, (b) 120, (c) 352 and (d) 629 nm in diameter in poly(styrene).<sup>40</sup>

### 2.2.6. Particle encapsulation by precipitation polymerization

Encapsulation of particles by precipitation polymerization has also been shown. Bon *et al.* selectively decorated Lycopodium spores by precipitation polymerization of divinylbenzene in acetonitrile (Figure 2.5).<sup>45</sup> Magnetic  $\text{Fe}_3\text{O}_4$  particles were encapsulated by precipitation polymerization by initially grafting methacrylate functionalized silanes to the surface then encapsulating in poly(methacrylic acid) and *N,N'*-methylenebisacrylamide in acetonitrile.<sup>46</sup> This method is very successful as no secondary latex particles are formed and all particles are encapsulated. This has not been demonstrated in water-based systems, which would be preferable.

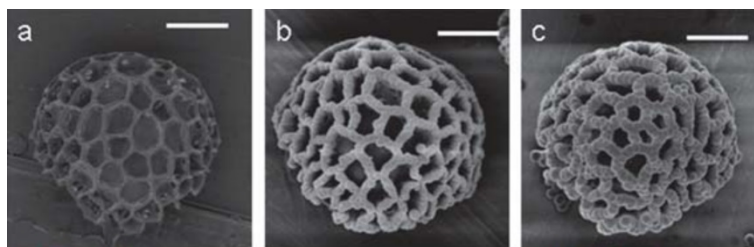


**Figure 2.5** SEM images of (a) bare Lycopodium spores, (b) and (c) spores selectively decorated with poly(DVB) (scale bar: 10µm).<sup>45</sup>



### 2.2.7. Particle encapsulation by emulsion polymerization using macro-RAFT agents

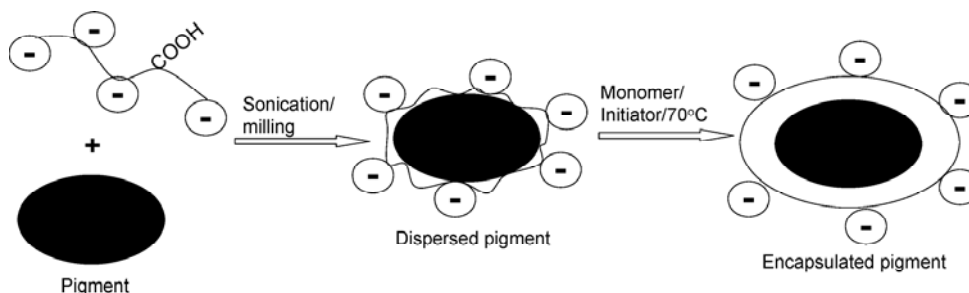


**Figure 2.6** Schematic representation of pigment dispersion and encapsulation by emulsion polymerization using a macro-RAFT agent.<sup>47</sup>

A key development, by Hawckett and co-workers, solved the two concerns of secondary nucleation and coverage of all pigment particles by using macro-RAFT agents. Macro-RAFT agents have been shown to be effective pigment dispersants,<sup>48-50</sup> this has been expanded on, to facilitate encapsulation through RAFT emulsion polymerization.<sup>47</sup> Macro-RAFT agents with acrylic acid moieties were initially employed to adhere to the surface of the pigment and aid dispersion in water-based systems. RAFT emulsion polymerization process was carried out under monomer starved-fed conditions and resulted in an efficient encapsulation (Figure 2.6). This approach has proven to be very versatile, with the ability to encapsulate a range of pigments including titanium dioxide,<sup>47</sup> phthalocyanine blue,<sup>47</sup> clay platelets,<sup>51</sup> cerium oxide,<sup>52</sup> calcium carbonate,<sup>53</sup> alumina and copper oxide<sup>54</sup> (Figure 2.7). The RAFT polymerization process, however, has a number of downsides; cost, colour and sulfur content being but a few.

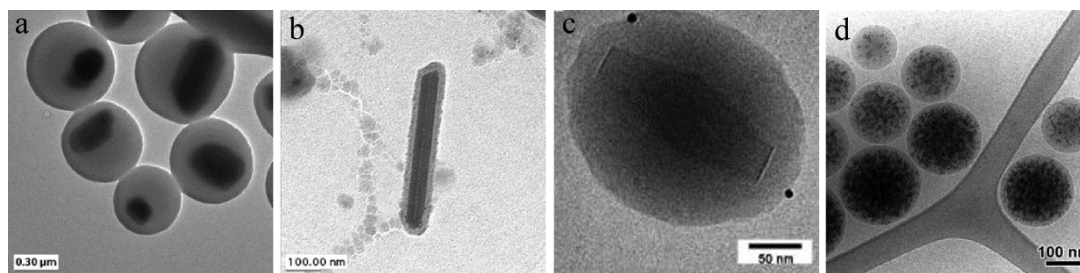


**Figure 2.7** TEM images of particles encapsulated by emulsion polymerization using macro-RAFT agents; (a) titanium dioxide,<sup>47</sup> (b) phthalocyanine blue,<sup>47</sup> (c) gibbsite platelets<sup>51</sup> and (d) cerium oxide.<sup>52</sup>

Our mission was to go back to the core question; could we devise an encapsulation method based on conventional free radical emulsion polymerization technology without the need to pre-treat the pigment particles or use surfactants? Here we show a method which achieves exactly that. The key step in our approach is that the surface of the pigment is primed with an initial layer of cross-linked polymer. This thin shell would then promote deposition of additional polymer material using free radical emulsion polymerization conditions. To fully cover the surface of the pigments with the primer: (1) its compatibility and thus wettability with the pigment surface needs to be tuned, (2) the primer layer is cross-linked to avoid potential dewetting in sequential reaction or modification steps, or in the end application (for example if the encapsulated pigments were to be used in polymer melt injection moulding or paper manufacturing). Note that in our studies we focus on the encapsulation of pigments of submicron size.

## 2.3. Results and Discussion

Herein we describe the encapsulation of sub-micron precipitated calcium carbonate particles in a polymeric shell. A protocol was devised to provide the dispersed pigment particles with a thin primer shell of heavily cross-linked polymer.

### 2.3.1. Characterization of calcium carbonate particles

SOCAL P3, a cheap, commercially available precipitated calcium carbonate of ellipsoidal morphology, was chosen to encapsulate as it is currently used as an extender in paint formulations and is thus industrially relevant. TEM and SEM analysis of the particles confirmed that the particles indeed had a “cigar shape” or ellipsoidal morphology and were sub-micron in size, with approximate width of a few hundred nm and a maximum length of 1  $\mu\text{m}$ , though it is clear that they are polydisperse (Figure 2.8 and Figure 2.9 respectively). TEM images show that the calcium carbonate particles have varying electron density and in some cases rings, this is due to the diffraction of the beam by a crystalline material producing artefacts in the image which change as the focus is adjusted.

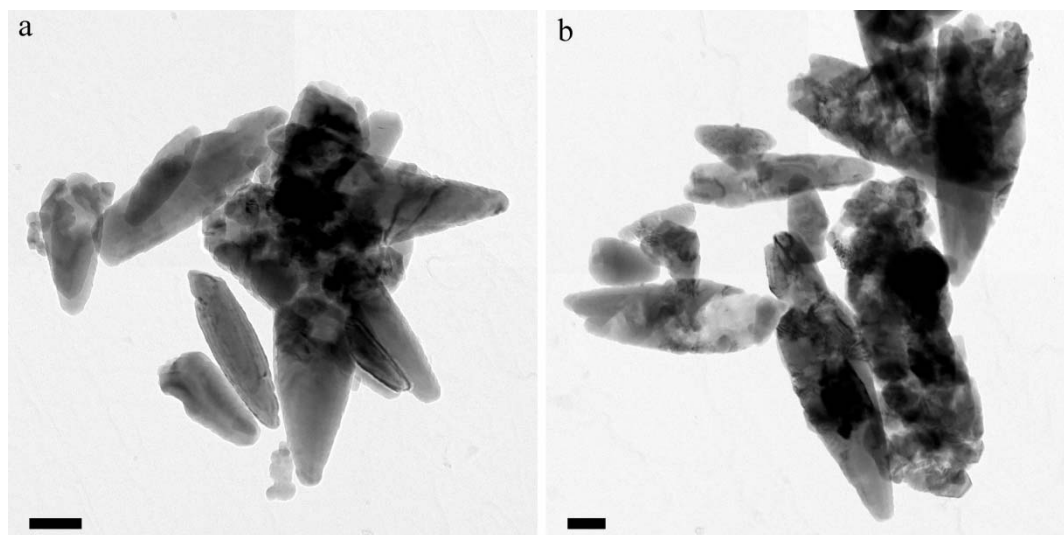


**Figure 2.8** TEM images of calcium carbonate (SOCAL P3) (scale bar: 200 nm).

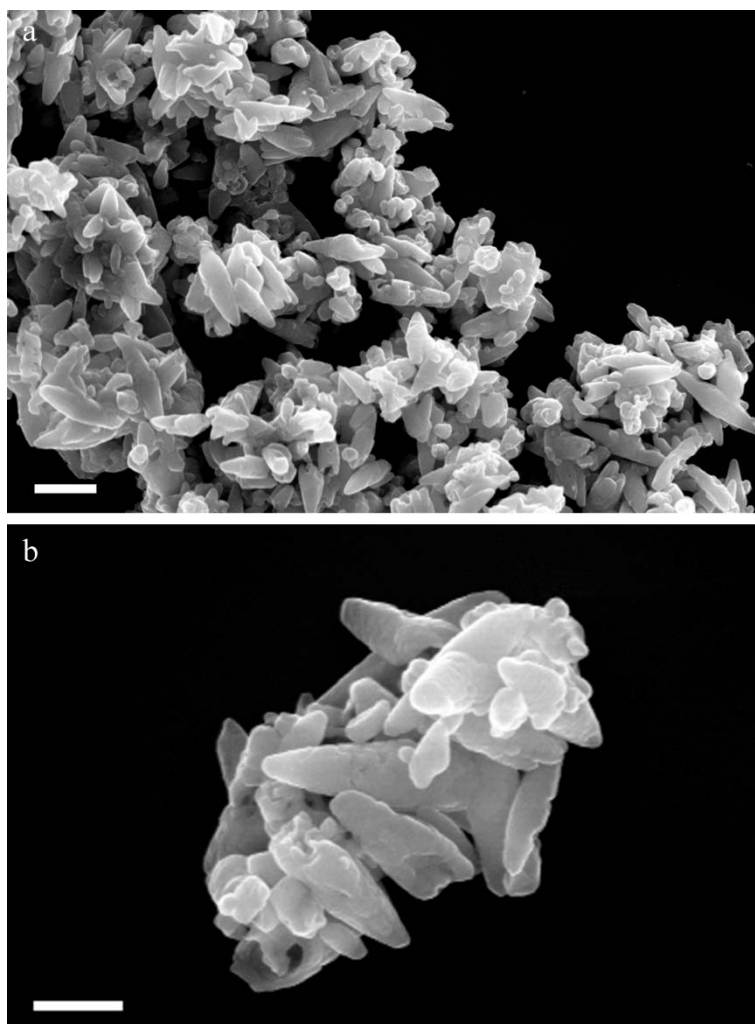


**Figure 2.9** SEM images of calcium carbonate (SOCAL P3) (scale bar: 200 nm).

Four polymorphs of calcium carbonate exist, calcite, aragonite, vaterite and amorphous, where calcite is the most abundant and stable. The polymorphs of calcium carbonate exhibit different surface structures which may affect the encapsulation approach.<sup>55</sup> Powder X-ray diffraction was used to determine the polymorph of the precipitated calcium carbonate, SOCAL P3. The analysis determined that SOCAL P3 is of the polymorph calcite (Figure 2.10), which has a rhombohedral crystal structure (Figure 2.11). Further analysis is required to determine the surface of the particles and thus the direction of the encapsulation approach.

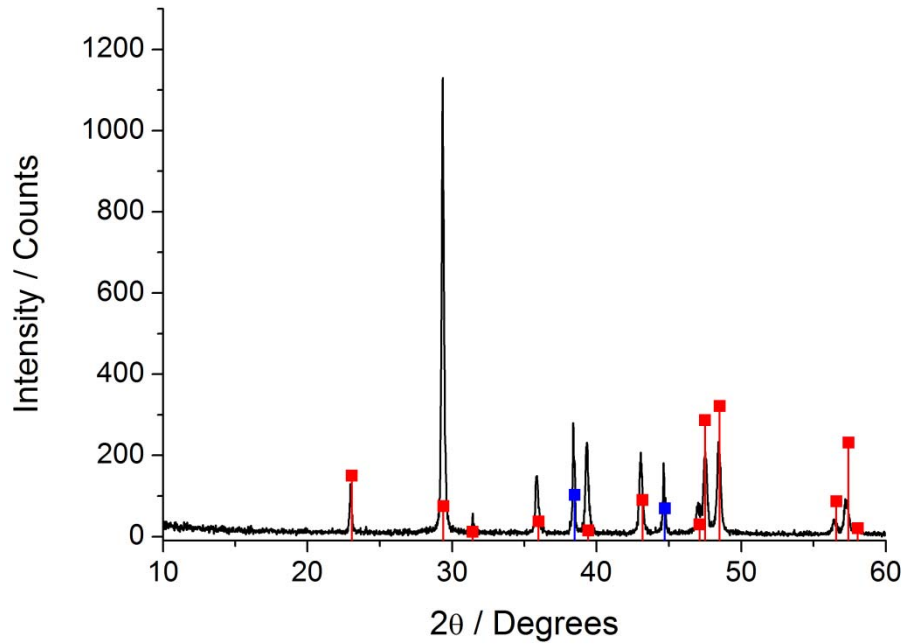


**Figure 2.10** X-ray diffraction spectra of SOCAL P3, the ■ represents the diffraction pattern of calcite and the ■ represent the diffraction of the aluminium holder, demonstrating that SOCAL P3 precipitated calcite.

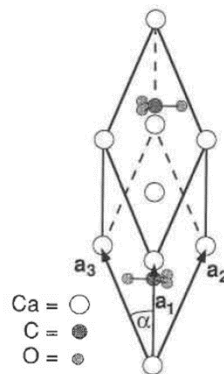


**Figure 2.11** Crystal structure of calcite.<sup>56</sup>

Surface area is a very important factor when considering encapsulating a particle, whether it be an *in-situ* polymerization or heterocoagulation; too low a surface area and the polymerization/heterocoagulation will not occur at the surface, too high and uneven coating and coagulation becomes a factor. Nitrogen porosimetry can be used to determine the surface area. Using BET analysis the surface area and BET constant can be found from the BET plot (Figure 2.12),  $1/[V_a(P_0/P-1)]$  versus  $P/P_0$ ; where  $P$  is the absolute pressure of bulk gas above the sample,  $P_0$  is the

saturation pressure of the adsorptive (in this case nitrogen) and  $V_a$  is the volume of gas adsorbed by the sample. The intercept of the straight line gives  $1/V_m C$  and the slope gives  $(C-1)/V_m C$  where  $C$  is the BET constant and  $V_m$  is the volume of gas adsorbed when the entire surface is covered with a monomolecular layer, from which the surface area can be calculated by knowing the area one unit of gas takes up on the surface.<sup>57</sup> The surface area of calcium carbonate was determined by this method, giving a surface area of  $8.92 \pm 0.05 \text{ m}^2 \text{ g}^{-1}$  (Figure 2.12). The BET constant, should be in the range of  $0 < C < 300$ , for SOCAL P3 it was determined to be 336 which is slightly above the desired range, it is possible that this is due to the presence of micropores.<sup>57</sup> The value is only slightly out of range and the correlation coefficient (0.9999) is suitably close to unity that the value for the surface area can be considered acceptable.

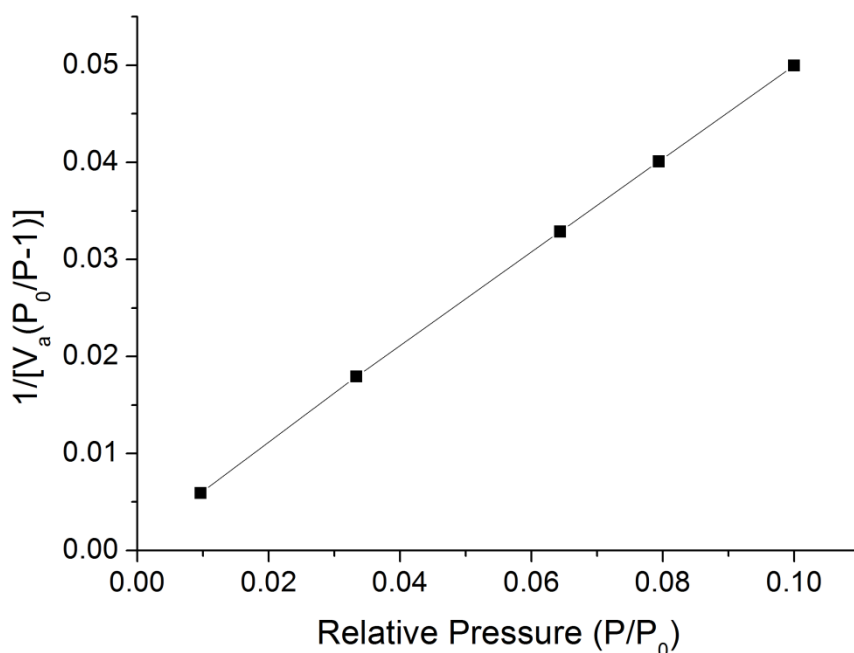


**Figure 2.12** BET transform plot of calcium carbonate (SOCAL P3) obtained by nitrogen porosimetry; quantity of gas adsorbed as a function of relative pressure. SOCAL P3 has a BET surface area of  $8.92 \pm 0.05 \text{ m}^2 \text{ g}^{-1}$  and a  $C$  value of 336.

The nitrogen adsorption isotherm of the particles, which is the volume of gas adsorbed ( $\text{cm}^3 \text{g}^{-1}$ ) onto the surface as a function of relative pressure ( $P/P_0$ ), shows that SOCAL P3 has a type II isotherm, meaning that the material is essentially non-porous (Figure 2.13). At low-mid relative pressure the quantity of gas absorbed is low and corresponds to a monolayer of gas, the sharp increase at higher relative pressure corresponds to the gas condensing as a liquid on the surface. The small increase in gas adsorbed at the low relative pressure range of 0-0.2 indicates there are hardly any micropores ( $< 2 \text{ nm}$ ), the slight hysteresis at the high relative pressure range of 0.7-1.00 is indicative of the presence of some macropores (50-1000 nm). Total pore volume measurements corroborate with this, showing that the calcium carbonate particles have a low pore volume of only  $0.03 \text{ cm}^3 \text{g}^{-1}$ .

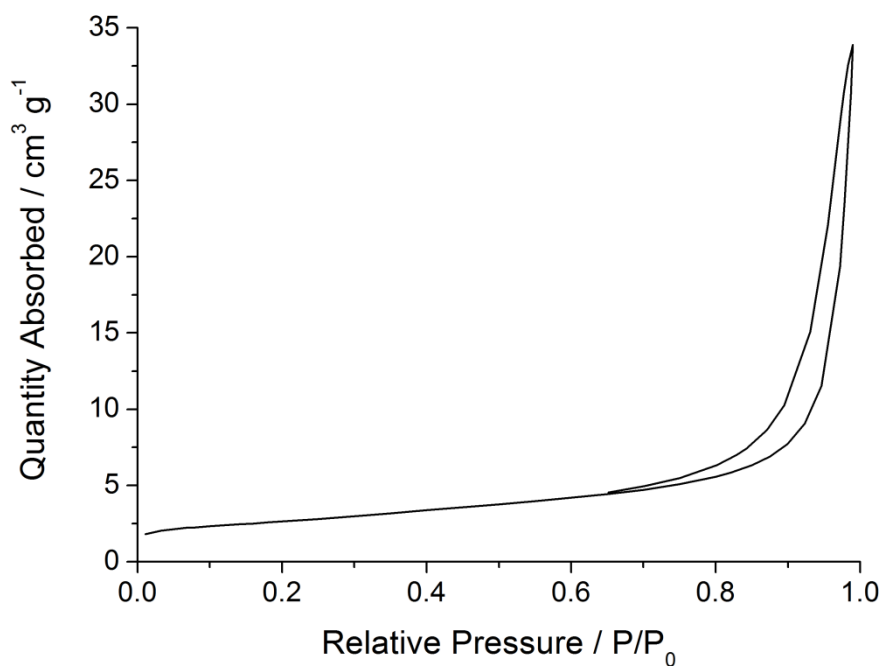


**Figure 2.13** Nitrogen adsorption isotherm of calcium carbonate (SOCAL P3); it has a type II isotherm meaning that is essentially non-porous.

The stability and surface charge are also important factors when encapsulating materials; surface functionality and charge can help determine what will stick to the surface and stability is important as the particles need to be fully

dispersed to encapsulate individual particles, however contrastingly if too stable it becomes difficult to wrap within a polymeric layer. Zeta potential is a characterization tool with which the magnitude of the zeta potential infers the stability of a particle and the sign describes the surface charge. Colloidal dispersions with zeta potentials greater than  $\pm 30$  mV are considered to be stable.<sup>58</sup> Zeta potential measurements of SOCAL P3 calcium carbonate particles were conducted at 25 °C and pH 9.3 at different salt concentrations (Figure 2.14). Salt affects the zeta potential as increasing the ionic strength of the medium decreases the thickness of the electric double layer, thus at very high salt concentrations, particles can become unstable and a zeta potential of 0 mV will be reached. The zeta potential for SOCAL P3 was determined to be positive, suggesting that in water the surface largely consists of  $\text{Ca}^{2+}$  or  $\text{CaOH}^+$  ions.

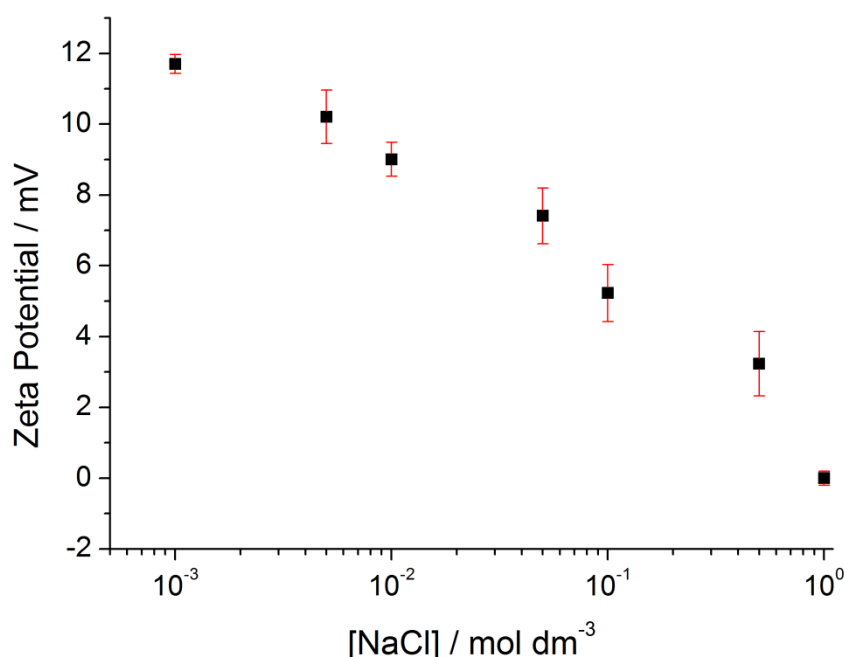


**Figure 2.14** Zeta potential of calcium carbonate (SOCAL P3) as a function of salt (NaCl) concentration. The zeta potentials were measured at pH 9.33, and an average of 6 measurements were recorded.



Changes in pH strongly affect the zeta potential of particles; typically at low pH positive charge builds up on the particles, resulting in a positive zeta potential. If the pH is increased, i.e. an alkali is added, the zeta potential will decrease (or become more negative) and surface charge will get to a point where it is neutralised. On the addition of more alkali the negative charge on the surface will increase resulting in a higher negative value. The point at which the zeta potential is equal to 0 mV is known as the isoelectric point (IEP) and is the pH at which the particles are least stable. The point of zero-charge (PZC) is defined as the point when the surface charge of the particle is equal to zero, often but not always this is the same as the isoelectric point; they differ when specific ion adsorption occurs, changing the IEP. Zeta potential measurements of calcium carbonate were also conducted at different pHs varying from 8.5 - 12.5, measurements at pH below 8.5 were not conducted as the calcium carbonate begins to dissolve at lower pH. As the pH was increased the zeta potential reduced, passing through the isoelectric point at pH 11.2. This falls within the range of reported isoelectric points for calcite, 8.2 – 11.5, the range being attributed to the variety of calcite surfaces, measurement techniques or presence of solubilised CO<sub>2</sub> and Ca<sup>2+</sup> ions.<sup>56, 59-65</sup>

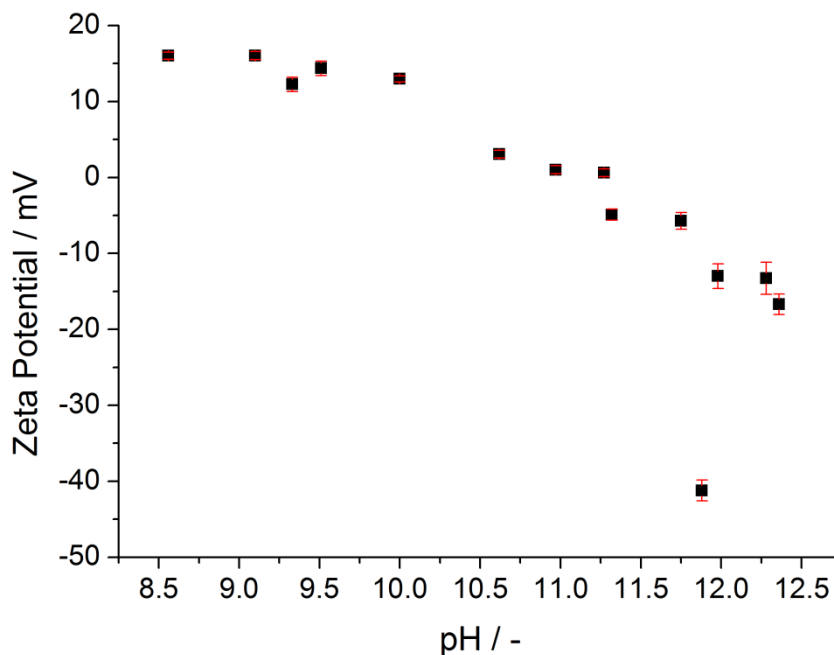


**Figure 2.15** Zeta potential as a function of pH of calcium carbonate (SOCAL P3). An average of 6 measurements were recorded.

### 2.3.2. Encapsulation of calcium carbonate particles

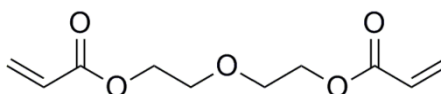


**Figure 2.16** Di(ethylene glycol) diacrylate.

Di(ethylene glycol) diacrylate (DEGDA) (Figure 2.16) was chosen as the primary encapsulating monomer. A di-functional monomer was desired to produce a fully cross-linked system so that the calcium carbonate core is kinetically trapped within the polymer shell and so that the composite material could potentially be processed since particles encapsulated in a non-cross-linked polymer shell exhibit dewetting when heated above the  $T_g$  of said polymer.<sup>66</sup> The monomer also needed to have slight water solubility so that it could be used in emulsion polymerization conditions. The solubility of DEGDA in water was of further interest as ethylene glycol based polymers have exhibited LCST behaviour.<sup>67, 68</sup> The solubility of DEGDA in water at various temperatures was measured by  $^1\text{H}$  NMR. 1.0 g DEGDA was added to 10.0 g  $\text{D}_2\text{O}$  and heated in an oil bath to the desired temperatures, the

mixture was left to stir for an hour to allow it to equilibrate, after which a known mass of the supernatant was extracted and diluted with a known mass of D<sub>2</sub>O containing an internal NMR standard sodium acetate trihydrate. The dilution was necessary to prevent any solubilised DEGDA crashing out of solution on cooling, and the NMR standard was added after solubilisation to prevent partitioning into the DEGDA phase. On increasing temperature, DEGDA exhibited a decreasing solubility, suggesting that it has an LCST (Figure 2.17). At reaction temperature of 70 °C it was found that DEGDA has a water solubility of 21 g L<sup>-1</sup>.

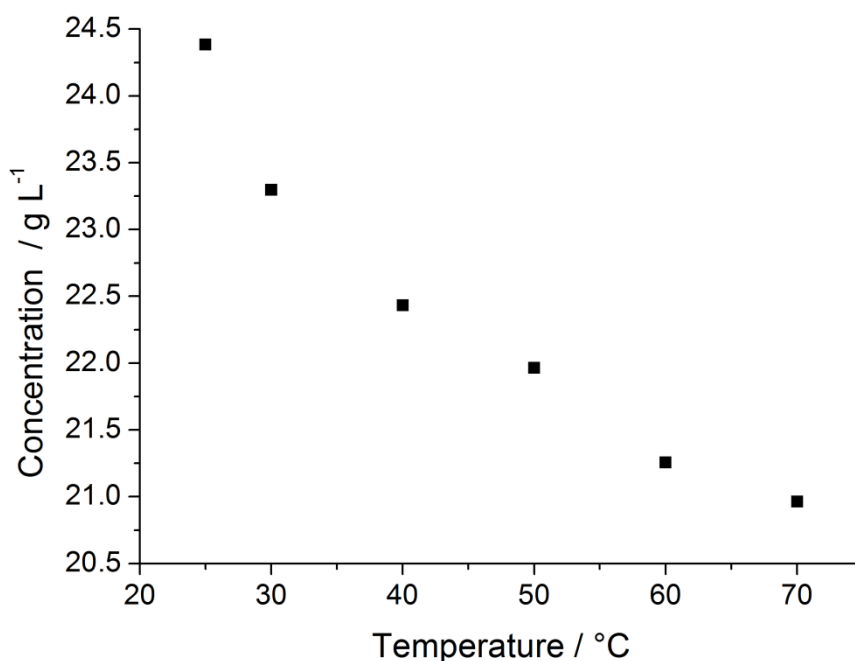


**Figure 2.17** Water solubility of DEGDA in D<sub>2</sub>O at varying temperatures, measured by <sup>1</sup>H NMR.

The initial encapsulation method proceeded as follows (HM-201). Typically, 60.0 g of 16 wt.% water-based slurries of the pigment was used as a starting point in a conventional free-radical seeded emulsion polymerization set up. To the calcium carbonate slurry, 1 mL DEGDA was fed at a rate of 0.5 mL h<sup>-1</sup>, the polymerization was initiated with APS simultaneously with the start of the feed and the polymerization was conducted at 70 °C. The emulsion polymerization was continued for an additional 30 minutes, after which the final product was obtained. Through

TEM analysis it was clear that the poly(DEGDA) did not wet the surface of the calcium carbonate: coagulated polymer (Figure 2.18a) is clearly observed, as are bare calcium carbonate particles (Figure 2.18b). It appears that where the polymer has interacted with the surface, only large blobs are observed suggesting that dewetting has occurred. To overcome this wetting dilemma methacrylic acid (MAA) was chosen as a secondary monomer to encourage wetting of the polymer to the calcite surface.

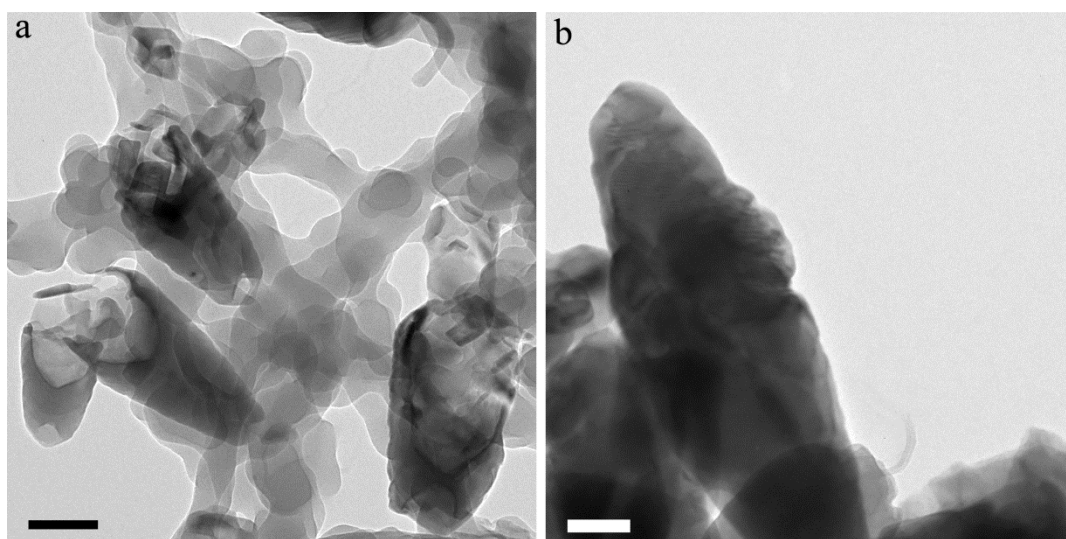


**Figure 2.18** TEM images of DEGDA polymerized in the presence of calcium carbonate. (a) poly(DEGDA) is unstable and coagulates, (b) calcium carbonate remains uncoated (HM-201) (scale bar: 100 nm).

In order to determine whether the methacrylic acid would adsorb onto the positively charged surface of the calcium carbonate particles, we calculated whether the methacrylic acid is deprotonated in the 17 wt.% solids calcium carbonate slurry using the Henderson-Hasselbalch equation (1.1). The  $pK_a$  of methacrylic acid is 4.66,<sup>69</sup> and the pH of the calcium carbonate slurry containing methacrylic acid is 7.10. Rearranging the Henderson-Hasselbalch equation to give  $[A^-]/[HA]$  (1.2) we can determine the extent to which the methacrylic acid is deprotonated. Under these conditions  $[A^-]/[HA]$  is equal to 275, thus the methacrylic acid is > 99.5 % deprotonated, and consequently adsorbs onto the positively charged surface of

calcium carbonate by means of electrostatic interactions (Figure 2.19). It is important to note that we are not only considering methacrylic acid monomer units adsorbing to the calcium carbonate surface but also polymeric (MAA-*co*-DEGDA) chains and primary particles.

$$pH = pK_a + \log \left( \frac{[A^-]}{[HA]} \right) \quad (1.1)$$

$$\frac{[A^-]}{[HA]} = 10^{pH-pK_a} \quad (1.2)$$

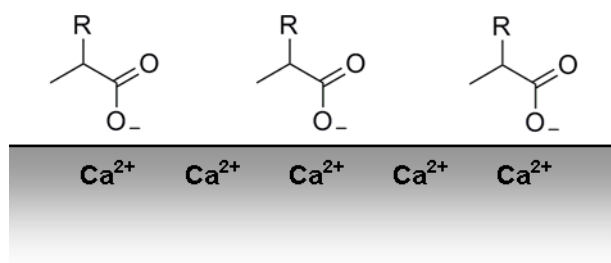


**Figure 2.19** Scheme depicting the adsorption of deprotonated methacrylic acid onto the positively charged surface of the calcium carbonate particles, where R is the poly(MAA-*co*-DEGDA) chains/particles.

The second encapsulation method proceeded as follows (HM-202). Typically, 60.0 g of 16 wt.% water-based slurries of the pigment was used as a starting point in a conventional free-radical seeded emulsion polymerization set up. To the calcium carbonate slurry, 1 mL of a 14:86 wt.% mixture of MAA and DEGDA was fed in at a rate of 0.5 mL h<sup>-1</sup>, the polymerization was initiated with APS and the polymerization was conducted at 70 °C. The emulsion polymerization was continued for an additional 30 minutes, after which the final product was obtained. Through TEM analysis it was clear that the wettability of the polymer to the calcium carbonate has substantially improved, however some dewetting is clearly observable (Figure 2.20). To overcome this apparent wetting problem the monomer feed was split into two; (1) 0.5 mL of a 30:70 wt.% mixture of MAA and DEGDA

and (2) 0.5 mL of pure DEGDA. This was chosen in order to maximise the effect of MAA improving the wettability of the polymer to the calcium carbonate surface without increasing total MAA content in the polymer composition.

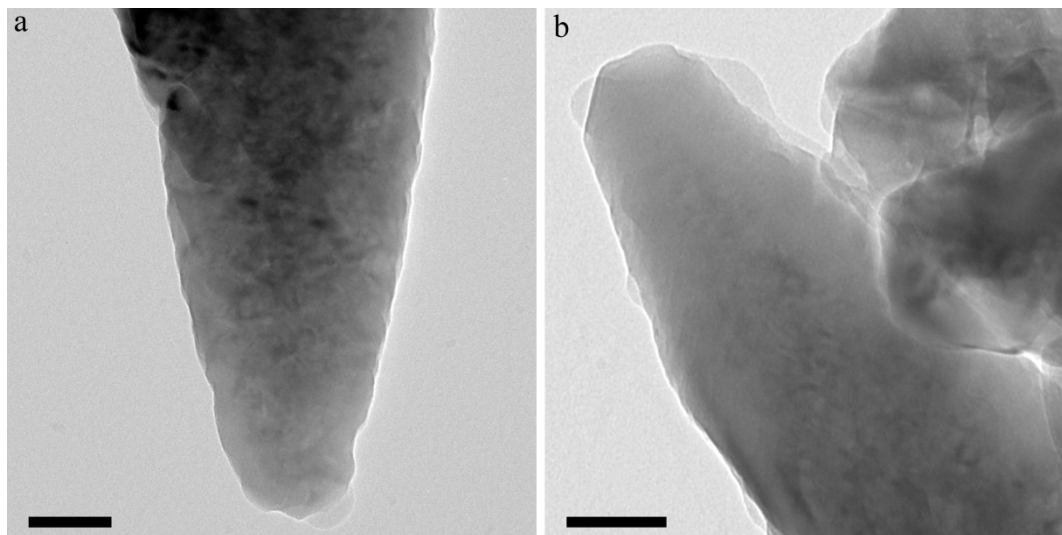


**Figure 2.20** TEM images of a 14:86 wt.% mixture of MAA and DEGDA polymerized in the presence of calcium carbonate (HM-202). The wettability of the polymer to the calcium carbonate surface has improved though dewetting is still observable (scale bar: 100 nm).

The encapsulation proceeded as follows (HM-203 - 206). Typically, 60.0 g of 16 wt.% water-based slurries of the pigment was used as a starting point in a conventional free-radical seeded emulsion polymerization set up. To the calcium carbonate slurry, monomer was starved-fed and polymerized in two steps at 70 °C. Firstly, 0.5 mL of 30:70 wt.% mixture of methacrylic acid (MAA) and di(ethylene glycol) diacrylate (DEGDA) was fed in using a syringe pump at a rate of 0.5 mL h<sup>-1</sup>. This was immediately followed by a second addition of 0.5 mL of pure DEGDA at the same feed rate (0.5 mL h<sup>-1</sup>). The emulsion polymerization was continued for an additional 30 minutes, after which the final product was obtained.

The slow monomer feed rate was chosen so that the reaction was under starved conditions, thus keeping the monomer concentration low, meaning that there are no monomer droplets present for the majority of the emulsion polymerization process. Monomer conversion measurements as function of time show indeed that

near starved-fed conditions have been achieved (Figure 2.21 and Appendix II Figure II.1).

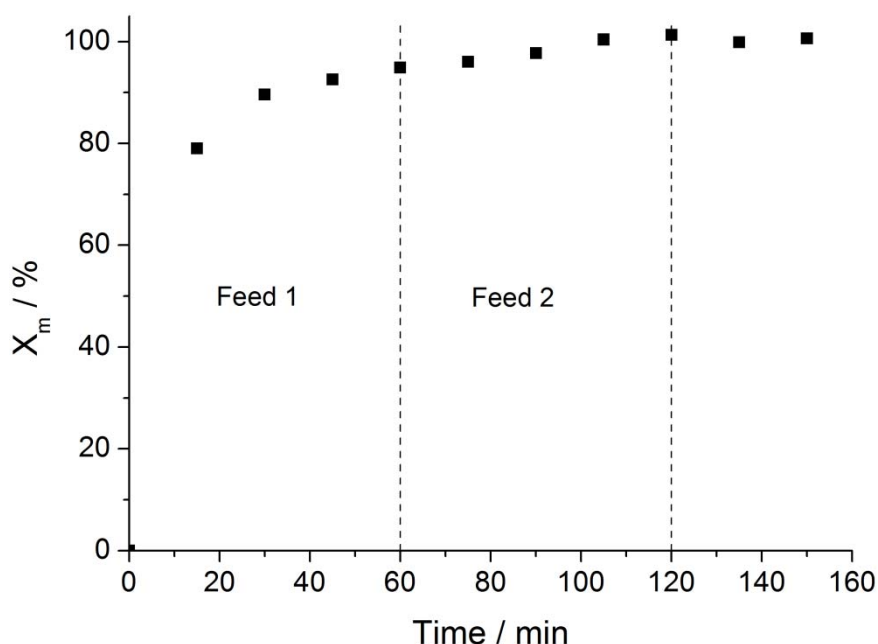


**Figure 2.21** Overall monomer conversion  $X_m$  vs. time of encapsulation of calcium carbonate (HM-204). Feed 1 represents the feed of MAA and DEGDA mixture and feed 2 represents the DEGDA feed. Monomer was fed at a rate of  $0.5 \text{ mL h}^{-1}$ .

Once the encapsulation was complete it was essential to determine the location of the polymer, to ensure the calcium carbonate particles were indeed encapsulated. Zeta potential measurements can be used to identify the surface charge of particles. This can be a useful tool in identifying whether particles have been encapsulated. The zeta potential measurements of the new composite particles indicate that the surface has in fact changed. The original calcium carbonate particles exhibited a low positive zeta potential of  $\sim 12 \text{ mV}$ , after the encapsulation process the new particles have a zeta potential of  $\sim -30 \text{ mV}$ . The change to negative surface charge is logical as an anionic initiator, ammonium persulfate, was used and acts as a surface charge stabilizer, also some MAA may exhibit itself on the surface. The increased stabilization is also promising, in that aggregation of the particles is likely to be much reduced.

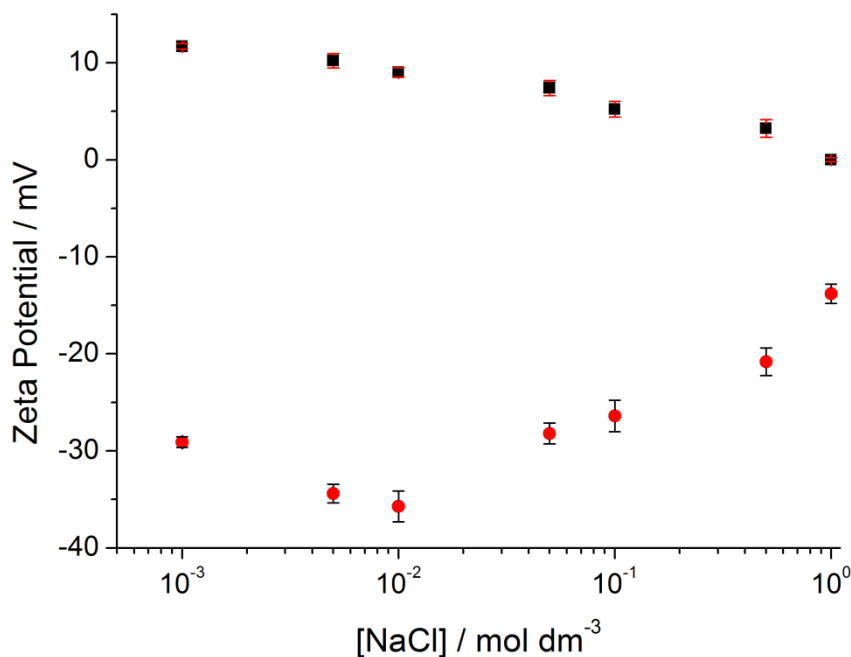


**Figure 2.22** Zeta potential of calcium carbonate (SOCAL P3) (■) and calcium carbonate encapsulated in poly(MAA-*co*-DEGDA) (HM-203) (●) as a function of salt (NaCl) concentration. Zeta potential measurements were performed at pH 9.3 and an average of 6 measurements were recorded.

To determine whether the particles were encapsulated in a polymeric shell, the morphology was analyzed by TEM; TEM is a very powerful tool in determining whether a surface is coated in a different species, as differences in electron density of materials can clearly be observed. TEM analysis showed that the calcium carbonate particles were indeed encapsulated in a polymeric shell with an approximate thickness of 10 nm, the polymer being clearly identifiable by its lower electron density and thus lighter in contrast to the calcium carbonate core (Figure 2.23).



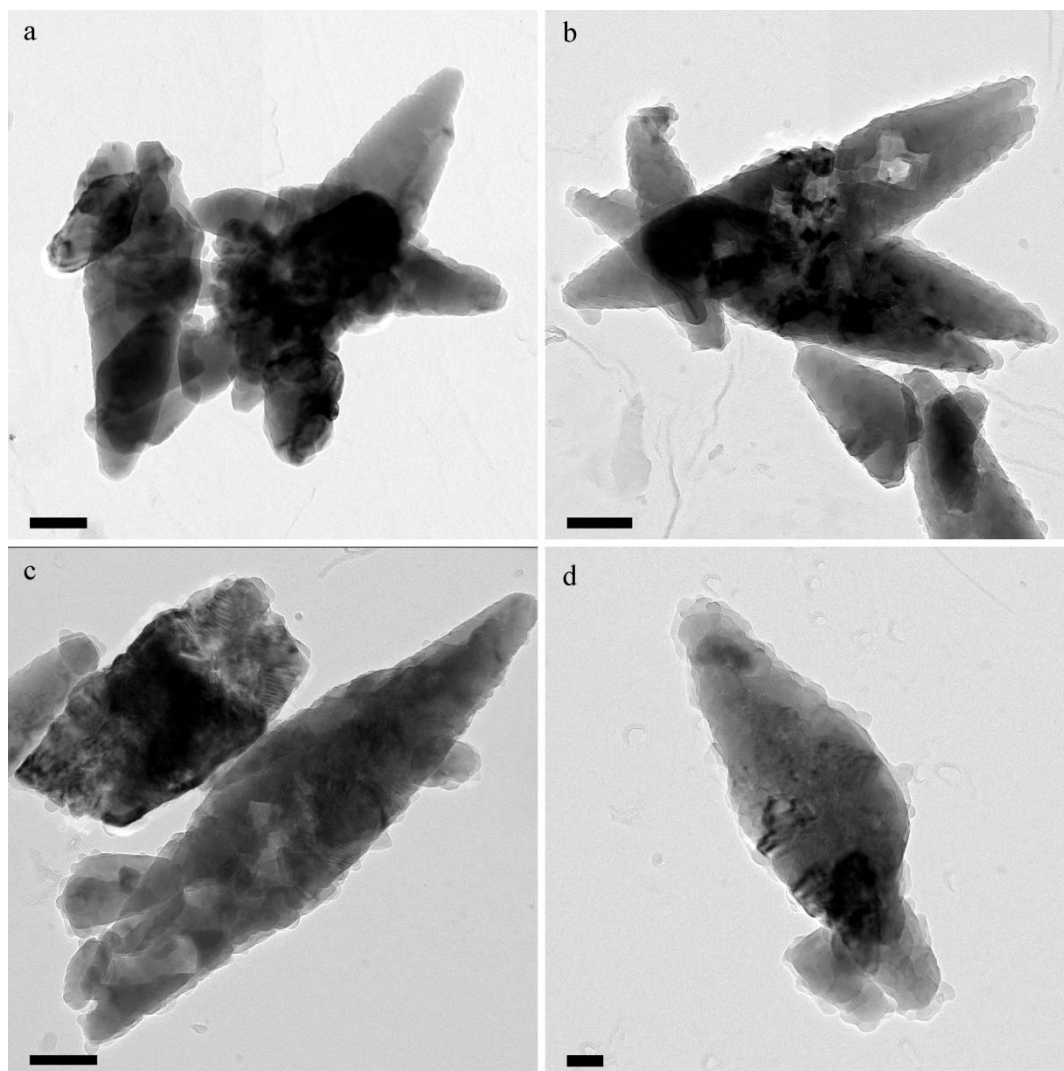


**Figure 2.23** TEM image of bare and encapsulated calcium carbonate. (a) Bare calcium carbonate particles. (b), (c) and (d) Calcium carbonate encapsulated in poly(MAA-*co*-DEGDA) (HM-203). (Images (a) (b) and (c) scale bar: 200 nm, image (d) scale bar: 100 nm).

On close inspection of the TEM images it is apparent that the shell is not smooth, but bumpy, whereas the underlying surface of the calcite does not have this rough texture (Figure 2.24). We postulate that the roughness of the coating is a result of the polymer not completely wetting the surface of calcium carbonate particles, however as they are completely coated in polymer, the cross-linking of the diacrylate has ensured that the calcium carbonate core is kinetically trapped in the polymeric cage.

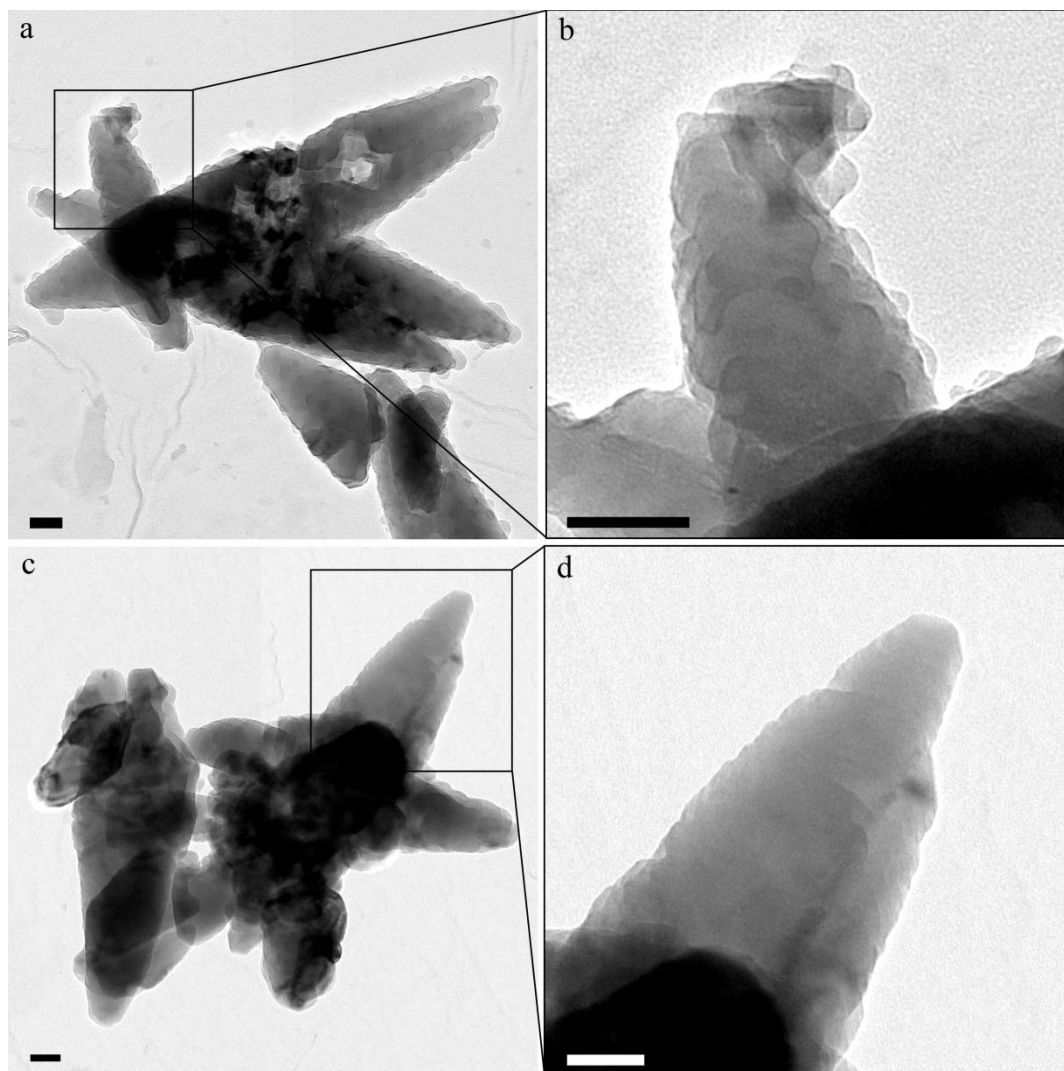


**Figure 2.24** TEM images of (a) calcium carbonate encapsulated in poly(MAA-*co*-DEGDA), (b) an increased magnification of image (a) (HM-203), (c) bare calcium carbonate and (d) an increased magnification of image (c) illustrating the bumpy surface of the encapsulated calcium carbonate compared to the relatively smooth surface of the bare calcium carbonate (scale bar: 100 nm).

SEM provides surface morphology information; typically this is of no use in analyzing encapsulated materials if the surface is smooth, though as the surface of the particles appears to have a rough texture SEM is now a valuable tool. SEM analysis of the particles supports that of the TEM, confirming that the surface of the particles are no longer smooth like that of the original calcium carbonate particles but is now bumpy (Figure 2.25).

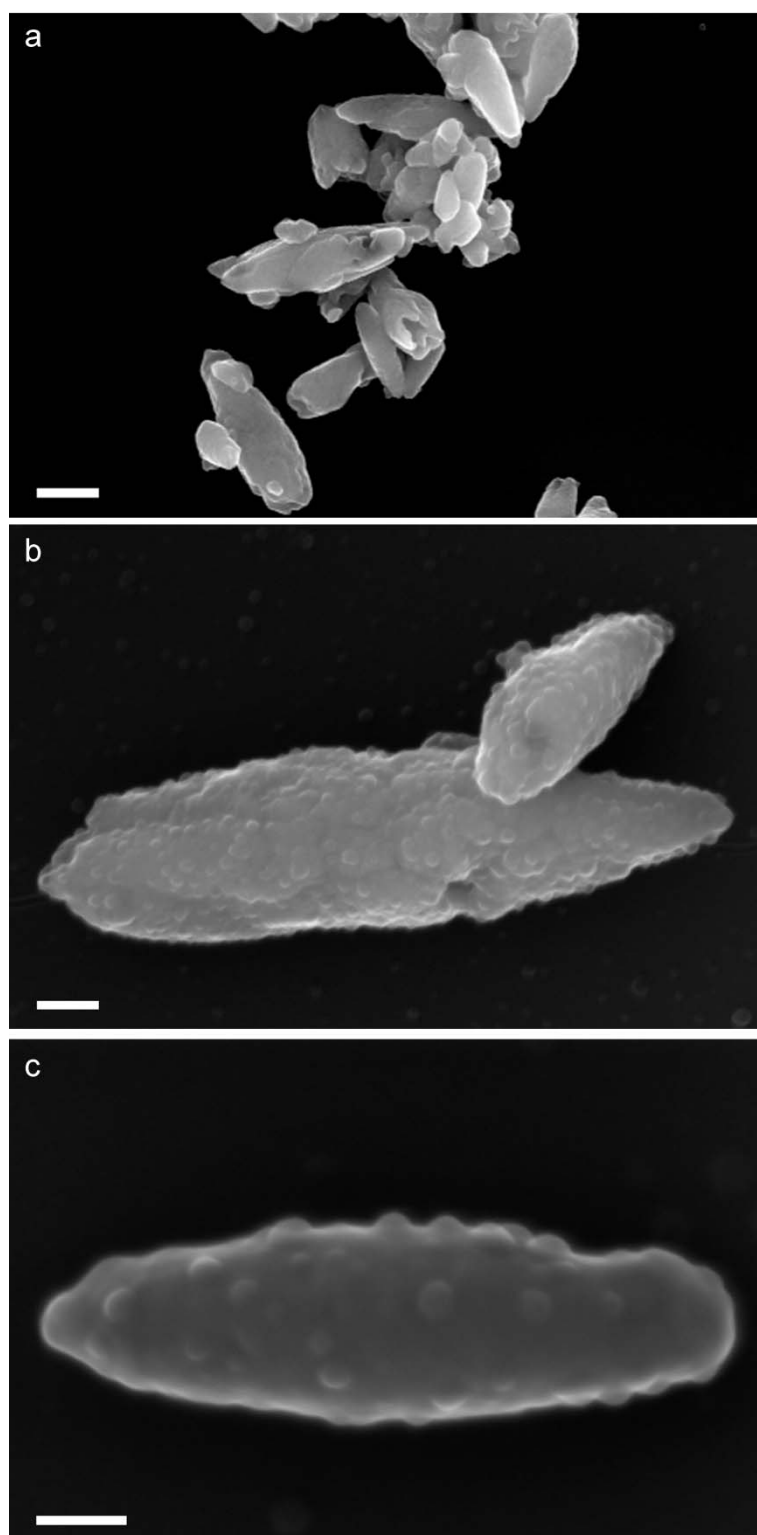


**Figure 2.25** SEM images of (a) bare calcium carbonate, (b) and (c) calcium carbonate encapsulated in poly(MAA-*co*-DEGDA) (HM-206) (scale bar (a): 500 nm, scale bar (b) and (c): 200 nm).

In lower magnification SEM images it is clear that some small non-spherical particles are present (Figure 2.26a). These particles are calcium carbonate fragments and are distinguishable from potential secondary polymer particles, as such secondary particles would be spherical. On closer inspection it is clear that these fragments are also coated in a polymer shell, in the same manner as the much larger, complete SOCAL particles (Figure 2.26b).

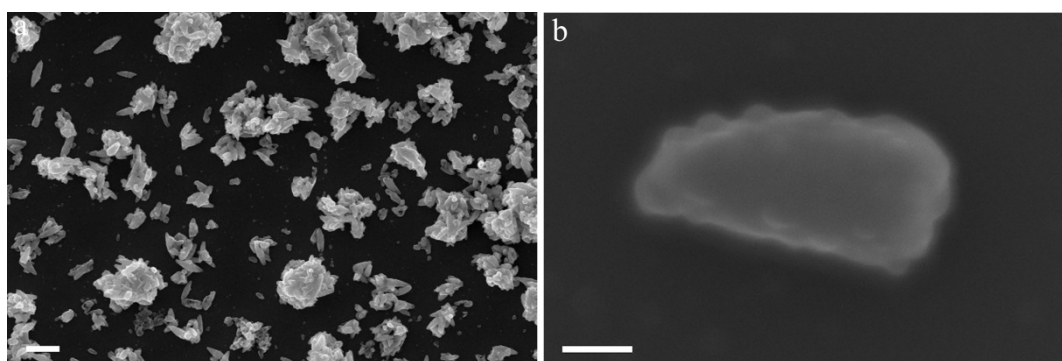
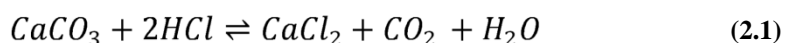


**Figure 2.26** SEM images of calcium carbonate encapsulated in poly(MAA-*co*-DEGDA) (HM-206) (a) broad overview of particles, showing small fragmented calcium carbonate particles and (b) small calcium carbonate fragment coated in a polymeric shell (scale bar (a): 2 $\mu$ m, scale bar (b): 100 nm)

We have discussed that the bumpy surface is due to the polymer not completely wetting the surface of the calcium carbonate, but that this does not impair the encapsulation as the core is kinetically trapped in a cross-linked shell. Removal of the core to yield a hollow polymeric particle helps to determine whether the particles are in fact completely encapsulated and thus kinetically trapped. It is well known that calcium carbonate reacts with acid to form carbon dioxide, calcium salts and water:



The calcium carbonate was etched out of the composite particles by adding 1 M HCl drop-wise, it was imperative that the acid was added slowly to prevent a sudden release of carbon dioxide blowing the comparatively delicate polymer shell apart (HM-207). The particles were subsequently cleaned by several centrifugation

cycles. The resulting hollow polymeric particles were analyzed by cryo-TEM so as to clearly observe them in aqueous conditions, as once dried it would become difficult to characterize the shape and determine whether the particles were truly hollow. The hollow polymer particles retained the original morphology of the ellipsoidal calcium carbonate, further corroborating that the location of the polymer is certainly around the calcium carbonate particles. Though it appears that the surface could be covered in individual polymeric particles due to the rough texture, the retention of the ellipsoidal morphology confirms that the entire surface is in fact cross-linked and trapped in that shape, otherwise a spherical morphology would likely be observed (Figure 2.27). Here we have shown that we can produce non-spherical hollow particles, such morphology is of great interest as they have been shown to have an increased cell-uptake compared to their spherical counterparts<sup>70-72</sup> and another for their increased opacity properties.<sup>73, 74</sup>

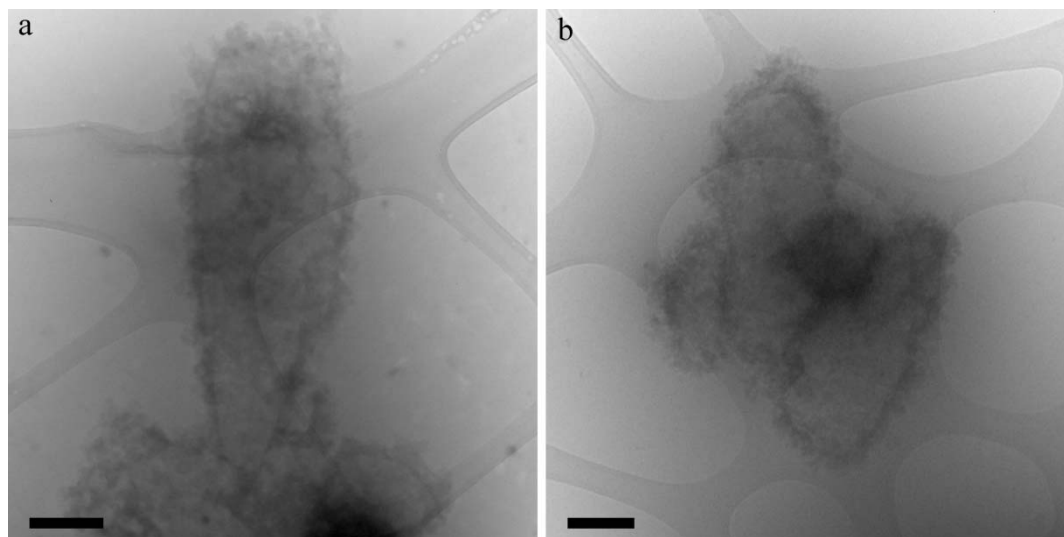


**Figure 2.27** Cryo-TEM images of calcium carbonate encapsulated in poly(MAA-*co*-DEGDA), with the calcium carbonate etched out with HCl (HM-207) (scale bar: 200 nm).

Energy dispersive X-ray (EDX) analysis on STEM was used to gain elemental analysis on the nanometre scale of the encapsulated particles. EDX analysis works by bombarding a sample with high energy electrons and the X-ray



spectrum emitted is unique to each element.<sup>75</sup> Line scans across the particles (Figure 2.28 a) produced micrographs illustrating the location of the elements (Figure 2.28 b). It is clear that the carbon based polymer shell extends past the core inorganic particle as seen by the extension of the carbon past that of the calcium in the line scans. The count rate for the lighter elements, carbon and oxygen were lower than that of the heavier calcium, which is logical as they produced lower energy x-rays. Despite this, the obvious enrichment of approximately 10 nm of carbon at the edges corroborates with the polymeric shell observed by TEM analysis (Figure 2.23).

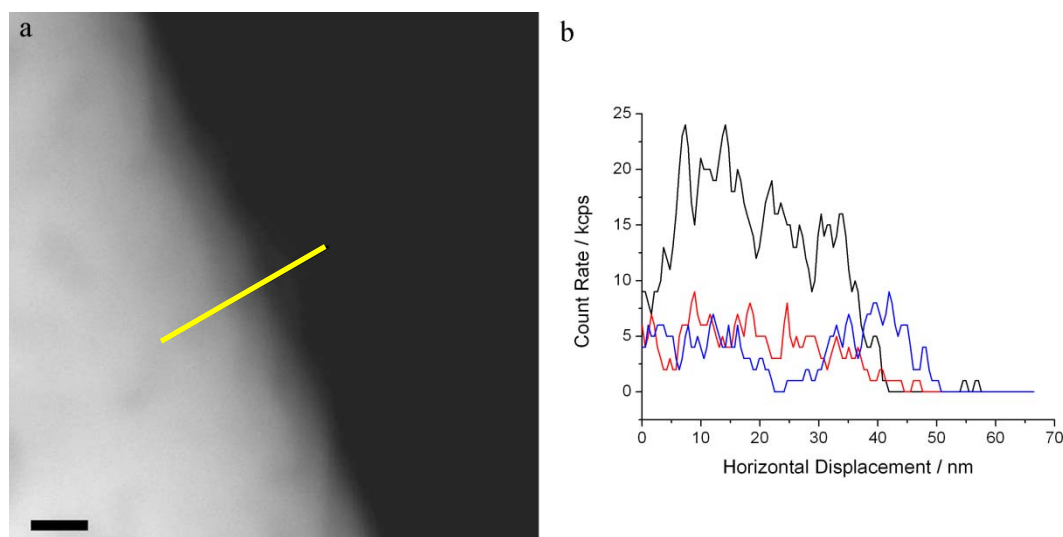


**Figure 2.28** STEM images of (a) calcium carbonate encapsulated in poly (MAA-co-DEGDA) (scale bar: 20 nm) where (b) is the corresponding EDX linescans (— calcium, — oxygen and — carbon). The yellow line across particles indicates place of linescan (HM-205).

### 2.3.2.1. Encapsulation Mechanism

We believe the encapsulation mechanism is as follows. The monomer concentration is kept low as a result of the starved-fed conditions, meaning that there are no monomer droplets present. A sulfate radical, which originates from the decomposition of the ammonium persulfate initiator, reacts with monomer in the water phase. Upon further propagation of this radical, the oligomer, becomes surface active and can adhere in this case to the pigment. It is also plausible that a fraction can propagate further in the water phase, becoming insoluble and thereby collapsing

initially on itself and then subsequently heterocoagulate onto the pigment particle where they become cross-linked with the surrounding polymer. This results in a thin cross-linked polymeric shell around individual calcium carbonate particles.

### **2.3.3. Control of shell thickness**

Now that this seeded emulsion polymerization strategy is able to encapsulate pigment with a thin shell of cross-linked polymer primer, we were interested to see if we could increase the polymer shell thickness.

In order to investigate this we extended the encapsulation protocol with an additional step in which we starve-fed methyl methacrylate (MMA) after the initial DEGDA feeds. The presence of the primer layer facilitates efficient encapsulation in that it locally enhances the monomer concentration in the existing shell through swelling, which promotes polymerization upon radical entry from the water phase. Typically, 6.0 mL methyl methacrylate (with respect to 10 g calcium carbonate) was fed into the reaction mixture under starved conditions (HM-208). The starved-fed conditions were verified by following conversion by gravimetry, the plot shows that the conversion of MMA is close to 100 % throughout the feed (Figure 2.29).

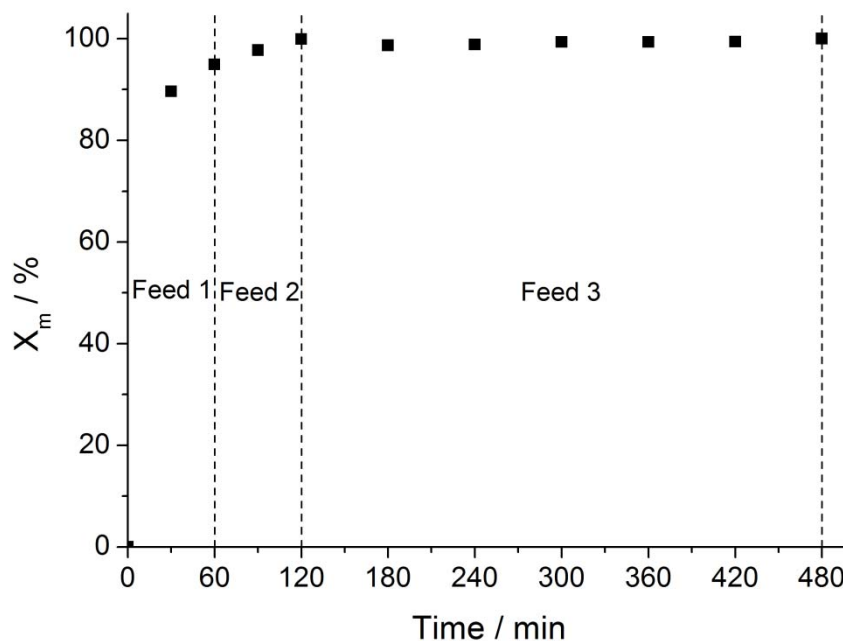


**Figure 2.29** Overall monomer conversion;  $X_m$  vs. time of encapsulation of calcium carbonate (HM-208). Feed 1 represents the feed of methacrylic acid and di(ethylene glycol) diacrylate mixture, feed 2 represents the di(ethylene glycol) diacrylate feed and feed 3 represents the MMA feed. In the first two feeds were fed at a rate of  $0.5 \text{ mL h}^{-1}$  and MMA was fed at a rate of  $1 \text{ mL h}^{-1}$ .

Zeta potential measurements after the shell extension with MMA show that the particles have a zeta potential of  $\sim -30 \text{ mV}$  at pH 9.3 and  $10^{-3} \text{ M NaCl}$ . The particles with a poly(MMA) shell extension exhibit very similar zeta potential to that of those encapsulated in poly(DEGDA-*co*-MAA); this is logical as the monomers are similar and the same initiator, ammonium persulfate, that acts as a charge stabilizer was used.



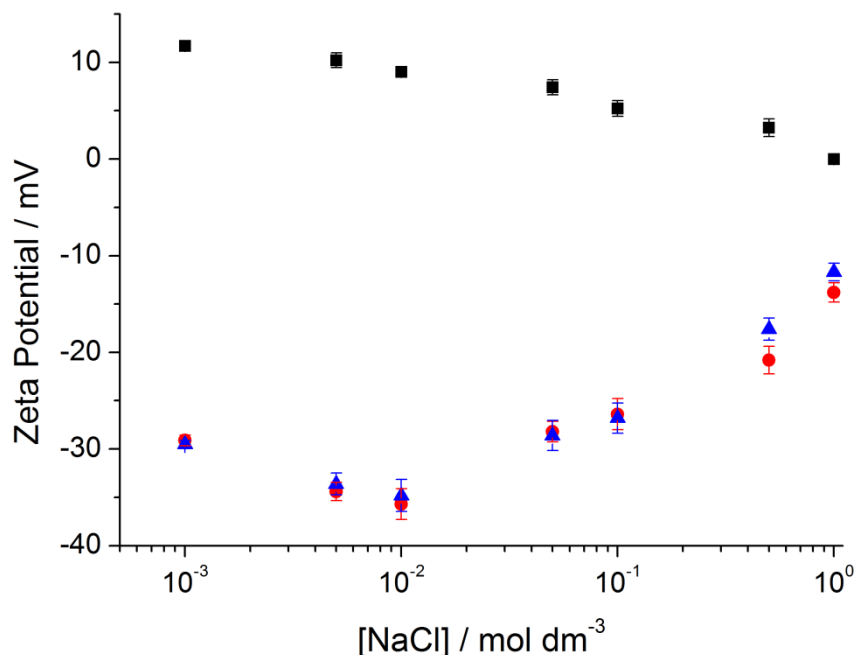


**Figure 2.30** Zeta potential of calcium carbonate (SOCAL P3) (■), calcium carbonate encapsulated in poly(MAA-*co*-DEGDA) (HM-203) (●) and calcium carbonate encapsulated in poly(MAA-*co*-DEGDA) primer with poly(MMA) shell extension (▲) (HM-208) as a function of salt (NaCl) concentration. Zeta potential measurements were performed at pH 9.3 and an average of 6 measurements were recorded.

Particle size was monitored by laser diffraction. The particle size distribution was measured for the growth of the polymer shell around calcium carbonate after 2, 3, 4, 5, and 6 mL of MMA was added, it is clear that the particle size is increasing on increasing amount of monomer fed in (Figure 2.31). For particles with less than 2 mL MMA no change was observed by laser diffraction. Particles smaller than the calcium carbonate were not observed, indicating that there was no secondary nucleation. Note that the shift toward higher particle sizes is only indicative as the particles are not spherical, the pigment size distribution is not monodisperse, and upon polymer shell growth the overall refractive index changes. Hence laser diffraction can only demonstrate the increasing trend in particle size rather than an accurate shell thickness.

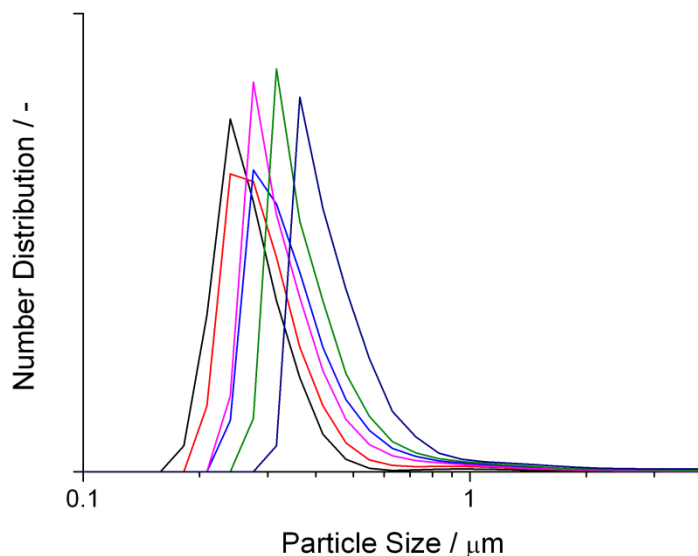


**Figure 2.31** Particle size analysis by laser diffraction of bare calcium carbonate (—), and encapsulated calcium carbonate; at 2 mL (—), 3 mL (—), 4 mL (—), 5 mL (—) and 6 mL (—) methyl methacrylate (HM-208).

Cryo-TEM analysis showed that the shell thickness had indeed substantially increased and that the surface remained bumpy, as was in the case of encapsulation with the primer (Figure 2.32). This is due to a combination of reasons, one of which is that the locus of polymerization is on the cross-linked poly(DEGDA)-based shell. This is combined with the fact that the polymerization is conducted below the  $T_g$  of poly(MMA) and is under starved conditions meaning that there is little monomer swelling, resulting in the polymer retaining the structure formed on initial polymerization. Under normal TEM conditions however the polymer surface appears smooth, this is likely a cause of capillary action on drying (Figure 2.33).<sup>76</sup> This is also observed when analyzed by SEM; although the surface is not completely smooth it is clearly much smoother than that seen in the wet-state of cryo-TEM, underlining that this is capillary pressure on drying smoothing out the polymer shell (Figure 2.34).

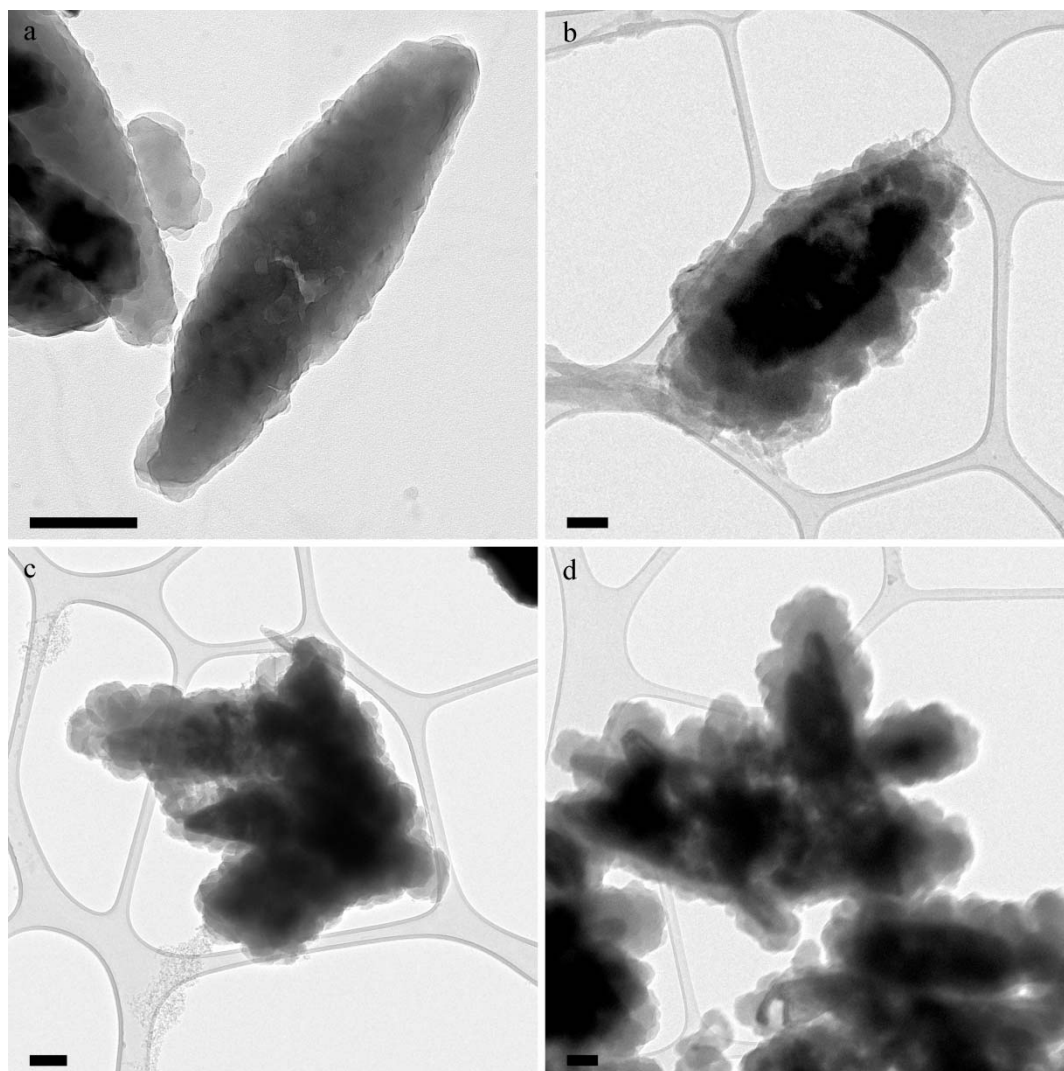


**Figure 2.32** (a) TEM image of calcium carbonate encapsulated in initial poly(MAA-*co*-DEGDA) (M-203), and (b), (c) and (d) corresponding cryo-TEM image of said encapsulated particles with shell extended with poly(MMA) (HM-208) (scale bar: 200 nm).

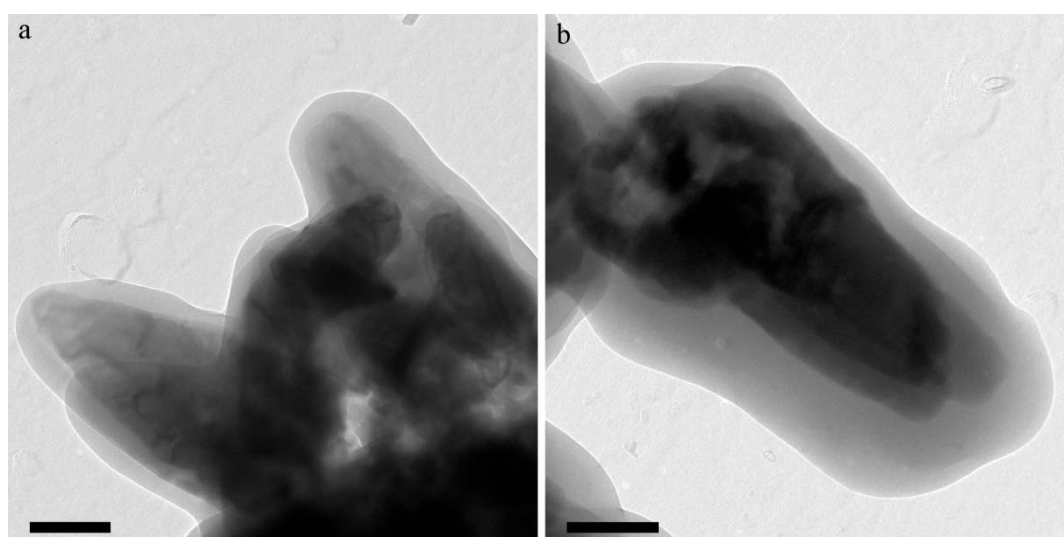


**Figure 2.33** TEM images of calcium carbonate encapsulated in initial poly(MAA-*co*-DEGDA) followed by shell extension with poly(MMA) (HM-208) (scale bar: 200 nm).

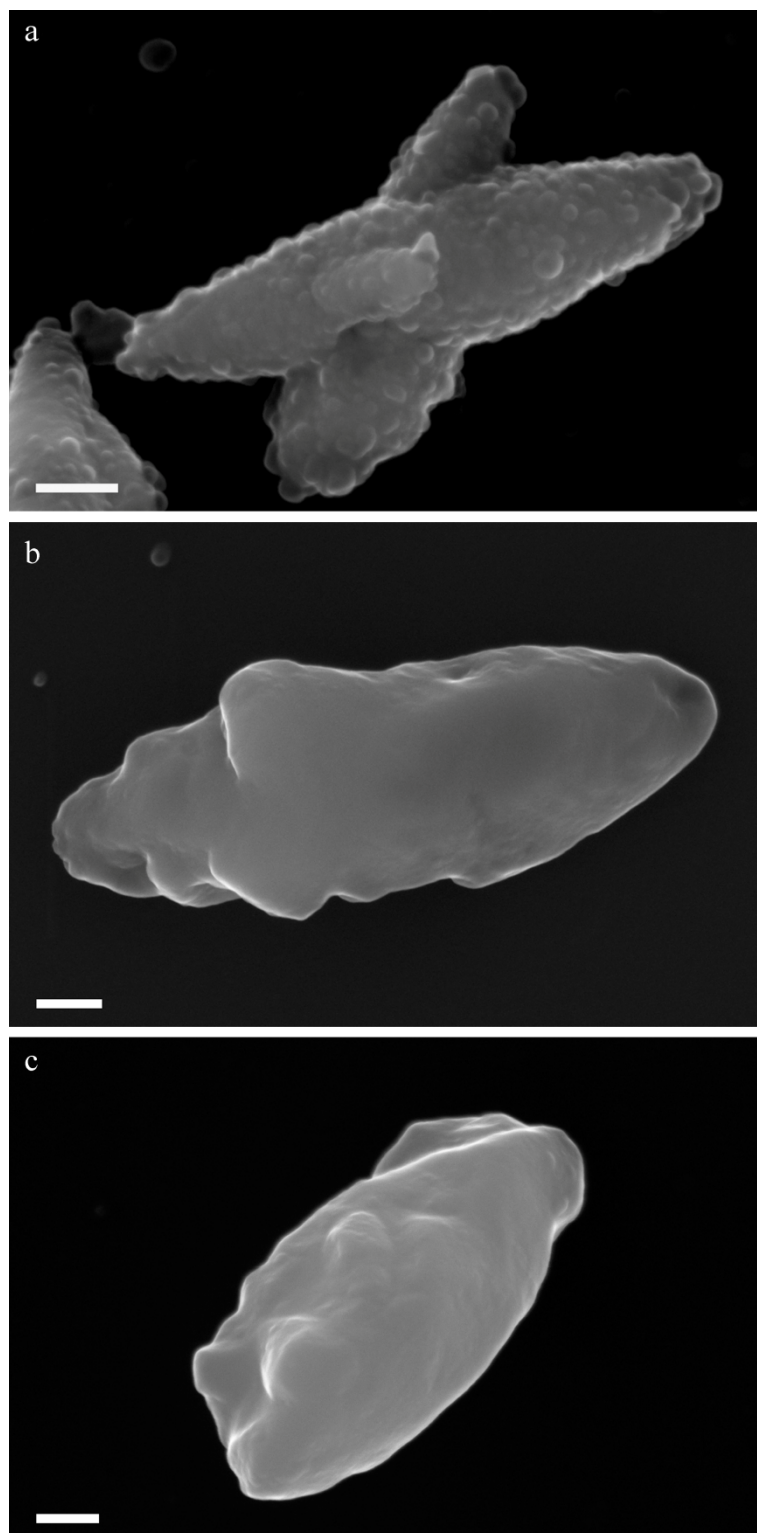


**Figure 2.34** (a) SEM image of calcium carbonate encapsulated in initial poly(MAA-*co*-DEGDA) (HM-206), and (b) and (c) the corresponding SEM image of said encapsulated particles with shell extended with poly(MMA) (HM-208) (scale bar: 200 nm).

### 2.3.4. $\text{CaCO}_3$ as a sacrificial template for nano-rattles

Now that we have illustrated encapsulation of calcium carbonate particles, we intend to use this method to create nano-rattles using the calcium carbonate as a sacrificial template. Amorphous calcium carbonate particles have been used as a sacrificial template in the preparation of loaded hollow polymer particles for applications in drug delivery.<sup>11, 13, 77</sup> Herein we load amorphous calcium carbonate with silica nanoparticles and encapsulate them in a polymeric shell.

#### 2.3.4.1. *Synthesis of amorphous calcium carbonate particles*

Amorphous calcium carbonate particles (HM-210) were synthesized in accordance with the method illustrated by Sukhorukov and co-workers;<sup>13</sup> a solution of calcium chloride (250 mL, 0.33 M) was added rapidly to a vigorously stirred solution of sodium carbonate (250 mL, 0.33 M), the mixture was stirred vigorously for 30 seconds, after which the particles were collected by Büchner filtration. Particles were cleaned by rinsing with water and then dried under vacuum. Spherical calcium carbonate particles which appeared porous were produced (Figure 2.35). Particles were also synthesized in the presence of silica nano-particles (Ludox TM-40), which had a diameter of 20 nm (HM-211). SEM analysis of HM-211 shows a different surface topology, however on cracking open the particles it was not possible to differentiate the silica nano-particles from the porous calcium carbonate (Figure 2.36).

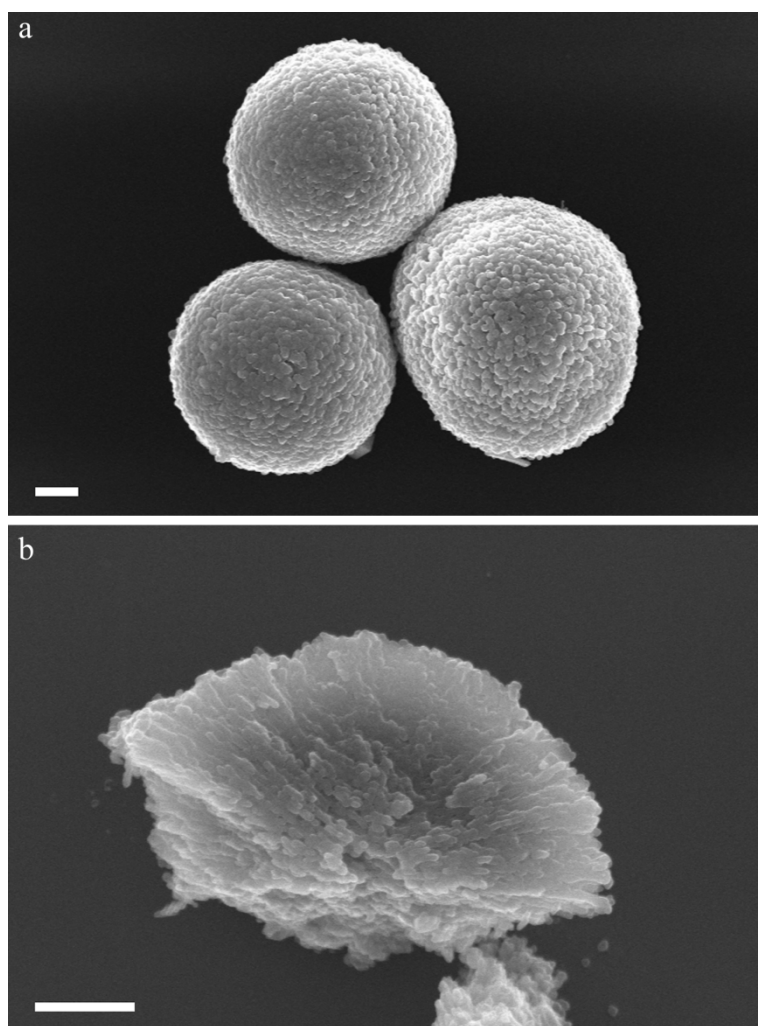


**Figure 2.35** SEM images of amorphous calcium carbonate particles; (a) whole particles and (b) broken particle (HM-210) (scale bar: 1  $\mu\text{m}$ )



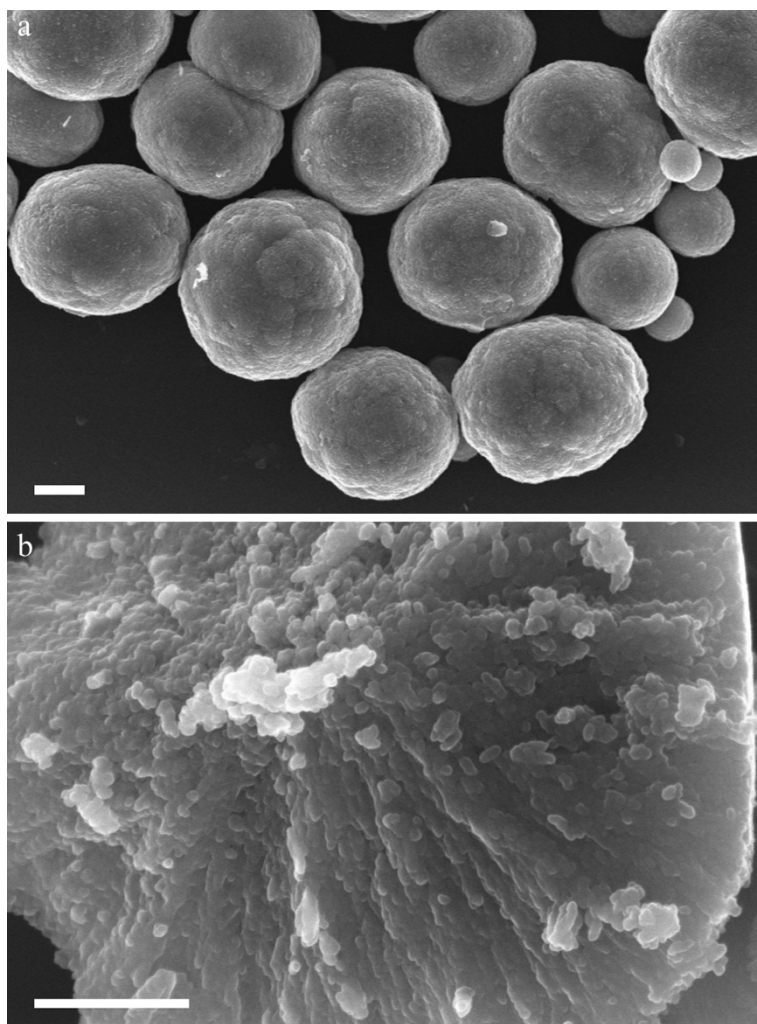


**Figure 2.36** SEM images of amorphous calcium carbonate particles formed in the presence of silica particles (Ludox); (a) whole particles and (b) broken particle (HM-211) (scale bar: 1  $\mu\text{m}$ ).

Though the presence of silica nanoparticles was not discernible by SEM for HM-211, EDAX analysis on the SEM indicated that silica was indeed present in the particles by the presence of the silicon peak (Figure 2.37). Silicon was not present in the EDAX of plain amorphous  $\text{CaCO}_3$  particles. Particles were loaded directly onto the aluminium stub, rather than on a silicon wafer as is typical, and EDAX measurements were taken from the centre of the particles. EDAX also provides quantitative data of the elemental analysis (Table 2.1).

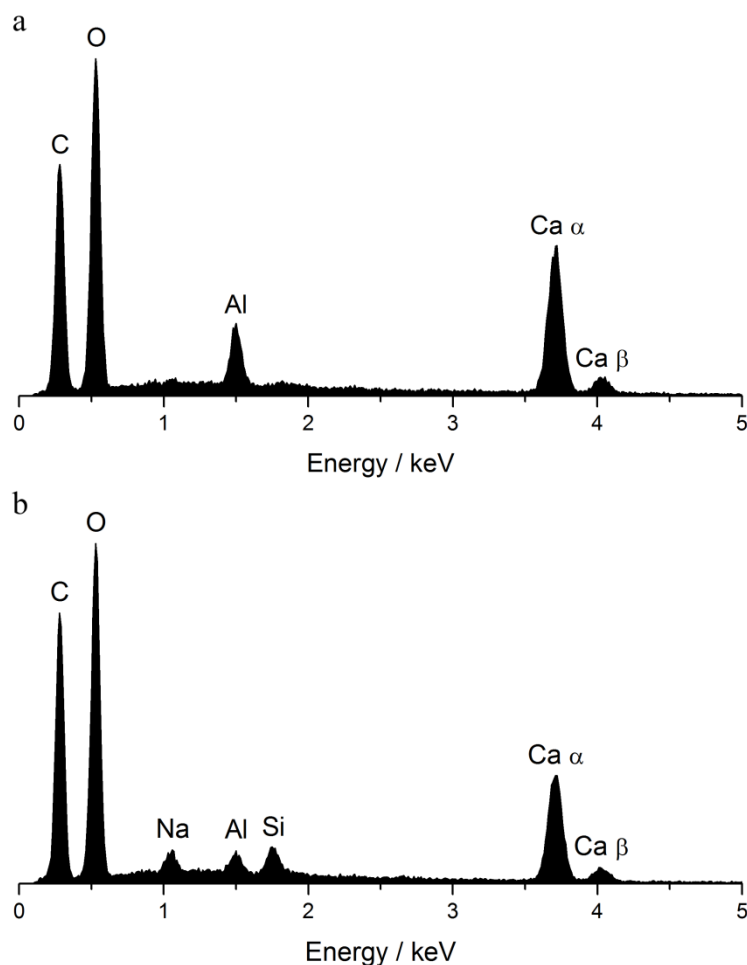


**Figure 2.37** EDAX spectrum of (a) amorphous calcium carbonate (HM-210) and (b) amorphous calcium carbonate formed in the presence of silica particles (Ludox) (HM-211). An average of 8 samples were taken.

TGA was performed on both samples to elucidate silica content (Figure 2.38). At  $\sim 650$  °C calcium carbonate combusts, releasing 44.0 % of its mass as  $\text{CO}_2$ , leaving a CaO pellet; TGA shows that the amorphous calcium carbonate completely combusts, leaving no carbon residue. As the mass loss at 650 °C provides information on how much of the particle is  $\text{CaCO}_3$ , silica content can be deduced (Table 2.1). The silica content was also determined by an average of 8 EDAX measurements to be 4.5 wt.%, this is not in keeping with silica determined by TGA, 6.4 wt.%. This is because the shape of the volume of sample that is measured by EDAX is a tear drop (Figure 2.39), thus if the silica is not evenly distributed over the sample the quantitative EDAX data will not be accurate.



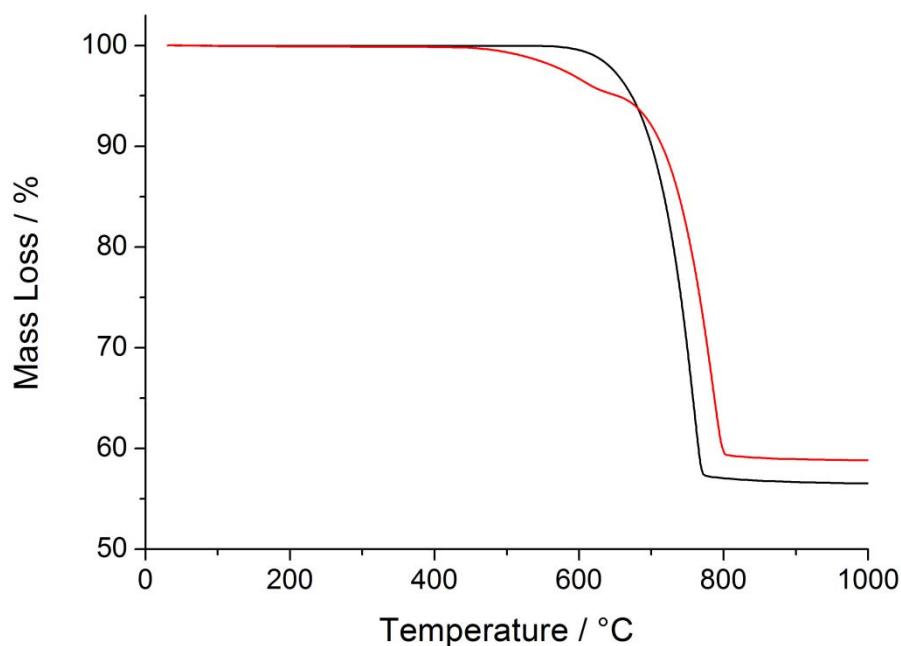


**Figure 2.38** TGA of amorphous calcium carbonate (HM-210) (—) and amorphous calcium carbonate formed in the presence of silica (Ludox) (HM-211) (—).

**Table 2.1** Table showing SiO<sub>2</sub> content determined by EDAX and TGA for amorphous calcium carbonate-silica particles.

| Particles | SiO <sub>2</sub> content (%) determined by: |     |
|-----------|---|-----|
|           | EDAX  | TGA |
| HM-211    | 4.5   | 6.4 |

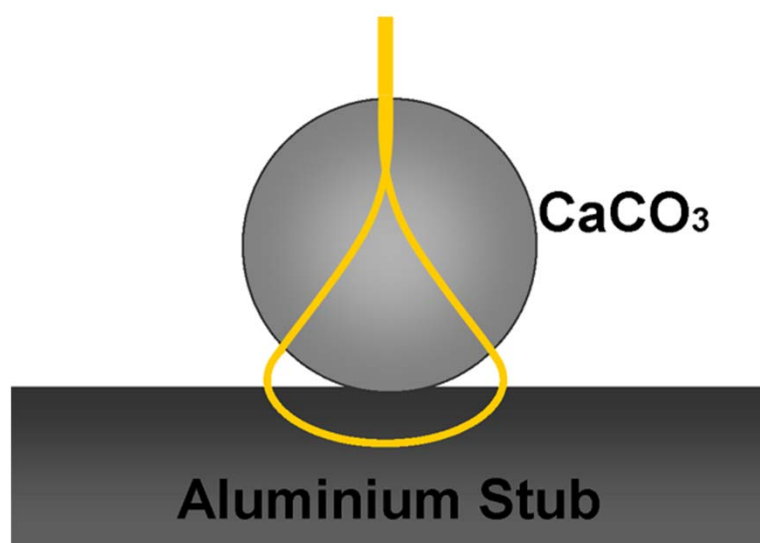


**Figure 2.39** Scheme illustrating the area (yellow outline) from which EDAX data is gained.

Zeta potential measurements show that the calcium carbonate based particles exhibit different surface potentials, indicating that when formed in the presence of silica nanoparticles the amorphous calcium carbonate particles potentially have some of the Ludox adsorbed to the surface (Figure 2.40).

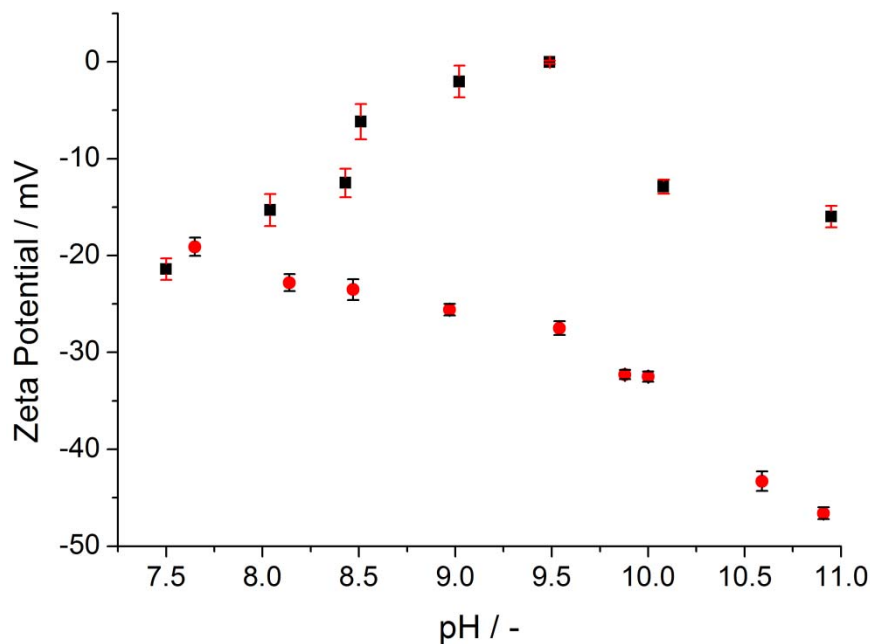


**Figure 2.40** Zeta potential as a function of pH of amorphous calcium carbonate particles (HM-210) (■) and amorphous calcium carbonate particles formed in the presence of silica nanoparticles (HM-211) (●). An average of 6 measurements were recorded.

The silica loaded calcium carbonate particles were etched with acetic acid (0.25 M fed at 0.3 mL h<sup>-1</sup>) to determine whether the silica had formed internal or external structures. SEM analysis suggests that small fractals of silica were formed during the precipitation of calcium carbonate (Figure 2.41). This explains why the EDAX analysis provided a lower value of silica wt.% than TGA; the presence of silica fractals of various sizes indicate that the silica is not evenly distributed through the calcium carbonate particles.

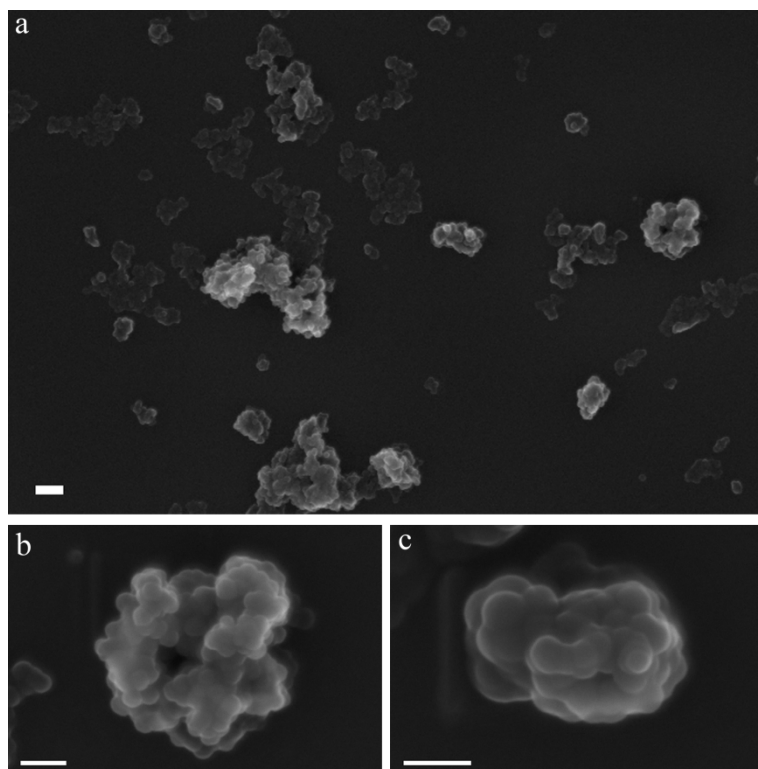


**Figure 2.41** SEM images of silica after the  $\text{CaCO}_3$  has been etched out using acetic acid ((a) scale bar: 200nm, (b) scale bar: 100 nm).

#### *2.3.4.2. Encapsulation of amorphous calcium carbonate particles*

The amorphous calcium carbonate particles were encapsulated in a poly(DEGDA-*co*-MAA) shell as described in section 2.3.2. SEM analysis of encapsulated amorphous calcium carbonate particles indicate that they have indeed been encapsulated in a polymeric shell (HM-212) (Figure 2.42).

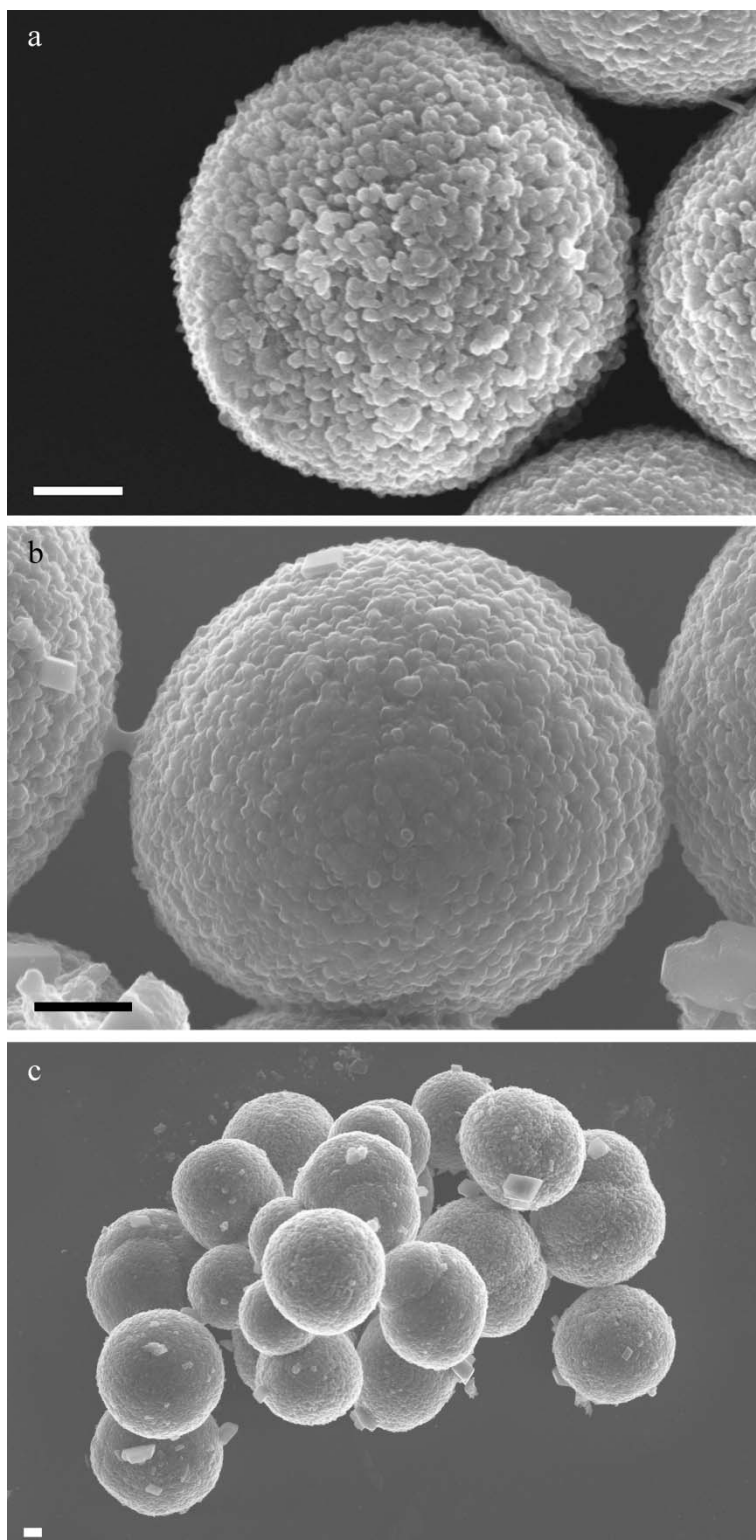


**Figure 2.42** SEM images of (a) amorphous calcium carbonate particle (HM-210), (b) and (c) amorphous calcium carbonate encapsulated in poly(DEGDA-*co*-MAA) (HM-212) (scale bar: 1  $\mu\text{m}$ ).

SEM samples of the encapsulated amorphous calcium carbonate particles (HM-212) prepared immediately after the 2.5 hour polymerization illustrate that the particles have maintained their spherical morphology. However, SEM samples of the same particles (HM-212) prepared three days later indicate that the calcium carbonate core is not stable (Figure 2.43). Calcium carbonate cubes and hollowed polymer particles with calcium carbonate crystals on their surface can be observed, indicating that the calcium carbonate is being etched from the core and re-precipitating elsewhere. This illustrates that these particles must be immediately removed from aqueous conditions if the core-shell morphology is to be maintained. Also, in the case of producing a hollow capsule, the core should be gently etched immediately to preserve the integrity of the polymer shell.

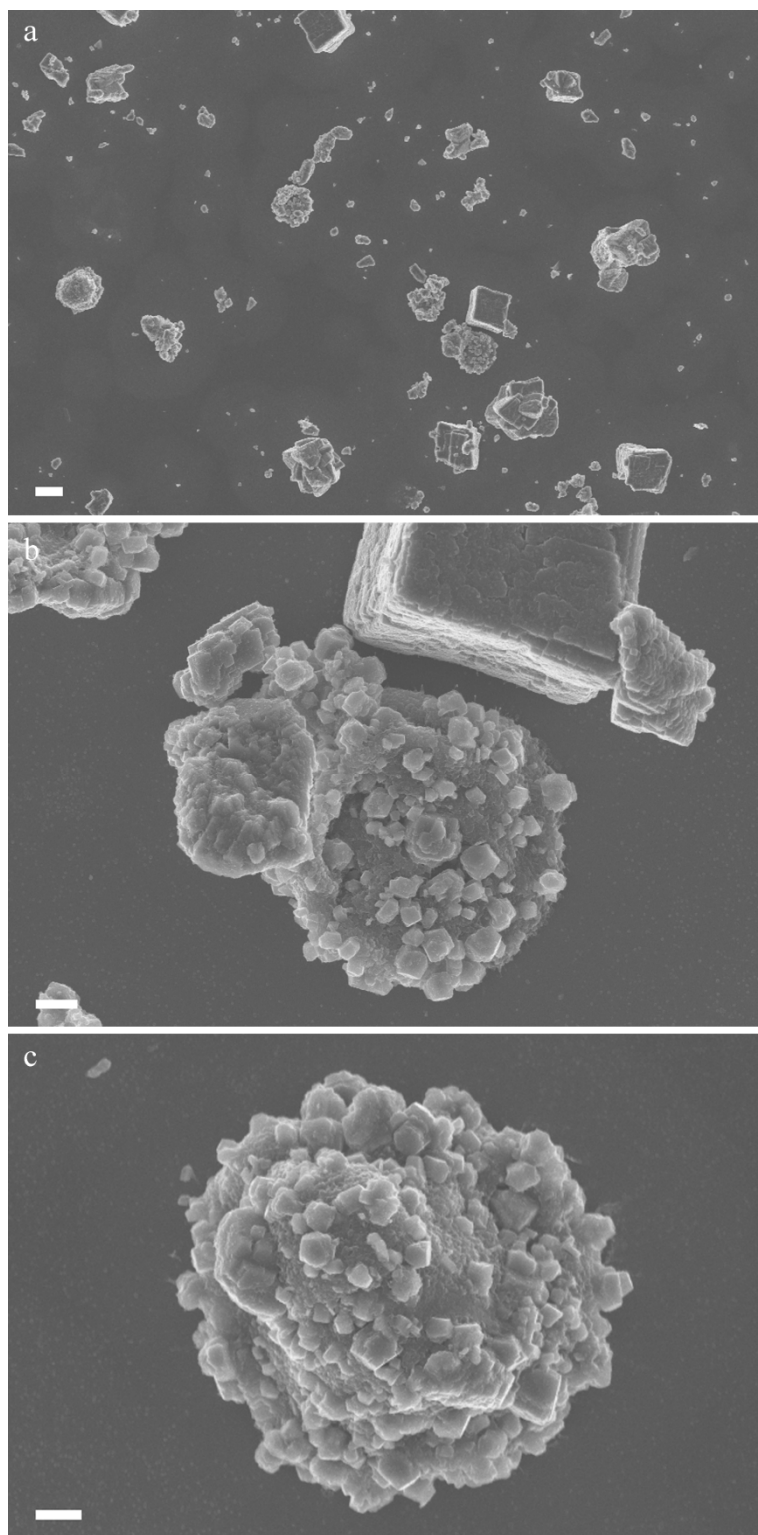


**Figure 2.43** SEM images of amorphous calcium carbonate encapsulated in poly(DEGDA-*co*-MAA) after 3 days in aqueous conditions ((a) scale bar: 10  $\mu\text{m}$ . (b-c) scale bar: 2  $\mu\text{m}$ ). It appears as though the calcium carbonate has been etched from the core and re-precipitated outside the polymer shell.



Silica loaded calcium carbonate particles were also encapsulated; SEM analysis indicated that the particles were coated in a polymer layer (Figure 2.44).

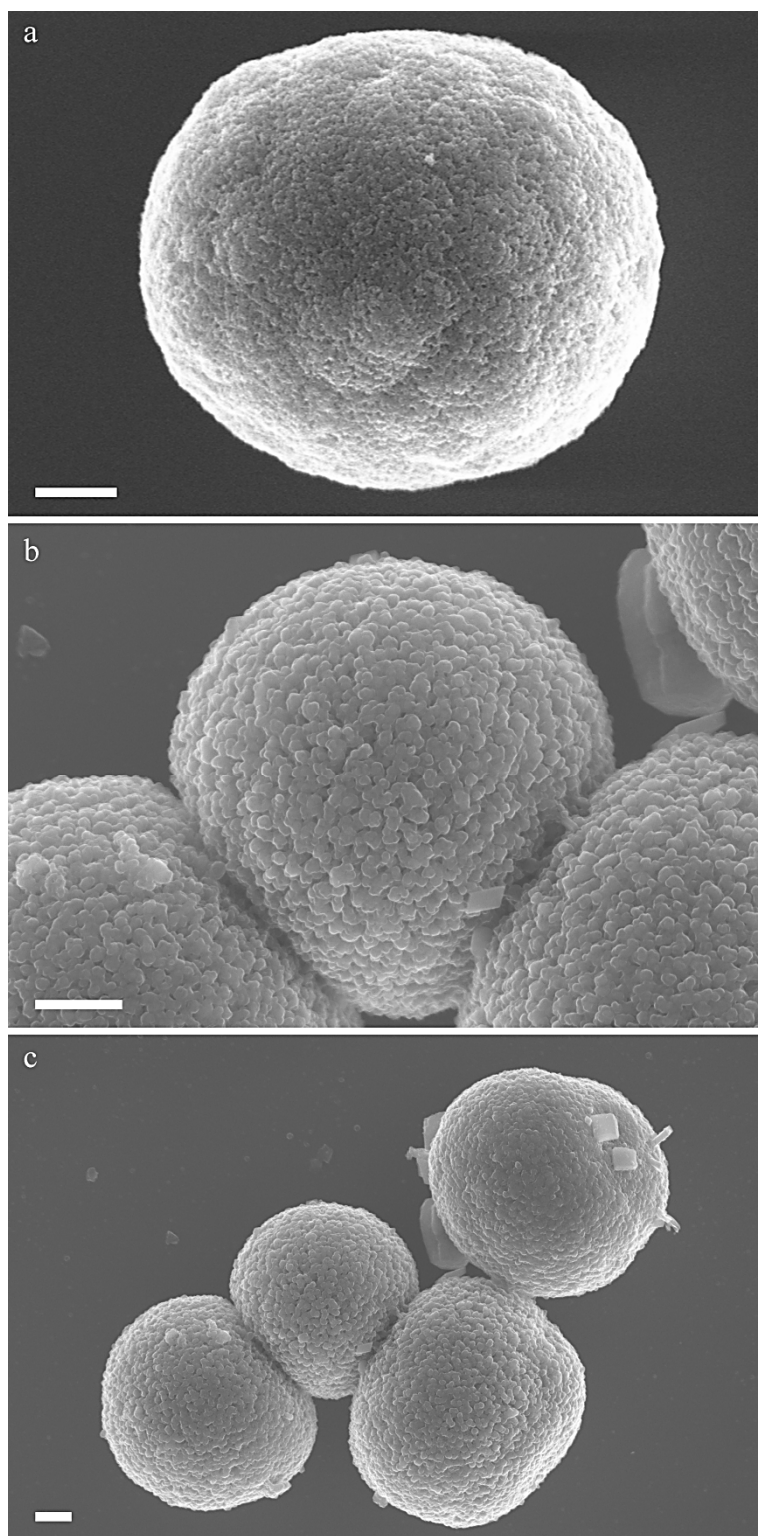


**Figure 2.44** SEM images of (a) amorphous calcium carbonate particle formed in the presence of silica (HM-211), (b) and (c) amorphous calcium carbonate formed in the presences of silica encapsulated in poly(DEGDA-*co*-MAA) (HM-213) (scale bar: 1  $\mu$ m).

#### 2.3.4.3. *Hollow particles template on amorphous calcium carbonate*

The calcium carbonate core was etched out of the composite particles (1.0 g) by feeding 100 mL of 0.25 M acetic acid at  $0.3 \text{ mL h}^{-1}$ . SEM analysis showed the collapsed polymer shell, indicating that the calcium carbonate had been removed (Figure 2.45 and Figure 2.46). Here we have touched upon the potential our encapsulation method has in preparation of nano-rattles by loading a sacrificial calcium carbonate core prior to encapsulation.

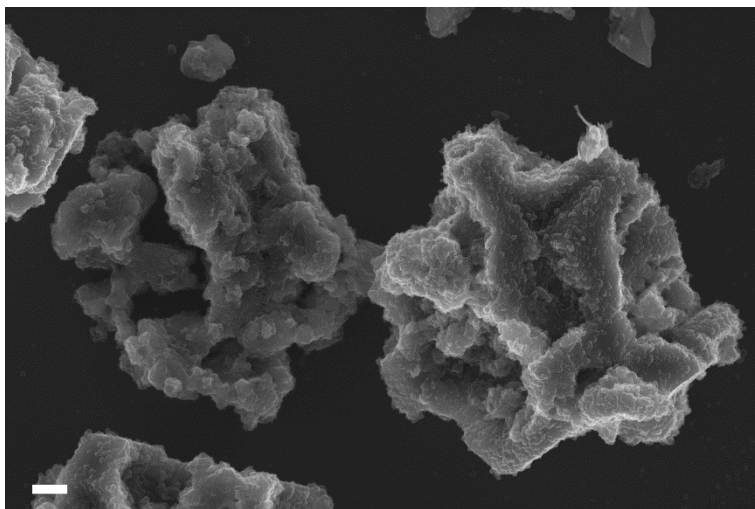


**Figure 2.45** SEM image of hollow poly(DEGDA-*co*-MAA) templated on amorphous calcium carbonate particles (HM-214) (scale bar: 1  $\mu\text{m}$ ).

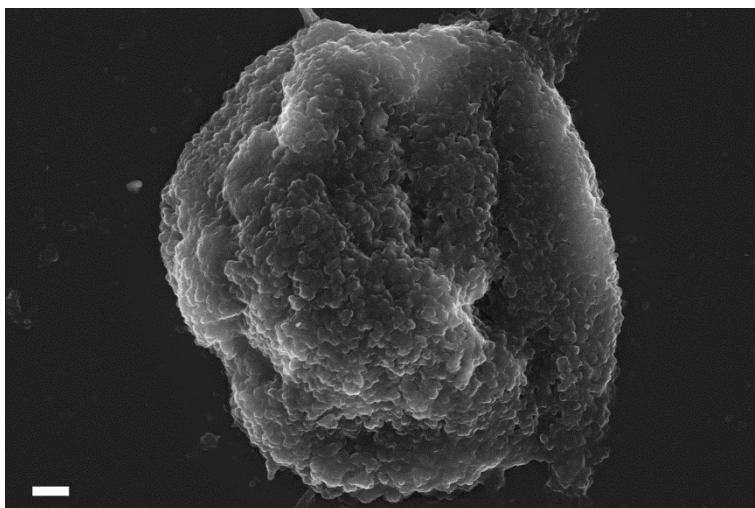


**Figure 2.46** SEM image of hollow poly(DEGDA-*co*-MAA) templated on amorphous calcium carbonate particles formed in the presence of silica (HM-215) (scale bar: 1  $\mu\text{m}$ ).



## 2.4. Conclusion

In conclusion, we have demonstrated a strategy to encapsulate calcium carbonate particles and provide them with a polymer shell in waterborne dispersions, without the need of pre-modification of pigment surfaces, or the necessity to use surfactants. We have shown the ability to produce non-spherical hollow polymer particles using ellipsoidal calcium carbonate particles as a template. We have also touched upon the potential to prepare nano-rattle structures by precipitating calcium carbonate in the presence of the “rattle” material, in this case silica nano-particles, prior to encapsulation. Having illustrated the encapsulation of calcium carbonate, we are interested in exploring the encapsulation of other pigments such as titanium dioxide or phthalocyanine blue. We believe that our method can be used to fabricate a wide range of hybrid core-shell pigment-polymer colloids, opening up interesting materials for photonic applications, such as opacifying agents in waterborne coating formulation.

## 2.5. Experimental

### 2.5.1. Materials

Di(ethylene glycol) dimethacrylate (75 %), methacrylic acid, methyl methacrylate (99 %), hydrochloric acid (37 %) and ammonium persulfate ( $\geq 98.0$  %) were purchased from Sigma-Aldrich and were used as received. Calcium chloride (granular) and sodium carbonate (anhydrous) were purchased from Fischer Scientific. Calcium carbonate (SOCAL P3) was kindly donated by AkzoNobel. Carbon film 200 copper mesh, lacey carbon film 300 copper mesh TEM grids and SEM specimen stubs were purchased from Agar Scientific.

### 2.5.2. Equipment

Monomer was fed into the reaction mixture with a Harvard Instrument PHD 2000 Infusion syringe pump. Transmission electron microscopy (TEM) and Cryo-TEM was performed on a Jeol 2010F TEM fitted with a Gatan Ultrascan 4000 camera; samples were prepared by adding a drop of diluted latex to a suspended carbon grid, wicking the excess liquid away with filter paper. Scanning transmission electron microscopy (STEM) was performed on a Jeol 2100 STEM fitted with an 80 mm<sup>2</sup> Oxford Instruments X-Max silicon drift detector; samples were prepared by adding a drop of diluted latex to a suspended lacey carbon grid, wicking the excess liquid away with filter paper. SEM was performed on a Zeiss SUPRA 55-VP FEGSEM fitted with an EDAX Genesis analytical system; samples were prepared by adding an aqueous drop of diluted sample to a silicon wafer and drying at room temperature for 12 hours, the sample was subsequently carbon coated with a carbon evaporator for 4 seconds. Particle size was measured with; a Malvern Mastersizer 2000 fitted with a hydro 2000  $\mu$ p wet dispersion unit and a Malvern Zetasizer Nano ZS. All <sup>1</sup>H and spectra were recorded on a Bruker DPX-400 spectrometer as

solutions in deuterated NMR solvents. Chemical shifts are cited as parts per million (ppm). The following abbreviations are used to abbreviate multiplicities; s = singlet, d = doublet, t = triplet, q = quartet, m = multiplet.

### **2.5.3. Encapsulation of calcium carbonate with polymer primer**

#### *2.5.3.1. Encapsulation with DEGDA (HM-201)*

Calcium carbonate (SOCAL P3) (10.00 g) was dispersed in water (50.00 g) and degassed by purging with nitrogen for 20 minutes. The reaction mixture was heated to 70 °C and initiated with ammonium persulfate (0.0203 g, 0.089 mmol) dissolved in water (1.0 g). Degassed di(ethylene glycol) diacrylate (1.12 g, 1.00 mL, 5.22 mmol) was fed into the reaction at 0.5 mL h<sup>-1</sup>. The reaction stopped 30 minutes after the monomer feed finished.

#### *2.5.3.2. Encapsulation with MAA and DEGDA (single feed) (HM-202)*

Calcium carbonate (SOCAL P3) (10.00 g) was dispersed in water (49.98 g) and degassed by purging with nitrogen for 20 minutes. The reaction mixture was heated to 70 °C and initiated with ammonium persulfate (0.0204 g, 0.089 mmol) dissolved in water (1.00 g). A degassed mixture of di(ethylene glycol) diacrylate (0.94 g, 0.84 mL, 4.40 mmol) and methacrylic acid (0.16 g, 0.16 mL, 1.84 mmol) was fed into the reaction at 0.5 mL h<sup>-1</sup>. The reaction stopped 30 minutes after the monomer feed finished.

#### *2.5.3.3. Encapsulation with MAA and DEGDA (Two feeds)*

Calcium carbonate (SOCAL P3) (10.00 g) was dispersed in water (50.30 g) and degassed by purging with nitrogen for 20 minutes. The reaction mixture was heated to 70 °C and initiated with ammonium persulfate (0.0204 g, 0.089 mmol) dissolved in water (1.00 g). A degassed mixture of di(ethylene glycol) diacrylate (0.38 g, 0.34 mL, 1.79 mmol) and methacrylic acid (0.16 g, 0.16 mL, 1.84 mmol)

was fed into the reaction at  $0.5 \text{ mL h}^{-1}$ , followed by di(ethylene glycol) diacrylate (0.56 g, 0.50 mL, 2.61 mmol) fed at  $0.5 \text{ mL h}^{-1}$ . The reaction stopped 30 minutes after the monomer feed finished. Conversion was determined by gravimetry.

**Table 2.2** Table of repeated reactions of the encapsulation of calcium carbonate in poly(DEGDA-co-MAA).

| Exp.   | MAA<br>(g) | DEGDA 1<br>(g) | DEGDA 2<br>(g) | CaCO <sub>3</sub><br>(g) | APS<br>(g) |
|--------|------------|----------------|----------------|--------------------------|------------|
| HM-203 | 0.16       | 0.38           | 0.56           | 10.00                    | 0.020      |
| HM-204 | 0.16       | 0.38           | 0.56           | 10.00                    | 0.020      |
| HM-205 | 0.16       | 0.38           | 0.56           | 10.00                    | 0.020      |
| HM-206 | 0.16       | 0.39           | 0.56           | 10.00                    | 0.021      |

#### 2.5.4. Etching of calcium carbonate core to yield hollow particles (HM-207)

To the encapsulated calcium carbonate particles (HM-204) (1.00 g) in water (5.00 g) an excess of 1 M HCl solution (20 mL) was added drop-wise with a dropping funnel. The particles were cleaned by 5 centrifugation cycles into water.

#### 2.5.5. Shell Growth (HM-208)

To increase shell thickness the initial encapsulation reactions for all pigments were repeated but with a total of 120.00 g water and after the di(ethylene glycol) diacrylate based feed degassed methyl methacrylate (5.62 g, 6.0 mL, 56.09 mmol) was fed at a rate of  $1 \text{ mL h}^{-1}$ . The reaction stopped 30 minutes after the monomer feed finished.

#### 2.5.6. Water solubility of DEGDA (HM-209)

Water solubility of di(ethylene glycol) diacrylate was calculated by NMR. Mixtures of DEGDA (1.00 g) in D<sub>2</sub>O (7 g) were heated to 25, 30, 40, 50, 60 and

70 °C and stirred for one hour, after which stirring was stopped and the mixture was left to separate. A sample of the D<sub>2</sub>O phase (0.40 g) was taken with an appropriately heated glass pipette and diluted with a solution of sodium acetate trihydrate in D<sub>2</sub>O (0.326 mol dm<sup>-3</sup>). Concentration of DEGDA was calculated from the resultant <sup>1</sup>H NMR (Figure 2.46 and Table 2.3).

<sup>1</sup>H NMR (D<sub>2</sub>O),  $\delta$  (PPM): 6.37 (d, 4H, HCHCHCO); 6.13 (q, 2H, 2xCH<sub>2</sub>CHCCOOC); 5.92 (d, 4H, HCHCHCO); 4.28 (t, 4H, COOCH<sub>2</sub>CH<sub>2</sub>O); 3.78 (t, 4H, 2xCOOCH<sub>2</sub>CH<sub>2</sub>O).

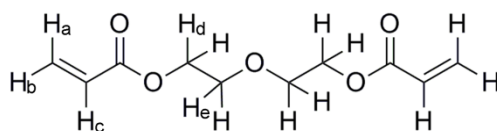


**Figure 2.47** Di(ethylene glycol) diacrylate (DEGDA).

**Table 2.3** Table of <sup>1</sup>H NMR data for the solubility of DEGDA in D<sub>2</sub>O

| Temp<br>(°C) | <sup>1</sup> H Integrals |      |      |      |      | Std. Conc.<br>(mol dm <sup>-3</sup> ) | DEGDA Conc.<br>(mol dm <sup>-3</sup> ) (g L <sup>-1</sup> ) |      |
|--------------|--------------------------|------|------|------|------|---------------------------------------|---|------|
|              | a                        | b    | c    | d    | e    | SA                                    |   |      |
| 25           | 2.00                     | 2.04 | 1.71 | 3.97 | 3.89 | 11.43                                 | 0.177   | 24.4 |
| 30           | 2.00                     | 2.04 | 1.72 | 3.95 | 3.74 | 11.11                                 | 0.173   | 23.3 |
| 40           | 2.00                     | 2.01 | 1.72 | 3.84 | 3.75 | 14.42                                 | 0.189   | 22.4 |
| 50           | 2.00                     | 2.08 | 1.67 | 4.03 | 3.85 | 12.65                                 | 0.176   | 22.0 |
| 60           | 2.00                     | 2.03 | 1.64 | 3.96 | 3.85 | 12.34                                 | 0.174   | 21.3 |
| 70           | 2.00                     | 2.05 | 1.68 | 4.05 | 3.92 | 13.38                                 | 0.177   | 21.0 |

### 2.5.7. Synthesis of amorphous calcium carbonate particles (HM-210)

Amorphous calcium carbonate particles were synthesized as follows. 250 mL of 0.33 M calcium chloride was rapidly added to a vigorously stirred beaker containing 250 mL of 0.33 M sodium carbonate. The mixture was vigorously stirred

for 30 seconds, after which the precipitated amorphous calcium carbonate was collected by filtration; the particles were washed with water and left to dry under vacuum.

#### **2.5.8. Synthesis of amorphous calcium carbonate particles containing silica nanoparticles (HM-211)**

250 mL of 0.33 M calcium chloride and 250 mL 0.33 M sodium carbonate were simultaneously added to a vigorously stirred beaker containing 13.6 g Ludox sol (40 wt.% silica). The mixture was vigorously stirred for 30 seconds, after which the precipitated amorphous calcium carbonate was collected by filtration; the particles were washed with water and left to dry under vacuum.

#### **2.5.9. Encapsulation of amorphous calcium carbonate particles**

A typical procedure for the encapsulation of amorphous calcium carbonate particles proceeded as follows. 24.0 g of water (adjusted to pH 8) was added to the amorphous calcium carbonate particles (5.0 g) (the pH was adjusted to 10.8 for HM-212 and 10.2 for HM-213 with aqueous NaOH). The mixture was degassed by purging with nitrogen for 20 minutes. The reaction mixture was heated to 70 °C and initiated with ammonium persulfate (0.02 g, 0.088 mmol) dissolved in water (1.0 g). 0.5 mL of a degassed mixture of di(ethylene glycol) diacrylate and methacrylic acid was fed into the reaction at 0.5 mL h<sup>-1</sup>, followed by 0.5 mL di(ethylene glycol) diacrylate fed at 0.5 mL h<sup>-1</sup> (see Table 2.4 for monomer quantities). The reaction was left for 30 minutes.

**Table 2.4** Encapsulated amorphous calcium carbonate particles within a polymeric shell monomer fed amounts fed into a mixture of 5.0 g calcium carbonate and 25.0 g water. Monomer feeds 1 and 2 were both 0.5 mL and fed at 0.5 mL h<sup>-1</sup>.

| Exp.   | Monomers | Mass (g) |        | mmol   |        |
|--------|----------|----------|--------|--------|--------|
|        |          | Feed 1   | Feed 2 | Feed 1 | Feed 2 |
| HM-212 | MAA      | 0.16     | 0      | 1.86   | 0      |
|        | DEGDA    | 0.39     | 0.56   | 1.82   | 2.61   |
| HM-213 | MAA      | 0.16     | 0      | 1.86   | 0      |
|        | DEGDA    | 0.38     | 0.56   | 1.82   | 2.61   |

#### 2.5.10. Hollow particles template on amorphous calcium carbonate

Hollow particles were synthesized by feeding 100 mL 0.25 M acetic acid into a 6.0 g solution containing 1.0 g composite particles at 0.3 mL h<sup>-1</sup>. Particles were cleaned by 5 centrifugation cycles into water.

## 2.6. References

1. Fernández-Varea, J. M.; Garcia-Molina, R. *J. Colloid Interface Sci.* **2000**, 231, 394-397.
2. Urban, D.; Takamura, K. *Polymer Dispersions and Their Industrial Applications* Wiley-VCH, Weinham, 2002.
3. Tiarks, F.; Frechen, T.; Kirsch, S.; Leuninger, J.; Melan, M.; Pfau, A.; Richter, F.; Schuler, B.; Zhao, C. L. *Macromol. Symp.* **2002**, 187, 739-752.
4. Yamaguchi, T.; Ono, T.; Ito, H. *Angew. Makromol. Chem.* **1973**, 32, 177-180.
5. Arai, M.; Arai, K.; Saito, S. *J. Polym. Sci. Polym. Chem. Ed.* **1982**, 20, 1021-1029.
6. Konno, M.; Shimizu, K.; Arai, K.; Saito, S. *J. Polym. Sci., Part A: Polym. Chem.* **1987**, 25, 223-230.
7. Hasegawa, M.; Arai, K.; Saito, S. *J. Polym. Sci., Part A: Polym. Chem.* **1987**, 25, 3117-3125.
8. Caruso, R. A.; Susha, A.; Caruso, F. *Chem. Mater.* **2001**, 13, 400-409.
9. Blomberg, E.; Poptoshev, E.; Claesson, P. M.; Caruso, F. *Langmuir* **2004**, 20, 5432-5438.
10. De Geest, B. G.; Vandenbroucke, R. E.; Guenther, A. M.; Sukhorukov, G. B.; Hennink, W. E.; Sanders, N. N.; Demeester, J.; De Smedt, S. C. *Adv. Mater.* **2006**, 18, 1005-1009.
11. De Geest, B. G.; Willart, M. A.; Hammad, H.; Lambrecht, B. N.; Pollard, C.; Bogaert, P.; De Filette, M.; Saelens, X.; Vervaet, C.; Remon, J. P.; Grooten, J.; De Koker, S. *ACS Nano* **2012**, 6, 2136-2149.
12. De Geest, B. G.; Willart, M. A.; Lambrecht, B. N.; Pollard, C.; Vervaet, C.; Remon, J. P.; Grooten, J.; De Koker, S. *Angew. Chem. Int. Ed.* **2012**, 51, 3862-3866.
13. Volodkin, D. V.; Petrov, A. I.; Prevot, M.; Sukhorukov, G. B. *Langmuir* **2004**, 20, 3398-3406.
14. Richardson, J. J.; Ejima, H.; Lörcher, S. L.; Liang, K.; Senn, P.; Cui, J.; Caruso, F. *Angew. Chem. Int. Ed.* **2013**, 52, 6455-6458.
15. Harley, S.; Thompson, D. W.; Vincent, B. *Colloids Surfaces* **1992**, 62, 163-176.



16. Hogg, R.; Healy, T. W.; Fuerstenau, D. W. *Trans. Faraday Soc.* **1966**, 62, 1638-1651.
17. Barouch, E.; Matijevic, E.; Wright, T. H. *J. Chem. Soc., Faraday Trans.* **1985**, 81, 1819-1832.
18. Ottewill, R. H.; Schofield, A. B.; Waters, J. A.; Williams, N. S. J. *Colloid. Polym. Sci.* **1997**, 275, 274-283.
19. Furusawa, K.; Anzai, C. *Colloid. Polym. Sci.* **1987**, 265, 882-888.
20. Furusawa, K.; Anzai, C. *Colloids Surfaces* **1992**, 63, 103-111.
21. Voorn, D. J.; Ming, W.; Herk, A. M. v.; Bomans, P. H. H.; Frederik, P. M.; Gasemjit, P.; Johanssmann, D. *Langmuir* **2005**, 21, 6950-6956.
22. Haga, Y.; Watanabe, T.; Yosomiya, R. *Angew. Makromol. Chem.* **1991**, 189, 23-34.
23. Yu, D.-G.; An, J. H.; Bae, J. Y.; Ahn, S. D.; Kang, S.-Y.; Suh, K. S. *J. Appl. Polym. Sci.* **2005**, 97, 72-79.
24. Lorimer, J. P.; Mason, T. J.; Kershaw, D.; Livsey, I.; Templeton-Knight, R. *Colloid. Polym. Sci.* **1991**, 269, 392-397.
25. Fu, S.; Xu, C.; Du, C.; Tian, A.; Zhang, M. *Colloids Surf. A* **2011**, 384, 68-74.
26. Fu, S.; Du, C.; Zhang, M.; Tian, A.; Zhang, X. *Prog. Org. Coat.* **2012**, 73, 149-154.
27. Luna-Xavier, J.-L.; Bourgeat-Lami, E.; Guyot, A. *Colloid. Polym. Sci.* **2001**, 279, 947-958.
28. Luna-Xavier, Guyot, J. A.; Bourgeat-Lami, E. *J. Colloid Interface Sci.* **2002**, 250, 82-92.
29. de Oliveira, A. M.; da Silva, M. L. C. P.; Alves, G. M.; de Oliveira, P. C.; dos Santos, A. M. *Polym. Bull.* **2005**, 55, 477-484.
30. Rong, Y.; Chen, H.-Z.; Li, H.-Y.; Wang, M. *Colloids Surf. A* **2005**, 253, 193-197.
31. Lelu, S.; Novat, C.; Graillat, C.; Guyot, A.; Bourgeat-Lami, E. *Polym. Int.* **2003**, 52, 542-547.
32. Steiert, N.; Landfester, K. *Macromol. Mater. Eng.* **2007**, 292, 1111-1125.
33. Erdem, B.; Sudol, E. D.; Dimonie, V. L.; El-Aasser, M. S. *J. Polym. Sci., Part A: Polym. Chem.* **2000**, 38, 4419-4430.

34. Erdem, B.; Sudol, E. D.; Dimonie, V. L.; El-Aasser, M. S. *J. Polym. Sci., Part A: Polym. Chem.* **2000**, 38, 4431-4440.
35. Erdem, B.; Sudol, E. D.; Dimonie, V. L.; El-Aasser, M. S. *J. Polym. Sci., Part A: Polym. Chem.* **2000**, 38, 4441-4450.
36. Al-Ghamdi, G. H.; Sudol, E. D.; Dimonie, V. L.; El-Aasser, M. S. *J. Appl. Polym. Sci.* **2006**, 101, 3479-3486.
37. Bourgeat-Lami, E.; Farzi, G. A.; David, L.; Putaux, J. L.; McKenna, T. F. L. *Langmuir* **2012**, 28, 6021-6031.
38. Bechthold, N.; Tiarks, F.; Willert, M.; Landfester, K.; Antonietti, M. *Macromol. Symp.* **2000**, 151, 549-555.
39. Bourgeat-Lami, E.; Lang, J. *J. Colloid Interface Sci.* **1998**, 197, 293-308.
40. Bourgeat-Lami, E.; Lang, J. *J. Colloid Interface Sci.* **1999**, 210, 281-289.
41. Yu, D.-G.; An, J. H. *Colloids. Surf. A* **2004**, 237, 87-93.
42. Yu, D.-G.; An, J. H.; Ahn, S. D.; Kang, S.-R.; Suh, K. S. *Colloids. Surf. A* **2005**, 266, 62-67.
43. Li, G.; Mai, K.-C.; Feng, K.-C.; Huang, Y.-P. *Polym. Int.* **2006**, 55, 891-897.
44. Gilbert, R. G. *Emulsion Polymerization: A Mechanistic Approach* Academic Press, London, 1995.
45. Ballard, N.; Bon, S. A. F. *Polym. Chem.* **2011**, 8, 301-318.
46. Ma, W.; Xu, S.; Li, J.; Guo, J.; Lin, Y.; Wang, C. *J. Polym. Sci., Part A: Polym. Chem.* **2011**, 49, 2725-2733.
47. Nguyen, D.; Zondanos, H. S.; Farrugia, J. M.; Serelis, A. K.; Such, C. H.; Hawket, B. S. *Langmuir* **2008**, 24, 2140-2150.
48. Loiseau, J.; Doërr, N.; Suau, J. M.; Egraz, J. B.; Llauro, M. F.; Ladavière, C.; Claverie, J. *Macromolecules* **2003**, 36, 3066-3077.
49. Loiseau, J.; Ladavière, C.; Suau, J. M.; Claverie, J. *Polymer* **2005**, 46, 8565-8572.
50. Zhang, L.; Fang, K.; Fu, S.; Zhang, X.; Tian, A. *J. Appl. Polym. Sci.* **2012**, 125, 915-921.
51. Ali, S. I.; Heuts, J. P. A.; Hawket, B. S.; van Herk, A. M. *Langmuir* **2009**, 25, 10523-10533.

52. Zgheib, N.; Putaux, J.-L.; Thill, A.; Bourgeat-Lami, E.; D'Agosto, F.; Lansalot, M. *Polym. Chem.* **2013**, 4, 607-614.
53. Shang, C.; Xu, J.; Wang, X.; Zhang, X.; Zhang, W.; Zhang, T. *Polymer* **2013**, 54, 614-622.
54. Daigle, J.-C.; Claverie, J. P. *J. Nanomater.* **2008**, 1-8.
55. de Leeuw, N. H.; Parker, S. C. *J. Phys. Chem. B* **1998**, 102, 2914-2922.
56. Skinner, A. J.; LaFemina, J. P.; Jansen, H. J. *Am. Mineral.* **1994**, 79, 205-214.
57. Webb, P. A.; Orr, C. *Analytical methods in fine particle technology* Micromeritics Instrument Corporation, Norcross U.S.A, 1997.
58. Fitch, R. *Polymer Colloids: A Comprehensive Introduction* Academic Press, London, 1997.
59. Moulin, P.; Roques, H. *J. Colloid Interface Sci.* **2003**, 261, 115-126.
60. Somasundaran, P.; Agar, G. E. *J. Colloid Interface Sci.* **1967**, 24, 433-440.
61. Fuerstenau, D. W.; Pradip; Herrera-Urbina, R. *Colloids Surfaces* **1992**, 68, 95-102.
62. Healy, T. W.; Fuerstenau, D. W. *J. Colloid Interface Sci.* **2007**, 309, 183-188.
63. Vdović, N. *Chem. Geol.* **2001**, 177, 241-248.
64. Planck, J.; Bassioni, G. *Z. Naturforsch.* **2007**, 62b, 1277-1284.
65. Heberling, F.; Trainor, T. P.; Lützenkirchen, J.; Eng, P.; Denecke, M. A.; Bosbach, D. *J. Colloid Interface Sci.* **2011**, 354, 843-857.
66. Mballa, M. M.; Heuts, J. A.; Herk, A. *Colloid. Polym. Sci.* **2013**, 291, 501-513.
67. Becer, C. R.; Hahn, S.; Fijten, M. W. M.; Thijs, H. M. L.; Hoogenboom, R.; Schubert, U. S. *J. Polym. Sci., Part A: Polym. Chem.* **2008**, 46, 7138-7147.
68. Luzon, M.; Boyer, C.; Peinado, C.; Corrales, T.; Whittaker, M.; Tao, L.; Davis, T. P. *J. Polym. Sci., Part A: Polym. Chem.* **2010**, 48, 2783-2792.
69. *Methacrylic acid* The MAK-Collection for Occupational Health and Safety. Wiley-VCH Verlag GmbH & Co., 2002, 216-227.
70. Geng, Y.; Dalhaimer, P.; Cai, S.; Tsai, R.; Tewari, M.; Minko, T.; Discher, D. E. *Nat. Nanotechnol.* **2007**, 2, 249-255.

71. Decuzzi, P.; Pasqualini, R.; Arap, W.; Ferrari, M. *Pharm. Res.* **2009**, 26, 235-243.
72. Decuzzi, P.; Ferrari, M. *Biophys. J.* **2008**, 94, 3790-3797.
73. Itou, N.; Masukawa, T.; Ozaki, I.; Hattori, M.; Kasai, K. *Colloids. Surf. A* **1999**, 153, 311-316.
74. Fuji, M.; Shin, T.; Watanabe, H.; Takei, T. *Adv. Powder Technol.* **2012**, 23, 562-565.
75. Goldstein, J. L.; Newbury, D. E.; Joy, D. C.; Lyman, C. E.; Echlin, P.; Lifshin, E.; Sawyer, L.; Michael, J. R. *Scanning Electron Microscopy and X-ray Microanalysis*, 3rd ed. Plenum Press, New York, 2003.
76. Tirumkudulu, M. S.; Russel, W. B. *Langmuir* **2004**, 20, 2947-2961.
77. Sukhorukov, G. B.; Volodkin, D. V.; Gunther, A. M.; Petrov, A. I.; Shenoy, D. B.; Mohwald, H. *J. Mater. Chem.* **2004**, 14, 2073-2081.

# Chapter 3: Composite Particle Surface Modification

---

## 3.1. Abstract

In Chapter 2 a method was developed to encapsulate calcium carbonate particles in a polymeric shell. Herein we develop this technique by incorporating a surface modification step utilizing thiol-ene “click” chemistry. Particle dispersion affects more than just waterborne systems; by tuning the surface of these composite particles we can broaden the applications in which they can be used, such as in polymer melts.

## 3.2. Introduction

The modification of polymers through “click” chemistry is well established, with a variety of reactions having been utilized, including; azide-alkyne cycloaddition,<sup>1</sup> azide-nitrile cycloaddition,<sup>2</sup> Diels-Alder,<sup>3</sup> thiol-alkyne<sup>4</sup> and thiol-ene<sup>5</sup> reactions. Herein we focus on the chemistry of thiol-ene “click” reactions and their applications within colloidal materials.

### 3.2.1. Click chemistry

Click chemistry, first reported by Sharpless, is defined as reactions which are simple, high yielding, selective, produce inoffensive by-products which are easily removed, involve readily available starting materials and use either no solvent, benign solvent or solvent that is easily removed.<sup>6</sup> The scope of click chemistry is wide; herein, we will only discuss the thiol-ene “click” chemistries which are relevant to this body of work. For a more detailed discussion on the various types of click reactions the reader is directed to the following reviews.<sup>6-8</sup>

Thiol-ene chemistry has proven to be a very versatile tool with uses in a wide range applications including polymer functionalization,<sup>9, 10</sup> dendrimer synthesis,<sup>11</sup> nanoimprinting<sup>12, 13</sup> and patterning.<sup>14, 15</sup> Herein we discuss in further detail the applications of functionalizing polymer particles. The reaction between thiols and alkenes can proceed by two manners: radical thiol addition or thiol Michael addition, described below.

#### 3.2.1.1. Radical thiol-ene click chemistry

The first reaction between thiols and alkenes was reported in 1905 by Posner,<sup>16</sup> the basic mechanism by which the radical reaction proceeds was later proposed by Kharasch *et al.* in 1938;<sup>17</sup> the mechanism has been further elucidated in more recent years.<sup>18-20</sup> The radical thiol-ene click process is described by the

alternation between a thiyl radical propagation across the “ene” with an anti-Markovnikov orientation and chain transfer, abstraction of a hydrogen from another thiol on the carbon centred radical, regenerating the thiyl radical (Figure 3.1). The reaction can be initiated by thermal or photo-initiator species and can undergo polymerization side reactions and termination.

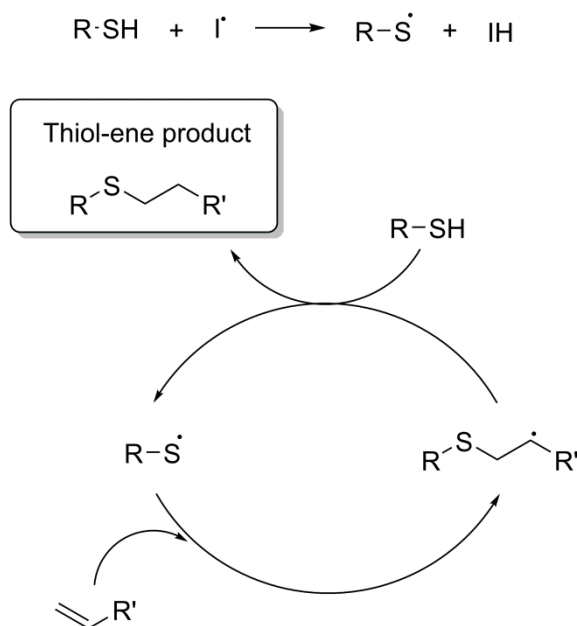


**Figure 3.1** Radical thiol-ene mechanism.

The choice of thiol and ene can greatly alter the kinetics of the reaction, specifically the rate limiting step and this is reflected in the concentration of the two radical species. Thiols with less abstractable hydrogens (higher  $\text{p}K_{\text{a}}$ ) have reduced chain transfer rates, thus the rate limiting step becomes the chain transfer, whereas less reactive enes will cause slow propagation and thus the rate limiting step becomes the propagation step (equations (3.1)-(3.3)).<sup>21, 22</sup>

$$k_{\text{CT}} \cong k_{\text{P}} \quad [R-S\cdot]/[R-S-C-C\cdot-R'] \approx 1 \quad \text{and} \quad R_{\text{p}} \propto [R-SH]^{1/2}[R'-C=C]^{1/2} \quad (3.1)$$

$$k_{\text{CT}} \ll k_{\text{P}} \quad [R-S\cdot]/[R-S-C-C\cdot-R'] \ll 1 \quad \text{and} \quad R_{\text{p}} \propto [R-SH]^1 \quad (3.2)$$

$$k_{CT} \gg k_p \quad (3.3)$$

$$[R-S^\bullet]/[R-S-C-C^\bullet-R'] \gg 1 \quad \text{and} \quad R_p \propto [R-C=C]^1$$

Where  $k_{CT}$  is the chain transfer rate constant,  $k_p$  is the propagation rate constant,  $[R-SH]$  is the thiol concentration,  $[R'-C=C]$  is the ene concentration,  $[R-S^\bullet]$  is the thiyl radical concentration and  $[R-S-C-C^\bullet-R']$  is the carbon centred radical concentration. The reaction is much faster for electron-rich alkenes, compared to electron-deficient alkenes.<sup>19, 23</sup> In the case of electron-deficient enes, such as (meth)acrylates, the intermediate carbon centred radical can react with other alkenes, propagating to form oligomer/polymer contaminants. This competing polymerization becomes a serious complication, making radical-mediated thiol-ene reactions unsuitable for such electron-deficient alkene species.

### 3.2.1.2. Thiol Michael addition

Thiol Michael addition involves the addition of a thiol to an electron-deficient ene and can proceed by either base or nucleophile catalyzed mechanisms. The addition of mercaptans to electron deficient alkenes using a base as a catalyst has been studied since the 1940s.<sup>24</sup> Base catalyzed thiol Michael addition proceeds *via* the deprotonation of the thiol by a base such as triethylamine, the thiolate anion created (a strong nucleophile) attacks the electron-deficient  $\beta$ -carbon of the ene, abstraction of a hydrogen from the conjugate acid completes the cycle, regenerating the base (Figure 3.2).

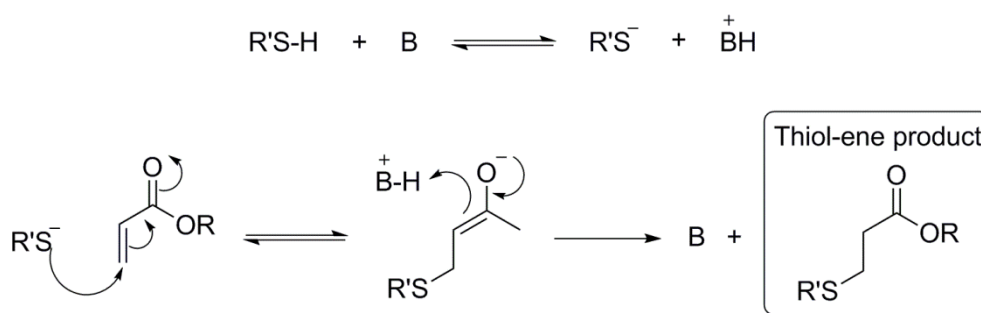


**Figure 3.2** Base catalysed thiol-Michael addition mechanism.



The rate-limiting step is the nucleophilic addition of the thiolate anion across the ene, thus the rate of reaction is dependent on the basicity of the catalyst, acidity of the thiol and electrophilicity of the vinyl group (equations (3.4) and (3.5)).<sup>25</sup>

$$R_{rxn} = k[R-S^{-}][C=C] \quad (3.4)$$

$$[R-S^{-}] = K_{eq} \left( \frac{[B]}{[B^{+}-H]} \right) [R-SH] \quad (3.5)$$

Where  $R_{rxn}$  is the rate of reaction,  $k$  is the rate constant,  $[R-S^{-}]$  is the concentration of the thiolate anion,  $[C=C]$  is the concentration of the ene,  $K_{eq}$  is the equilibrium constant,  $[B]$  is the concentration of the base,  $[B^{+}-H]$  is the concentration of the protonated base and  $[R-SH]$  is the concentration of the thiol. In some cases the base-mediated method can have significant drawbacks including less than quantitative conversion, lengthy reaction times and the requirement of high catalyst concentrations; the nucleophilic-mediated thiol Michael addition significantly overcomes these issues.

The use of a nucleophilic catalyst in thiol Michael addition was first reported in 1967,<sup>26</sup> and was first reported for use in materials in 2003 in an AkzoNobel patent.<sup>27</sup> In the case of nucleophilic catalyzed thiol Michael addition, a nucleophile such as primary amines<sup>25</sup> or tertiary phosphines,<sup>28</sup> reacts with an electron-deficient ene to generate the thiolate anion which undergoes a Michael addition to the ene (Figure 3.3).<sup>29-31</sup> However, it is important to note that a nucleophile-vinyl adduct is formed as a by-product of this mechanism.<sup>32</sup> It was found by Bowman *et al.* that primary amines, specifically hexylamine, did not catalyze the thiol-ene reaction as expected.<sup>25</sup> The experimental kinetics of the reaction of hexyl acrylate and hexanethiol was measured for different amines and phosphines. It was expected that reaction rates should follow the order of *n*-dipropylamine > triethylamine >

hexylamine due to decreasing base strength of the amines, however it was found experimentally that the order was hexylamine > triethylamine > *n*-dipropylamine. When hexylamine was used, the reaction reached 100 % conversion within 500 seconds, correspondingly triethylamine only reached 1 % conversion in this time. This prompted the understanding that primary amines, such as hexylamine, catalyzed the reaction as a nucleophile rather than a base. In the same body of work it was determined that trialkyl phosphines, weaker bases than alkylamines though stronger nucleophiles, prompted faster reaction times still, with the reactivity following the order of  $P\text{-}n\text{-Pr}_3 > P\text{Me}_2\text{Ph} > P\text{Ph}_3$ .

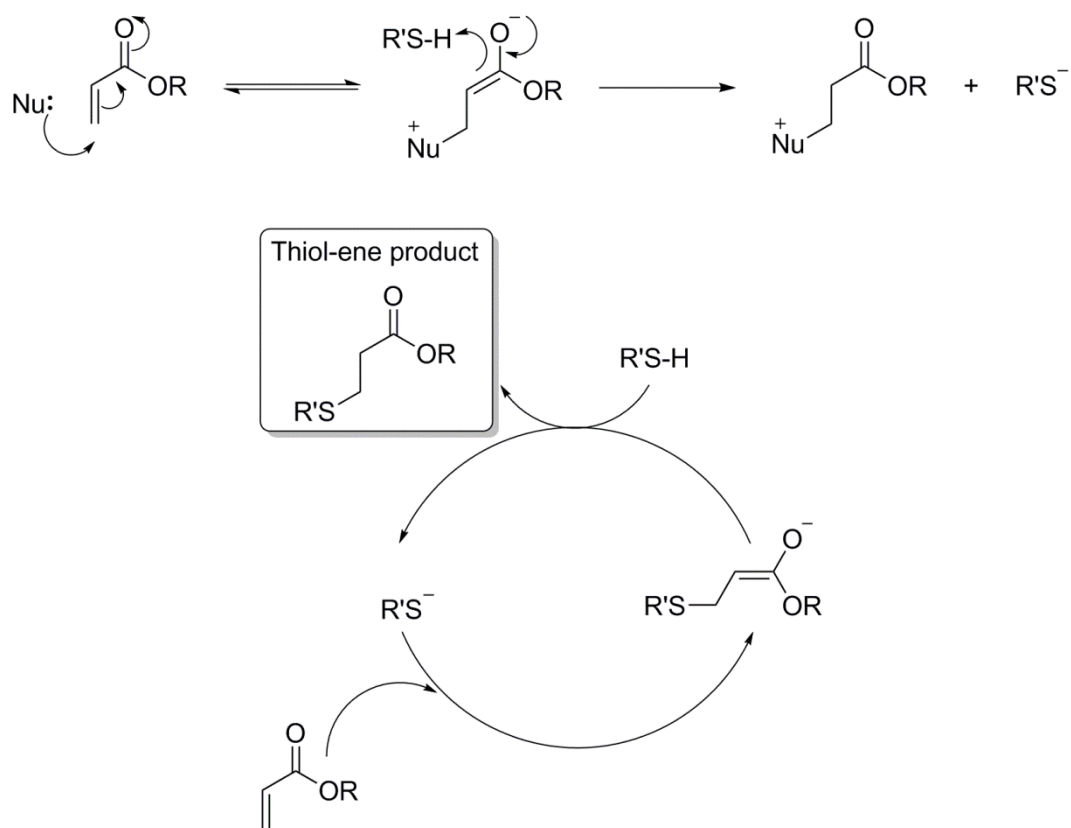


**Figure 3.3** Nucleophile catalyzed thiol-Michael addition mechanism.

The nucleophile initiated thiol Michael addition has significant advantages over the base catalyzed process, including very low concentrations of catalyst and much faster reaction times. It is important to note that unlike traditional Michael reactions, the presence of water is not a concern in the thiol-ene case, due to the low

$pK_a$  of thiols.<sup>25</sup> The nucleophilic method is also of particular interest in certain “one-pot” reactions; phosphine catalysts are distinctly useful when using reagents containing disulphide bridges; they can reduce the disulphide bridge and catalyse the thiol-Michael addition, similarly primary amines will react with RAFT polymers to form thiol  $\omega$ -end functionalized polymers and then subsequently catalyze the thiol-Michael addition.<sup>33-36</sup>

### 3.2.2. Particle modification

Much work has been done on the functionalization of polymers using thiol-ene chemistry.<sup>32, 33, 37-39</sup> Herein we focus on the use of such chemistry to modify particles.

Polymerization of difunctional monomer species results in polymers with pendant vinyl groups; these can be exploited by thiol-ene click chemistry.<sup>40, 41</sup> Poly(divinylbenzene) particles are a common substrate for such reactions, due to their well understood characterization and ease of synthesis *via* precipitation polymerization.<sup>42, 43</sup> Radical thiol-ene chemistry has been widely employed for the modification of such functionalized particles using both thermal and photo-initiator pathways. Hawker and co-workers utilized thiol-ene click chemistry to modify multimodal composite poly(divinylbenzene) particles in order to disperse them in various organic media.<sup>44, 45</sup> Charge stabilized poly(divinylbenzene) particles containing  $MnFe_2O_4$  and Au nanoparticles were synthesized by miniemulsion polymerization in water (Figure 3.4 a); on redispersion in THF the particles were found to be unstable. By reacting the pendant vinyl groups on the surface of the poly(divinyl benzene) particle with thiol functionalized PEG, using a thermal radical initiator (V-50), particles were found to be dispersible in a number of solvents including water, THF, chloroform and DMF (Figure 3.4 b).

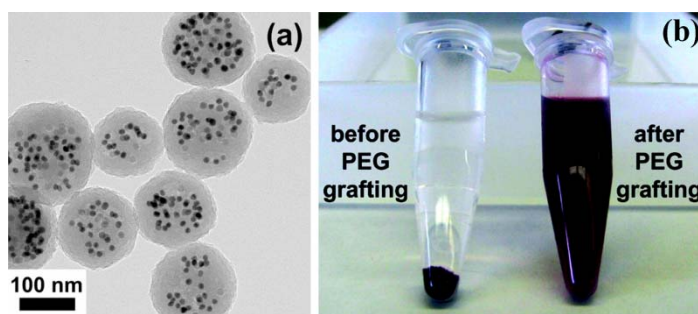


**Figure 3.4** (a) TEM image of composite multimodal composite poly(divinylbenzene)-inorganic latex particles prepared by co-encapsulation of  $\text{MnFe}_2\text{O}_4$  and Au nanoparticles and (b) photograph of composite latex particles redispersed in THF; (left) before and (right) after attachment of PEG.<sup>44</sup>

Aiding particle dispersion is a common goal in the surface modification of particles. Mecking *et al.* post-functionalised poly(butadiene) particles with various hydrophilic moieties; including 3-mercaptopropionic acid methyl ester, 3-mercaptopropanesulfonic acid sodium salt and glutathione (Figure 3.5).<sup>46</sup> Modification was achieved using a thermal radical initiator, in order to produce stable nanoparticles which were redispersible in water. Grafting of the more polar mercaptans (glutathione and 3-mercaptopropanesulfonic acid sodium salt) resulted in modification of the surface pendant vinyl groups on the poly(butadiene) particles. Using less polar mercaptans (3-mercaptopropionic acid methyl ester) resulted in complete conversion of all vinyl groups, due to permeability of the thiol into the polymer particle.

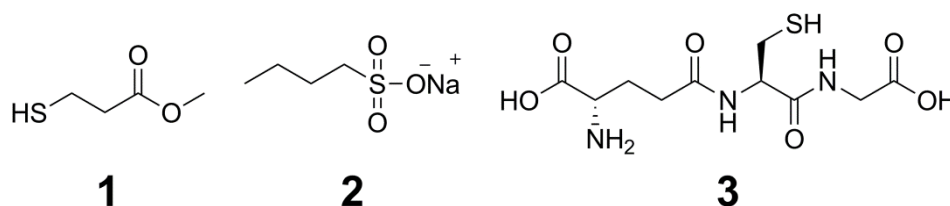


**Figure 3.5** (1) 3-mercaptopropionic acid methyl ester, (2) 3-mercaptopropanesulfonic acid sodium salt and (3) glutathione.

The grafting of polymers prepared by RAFT has proven a popular tool as highly controlled and well defined polymers can be converted to thiol  $\omega$ -end functional polymers *via* aminolysis.<sup>47</sup> Müller and co-workers modified

poly(divinylbenzene) particles, prepared by precipitation polymerization in acetonitrile, with poly(NIPAAm) in order to produce particles which were dispersible in water and had thermo-responsive behaviour.<sup>48</sup> Thiol functionalized poly(NIPAAm) was prepared by RAFT polymerization and cleavage of the RAFT group to yield a thiol using NaBH<sub>4</sub>; the subsequent grafting reaction proceeded by radical thiol-ene click using AIBN as an initiator. In a similar manner, Kang *et al.* prepared fluorescent hollow particles with temperature responsive brushes.<sup>49</sup> Encapsulation of silica nanoparticles in poly(divinylbenzene-*co-n*-vinylcarbazole) was followed by AIBN initiated click of thiol functionalized poly(NIPAM) to the pendant vinyl groups; where poly(NIPAAm) was prepared by RAFT polymerization followed by reduction of the RAFT group using NaBH<sub>4</sub>. The silica core was etched out with hydrofluoric acid to yield multifunctional hollow particles.

Caruso and co-workers prepared hollow particles by layer-by layer assembly, where thiol-ene chemistry was used to cross-link polymer layers and to functionalize the surface with PEG to achieve anti-fouling properties.<sup>50</sup> Silica particles were encapsulated by LbL assembly of poly(methacrylic acid) containing either thiol or ene functionality with poly(vinylpyrrolidone), using UV-light as an initiator (thiol self-initiates forming a radical). Thiol-ene chemistry was used to cross-link the poly(methacrylate) layers and the silica was etched out on addition of hydrofluoric acid and on increasing the pH to 7 the non-cross-linked layers of poly(vinylpyrrolidone) were released. The particles were further reacted with ene functionalized PEG, again using UV light, to create the thiol radical to achieve the anti-fouling finish (Figure 3.6). Yogo and co-workers modified Fe<sub>3</sub>O<sub>4</sub> nanoparticles expressing vinyl groups on the surface to yield biofunctional magnetic particles by

radical click chemistry of cysteine using AIBN, for use in biomedical applications such as an MRI contrast agent.<sup>51</sup>

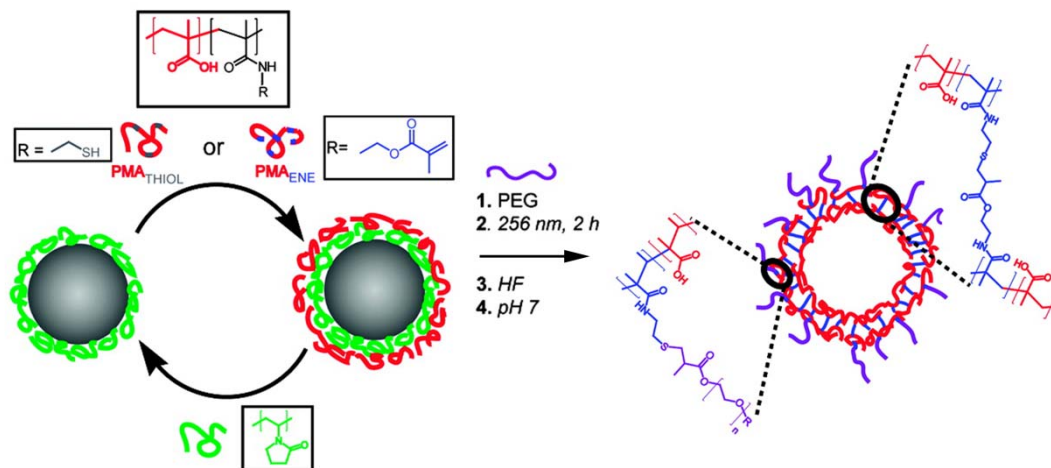


**Figure 3.6** Preparation of (PVP/PMA<sub>Thiol</sub>/PVP/PMA<sub>Ene</sub>)-coated particles, (1-2) PEGylation and stabilization using thiol-ene chemistry, (3) removal of silica core and (4) removal of PVP.<sup>50</sup>

Though not as widely employed as the radical thiol-ene reaction, the thiol-ene Michael addition has also been used in polymer synthesis and modification. Stenzel and co-workers synthesized ethylene glycol dimethacrylate (EGDMA) particles by suspension polymerization and subsequently surface modified them with glucothiose to achieve bioactive particles using tris(2-carboxyethyl)phosphine (TCEP) as the nucleophilic catalyst.<sup>52</sup> Boyer and co-workers used thiol-ene chemistry to modify the surface of titanium dioxide nanoparticles with polymeric chains to aid dispersibility in biological media and aid cell uptake.<sup>53</sup> The TiO<sub>2</sub> nanoparticles were modified to yield surface thiol groups by functionalizing with (3-mercaptopropyl) trimethoxysilane, thiol Michael addition with poly(oligo(ethylene glycol) methyl ether methacrylate) comb polymers with vinyl functionality (prepared by catalytic chain transfer) was achieved using hexylamine as a nucleophilic catalyst in acetonitrile (Figure 3.7).

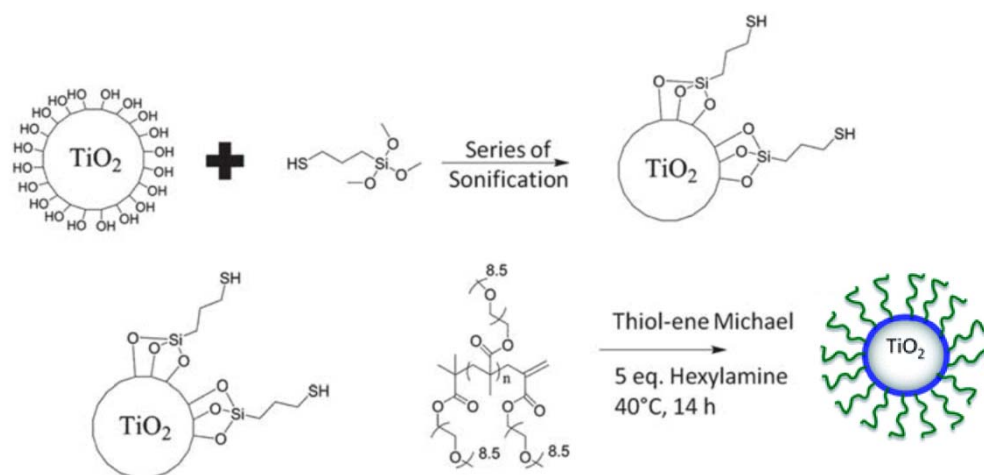


**Figure 3.7** Overall synthetic approach for the surface modification of  $\text{TiO}_2$  nanoparticles.<sup>53</sup>

In this body of work we describe the encapsulation of calcium carbonate particles with multi-functional acrylate monomers to achieve particles with pendant vinyl groups. Utilizing the pendant vinyl groups to modify the particles with thiol “click” chemistry, we demonstrate both hydrophilic and hydrophobic modification and the Michael addition of thiol functionalized poly(styrene) synthesized by RAFT polymerization.

### 3.3. Results and Discussion

#### 3.3.1. Encapsulation of calcium carbonate particles with multi-acrylate monomers to afford pendant vinyl groups

We have previously shown the encapsulation of calcium carbonate particles by starved-fed emulsion polymerization; through initially encapsulating in a cross-linked primer polymeric shell, which on addition of further monomer led to a thick polymeric shell. To form the primer shell a diacrylate monomer was used; often such divinyl monomers yield pendant vinyl groups on the surface.<sup>43</sup> These pendant acrylate groups can be used to tune the surface of the particles through thiol Michael addition reactions, in doing so we may be able to adjust the dispersibility of the particles in various media. We believed that the number of pendant vinyl groups on the encapsulated particles could be controlled by introducing monomers with multiple acrylate functionality such as pentaerythritol triacrylate (PETA) and dipentaerythritol penta-/hexa-acrylate (DPEPHA) (Figure 3.8).

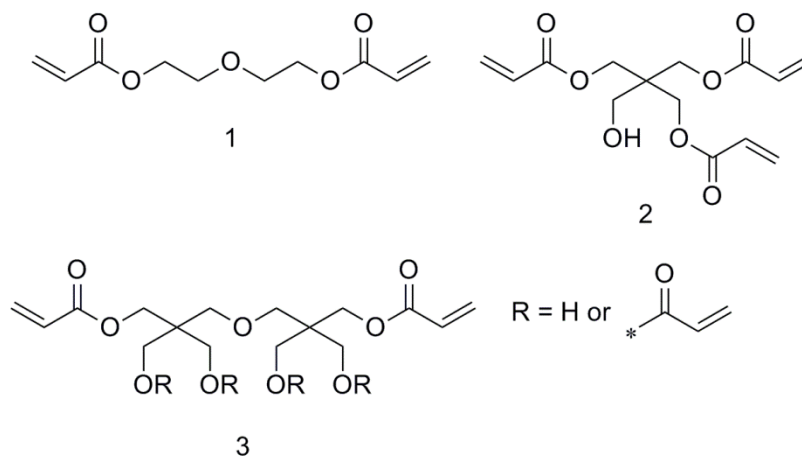


**Figure 3.8** Multiple acrylate containing monomers; (1) di(ethylene glycol) diacrylate (DEGDA), (2) pentaerythritol triacrylate (PETA), (3) dipentaerythritol penta-/hexa-acrylate (DPEPHA).

The sub-micron calcium carbonate particles were encapsulated in the same manner as described in Chapter 2. In an effort to increase the number of pendant vinyl groups, PETA and DPEPHA were incorporated into both feeds (Table 3.1).



However, the PETA and DPEPHA monomers were too viscous to feed in alone; they were diluted by 50 wt. % with DEGDA to decrease the viscosity. Particles were dialysed into water and then collected by freeze-drying. Table 3.2 describes the abbreviations for the composite particle which shall be used from here.

**Table 3.1** Encapsulated calcium carbonate particles within a polymeric shell with various multiple acrylate containing monomers, monomer feed amounts fed into a mixture of 10.0 g calcium carbonate and 50.0 g water. Monomer feeds 1 and 2 were both 0.5 mL and fed at 0.5 mL h<sup>-1</sup>.

| Exp.   | Monomers | Mass (g) |        | mmol   |        |
|--------|----------|----------|--------|--------|--------|
|        |          | Feed 1   | Feed 2 | Feed 1 | Feed 2 |
| HM-301 | MAA      | 0.16     | 0      | 1.84   | 0      |
|        | DEGDA    | 0.39     | 0.34   | 1.80   | 2.61   |
| HM-302 | MAA      | 0.16     | 0      | 1.88   | 0      |
|        | DEGDA    | 0.20     | 0.29   | 0.91   | 1.34   |
|        | PETA     | 0.20     | 0.29   | 0.65   | 0.96   |
| HM-303 | MAA      | 0.16     | 0      | 1.86   | 0      |
|        | DEGDA    | 0.20     | 0.29   | 0.91   | 1.33   |
|        | DPEPHA   | 0.19     | 0.28   | 0.37   | 0.54   |

**Table 3.2** Table listing composite particles synthesized and their abbreviations.

| Exp.   | Abbrev. Name   | Full Description of Particles  |
|--------|----------------|--|
| HM-301 | Poly(DEGDA)-C  | CaCO <sub>3</sub> encapsulated in poly(DEGDA- <i>co</i> -MAA)                    |
| HM-302 | Poly(PETA)-C   | CaCO <sub>3</sub> encapsulated in poly(PETA- <i>co</i> -DEGDA- <i>co</i> -MAA)   |
| HM-303 | Poly(DPEPHA)-C | CaCO <sub>3</sub> encapsulated in poly(DPEPHA- <i>co</i> -DEGDA- <i>co</i> -MAA) |

Particle morphology was characterized by TEM (Figure 3.9-Figure 3.10) and SEM (see Appendix III, Figure III.1). TEM and SEM analysis show that the particles are encapsulated in a polymeric shell. As illustrated in Chapter 2, etching out the  $\text{CaCO}_3$  core with 0.25 M acetic acid yielded hollow non-spherical polymer particles, further illustrating encapsulation of the calcium carbonate core (see Appendix III, Figure III.2 for cryo-TEM images). Zeta potential measurements were also performed to determine whether the calcium carbonate particles were coated in a polymeric shell. The bare calcium carbonate exhibited a low positive zeta potential of 12 mV, after encapsulation all particles had a zeta potential of  $\sim -30$  mV, suggesting that the surface was coated in a negatively charged polymer, in-line with negative charge stabilization of particles by the initiator, APS (see Appendix III, Figure III.3).

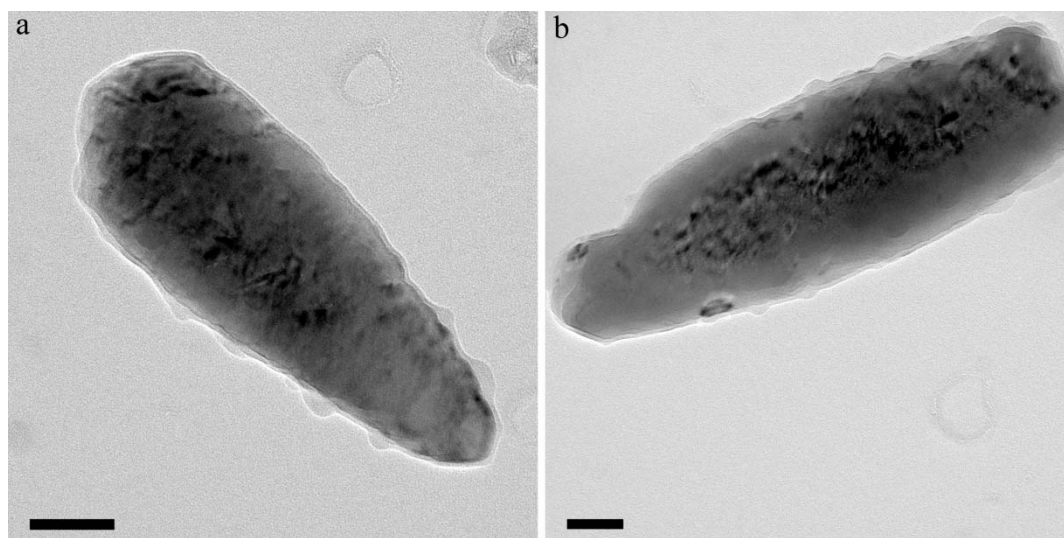


**Figure 3.9** TEM image of poly(DEGDA)-C particles (HM-301) (scale bar: 100 nm).

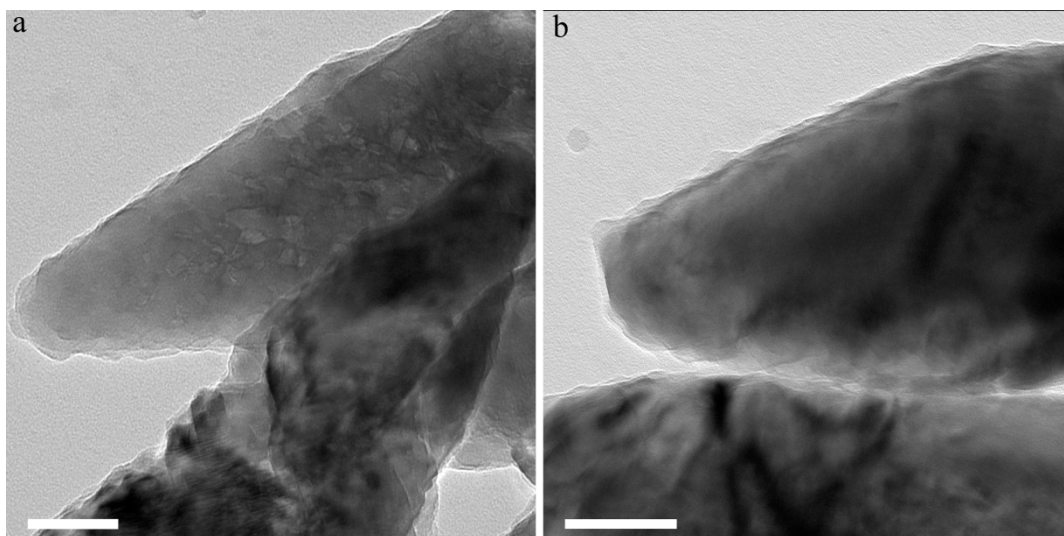


**Figure 3.10** TEM images of poly(PETA)-C particles (HM-302) (scale bar: 100 nm).

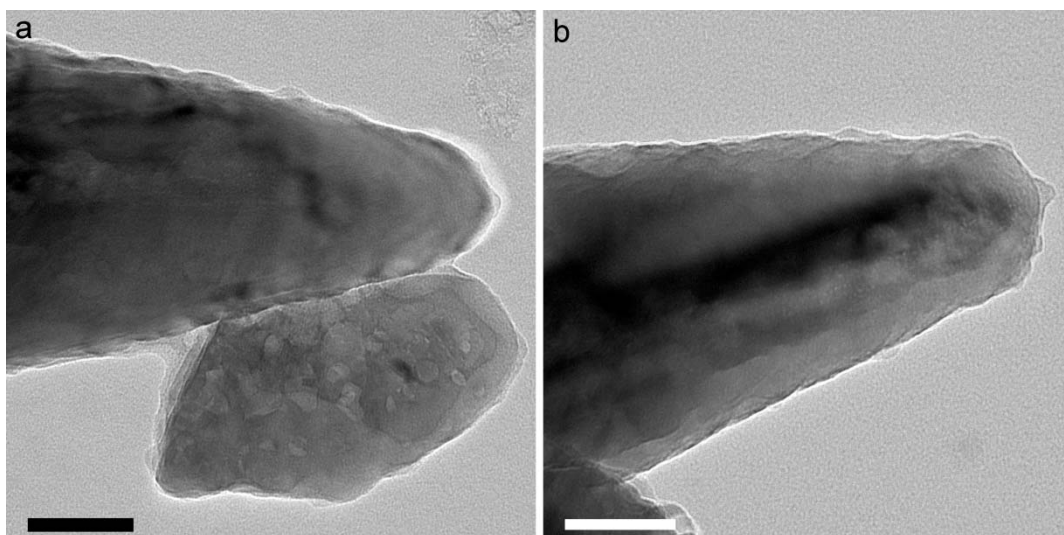


**Figure 3.11** TEM images of poly(DPEPHA)-C particles (HM-303) (scale bar: 100 nm).

FTIR and Raman spectroscopy were used to determine the presence of pendant vinyl groups on the encapsulated particles. Particles were cleaned by dialysis to remove any potential residual monomer which may potentially skew the data. FTIR analysis proved to be a poor tool for the determination of alkene groups, showing only very weak vinylic and  $\alpha,\beta$  unsaturated carbonyl  $-C-H$  peaks at  $809\text{ cm}^{-1}$  and  $983\text{ cm}^{-1}$  respectively,  $C=C$  double bonds were not observed at all. These weak vinylic and  $\alpha,\beta$  unsaturated carbonyl  $-C-H$  peaks were only observed in the poly(PETA)-C (HM-302) and poly(DPEPHA)-C (HM-303) particles, the

poly(DEGDA)-C particles (HM-301) exhibited no such peaks (Figure 3.12). Raman spectroscopy, however, proved far more effective in determining the presence of vinyl groups, with strong C=C peaks at  $1637\text{ cm}^{-1}$  and vinylic -C-H peaks at  $1409$ ,  $3040$ ,  $3075$  and  $3109\text{ cm}^{-1}$ . Raman analysis showed that the poly(DEGDA)-C particles had no pendant vinyl groups, however, on incorporation of PETA and DPEPHA monomers the presence of pendant vinyl groups was evident (Figure 3.13). It is important to note that the baseline of the Raman spectra is not completely flat, this is due to fluorescence of the material at the wavelength of the laser (in this case  $514\text{ nm}$ ) causing a strong background and distorting the baseline; this has no impact on the peak location.<sup>54</sup> The wavelength of  $514\text{ nm}$  was chosen as it is the most suitable for inorganic materials such as calcium carbonate and produced the best resolution of peaks for the vinyl groups of the polymer encapsulated calcium carbonate particles.

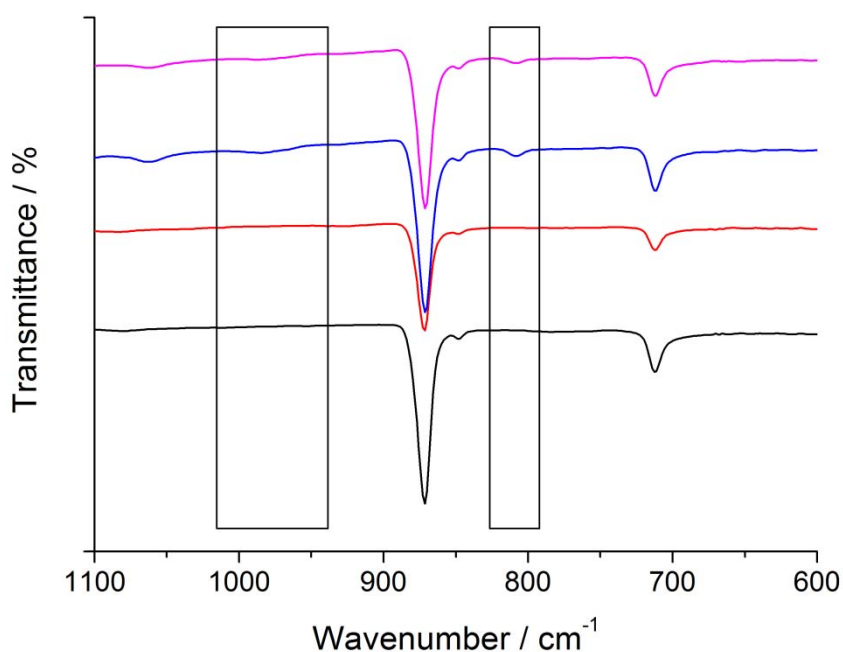


**Figure 3.12** FTIR spectra of bare  $\text{CaCO}_3$  particles (—), poly(DEGDA)-C particles (HM-301) (—), poly(PETA)-C particles (HM-302) (—) and poly(DPEPHA)-C particles (HM-303) (—). Very weak vinyl -CH stretches at  $809$  and  $984\text{ cm}^{-1}$  are observed in the cases for the poly(PETA)-C and poly(DPEPHA)-C particles (illustrated by the black boxes).

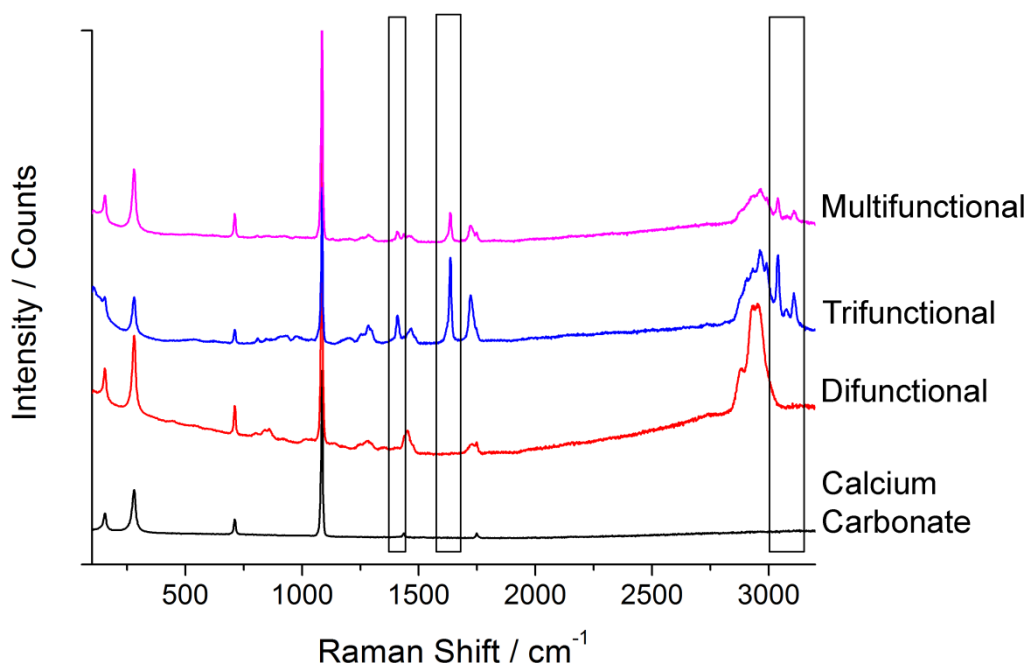


**Figure 3.13** Raman spectra of bare  $\text{CaCO}_3$  particles (—), poly(DEGDA)-C (HM-301) (—), poly(PETA)-C (HM-302) (—) and poly(DPEPHA)-C particles (HM-303) (—). The presence of C=C double bonds in HM-302 and HM-303 are observed with  $1637\text{ cm}^{-1}$  indicating C=C stretch and vinyl C-H stretches at  $1409$ ,  $3040$ ,  $3075$  and  $3109\text{ cm}^{-1}$  (illustrated by the black boxes). No vinyl groups were observed for the poly(DEGDA)-C particles.

Raman spectroscopy clearly determined the presence of vinyl groups on the encapsulated particles; however, it is not a quantitative tool. Pendant vinyl groups can be quantified by bromination of alkenes followed by titration to calculate bromate consumption and thus the number of alkene groups.<sup>55</sup> Bromine formed *in-situ*, by reacting potassium bromate with potassium bromide in the presence of acetic acid (3.1), reacts with the pendant vinyl groups, permanently removing bromine and thus bromate ions from the solution (Figure 3.14). Once the bromination is complete, hydrochloric acid and potassium iodide are introduced to the reaction mixture; under acidic conditions the iodide reacts with the excess potassium bromate to produce iodine (3.2), against which sodium thiosulfate is titrated. The iodine reacts with the sodium thiosulfate to produce sodium iodide; starch is used as an indicator to qualify the complete consumption of iodine and thus potassium bromate (3.3). For every six moles sodium thiosulfate, there is one mole of potassium bromate. The reaction was

conducted in the dark to prevent the homolytic fission of  $\text{Br}_2$  to  $2\text{Br}^\bullet$  which can in turn abstract a hydrogen forming  $\text{HBr}$ ; if formed,  $\text{HBr}$  will react with the vinyl groups and alter the results. Light also catalyzes the reaction of iodide to iodine which would increase the amount of sodium thiosulfate required. As the reaction is under acidic conditions, the calcium carbonate was etched out of the composite particles prior to the bromination.

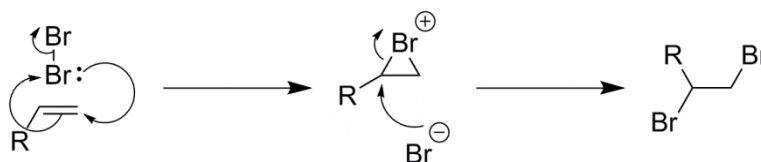
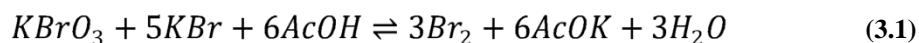
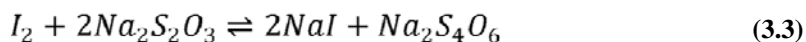


**Figure 3.14** Mechanism of alkene bromination.



Vinyl groups present are then quantified using the Bromine Index (BI):

$$\text{BI} = \frac{7990 \times (V_1 - V_2) \times c}{m} \quad (3.4)$$

Where the Bromine Index quantifies the amount of (molecular) bromine (mg) consumed by 100 g of composite particles,  $V_1$  and  $V_2$  denote the volume (mL) of  $\text{Na}_2\text{S}_2\text{O}_3$  titrated in the blank and sample solutions respectively,  $c$  denotes the concentration ( $\text{mol dm}^{-3}$ ) of  $\text{Na}_2\text{S}_2\text{O}_3$ ,  $m$  the mass (g) of particles and 7990 is the molecular weight of molecular bromine multiplied by 100. There is a conversion factor of 0.1 within the equation that provides the units of mg per 100 g of sample. The Bromine Index (mg per 100 g) value can be converted to mmol per 100 g of sample by dividing by the molecular weight of dibromine, this mmol of dibromine per 100 g of composite particles is equal to the mmol of pendant vinyl groups per

100 g of composite particles; from this the percentage of pendant vinyl groups with respect to monomer vinyl groups can be calculated.

To calculate the percentage of vinyl groups remaining with respect to the monomer, the moles of vinyl groups on the specific multi-acrylate monomer in 100 g of composite particles needs to be known (Table 3.3). In agreement with the Raman analysis, the titration determined that the poly(DEGDA)-C particles exhibited no pendant vinyl groups (Table 3.4). As DEGDA does not express any pendant vinyl groups in the polymer, the moles of pendant vinyl groups calculated from the Bromine Index for the poly(PETA)-C and poly(DPEPHA)-C particles pertains to the contribution of PETA and DPEPHA monomers only. It is important to note that for DPEPHA (dipentaerythritol penta-/hexa-acrylate) the number of vinyl groups used for this calculation was chosen as 5 rather than 6 as that corresponds to the molecular weight of the monomer. By dividing the mmol per 100 g of vinyl groups in the particles by the mmol of vinyl groups in said monomer (i.e. PETA or DPEPHA) present in 100 g of particles, a percentage of remaining pendant vinyl groups with respect to the initial monomer is given. The poly(PETA)-C and poly(DPEPHA)-C particles show that, respectively, 32.6 and 11.9 % of the vinyl groups of said monomer remain on the composite particles (Table 3.4).

**Table 3.3** Table of multi-acrylate monomer and multi-acrylate monomer vinyl groups present in the composite particles, where MA<sub>x</sub> is the multi-acrylate in question.

| Particles | MA <sub>x</sub> | No. Vinyl Groups | MA <sub>x</sub> in Particles (wt.%) | MA <sub>x</sub> in Particle (mmol/100 g) | MA <sub>x</sub> (C=C) in Particle (mmol/100 g) |
|-----------|-----------------|------------------|-------------------------------------|--|--|
| HM-301    | DEGDA           | 2                | 8.51                                | 39.7                                     | 79.4   |
| HM-302    | PETA            | 3                | 4.34                                | 14.6                                     | 43.7   |
| HM-303    | DPEPHA          | 5                | 4.31                                | 8.22                                     | 41.1   |



**Table 3.4** Table of Bromine Index values and the % of vinyl groups remaining from the addition of multi-acrylate, where monomer vinyl groups is the total possible mmol of vinyl groups in the specific monomer in 100 g of particles.

| Exp.   | Particles      | BI<br>(mg/100 g) | Vinyl Groups<br>(mmol/100 g) | MA <sub>x</sub> (C=C)<br>(mmol/100 g) | % Vinyl<br>Remaining |
|--------|----------------|------------------|------------------------------|---------------------------------------|----------------------|
| HM-307 | Poly(DEGDA)-C  | 0                | 0                            | 79.4                                  | 0                    |
| HM-308 | Poly(PETA)-C   | 2280             | 14.3                         | 43.7                                  | 32.6                 |
| HM-309 | Poly(DPEPHA)-C | 799              | 4.88                         | 41.1                                  | 11.9                 |

To ensure that all of the vinyl groups had reacted with the bromine and thus the bromine analysis is accurate, FTIR and Raman analysis were performed. For accurate comparison, FTIR and Raman analysis were performed on hollowed encapsulated particles. To achieve optimum results, the Raman analysis of the hollowed particles were performed with a 754 nm wavelength laser, as this ensured minimum fluorescence and produced a superior spectra; the 514 nm wavelength laser did not produce a clear spectra once the calcium carbonate had been removed. The very weak vinyl peaks in the FTIR spectra for the poly(PETA)-C (HM-308) (Figure 3.15) and poly(DPEPHA)-C particles (HM-309) (Figure 3.17) disappear after the bromination. Raman analysis clearly showed the loss of vinyl groups; C=C stretches at  $1634\text{ cm}^{-1}$  and vinyl C-H stretches at  $733$ ,  $1380$ ,  $1408$  and  $3036\text{ cm}^{-1}$  were lost after bromination and C-Br stretch at  $758\text{ cm}^{-1}$  appeared (Figure 3.16 and Figure 3.18 for the poly(PETA)-C and poly(DPEPHA)-C particles respectively).



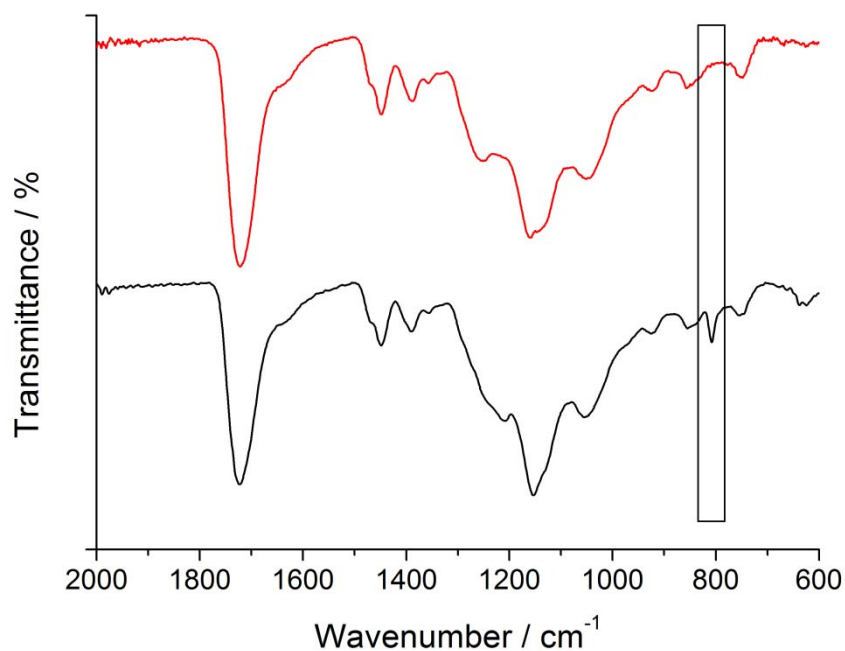


**Figure 3.15** FTIR spectra of hollowed poly(PETA)-C particles (HM-305) (—) and said particles after bromination (HM-308) (—). After the bromination the vinyl -CH shift at 808 cm<sup>-1</sup> is lost (illustrated by the black boxes).

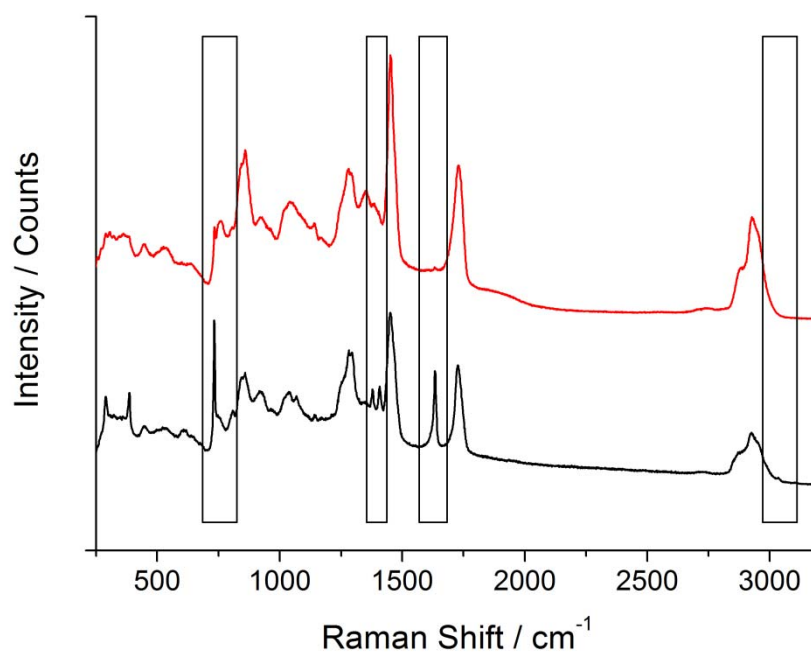


**Figure 3.16** Raman spectra of hollowed poly(PETA)-C particles (HM-305) (—) and said particles after bromination (HM-308) (—). After the bromination the vinyl C-H shifts at 733, 1380, 1408 and 3036 cm<sup>-1</sup> and vinyl C=C shift at 1634 cm<sup>-1</sup> are lost and a C-Br shift at 758 cm<sup>-1</sup> is gained (illustrated by the black boxes).

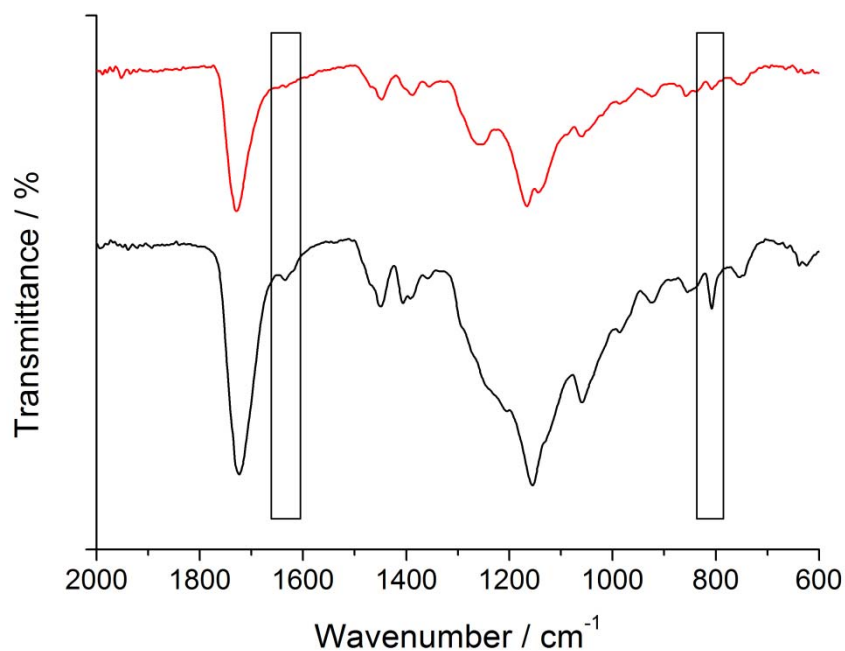


**Figure 3.17** FTIR spectra of hollowed poly(DPEPHA)-C particles (HM-306) (—) and said particles after bromination (HM-309) (—). After the bromination the vinyl shift at  $1634\text{ cm}^{-1}$  and vinyl  $\text{—CH}$  shift at  $808\text{ cm}^{-1}$  is lost (illustrated by the black boxes).

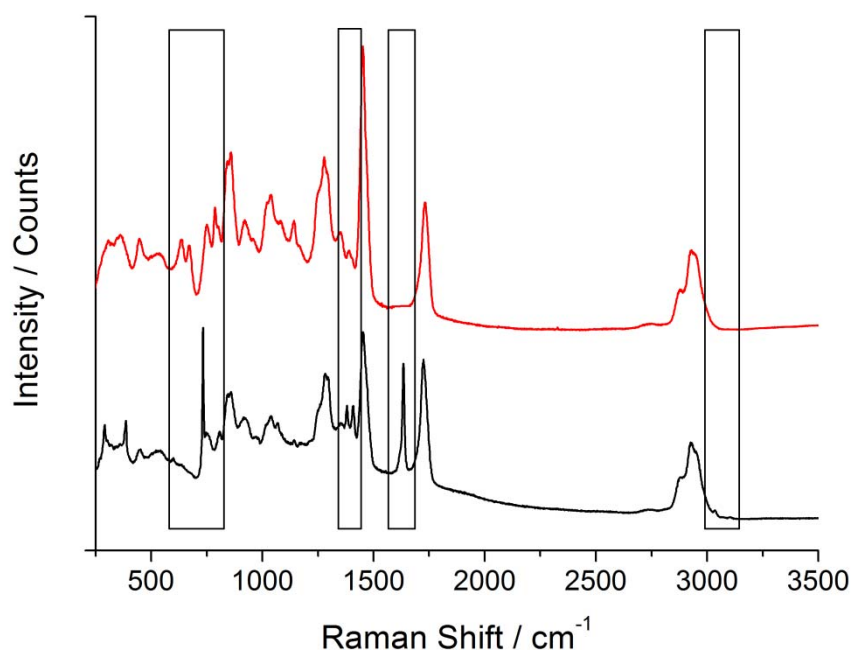


**Figure 3.18** Raman spectra of hollowed poly(DPEPHA)-C particles (HM-306) (—) and said particles after bromination (HM-309) (—). After the bromination the vinyl  $\text{C—H}$  shifts at  $733$ ,  $1380$ ,  $1408$  and  $3036\text{ cm}^{-1}$  and vinyl  $\text{C=C}$  shifts at  $1634\text{ cm}^{-1}$  are lost,  $\text{C—Br}$  shifts at  $635$  and  $758\text{ cm}^{-1}$  are gained, (illustrated by the black boxes).

We postulate that the lack of vinyl groups on the DEGDA-c particles is due to flexibility of the chain, this flexibility allows looping/backbiting of the polymer

chain to occur (Figure 3.19). In starved-fed conditions the likelihood of backbiting occurring over addition of a new monomer unit is increased. We believe that the looping also results in a lower, though not altogether absent, cross-linking density. An issue arises in determining the presence of loops, as the looped DEGDA chain and an un-looped chain are chemically the same, making them very difficult to differentiate (for further discussion the reader is referred to Chapter 4).

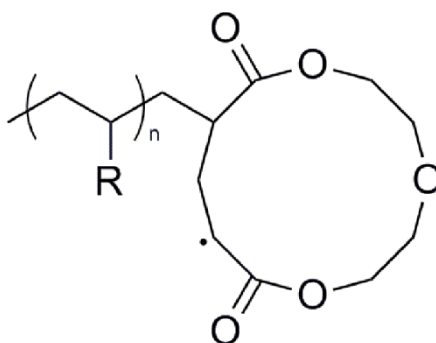


**Figure 3.19** Scheme depicting the looping of DEGDA, where R is the rest of the DEGDA unit.

### 3.3.2. Thiol-Michael addition to pendant vinyl groups

Nucleophilic thiol-Michael addition was chosen for modification of the pendant vinyl groups on the composite particles as it has been shown to be successful when used in conjunction with acrylates.<sup>25, 29, 32</sup> The reaction with hexylamine, the chosen catalyst, proceeds *via* the nucleophile catalyzed mechanism, resulting in only needing 1-2 % of the catalyst and much faster reaction times.<sup>29, 32</sup>

The reaction proceeded by stirring an aqueous solution containing 0.5 g of composite particles, 0.2 mg hexylamine (~3 % with respect to pendant vinyl groups) and 1.0 g mercaptoethanol. As the composite particles were added in a dried state, the reaction was left for 24 hours; although the thiol-Michael addition is fast, the dispersion of the particles (aided by the mercaptoethanol modification) and thus access to the pendant vinyl groups is slower. The particles were cleaned by several centrifugation cycles and FTIR and Raman spectroscopy were used to determine the

loss of vinyl groups. For both poly(PETA)-C and poly(DPEPHA)-C particles FTIR showed a loss in the very weak vinylic and  $\alpha,\beta$  unsaturated carbonyl  $-C-H$  peaks at 809 and 984  $\text{cm}^{-1}$  (Figure 3.20 and Figure 3.22 respectively). Raman proved far more conclusive with the clear loss of  $C=C$  (1409  $\text{cm}^{-1}$ ) and vinylic  $-C-H$  peaks at (1637, 3040, 3075 and 3109  $\text{cm}^{-1}$ ) after the thiol-Michael addition (Figure 3.21 for poly(PETA)-C and Figure 3.23 for poly(DPEPHA)-C).

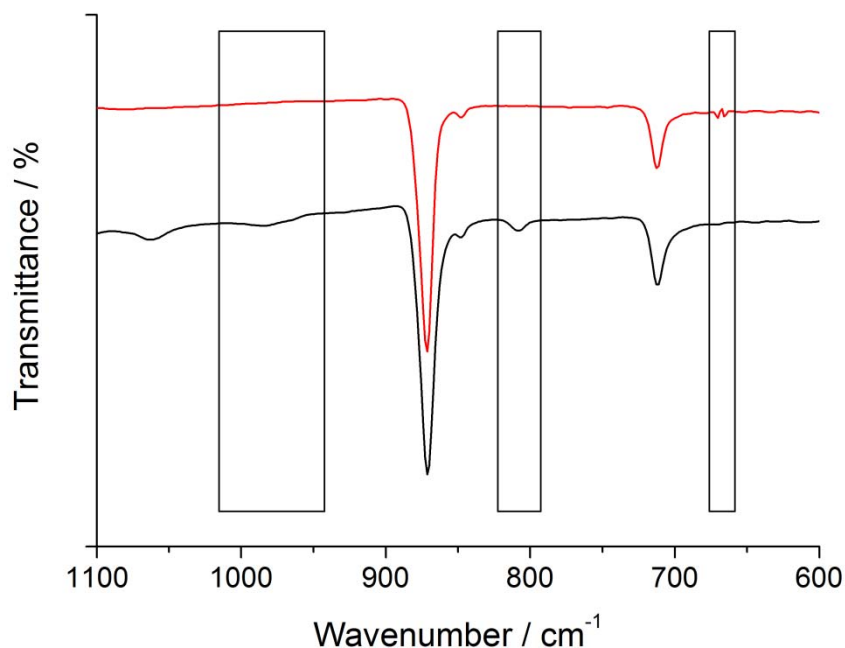


**Figure 3.20** FTIR spectra of poly(PETA)-C particles (HM-302) (—) and said particles after the thiol Michael addition with 2-mecapto ethanol (HM-310) (—). Very weak vinyl  $-CH$  stretches at 809 and 984  $\text{cm}^{-1}$  are lost and thioether stretch at 667  $\text{cm}^{-1}$  gained after the Michael addition.

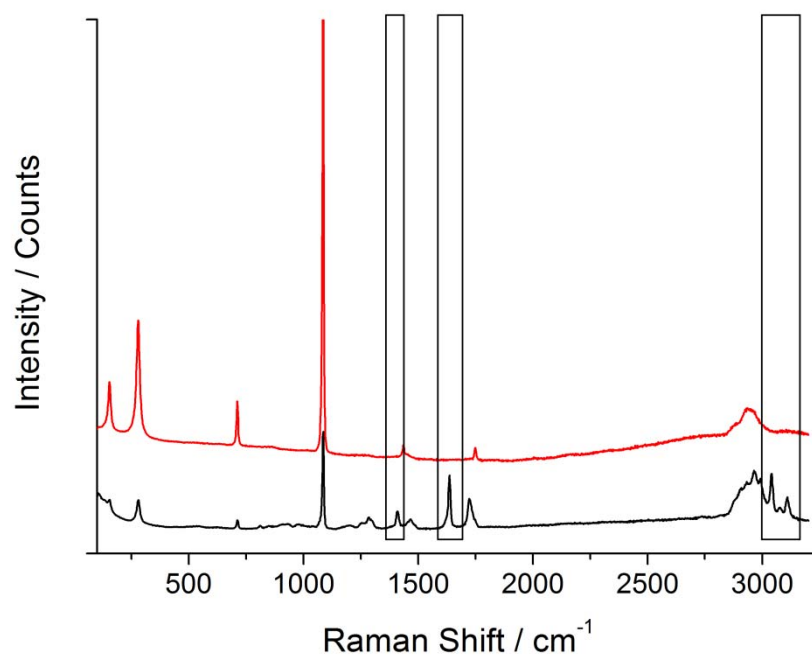


**Figure 3.21** Raman spectra of poly(PETA)-C particles (HM-302) (—) and said particles after the thiol Michael addition with 2-mecapto ethanol (HM-310) (—). After the thiol Michael addition the vinyl C-H shifts at 1409, 3075, 3109 cm<sup>-1</sup> and vinyl C=C shifts at 1637 cm<sup>-1</sup> are lost (illustrated by the black boxes).

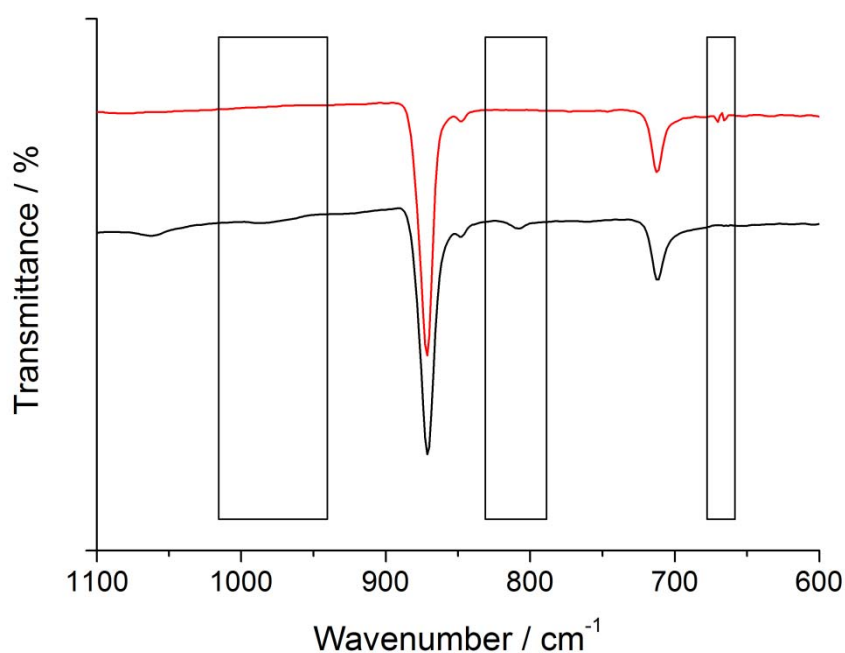


**Figure 3.22** FTIR spectra of poly(DPEPHA)-C particles (HM-303) (—) and said particles after the thiol Michael addition with 2-mecapto ethanol (HM-311) (—). Vinyl –CH stretches at 809 and 984 cm<sup>-1</sup> are lost after the Michael addition.

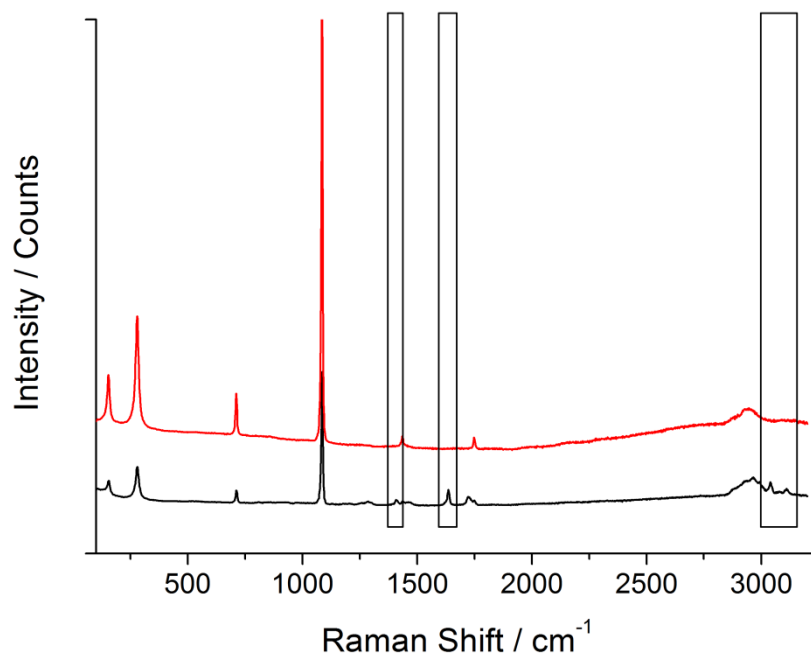


**Figure 3.23** Raman spectra of poly(DPEPHA)-C particles (HM-303) (—) and said particles after the thiol Michael addition with 2-mecapto ethanol (HM-311) (—). After the thiol Michael addition the vinyl C-H shifts at 1409, 3040, 2075 and 3109 cm<sup>-1</sup> and vinyl C=C shifts 1637 cm<sup>-1</sup> are lost (illustrated by the black boxes).

After the thiol Michael addition the calcium carbonate was etched out of the particles with 0.25 M acetic acid to afford hollow polymeric ellipsoids, the resulting particles were thoroughly cleaned by several centrifugation cycles to remove all of the dissolved calcium ions and excess acid. FTIR and Raman analysis was repeated on these hollow particles in an effort to determine the presence of C-S stretches which were previously unobserved. In both cases, FTIR only showed the loss of the very weak vinyl C-H stretches (see Figure 3.24 and Figure 3.26 for the hollow poly(PETA)-C and poly(DPEPHA)-C after thiol Michael addition). Raman once again illustrated the loss of the very strong vinyl C=C stretch at 1634 cm<sup>-1</sup> and vinyl C-H stretches at 733, 1380, 1408 and 3036 cm<sup>-1</sup>, Raman spectroscopy also indicated the presence of C-S stretches at 646 and 748 cm<sup>-1</sup> (see Figure 3.25 and Figure 3.27 for the hollow poly(PETA)-C and poly(DPEPHA)-C after thiol Michael addition), clearly indicating that the loss of vinyl groups was due to the thiol Michael addition.

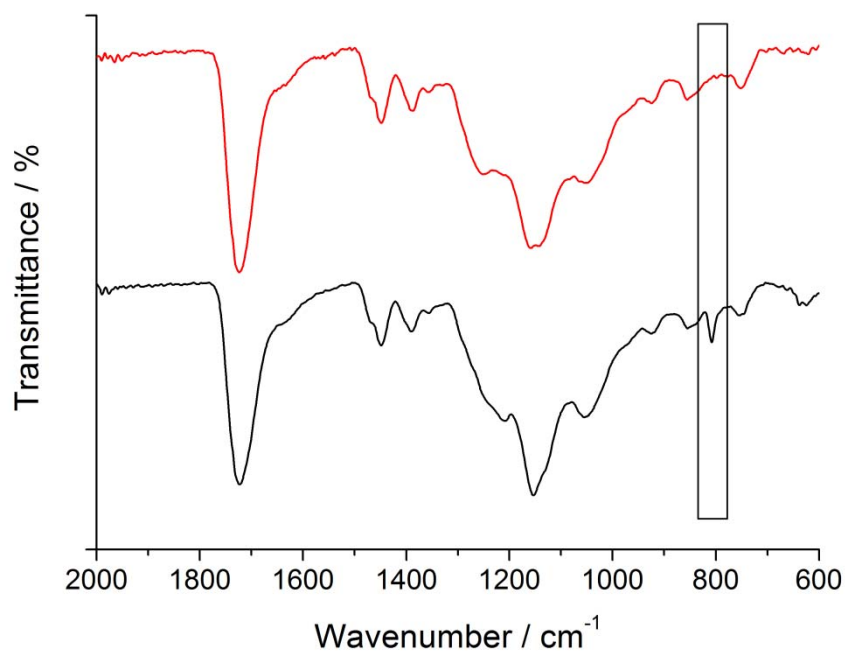


**Figure 3.24** FTIR spectra of hollowed poly(PETA)-C particles (HM-305) (—) and said particles after the thiol Michael addition with 2-mecapto ethanol (HM-312) (—). After the thiol Michael addition, the vinyl -CH shift at 808  $\text{cm}^{-1}$  is lost.

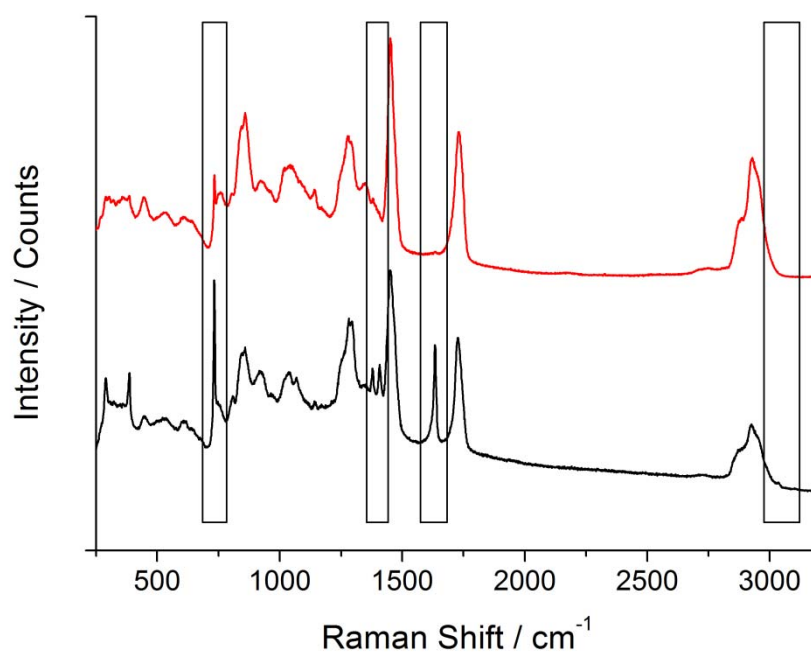


**Figure 3.25** Raman spectra of hollowed poly(PETA)-C particles (HM-305) (—) and said particles after the thiol Michael addition with 2-mecapto ethanol (HM-312) (—). After the thiol Michael addition the vinyl C-H shifts at 733, 1380, 1408 and 3036  $\text{cm}^{-1}$  and vinyl C=C shift at 1634  $\text{cm}^{-1}$  are lost, C-S shifts at 646 and 748 are gained, (illustrated by the black boxes).

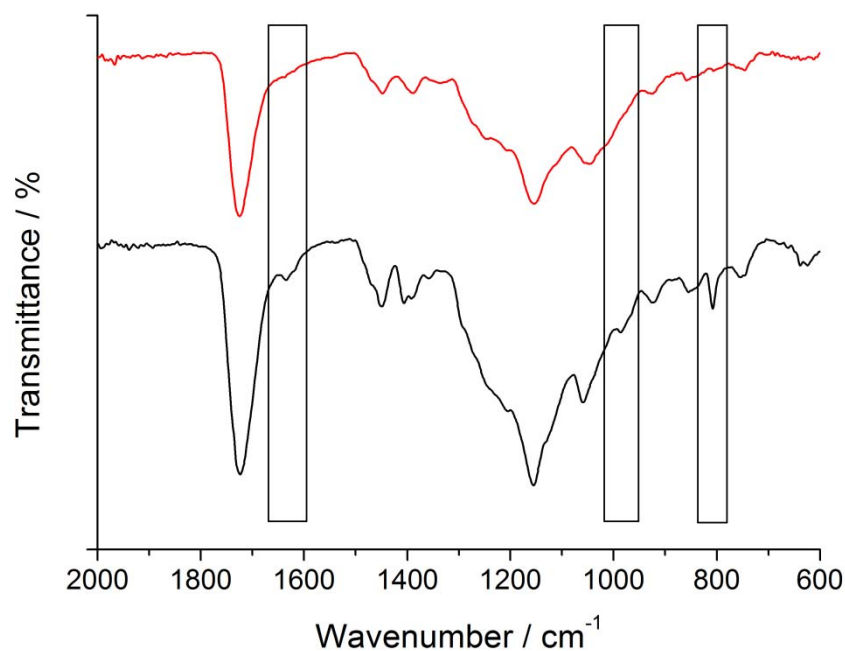


**Figure 3.26** FTIR spectra of hollowed poly(DPEPHA)-C particles (HM-306) (—) and said particles after the thiol Michael addition with 2-mecapto ethanol (HM-313) (—). After the thiol Michael addition the vinyl C=C shift at 1634 cm<sup>-1</sup> and the vinyl –CH shift at 987 and 808 cm<sup>-1</sup> are lost.

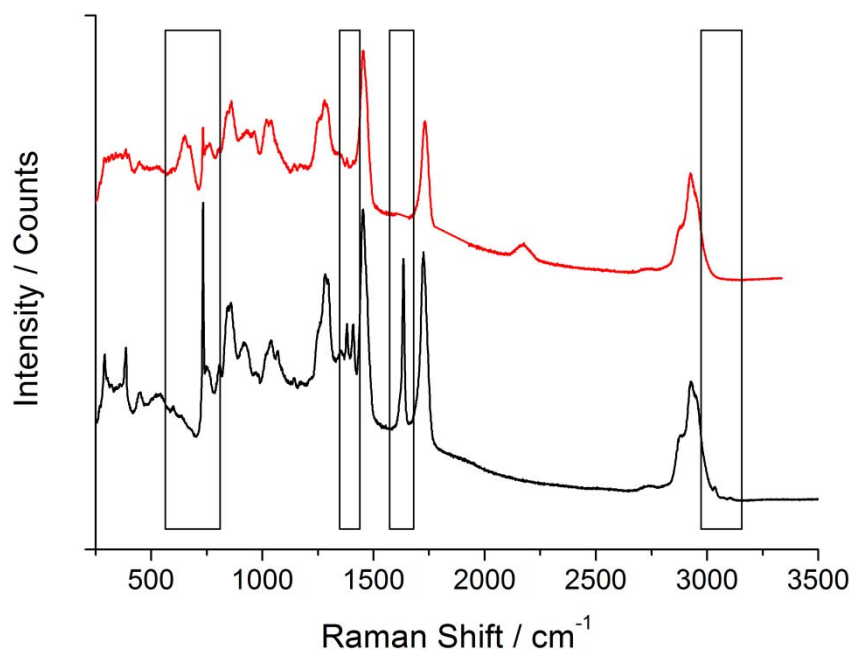


**Figure 3.27** Raman spectra of hollowed particles of poly(DPEPHA)-C particles (HM-306) (—) and said particles after the thiol Michael addition with 2-mecapto ethanol (HM-313) (—). After the thiol Michael addition the vinyl C-H shifts at 733, 1380, 1408, and 2036 cm<sup>-1</sup> and vinyl C=C shift at 1634 cm<sup>-1</sup> are lost, C-S shifts at 651, and 758 cm<sup>-1</sup> are gained, (illustrated by the black boxes).



Bromination titrations were repeated to corroborate the findings of the FTIR and Raman analysis. As expected, the titrations confirmed that all the vinyl groups had been consumed in the thiol Michael addition (Table 3.5).

**Table 3.5** Table of Bromine Index values and the % of vinyl groups remaining after thiol-ene Michael of 2-mercapto ethanol. BI of 0 for both particles indicates that the all vinyl groups are consumed in the thiol-ene Michael addition.

| Exp.   | Particles                          | BI<br>(g / 100 g) | Vinyl Groups<br>(mmol / 100 g) |
|--------|------------------------------------|-------------------|--------------------------------|
| HM-314 | Poly(PETA)-C—<br>mercaptoethanol   | 0                 | 0                              |
| HM-315 | Poly(DPEPHA)-C—<br>mercaptoethanol | 0                 | 0                              |

We found it surprising that all the pendant vinyl groups appeared to disappear. It suggests that the thiol Michael addition was not only occurring at the surface of the particles, as expected, but throughout, signifying that the polymer shell was swollen with water. This is logical as the polymer consists of approximately 14 wt.% methacrylic acid; considering that the pH of the latex is 7.8, it can be determined from the Henderson-Hasselbalch equation (equations (3.6) and (3.7)) that greater than 99.9 % of the methacrylic acid is deprotonated. Thus the polymer shell, swollen with water, is permeable to the thiol Michael addition reagents allowing the reaction to penetrate to all the pendant vinyl groups.

$$pH = pK_a + \log \left( \frac{[A^-]}{[HA]} \right) \quad (3.6)$$

$$\frac{[A^-]}{[HA]} = 10^{pH - pK_a} \quad (3.7)$$

It is apparent that the particles can be modified hydrophilically in water, though we also wanted to modify the particles hydrophobically; dodecanethiol was chosen as a hydrophobic test. The thiol Michael addition was performed in the same manner, as above, but in acetone rather than water.

FTIR for poly(PETA)-C and poly(DPEPHA)-C showed the loss in the very weak vinylic and  $\alpha,\beta$  unsaturated carbonyl  $-C-H$  peaks at 809 and 984  $\text{cm}^{-1}$  (Figure 3.28 for poly(PETA)-C particles and Figure 3.30 for poly(DPEPHA)-C particles). In the case of poly(PETA)-C particles a very weak thioester stretch at 667  $\text{cm}^{-1}$  was also observed. In both cases, Raman clearly showed the loss of  $C=C$  stretch at 1409  $\text{cm}^{-1}$  and vinylic  $-C-H$  peaks at 1637, 3040, 3075 and 3109  $\text{cm}^{-1}$  after the thiol-Michael addition (Figure 3.29 for poly(PETA)-C particles and Figure 3.31 for poly(DPEPHA)-C particles).

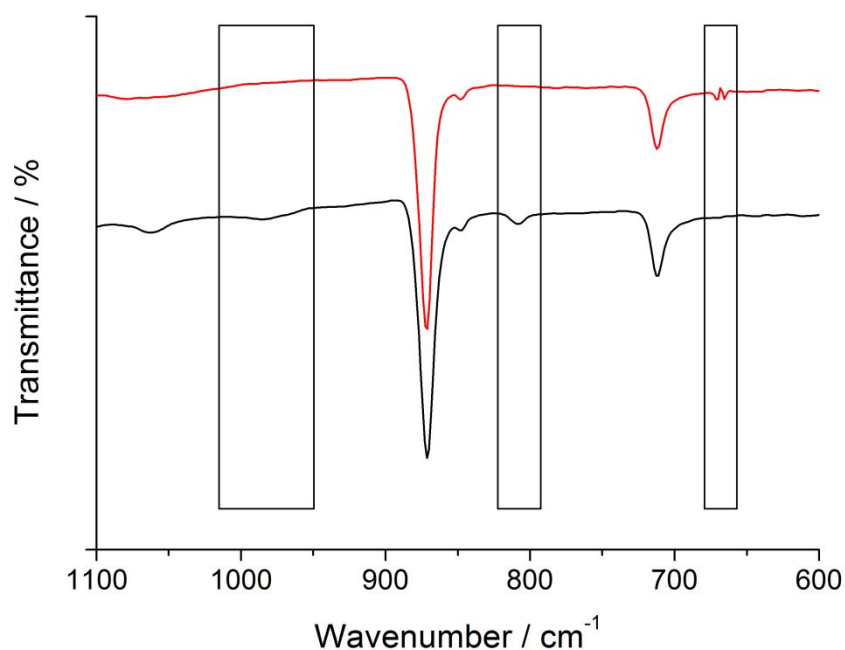


**Figure 3.28** FTIR spectra of poly(PETA)-C particles (HM-302) (—) and said particles after the thiol Michael addition with dodecanethiol in acetone (HM-316) (—). Vinyl  $-CH$  stretches at 809 and 984  $\text{cm}^{-1}$  are lost and thioether stretch at 667  $\text{cm}^{-1}$  gained after the Michael addition.

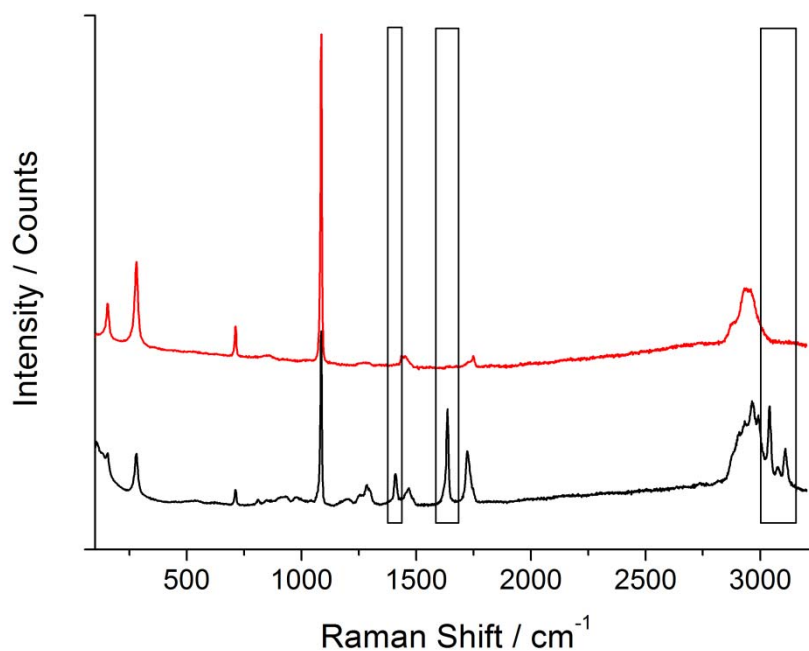


**Figure 3.29** Raman spectra of poly(PETA)-C particles (HM-302) (—) and said particles after the thiol Michael addition with dodecane thiol in acetone (HM-316) (—). After the thiol Michael addition the vinyl shifts at 1409, 1637, 3040, 3075 and 3109 cm<sup>-1</sup> are lost (illustrated by the black boxes).

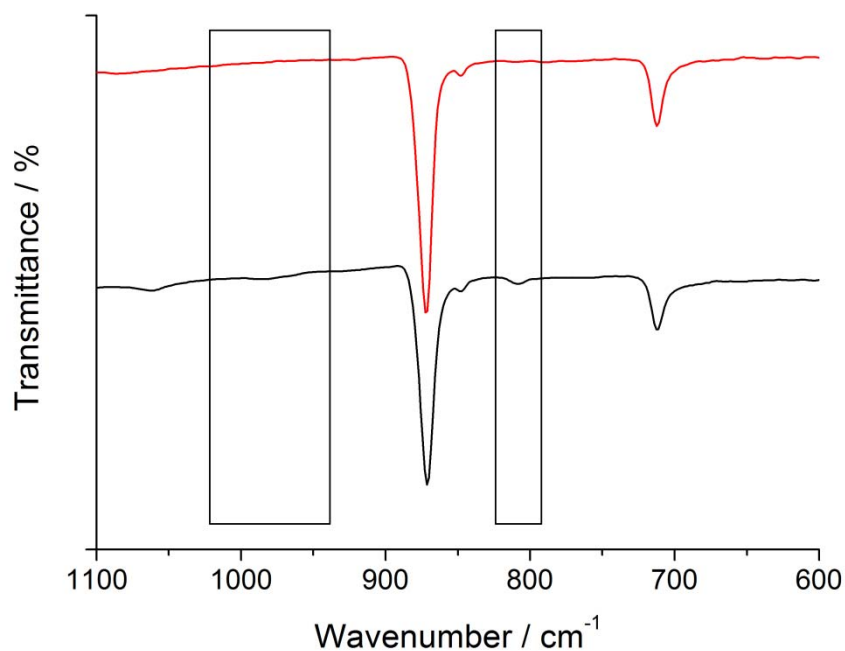


**Figure 3.30** FTIR spectra of poly(DPEPHA)-C particles (HM-303) (—) and said particles after the thiol Michael addition with dodecane thiol in acetone (HM-317) (—). Vinyl –CH stretches at 809 and 984 cm<sup>-1</sup> are lost after the Michael addition (illustrated by the black boxes).

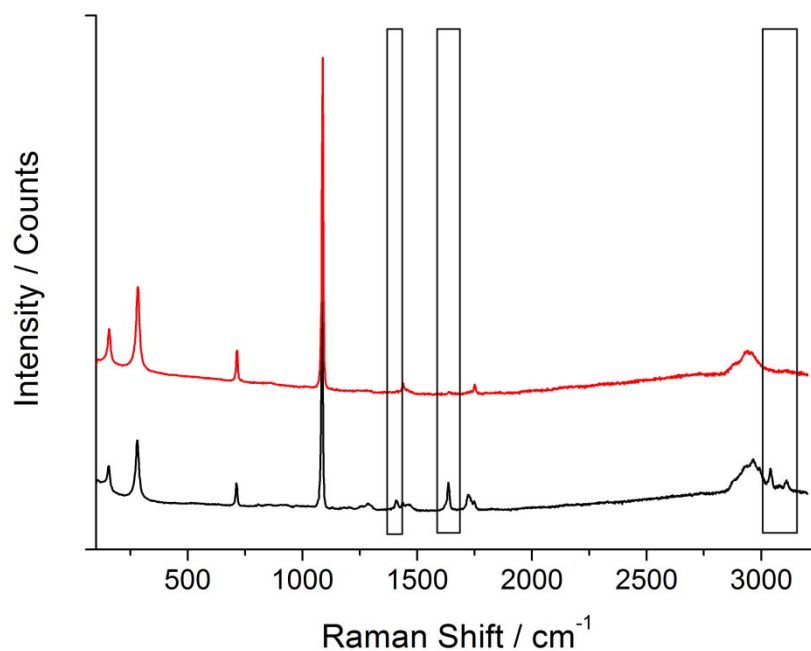


**Figure 3.31** Raman Spectra of poly(DPEPHA)-C particles (HM-303) (—) and said particles after the thiol Michael addition with dodecanethiol in acetone (HM-317) (—). After the thiol Michael addition the vinyl shifts at 1409, 1637, 3040, 3075 and 3109  $\text{cm}^{-1}$  are lost (illustrated by the black boxes).

Bromination titrations were repeated to corroborate the findings of the FTIR and Raman analysis. As expected, the titrations confirmed that all the vinyl groups had been consumed in the thiol Michael addition (Table 3.6). In this case, complete conversion of pendant vinyl groups is attributed to the particles swelling with acetone.

**Table 3.6** Table of Bromine Index values and the % of vinyl groups remaining after thiol-ene Michael addition of 1-dodecane thiol. BI of 0 for both particles indicates that the all vinyl groups are consumed in the thiol-ene Michael addition.

| Exp.   | Particles                         | BI<br>(g / 100 g) | Vinyl Groups<br>(mmol / 100 g) |
|--------|-----------------------------------|-------------------|--------------------------------|
| HM-318 | Poly(PETA)-C—<br>dodecane thiol   | 0                 | 0                              |
| HM-319 | Poly(DPEPHA)-C—<br>dodecane thiol | 0                 | 0                              |

### 3.3.3. Synthesis and thiol Michael addition of $\omega$ -thiol functionalized poly(styrene) to composite particles

RAFT polymers (containing a di/trithiocarbonate) can undergo  $\omega$ -end modification to achieve thiol functionality through reactions with nucleophiles.<sup>47, 56-59</sup> With this in mind we aimed to prepare poly(styrene) by RAFT polymerization, with the intention to produce thiol  $\omega$ -end functionalized poly(styrene) which could be used to react with pendant vinyl groups on the composite particles *via* thiol Michael addition. By “clicking” a specific polymer chain to the encapsulated calcium carbonate particles, the surface can be tuned for a desired application. For example, by attaching poly(styrene) chains to calcium carbonate, one could aid dispersion in a poly(styrene) polymer melt. Calcium carbonate is used in polymer melts to improve mechanical strength; the strength of the material can be greatly improved upon by improving the dispersion of the particles.<sup>60-65</sup>

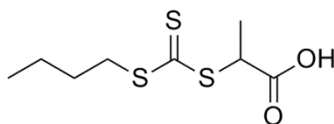


**Figure 3.32** RAFT agent (Propanoic acid)-2-yl butyl trithiocarbonate (PABTC).

The choice of RAFT agent is very important; for the polymerization of styrene, (propanoic acid)-2-yl butyl trithiocarbonate (PABTC) (Figure 3.32) was chosen.<sup>66</sup> PABTC was synthesised by deprotonating the thiol, in this case 1-butanethiol, with sodium hydroxide, following this carbon disulfide was introduced, to which the deprotonated mercaptan adds by nucleophilic addition turning the colourless solution bright yellow. Once this was complete bromopropionic acid is added which adds to the trithiocarbonate by nucleophilic addition ( $S_N2$ ), a bright yellow precipitate is formed which was recrystallized from hexane and the product was dried under vacuum to give a bright yellow powder (Figure 3.33).<sup>67</sup>

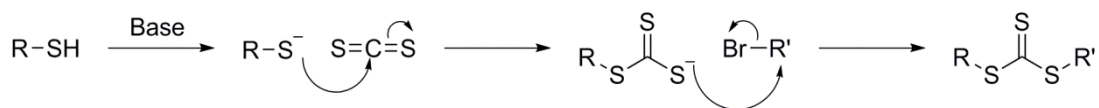


**Figure 3.33** Mechanism of RAFT agent synthesis.

Poly(styrene) was synthesized with a target molecular weight of 10,000 g mol<sup>-1</sup> at 60 % monomer conversion under the following conditions. A mixture of PABTC, VA-088 (10 mol. % w.r.t. PABTC), styrene (8 M w.r.t. solvent) and 1,4-dioxane was degassed by four freeze-pump-thaw cycles, after which the chamber was flooded with nitrogen gas and the polymerization was started by heating to 90 °C. Monomer conversion was followed by <sup>1</sup>H NMR and molecular weight by THF SEC from samples taken every hour.

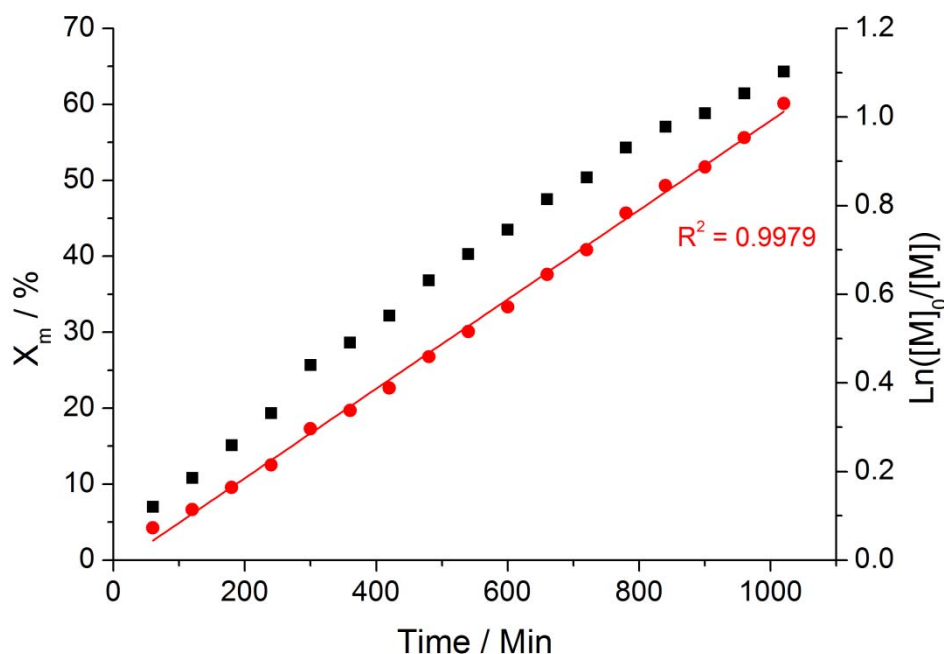


**Figure 3.34** Overall monomer conversion,  $X_m$ , (■) and  $\ln([M]_0/[M])$  (●) versus time for the RAFT polymerization of styrene where the expected molecular weight at 60 % monomer conversion is 10,000 (HM-321).  $R^2$  for the linear fit of the  $\ln([M]_0/[M])$  plot is 0.9979.

Kinetic plot of  $\ln([M]_0/[M])$  versus time for the polymerization shows a “linear” behaviour, hereby indicating that the radical concentration in the RAFT polymerization is constant (Figure 3.34).<sup>68, 69</sup>  $M_n$  increased linearly with monomer conversion (Figure 3.35). The dispersity decreases from 1.21 to 1.10. This follows

typical RAFT polymerization kinetics; thus the polymerization of styrene using the PABTC RAFT agent is controlled. The molecular weight distributions shift to higher average molar masses with no clear broadening (Figure 3.36), that is no marked development of a high molar mass shoulder as a result of long-long termination and no clear tailing towards lower molar masses as a result of short-short termination or transfer to monomer and/or solvent. As the reaction proceeds it is apparent that dispersity is reducing as is expected in a RAFT controlled polymerization.

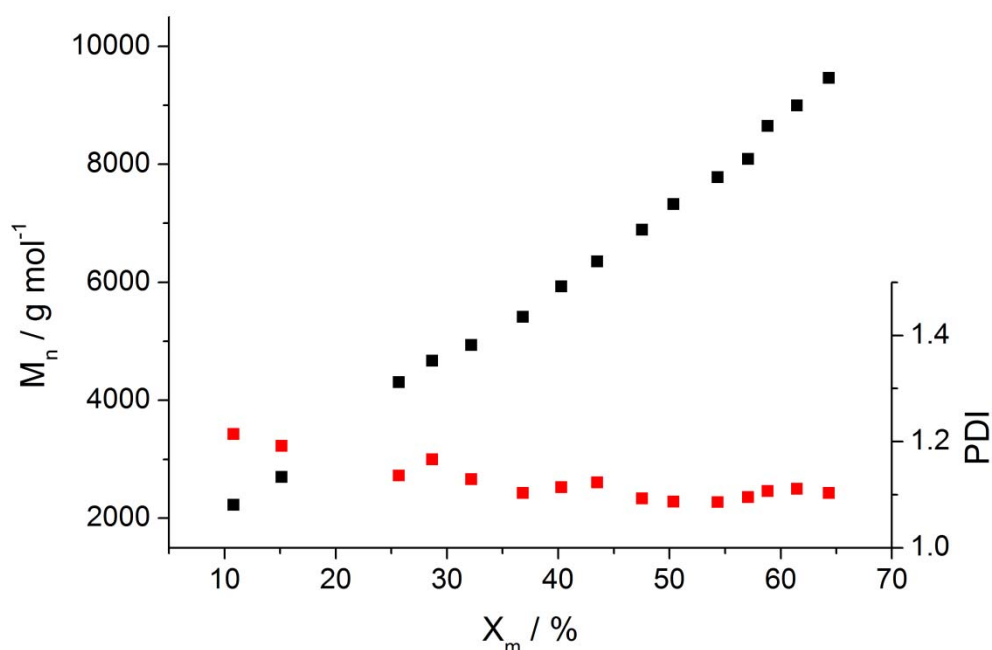


**Figure 3.35**  $M_n$  versus conversion for poly(styrene) synthesized using PABTC RAFT agent with a target molecular weight at 60 % conversion of  $10,000 \text{ g mol}^{-1}$  (HM-321); (■)  $M_n$  and (■) PDI, where for  $M_n$   $R^2=0.995$ .

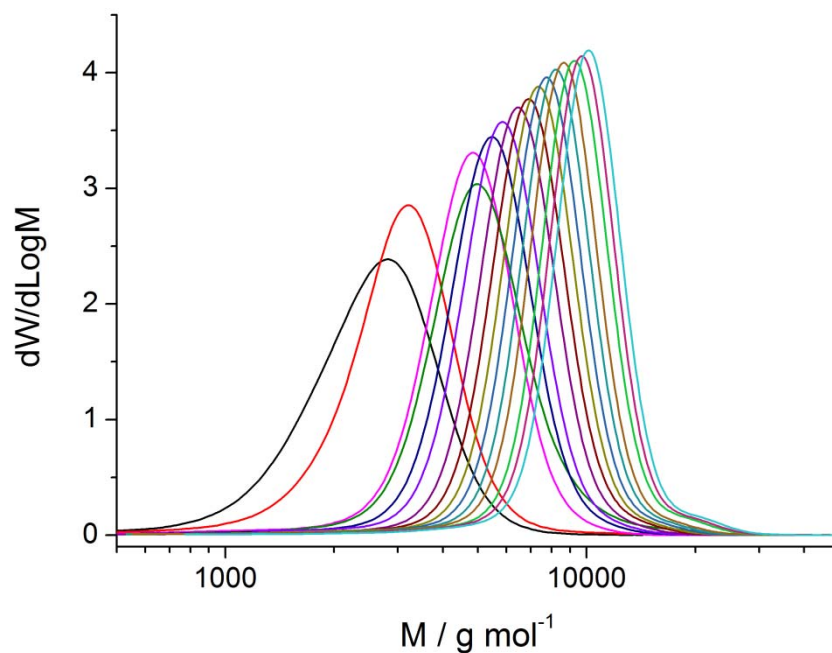


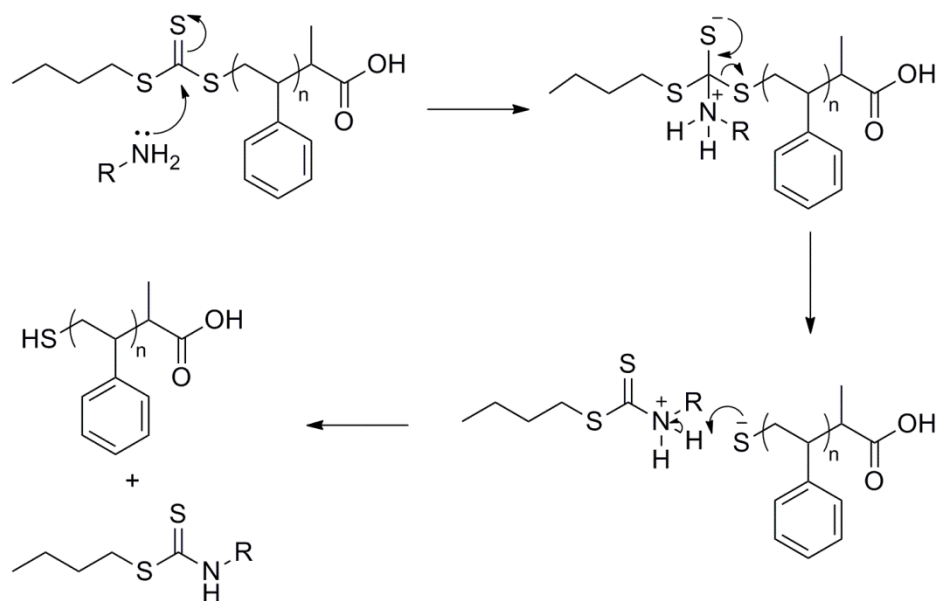
**Figure 3.36** Molecular weight distributions of poly(styrene) synthesized using PABTC RAFT agent with a target molecular weight at 60 % conversion of  $10,000 \text{ g mol}^{-1}$  (HM-321). Samples taken at 2 (—), 3 (—), 5 (—), 6 (—), 7 (—), 8 (—), 9 (—), 10 (—), 11 (—), 12 (—), 13 (—), 14 (—), 15 (—), 16 (—) and 17 (—) hours, before this samples could not be accurately analyzed by SEC. As conversion increases so does molecular weight, whilst dispersity decreases.

The polymerization was repeated and the reaction was stopped at ~60 % monomer conversion (16 hours) to limit termination and produce polymers with maximum trithiocarbonate functionality. Monomer conversion was determined by  $^1\text{H}$  NMR and molecular weight by THF SEC (Table 3.7). The polymer was purified by precipitation in methanol and collected by Büchner filtration.

**Table 3.7** Table of monomer conversion (measured by  $^1\text{H}$  NMR) and molecular weights (measured by THF SEC) for poly(styrene) synthesized by RAFT polymerization.

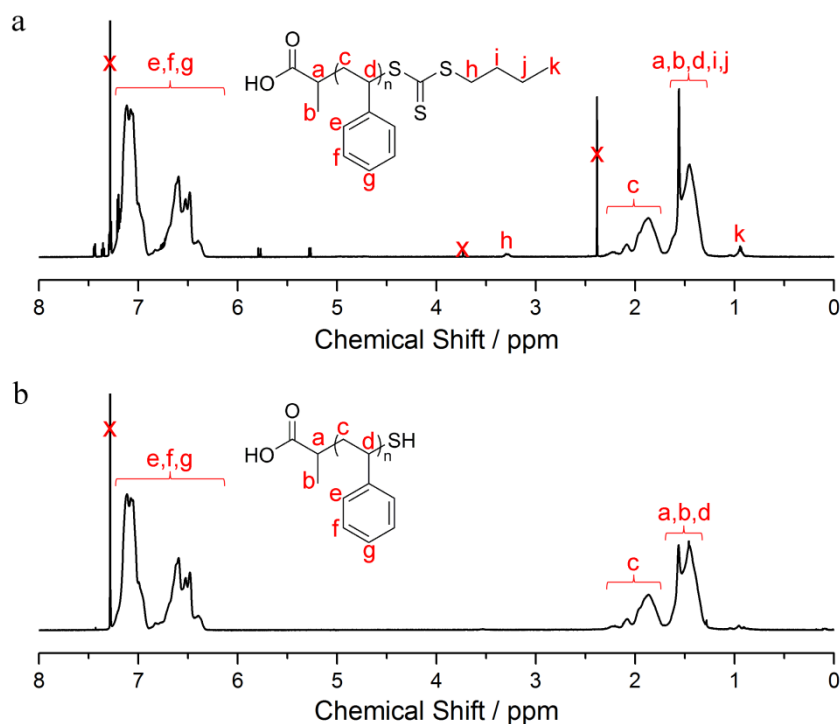
| Exp.   | Conversion | $M_{n(\text{theory})}$ | $M_n$ | $M_p$ | $M_w$ | PD   |
|--------|------------|------------------------|-------|-------|-------|------|
| HM-322 | 63         | 10020                  | 9610  | 10200 | 10400 | 1.08 |





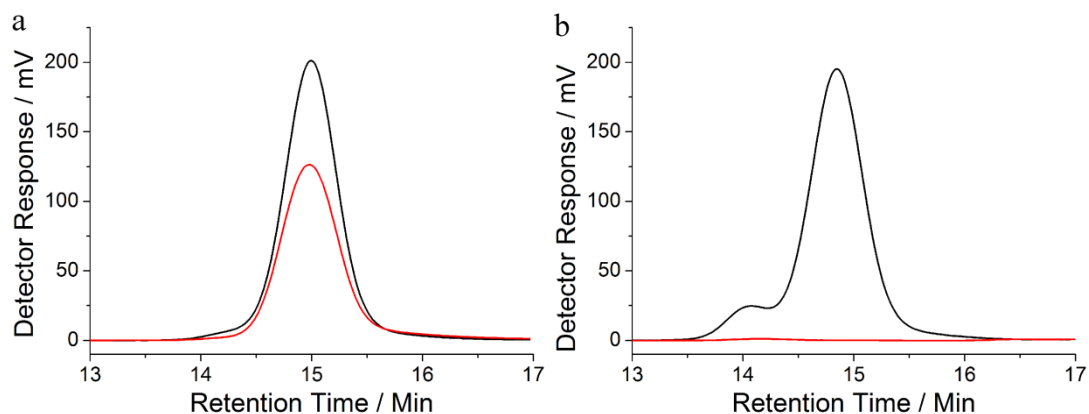
**Figure 3.37** Mechanism of aminolysis of the trithiocarbonate to achieve thiol  $\omega$ -end functionalized poly(styrene).

Thiol  $\omega$ -end functionalized poly(styrene) was synthesized by aminolysis of the precursor trithiocarbonate functionalized poly(styrene), using hexylamine as the nucleophile (Figure 3.37).<sup>47</sup> A solution of the polymer in THF was degassed by purging with nitrogen, after which hexylamine was injected into the polymer solution. The yellow solution turned colourless overnight. The polymer was precipitated in methanol to yield a white powder.



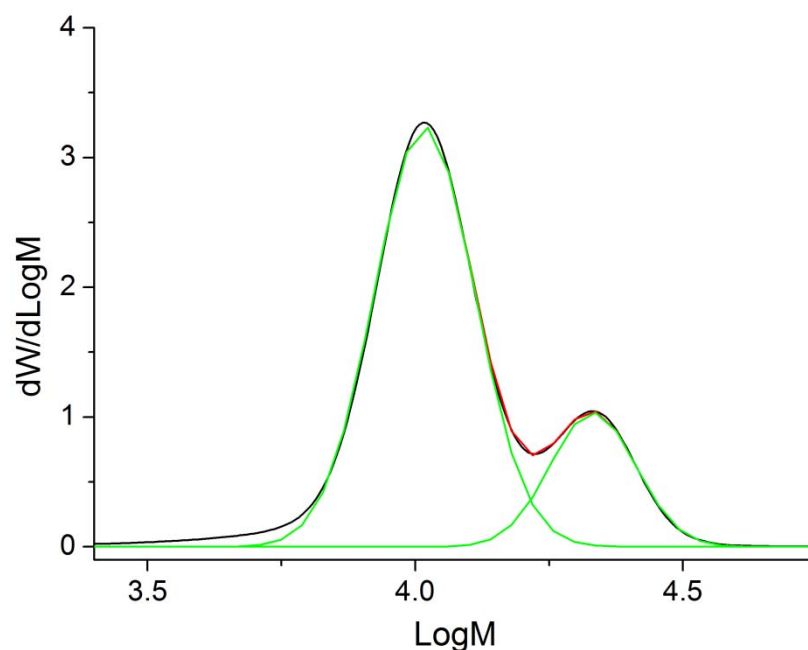
**Figure 3.38**  $^1\text{H}$  NMR (a)  $\omega$ -RAFT functionalized poly(styrene) and (b)  $\omega$ -thiol functionalized poly(styrene) yielded after aminolysis.

$^1\text{H}$  NMR analysis indicated that the RAFT group had been cleaved by aminolysis, by the loss of butyl peaks associated with the trithiocarbonate (Figure 3.38). SEC with UV detection, measuring  $\lambda = 309$  nm, was used to determine the loss of the RAFT end group. A chromophore is observed at 15 minutes retention time, corresponding to the SEC eluent (THF), for the poly(styrene)-PABTC (HM-322) (Figure 3.39 a). No chromophore is observed after aminolysis (HM-323), indicating that the RAFT group has been cleaved (Figure 3.39 b).



**Figure 3.39** SEC of (a) RAFT-functionalized poly(styrene) (HM-322) and (b) poly(styrene) after aminolysis of trithiocarbonate group and reduction with DTT (HM-324). RI (—) and UV ( $\lambda = 309$  nm) detector response (—) vs. retention time. After aminolysis the UV trace disappears, suggesting that the trithiocarbonate group has been cleaved.

After aminolysis of the RAFT group, SEC analysis showed a large shoulder with an  $M_p$  with approximately twice that of the  $M_p$  of the main peak; a portion of the polymers had coupled to form disulfides (Figure 3.40 and Table 3.8). The peaks were deconvoluted using Origin 6 software and the area ratios were used to calculate the approximate proportion of coupled polymers, which was found to be ~35 %.

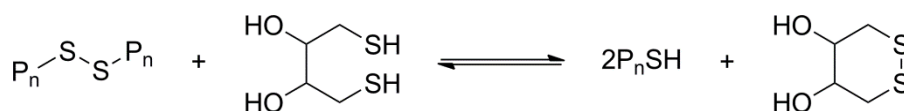
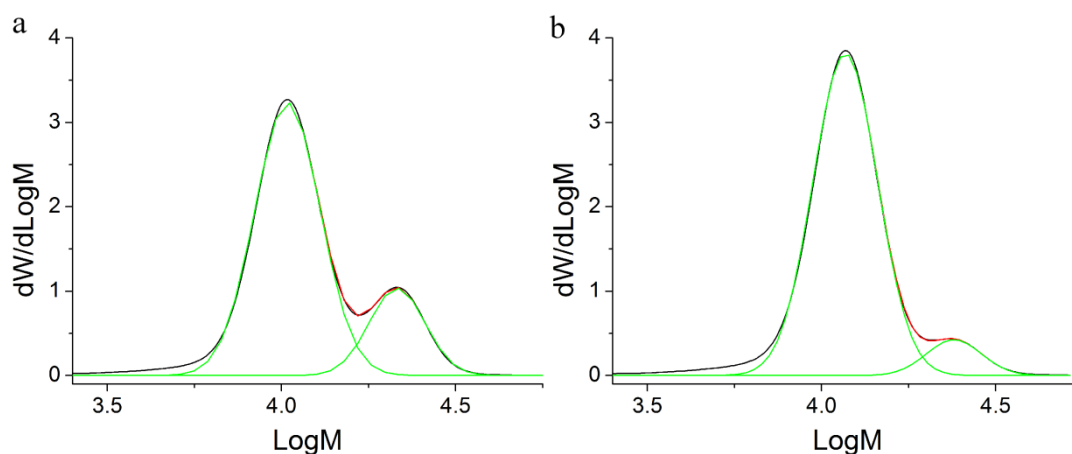


**Figure 3.40** SEC chromatogram of poly(styrene) after aminolysis of trithiocarbonate group (HM-323) (—), deconvolution (Gaussian fit) of bimodal plot (—) and the sum of the deconvoluted plots (—).

**Table 3.8** Table of molecular weights and % of coupled polymer chains for poly(styrene) after aminolysis of trithiocarbonate group (HM-323). Where reported  $M_n$  and  $M_w$  are of the system.

| Exp.   | $M_n$ | $M_w$ | $M_{p1}$ | $M_{p2}$ | Dispersity | % Coupled |
|--------|-------|-------|----------|----------|------------|-----------|
| HM-323 | 10800 | 13000 | 10400    | 21300    | 1.20       | 35        |

The disulfides were cleaved by reacting with dithiothreitol (DTT) (Figure 3.41).<sup>70-72</sup> SEC analysis showed that the shoulder remained, though deconvolution showed that the amount of disulfides had reduced to ~16 % (Figure 3.42 and Table 3.9).

**Figure 3.41** Reaction scheme of disulfide reduction by DTT.<sup>73</sup>**Figure 3.42** (a) poly(styrene) after aminolysis of trithiocarbonate group (HM-323) and (b) after reduction of disulfide bonds with DTT (HM-324); SEC chromatogram (—), deconvolution (Gaussian fit) of bimodal plot (—) and the sum of the deconvoluted plots (—).**Table 3.9** Table of molecular weights and % of coupled polymer chains for poly(styrene) after aminolysis of trithiocarbonate group (HM-323) and after reduction of disulfide bonds with DTT (HM-324). Where reported  $M_n$  and  $M_w$  are of the system.

| Exp.   | $M_n$ | $M_w$ | $M_{p1}$ | $M_{p2}$ | Dispersity | % Coupled |
|--------|-------|-------|----------|----------|------------|-----------|
| HM-323 | 10800 | 13000 | 10400    | 21300    | 1.20       | 35        |
| HM-324 | 11400 | 12900 | 11700    | 23400    | 1.13       | 16        |

Thiol Michael addition proceeded as follows: 40 mL solution of acetone containing hexylamine (0.7 mg, 0.007 mmol, ~3 % w.r.t. vinyl groups) was added to poly(styrene)-SH (HM-324) (3.4 g, 0.3 mmol) and poly(PETA)-C (HM-302) (1.5g, ~0.214 mmol of vinyl groups) particles, and heated to 40 °C. After four days the reaction was stopped and the particles were cleaned by 6 centrifugation cycles. Poly(styrene) of  $\sim 10,300 \text{ g mol}^{-1}$  has a UCST and LCST of -2 and 144 °C respectively, thus under these reaction conditions the poly(styrene) is completely dissolved in the continuous phase.<sup>74</sup> Unlike with the relatively small thiols (2-mercapto ethanol and 1-dodecanethiol), we expected the poly(styrene)-SH to only react with surface vinyl groups, rather than penetrating the polymer.

FTIR analysis showed the disappearance of the vinylic and  $\alpha,\beta$  unsaturated carbonyl –C-H peak at  $984 \text{ cm}^{-1}$ , however the peak at  $809 \text{ cm}^{-1}$  appears to remain, in addition to this an aromatic C-H stretch at  $698 \text{ cm}^{-1}$  appears after the thiol Michael addition, indicating the presence of poly(styrene) chains (Figure 3.43).

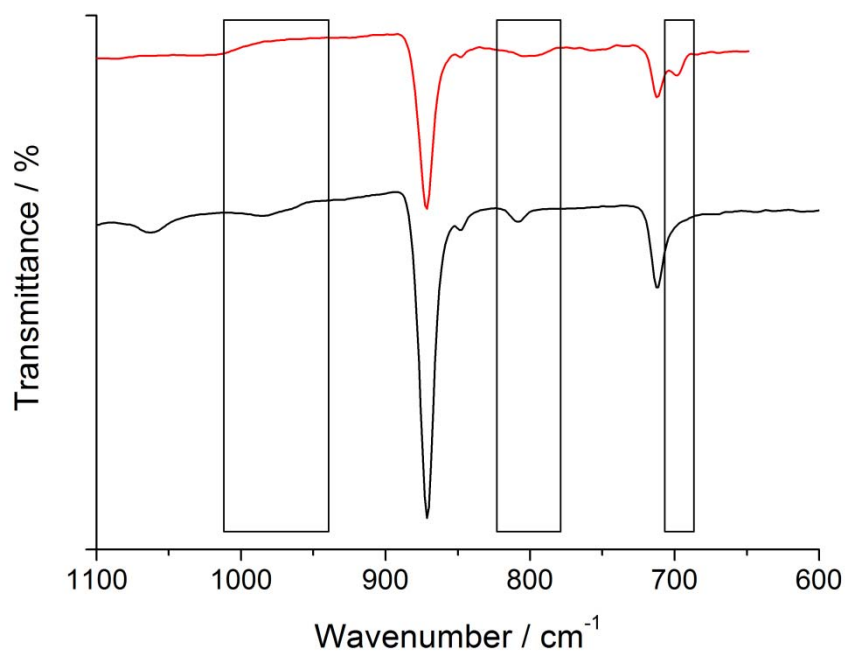


**Figure 3.43** FTIR spectra of poly(PETA)-C particles (HM-302) (—) and said particles after the thiol Michael addition with poly(styrene)-SH (HM-325) (—). Very weak vinyl –CH stretch at  $984\text{ cm}^{-1}$  is lost, however the very weak vinyl –CH stretch at  $809\text{ cm}^{-1}$  remains and aromatic C-H stretch from styrene at  $698\text{ cm}^{-1}$  is gained after the Michael addition.

After the thiol Michael addition, Raman analysis shows the loss of C=C peak at  $1409\text{ cm}^{-1}$  and vinylic -C-H peaks at  $1637$ ,  $3040$ ,  $3075$  and  $3109\text{ cm}^{-1}$ , which is in contrast to the FTIR analysis. Appearance of aromatic C=C peaks at  $837$  and  $1000\text{ cm}^{-1}$  suggests that poly(styrene) chains are present.

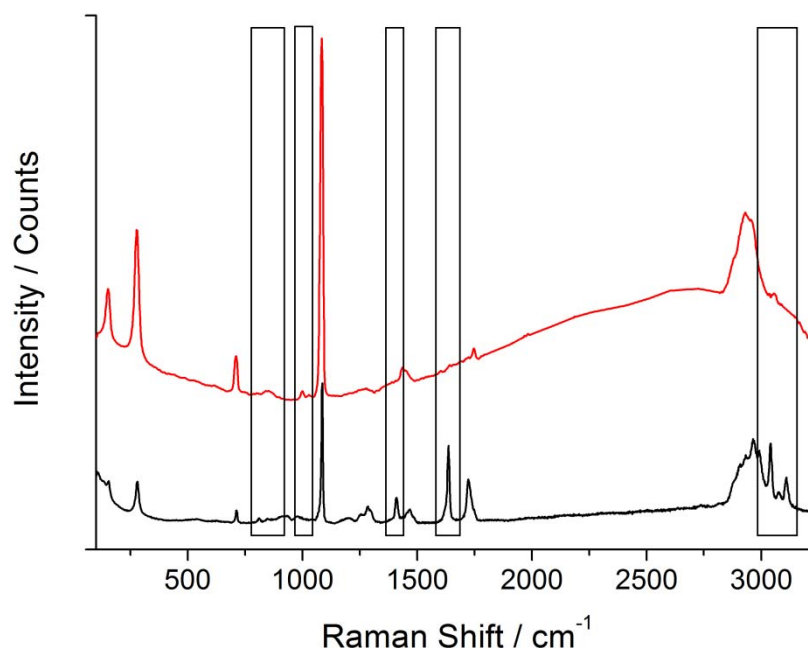


**Figure 3.44** Raman spectra of poly(PETA)-C particles (HM-302) (—) and said particles after the thiol Michael addition with poly(styrene)-SH in acetone (HM-316) (—). After the thiol Michael addition the vinyl shifts at 1409, 1637, 3040, 3075 and 3109  $\text{cm}^{-1}$  diminish and aromatic C-H shifts at 837 and 1000  $\text{cm}^{-1}$  appear (illustrated by the black boxes); indicating that some polystyrene chains have “clicked” to the particles.

Bromination titrations were performed to determine whether any vinyl groups remained after the thiol Michael addition. As expected, the titrations confirmed that not all the vinyl groups had been consumed. Comparing vinyl groups (mmol / 100 g) calculated from the bromine index of poly(PETA)-C particles (HM-301) to particles after thiol Michael addition with poly(styrene)-SH (HM-326), indicates that approximately 22 % of the vinyl groups were consumed by the thiol Michael addition (Table 3.10).

**Table 3.10** Table of Bromine Index of poly(PETA)-C particles and poly(PETA)-C particles after thiol Michael addition with poly(styrene)-SH.

| Exp.   | Particles     | BI<br>(mg/100 g) | Vinyl Groups<br>(mmol/100 g) |
|--------|---------------|------------------|------------------------------|
| HM-308 | PETA-c        | 2280             | 14.3                         |
| HM-326 | PETA-c-p(Sty) | 1800             | 11.2                         |

### 3.4. Conclusions

We have developed the encapsulation of calcium carbonate nanoparticles to incorporate pendant vinyl groups from which the particles were modified by thiol Michael addition. We have illustrated the surface modification of these composite particles with various thiols. We determined, by Raman spectroscopy and quantitative analysis of pendant vinyl groups by bromination titrations, that small hydrophilic (2-mercaptoethanol) and hydrophobic (1-dodecanethiol) molecules were found to not only react with the surface vinyl groups but penetrated the polymer shell to consume all pendant vinyl groups. However, thiol Michael addition of  $\omega$ -thiol functionalized poly(styrene) with a molecular weight of approximately  $10,000 \text{ g mol}^{-1}$ , we found that only 22 % of the vinyl groups were consumed. We have yet to test our hypothesis that the surface modification could be used as a tool to tune the particle surface for dispersion in various media; this would be achieved by preparing poly(styrene) melts with bare calcium carbonate, poly(PETA)-C and poly(PETA)-C particles modified with poly(styrene) and determining particle dispersion.



## 3.5. Experimental

### 3.5.1. Materials

Di(ethylene glycol) diacrylate (75 %), methacrylic acid (99 %), pentaerythritol triacrylate, dipentaerythritol penta-/hexa-acrylate, styrene (99.9 %), 2-mercaptoethanol ( $\geq 99.0$  %), dodecanethiol ( $\geq 98.0$  %), 2-bromopropionic acid ( $\geq 99.0\%$ ), 1-butanethiol (99 %), carbon disulfide (anhydrous,  $\geq 99$  %), hydrochloric acid (37%), sodium hydroxide pellets ( $\geq 99$  %), hexane (95 %), dithiothreitol (DTT) (99.0 %), 1,1'-azobis(cyclohexanecarbonitrile) (VA-088) (98 %) and ammonium persulfate (APS) ( $\geq 98.0$  %) were purchased from Sigma-Aldrich and were used as received. Calcium carbonate (SOCAL P3) was kindly donated by AkzoNobel. Carbon film 200 copper mesh, lacey carbon film 300 copper mesh TEM grids and SEM specimen stubs were purchased from Agar Scientific. Silicon wafers for mounting SEM samples were kindly donated by Wacker Chemie AG.

### 3.5.2. Equipment

Monomer was fed into the reaction mixture with a Harvard Instrument PHD 2000 Infusion syringe pump. TEM was performed on a Jeol 2010F TEM fitted with a Gatan Ultrascan 4000 camera; samples were prepared by adding a drop of diluted latex to a suspended carbon grid, the excess liquid was wicked away with filter paper. SEM was performed on a Zeiss SUPRA 55-VP FEGSEM; samples were prepared by adding an aqueous drop of diluted sample to a silicon wafer and drying at room temperature for 12 hours, the sample was subsequently carbon coated with a carbon evaporator for 4 seconds. Raman Measurements were conducted on a Renishaw inVia Raman Microscope fitted with a 514.5 nm  $\text{Ar}^+$  laser and Renishaw CCD detector. FTIR measurements were conducted on a Bruker Alpha Platinum ATR FTIR.  $^1\text{H}$  and  $^{13}\text{C}$  NMR spectra were recorded on a Bruker DRX500 and an

AV700 spectrometers as solutions in deuterated NMR solvents. Chemical shifts are cited as parts per million (ppm). The following abbreviations are used to abbreviate multiplicities; s = singlet, d = doublet, t = triplet, q = quartet, m = multiplet.

All SEC experiments were performed on Agilent 390-LC multi-detector suites equipped with a PL-AS RT/MT autosampler, fitted with a PLgel 5  $\mu\text{m}$  guard column and two PLgel 5  $\mu\text{m}$  Mixed D columns (with an exclusion limit of  $2.0 \times 10^6 \text{ g mol}^{-1}$ ). All data was collected and analysed using Agilent GPC software. Solvent used was THF with 2 % TEA and 0.01 % BHT, with a flow rate of  $1 \text{ ml min}^{-1}$  and an injection volume of 100  $\mu\text{L}$ . The column sets were maintained at ambient temperature and 50  $^{\circ}\text{C}$ . A DRI detector was used for conventional calibration. Calibrations were created using poly(styrene) EasiVial standards ( $162\text{-}508,000 \text{ g mol}^{-1}$ ) purchased from Agilent, with a minimum of 9 points fitted with a third order calibration curve. Points with an error greater than 10 % were not included in the final calibration. Samples were prepared by diluting one drop of aqueous polymer solution in 1.5 mL SEC solvent, allowing the solution to equilibrate for 30 minutes after which the solution was filtered.

### **3.5.3. Calcium carbonate encapsulated in a polymeric shell with pendant vinyl groups**

Typical method for encapsulation of calcium carbonate particles: Calcium carbonate (10.00 g) was dispersed in water (49.00 g) and degassed by purging with nitrogen for 20 minutes. The reaction mixture was heated to 70  $^{\circ}\text{C}$  and initiated with ammonium persulfate (0.0216 g, 0.095 mmol) dissolved in water (1.00 g). 0.5 mL of a degassed mixture of DEGDA and MAA was fed into the reaction at  $0.5 \text{ mL h}^{-1}$ , followed by a 0.5 mL DEGDA feed at  $0.5 \text{ mL h}^{-1}$  (see Table 3.1 for monomer quantities). The polymerization was stopped 30 minutes after the monomer feed had

finished. The composite latex was dialysed into water. Particles were collected by freeze-drying.

**Table 3.11** Encapsulated calcium carbonate particles within a polymeric shell with various multiple acrylate containing monomers, monomer fed amounts fed into a mixture of 10.0 g calcium carbonate and 50.0 g water. Monomer feeds 1 and 2 were both 0.5 mL and fed at 0.5 mL h<sup>-1</sup>.

| Exp.   | Monomers | Particle<br>Acronym | Mass (g) |        | mmol   |        |
|--------|----------|---------------------|----------|--------|--------|--------|
|        |          |                     | Feed 1   | Feed 2 | Feed 1 | Feed 2 |
| HM-301 | MAA      | Poly(DEGDA)-<br>C   | 0.16     | 0      | 1.84   | 0      |
|        | DEGDA    |                     | 0.38     | 0.34   | 1.80   | 2.61   |
| HM-302 | MAA      | Poly(PETA)-C        | 0.16     | 0      | 1.88   | 0      |
|        | DEGDA    |                     | 0.20     | 0.29   | 0.91   | 1.34   |
|        | PETA     |                     | 0.20     | 0.29   | 0.65   | 0.96   |
| HM-303 | MAA      | Poly(DPEPHA)-<br>C  | 0.16     | 0      | 1.86   | 0      |
|        | DEGDA    |                     | 0.19     | 0.28   | 0.91   | 1.33   |
|        | DPEPHA   |                     | 0.19     | 0.28   | 0.37   | 0.54   |

### 3.5.3.1. Bare calcium carbonate

Raman data was analysed from literature; calcium carbonate<sup>75, 76</sup> and organic groups.<sup>77, 78</sup>

Raman spectra (cm<sup>-1</sup>): 155 (T[Ca, CO<sub>3</sub>]); 280 (T[Ca, CO<sub>3</sub>]); 712 (v<sub>4</sub> [CO<sub>3</sub>] bending vibrations); 1086 (v<sub>1</sub> [CO<sub>3</sub>] symmetric stretch); 1436 (v<sub>3</sub> [CO<sub>3</sub>] asymmetric stretch); 1749 (v<sub>1</sub> and v<sub>4</sub>).

FTIR spectra (cm<sup>-1</sup>): 712 (w, v<sub>4</sub> [CO<sub>3</sub>] symmetric deformation); 871 (s, v<sub>2</sub> [CO<sub>3</sub>] asymmetric deformation); 1079 (vw, v<sub>1</sub> [CO<sub>3</sub>] symmetric stretch); 1402 (vs, v<sub>3</sub> [CO<sub>3</sub>] asymmetric stretch); 1793 (vw, v<sub>1</sub> and v<sub>4</sub>); 2515 (vw, 2v<sub>2</sub> and v<sub>4</sub>).

### 3.5.3.2. DEGDA-*c* particles (HM-301)

Raman spectra ( $\text{cm}^{-1}$ ): 155 (T[Ca,  $\text{CO}_3$ ]); 280 (T[Ca,  $\text{CO}_3$ ]); 712 ( $\nu_4$  [ $\text{CO}_3$ ] bending vibrations); 841 (-C-O-C- stretch); 1086 ( $\nu_1$  [ $\text{CO}_3$ ] symmetric stretch); 1285 (C-C<sub>aliph</sub> stretch); 1452 ( $\nu_3$  [ $\text{CO}_3$ ] asymmetric stretch); 1729 ( $\nu_1$  and  $\nu_4$ ); 2876 (-CH<sub>2</sub> symmetric stretch); 2926 (-CH<sub>2</sub> asymmetric stretch); 2960 (-CH<sub>2</sub> asymmetric stretch).

FTIR spectra ( $\text{cm}^{-1}$ ): 712 (w,  $\nu_4$  [ $\text{CO}_3$ ] symmetric deformation); 871 (s,  $\nu_2$  [ $\text{CO}_3$ ] asymmetric deformation); 1079 (vw,  $\nu_1$  [ $\text{CO}_3$ ] symmetric stretch); 1178 (w, C-O- stretch); 1402 (vs,  $\nu_3$  [ $\text{CO}_3$ ] asymmetric stretch); 1725 (w, -(CO)-O- stretch) 1793 (vw,  $\nu_1$  and  $\nu_4$ ); 2515 (vw,  $2\nu_2$  and  $\nu_4$ ).

### 3.5.3.3. PETA-*c* particles (HM-302)

Raman spectra ( $\text{cm}^{-1}$ ): 155 (T[Ca,  $\text{CO}_3$ ]); 280 (T[Ca,  $\text{CO}_3$ ]); 712 ( $\nu_4$  [ $\text{CO}_3$ ] bending vibrations); 1086 ( $\nu_1$  [ $\text{CO}_3$ ] symmetric stretch); 1284 (C-C<sub>aliph</sub> stretch); 1409 (C=C-H deformation); 1468 ( $\nu_3$  [ $\text{CO}_3$ ] asymmetric stretch); 1637 (C=C stretch); 1722 ( $\nu_1$  and  $\nu_4$ ); 2904 (-CH<sub>2</sub> symmetric stretch); 2932 (-CH<sub>2</sub> asymmetric stretch); 2966 (-CH<sub>2</sub> asymmetric stretch); 2993 (-OH stretch); 3040 (C=C-H stretch); 3075 (C=C-H stretch); 3109 (C=C-H stretch).

FTIR spectra ( $\text{cm}^{-1}$ ): 712 (w,  $\nu_4$  [ $\text{CO}_3$ ] symmetric deformation); 809 (vw, vinyl -C-H deformation); 871 (s,  $\nu_2$  [ $\text{CO}_3$ ] asymmetric deformation); 983 (vw, vinyl -C-H conjugated to C=O deformation); 1061 (vw, C-O stretch); 1079 (vw,  $\nu_1$  [ $\text{CO}_3$ ] symmetric stretch); 1178 (w, -C-O- stretch); 1298 (vw, -O-H stretch); 1402 (vs,  $\nu_3$  [ $\text{CO}_3$ ] asymmetric stretch); 1725 (w, unsaturated -(CO)-O- stretch); 1793 (vw,  $\nu_1$  and  $\nu_4$ ); 2515 (vw,  $2\nu_2$  and  $\nu_4$ ).

#### 3.5.3.4. DPEPHA-*c* particles (HM-303)

Raman spectra ( $\text{cm}^{-1}$ ): 155 (T[Ca,  $\text{CO}_3$ ]); 280 (T[Ca,  $\text{CO}_3$ ]); 712 ( $\nu_4[\text{CO}_3]$  bending vibrations); 1086 ( $\nu_1[\text{CO}_3]$  symmetric stretch); 1285 (C-C<sub>aliph</sub> stretch); 1408 (m, C=C-H deformation); 1435( $\nu_3[\text{CO}_3]$  asymmetric stretch); 1637 (C=C stretch); 1727 ( $\nu_1$  and  $\nu_4$ ); 2963 (-CH<sub>2</sub> asymmetric stretch); 3040 (C=C-H stretch); 3075 (C=C-H stretch); 3109 (C=C-H stretch).

FTIR spectra ( $\text{cm}^{-1}$ ): 712 (w,  $\nu_4$  [ $\text{CO}_3$ ] symmetric deformation); 809 (vw, vinyl -C-H deformation); 871 (s,  $\nu_2$  [ $\text{CO}_3$ ] asymmetric deformation); 983 (vw, vinyl -C-H conjugated to C=O deformation); 1061 (vw, C-O stretch); 1079 (vw,  $\nu_1$  [ $\text{CO}_3$ ] symmetric stretch); 1178 (w, -C-O- stretch); 1298 (vw, -OH stretch); 1402 (vs,  $\nu_3$  [ $\text{CO}_3$ ] asymmetric stretch); 1725 (w, -(CO)-O- stretch); 1793 (vw,  $\nu_1$  and  $\nu_4$ ); 2515 (vw,  $2\nu_2$  and  $\nu_4$ ).

#### 3.5.4. Hollow particles

Typical method of preparing hollow polymer particles: To 0.50 g of composite particles (HM-301-303) in 2.50 g water, acetic acid (40 mL, 0.25 M) was added at a rate of 3 mL h<sup>-1</sup> using a syringe pump. The hollow particles were cleaned by 5 centrifugation cycles.

##### 3.5.4.1. Hollow DEGDA-*c* particles (HM-304)

Raman spectra ( $\text{cm}^{-1}$ ): 752 (w, CH<sub>2</sub> rocking); 802 (w, C-C<sub>aliph</sub> stretch); 837 (w, symmetric C-O-C stretch); 860 (m, C-C stretch); 919 (w, C-C<sub>aliph</sub> stretch); 1016 (m, ester C-O stretch); 1040 (m, C-O-C stretch); 1085 (m, C-O-C stretch); 1277 (s, C-C<sub>aliph</sub> stretch); 1380 (m, C=O stretch); 1451 (vs, CH<sub>2</sub> bending); 1730 (vs, C=O asymmetric stretch); 2867 (s, CH<sub>2</sub> stretch); 2920 (vs, CH<sub>2</sub> asymmetric stretch).

FTIR spectra ( $\text{cm}^{-1}$ ): 758 (vw, -CH<sub>2</sub> rocking); 854 (vw, symmetric -C-O-C stretch); 919 (vw, symmetric C-O-C stretch); 1045 (s, C-O stretch); 1132 (vs, C-O

stretch); 1163 (vs, C-O stretch); 1245 (s, C-O stretch); 1355 (m, C=O stretch); 1385 (m, C=O stretch); 1446 (m -CH<sub>2</sub> deformation); 1724 (vs, -(CO)O- stretch); 2869 (s, -CH<sub>2</sub> stretch); 2953 (s, -CH<sub>2</sub> stretch).

#### 3.5.4.2. Hollow PETA-*c* particles (HM-305)

Raman spectra (cm<sup>-1</sup>): 622 (w, 733 (s, -CH=CH<sub>2</sub>); 758 (w, CH<sub>2</sub> rocking); 807 (w, C-C<sub>aliph</sub> stretch); 839 (w, symmetric C-O-C stretch); 860 (m, C-C stretch); 915 (m, RHC=CH<sub>2</sub> deformation); 925 (w, C-C<sub>aliph</sub> stretch); 1011 (m, ester C-O stretch); 1031 (m, C-O-C stretch); 1069 (m, C-O-C stretch); 1281 (s, C-C<sub>aliph</sub> stretch); 1380 (m, C=C-H deformation); 1408 (m, C=C-H deformation); 1454 (vs, CH<sub>2</sub> bending); 1634 (s, C=C stretch); 1729 (vs, C=O asymmetric stretch); 2928 (vs, CH<sub>2</sub> asymmetric stretch); 3036 (w, C=C-H stretch).

FTIR spectra (cm<sup>-1</sup>): 748 (vw, -CH<sub>2</sub> rocking); 860 (vw, symmetric -C-O-C stretch); 923 (vw, symmetric C-O-C stretch); 1052 (s, C-O stretch); 1153 (vs, C-O stretch); 1208 (s, C-O stretch); 1388 (m, C=O stretch); 1449 (m -CH<sub>2</sub> deformation); 1722 (vs, -(CO)O- stretch); 2885 (s, -CH<sub>2</sub> stretch); 2952 (s, -CH<sub>2</sub> stretch); 3523 (b, O-H stretch).

#### 3.5.4.3. Hollow DPEPHA-*c* particles (HM-306)

Raman spectra (cm<sup>-1</sup>): 733 (s, -CH=CH<sub>2</sub> rocking); 758 (w, CH<sub>2</sub> rocking); 807 (w, C-C<sub>aliph</sub> stretch); 839 (w, symmetric C-O-C stretch); 861 (m, C-C stretch); 915 (m, RHC=CH<sub>2</sub> deformation); 925 (w, C-C<sub>aliph</sub> stretch); 1011 (m, ester C-O stretch); 1034 (m, C-O-C stretch); 1069 (m, C-O-C stretch); 1281 (s, C-C<sub>aliph</sub> stretch); 1380 (m, C=C-H deformation); 1408 (m, C=C-H deformation); 1455 (vs, CH<sub>2</sub> bending); 1634 (s, C=C stretch); 1726 (vs, C=O asymmetric stretch); 2927 (vs, CH<sub>2</sub> asymmetric stretch); 3036 (w, C=C-H stretch).

FTIR spectra ( $\text{cm}^{-1}$ ): 755 (vw,  $-\text{CH}_2$  rocking); 808 (w, vinyl  $-\text{CH}$  deformation); 855 (vw, symmetric  $-\text{C}-\text{O}-\text{C}-$  stretch); 925 (vw, symmetric  $\text{C}-\text{O}-\text{C}$  stretch); 987 (w, vinyl  $-\text{CH}$  conjugated to  $\text{C}=\text{O}$  deformation); 1059 (s,  $\text{C}-\text{O}$  stretch); 1158 (vs,  $\text{C}-\text{O}$  stretch); 1205 (s,  $\text{C}-\text{O}$  stretch); 1358 (m,  $\text{C}=\text{O}$  stretch); 1406 (m,  $\alpha\beta$ -unsaturated  $\text{C}=\text{O}$ ); 1449 (m  $-\text{CH}_2$  deformation); 1634 (m,  $\text{C}=\text{C}$  stretch), 1724 (vs,  $-(\text{CO})\text{O}-$  stretch), 2876 (s,  $-\text{CH}_2$  stretch), 2956 (s,  $-\text{CH}_2$  stretch), 3521 (b,  $\text{O}-\text{H}$  stretch).

### 3.5.5. Quantifying pendant vinyl groups on encapsulated particles

Typical Bromination reaction proceeded as follows. The calcium carbonate of 0.20 g of composite particles was etched out with acetic acid. The now hollow particles were added to a 50 mL solution containing  $\text{KBrO}_3$  (0.139 g, 0.835 mmol) and  $\text{KBr}$  (0.496 g, 4.17 mmol) along with 9 mL water, 0.5 mL methanol and 0.5 mL glacial acetic acid. This was left in the dark for 6 hours whilst stirring at room temperature.

Typical titration proceeded as follows. Once the bromination was complete, the solution was cooled to  $0-3^\circ\text{C}$ , 2 mL concentrated  $\text{HCl}$  was added to the solution and was left for 30 minutes. Potassium iodide (1.5 g) was added and stirred until homogenous. The solution was titrated with 0.1 M sodium thiosulfate solution, 0.5 mL of 1 % starch solution was added after the solution changed colour from brown to yellow, and the end point was when the solution turned from black to colourless. Throughout the titration the mixture was kept in the dark.

**Table 3.12** Table of average titration volumes and corresponding Bromine Index for composite particles.  $V_1$  and  $V_2$  denote the volume of  $\text{Na}_2\text{S}_2\text{O}_3$  titrated in the blank and sample solution respectively.

| Exp.   | Particles                  | $V_1 - V_2$<br>(mL) | BI<br>(mg / 100 g) |
|--------|----------------------------|---------------------|--------------------|
| HM-307 | Poly(DEGDA)-C<br>(HM-301)  | 0                   | 0                  |
| HM-308 | Poly(PETA)-C<br>(HM-302)   | 0.57                | 2220               |
| HM-309 | Poly(DPEPHA)-C<br>(HM-303) | 0.20                | 779                |

#### 3.5.5.1. Brominated PETA-c particles (HM-308)

Raman spectra ( $\text{cm}^{-1}$ ): 758 (s, C-Br stretch), 839 (w, symmetric C-O-C stretch), 861 (m, C-C stretch), 921 (w, C-C<sub>aliph</sub> stretch), 1018 (m, ester C-O stretch); 1142 (m, C-O stretch); 1276 (s, C-C<sub>aliph</sub> stretch); 1356 (m, C=O stretch); 1453 (vs, CH<sub>2</sub> bending); 1730 (vs, C=O asymmetric stretch); 2873 (s, CH<sub>2</sub> asymmetric stretch); 2940 (vs, CH<sub>2</sub> asymmetric stretch).

FTIR spectra ( $\text{cm}^{-1}$ ): 748 (vw, -CH<sub>2</sub> rocking); 854 (vw, symmetric -C-O-C stretch); 923 (vw, symmetric C-O-C stretch); 1059 (s, C-O stretch); 1166 (vs, C-O stretch); 1253 (s, C-O stretch); 1387 (m, C=O stretch); 1447 (m -CH<sub>2</sub> deformation); 1729 (vs, -(CO)O- stretch); 2876 (s, -CH<sub>2</sub> stretch); 2944 (s, -CH<sub>2</sub> stretch).

#### 3.5.5.2. HM-309 Brominated DPEPHA-c particles

Raman spectra ( $\text{cm}^{-1}$ ): 635 (m, C-Br stretch); 673 (m, C-Br stretch); 748 (s, C-Br stretch); 786 (w, CH<sub>2</sub> rocking); 802 (vw, C-C<sub>aliph</sub> stretch); 837 (w, symmetric C-O-C stretch); 860 (m, C-C stretch); 920 (w, C-C<sub>aliph</sub> stretch); 1028 (m, ester C-O stretch); 1085 (m, C-O-C stretch); 1142 (m, C-O stretch); 1281 (s, C-C<sub>aliph</sub> stretch);



1452 (vs, CH<sub>2</sub> bending); 1732 (vs, C=O asymmetric stretch); 2878 (s, CH<sub>2</sub> asymmetric stretch); 2931 (vs, vs, CH<sub>2</sub> asymmetric stretch).

FTIR spectra (cm<sup>-1</sup>): 748 (vw, -CH<sub>2</sub> rocking); 854 (vw, symmetric -C-O-C- stretch); 923 (vw, symmetric C-O-C stretch); 1059 (s, C-O stretch); 1166 (vs, C-O stretch); 1253 (s, C-O stretch); 1387 (m, C=O stretch); 1447 (m -CH<sub>2</sub> deformation); 1729 (vs, -(CO)O- stretch); 2876 (s, -CH<sub>2</sub> stretch); 2944 (s, -CH<sub>2</sub> stretch).

### **3.5.6. Typical method for thiol Michael addition of 2-mercapto ethanol to pendant vinyl groups on encapsulated CaCO<sub>3</sub> particles**

To the particles (0.50 g) (HM-302-303), 2-mercaptoethanol (0.56 g, 7.17 mmol) was added, followed by a 10 mL solution of water containing hexylamine (0.2 mg, 0.002 mmol), the reaction was left overnight. The particles were cleaned by centrifugation cycles.

#### *3.5.6.1. HM-310 Thiol Michael addition of 2-mercaptoethanol to PETA-c particles*

Raman spectra (cm<sup>-1</sup>): 154 (T[Ca, CO<sub>3</sub>]); 279 (T[Ca, CO<sub>3</sub>]); 711 (v<sub>4</sub> [CO<sub>3</sub>] bending vibrations); 1085 (v<sub>1</sub> [CO<sub>3</sub>] symmetric stretch); 1435 (v<sub>3</sub> [CO<sub>3</sub>] asymmetric stretch); 1748 (v<sub>1</sub> and v<sub>4</sub>); 2927 (-CH<sub>2</sub> asymmetric stretch); 2960 (-CH<sub>2</sub> asymmetric stretch); 2993 (-OH stretch).

FTIR spectra (cm<sup>-1</sup>): 667 (vw -C-S- stretch); 712 (w, v<sub>4</sub> [CO<sub>3</sub>] symmetric deformation); 871 (s, v<sub>2</sub> [CO<sub>3</sub>] asymmetric deformation); 1061 (vw, C-O stretch); 1067 (vw, v<sub>1</sub> [CO<sub>3</sub>] symmetric stretch); 1167 (w, -C-O- stretch); 1298 (vw, -O-H stretch); 1398 (vs, v<sub>3</sub> [CO<sub>3</sub>] asymmetric stretch); 1732 (w, -(CO)-O- stretch); 1794 (vw, v<sub>1</sub> and v<sub>4</sub>); 2510 (vw, 2v<sub>2</sub> and v<sub>4</sub>).

### 3.5.6.2. HM-312 Hollowed PETA-c particles after thiol Michael addition of 2-mercaptoethanol

Raman spectra ( $\text{cm}^{-1}$ ): 646 (w, C-S stretch); 748 (w, C-S stretch); 839 (w, symmetric C-O-C stretch); 860 (m, C-C stretch); 925 (w, C-C<sub>aliph</sub> stretch); 1015 (m, ester C-O stretch); 1041 (m, C-O-C stretch); 1247 (m, ester C-O stretch); 1279 (s, C-C<sub>aliph</sub> stretch); 1456 (vs, CH<sub>2</sub> bending); 1728 (vs, C=O asymmetric stretch); 2927 (vs, CH<sub>2</sub> asymmetric stretch).

FTIR spectra ( $\text{cm}^{-1}$ ): 746 (vw, -CH<sub>2</sub> rocking); 858 (vw, symmetric -C-O-C- stretch); 932 (vw, symmetric C-O-C stretch); 1047 (s, C-O stretch); 1154 (vs, C-O stretch); 1245 (s, C-O stretch); 1389 (m, C=O stretch); 1447 (m -CH<sub>2</sub> deformation); 1725 (vs, -(CO)O- stretch); 2876 (s, -CH<sub>2</sub> stretch); 2949 (s, -CH<sub>2</sub> stretch); 3521 (b, O-H stretch).

### 3.5.6.3. HM-311 Thiol Michael addition of 2-mercaptoethanol to DPEPHA-c particles

Raman spectra ( $\text{cm}^{-1}$ ): 154 (T[Ca, CO<sub>3</sub>]); 279 (T[Ca, CO<sub>3</sub>]); 711 ( $\nu_4$ [CO<sub>3</sub>] bending vibrations); 1085 ( $\nu_1$ [CO<sub>3</sub>] symmetric stretch); 1435 ( $\nu_3$ [CO<sub>3</sub>] asymmetric stretch); 1748 ( $\nu_1$  and  $\nu_4$ ); 2927 (-CH<sub>2</sub> asymmetric stretch); 2963 (-CH<sub>2</sub> asymmetric stretch).

FTIR spectra ( $\text{cm}^{-1}$ ): 667 (vw, -C-S- stretch); 712 (w,  $\nu_4$  [CO<sub>3</sub>] symmetric deformation); 871 (s,  $\nu_2$  [CO<sub>3</sub>] asymmetric deformation); 1061 (vw, C-O stretch); 1067 (vw,  $\nu_1$  [CO<sub>3</sub>] symmetric stretch); 1167 (w, -C-O- stretch); 1298 (vw, -O-H stretch); 1398 (vs,  $\nu_3$  [CO<sub>3</sub>] asymmetric stretch); 1730 (w, -(CO)-O- stretch); 1795 (vw,  $\nu_1$  and  $\nu_4$ ); 2510 (vw,  $2\nu_2$  and  $\nu_4$ ).

#### 3.5.6.4. HM-313 Hollowed DPEPHA-c particles after thiol Michael addition of 2-mercaptoethanol

Raman spectra ( $\text{cm}^{-1}$ ): 651 (w, C-S stretch); 758 (w, C-S stretch); 834 (w, symmetric C-O-C stretch); 862 (m, C-C stretch); 965 (w, C-C<sub>aliph</sub> stretch); 1015 (m, ester C-O stretch); 1041 (m, C-O-C stretch); 1247 (m, ester C-O stretch); 1279 (s, C-C<sub>aliph</sub> stretch); 1456 (vs, CH<sub>2</sub> bending); 1731 (vs, C=O asymmetric stretch); 2168 (m, -OH stretch); 2923 (vs, CH<sub>2</sub> asymmetric stretch).

FTIR spectra ( $\text{cm}^{-1}$ ): 746 (vw, -CH<sub>2</sub> rocking); 858 (vw, symmetric -C-O-C stretch); 932 (vw, symmetric C-O-C stretch); 1047 (s, C-O stretch); 1154 (vs, C-O stretch); 1245 (s, C-O stretch); 1389 (m, C=O stretch); 1447 (m -CH<sub>2</sub> deformation); 1725 (vs, -(CO)O- stretch); 2876 (s, -CH<sub>2</sub> stretch); 2949 (s, -CH<sub>2</sub> stretch); 3521 (b, -OH stretch).

#### 3.5.6.5. Quantifying pendant vinyl groups by bromination after thiol Michael addition of 2-mercapto ethanol

See section 3.4.5. for experimental protocol.

**Table 3.13** Table of average titration volumes and corresponding Bromine Index for composite particles after thiol Michael addition of 2-mercapto ethanol.  $V_1$  and  $V_2$  denote the volume of  $\text{Na}_2\text{S}_2\text{O}_3$  titrated in the blank and sample solution respectively.

| Exp.   | Particles                                      | $V_1 - V_2$<br>(mL) | BI<br>(mg / 100 g) |
|--------|--|---------------------|--------------------|
| HM-314 | Poly(PETA)-C—<br>mercaptoethanol<br>(HM-310)   | 0                   | 0                  |
| HM-315 | Poly(DPEPHA)-C—<br>mercaptoethanol<br>(HM-311) | 0                   | 0                  |

### 3.5.7. Typical method for thiol Michael addition of dodecanethiol to pendant vinyl groups on encapsulated $\text{CaCO}_3$

To the particles (0.65 g) (HM-301-303), 1-dodecanethiol (1.54 g, 7.62 mmol) was added, followed by a 10 mL solution of acetone containing hexylamine (0.2 mg, 0.002 mmol), the reaction was left overnight. The particles were cleaned by centrifugation cycles.

#### 3.5.7.1. HM-314 Thiol Michael addition of 1-dodecanethiol to PETA-c particles

Raman spectra ( $\text{cm}^{-1}$ ): 155 (T[Ca,  $\text{CO}_3$ ]); 280 (T[Ca,  $\text{CO}_3$ ]); 712 ( $\nu_4$  [ $\text{CO}_3$ ] bending vibrations); 1086 ( $\nu_1$  [ $\text{CO}_3$ ] symmetric stretch); 1435 ( $\nu_3$  [ $\text{CO}_3$ ] asymmetric stretch); 1748 ( $\nu_1$  and  $\nu_4$ ); 2927 ( $-\text{CH}_2$  asymmetric stretch); 2960 ( $-\text{CH}_2$  asymmetric stretch); 2993 ( $-\text{OH}$  stretch).

FTIR spectra ( $\text{cm}^{-1}$ ): 667 (vw  $-\text{C}-\text{S}-$  stretch); 712 (w,  $\nu_4$  [ $\text{CO}_3$ ] symmetric deformation); 871 (s,  $\nu_2$  [ $\text{CO}_3$ ] asymmetric deformation); 1061 (vw,  $\text{C}-\text{O}$  stretch); 1079 (vw,  $\nu_1$  [ $\text{CO}_3$ ] symmetric stretch); 1167 (w,  $-\text{C}-\text{O}-$  stretch); 1298 (vw,  $-\text{O}-\text{H}$  stretch); 1410 (vs,  $\nu_3$  [ $\text{CO}_3$ ] asymmetric stretch); 1733 (w,  $-(\text{CO})-\text{O}-$  stretch); 1793 (vw,  $\nu_1$  and  $\nu_4$ ); 2508 (vw,  $2\nu_2$  and  $\nu_4$ ); 2873 (m,  $-\text{CH}_2$  stretch); 2977 (m,  $-\text{CH}_2$  stretch); 3521 (b,  $-\text{OH}$ ).

#### 3.5.7.2. HM-315 Thiol Michael addition of 1-dodecanethiol to DPEPHA-c particles

Raman spectra ( $\text{cm}^{-1}$ ): 157 (T[Ca,  $\text{CO}_3$ ]); 282 (T[Ca,  $\text{CO}_3$ ]); 714 ( $\nu_4$  [ $\text{CO}_3$ ] bending vibrations); 1088 ( $\nu_1$  [ $\text{CO}_3$ ] symmetric stretch); 1437 ( $\nu_3$  [ $\text{CO}_3$ ] asymmetric stretch); 1751 ( $\nu_1$  and  $\nu_4$ ); 2927 ( $-\text{CH}_2$  asymmetric stretch); 2960 ( $-\text{CH}_2$  asymmetric stretch).

FTIR spectra ( $\text{cm}^{-1}$ ): 712 (w,  $\nu_4$  [ $\text{CO}_3$ ] symmetric deformation); 872 (s,  $\nu_2$  [ $\text{CO}_3$ ] asymmetric deformation); 1061 (vw,  $\text{C}-\text{O}$  stretch); 1086 (vw,  $\nu_1$  [ $\text{CO}_3$ ]

symmetric stretch); 1173 (w, -C-O- stretch); 1405 (vs,  $\nu_3$  [CO<sub>3</sub>] asymmetric stretch); 1732 (w, -(CO)-O- stretch); 1796 (vw,  $\nu_1$  and  $\nu_4$ ); 2512 (vw,  $2\nu_2$  and  $\nu_4$ ).

### 3.5.7.3. Quantifying pendant vinyl groups by bromination after thiol Michael addition of 1-dodecane thiol

See section 3.4.5. for experimental protocol.

**Table 3.14** Table of average titration volumes and corresponding Bromine Index for composite particles after thiol Michael addition of 1-dodecane thiol.  $V_1$  and  $V_2$  denote the volume of Na<sub>2</sub>S<sub>2</sub>O<sub>3</sub> titrated in the blank and sample solution respectively.

| Exp.   | Particles                                     | $V_1 - V_2$<br>(mL) | BI<br>(mg / 100 g) |
|--------|---|---------------------|--------------------|
| HM-318 | Poly(PETA)-C—<br>dodecane thiol<br>(HM-316)   | 0                   | 0                  |
| HM-319 | Poly(DPEPHA)-C—<br>dodecane thiol<br>(HM-317) | 0                   | 0                  |

### 3.5.8. Synthesis of RAFT agent (propanoic acid)-2-yl butyl trithiocarbonate (PABTC) (HM-320)

(Propanoic acid)-2-yl butyl trithiocarbonate (PABTC) was synthesized as follows.<sup>67</sup> A 50 % NaOH solution (32.06 g, containing 16.03 g, 401 mmol of NaOH) was added to a stirred mixture of 1-butanethiol (36.10 g, 400 mmol), water (60 mL) and acetone (20 mL), the resulting clear, colourless solution was stirred for 30 minutes. Carbon disulfide (34.22 g, 449 mmol) was added and the now clear orange solution was left to stir for 30 minutes. The solution was cooled to <10 °C, after which 2-bromopropionic acid (63.06 g, 412 mmol) was added at a rate so that the temperature did not exceed 30 °C, followed by 50 % NaOH (32.83 g containing 16.42 g, 410 mmol NaOH) at a rate so that the temperature did not exceed 30 °C. When the exotherm had stopped the ice bath was removed, water (60 mL) was added

and the mixture was left to stir for 24 hours at ambient temperature. Water (100 mL) was added to the mixture and it was cooled to  $<10\text{ }^{\circ}\text{C}$ , after which 10 M HCl (60 mL) was added at a rate so that the temperature did not exceed  $10\text{ }^{\circ}\text{C}$ . A yellow oil separated and on further cooling solidified. The yellow solid was collected by suction filtration, washed with ice cold water and dried under reduced pressure. The lumps were crushed with a spatula and the solid was re-suspended in cold water and stirred for 15 minutes. The solid was collected by suction filtration and dried under reduced pressure. The powdery yellow solid was recrystallized from hexane (180 mL) to give bright yellow microcrystals.

Yield: 75.71 g, 79.34 %

$^1\text{H}$  NMR ( $\text{CDCl}_3$ ),  $\delta$  (ppm): 0.95 (t,  $J=7.3\text{ Hz}$ , 3H,  $\text{CH}_3\text{CH}_2-$ ); 1.44 (sext,  $J=7.5\text{ Hz}$ , 2H,  $\text{CH}_3\text{CH}_2\text{CH}_2-$ ); 1.64 (d,  $J=7.3\text{ Hz}$ , 3H,  $\text{SCHCH}_3$ ); 1.70 (quint,  $J=7.5\text{ Hz}$ , 2H,  $\text{CH}_2\text{CH}_2\text{S}-$ ); 3.38 (t,  $J=7.5\text{ Hz}$ , 2H,  $\text{CH}_2\text{S}-$ ); 4.88 (q,  $J=7.5\text{ Hz}$ , 1H,  $\text{SCH}$ ); 10.6 (b, 1H,  $\text{CO}_2\text{H}$ ).

$^{13}\text{C}$  NMR ( $\text{CDCl}_3$ ),  $\delta$  (ppm): 13.88 (1C,  $\text{CH}_2\text{CH}_3$ ); 16.89 (1C,  $\text{SCHCH}_3$ ); 22.36 (1C,  $\text{CH}_3\text{CH}_2$ ); 30.18 (1C,  $\text{CH}_2\text{CH}_2\text{S}$ ); 37.44 (1C,  $\text{CH}_2\text{S}$ ); 47.72 (1C,  $\text{SCH}$ ); 177.14 (1C  $\text{C=O}$ ); 221.89 (1C,  $\text{C=S}$ ).

FTIR ( $\text{cm}^{-1}$ ): 2953 (s,  $\text{CH}_3$  stretch); 2926 (s,  $\text{CH}_2$  stretch); 2865 (s, CH stretch); 2712 (m, CHO stretch); 2597 (m, COOH); 1705 (s,  $\text{C=O}$  stretch); 1450 (m,  $\text{CH}_2$  stretch); 1418 (s, OH bending); 1316 (m, C-O stretch), 1304 (s,  $\text{CO}_2\text{H}$ ); 1208 (s,  $\text{C=S}$  stretch); 1105 (s, C-O); 1087 (m, S-CS-S); 1065 (m, S-CS-S); 1041 (m, C-O); 910 (w, C-C stretch); 823 (s, C-C stretch); 647 (w, C-S stretch).

ESI-MS  $m/z$ : Calculated: 237.40 ( $\text{H}^+$ ). Found: 237.00.

### 3.5.9. RAFT polymerization of styrene using PABTC

Typical polymerization of polystyrene using PABTC was conducted as follows (see Table 3.15 for values). PABTC (HM-320) and VA-088 (10 mol.% w.r.t. PABTC) was dissolved in 1,4-dioxane (0.80 g), to this styrene (8.00 g, 76.8 mmol, 8 M w.r.t. solvent) was added. The solution was degassed by four freeze-pump-thaw cycles, after which the chamber was flooded with nitrogen gas and the polymerization was started by heating to 90 °C. Monomer conversion was followed by  $^1\text{H}$  NMR and molecular weight by THF SEC. Polymer was purified by precipitation in methanol.

**Table 3.15** Table of polymerization of styrene using PABTC RAFT agent. The number in the brackets denotes the molecular weight aim at 60 % monomer conversion.

| Polymer | PABTC |        | VA-088 |        | Styrene |        | Dioxane |
|---------|-------|--------|--------|--------|---------|--------|---------|
|         | (g)   | (mmol) | (g)    | (mmol) | (g)     | (mmol) |         |
| HM-321  | 0.114 | 0.479  | 0.0116 | 0.047  | 8.04    | 77.2   | 0.80    |
| HM-322  | 0.114 | 0.479  | 0.0113 | 0.046  | 8.00    | 76.8   | 0.80    |

$^1\text{H}$  NMR ( $\text{CDCl}_3$ ),  $\delta$  (ppm): 0.94 (t, 3H,  $\text{CH}_3\text{CH}_2$ - RAFT agent); 1.25-1.71 (bm, 1nH, backbone); 1.73-2.30 (bm, 2nH, backbone); 3.29 (t, 2H,  $\text{CH}_2\text{S}$ - RAFT agent); 6.35-7.20 (bm, 5nH, Ar-H).

$^{13}\text{C}$  NMR ( $\text{CDCl}_3$ ),  $\delta$  (ppm): 13.66 (1C,  $\text{CH}_2\text{CH}_3$ , RAFT agent); 21.51 (1C,  $\text{SCHCH}_3$ , RAFT agent); 22.10 (1C,  $\text{CH}_3\text{CH}_2$ , RAFT agent); 30.02 (1C,  $\text{SCH}_2\text{CH}_2$ , RAFT agent); 36.48 (1C,  $\text{CH}_2\text{S}$ , RAFT agent); 40.39 (1nC,  $\text{CH}_2\text{CH}$ , backbone); 41.52-4.04 (1nC,  $\text{CH}_2\text{CH}$ , backbone); 52.90 (1C,  $\text{SCH}$ , RAFT agent); 125.68 (2nC, ortho-Ar); 127.46 (1nC, para-Ar); 129.08 (2nC, meta-Ar); 145.35 (1nC, Ar); 179.64 (1C,  $\text{C=O}$ , RAFT agent); 222.33 (1C,  $\text{C=S}$ , RAFT agent).

FTIR ( $\text{cm}^{-1}$ ): 696 (s, aromatic C-H); 752 (s, aromatic C-H); 841 (vw, C-C stretch); 907 (w, C-C stretch); 1027 (m, aromatic C=C); 1452 (m,  $\text{CH}_2$  asymmetrical deformation); 1492 (m, aromatic C=C stretch); 1582 (w, aromatic C=C stretch); 1601 (m, aromatic C=C stretch); 2841 (w, C-H stretch); 2919 (m, C-H stretch); 3003 (w, aryl C-H); 3024 (m, aryl C-H); 3060 (w, aryl C-H); 3082 (w, aryl C-H).

### 3.5.10. Aminolysis of RAFT functionalized poly(styrene) (HM-323)

Trithiocarbonate functionalized poly(styrene) (HM-322) (5.00) was dissolved in THF (50 mL) and was degassed by purging with nitrogen. Degassed hexylamine (0.5 mL) was injected into the poly(styrene) solution, the reaction was left overnight to complete during which the yellow solution turned colourless. The polymer was purified by precipitating into methanol and was collected by Buchner filtration.

$^1\text{H}$  NMR ( $\text{CDCl}_3$ ),  $\delta$  (ppm): 1.22-1.68 (bm, 1nH,  $\text{CH}_2\text{CH}$  backbone); 1.70-2.25 (bm, 2nH,  $\text{CH}_2\text{CH}$  backbone); 6.35-7.20 (bm, 5nH, Ar-H).

$^{13}\text{C}$  NMR ( $\text{CDCl}_3$ ),  $\delta$  (ppm): 29.30 (1C,  $\text{SCHCH}_3$ , RAFT agent); 39.49 (1nC,  $\text{CH}_2\text{CH}$ , backbone); 40.69-43.15 (1nC,  $\text{CH}_2\text{CH}$ , backbone); 45.38 (1C,  $\text{SCH}$ , RAFT agent); 124.62 (2nC, ortho-Ar); 126.83 (1nC, para-Ar); 128.97 (2nC, meta-Ar); 144.66 (1nC, Ar); 178.46 (1C, C=O, RAFT agent).

FTIR ( $\text{cm}^{-1}$ ): 697 (s, aromatic C-H); 755 (s, aromatic C-H); 841 (vw, C-C stretch); 907 (w, C-C stretch); 1028 (m, aromatic C=C); 1452 (m,  $\text{CH}_2$  asymmetrical deformation); 1493 (m, aromatic C=C stretch); 1584 (w, aromatic C=C stretch); 1601 (m, aromatic C=C stretch); 2849 (w, C-H stretch); 2922 (m, C-H stretch); 3002 (w, aryl C-H); 3026 (m, aryl C-H); 3060 (w, aryl C-H); 3082 (w, aryl C-H).



**3.5.11. Reduction of disulfides with DTT (HM-324)**

Cleavage of disulfides proceeded as follows.<sup>72</sup> Poly(styrene) (HM-323) (4.62 g) and DTT (0.94 g) was dissolved in THF (50 mL) and placed under a nitrogen atmosphere by purging for 15 minutes. The solution was heated to 60 °C and stirred for 7 days. The polymer was purified by precipitating into methanol and was collected by Büchner filtration.

**3.5.12. Method for thiol Michael addition of  $\omega$ -thiol functionalized poly(styrene) to pendant vinyl groups on encapsulated CaCO<sub>3</sub> (HM-325)**

To a mixture of poly(PETA)-C particles (HM-302) (1.50 g) and poly(styrene) (HM-324) (3.44 g, 0.30 mmol) a 40 mL solution of acetone containing hexylamine (0.7 mg, 0.007 mmol) was added, the mixture was heated to 40 °C and was left for four days. The particles were cleaned by centrifugation cycles.

Raman spectra (cm<sup>-1</sup>): 152 (T[Ca, CO<sub>3</sub>]); 278 (T[Ca, CO<sub>3</sub>]); 712 (v<sub>4</sub> [CO<sub>3</sub>] bending vibrations); 837 (aromatic C=C); 1000 (aromatic C=C); 1085 (v<sub>1</sub> [CO<sub>3</sub>] symmetric stretch); 1438 (v<sub>3</sub> [CO<sub>3</sub>] asymmetric stretch); 1746 (v<sub>1</sub> and v<sub>4</sub>); 2926 (-CH<sub>2</sub> asymmetric stretch); 2963 (-CH<sub>2</sub> asymmetric stretch).

FTIR spectra (cm<sup>-1</sup>): 698 (w, aromatic C-H); 712 (w, v<sub>4</sub> [CO<sub>3</sub>] symmetric deformation); 758 (w, aromatic C-H); 805 (vw, vinyl -C-H deformation); 871 (s, v<sub>2</sub> [CO<sub>3</sub>] asymmetric deformation); 1021 (vw, C-O stretch); 1087 (vw, v<sub>1</sub> [CO<sub>3</sub>] symmetric stretch); 1170 (w, -C-O- stretch); 1262 (vw, -O-H stretch); 1404 (vs, v<sub>3</sub> [CO<sub>3</sub>] asymmetric stretch); 1731 (w, unsaturated -(CO)-O- stretch); 1796 (vw, v<sub>1</sub> and v<sub>4</sub>); 2510 (vw, 2v<sub>2</sub> and v<sub>4</sub>).

*3.5.12.1. Quantifying pendant vinyl groups by bromination after thiol Michael addition of poly(styrene)-SH*

See section 3.4.5. for experimental protocol.

**Table 3.16** Table of average titration volumes and corresponding Bromine Index for poly(PETA)-C particles after thiol Michael addition of poly(styrene)-SH.  $V_1$  and  $V_2$  denote the volume of  $\text{Na}_2\text{S}_2\text{O}_3$  titrated in the blank and sample solution respectively.

| Exp.   | Particles        | $V_1 - V_2$<br>(mL) | BI<br>(mg / 100 g) |
|--------|------------------|---------------------|--------------------|
| HM-326 | PETA-c—p(Sty)-SH | 0.45                | 1800               |

### 3.6. References

1. Ranjan, R.; Brittain, W. J. *Macromolecules* **2007**, 40, 6217-6223.
2. Tsarevsky, N. V.; Bernaerts, K. V.; Dufour, B.; Du Prez, F. E.; Matyjaszewski, K. *Macromolecules* **2004**, 37, 9308-9313.
3. Tasdelen, M. A. *Polym. Chem.* **2011**, 2, 2133-2145.
4. Hensarling, R. M.; Doughty, V. A.; Chan, J. W.; Patton, D. L. *J. Am. Chem. Soc.* **2009**, 131, 14673-14675.
5. Lowe, A. B. *Polym. Chem.* **2010**, 1, 17-36.
6. Kolb, H. C.; Finn, M. G.; Sharpless, K. B. *Angew. Chem. Int. Ed.* **2001**, 40, 2004-2021.
7. Moses, J. E.; Moorhouse, A. D. *Chem. Soc. Rev.* **2007**, 36, 1249-1262.
8. Kolb, H. C.; Sharpless, K. B. *Drug Discovery Today* **2003**, 8, 1128-1137.
9. Justynska, J.; Hordyjewicz, Z.; Schlaad, H. *Polymer* **2005**, 46, 12057-12064.
10. Gress, A.; Völkel, A.; Schlaad, H. *Macromolecules* **2007**, 40, 7928-7933.
11. Killops, K. L.; Campos, L. M.; Hawker, C. J. *J. Am. Chem. Soc.* **2008**, 130, 5062-5064.
12. Hagberg, E. C.; Malkoch, M.; Ling, Y.; Hawker, C. J.; Carter, K. R. *Nano Lett.* **2007**, 7, 233-237.
13. Campos, L. M.; Meinel, I.; Guino, R. G.; Schierhorn, M.; Gupta, N.; Stucky, G. D.; Hawker, C. J. *Adv. Mater.* **2008**, 20, 3728-3733.
14. Khire, V. S.; Harant, A. W.; Watkins, A. W.; Anseth, K. S.; Bowman, C. N. *Macromolecules* **2006**, 39, 5081-5086.
15. Jonkheijm, P.; Weinrich, D.; Köhn, M.; Engelkamp, H.; Christianen, P. C. M.; Kuhlmann, J.; Maan, J. C.; Nüsse, D.; Schroeder, H.; Wacker, R.; Breinbauer, R.; Niemeyer, C. M.; Waldmann, H. *Angew. Chem. Int. Ed.* **2008**, 47, 4421-4424.
16. Posner, T. *Ber. Dtsch. Chem. Ges.* **1905**, 38, 646-657.
17. Kharasch, M. S.; Mayo, F. R. *J. Am. Chem. Soc.* **1933**, 55, 2468-2496.
18. Marvel, C. S.; Chambers, R. R. *J. Am. Chem. Soc.* **1948**, 70, 993-998.

19. Morgan, C. R.; Magnotta, F.; Ketley, A. D. *J. Polym. Sci. Polym. Chem. Ed.* **1977**, 15, 627-645.
20. Cramer, N. B.; Bowman, C. N. *J. Polym. Sci., Part A: Polym. Chem.* **2001**, 39, 3311-3319.
21. Griesbaum, K. *Angew. Chem. Int. Ed.* **1970**, 9, 273-287.
22. Cramer, N. B.; Reddy, S. K.; O'Brien, A. K.; Bowman, C. N. *Macromolecules* **2003**, 36, 7964-7969.
23. Hoyle, C. E.; Lee, T. Y.; Roper, T. *J. Polym. Sci., Part A: Polym. Chem.* **2004**, 42, 5301-5338.
24. Hurd, C. D.; Gershbein, L. L. *J. Am. Chem. Soc.* **1947**, 69, 2328-2335.
25. Chan, J. W.; Hoyle, C. E.; Lowe, A. B.; Bowman, M. *Macromolecules* **2010**, 43, 6381-6388.
26. Sanui, K.; Ogata, N. *Bull. Chem. Soc. Jpn.* **1967**, 40, 1727-1727.
27. Van Dijk, J. T. M.; AkzoNobel. Composition comprising mercapto-functional compounds US6639046 B1 **2003**.
28. Gimbert, C.; Lumbierres, M.; Marchi, C.; Moreno-Mañas, M.; Sebastián, R. M.; Vallribera, A. *Tetrahedron* **2005**, 61, 8598-8605.
29. Chan, J. W.; Wei, H.; Zhou, H.; Hoyle, C. E. *Eur. Polym. J.* **2009**, 45, 2717-2725.
30. Chan, J. W.; Yu, B.; Hoyle, C. E.; Lowe, A. B. *Polymer* **2009**, 50, 3158-3168.
31. Liu, M.; Tan, B. H.; Burford, R. P.; Lowe, A. B. *Polym. Chem.* **2013**, 4, 3300-3311.
32. Li, G.-Z.; Randev, R. K.; Soeriyadi, A. H.; Rees, G.; Boyer, C.; Tong, Z.; Davis, T. P.; Becer, C. R.; Haddleton, D. M. *Polym. Chem.* **2010**, 1, 1196-1204.
33. Jones, M. W.; Mantovani, G.; Ryan, S. M.; Wang, X.; Brayden, D. J.; Haddleton, D. M. *Chem. Commun.* **2009**, 5272-5274.
34. Boyer, C.; Davis, T. P. *Chem. Commun.* **2009**, 6029-6031.
35. Qiu, X.-P.; Winnik, F. M. *Macromol. Rapid Commun.* **2006**, 27, 1648-1653.
36. Dalmont, H.; Pinprayoon, O.; Saunders, B. R. *Langmuir* **2008**, 24, 2834-2840.

37. Syrett, J. A.; Jones, M. W.; Haddleton, D. M. *Chem. Commun.* **2010**, 46, 7181-7183.
38. Soeriyadi, A. H.; Li, G.-Z.; Slavin, S.; Jones, M. W.; Amos, C. M.; Becer, C. R.; Whittaker, M. R.; Haddleton, D. M.; Boyer, C.; Davis, T. P. *Polym. Chem.* **2011**, 2, 815-822.
39. Rieger, J.; Van Butsele, K.; Lecomte, P.; Detrembleur, C.; Jerome, R.; Jerome, C. *Chem. Commun.* **2005**, 274-276.
40. Saunders, B. R.; Vincent, B. *Adv. Colloid Interface Sci.* **1999**, 80, 1-25.
41. Saunders, B. R.; Vincent, B. *Colloid. Polym. Sci.* **1997**, 275, 9-17.
42. Downey, J. S.; Frank, R. S.; Li, W.-H.; Stöver, H. D. H. *Macromolecules* **1999**, 32, 2838-2844.
43. Hubbard, K. L.; Finch, J. A.; Darling, G. D. *React. Funct. Polym.* **1998**, 36, 1-16.
44. van Berkel, K. Y.; Piekarski, A. M.; Kierstead, P. H.; Pressly, E. D.; Ray, P. C.; Hawker, C. J. *Macromolecules* **2009**, 42, 1425-1427.
45. van Berkel, K. Y.; Hawker, C. J. *J. Polym. Sci., Part A: Polym. Chem.* **2010**, 48, 1594-1606.
46. Korthals, B.; Morant-Miñana, M. C.; Schmid, M.; Mecking, S. *Macromolecules* **2010**, 43, 8071-8078.
47. Willcock, H.; O'Reilly, R. K. *Polym. Chem.* **2010**, 1, 149-157.
48. Goldmann, A. S.; Walther, A.; Nebhani, L.; Joso, R.; Ernst, D.; Loos, K.; Barner-Kowollik, C.; Barner, L.; Müller, A. H. E. *Macromolecules* **2009**, 42, 3707-3714.
49. Li, G. L.; Xu, L. Q.; Tang, X.; Neoh, K. G.; Kang, E. T. *Macromolecules* **2010**, 43, 5797-5803.
50. Connal, L. A.; Kinnane, C. R.; Zelikin, A. N.; Caruso, F. *Chem. Mater.* **2009**, 21, 576-578.
51. Hayashi, K.; Ono, K.; Suzuki, H.; Sawada, M.; Moriya, M.; Sakamoto, W.; Yogo, T. *Chem. Mater.* **2010**, 22, 3768-3772.
52. Gu, W.; Chen, G.; Stenzel, M. H. *J. Polym. Sci., Part A: Polym. Chem.* **2009**, 47, 5550-5556.
53. Tedja, R.; Soeriyadi, A. H.; Whittaker, M. R.; Lim, M.; Marquis, C.; Boyer, C.; Davis, T. P.; Amal, R. *Polym. Chem.* **2012**, 3, 2743-2751.

54. Vandenabeele, P. *Practical Raman Spectroscopy - An Introduction* John Wiley & Sons Ltd., Chichester, 2013.
55. Yang, X.; Zhu, L.-W.; Wan, L.-S.; Zhang, J.; Xu, Z.-K. *J. Mater. Res.* **2013**, 28, 642-650.
56. Moad, G.; Rizzardo, E.; Thang, S. H. *Polym. Int.* **2011**, 60, 9-25.
57. Deletre, M.; Levesque, G. *Macromolecules* **1990**, 23, 4733-4741.
58. Patton, D. L.; Mullings, M.; Fulghum, T.; Advincula, R. C. *Macromolecules* **2005**, 38, 8597-8602.
59. Xu, J.; He, J.; Fan, D.; Wang, X.; Yang, Y. *Macromolecules* **2006**, 39, 8616-8624.
60. Tanaka, H.; White, J. L. *Polym. Eng. Sci.* **1980**, 20, 949-956.
61. White, J. I.; Tanaka, H. *J. Non-Newton. Fluid* **1981**, 8, 1-10.
62. Suetsugu, Y.; White, J. L. *J. Appl. Polym. Sci.* **1983**, 28, 1481-1501.
63. Li, G.; Mai, K.; Feng, K. *J. Appl. Polym. Sci.* **2006**, 99, 2138-2143.
64. Zuiderduin, W. C. J.; Westzaan, C.; Huétink, J.; Gaymans, R. J. *Polymer* **2003**, 44, 261-275.
65. Wang, G.; Chen, X.; Huang, R.; Zhang, L. *J. Mater. Sci. Lett.* **2002**, 21, 985-986.
66. Moraes, J.; Maschmeyer, T.; Perrier, S. *J. Polym. Sci., Part A: Polym. Chem.* **2011**, 49, 2771-2782.
67. Ferguson, C. J.; Hughes, R. J.; Nguyen, D.; Pham, B. T. T.; Gilbert, R. G.; Serelis, A. K.; Such, C. H.; Hawket, B. S. *Macromolecules* **2005**, 38, 2191-2204.
68. Moad, G.; Solomon, D. H. *The Chemistry of Radical Polymerization: Second Fully Revised Edition* Elsevier, Amsterdam, 2006.
69. Barner-Kowollik, C.; Buback, M.; Charleux, B.; Coote, M. L.; Drache, M.; Fukuda, T.; Goto, A.; Klumperman, B.; Lowe, A. B.; McLeary, J. B.; Moad, G.; Monteiro, M. J.; Sanderson, R. D.; Tonge, M. P.; Vana, P. *J. Polym. Sci., Part A: Polym. Chem.* **2006**, 44, 5809-5831.
70. Cleland, W. W. *Biochemistry* **1964**, 3, 480-482.
71. Bulter, J.; Spielberg, S. P.; Schulman, J. D. *Anal Biochem* **1976**, 75, 674-675.
72. Li, Y.; Armes, S. P. *Macromolecules* **2005**, 38, 8155-8162.

73. Tsarevsky, N. V.; Matyjaszewski, K. *Macromolecules* **2002**, 35, 9009-9014.
74. Siow, K. S.; Delmas, G.; Patterson, D. *Macromolecules* **1972**, 5, 29-34.
75. Buzgar, N.; Apopei, A. I. *Geologie. Tomul LV* **2009**, 2, 97-112.
76. Gunasekaran, S.; Anbalagan, G.; Pandi, S. *J. Raman. Spectrosc.* **2006**, 37, 892-899.
77. Baranska, H.; Labudzinska, A.; Terpinski, J. *Laser raman spectrometry: analytical applications* John Wiley&Sons, Chichester, 1987.
78. Kuptsov, A. H.; Zhizhin, G. N. Polymer classification;. *Handbook of Fourier transform Raman and infrared spectra of polymers* Physical Sciences Data. Elsevier, 1998, xxi-xxii.

# Chapter 4: pH Responsive Microgel Particles

---

## 4.1. Abstract

In Chapters 2 and 3 we have demonstrated encapsulation of calcium carbonate particles in a DEGDA and MAA based polymer shell. Polymerization in the absence of the calcium carbonate core yielded stable microgel particles. We demonstrate the pH responsive behaviour of these particles and their applications in gel formation and as Pickering stabilizers for oil-in-water emulsions. Through analysing the swelling behaviour of these microgels we elucidate upon the encapsulation mechanism discussed in Chapter 2 and why DEGDA yielded no pendant vinyl groups in Chapter 3.



## 4.2. Introduction

Microgels are cross-linked latex particles that swell in a good solvent and were first reported by Staudinger *et al.* in 1935; where divinylbenzene was polymerized at high dilution in a good solvent (Figure 4.1).<sup>1</sup> The term “microgel” to describe these particles was first reported in 1949 by Baker.<sup>2</sup> Microgels have been synthesized to not only respond to a good solvent but to changes in temperature,<sup>3-5</sup> pH,<sup>6-9</sup> light,<sup>10, 11</sup> electric fields<sup>12, 13</sup> and biomolecules.<sup>14</sup>

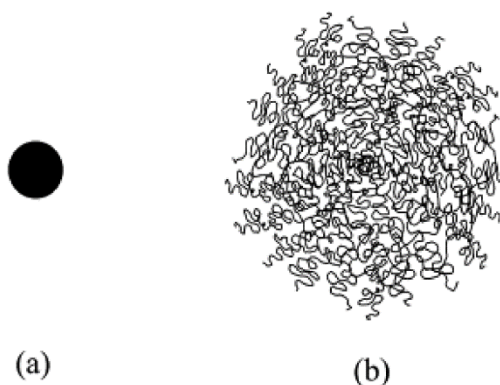


**Figure 4.1** Illustration of a microgel particle in a (a) poor and (b) good solvent.<sup>15</sup>

Flory's theory of swelling of a neutral polymer network has been used to describe the swelling of microgels in organic solvents.<sup>16</sup> Swelling is a result of a balance in osmotic pressure and elastic forces, where cross-links restrict the extent to which the microgel can swell. Ionic networks have an additional contribution to swelling as a result of a higher concentration of non-associated ions within the network as a consequence of the Donnan equilibrium. Thus incorporation of charged species within the network results in greater swelling.<sup>6, 15, 17</sup>

A combination of sufficient particle swelling, particle concentration and particle-particle interaction can lead to gel formation, where colloidal particles form a solid network which is interspersed with background fluid. Gel formation is attributed to swelling of the particles to the point where a critical jamming volume is

exceeded.<sup>18</sup> In rheological terms, the particles are described by the storage (elastic) modulus ( $G'$ ) and the background fluid is described by the loss (viscous) modulus ( $G''$ ). Colloidal gels can be identified by their rheological properties;  $G'$  is higher in value (Pa) than the  $G''$  below a critical frequency. Where  $G' > G''$  the phase angle ( $\delta$ , the lag between applied and measures stress) is less than  $45^\circ$ , this describes solid-like behaviour; a strong gel can be identified by  $\delta$  being independent of frequency.<sup>19</sup> Rheological properties are affected by the deformability of the microgel particles. In non-gelled systems the rheology of hard spheres is largely affected by long range particle interactions and particle volume fraction. Buscall described the rheological behaviour of microgel particles to be equivalent to hard spheres with a thin soft shell.<sup>20</sup> This is in contrast to work by Ballauf *et al.* and Weitz *et al.* where they describe the particles as hard spheres when contracted but as deformable and “soft” when swollen.<sup>21, 22</sup>

Saunders and co-workers investigated the parameters that effect gel formation of methacrylic acid based microgels.<sup>23</sup> Microgels were prepared by batch emulsion polymerization with 37 mol% methacrylic acid with the formula poly(MAA-*co*-X-*co*-Y) where X is either methyl methacrylate (MMA), butyl methacrylate (BMA) or ethyl acrylate (EA) and cross-linker Y is ethylene glycol dimethacrylate (EGDMA) or butanediol diacrylate (BDDA). Saunders proposed that microgels with a higher  $T_g$  (where MMA is incorporated when compared to BMA) exhibit poorer swelling described through the relation of  $T_g$  to polymer chain flexibility, where reduced flexibility will limit the particle’s ability to swell. The reactivity of the cross-linker was also shown to influence particle swelling when microgels are synthesized by batch polymerization; particles cross-linked with EGDMA were found to swell more than when BDDA was used. This swelling

behaviour was attributed to differences in cross-link density; EGDMA is more reactive than BDDA and thus forms a core-shell morphology where the core is more highly cross-linked than the shell, whereas particles containing BDDA were evenly cross-linked. Tan *et al.* illustrated the effect of cross-link density in MAA-EA microgels where di-allyl phthalate (DAP) was the cross-linker.<sup>24</sup> 1 wt.% was found to be the ideal incorporation of DAP, below 1 wt.% insufficient cross-linked junctions were present to achieve stable microgels and above 1 wt.% swelling was restricted due to excessive cross-linked junctions.

Weitz and co-workers synthesized doubly cross-linked microgels by creating covalent bonds between microgel particles, yielding permanent gel structures that do not redisperse.<sup>25</sup> Poly(NIPAAm) microgel particles were synthesized with allyl amine to produce temperature responsive microgels with amine functionality; microgel clusters were formed on addition of poly(acrylic acid) and the clusters were covalently linked on addition of glutaldehyde (Figure 4.2). Saunders and co-workers prepared methacrylic acid based microgels doubly cross-linked by polymerizing pendant vinyl groups, in order to prepare gels that did not re-disperse on dilution, for applications in restoring mechanical strength in damaged intervertebral discs.<sup>26</sup> The doubly cross-linked gels exhibited higher  $G'$  values than their parent singly cross-linked gels, this is logical as inter-particle interactions influence gel strength.<sup>27, 28</sup>

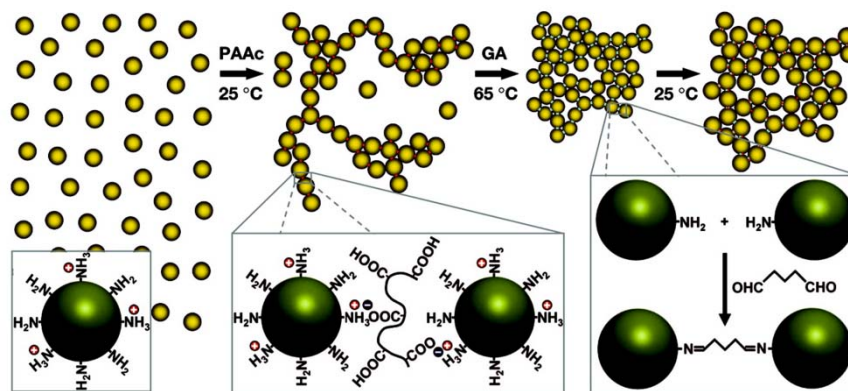


**Figure 4.2** Scheme of controlled aggregation and colloidal gelation of microgel particles, to prepare doubly cross-linked gels.<sup>25</sup>

Responsive microgels have been synthesized for a range of applications including: mechanical support for degenerated intervertebral discs,<sup>29</sup> drug delivery<sup>30-32</sup> and catalysis.<sup>33-35</sup> We are interested in their application as responsive Pickering stabilizers. Ngai and co-workers prepared octanol-in-water emulsions stabilized by poly(NIPAAm) microgels cross-linked with bisacrylamide and containing 5 wt.% MAA.<sup>36, 37</sup> Destabilization of the emulsions was reported below pH 6, attributed to protonation of the carboxylic acid groups resulting in more hydrophobic particles which partitioned deeper into the oil phase. Temperature dependant instability was also reported; emulsion at pH 6.1 and 9.4 were stable at 25 °C, however, on heating to 60 °C emulsions at pH 6.1 coarsened (Figure 4.3). Poly(NIPAAm) undergoes an LCST at 32 °C,<sup>38</sup> thus on heating the microgels contract, resulting in insufficient coverage of the octanol droplets and subsequent ripening. At pH 9.4 the microgels were charged enough to inhibit contraction leading to a stable emulsion. Ngai and co-workers also prepared high internal phase emulsions (HIPEs) using poly(NIPAAm-*co*-MAA) microgels with a maximum internal phase volume of 80 %.<sup>39</sup> The rheological properties of the HIPE were shown to be tuneable by adjusting the pH and temperature; below the LCST of poly(NIPAAm) solid-like behaviour was observed independent of frequency, suggesting that the material was a

gel, with  $G'$  increasing with pH, however, on heating to 60 °C a gel-fluid transition occurred. This transition was attributed to collapse of the microgels leading to reduced interfacial coverage.

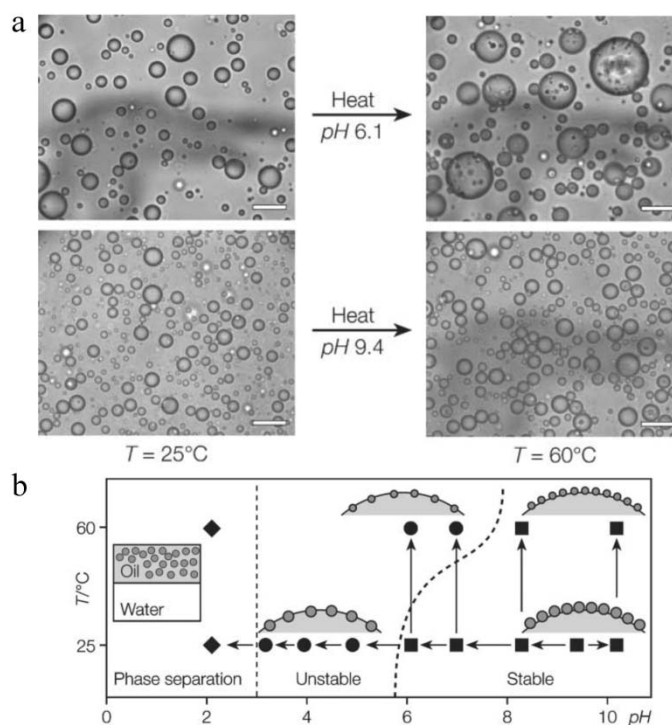


**Figure 4.3** (a) Optical micrographs illustrating temperature dependent stability of poly(NIPAAm-*co*-MAA) microgel stabilized emulsion at pH 6.1 and 9.4 (scale bar: 20  $\mu$ m). (b) Illustration of temperature and pH dependent stability of poly(NIPAAm-*co*-MAA) microgel stabilized emulsion.<sup>36</sup>

Armes *et al.* demonstrated reversible emulsification of dodecane-in-water emulsions stabilized by poly(*tert*-butylaminoethyl methacrylate-*co*-divinylbenzene) microgels, which were sterically stabilized by PEGMA.<sup>40</sup> Stable emulsions were formed at pH 10, but on addition of acid the microgels swelled with water and immediate demulsification occurred, as a result of spontaneous desorption of the microgels from the interface. Four successive demulsification/emulsification cycles were achieved without loss of performance; however, the fifth cycle could not be demulsified on addition of acid due to a build-up of background salt. Stöver and co-workers used doubly cross-linked microgels poly(divinylbenzene-*co*-maleic anhydride) as a Pickering stabilizer in order to prepare tectocapsules (capsules of

cross-linked microgel particles).<sup>41</sup> Microgel stabilized propyl acetate-in-water emulsions were prepared in the presence of PVA, on addition of polyamines the shell was cross-linked. Increasing the molecular weight of the polyamine resulted in stronger capsules, up to a critical point; with the highest molecular weight polyamine (60,000 g mol<sup>-1</sup>) flocculation was observed, due to inter-particle bridging.

In this body of work we prepare pH responsive microgel particles based on MAA and DEGDA. In exploring their swelling behaviour as a response to pH change, we probe the mechanism of calcium carbonate encapsulation discussed in Chapter 2 and the open question left in Chapter 3 regarding the lack of pendant vinyl groups in poly(DEGDA-*co*-MAA) composite particles. We demonstrate the performance of colloidal gels by investigating their rheological properties. We also demonstrate their feasibility as Pickering stabilizers for dodecane-in-water emulsions.

### 4.3. Results and Discussion

In Chapters 2 and 3 we discussed the encapsulation of calcium carbonate in DEGDA and methacrylic acid based polymeric shells. On performing these polymerizations in the absence of calcium carbonate, we were surprised to find that stable particles were formed. Herein, we abandon the calcium carbonate core and synthesize microgels without spacers and investigate their responsive behaviour and performance as Pickering stabilizers.

#### 4.3.1. Particle synthesis

Four particles were synthesized; poly(DEGDA), poly(DEGDA-*co*-MAA), poly(PETA-*co*-DEGDA-*co*-MAA) and poly(DPEPHA-*co*-DEGDA-*co*-MAA). Typical polymerization proceeded as follows: 1 mL of a monomer mixture (see Table 4.1 for monomer quantities) was fed at a rate of 0.5 mL h<sup>-1</sup> into a degassed solution of 0.02 g APS in 50 mL of water, which had been heated to 70 °C. The polymerization was stopped 30 minutes after the feed had finished. Monomer conversion of poly(DEGDA) (HM-401) and poly(DEGDA-*co*-MAA) (HM-402) were followed by gravimetry. By feeding the monomer into the polymerization reaction, an even distribution of monomers throughout each particle is ensured.<sup>42</sup>

**Table 4.1** Table of monomer quantities in starved-fed emulsion polymerization.

| Exp.   | Particles                                      | Monomer | Mass<br>(g) | mmol |
|--------|--|---------|-------------|------|
| HM-401 | Poly(DEGDA)                                    | DEGDA   | 1.118       | 5.22 |
| HM-402 | Poly(DEGDA- <i>co</i> -MAA)                    | DEGDA   | 0.940       | 4.39 |
|        |  | MAA     | 0.162       | 1.88 |
| HM-403 | Poly(PETA- <i>co</i> -DEGDA- <i>co</i> -MAA)   | PETA    | 0.491       | 1.64 |
|        |  | DEGDA   | 0.492       | 2.30 |
|        |  | MAA     | 0.147       | 1.71 |
| HM-404 | Poly(DPEPHA- <i>co</i> -DEGDA- <i>co</i> -MAA) | DPEPHA  | 0.493       | 0.94 |
|        |  | DEGDA   | 0.493       | 2.30 |
|        |  | MAA     | 0.147       | 1.71 |

**Table 4.2** Methacrylic acid content (mol%) in microgels.

| Exp.   | Particles                                      | MAA<br>(mol%) |
|--------|--|---------------|
| HM-401 | Poly(DEGDA)                                    | 0             |
| HM-402 | Poly(DEGDA- <i>co</i> -MAA)                    | 30.0          |
| HM-403 | Poly(PETA- <i>co</i> -DEGDA- <i>co</i> -MAA)   | 30.3          |
| HM-404 | Poly(DPEPHA- <i>co</i> -DEGDA- <i>co</i> -MAA) | 34.5          |

Monomer conversion versus time plots show that the polymerization is under starved conditions with an inhibition period during the first 30 minutes. Monomer conversion for poly(PETA-*co*-DEGDA-*co*-MAA) (HM-403) and poly(DPEPHA-*co*-DEGDA-*co*-MAA) (HM-404) could not be followed as monomer evaporation did not occur.



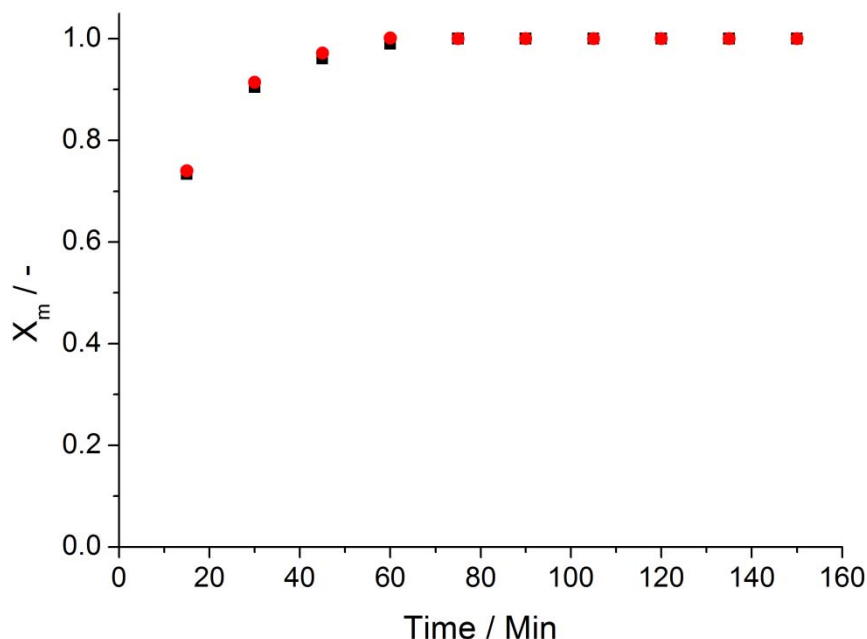


**Figure 4.4** Overall monomer conversion,  $X_m$ , versus time for poly(DEGDA) particles (HM-401) (■) and poly(DEGDA-co-MAA) (HM-402) (●). Monomer was fed at a rate of  $0.5 \text{ mL h}^{-1}$ .

Particle size was followed by DLS, and measurements were performed at pH 5.5. The narrow particle size distribution for all polymerizations suggests that nucleation period is fast compared to particle growth (Figure 4.5 b).<sup>43</sup> Particle size varies with monomer composition (Figure 4.5 a), deeper insight can be gained by analysing the  $d_z^3$  versus monomer fed into the reaction (Figure 4.6). If the number of latex particles is constant, we can assume that the plot of  $d_z^3$  vs. volume of monomer fed into the polymerization will be linear; as particle volume should scale linearly to volume of monomer introduced. All four polymerizations show a linear relationship between particle volume and monomer fed into the reaction with  $R^2$  values of 0.994 for poly(DEGDA), 0.993 for poly(DEGDA-co-MAA) and 0.992 for both poly(PETA-co-DEGDA-co-MAA) and poly(DPEPHA-co-DEGDA-co-MAA). This combined with low dispersity throughout the polymerizations suggests that particle size is increasing as would be expected and after particle nucleation no secondary particles are formed.

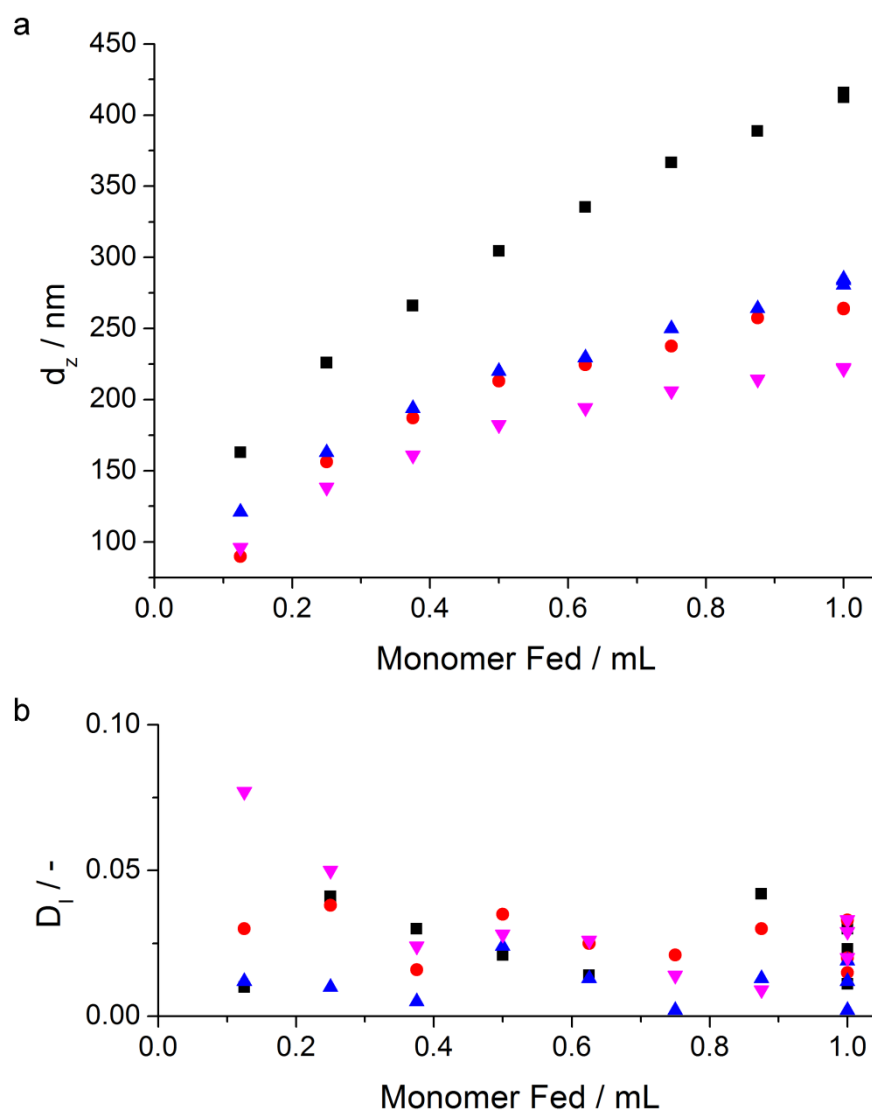


**Figure 4.5** (a) Average particle diameter,  $d_z$  and  $d_z^3$ , and (b) dispersity,  $D_i$ , versus monomer fed into the reaction (mL), of poly(DEGDA) (HM-401) (■), poly(DEGDA-co-MAA) (HM-402) (●), poly(PETA-co-DEGDA-co-MAA) (HM-403) (▲) and poly(DPEPHA-co-DEGDA-co-MAA) (HM-404) (▼). DLS measurements were performed at pH 5.5.

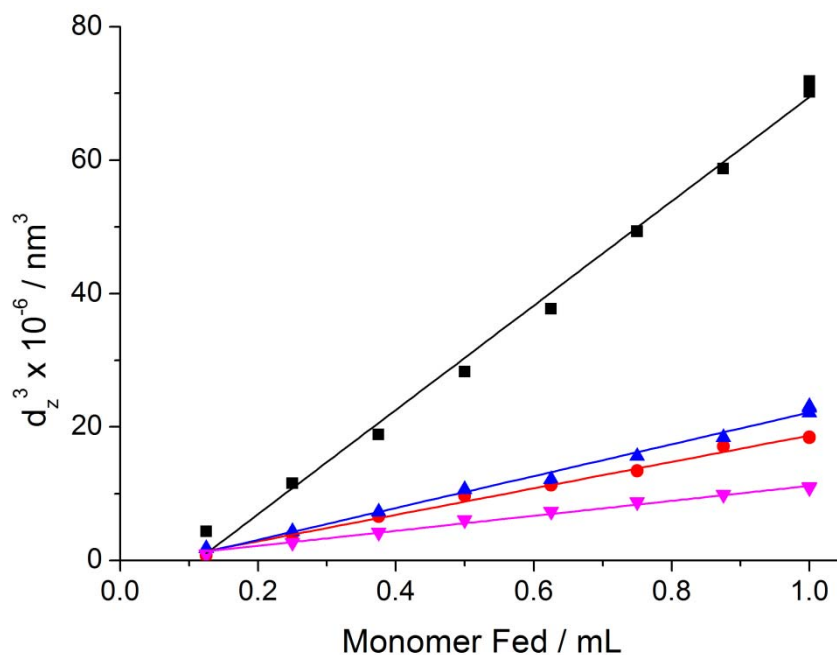


**Figure 4.6**  $d_z^3$  versus monomer fed into the reaction (mL) of poly(DEGDA) (HM-401) (■), poly(DEGDA-co-MAA) (HM-402) (●), poly(PETA-co-DEGDA-co-MAA) (HM-403) (▲) and poly(DPEPHA-co-DEGDA-co-MAA) (HM-404) (▼). Linear fit of  $d_z^3$ ;  $R^2 = 0.994$  for poly(DEGDA),  $R^2 = 0.993$  for poly(DEGDA-co-MAA),  $R^2 = 0.992$  for poly(PETA-co-DEGDA-co-MAA) and  $R^2 = 0.992$  for poly(DPEPHA-co-DEGDA-co-MAA). DLS measurements were performed at pH 5.5.

SEM analysis of particle morphology showed a smaller particle size than was measured by DLS (Figure 4.7-Figure 4.10). The particles were also creased, suggesting that particles were swollen when dispersed in water; on drying the water would be expelled forming this crinkled morphology.

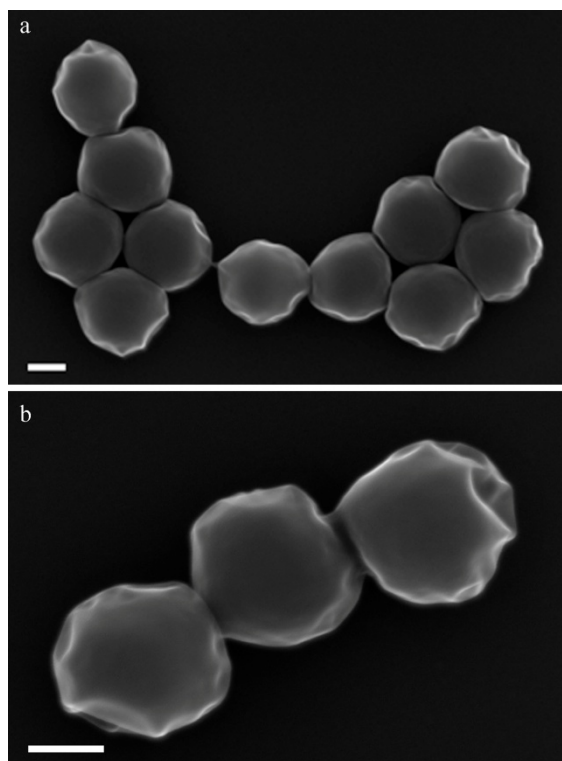


**Figure 4.7** SEM images of poly(DEGDA) particles (HM-401) (scale bar: 200 nm).

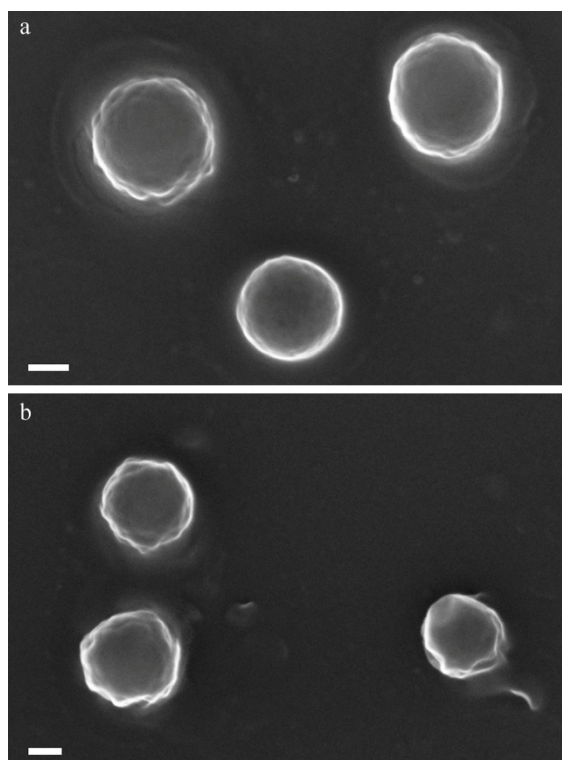


**Figure 4.8** SEM images of poly(DEGDA-co-MAA) particles (HM-402) (scale bar: 100 nm).

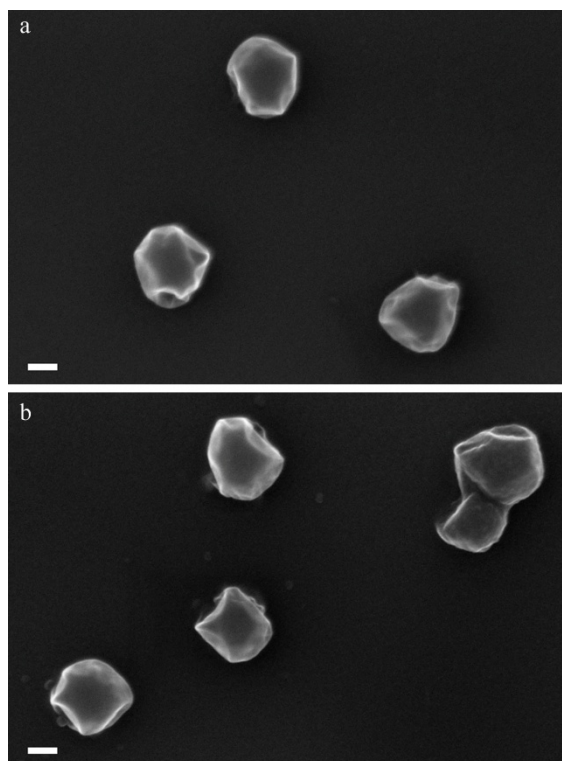


**Figure 4.9** SEM images of poly(PETA-*co*-DEGDA-*co*-MAA) (HM-403) (scale bar: 100 nm).

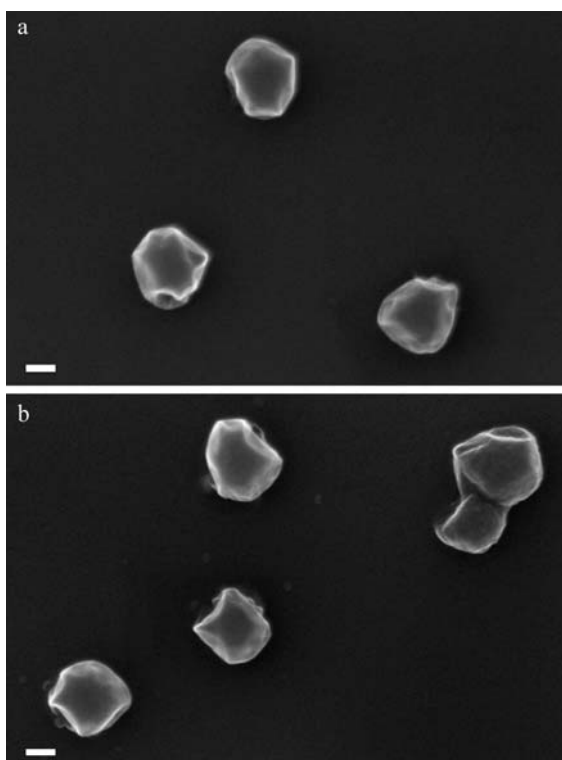


**Figure 4.10** SEM images of poly(DPEPHA-*co*-DEGDA-*co*-MAA) particles (HM-404) (scale bar: 100 nm).

### 4.3.2. Responsive behaviour

Particles containing methacrylic acid are known to display a responsive behaviour with respect to pH. Alkali soluble emulsions (ASE) irreversibly dissociate on addition of base,<sup>44</sup> and microgels containing methacrylic acid show reversible swelling behaviour.<sup>15, 17, 22, 23, 36, 42</sup> Latexes were diluted to 0.05 wt.% and the pH was adjusted with aqueous HCl or NaOH (Figure 4.11). All dispersions showed low turbidity at pH 2, this was due to observed coagulation. From pH 7.5 poly(DEGDA-*co*-MAA) latexes showed a much decreased turbidity, this was also observed for poly(DPEPHA-*co*-DEGDA-*co*-MAA) from pH 8. This was due to particle swelling as methacrylic acid is deprotonated. As expected on increasing the pH poly(DEGDA) showed no change in turbidity, however poly(PETA-*co*-DEGDA-*co*-MAA) also showed no change in turbidity on increasing pH.

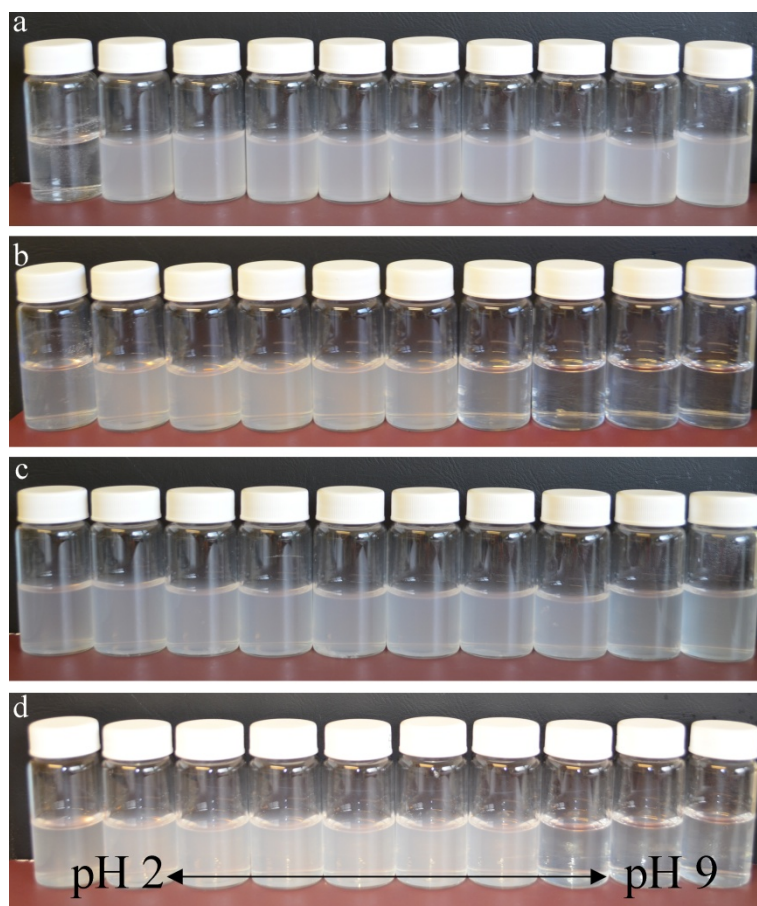


**Figure 4.11** Images of (a) poly(DEGDA) (HM-401), (b) poly(MAA-*co*-DEGDA) (HM-402), (c) poly(PETA-*co*-MAA-*co*-DEGDA) (HM-403) and (d) poly(DPEPHA-*co*-MAA-*co*-DEGDA) (HM-404) at pH's from left to right: 2, 3, 4, 5, 6, 7, 7.5, 8, 8.5 and 9.

DLS measurements were performed without dilution. It is immediately apparent that poly(DEGDA) and poly(PETA-*co*-DEGDA-*co*-MAA) do not show pH-responsive behaviour (Figure 4.12). At this point we postulate poly(PETA-*co*-DEGDA-*co*-MAA) does not swell due to a high degree of cross-linking. Size measurements of poly(DEGDA-*co*-MAA) were not possible above pH 8 due to low refractive index. It should be noted that as the particles begin to swell the DLS measurements become less reliable. This is due to reduced drag on the swollen microgel particles; the swollen particles can be described as polymer nets through which some of the continuous phase can flow, resulting in a degree of error in the drag factor in the Stokes-Einstein equation used to determine particle size (see Appendix I.3.1 for full DLS theory). Above pH 9 particle dispersity increases, this

suggests that at 0.05 wt.%, the particles are becoming unstable at high salt concentration. Increase in volume from pH 4-8 indicates that the poly(DEGDA-*co*-MAA) particles undergo a huge size increase of ~49x its original volume and poly(DPEPHA-*co*-DEGDA-*co*-MAA) particles swell ~4x their volume (Table 4.3). Swelling as a result of pH change is minimal for poly(DEGDA) and poly(PETA-*co*-DEGDA-*co*-MAA) particles. The extensive swelling of poly(DEGDA-*co*-MAA) particles suggests that DEGDA is a poor cross-linker. In Chapter 3 we postulated that the lack of pendant vinyl groups poly(DEGDA-*co*-MAA) composite particles were potentially due to DEGDA looping with itself, exacerbated by the starved conditions. We suggest that this swelling behaviour and thus low cross-linking density is a result of DEGDA units intramolecular looping. As poly(DPEPHA-*co*-DEGDA-*co*-MAA) and particularly poly(PETA-*co*-DEGDA-*co*-MAA) show substantially less swelling on addition of base we can infer that DPEPHA is a better cross-linking monomer than DEGDA, with PETA outperforming both. This also links back to Chapter 3, where particles containing PETA exhibited a greater proportion of pendant vinyl groups than DPEPHA.

DLS measurements were also performed in THF; 20  $\mu$ L of 2 wt.% latex at pH 5.5 were dispersed in 1 mL THF (Table 4.4). Particle swelling was exhibited by all particles; poly(DEGDA-*co*-MAA) and poly(DPEPHA-*co*-DEGDA-*co*-MAA) particles did not swell to the extent observed in water, however, poly(DEGDA) and poly(PETA-*co*-DEGDA-*co*-MAA) swelled to a greater extent than observed in water.



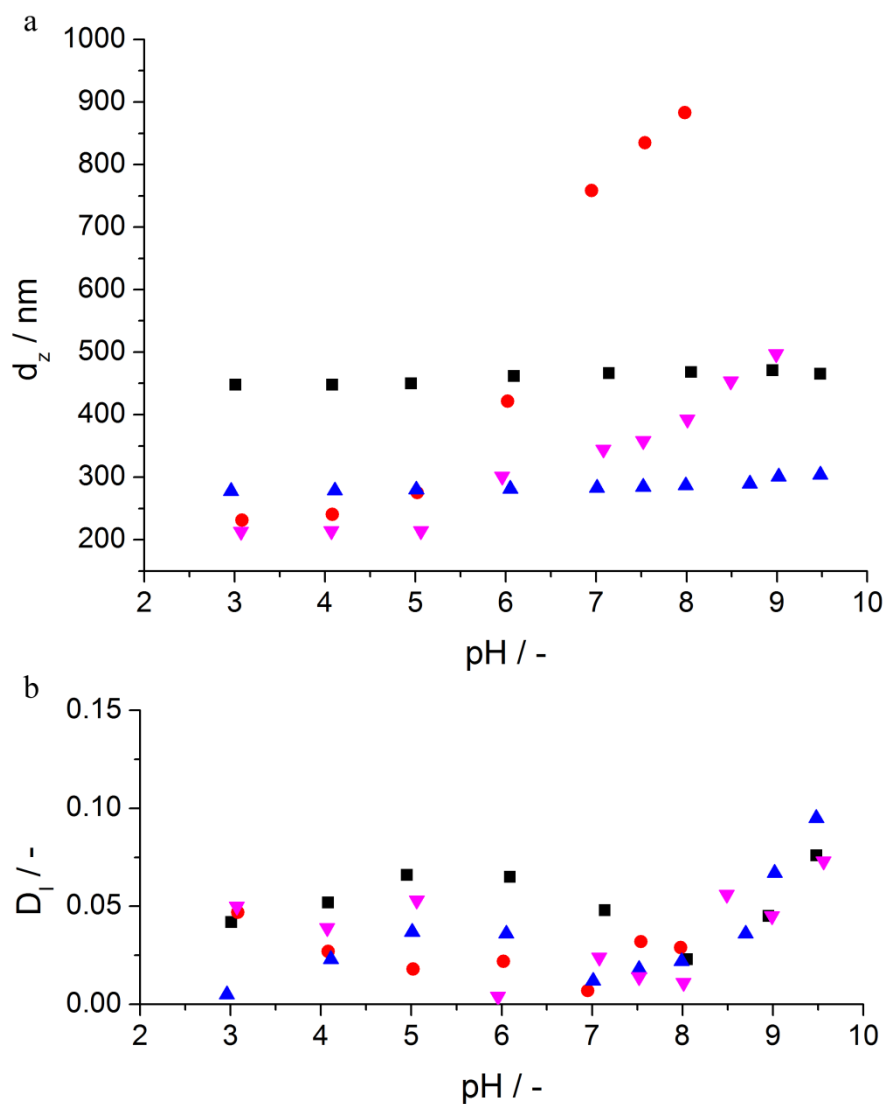


**Figure 4.12** (a) Average particle diameter,  $d_z$ , and (b) dispersity,  $D_l$ , versus pH of poly(DEGDA) (HM-401) (■), poly(DEGDA-*co*-MAA) (HM-402) (●), poly(PETA-*co*-DEGDA-*co*-MAA) (HM-403) (▲), poly(DPEPHA-*co*-DEGDA-*co*-MAA) (HM-404) (▼).

**Table 4.3** Table of % change in particle hydrodynamic volume with respect to pH.

| Exp.   | Particles                                   | $d_z$ at pH 4<br>(nm) | $d_z$ at pH 8<br>(nm) | Volume<br>Change<br>(%) |
|--------|---|-----------------------|-----------------------|-------------------------|
| HM-401 | P(DEGDA)                                    | 448.1                 | 468.3                 | 114                     |
| HM-402 | P(DEGDA- <i>co</i> -MAA)                    | 240.6                 | 883.0                 | 4940                    |
| HM-403 | P(PETA- <i>co</i> -DEGDA- <i>co</i> -MAA)   | 278.6                 | 286.9                 | 109                     |
| HM-404 | P(DPEPHA- <i>co</i> -DEGDA- <i>co</i> -MAA) | 200.3                 | 392.3                 | 423                     |

**Table 4.4** Particle size measurements of microgels in water (at pH 5.5) and after swelling in THF.

| Exp.   | Particles                                   | Water (pH 5.5) |       | THF        |       | Volume Change (%) |
|--------|---|----------------|-------|------------|-------|-------------------|
|        |   | $d_z$ (nm)     | $D_I$ | $d_z$ (nm) | $D_I$ |                   |
| HM-401 | P(DEGDA)                                    | 449.8          | 0.066 | 515.8      | 0.053 | 151               |
| HM-402 | P(DEGDA- <i>co</i> -MAA)                    | 275.2          | 0.018 | 507.6      | 0.028 | 628               |
| HM-403 | P(PETA- <i>co</i> -DEGDA- <i>co</i> -MAA)   | 280.1          | 0.037 | 313.6      | 0.035 | 140               |
| HM-404 | P(DPEPHA- <i>co</i> -DEGDA- <i>co</i> -MAA) | 200.3          | 0.053 | 244.5      | 0.027 | 183               |

Particle size was measured as a function of temperature at pH 8 (Figure 4.13). The particles that show no pH responsive behaviour, i.e. poly(DEGDA) and poly(PETA-*co*-DEGDA-*co*-MAA), also show no change in particle size on heating. However, poly(DEGDA-*co*-MAA) and poly(DPEPHA-*co*-DEGDA-*co*-MAA) appear to increase in size around 60 °C, a corresponding increase in PDI is also observed, indicating that the particles become unstable. When particle size, with respect to temperature is measured at a lower pH, an instability in response to temperature is not observed (Figure 4.14). In Chapter 2 we suggested that monomeric DEGDA may exhibit LCST behaviour, we suggest on heating that the particles interaction with water becomes unfavourable; swollen particles expel water and coagulate, whereas non-swollen particles have a much lower polymer-water interface thus do not exhibit coagulation at low solids content. This behaviour could help describe the mechanism by which we observe encapsulation of calcium carbonate particles in Chapter 2; the pH of the calcium carbonate in water is 9.3, thus the methacrylic acid once fed into the reaction is largely deprotonated, we suggest

that swollen polymer fractals of poly(DEGDA-*co*-MAA) formed in the continuous phase are unstable at the reaction temperature, which drives collapse onto the surface of calcium carbonate particles resulting in the encapsulation

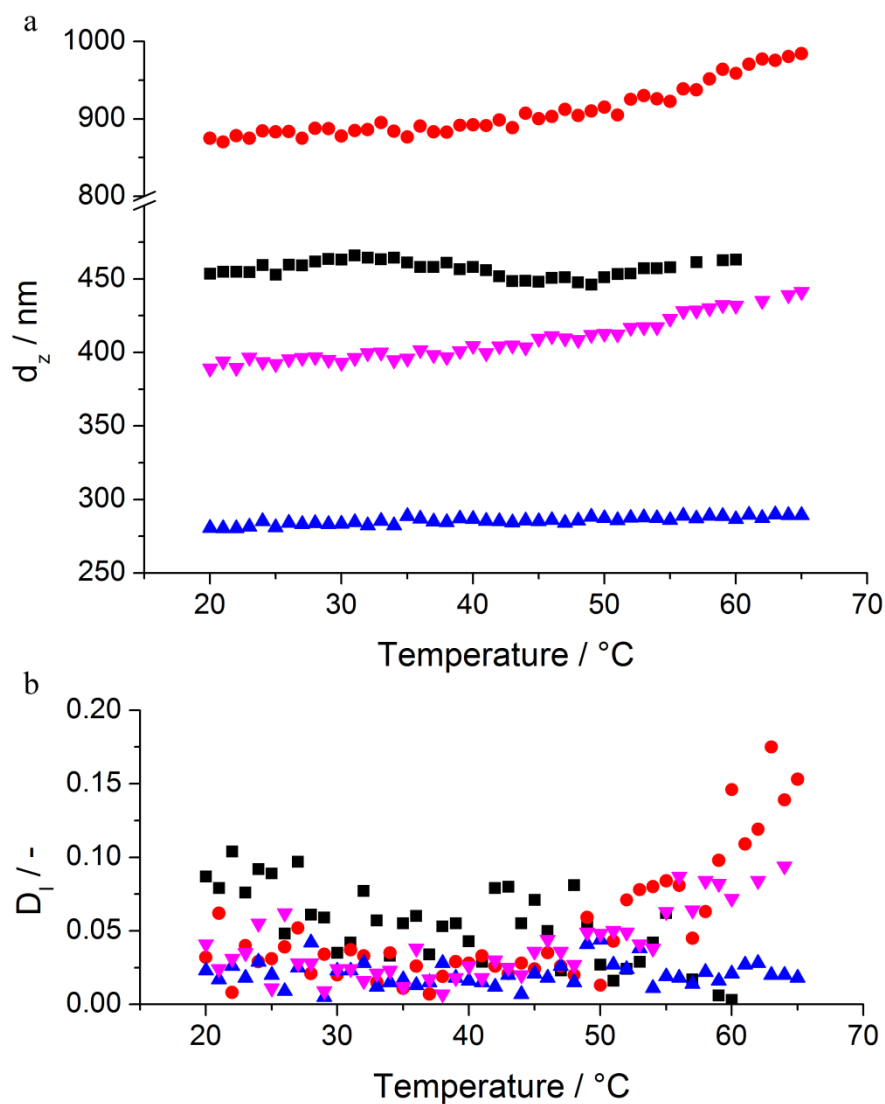


**Figure 4.13** (a) Average particle diameter,  $d_z$ , and (b) dispersity,  $D_I$ , versus temperature of poly(DEGDA) (HM-401) (■), poly(DEGDA-*co*-MAA) (HM-402) (●), poly(PETA-*co*-DEGDA-*co*-MAA) (HM-403) (▲), poly(DPEPHA-*co*-DEGDA-*co*-MAA) (HM-404) (▼) at pH 8.

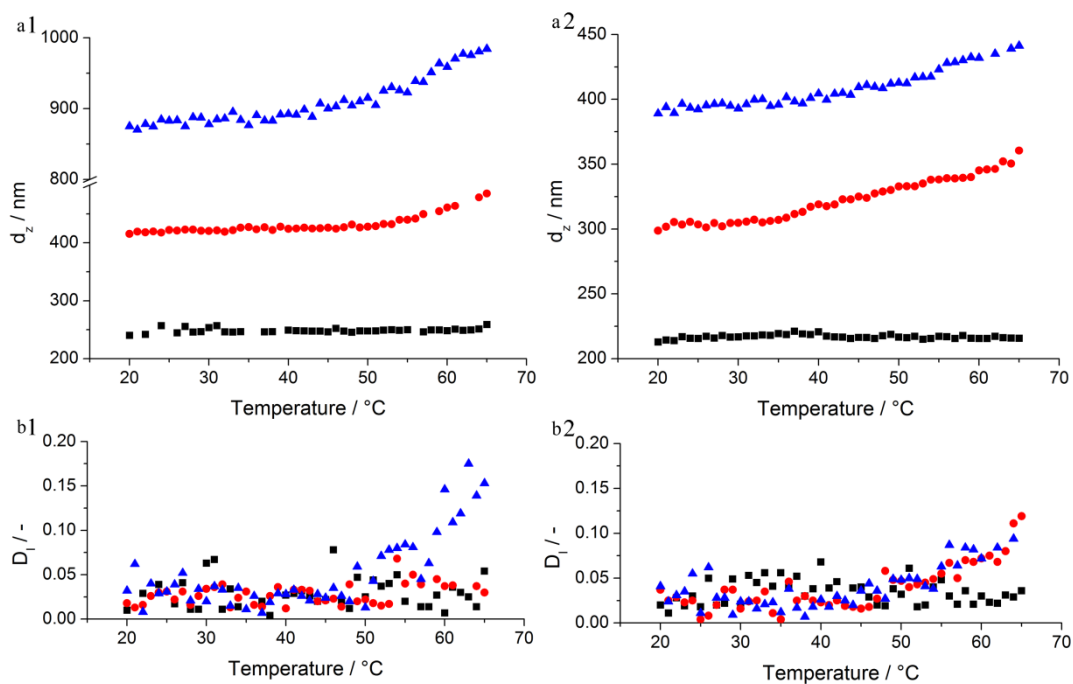


**Figure 4.14** (a) Average particle diameter,  $d_z$ , and (b) dispersity,  $D_i$ , versus temperature of (1) poly(DEGDA-*co*-MAA) (HM-402) and (2) poly(DPEPHA-*co*-DEGDA-*co*-MAA) (HM-404) at pH values 4 (■), 6 (●) and 8 (▲).

We now focus on the poly(DEGDA-*co*-MAA) particles as they exhibit the greatest swelling response to pH changes. Pycnometry, a method used to measure the volume, of poly(DEGDA-*co*-MAA) determined that the polymer had a density of  $1.4252 \text{ g cm}^{-3}$ , from this we can determine the polymer volume fractions of microgel dispersions.

Shear rate sweep rheology measurements were performed on 1 wt.% (polymer volume fraction of 0.0070) of particles in water which had been adjusted to pH 4, 6, 8 and 10, where three sweeps of  $1\text{-}1000\text{-}1 \text{ s}^{-1}$  were performed. Shear viscosity is dependent on particle volume fraction and particle-particle interactions thus on particle swelling we should expect the viscosity to increase, despite keeping particle mass concentration constant.<sup>45</sup> On increasing the pH from 4-6-8 an increase in viscosity is observed, however the viscosity appears to decrease at pH 10 with respect to pH 8 (Figure 4.15 and Figure 4.16). This could be a result of syneresis, where an excess of salt in the bulk water causes the expulsion of water and thus

potentially contraction of the microgel or it could be a result of dilution as a result of increasing the pH.<sup>23, 46</sup>

The plot of log shear viscosity vs. log shear rate show shear thinning at low shear rate, followed by a plateau which indicates liquid-like behaviour, at high shear rate shear thickening is observed as the viscosity increases. We can describe the increase in viscosity as shear rate dependent coagulation of particles. The onset of shear thickening for the smaller particles (i.e. at pH 4 and 6) occurs at a lower shear rate than for the more swollen particles (i.e. at pH 8 and 10) (Figure 4.16). This suggests that the swollen particles have less particle-particle interaction than their smaller counterparts; the small particles are hard and, due to protonation of the acid groups, can hydrogen bond leading to shear thickening at a lower shear rate. The more swollen particles (i.e. at higher pH) cannot hydrogen bond and could almost be described as sterically stabilized, thus they are stabilized against coagulation until a higher shear rate is applied.<sup>47, 48</sup>

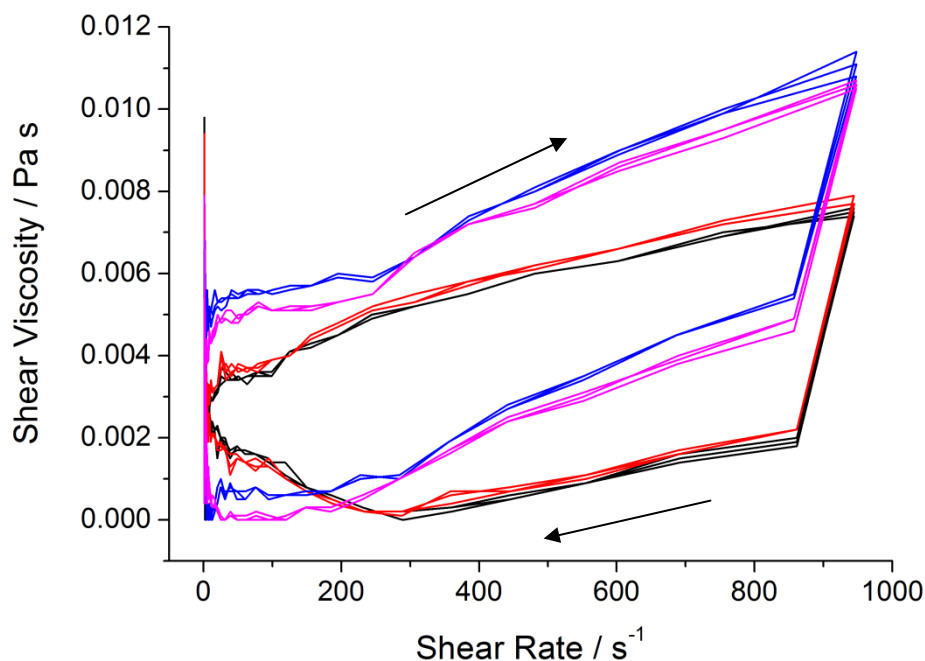


**Figure 4.15** Shear viscosity vs. shear rate of 1 wt.% poly(MAA-*co*-DEGDA) latex at pH values 4 (—), 6 (—), 8 (—) and 10 (—). Three cycles of 0-1000-0 s<sup>-1</sup> were performed.

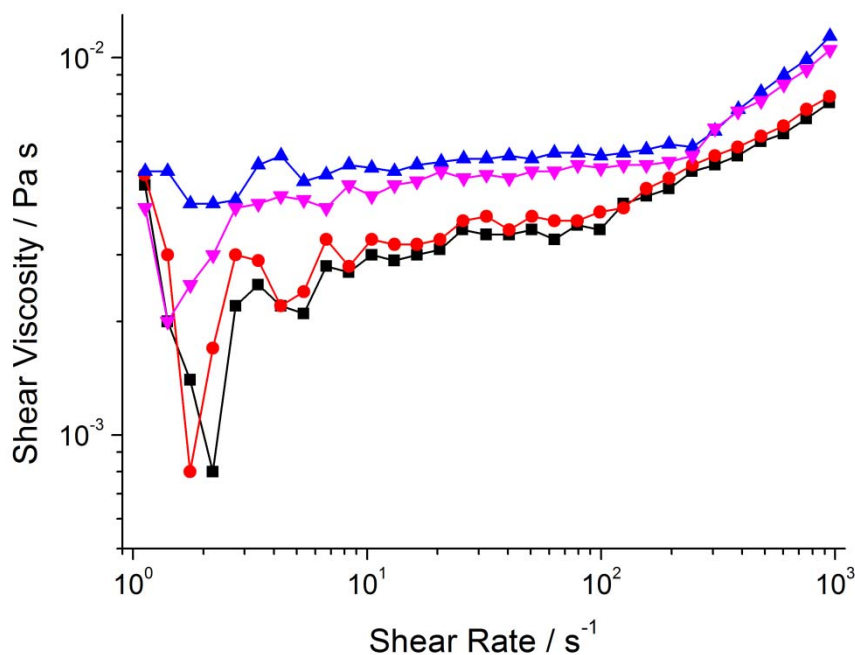


**Figure 4.16** Log plot of shear viscosity vs. shear rate of 1 wt.% poly(MAA-*co*-DEGDA) latex at pH values 4 (■), 6 (●), 8 (▲) and 10 (▼).

The shape of the plot of shear stress vs. shear rate further illuminates whether the dispersion is Newtonian or non-Newtonian (Figure 4.17). At 1 wt.% these microgels are shear thickening (Figure 4.18). Microgel dispersions are often reported as shear thinning,<sup>7, 24, 48</sup> however shear thickening behaviour has also been reported.<sup>47, 49, 50</sup>

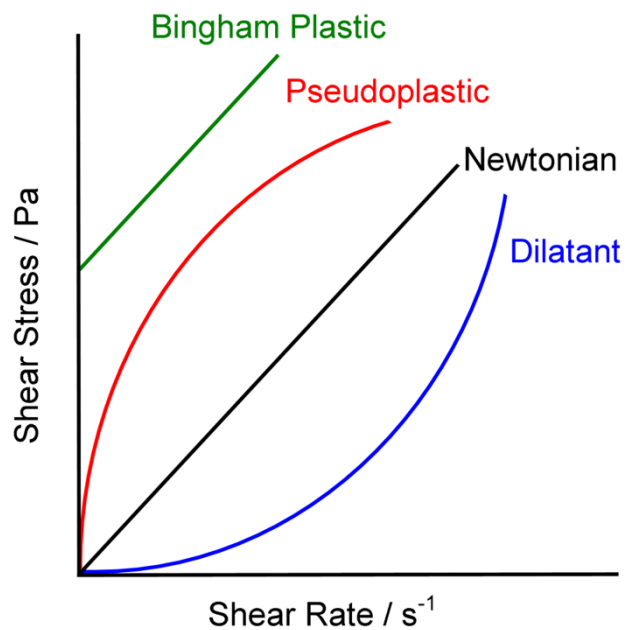


**Figure 4.17** Scheme illustrating the relationship between shear stress and shear rate for Newtonian and non-Newtonian liquids.

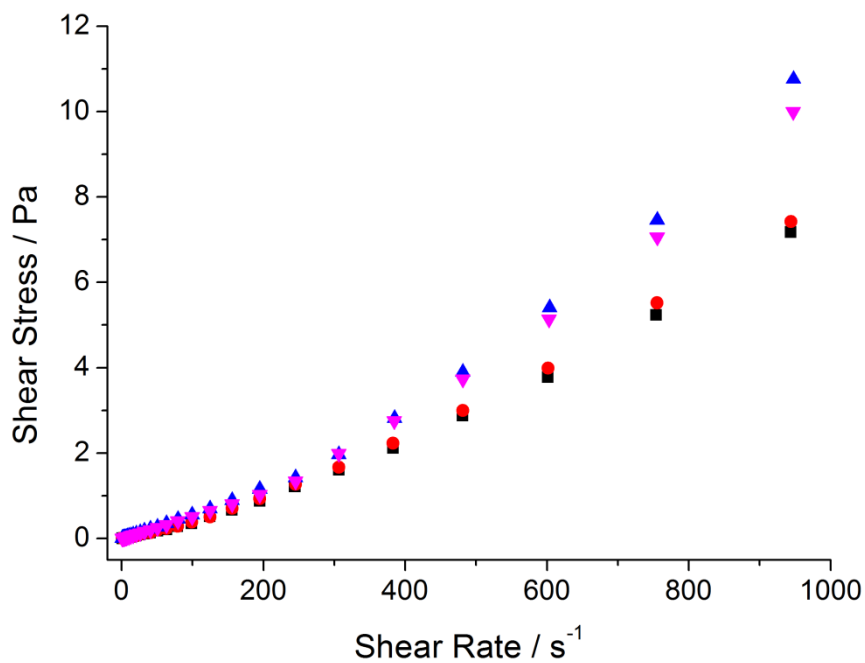


**Figure 4.18** Shear stress vs. shear rate of 1 wt.% poly(MAA-*co*-DEGDA) latex at pH values 4 (■), 6 (●), 8 (▲) and 10 (▼). The plot indicates that the latexes are dilatants or shear thickening.

DLS measurements showed that poly(DEGDA-*co*-MAA) particles increased dramatically in size at high pH, thus we were interested in their gelling behaviour. Poly(DEGDA-*co*-MAA) gels were prepared by dispersing freeze-dried particles in water (which had been pre-adjusted to pH 13) (Table 4.5) by alternating between a vortex mixer and sonic bath.

**Table 4.5** Wt.% of poly(DEGDA-*co*-MAA) microgels in preparation of gels (HM-407).

| Microgel<br>(g) | Water (pH 13)<br>(g) | Microgel<br>(wt.%) | Microgel<br>(Vol. Fraction) |
|-----------------|----------------------|--------------------|-----------------------------|
| 0.0125          | 0.4869               | 2.5                | 0.0177                      |
| 0.0200          | 0.4811               | 4                  | 0.0283                      |
| 0.0250          | 0.4746               | 5                  | 0.0356                      |
| 0.0300          | 0.4709               | 6                  | 0.0428                      |
| 0.0375          | 0.4618               | 7.5                | 0.0539                      |
| 0.0500          | 0.4500               | 10                 | 0.0723                      |



**Figure 4.19** Image of poly(DEGDA-*co*-MAA) particles dispersed in water adjusted to pH 13 (prior to addition of particles) at 2.5, 4, 5, 6, 7.5 and 10 wt.% solids (HM-407). From 5 wt.% solids the solution gels.

It was apparent that poly(DEGDA-*co*-MAA) microgels at 5 wt.% solids (polymer volume fraction of 0.0356) content and higher did not flow (Figure 4.19). To confirm whether that these dispersions were in fact gels, viscoelastic rheological measurements were performed. First the linear viscoelastic region (LVR) was



identified by performing an amplitude sweep of strain at a constant frequency of 1 Hz (Figure 4.20). The LVR is the region, on a log plot of  $G'$  vs. shear-strain, where  $G'$  is independent of applied strain; within the LVR the sample is stable.<sup>45</sup> All samples showed a similar LVR region (up to  $\sim 2.5$  % shear strain), with  $G'$  increasing with increasing microgel content. The magnitude of  $G'$  is dependent on the volume fraction of the particles and the attractive energy between particles, thus it is logical that as we increase the particle concentration that  $G'$  increases.<sup>18</sup> The increasing  $G'$  with solids content suggests that the material is getting tougher with increasing solids content. As all concentrations of particles exhibit failure at the same shear-strain, we suggest that the LVR for gelled poly(DEGDA-*co*-MAA) particles is independent of solids content or gel strength.

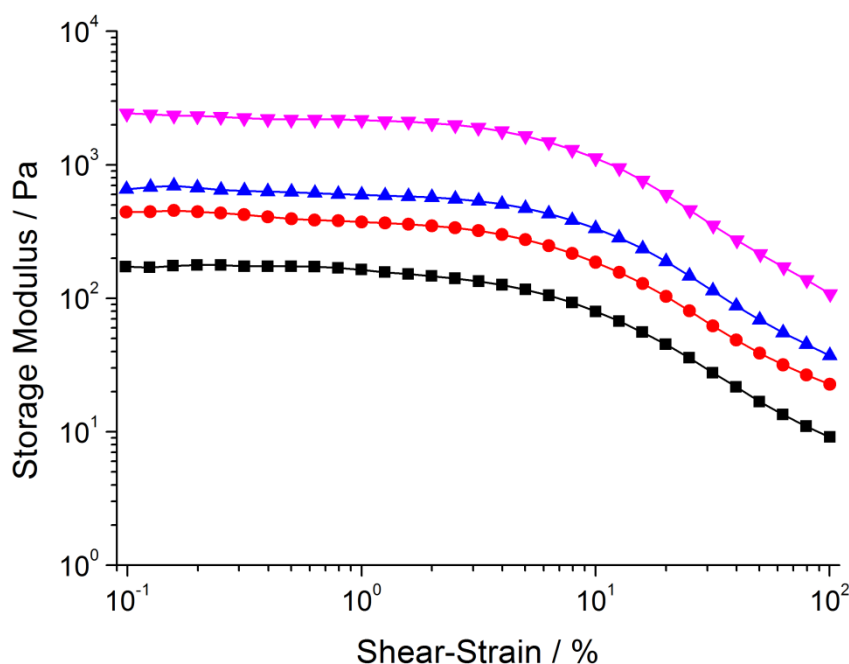


**Figure 4.20** Amplitude sweep of 5 (■), 6 (●), 7.5 (▲) and 10 (▼) wt.% microgels.

A frequency sweep at constant shear-strain identifies whether the material is a gel, viscoelastic solid or viscoelastic liquid; a gel is described by  $G' > G''$  independent of frequency. Properties can also be described by the phase angle; if the phase angle ( $\delta$ ) is  $0^\circ$  at 0 Hz the material is a viscoelastic solid,  $90^\circ$  at 0 Hz the material is a viscoelastic liquid and if the phase angle is independent of frequency the material is a strong gel. It is important to note that frequency dependent gels have been reported.<sup>23, 51</sup> Frequency sweeps were performed in the range of 1-100 Hz and at 0.05 % shear-strain (within the LVR). The poly(DEGDA-*co*-MAA) dispersions from 5 wt.% solids appear to be gels, which increase in “toughness” (illustrated by increasing  $G'$ ) on increasing solids content (Figure 4.21). At 5 wt.% (0.0356 polymer volume fraction) the gel appears to deteriorate at higher frequencies, though above 5 wt.% the gels become increasingly frequency independent with respect to solids content. Saunders *et al.* prepared a series of methacrylic acid based gels with the composition poly(MAA-*co*-X-*co*-Y) where X was either MMA, EA or BMA and Y was EGDMA or BDDA with 37 mol% MAA.<sup>23</sup> All the formed gels showed frequency dependent  $\delta$  indicating that they were weaker than the poly(DEGDA-*co*-MAA) (30 mol% MAA); this could be because the microgels prepared by Saunders *et al.* were synthesized by batch polymerization resulting in non-homogenous particles, whereas poly(DEGDA-*co*-MAA) were synthesized under starved conditions, ensuring a homogeneous distribution of methacrylic acid and cross-linking density. The lowest polymer volume fraction Saunders *et al.* report for gel formation was 0.05 for poly(BMA-*co*-MAA-*co*-BDDA) microgels; poly(DEGDA-*co*-MAA) microgels formed gels at the lower polymer volume fraction of 0.0356.

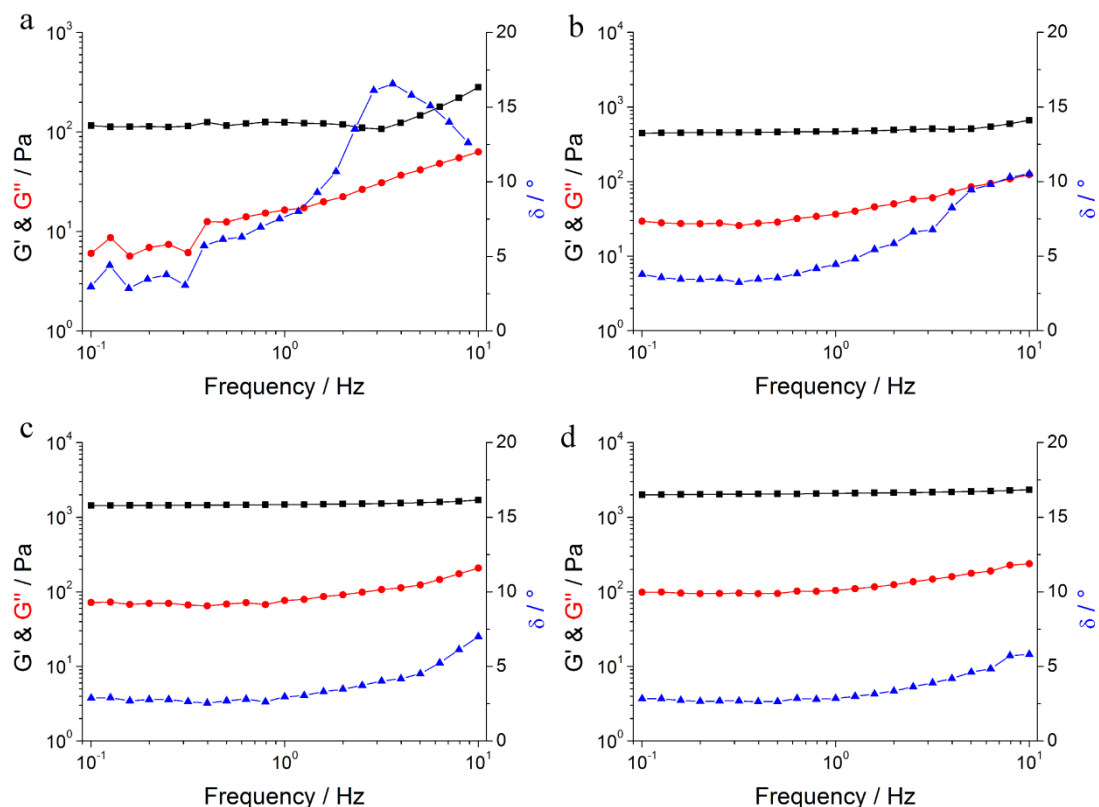


**Figure 4.21** Frequency sweeps of (a) 5, (b) 6, (c) 7.5 and (d) 10 wt.% poly(DEGDA-co-MAA) microgels; storage modulus,  $G'$ , (■), loss modulus,  $G''$ , (●) and phase angle,  $\delta$ , (▲).

In order to determine whether gelation of the microgels was reversible, addition of acid and base was repeated until the gels ceased to form (Figure 4.22 and Table 4.6). Acid and base were added in 10  $\mu$ L aliquots until a change was observed. After addition of 20  $\mu$ L 1 M HCl solution the gels at 5 and 6 wt.% did not reform, 7.5 wt.% gels did not reform after two acid/base cycles and 10 wt.% gels did not reform after three acid/base cycles. We suggest that the loss of gel structure was due to either dilution or syneresis, where the high salt concentration with respect to particles resulted in expulsion of liquid from the microgel particles, decreasing volume fraction of the particles.

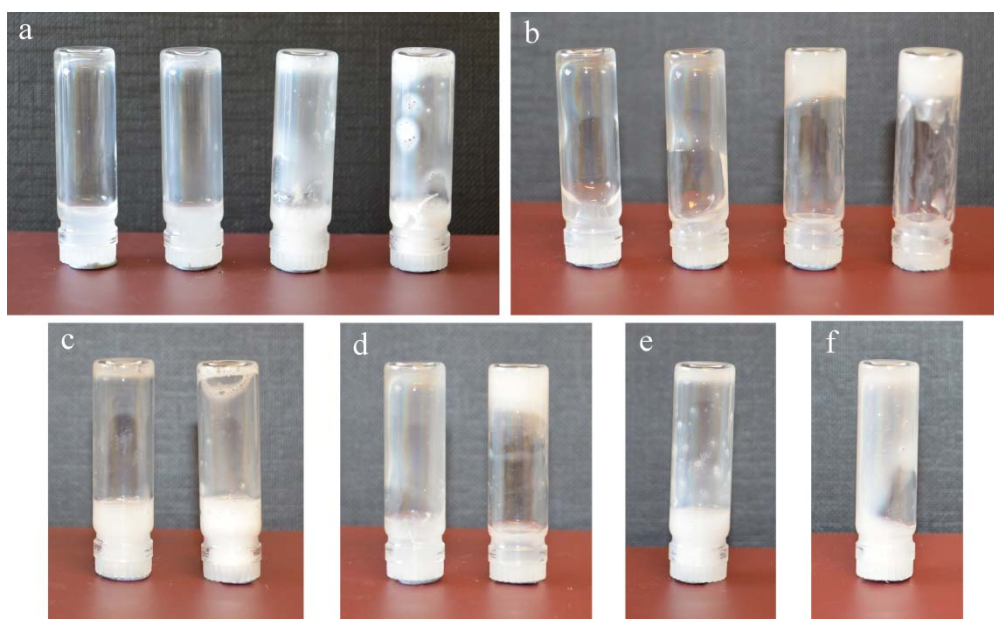


**Figure 4.22** Image of poly(DEGDA-*co*-MAA) particles dispersed in water adjusted to pH 13 (prior to addition of particles) showing repeatable destruction and reformation of the gel by adjusting the pH; (a) 5, 6, 7.5 and 10 wt.% solids after addition of 20  $\mu$ L 1M HCl, gel is lost; (b) 5, 6, 7.5 and 10 wt.% solids after addition of 30  $\mu$ L 1M NaOH, gel reforms for 7.5 and 10 wt.% solids only; (c) 7.5 and 10 wt.% solids after addition of 20  $\mu$ L 1M HCl, gel is lost; (d) 7.5 and 10 wt.% solids after addition of 30  $\mu$ L 1M NaOH, gel reforms for 10 wt.% solids only; (e) 10 wt.% solids after addition of 10  $\mu$ L 1M HCl, gel is lost; (f) 10 wt.% solids after addition of 50  $\mu$ L 1M HCl, gel is lost. Acid and base were added 10  $\mu$ L at a time until change was observed.

**Table 4.6** Table of quantities of 1 M HCl and 1 M NaOH added in reversible gel experiment. HCl and NaOH were added 10  $\mu$ L at a time until a response was observed.

| Exp.     | Wt.% | 1          | 2           | 3          | 4           | 5          | 6           |
|----------|------|------------|-------------|------------|-------------|------------|-------------|
|          |      | HCl<br>1 M | NaOH<br>1 M | HCl<br>1 M | NaOH<br>1 M | HCl<br>1 M | NaOH<br>1 M |
| HM-408-1 | 5    | 20 $\mu$ L | 30 $\mu$ L  | -          | -           | -          | -           |
| HM-408-2 | 6    | 20 $\mu$ L | 30 $\mu$ L  | -          | -           | -          | -           |
| HM-408-3 | 7.5  | 20 $\mu$ L | 30 $\mu$ L  | 20 $\mu$ L | 30 $\mu$ L  | -          | -           |
| HM-408-4 | 10   | 20 $\mu$ L | 30 $\mu$ L  | 20 $\mu$ L | 30 $\mu$ L  | 10 $\mu$ L | 50 $\mu$ L  |

### 4.3.3. Pickering emulsions

We investigated the potential of these microgels as Pickering stabilizers in dodecane-in-water emulsions. Emulsions were prepared from 1 wt.% microgels at pH 4, 6, 8 and 10. Dodecane (2 mL) was added to the microgel dispersion (10 mL); emulsions were prepared by mixing with an Ultra-Turrax at 24,000 rpm for 60 seconds. It was immediately clear that at low pH the emulsions were unstable (Figure 4.23).



**Figure 4.23** Image of dodecane emulsions stabilized by poly(DEGDA-*co*-MAA) microgels. From left to right: pH; 4, 6, 8 and 10. At pH 8 and 10 the Pickering emulsions were stable, however, at pH 4 and 6 they were unstable.

Optical microscopy illustrated that at high pH (pH 8 and 10) a stable emulsions were formed (Figure 4.24 c and d). At low pH (4 and 6) coalescence was observed (Figure 4.24 a and b); the flocculation is a result of hydrogen bonding between microgel particles as the acid groups at pH 4 and 6 are partially protonated.<sup>36, 52</sup> Laser scattering of the emulsions indicate the formation of aggregates at low pH, with emulsions formed at pH 4 containing the greatest proportion of aggregates by volume % (Figure 4.25). The emulsions formed at pH 8 and 10, though they do not contain aggregates, are not monomodal.

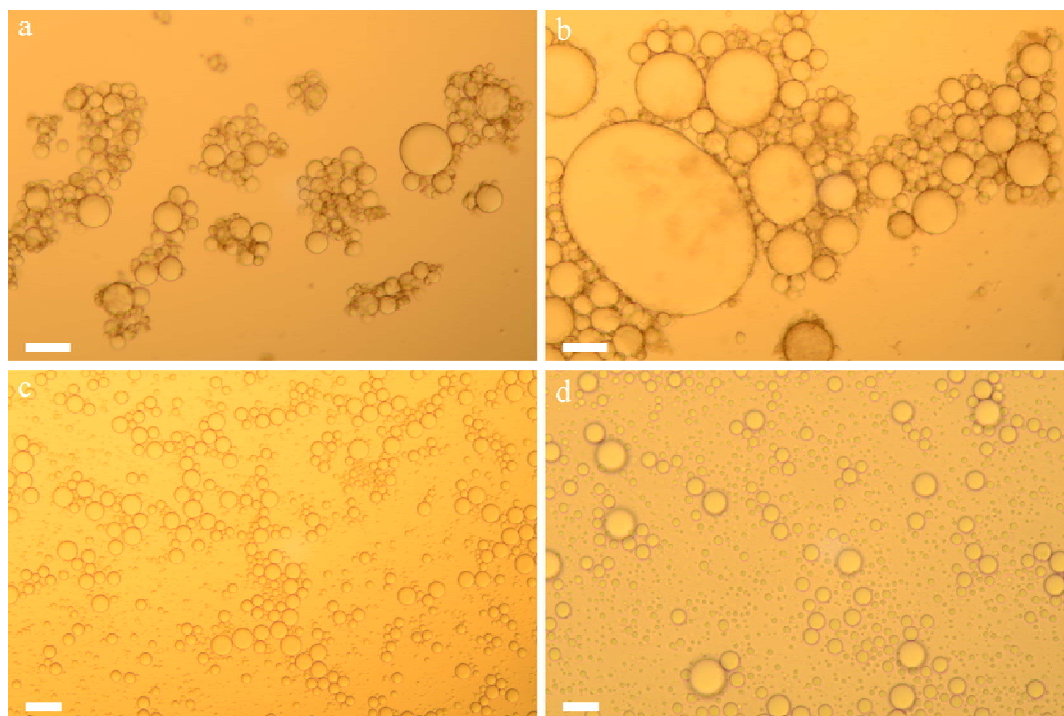


**Figure 4.24** Optical microscope image of dodecane emulsions stabilized by poly(DEGDA-*co*-MAA) microgels at (a) pH 4, (b) pH 6, (c) pH 8 and (d) pH 10 ((a-b) scale bar: 50  $\mu\text{m}$ . (c-d) scale bar: 20  $\mu\text{m}$ ). At low pH (pH 4 and 6) flocculation occurs, at high pH (pH 8 and 10) particles are well dispersed.

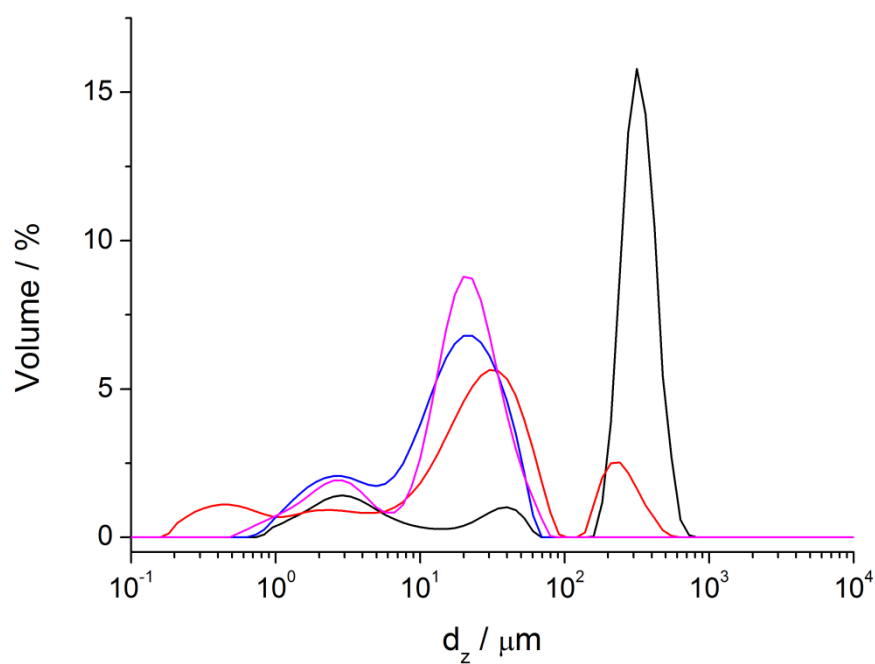


**Figure 4.25** Laser scattering of dodecane emulsions stabilized by poly(DEGDA-*co*-MAA) microgels at pH 4 (—), pH 6 (—), pH 8 (—) and pH 10 (—).



Addition of base (50  $\mu\text{L}$  1 M NaOH) to the unstable emulsion formed at pH 4 results in stabilization of the microgel armoured droplets (Figure 4.26). Optical microscopy shows that the coagulated droplets are replaced by well dispersed droplets (Figure 4.27), indicating that on addition of base the acidic groups of the microgel particles become deprotonated, reversing aggregation. Laser scattering indicates that the range of particle sizes is unchanged; however, the volume of aggregates is much reduced (Figure 4.28).

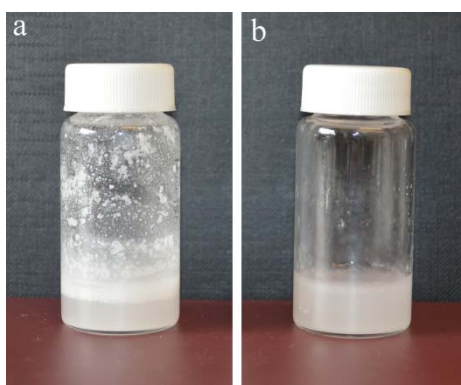


**Figure 4.26** Images of responsive Pickering emulsion (a) emulsion formed with poly(DEGDA-*co*-MAA) particles at pH 4, (b) adjusted to pH 10.

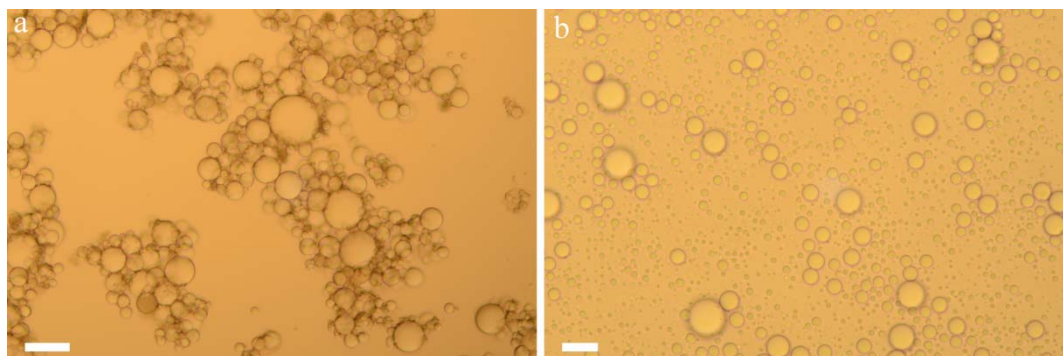


**Figure 4.27** Optical microscope image of dodecane emulsion (a) formed with poly(DEGDA-*co*-MAA) particles at pH 4, (b) adjusted to pH 10. ((a) scale bar: 50  $\mu\text{m}$ . (b) scale bar: 20  $\mu\text{m}$ ).

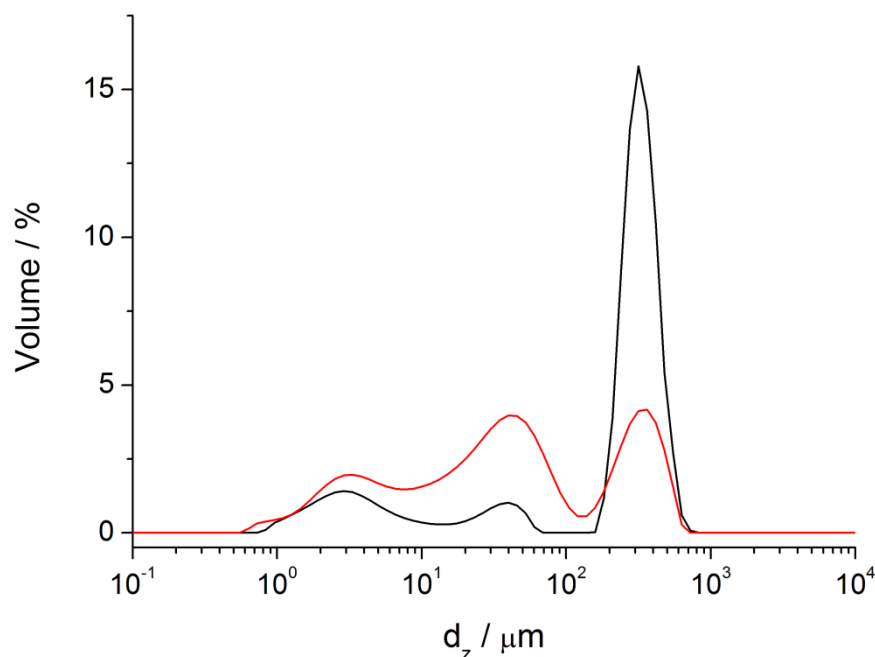


**Figure 4.28** Laser scattering of responsive Pickering emulsion of dodecane emulsion formed with poly(DEGDA-*co*-MAA) particles at pH 4 (—) and adjusted to pH 10 (—).

In a similar manner we destabilized and re-stabilized the emulsions formed at pH 10 by addition of HCl (50  $\mu\text{L}$ , 1 M) followed by NaOH (100  $\mu\text{L}$ , 1M). It is immediately clear that the emulsion is destabilized by addition of acid and re-stabilized by addition of base (Figure 4.29). Optical microscopy and laser scattering shows that on addition of acid aggregates similar to those observed for emulsions formed at pH 4 and 6 are produced (Figure 4.30 and Figure 4.31). On addition of base and mixing using the vortex-mixer for 30 seconds, the droplets appear to become stabilized and the aggregates disappear, however, they appear to have coarsened. This is likely due to ripening, as on addition of acid the microgel particles stabilizing the dodecane droplets shrink in size, reducing coverage. It is likely that at this point coarsening occurs to compensate for the loss of stabilized surface area, on addition of base the particles swell, increasing coverage, however higher shear is required to form the original size distribution.



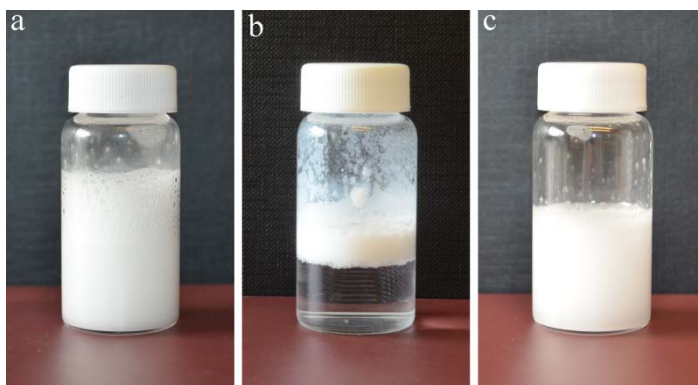


**Figure 4.29** Images of responsive Pickering emulsion of dodecane (a) emulsion formed with poly(DEGDA-*co*-MAA) particles at pH 10, (b) adjusted to pH 4 and (c) adjusted back to pH 10.

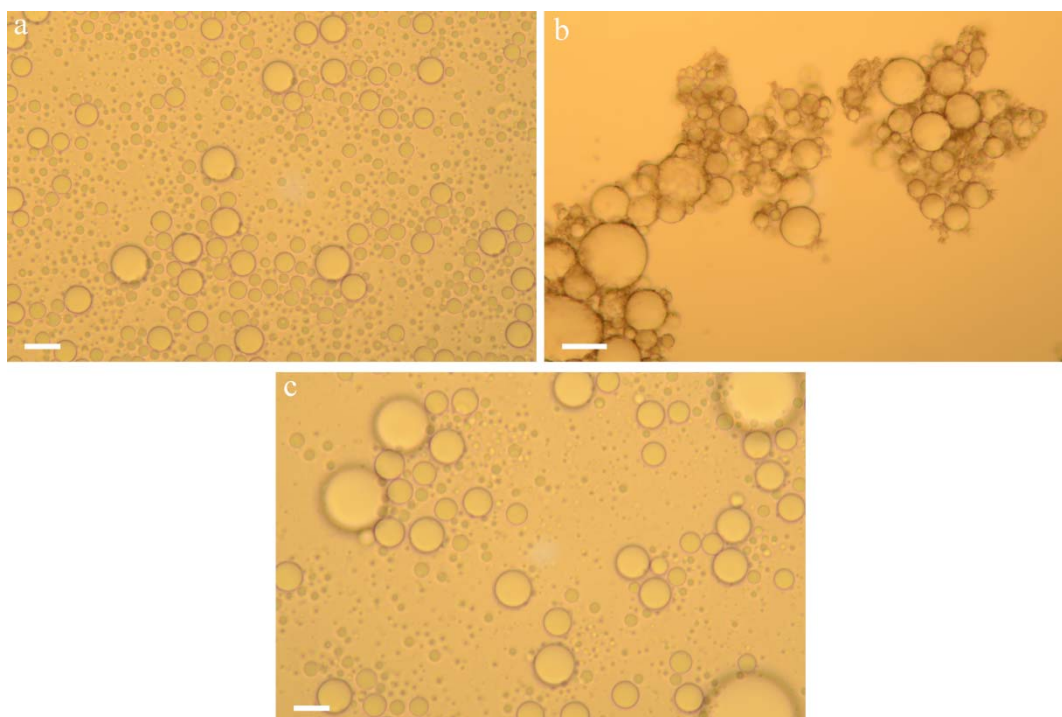


**Figure 4.30** Optical microscope images of dodecane emulsion (a) formed with poly(DEGDA-*co*-MAA) particles at pH 10, (b) adjusted to pH 4 and (c) adjusted back to pH 10 ((a and c) scale bar (a): 20  $\mu\text{m}$ . (b) scale bar: 50  $\mu\text{m}$ ).

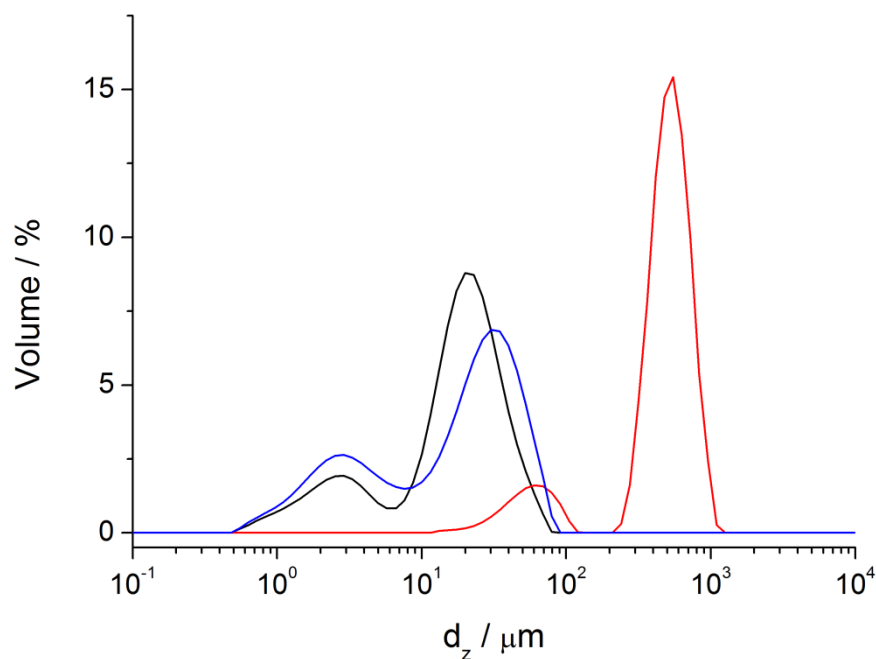


**Figure 4.31** Laser scattering of responsive Pickering emulsion of dodecane emulsion formed with poly(DEGDA-*co*-MAA) particles at pH 10 (—), adjusted to pH 4 (—) and adjusted back to pH 10 (—).

Concentrated emulsions of poly(DEGDA-*co*-MAA) stabilized dodecane were prepared by adding 1 mL dodecane to 1 mL 2.5 wt.% poly(DEGDA-*co*-MAA) latex which had been adjusted to pH 8, this was followed by mixing with an Ultra-Turrax at 11,000 rpm for 60 seconds. The initial emulsion flowed, though on addition of acid (4 drops, 1M HCl) the emulsion gelled; gelation was reversible on addition of base (4 drops, 1 M NaOH) (Figure 4.32). The carboxylic acid groups were protonated on the addition of acid, as a result of this hydrogen bonding between microgels occurred resulting in gelation of the emulsion; addition of base deprotonated the acid groups resulting in loss of hydrogen bonding and thus gel structure. A monolith was created from the gelled emulsion; addition of base (2 drops, 1 M NaOH) resulted in the collapse of the monolith (Figure 4.33).

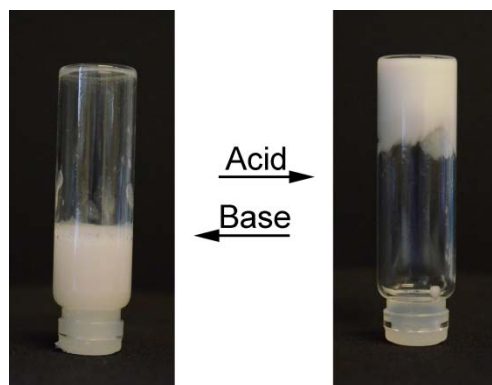


**Figure 4.32** Image of HIPE prepared from concentrated Pickering stabilized emulsions.

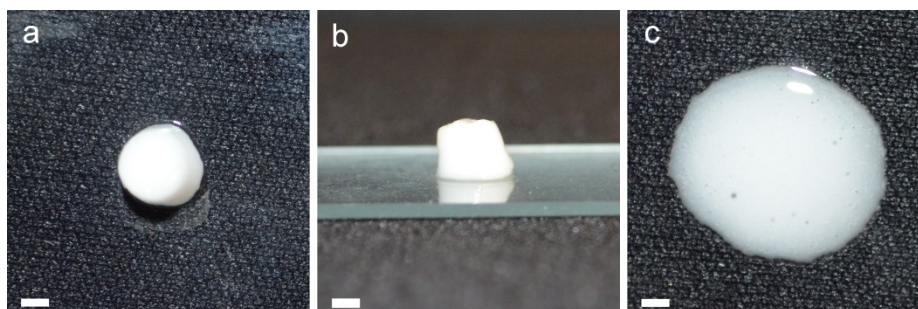


**Figure 4.33** (a) and (b) monolith of poly(DEGDA-*co*-MAA) stabilized dodecane concentrated emulsion gel and (c) collapse of monolith after addition of base (scale bar: 2 mm).

Hollow Pickering stabilized particles have been synthesised by polymerization of particle stabilized emulsions of monomer, initiator and a non-solvent in order to prepare capsules.<sup>53</sup> Emulsions were prepared from 1 wt.% microgels at pH 10. A solution of methyl methacrylate (0.22 g), dodecane (2.01 g) and AIBN (3.7 mg) was added to the microgel dispersion (10 mL); emulsions were prepared by mixing with an Ultra-Turrax at 24,000 RPM for 60 seconds. The resulting emulsion was heated to 60 °C and left overnight. Optical microscopy suggested that stable particles had been formed (Figure 4.34). SEM analysis does indicate that the particles are hollow (Figure 4.35). However, SEM analysis also shows that the resultant polymer particles have a very rough surface and it appears that the microgel particles are not on the interface (Figure 4.36). Desorption of the microgel particles from the interface could be due to the change in interfacial tension on polymerization of MMA or as a result of particle instability on heating. The

polymerization is conducted below the  $T_g$  of methyl methacrylate, thus it is possible that on polymerization and change in interfacial tension that the microgels move from the interface to the aqueous phase, leaving behind an imprint on the polymer. Swollen microgels can be considered as deformable, this deformability can perhaps describe the non-uniform patterning of the hollow particles.<sup>45, 54</sup> Another explanation for the rough surface could be that it is a result of the immiscibility between poly(methyl methacrylate) and dodecane.

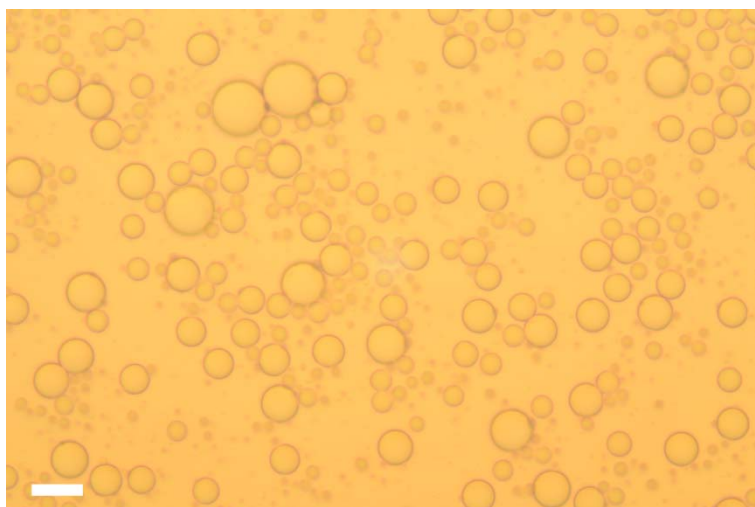


**Figure 4.34** Optical microscope image of hollow poly(methyl methacrylate) stabilized with poly(DEGDA-*co*-MAA) (HM-414) (scale bar: 20  $\mu\text{m}$ ).

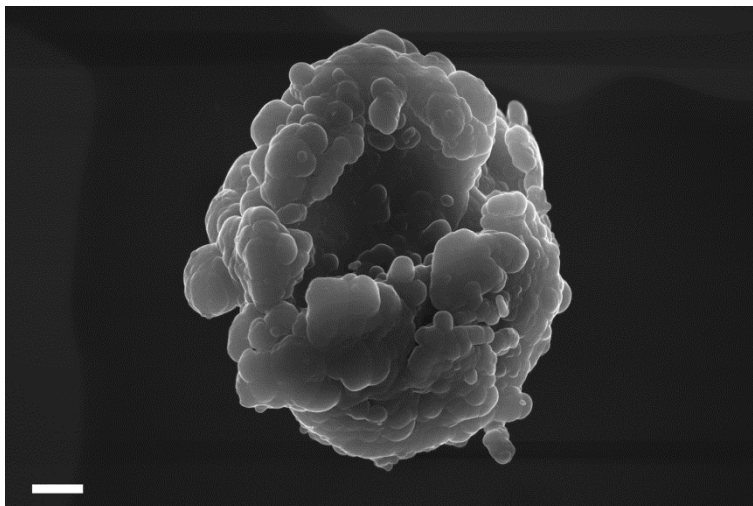


**Figure 4.35** SEM image of hollow poly poly(methyl methacrylate) prepared from microgel Pickering emulsion polymerization with a non-solvent (dodecane), illustrating cavity (HM-414) (scale bar: 1  $\mu\text{m}$ ).

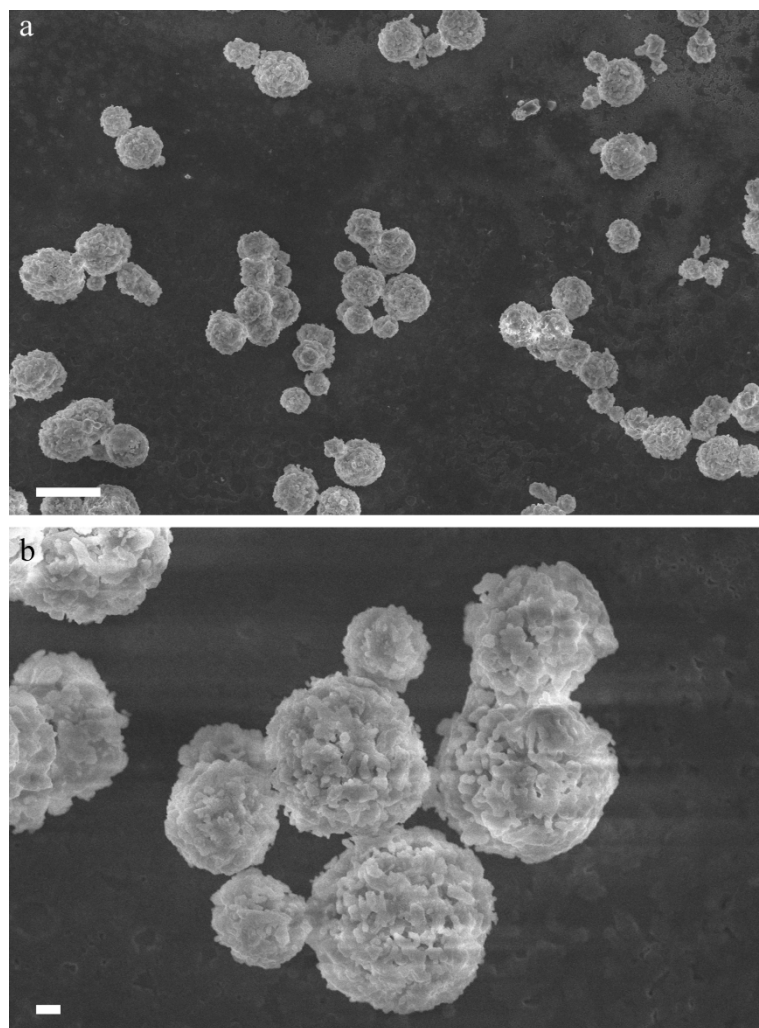


**Figure 4.36** SEM images of hollow poly(methyl methacrylate) prepared from microgel Pickering emulsion polymerization with a non-solvent (dodecane) (HM-414) ((a) scale bar: 10  $\mu\text{m}$ . (b) scale bar: 1  $\mu\text{m}$ ).

## 4.4. Conclusions

In conclusion we have illustrated the surprising pH responsive behaviour of poly(DEGDA-*co*-MAA) microgels with 30 mol% methacrylic acid. In doing so we have begun to elucidate upon the mechanism by which the calcium carbonate particles were encapsulated in Chapter 2; driven by instability of swollen fractal-like poly(DEGDA-*co*-MAA). We also begin to understand possible reasons for the lack of pendant vinyl groups in poly(DEGDA-*co*-MAA) composite particles, through illustrating DEGDA's poor cross-linking capabilities when polymerized under starved conditions. We utilized these microgels to form gels, Pickering stabilized emulsions and highly concentrated Pickering emulsions from which gels could be formed.



## 4.5. Experimental

### 4.5.1. Materials

Di(ethylene glycol) diacrylate (DEGDA), methacrylic acid (MAA), pentaerythritol triacrylate (PETA), dipentaerythritol penta-/hexa-acrylate (DPEPHA), methyl methacrylate (MMA) (99 %), ammonium persulfate (APS), ( $\geq 98.0$  %), dodecane ( $> 99$  %), HCl (37 %) and NaOH pellets were purchased from Aldrich. Azobisisobutyronitrile (AIBN) (97 %) was purchased from VWR. All chemicals were used as received unless otherwise stated. Silicon wafers (used as sample holders for SEM) were kindly donated by Wacker Chemie AG.

### 4.5.2. Equipment

Monomer was fed into the reaction mixture with a Harvard Instrument PHD 2000 Infusion syringe pump. Particle sizes and dispersities were measured by dynamic light scattering using a Malvern Zetasizer Nano using a  $173^\circ$  backscattering angle, at  $25^\circ\text{C}$ , with an equilibration time of 120 s and an average of 3 measurements each with a minimum of 12 sub-runs were taken. SEM was performed on a Zeiss SUPRA 55-VP FEGSEM; sample were prepared by adding a aqueous drop of diluted sample to a silicon wafer and drying at room temperature for 12 hours, the sample was subsequently carbon coated with a carbon evaporator for 4 seconds. Rheological measurements were performed on a Malvern Kinexus Ultra Rheometer. Viscosity measurements were performed at  $25^\circ\text{C}$ , on 20 mL of 1 wt.% latex, shear rate was ramped from  $1\text{-}1000\text{ s}^{-1}$  in three cycles, using geometries C25 BC002 SS and PC25 C0015 SS. Amplitude and frequency sweeps were performed at  $25^\circ\text{C}$ , using parallel geometries PL40 C00007 SS and PU20SC002 SS with a gap size of 1 mm on 0.5 g of sample. Amplitude sweeps were performed with a frequency of 1 Hz and shear strain was ranged from 0.1-100 % at  $25^\circ\text{C}$ . Frequency

sweeps were in the range of 0.1-10 Hz at 0.05 % strain at 25 °C. A QII Kerry Ultrasonics Limited sonic bath was used to disperse particles. A Hook and Tucker Instruments Ltd. Rotamixer De Luxe was used to disperse particles and for reforming emulsions. Pickering emulsions were formed using an Ultra-Turrax basic set at 24,000 RPM. The pH measurements were recorded using a Knick pH meter 765 Calimetic. Optical microscopy was performed on a Leica DM2500M using a Nikon D5100 camera. Particles were collected by freeze-drying on a Thermo Scientific Heto PowerDry LL1500 freeze dryer.

#### **4.5.3. Microgel synthesis**

50.0 g of deionised water was placed under a nitrogen atmosphere in a 100 mL RBF by purging for 20 minutes. The water was heated to 70 °C, polymerization was initiated on addition of APS (0.02 g, 0.09 mmol) dissolved in water (0.50 g) as 1 mL of a degassed mixture of monomer (Table 4.7) was fed into the reaction mixture at 0.5 mL h<sup>-1</sup>. Latexes were dialysed at pH 8 (by adding NaOH to the dialysis water) and then dialysed back to water. Particles were collected by freeze-drying.



**Table 4.7** Table of monomer quantities for microgel synthesis.

| Exp.   | Particles                                      | Monomer | Mass<br>(g) | mmol |
|--------|--|---------|-------------|------|
| HM-401 | Poly(DEGDA)                                    | DEGDA   | 1.118       | 5.22 |
| HM-402 | Poly(DEGDA- <i>co</i> -MAA)                    | DEGDA   | 0.940       | 4.39 |
|        |  | MAA     | 0.162       | 1.88 |
| HM-403 | Poly(PETA- <i>co</i> -DEGDA- <i>co</i> -MAA)   | PETA    | 0.491       | 1.64 |
|        |  | DEGDA   | 0.492       | 2.30 |
|        |  | MAA     | 0.147       | 1.71 |
| HM-404 | Poly(DPEPHA- <i>co</i> -DEGDA- <i>co</i> -MAA) | DPEPHA  | 0.493       | 0.94 |
|        |  | DEGDA   | 0.493       | 2.30 |
|        |  | MAA     | 0.147       | 1.71 |
| HM-405 | Poly(DEGDA- <i>co</i> -MAA)                    | DEGDA   | 0.9410      | 3.39 |
|        |  | MAA     | 0.1607      | 1.87 |
| HM-406 | Poly(DEGDA- <i>co</i> -MAA)                    | DEGDA   | 0.9409      | 4.39 |
|        |  | MAA     | 0.1608      | 1.87 |

#### 4.5.4. Gels

Gels were prepared by adding water pre-adjusted to pH 13.0 to freeze-dried poly(MAA-*co*-DEGDA) particles (see table Figure 4.8). Particles were dispersed by placing on the vortex mixer for 2 minutes and in the sonic bath for 4 minutes and repeating until fully dispersed.

**Table 4.8** Table of reagent quantities for microgel gels; reversible gel experiment (HM-407).

| Microgel<br>(wt.%) | Microgel<br>(g) | Water (pH 13)<br>(g) | Microgel ratio<br>(g g <sup>-1</sup> ) | Microgel<br>(Vol. Fraction) |
|--------------------|-----------------|----------------------|--|-----------------------------|
| 2.5                | 0.0125          | 0.4869               | 0.0250                                 | 0.0177                      |
| 4                  | 0.0200          | 0.4811               | 0.0399                                 | 0.0283                      |
| 5                  | 0.0250          | 0.4746               | 0.0500                                 | 0.0356                      |
| 6                  | 0.0300          | 0.4709               | 0.0599                                 | 0.0428                      |
| 7.5                | 0.0375          | 0.4618               | 0.0751                                 | 0.0539                      |
| 10                 | 0.0500          | 0.4500               | 0.1000                                 | 0.0723                      |

**Table 4.9** Table of quantities of 1 M HCl and 1 M NaOH added in reversible gel experiment. HCl and NaOH were added 10  $\mu$ L at a time until a response was observed.

| Exp.     | Wt.% | 1          | 2          | 3          | 4          | 5          | 6          |
|----------|------|------------|------------|------------|------------|------------|------------|
|          |      | HCl        | NaOH       | HCl        | NaOH       | HCl        | NaOH       |
|          |      | 1 M        | 1 M        | 1 M        | 1 M        | 1 M        | 1 M        |
| HM-408-1 | 5    | 20 $\mu$ L | 30 $\mu$ L | -          | -          | -          | -          |
| HM-408-2 | 6    | 20 $\mu$ L | 30 $\mu$ L | -          | -          | -          | -          |
| HM-408-3 | 7.5  | 20 $\mu$ L | 30 $\mu$ L | 20 $\mu$ L | 30 $\mu$ L | -          | -          |
| HM-408-4 | 10   | 20 $\mu$ L | 30 $\mu$ L | 20 $\mu$ L | 30 $\mu$ L | 10 $\mu$ L | 50 $\mu$ L |

**Table 4.10** Table of reagent quantities for microgel gels for rheological experiments.

| Exp.     | Microgel<br>(wt.%) | Microgel<br>(g) | Water<br>(pH 13)<br>(g) | Microgel<br>ratio<br>(g g <sup>-1</sup> ) | Microgel<br>Vol. Fraction |
|----------|--------------------|-----------------|-------------------------|---|---------------------------|
| HM-409-1 | 5                  | 0.0250          | 0.4726                  | 0.0502                                    | 0.0358                    |
| HM-409-2 | 6                  | 0.0300          | 0.4700                  | 0.0600                                    | 0.0429                    |
| HM-409-3 | 7.5                | 0.0375          | 0.4616                  | 0.0752                                    | 0.0539                    |
| HM-409-4 | 10                 | 0.0500          | 0.4504                  | 0.0999                                    | 0.0723                    |
| HM-410-1 | 5                  | 0.0250          | 0.4752                  | 0.0500                                    | 0.0356                    |
| HM-410-2 | 6                  | 0.0300          | 0.4699                  | 0.0600                                    | 0.0429                    |
| HM-410-3 | 7.5                | 0.0375          | 0.4626                  | 0.0750                                    | 0.0538                    |
| HM-410-4 | 10                 | 0.0500          | 0.4498                  | 0.1000                                    | 0.0724                    |
| HM-411-1 | 5                  | 0.0250          | 0.4776                  | 0.0497                                    | 0.0354                    |
| HM-411-2 | 6                  | 0.0300          | 0.4698                  | 0.0600                                    | 0.0429                    |
| HM-411-4 | 7.5                | 0.0375          | 0.4620                  | 0.0751                                    | 0.0539                    |
| HM-411-5 | 10                 | 0.0500          | 0.4501                  | 0.1000                                    | 0.0723                    |

#### 4.5.5. Microgel Pickering emulsions (HM-412)

1 wt.% poly(DEGDA-*co*-MAA) microgel dispersions were adjusted to pH 4, 6, 8 and 10. Emulsions were prepared by adding 2.0 mL of dodecane to 10.0 mL of the microgel dispersion and mixing with an Ultra-Turrax at 24,000 RPM for 60 seconds.

#### 4.5.6. Monoliths prepared from concentrated microgel Pickering emulsions (HM-413)

A 2.5 wt.% poly(DEGDA-*co*-MAA) microgel dispersion was adjusted to pH 8. HIPEs were prepared by adding 1.0 mL of dodecane to 1.0 mL of the microgel

dispersion and mixing with an Ultra-Turrax at 11,000 rpm for 60 seconds. The emulsion was gelled on addition of 4 drops of 1 M HCl.

#### **4.5.7. Microgel Pickering emulsion polymerizations (HM-414)**

1 wt.% microgel dispersions were adjusted to pH 10. A solution of methyl methacrylate (0.22 g, 2.2 mmol) dodecane (2.01 g) and AIBN (3.7 mg, 0.023 mmol) was added to 10.0 mL of the microgel dispersion and mixed with an Ultra-Turrax at 24,000 RPM for 60 seconds. The resulting emulsion was heated to 60 °C and gently stirred with a stirrer bar (300 rpm) overnight.

## 4.6. References

1. Staudinger, H.; Husemann, E. *Ber. Dtsch. Chem. Ges.* **1935**, 68, 1618-1634.
2. Baker, W. O. *Ind. Eng. Chem.* **1949**, 41, 511-520.
3. Pelton, R. H.; Chibante, P. *Colloids Surfaces* **1986**, 20, 247-256.
4. Pelton, R. *Adv. Colloid Interface Sci.* **2000**, 85, 1-33.
5. Kawaguchi, H. *Polym. Int.* **2014**, 63, 925-932.
6. Fernández-Nieves, A.; Fernández-Barbero, A.; Vincent, B.; de las Nieves, F. J. *Macromolecules* **2000**, 33, 2114-2118.
7. Wolfe, M. S. *Prog. Org. Coat.* **1992**, 20, 487-500.
8. Rodriguez, B. E.; Wolfe, M. S.; Fryd, M. *Macromolecules* **1994**, 27, 6642-6647.
9. Hoare, T.; Pelton, R. *Macromolecules* **2004**, 37, 2544-2550.
10. Suzuki, A.; Tanaka, T. *Nature* **1990**, 346, 345-347.
11. Juodkasis, S.; Mukai, N.; Wakaki, R.; Yamaguchi, A.; Matsuo, S.; Misawa, H. *Nature* **2000**, 408, 178-181.
12. Tanaka, T.; Nishio, I.; Sun, S.; Ueno-Nishio, S. *Science* **1982**, 218, 467-469.
13. Kwon, I. C.; Bae, Y. H.; Kim, S. W. *Nature* **1991**, 354, 291-293.
14. Miyata, T.; Asami, N.; Uragami, T. *Nature* **1999**, 399, 766-769.
15. Saunders, B. R.; Vincent, B. *Adv. Colloid Interface Sci.* **1999**, 80, 1-25.
16. Flory, P. J. *Principles of Polymer Chemistry* Cornell University Press, London, 1986.
17. Saunders, B. R.; Crowther, H. M.; Vincent, B. *Macromolecules* **1997**, 30, 482-487.
18. Prasad, V.; Trappe, V.; Dinsmore, A. D.; Segre, P. N.; Cipelletti, L.; Weitz, D. A. *Faraday Discuss.* **2003**, 123, 1-12.
19. Senff, H.; Richtering, W. *J. Chem. Phys.* **1999**, 111, 1705-1711.
20. Buscall, R. *Colloids. Surf. A* **1994**, 83, 33-42.

21. Bolisetty, S.; Hoffmann, M.; Lekkala, S.; Hellweg, T.; Ballauff, M.; Harnau, L. *Macromolecules* **2009**, 42, 1264-1269.
22. Mattsson, J.; Wyss, H. M.; Fernandez-Nieves, A.; Miyazaki, K.; Hu, Z.; Reichman, D. R.; Weitz, D. A. *Nature* **2009**, 462, 83-86.
23. Lally, S.; Bird, R.; Freemont, T.; Saunders, B. *Colloid. Polym. Sci.* **2009**, 287, 335-343.
24. Tan, B. H.; Tam, K. C.; Lam, Y. C.; Tan, C. B. *Adv. Colloid Interface Sci.* **2005**, 113, 111-120.
25. Cho, E. C.; Kim, J.-W.; Fernández-Nieves, A.; Weitz, D. A. *Nano Lett.* **2007**, 8, 168-172.
26. Liu, R.; Milani, A. H.; Freemont, T. J.; Saunders, B. R. *Soft Matter* **2011**, 7, 4696-4704.
27. Liu, R.; Milani, A. H.; Saunders, J. M.; Freemont, T. J.; Saunders, B. R. *Soft Matter* **2011**, 7, 9297-9306.
28. Supasuteekul, C.; Milani, A. H.; Saunders, J. M.; Lally, S.; Freemont, T.; Saunders, B. R. *Soft Matter* **2012**, 8, 7234-7242.
29. Saunders, J. M.; Tong, T.; Le Maitre, C. L.; Freemont, T. J.; Saunders, B. R. *Soft Matter* **2007**, 3, 486-494.
30. Das, M.; Mardyani, S.; Chan, W. C. W.; Kumacheva, E. *Adv. Mater.* **2006**, 18, 80-83.
31. Nayak, S.; Lee, H.; Chmielewski, J.; Lyon, L. A. *J. Am. Chem. Soc.* **2004**, 126, 10258-10259.
32. Soppimath, K. S.; Tan, D. C. W.; Yang, Y. Y. *Adv. Mater.* **2005**, 17, 318-323.
33. Biffis, A.; Orlandi, N.; Corain, B. *Adv. Mater.* **2003**, 15, 1551-1555.
34. Lu, Y.; Mei, Y.; Drechsler, M.; Ballauff, M. *Angew. Chem. Int. Ed.* **2006**, 45, 813-816.
35. Ballauff, M.; Lu, Y. *Polymer* **2007**, 48, 1815-1823.
36. Ngai, T.; Behrens, S. H.; Auweter, H. *Chem. Commun.* **2005**, 331-333.
37. Ngai, T.; Auweter, H.; Behrens, S. H. *Macromolecules* **2006**, 39, 8171-8177.
38. Heskins, M.; Guillet, J. E. *J. Macromol. Sci. Chem.* **1968**, 2, 1441-1455.
39. Li, Z.; Ngai, T. *Colloid. Polym. Sci.* **2011**, 289, 489-496.

40. Morse, A. J.; Dupin, D.; Thompson, K. L.; Armes, S. P.; Ouzineb, K.; Mills, P.; Swart, R. *Langmuir* **2012**, 28, 11733-11744.
41. Croll, L. M.; Stöver, H. D. H. *Langmuir* **2003**, 19, 10077-10080.
42. Lally, S.; Mackenzie, P.; LeMaitre, C. L.; Freemont, T. J.; Saunders, B. R. *J. Colloid Interface Sci.* **2007**, 316, 367-375.
43. Fitch, R. M. *Brit. Poly. J.* **1973**, 5, 467-483.
44. Muroi, S.; Hosoi, K.; Ishikawa, T. *J. Appl. Polym. Sci.* **1967**, 11, 1963-1978.
45. Öle Kiminta, D. M.; Luckham, P. F.; Lenon, S. *Polymer* **1995**, 36, 4827-4831.
46. Zhang, J.; Peppas, N. A. *Macromolecules* **1999**, 33, 102-107.
47. Wagner, N. J.; Brady, J. F. *Physics Today* **2009**, 62, 27-32.
48. Wolfe, M. S.; Scopazzi, C. *J. Colloid Interface Sci.* **1989**, 133, 265-277.
49. Bergenholtz, J.; Brady, J. F.; Vicic, M. *J. Fluid Mech.* **2002**, 456, 239-275.
50. Lee, Y.; Wagner, N. *Rheol. Acta* **2003**, 42, 199-208.
51. Seetapan, N.; Mai-ngam, K.; Plucktaveesak, N.; Sirivat, A. *Rheol. Acta* **2006**, 45, 1011-1018.
52. Liu, T.; Seiffert, S.; Thiele, J.; Abate, A. R.; Weitz, D. A.; Richtering, W. *PNAS* **2012**, 109, 384-389.
53. Chen, T.; Colver, P. J.; Bon, S. A. F. *Adv. Mater.* **2007**, 19, 2286-2289.
54. Frith, W. J.; Lips, A.; Melrose, J. R.; Ball, R. C. 11. *Shear-Thickening in Suspensions of Deformable Particles* Modern Aspects of Colloidal Dispersions. Springer Netherlands, 1998, 123-132.

# Chapter 5: Hybrid Multi-Layered Particles

---

## 5.1. Abstract

Herein we describe the synthesis of multi-layered particles by a one-pot Pickering emulsion polymerization approach. The aim was to produce particles consisting of three layers where the inner-shell is a layer of Laponite clay and the core and outer-shell is poly(styrene-*co*-*n*-butyl acrylate) in order to form polymer films with a controlled structure on the nano-metre scale. Immobilization of the clay layer was a pivotal step in achieving the multi-layered morphology and was achieved with methacrylate functionalised silanes. Mechanical strength, thermal stability and structure of the polymer films were investigated to determine the effect of particle morphology. Ultimately we show that through controlling particle morphology of Laponite composite nano-particles we can alter and perhaps even tune the thermal and mechanical properties of their corresponding films.



## 5.2. Introduction

Polymer-clay composite particles are of great interest and are a very promising class of materials; they have the potential to offer significant improvements to gas barrier,<sup>1, 2</sup> thermal stability<sup>3-5</sup> and mechanical<sup>5-7</sup> properties. To achieve and improve upon these properties clay armoured latexes and clay particles encapsulated in polymeric shells have been synthesized. Both morphologies have shown desirable properties, so we were interested in synthesizing soft multi-layered particles, where the inner-shell is a layer of clay, and investigating their properties.

### 5.2.1. Clay armoured particles

One method to produce clay armoured particles is heterocoagulation of large cationic latex particles and small anionic clay platelets.<sup>8</sup> An alternative one-pot approach is Pickering emulsion polymerization; it differs from the heterocoagulation method in that the particles become armoured during the polymerization process. The term “Pickering” describes the stabilization of an interface by solid particles, it was first reported independently by Ramsden in 1903 and then by Pickering in 1907, whom it was subsequently named after.<sup>9, 10</sup> Pickering stabilization has been used to produce armoured droplets and particles with a variety of solid stabilizers including  $\text{SiO}_2$ ,<sup>11-17</sup>  $\text{TiO}_2$ <sup>18-20</sup>,  $\text{Fe}_3\text{O}_4$ <sup>21-24</sup> and graphene oxide<sup>25-28</sup> nanoparticles (Figure 5.1). Laponite clay particles have proven to be excellent Pickering stabilizers, first illustrated by Binks and co-workers in the stabilization of oil-in-water emulsions.<sup>29</sup> Later work showed Laponite armoured polymer particles could be prepared by Pickering stabilized emulsion,<sup>30-34</sup> miniemulsion,<sup>35-40</sup> and inverse miniemulsion<sup>41, 42</sup> polymerization methods.

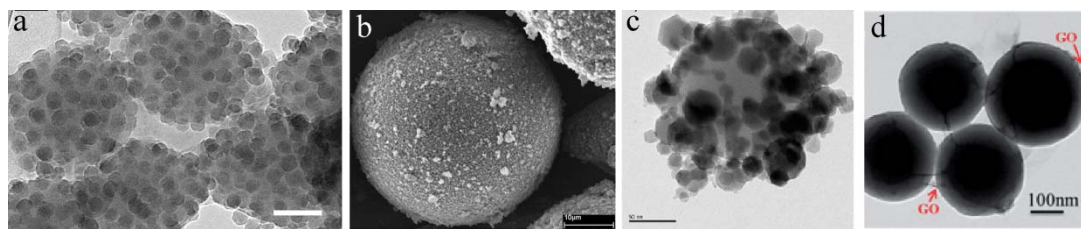


**Figure 5.1** (a) TEM image of silica armoured poly(MMA) prepared by emulsion polymerization.<sup>13</sup> (b) SEM image of TiO<sub>2</sub>-stabilized poly(styrene) with hollow core prepared by miniemulsion polymerization with a sacrificial solvent (scale bar: 10  $\mu$ m).<sup>18</sup> (c) TEM image of Fe<sub>2</sub>O<sub>3</sub>/poly(styrene) particles prepared by miniemulsion polymerization (scale bar: 50 nm).<sup>24</sup> (d) TEM image of GO/poly(styrene) particles prepared by miniemulsion polymerization (scale bar: 100 nm).<sup>28</sup>

Bon and co-workers showed that, in the synthesis of Laponite armoured particles by Pickering emulsion polymerization, the concentration of Laponite plays a crucial role in the particle nucleation step. Increasing the concentration of Laponite was shown to reduce particle size, but it also increased the length of the nucleation period, resulting in a broader particle size distribution. At low initiator flux a disastrous coagulation event was observed within a small window of clay:monomer ratios (0.009-0.025); this window of particle instability was not observed at higher initiator flux. Bon *et al.* hypothesized that the instability of the electrostatically stabilized particles was due to a combination of low concentration of initiator derived sulfonate groups and Laponite resulting in coagulation of unstable particles.<sup>43</sup>

Films formed from clay armoured soft latex particles have been found to have a honey-comb structure of the Pickering stabilizer throughout the film; the honey-comb structure has been determined through examining ultrathin cross-sections using cryo-TEM (Figure 5.2 b).<sup>5, 44, 45</sup> When the polymer inter-diffuses in step three of film formation, the armour (in this case Laponite clay) boundary remains at its original location (from step two of film formation: particle deformation). This results in the formation of the honey-comb structure, with the excess Laponite moving to the surface of the film.<sup>5</sup> This affect is also observed when

particles are stabilized by surfactants.<sup>46</sup> Bourgeat-Lami and co-workers showed that films with a Laponite honey-comb structure showed significantly improved thermal and mechanical properties in poly(styrene) films; DSC measurements showed an increase in  $T_g$  by 12 °C for films formed from the armoured particles when compared to corresponding plain latex films and stress-strain analysis illustrated a 50-fold increase in Young's modulus.<sup>5</sup> The increase in  $T_g$  is attributed to reduced mobility of polymer chains in the vicinity of the clay platelets and the increased mechanical strength is attributed to the Laponite network throughout the film.<sup>47, 48</sup>

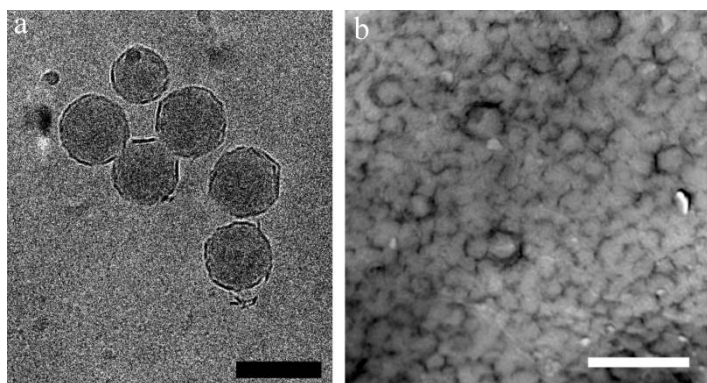


**Figure 5.2** (a) Cryo-TEM image of Laponite armoured poly(Sty-*co*-BA) particles (scale bar: 100 nm).<sup>43</sup> (b) Cryo-TEM of a monolayer film of poly(Sty-*co*-BA) latex particles armoured with Laponite clay, illustrating the honey-comb structure of Laponite (dark lines) produced on film formation (scale bar: 500 nm).<sup>45</sup>

Bon and co-workers have shown that low concentrations of Laponite armoured soft particles can improve the mechanical strength of materials. Small quantities of Laponite armoured particles were incorporated into pressure sensitive adhesives, resulting in increased tack adhesion properties by raising the plateau stress and increasing the strain at point of failure. These properties were not observed when clay particles were simply mixed into the adhesive formulation. Increased tack adhesion on incorporation of armoured particles was attributed to the dissipation of energy by slippage of the clay from the interface during deformation.<sup>6</sup>

### 5.2.2. Multi-layered particles

Multi-layered particles are defined here as particles consisting of a minimum of three layers (a core, inner-shell and outer-shell). Herein, current methods of synthesizing multi-layered particles are described.

Multi-layered core-shell particles with an inorganic core, organic inner-shell and inorganic outer-shell have been synthesized by Wakiya *et al.* for applications in cosmetics and construction materials. The particles were made in three steps (1) surface modification of silica nanoparticles with MPTMS, (2) surface-seeded polymerization of styrene and (3) surface sol-gel reaction of tetraethoxysilane (TEOS) to produce a silica shell (Figure 5.3).<sup>49</sup> A fourth step of heating to 500 °C to calcine the organic layer produced a rattle-like structure. This method produced well-defined, monodisperse multi-layered particles; however a drawback of this method is the requirement of four separate steps to achieve the final product.

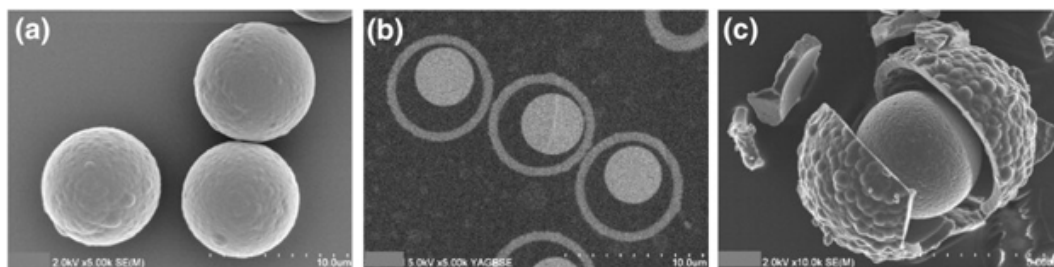


**Figure 5.3** SEM images of multi-layered particle with silica outer shell, (b) cross-section of multi-layered particle and (c) microcapsular structure after removal of organic inner-shell by calcinations.<sup>49</sup>

The layer-by-layer approach (described in detail in Chapter 2) has been used by Caruso and co-workers to prepare multi-layered particles from a range of sub-micron polystyrene cores (210-640 nm in diameter).<sup>50, 51</sup> The multi-layered morphology was achieved by alternating layers of oppositely charged polyelectrolyte with various inorganic particles; including titania, silica and Laponite clay. The multi-layered particles were synthesized in order to produce hollow inorganic particles by calcination of the organic core for applications as photonic band gap

crystals and as fillers and pigments. The layer-by layer technique offers a simple synthesis method with nanometre-scale control over particle diameter and shell thickness. However, the need for dilute conditions (0.5 wt.%) and time consuming cleaning cycles between each deposition make this method unsuitable to large scale production. Anzai and co-workers synthesized magnetic multi-layered composite particles for separation of T- and B-cells by a heterocoagulation approach.<sup>52</sup> The seed particles were produced by heterocoagulation of positively charged magnetic nanoparticles (20 nm) to anionic latex particles (180-900 nm). The resultant raspberry-like structures were encapsulated in a polymer shell by surface modification with sodium oleate, followed by emulsion polymerization of styrene. Very low solids content (0.1 wt.%) were used in the encapsulation step and desorption of some of the magnetic particles was observed, suggesting that this process was not optimal. Kumacheva and co-workers synthesized similar structures with metal nanoparticles in the middle phase, to achieve periodic structured nanocomposite films (where the periodicity is governed by the thickness of the outermost shell) for use as optically responsive materials.<sup>53</sup> The multi-layered particles were produced by *in-situ* synthesis of nanoparticles (cadmium sulphide and silver) on poly(methyl methacrylate-*co*-methacrylic acid) latex particles followed by polymerization of methyl methacrylate and butyl methacrylate at the surface of the composite particles (Figure 5.4).

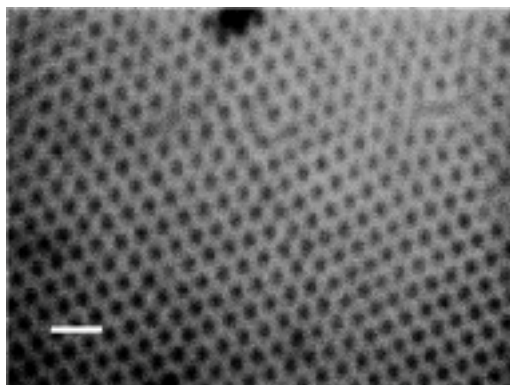


**Figure 5.4** Laser confocal fluorescent microscopy image of CdS-polymer nanocomposites, illustrating the periodic array of the metal inner-shell, where the spacing is controlled by the thickness of the polymer shell (scale bar: 2  $\mu\text{m}$ ).<sup>53</sup>

A Pickering template approach has been used to form multi-layered capsules by Stöver and co-workers. Silica stabilized oil-in-water emulsions were encapsulated in a polymer shell by either layer-by-layer assembly<sup>54</sup> or interfacial ATRP polymerization,<sup>55</sup> in order to produce large microcapsules ( $\sim 30\text{--}100\text{ }\mu\text{m}$ ). The microcapsules were designed for encapsulation of hydrophobic moieties for applications in pesticide delivery, food science and self-healing materials by changing the contents of the core. The layer-by-layer approach proceeded first by adsorbing a negatively charged polyelectrolyte, poly(sodium styrenesulfonate), to the positively charged silica particles; these particles were then used to stabilize a xylene-in-water emulsion. Once the Pickering emulsion was formed, layer-by-layer assembly of alternating polyelectrolytes, poly(diallyldimethylammonium chloride) and poly(sodium styrenesulfonate), were used to build up the outer polymeric shell.<sup>54</sup> This method only produces a thin polymeric shell and faces the difficulties associated with the layer-by-layer technique mentioned above. The interfacial ATRP approach proceeded in a similar manner, however the initial polyelectrolyte for modification of the silica particles contained an ATRP initiating group in the polymer chain (poly(sodium styrenesulfonate-*co*-2-(2-bromoisobutyloxy) ethyl methacrylate) to localize polymerization at the surface of the microcapsule. Once the

Pickering emulsion had been made, a batch surface-initiated ATRP polymerization of *N,N'*-methylene bisacrylamide was used to create the outer-shell. The divinyl monomer was used to prevent migration of the silica particles from the core-shell boundary, and a hydrophilic ligand (hexamethyltriethylenetetraamine) was used to ensure polymerization occurred on the aqueous side of the interface, thus preventing any partitioning to the xylene core.<sup>55</sup>

Philipse and co-workers prepared multi-layered particles with a  $\text{Fe}_2\text{O}_3$  inner-shell for biomedical applications (Figure 5.5).<sup>56</sup> The particles were synthesized by gentle stirring of an MPTMS,  $\text{Fe}_2\text{O}_3$  and methyl methacrylate solution. The reaction yielded  $\text{Fe}_2\text{O}_3$  stabilized MPTMS droplets with the methyl methacrylate forming a secondary phase floating on the aqueous phase. Addition of KPS and heating to 70 °C polymerized the core and triggered polymerization of methyl methacrylate at the  $\text{Fe}_2\text{O}_3$  boundary, with the floating methyl methacrylate acting as a monomer source.

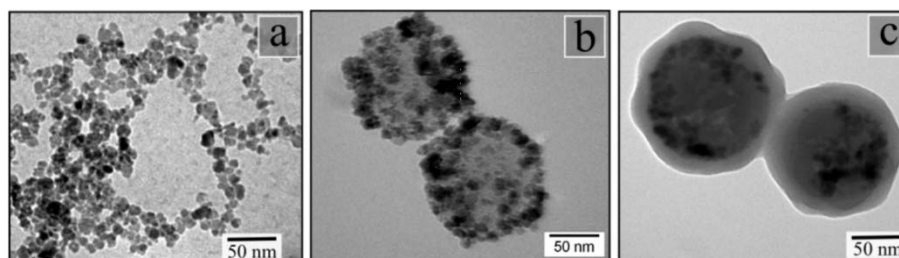


**Figure 5.5** TEM images of (a)  $\text{Fe}_2\text{O}_3$  nanoparticles, (b)  $\text{Fe}_2\text{O}_3$  stabilized MPTMS and (c) multi-layered particles with a poly(MMA) shell.<sup>56</sup>

Bon and co-workers produced multi-layered particles for applications in waterborne coatings and adhesives, to improve properties such as scratch resistance.<sup>57</sup> The multi-layered morphology was achieved by starved-fed seeded emulsion polymerization, where the seed was a silica armoured poly(MMA) latex synthesized by Pickering emulsion polymerization (Figure 5.6 a). Two different morphologies were created by changing the encapsulating monomer; where acrylonitrile was used to create the outer-shell, hairy multi-layered particles were



formed (Figure 5.6 b) and where *n*-butyl acrylate was used, an evenly distributed soft shell was produced (Figure 5.6 c). Surfactant was required in the starved fed process to maintain particle stability; this surfactant can however lead to potentially undesirable properties in waterborne coatings. In the case of the soft poly(BA) shell, slow migration of the silica particles to the outer surface was observed, illustrating a need to lock the inorganic inner-shell in place in soft systems.

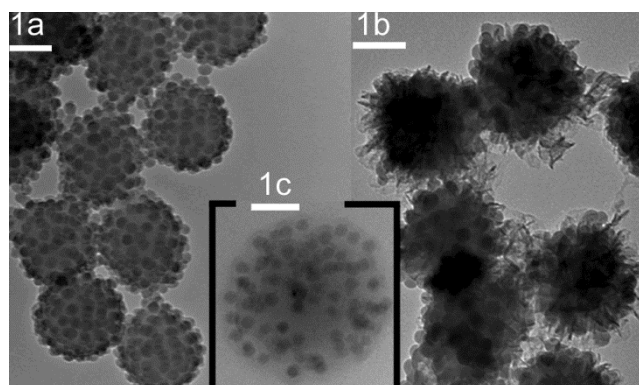


**Figure 5.6** TEM images of (a) silica armoured poly(MMA) latex, (b) hairy outer-layer of poly(acrylonitrile) and (c) a soft shell of poly(BA) (scale bar: 100 nm).<sup>57</sup>

### 5.2.3. Encapsulation of clay particles

Once the clay armoured latex core of a multi-layered particle has been synthesized, we can describe the armoured particle as a clay surface. From this we assume that the encapsulation step to produce a multi-layered morphology is similar to the encapsulation of clay particles. It is therefore important to understand the difficulties faced by encapsulation of clay particles, so that they can be avoided in the synthesis of multi-layered particles.

One encapsulation method that proved successful was the heterocoagulation of oppositely charged particles; small anionic butyl methacrylate latex particles were heterocoagulated onto the larger cationic Gibbsite particles at low solids content (~0.005 wt. %) resulting in encapsulated clay particles with a raspberry-like morphology. A smooth shell was achieved by heating the particles at low



concentration to slightly above the  $T_g$  of the polymer.<sup>58</sup> This method only works for relatively large clay particles, as smaller clays will result in armoured latex particles, due to their relative sizes. The heterocoagulation technique also requires very low solids content to prevent uncontrolled aggregation and several cleaning cycles by centrifugation to remove the unwanted excess latex particles. All-in-all it is an unscalable and time consuming approach.

Encapsulation by *in-situ* polymerization is a more desirable approach as it is easier to scale up and a higher solids content is possible (up to 40 wt.% for batch emulsion polymerization in the presence of Laponite clay has been reported).<sup>30</sup> In an attempt to encapsulate Laponite clay platelets by emulsion polymerization, Bourgeat-Lami *et al.* edge modified the platelets prior to polymerization with vinyl functionalized tri- and mono-functional silanes:  $\gamma$ -methacryloxy propyl trimethoxysilane (MPTMS) (Figure 5.7 1) and  $\gamma$ -methacryloxy propyl dimethyl ethoxysilane (MPDES) (Figure 5.7 2) respectively.<sup>59</sup> Modification with MPTMS resulted in poly-condensates, i.e. flocks of platelets, with a stacked structure which was not observed with the MPDES; the stacked structure was attributed to the presence of more than one functional silylating group binding the clays together. On batch emulsion polymerization with styrene and *n*-butyl acrylate, the Laponite clusters modified with MPTMS showed no interaction with the polymer and those modified with MPDES resulted in an armoured structure where the clay was located on the surface of the particles, typical of a Pickering emulsion polymerization. Thus, batch emulsion polymerization of modified platelets proved an unsuccessful approach for encapsulation.

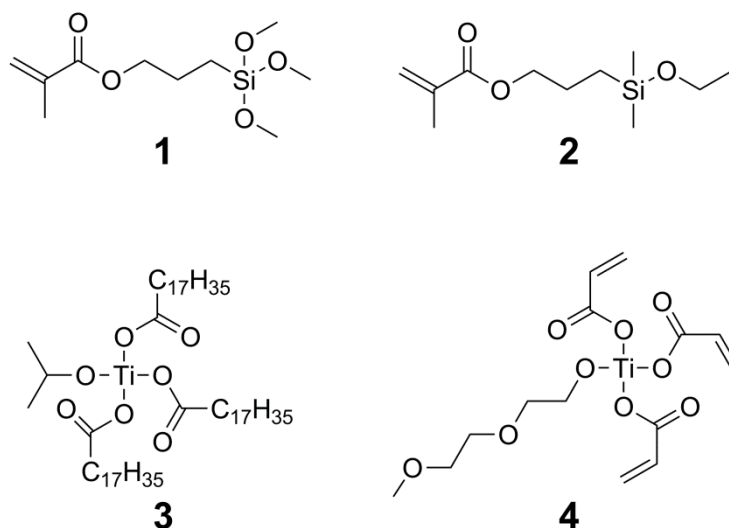


**Figure 5.7** (1) MPTMS, (2) MPDES, (3) KRTTS and (4) isopropyl triacryl titanate.

It was shown by van Herk and co-workers that encapsulation of montmorillonite can be achieved after modification with titanates with and without methacrylate functionality, thus in the latter case the encapsulating polymer was not grafted to the surface of the clay.<sup>60</sup> The titanates used were isopropyl triisostearoyl titanate (KRTTS) (Figure 5.2 3) and isopropyl triacryl titanate (Figure 5.7 4). It is important to note that surfactants (a mixture of anionic sodium dodecylbenzenesulfonate and non-ionic polyethylene glycol tert-octylphenyl ether) were used in these emulsion polymerizations, at concentrations below the CMC. Encapsulation attempts were made with various compositions of methyl methacrylate and *n*-butyl acrylate, to illustrate the effect of  $T_g$  of the encapsulating co-polymer on the encapsulation process. Encapsulation was successful when the monomer was fed under starved conditions and the reaction temperature was below that of the  $T_g$  of the encapsulating co-polymer (i.e. higher methyl methacrylate content compared to *n*-butyl acrylate). When the reaction temperature is above the  $T_g$  of the encapsulating co-polymer (i.e. higher *n*-butyl acrylate content compared to methyl methacrylate), the clay was found on the surface of polymer particles, suggesting migration of the clay through the polymer.<sup>60</sup> van Herk and co-workers

have also shown Laponite and montmorillonite platelets modified with methacrylate containing silanes and titanates can be successfully encapsulated in poly(methyl methacrylate) under surfactant-free conditions.<sup>61</sup> The polymerization was conducted under starved-fed conditions and the temperature was below the  $T_g$  of poly(methyl methacrylate). In this case, encapsulation of the smaller Laponite clay produced spherical particles (Figure 5.8 a) and the encapsulation of the larger montmorillonite resulted in dumbbell shaped particles with the clay located between the two spheres (Figure 5.8 b). It was noted that though encapsulated particles were observed, it could not be determined whether all the polymer particles contained encapsulated clay particles due to the thin nature of Laponite and thus the difficulty in visualising it face on by TEM.<sup>61</sup>

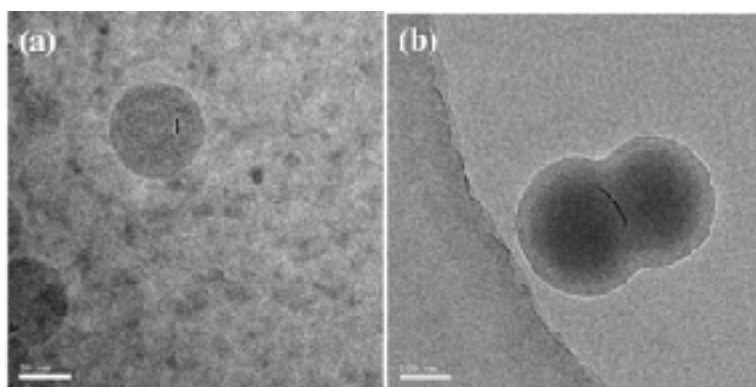


**Figure 5.8** Cryo-TEM image of poly(MMA) particles containing (a) Laponite (scale bar: 50 nm) and (b) montmorillonite (scale bar: 100 nm).<sup>61</sup>

#### 5.2.4. Laponite clay

The choice of clay is a very important consideration, as size and dispersibility are key factors in Pickering emulsion polymerizations. Various types of natural and synthetic clays exist; the clay chosen for this body of work was Laponite XLS as its use as a Pickering stabilizer is established.<sup>32, 34, 36, 43</sup> Laponite XLS is a synthetic hectorite clay of dimensions 25 nm in diameter and 0.92 nm thick. The crystal lattice consists of an octahedral sheet of magnesia fused between two tetrahedral silica

sheets, where the tip of the oxygen ions of the octahedral sheet also belongs to the tetrahedral sheet (Figure 5.9).<sup>62</sup> Laponite clay has the formula  $[(\text{Si}_8\text{Mg}_{5.5}\text{Li}_{0.3})\text{O}_{20}(\text{OH})_4]\text{Na}_{0.7}$ ; where some of the divalent magnesium ions are substituted with monovalent lithium ions, resulting in the particles having an overall negative charge which is quenched by  $\text{Na}^+$  ions adsorbed to the edges.<sup>63</sup> The XLS grade has tetrasodium pyrophosphate (Figure 5.10) adsorbed to the  $\delta^+$  edges in order to aid dispersion in water. The edges of the discs also exhibit reactive hydroxyl groups in the form of Si-OH, Mg-OH and Li-OH. Full dispersion of the XLS grade (also described as exfoliation), where the individual clay platelets are completely separated, is achieved through vigorous stirring in water for a minimum of 10 minutes.<sup>64</sup>

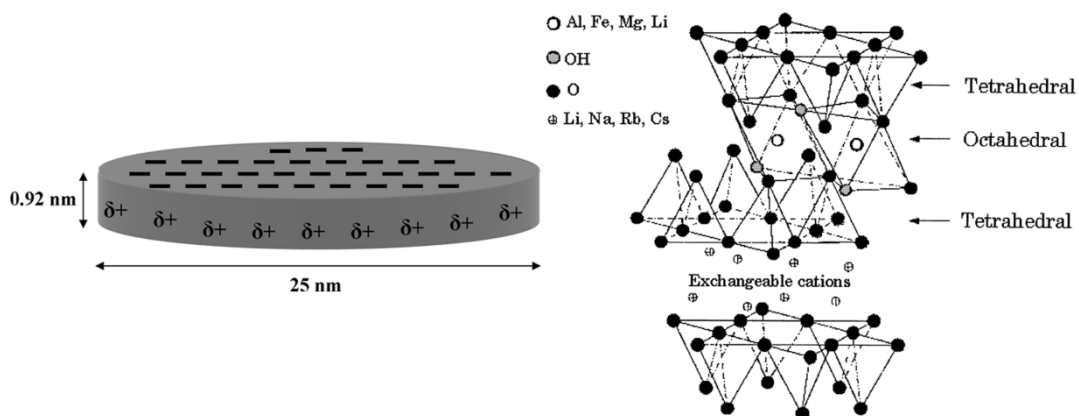


**Figure 5.9** (Left) Single Laponite particle, (right) structure of Laponite.<sup>62</sup>

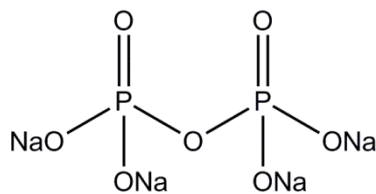


**Figure 5.10** Tetrasodium pyrophosphate; used to edge modify Laponite clay discs to aid dispersion.

Herein we describe a one-pot free-radical polymerization synthesis of multi-layered particles consisting of a soft polymer core, Laponite clay inner-shell and a soft polymer outer-shell. We intend to use Pickering emulsion polymerization to

synthesize a seed, which on encapsulation will yield multi-layered particles. Immobilization of the clay will be a vital step in order to overcome migration of the inner-shell through the soft outer-shell medium. The mechanical and thermal properties will be studied to investigate the effect of particle morphology in thin films.

## 5.3. Results and Discussion

### 5.3.1. Synthesis of armoured and multi-layered particles

Laponite armoured soft latex particles (HM-502) were synthesized by a typical Pickering emulsion polymerization;<sup>43</sup> 2.0 g of Laponite discs were dispersed in 180 g of water by stirring at 250 rpm, the mixture was then degassed for 20 minutes by purging with nitrogen, 20 g of a styrene and *n*-butyl acrylate mixture (40:60 wt. %) was introduced and the mixture was degassed for a further 5 minutes after which it was heated to 70 °C, stirred at 250 rpm and initiated by 0.15 g ammonium persulfate dissolved in 1.0 g water. Monomer conversion was followed by gravimetry, particle size was determined by DLS and particle morphology was determined by cryo-TEM.

The monomer conversion vs. time plot (Figure 5.11) showed the typical sigmoidal curve for an emulsion polymerization, which can be described by splitting it into three intervals.<sup>65</sup> (1) Nucleation period, the rate of reaction is increasing due to increasing particle number; this describes the first (non-linear) section of the plot. (2) Rate of reaction is constant, producing the linear section of the plot, as the number of particles is constant and monomer droplets behave as reservoirs. (3) Monomer droplets have been exhausted; all monomer is found in the latex particles, the concentration of monomer decreases with time, explaining the decrease in the rate of polymerization. It is important to note however, that an increase in rate in the final stage often occurs due to the Trommsdorff-Norrish effect.<sup>66</sup>

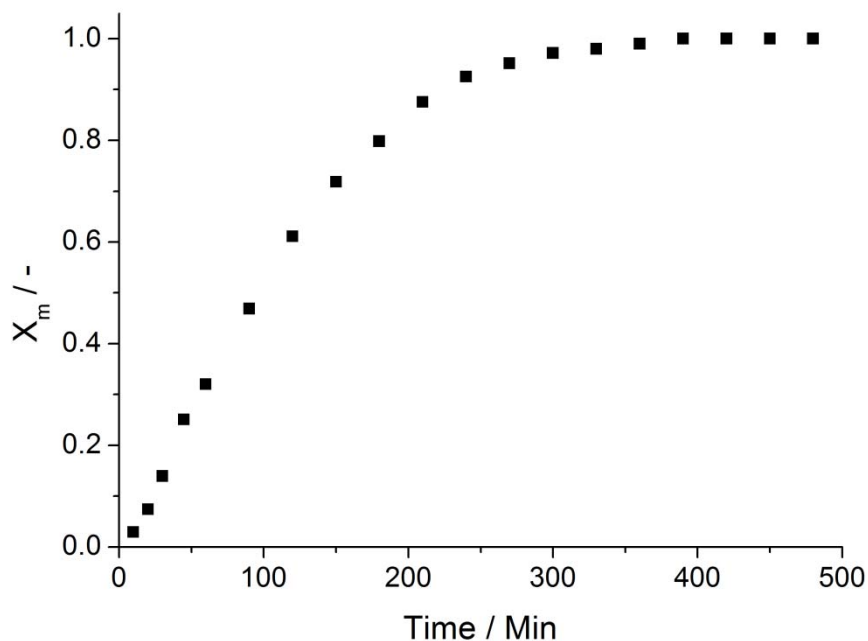


**Figure 5.11** Overall monomer conversion,  $X_m$ , versus time of Laponite armoured poly(Sty-co-BA) particles (HM-502).

When we assume that the number of latex particles stays constant, average particle size ( $d_z$ ) vs. monomer conversion should show 3<sup>rd</sup> order dependence (ignoring monomer swelling). This relation occurs because the conversion scales to mass, which scales to volume, and volume scales to  $d_z^3$ . Such behaviour was observed here, as the plot of  $d_z^3$  vs. monomer conversion shows a linear fit with an  $R^2$  value of 0.998 (Figure 5.12 a). The narrow particle size distribution suggests that nucleation period is fast compared to particle growth (Figure 5.12 b), where the initial broad dispersity is a result of the nucleation period, once complete (i.e. interval 2 has begun) the dispersity narrows.<sup>65</sup>

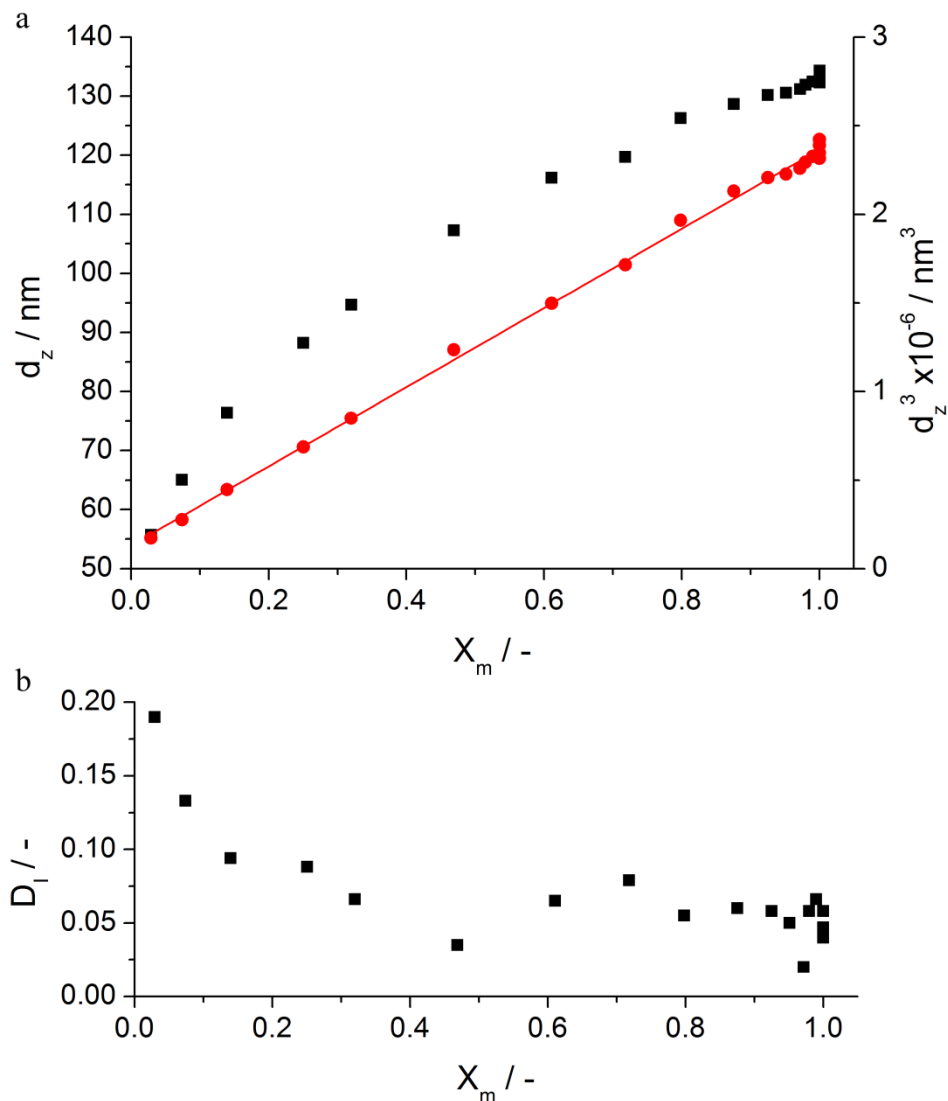


**Figure 5.12** (a) Average particle diameter,  $d_z$  (■) and  $d_z^3$  (●), and (b) dispersity,  $D_i$ , versus monomer conversion,  $X_m$ , of Laponite armoured poly(Sty-*co*-BA) particles (HM-502).  $R^2$  for linear fit of  $d_z^3$  is 0.998.

Cryo-TEM images clearly show that the morphology is indeed that of Laponite armoured latex particles (Figure 5.13); dark lines are observed around the edges of the spherical polymer particles, these are Laponite discs. The discs can only be observed when their basal plane is parallel to the electron beam, as they are too thin to be detected by TEM face on, thus can only be observed around the edges of the particles. For clarity, we show that these lines are not observed for the plain poly(styrene-*co*-*n*-butyl acrylate) latex particles (Figure 5.14).



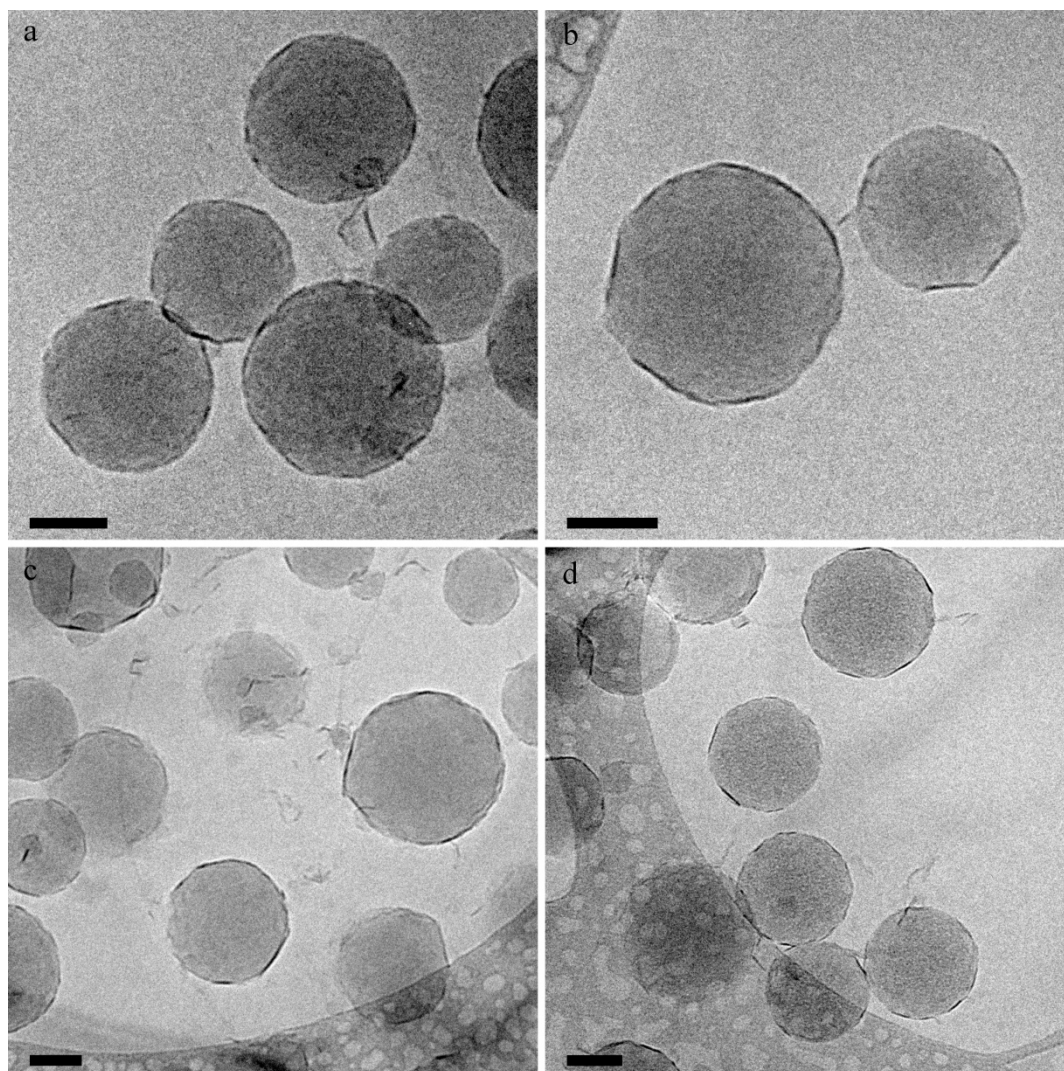


**Figure 5.13** Cryo-TEM images of Laponite armoured poly(Sty-co-BA) particles (HM-502) (scale bar: 50 nm).

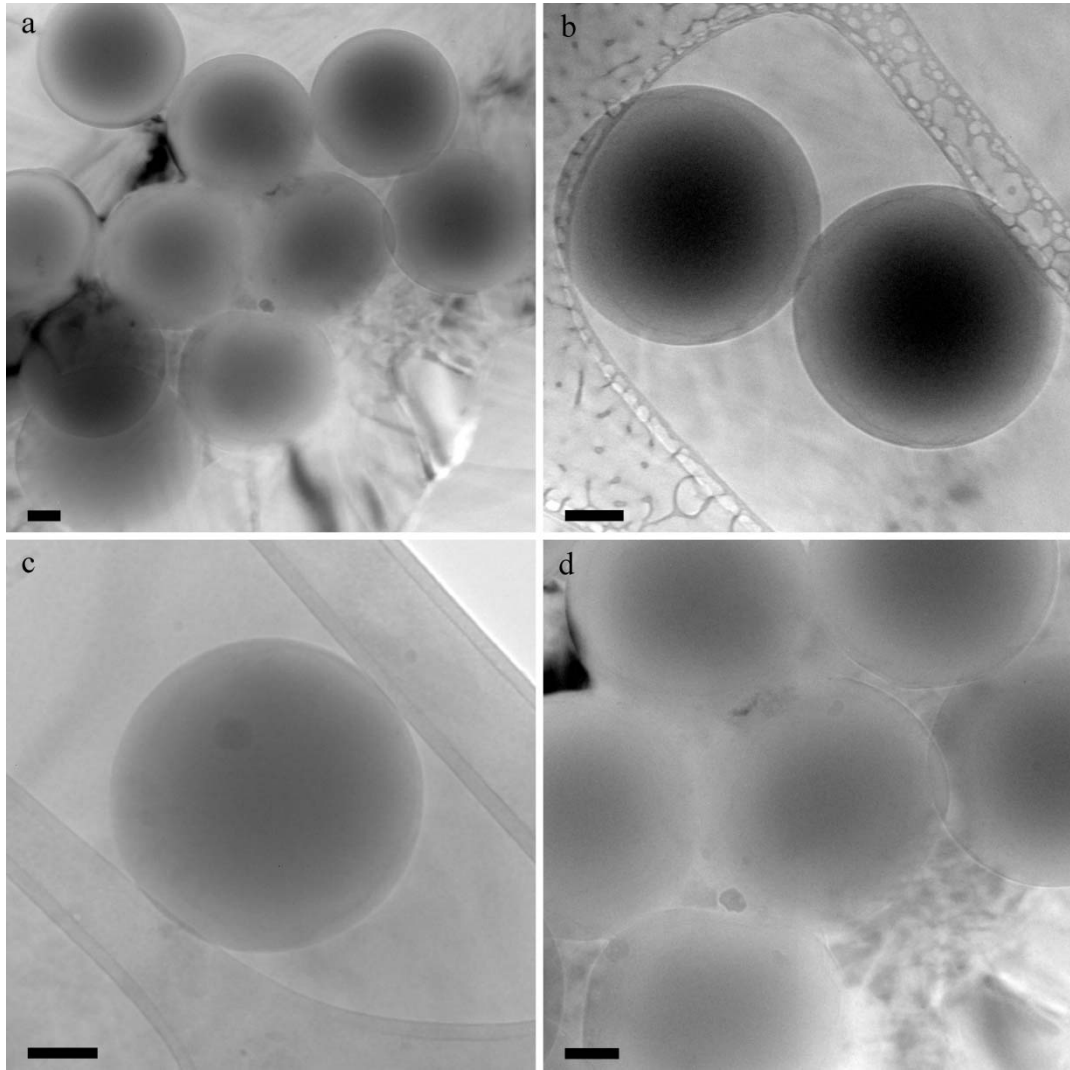


**Figure 5.14** Cryo-TEM images of poly(Sty-co-BA) particles (HM-501) (scale bar: 100 nm).

It is important to note that there is an excess of Laponite in the continuous phase of the Laponite Pickering emulsion polymerization, the amount of which can be calculated.<sup>36</sup> The total concentration of Laponite is the sum of the concentration of Laponite on the surface of the polymer particles and the concentration of the excess Laponite in the continuous phase.

$$C_0 = C_{surf} + C_{excess} \quad (5.1)$$

Where  $C_0$  is the overall concentration of Laponite in water ( $\text{g g}^{-1}$ , i.e.  $m_0/m_{\text{water}}$  where  $m$  is mass),  $C_{surf}$  is the concentration of Laponite on the surface of the polymer particles with respect to the water phase ( $\text{g g}^{-1}$ , i.e.  $m_{\text{surf}}/m_{\text{water}}$ ) and  $C_{excess}$  is the excess concentration of Laponite that remains in the continuous phase

(g g<sup>-1</sup>, i.e.  $m_{\text{excess}}/m_{\text{water}}$ ). The total concentration of Laponite is known, thus an expression defining the concentration of Laponite on the surface of the polymer particles ( $C_{\text{surf}}$ ) is required. In calculating  $C_{\text{surf}}$  we need to make some assumptions; (1) the total surface of the polymer particles are covered in a monolayer of Laponite discs, (2) the polymer particles and Laponite particles are uniform in size, (3) the dimensions of the Laponite discs are negligible with respect to the size of the polymer particles, i.e. we assume that the surface of the polymer particle is flat, thus the Laponite discs will lie flat and (4) a function for the packing of the Laponite discs is required, in this case we assume 2D square packing.

The interfacial area of one polymer particle ( $a_{\text{part}}$ ) is defined as:

$$a_{\text{part}} = 4\pi r_{\text{part}}^2 \quad (5.2)$$

Where  $r_{\text{part}}$  is the radius of the polymer particle. The area covered by one Laponite disc ( $a_{\text{Lap}}$ ) is defined as:

$$a_{\text{Lap}} = \pi r_{\text{Lap}}^2 \quad (5.3)$$

Where  $r_{\text{Lap}}$  is the radius of a Laponite disc. The total number of polymer particles ( $N_{\text{part}}$ ) is defined as the total volume of polymer divided by the volume of one polymer particle:

$$N_{\text{part}} = \frac{\frac{m_{\text{part}}}{\rho_{\text{part}}}}{\frac{4}{3}\pi r_{\text{part}}^3} \quad (5.4)$$

Where  $m_{\text{part}}$  is the total mass of polymer and  $\rho_{\text{part}}$  is the density of the (co)polymer. The total number of Laponite discs adhered to the water-polymer interface ( $N_{\text{Lap}}$ ) is defined as the volume of Laponite on the polymer-water interface divided by the volume of one Laponite disc:

$$N_{Lap} = \frac{\frac{m_{surf}}{\rho_{Lap}}}{\pi r_{Lap}^2 h} \quad (5.5)$$

Where  $m_{surf}$  is the mass of Laponite adhered to the polymer particle surface,  $\rho_{Lap}$  is the density of Laponite and  $h$  is the height of one Laponite disc. If complete coverage is assumed then the following relationship applies:

$$\frac{\pi}{4} N_{part} a_{part} = N_{Lap} a_{Lap} \quad (5.6)$$

The  $\pi/4$  term is the packing parameter for 2D square packing of circles, the term changes to  $\pi/(2\sqrt{3})$  if we assume hexagonal packing. Substituting equations (5.2) – (5.5) into equation (5.6) and rearranging gives the amount of Laponite adhered to the polymer-water interface ( $m_{surf}$ ):

$$m_{surf} = \frac{3\pi}{4} \left( \frac{\rho_{Lap}}{\rho_{part}} \right) \left( \frac{h}{r_{part}} \right) m_{part} \quad (5.7)$$

Equation (5.7) can be inserted into equation (5.1) to give the concentration of excess Laponite:

$$C_{excess} = C_0 - \frac{3\pi}{4} \left( \frac{\rho_{Lap}}{\rho_{part}} \right) \left( \frac{h}{r_{part}} \right) C_{part} \quad (5.8)$$

The following values were used to calculate the concentration of excess Laponite in HM-502;  $C_0 = 0.0099 \text{ g g}^{-1}$ ,  $\rho_{Lap} = 2570 \text{ kg m}^{-3}$ ,  $\rho_{part} = 1050 \text{ kg m}^{-3}$ ,  $h = 0.92 \times 10^{-9} \text{ m}$ ,  $r_{part} = 65.95 \times 10^{-9} \text{ m}$ ,  $C_{part} = 0.0990 \text{ g g}^{-1}$ . The concentration of excess Laponite was found to be:

$$C_{excess} = 0.0019 \text{ g g}^{-1} \quad (5.9)$$

From this the mass of excess Laponite in the continuous phase is calculated to be 0.3910 g which is 19.6 wt.% of the total Laponite content.

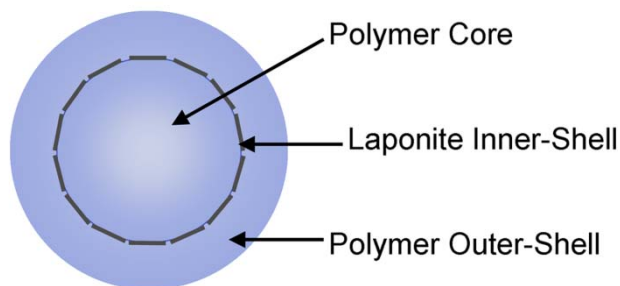


**Figure 5.15** Scheme illustrating multi-layered particle morphology.

In order to prepare multi-layered particles where the clay forms the inner shell (Figure 5.15) the preference of the clay particles to remain at the polymer-water interface must be overcome. The platelets must be kinetically trapped between the two polymeric regions (the core and outer shell); an obvious method to achieve this is to immobilize the clay, thus limiting its movement. If the clay is not immobilized migration to the surface will occur.<sup>57, 67</sup>

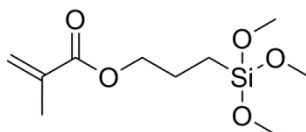


**Figure 5.16** 3-(trimethoxysilyl) propyl methacrylate (MPTMS).

The modification of clay particles by silanes has been well documented, in particular multifunctional silanes such as MPTMS (Figure 5.16) where the silane reacts with the Si-OH groups on the edges of the clay platelets (Figure 5.17).<sup>63, 68, 69</sup> Silanes have previously been used in this manner to immobilize a monolayer of Laponite on the surface of polymer particles, illustrated by removing the core to achieve hollow Laponite particles.<sup>8</sup> When MPTMS has been used to bind to Laponite dispersed in water small aggregates are formed, where the Laponite appears to be stacked; illustrating that multi-functional silanes can bind multiple Laponite discs together.<sup>59</sup> MPTMS was chosen as the agent to immobilize the clay as its reaction with Laponite clay is established and the multiple silylating groups could



link neighbouring clay platelets together, and potentially even scoop up the excess Laponite present in the aqueous phase.

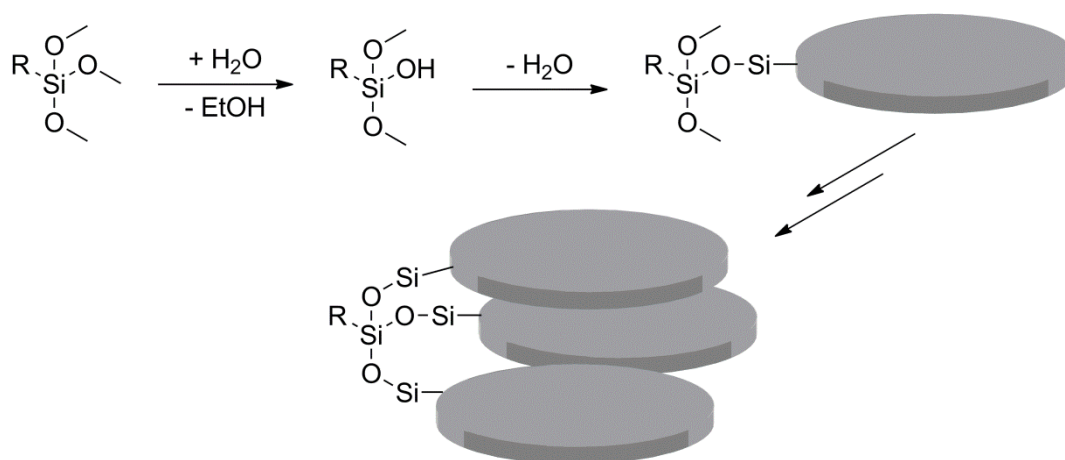


**Figure 5.17** Scheme illustrating the reaction of MPTMS and Laponite in water and potential to react with more than one Laponite disc.

On introduction of MPTMS the presence of a small amount of monomer was desired, as the MPTMS would not only bind to neighbouring Laponite particles but would also have the potential to increase binding through the presence of multiple MPTMS units on a poly(styrene-*co*-*n*-butyl acrylate) chain, thereby immobilizing the Laponite discs on the surface of the polymer particles. The hydrolysis of MPTMS is fast, for studies in water in the concentration range of 0.042-0.168 M at pH 9 the half-life was found to be in the order milliseconds.<sup>70, 71</sup> We intended to introduce MPTMS at approximately 95 % monomer conversion; from the monomer conversion vs. time plot of the Laponite armoured poly(styrene-*co*-*n*-butyl acrylate) reaction (Figure 5.11) conversion reaches approximately 95 % at 6 hours ( $t_6$ ).

We have shown that there is an excess of Laponite in the system (19.6 wt.% with respect to total Laponite content), that is Laponite not associated with the surface of the particles (equation (5.8)). We believed that MPTMS, with its three silylating groups could react with Laponite on the surface of the particles and the excess Laponite in the continuous phase to form stacks similar to those observed by

Bourgeat-Lami and co-workers when they pre-modified Laponite platelets with MPTMS.<sup>59</sup> The ability for the Laponite to form stacks could potentially result in a second patchy layer of Laponite around the soft core producing a new morphology (herein described as core-shell) (Figure 5.18). We define this potential second layer of Laponite as patchy as the 19.6 wt.% excess of Laponite is not enough to completely cover all particles.

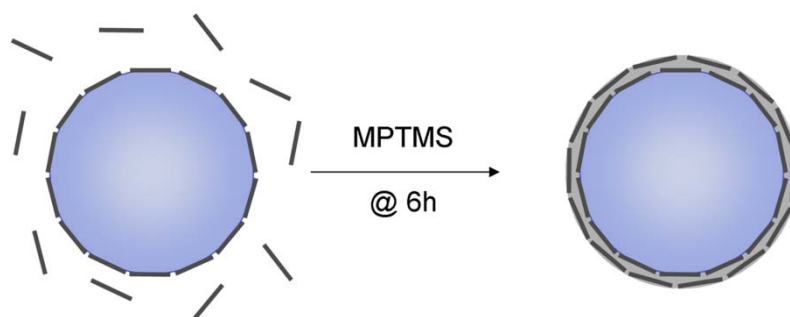


**Figure 5.18** Scheme depicting effect of MPTMS on particle morphology of Laponite armoured poly(Sty-*co*-BA) particles.

At 6 hours ( $t_6$ ) 0.10 g of MPTMS (0.5 wt.% with respect to monomer, 2.83 mM with respect to water) was introduced to the Pickering emulsion polymerization by shot addition. Monomer conversion vs. time plot for HM-503 is comparable to that of HM-502; the slight decrease in reaction rate at high conversion for HM-503 is likely due to the presence of a small amount of oxygen gained during sampling as it is not present early on in the polymerization (Figure 5.19). The conversion plot shows that at the time MPTMS was introduced the monomer conversion was ~95 % as desired, thus the MPTMS methacrylate group would likely copolymerize with the remaining monomer as anticipated.

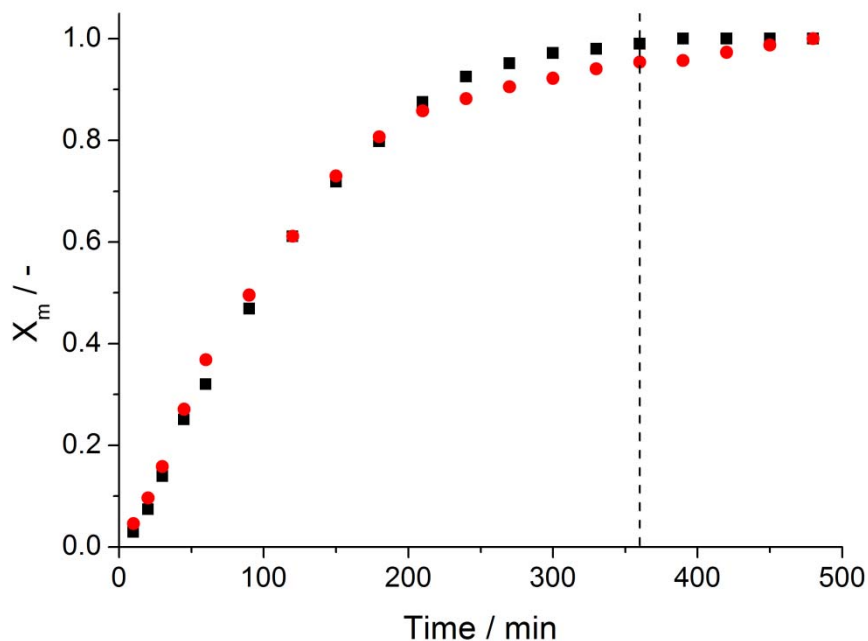


**Figure 5.19** Overall monomer conversion,  $X_m$ , versus time for Laponite armoured poly(Sty-co-BA) particles (HM-502) (■) and the same polymerization reaction with MPTMS (0.1 g) added at  $t_6$  (HM-503) (●). The dashed line indicates the time at which 0.1 g MPTMS was added to the reaction.

Again a linear fit ( $R^2 = 0.996$ ) was found for the plot of  $d_z^3$  vs. monomer conversion, suggesting that particle growth occurs with no secondary nucleation (Figure 5.20 a). The particle size distribution is narrow, and remains so after the shot addition of MPTMS (Figure 5.20 b). The introduction of MPTMS at  $t_6$  appears to have had very little, if any, effect on the particle size or particle size distribution (Figure 5.20).



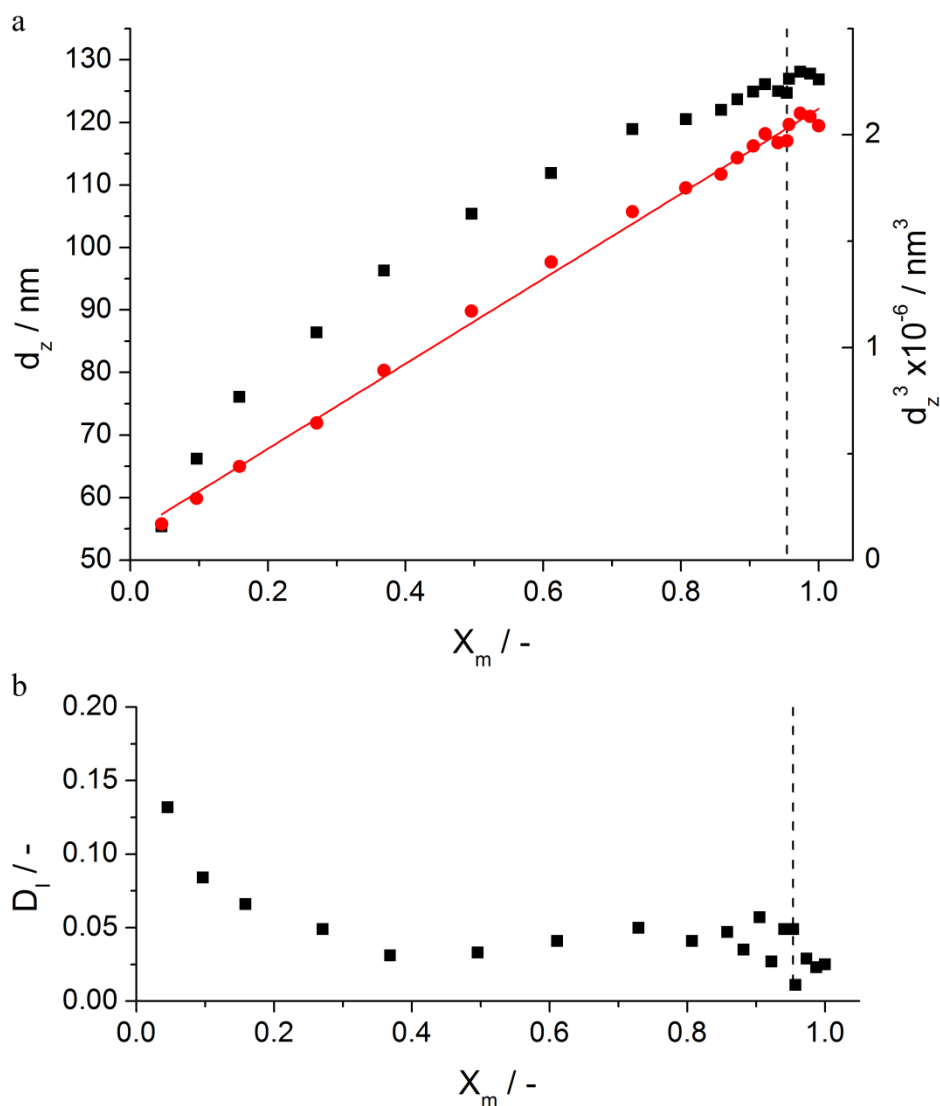


**Figure 5.20** (a) Average particle diameter,  $d_z$  (■) and  $d_z^3$  (●), and (b) dispersity,  $D_i$ , versus monomer conversion,  $X_m$ , of Laponite armoured poly(Sty-*co*-BA) where of MPTMS has been added at  $t_6$  (HM-503). The dashed line indicates the time at which 0.1 g MPTMS was shot added to the reaction.  $R^2$  for linear fit of  $d_z^3$  is 0.996.

Analysis by cryo-TEM shows the particles to have a core-shell morphology, where it appears as though there is a shell consisting of a double layer of Laponite and poly(MPTMS) around the poly(styrene-*co*-*n*-butyl acrylate) core (Figure 5.21). Thus it seems that the introduction of MPTMS effectively scoops up the excess Laponite, by a heterocoagulation method, forming a patchy second Laponite shell which is logical as there is approximately 19.6 wt.% excess of Laponite calculated for HM-501. In alkaline solutions (reaction pH at point of introduction of MPTMS is

pH 9.4) highly cross-linked inorganic networks of MPTMS are known to be formed which are not observed in acidic conditions.<sup>72, 73</sup> However, by keeping the concentration of MPTMS low (0.5 wt.% with respect to total monomer content) the likelihood of MPTMS reacting at the surface of the armoured particles rather than with itself in the continuous phase is increased. We previously suggested that MPTMS could copolymerize with the remaining monomer and copolymerization of MPTMS with styrene and methyl methacrylate have been reported.<sup>74-76</sup> However, a preference for blocks of MPTMS interrupted with co-monomer units was found; random copolymers were only produced by reducing the concentration of MPTMS with respect to the copolymer.<sup>77-79</sup> At the point of introduction of MPTMS monomer conversion is 95%, thus the concentration of MPTMS with respect to remaining monomer is ~9%, therefore it is likely the shell is not pure Laponite bound with MPTMS, but blocks of poly(MPTMS) partitioned along a poly(styrene-*co*-*n*-butyl acrylate) chain (Figure 5.19).

This method proposes an interesting means of removing excess Laponite from the continuous phase, which cannot be removed by conventional purifying processes such as dialysis or centrifugation. It appears that Laponite is present below the surface of the composite particle suggesting that the Laponite has been immobilized as desired within this composite shell.

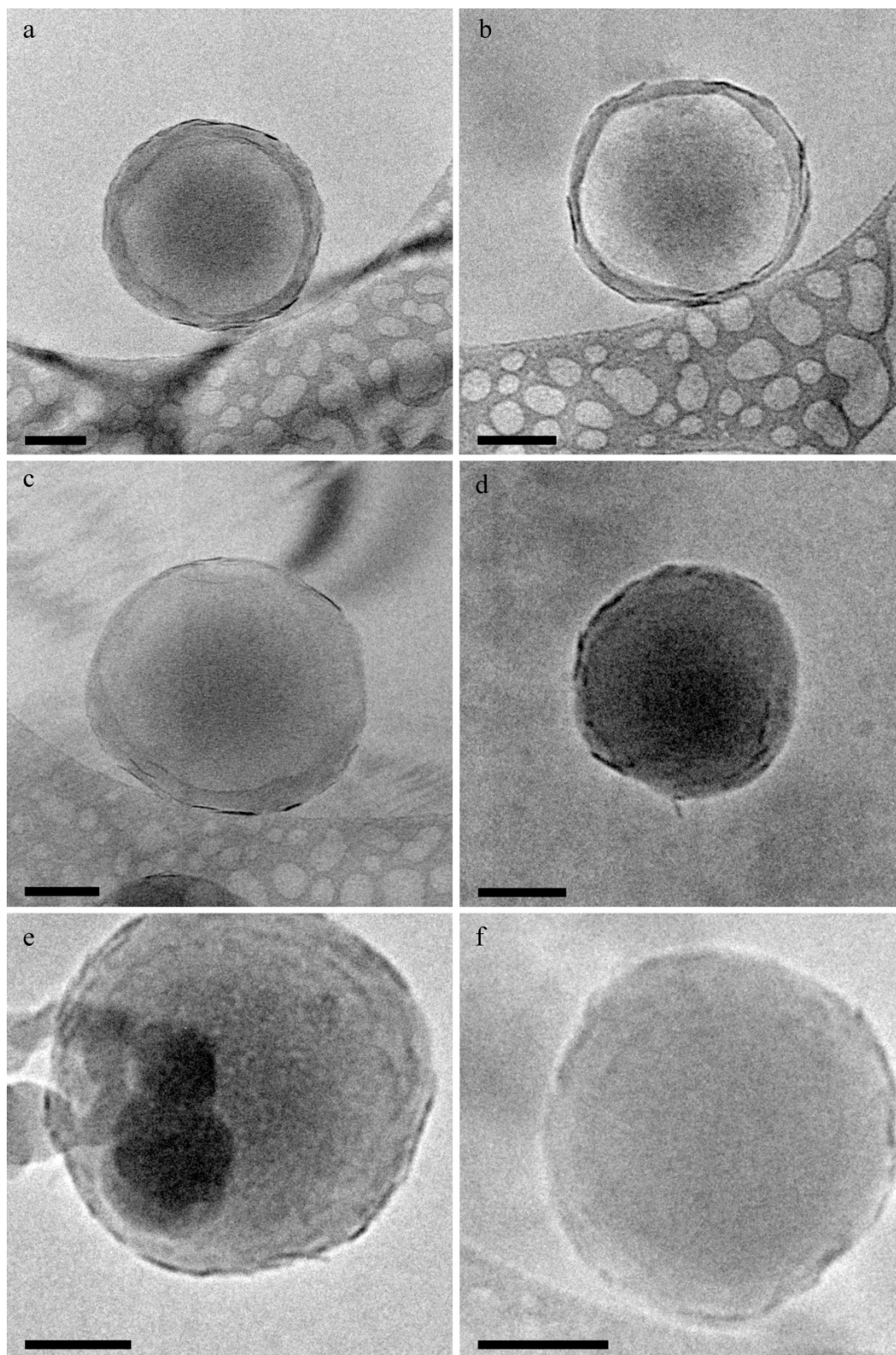


**Figure 5.21** Cryo-TEM images of Laponite armoured poly(Sty-co-BA) where MPTMS is added at  $t_6$  (scale bar: 50 nm) (BL-067). It appears as though particles have core-shell morphology with a double layer of Laponite in the “shell”.

A secondary experiment was conducted where MPTMS was introduced on initiation ( $t_0$ ) to determine whether this would lead to encapsulated clay platelets. By introducing MPTMS on initiation it was thought that the Laponite would not have time to form clusters as have been previously observed<sup>59</sup> and would become trapped within the polymer matrix. A typical Laponite Pickering emulsion polymerization was conducted where 0.10 g MPTMS (0.5 wt.% with respect to monomer) was added on initiation. Monomer conversion vs. time plot for HM-504 is comparable in shape to that of HM-502 and HM-503, however, the rate of polymerization appears to be much faster (Figure 5.22). The increased rate could be explained in terms of modification of the Laponite discs; on introduction of MPTMS hydrolysis followed by condensation with Laponite edges occurs, effectively hydrophobically modifying the clay discs, this results in a greater number of polymer particles in order to stabilize the modified clay discs, the increased particle number increases the rate of polymerization. To investigate further particle size needs to be considered.

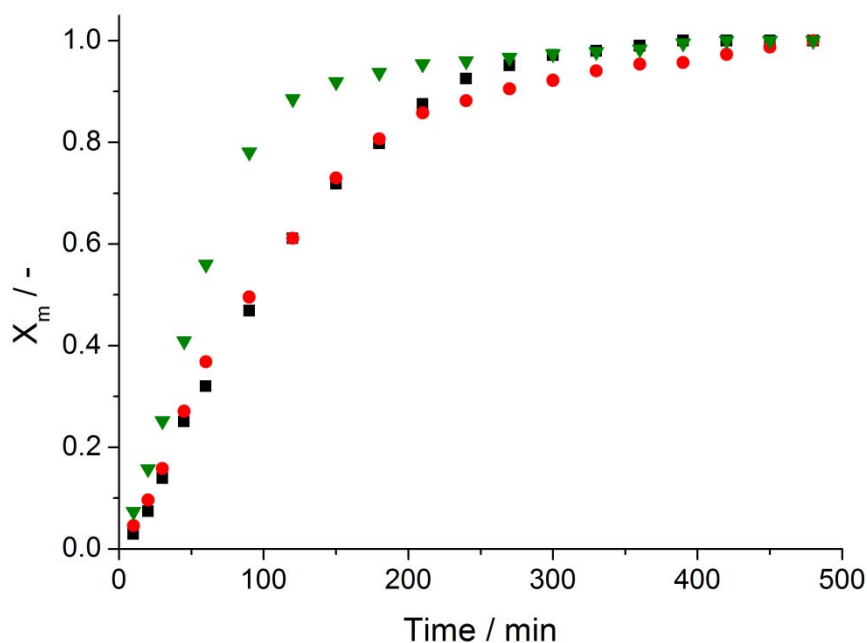


**Figure 5.22** Overall monomer conversion,  $X_m$ , versus time for Laponite armoured poly(Sty-co-BA) (HM-502) (■) and the same polymerization reaction with MPTMS (0.1 g) added at  $t_6$  (HM-503) (●) and with the MPTMS added at  $t_0$  (HM-504) (▼).

The final particle size for HM-504 is 160.2 nm, this is significantly larger than the particle sizes found for HM-502 and HM-503 (131.9 and 126.9 nm respectively), thus the hypothesis that there is a greater number of particles doesn't add up (Figure 5.23a). The plot of  $d_z^3$  vs. monomer conversion shows a slight deviation from linearity with  $R^2=0.986$  suggesting that particle size isn't increasing as would be expected (Figure 5.23a). These factors combined with a broader size dispersity ( $D_1 = 0.059$ ), suggests that further investigation is required into the morphology to determine the cause of increased particle size and increased rate of reaction.

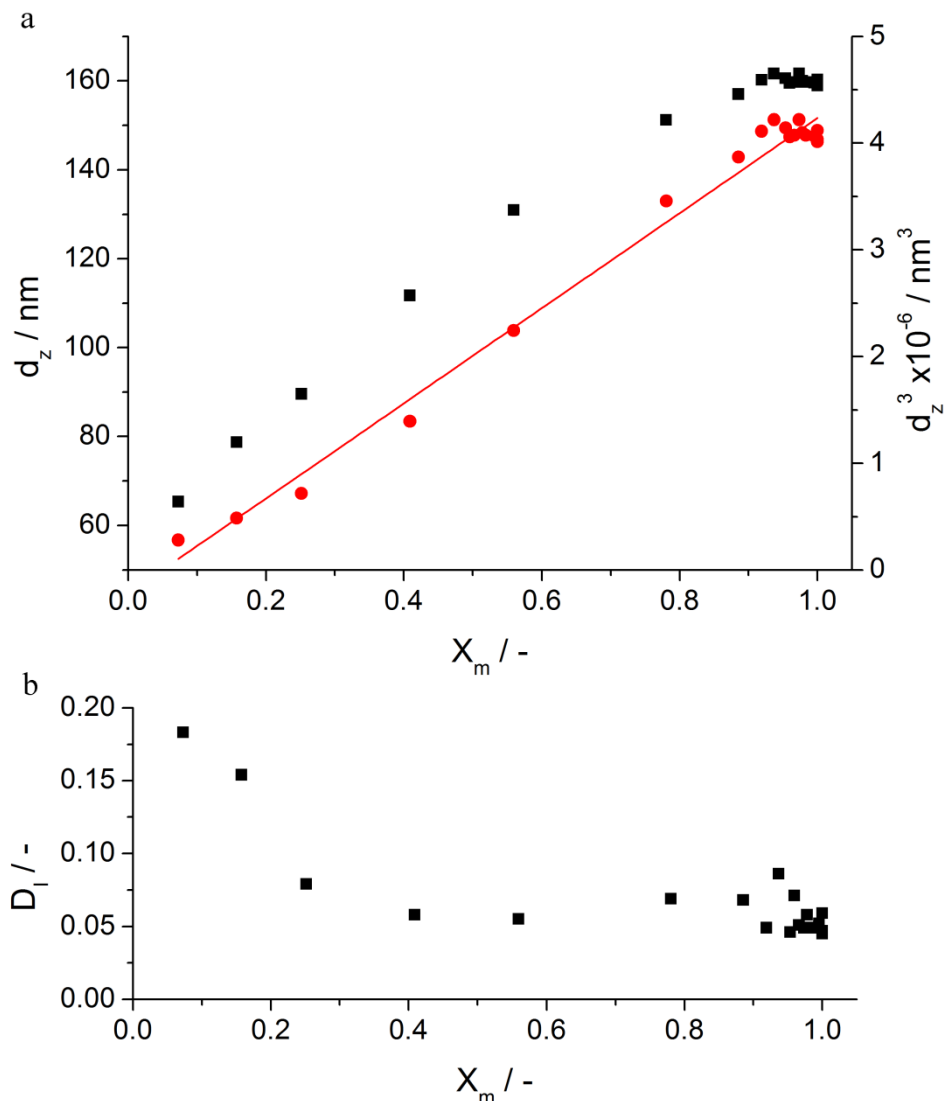


**Figure 5.23** (a) Average particle diameter,  $d_z$  (■) and  $d_z^3$  (●), and (b) dispersity,  $D_i$ , versus monomer conversion,  $X_m$ , of Laponite armoured poly(Sty-*co*-BA) particles where MPTMS is added at  $t_0$  (HM-504).  $R^2$  for linear fit of  $d_z^3$  is 0.986.

Cryo-TEM analysis shows that the polymer particles are armoured in clay discs in the same manner as HM-502 and HM-503, however, the odd Laponite particle can be observed within the polymer matrix, resulting in a dumbbell morphology (Figure 5.24). The formation of dumbbells explains the larger than expected particle size, deviation from linearity of the  $d_z^3$  vs.  $X_m$  plot and the broad particle size distribution. Thus the hypothesis that the increased rate in reaction observed could still be attributed to an increased number of particles formed due to hydrophobic modification of the Laponite clay. Dumbbell morphologies have

previously been reported in the encapsulation of clays and have been attributed to the clay preventing uniform growth of the polymer particle.<sup>34, 61</sup> As expected stacks of Laponite on modification with MPTMS observed by Bourgeat-Lami and co-workers were not found in this case, likely due simultaneous initiation of polymerization and MPTMS addition resulting in a reduced possibility of clay-clay interaction.<sup>68</sup> It is difficult to fully qualify the amount of clay encapsulated within the particles as only those with their basal plane parallel to the electron beam are visible, nevertheless as the particles surface appears to be fully coated in Laponite it is likely that this is the location for the bulk of Laponite and thus this method did not work as an encapsulating technique as anticipated.



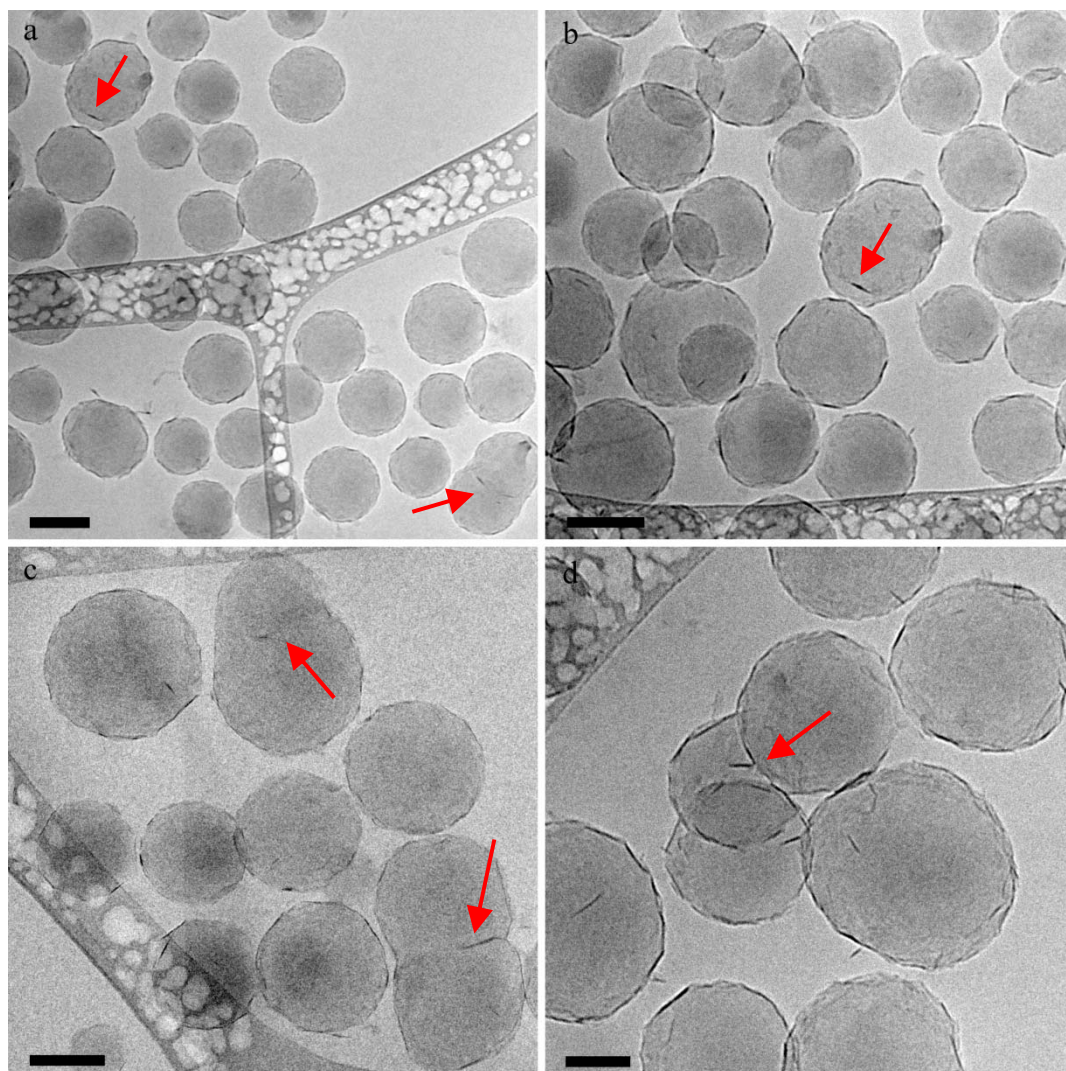


**Figure 5.24** Cryo-TEM images of Laponite armoured poly(styrene-*co-n*-butyl acrylate) with MPTMS added at  $t_0$  (scale bar a-c: 100 nm; scale bar d: 50 nm) (BL-050). Dumbbell shaped particles are highlighted by the red arrows.

As discussed above, it appeared that the introduction of MPTMS at  $t_6$  (HM-503) immobilized the Laponite clay on the surface of the polymer particles, thus an attempt was made to form multi-layered particles where a Laponite ring forms the inner-shell (Figure 5.25). Multi-layered particles were synthesized as follows; a typical Laponite Pickering emulsion polymerization with 40:60 ratio of styrene and *n*-butyl acrylate was performed, at  $t_6$  0.10 g MPTMS was introduced by shot addition, at  $t_7$  20 mL of a 40:60 wt.% mixture of styrene and *n*-butyl acrylate were fed into the reaction mixture at  $2.5 \text{ mL h}^{-1}$  without any dilution (HM-505).



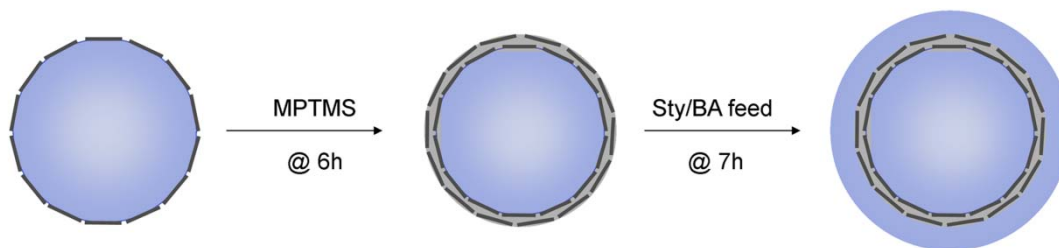


**Figure 5.25** Scheme depicting steps to form multi-layered particles.

Starved-fed emulsion polymerization is where the polymerization rate is controlled by the feed rate of monomer, so that the rate of polymerization equals the feed rate.<sup>80</sup> The starved condition under which the monomer was introduced was required to encourage encapsulation. Monomer conversion vs. time plots show that during the feed of the styrene *n*-butyl acrylate mixture conversion is consistently at approximately 90 %, (Figure 5.26), where the blue line represents zero conversion of the monomer feed. As the polymerization reaches 100% conversion after being left over night (1440 minutes) monomer evaporation is not the cause for the lower than expected conversion. The reaction was repeated with a slower monomer feed rate of  $1.5 \text{ mL h}^{-1}$ ; the same reduced conversion was observed, in this case however the reaction coagulated after 9 mL of monomer was fed into the reaction (6 hours), at which point samples could not be taken (Figure 5.27).

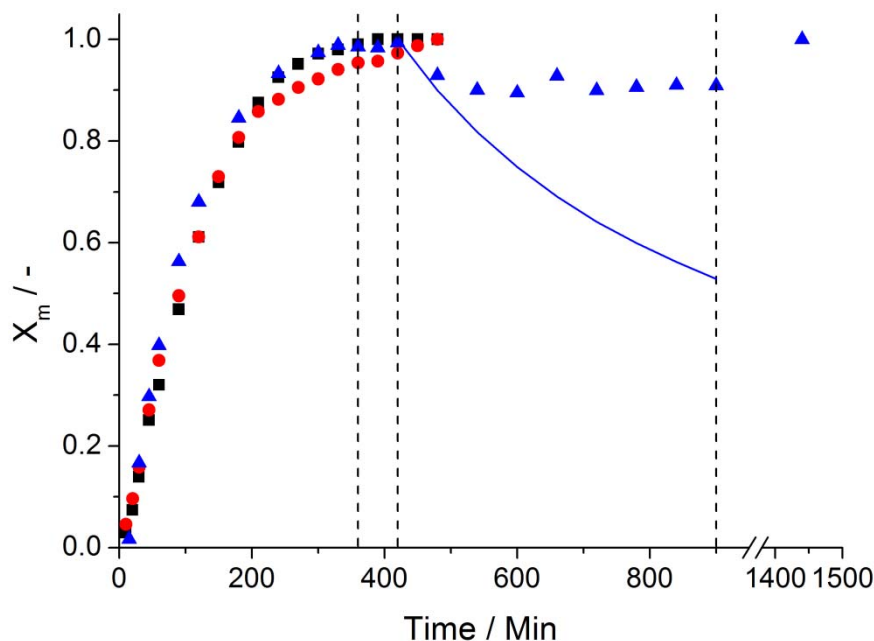


**Figure 5.26** Overall monomer conversion,  $X_m$ , versus time for Laponite armoured poly(Sty-co-BA) (HM-502) (■), the same polymerization reaction but where MPTMS (0.1 g) was added at  $t_6$  (HM-503) (●) and the multi-layered particles (HM-505) (▲). The dashed line at 360 minutes indicates the shot addition of 0.1 g MPTMS, the dashed line at 420 minutes indicates the beginning of encapsulating feed of styrene and *n*-butyl acrylate and the dashed line at 900 minutes indicates the end of the monomer feed. The blue line (—) represents the 0 % conversion line during the monomer feed. Monomer was fed at a rate of 2.5 mL h<sup>-1</sup>.

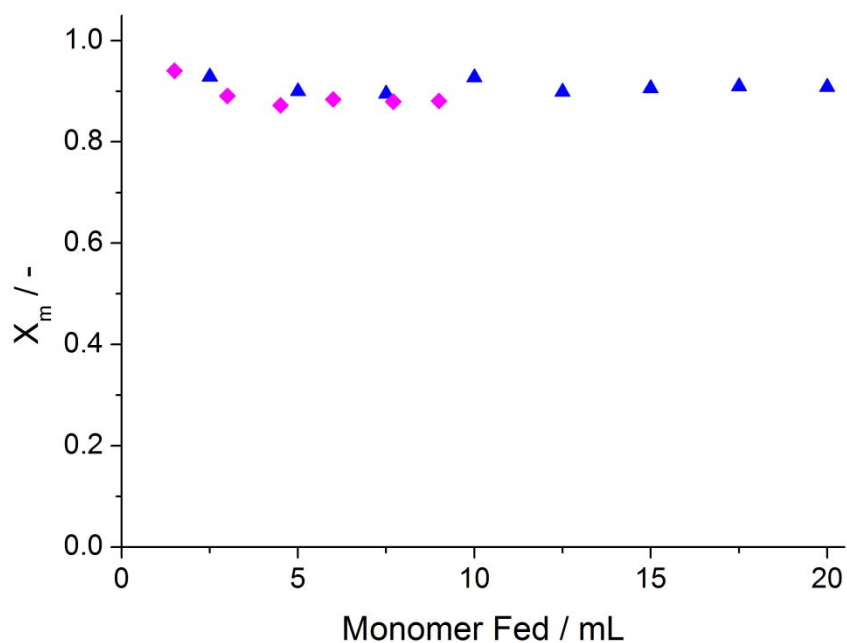


**Figure 5.27** Overall monomer conversion,  $X_m$ , versus monomer fed into the reaction mixture for multi-layered particles; where monomer was fed at 2.5 mL h<sup>-1</sup> (HM-505) (▲) and 1.5 mL h<sup>-1</sup> (HM-507) (◆). HM-507 coagulated after 9 mL of monomer was fed in.

As during the monomer feed conversion is maintained at  $\sim 90\%$  the graph of particle size versus conversion could not be plotted, thus particle size and dispersity were plotted against time (Figure 5.28). On feeding monomer the average diameter increases, whilst the dispersity remains consistently low. The maintained low dispersity throughout suggests that no secondary particles are being formed during the monomer feed.

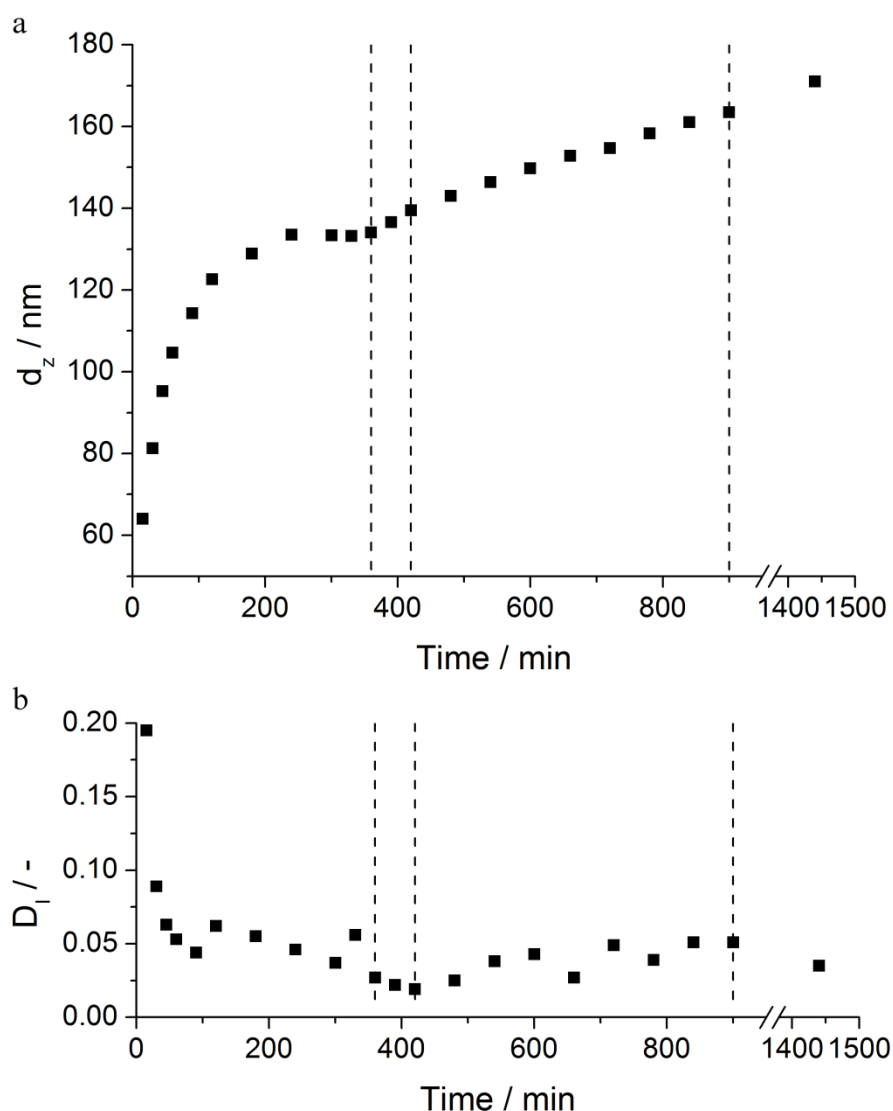


**Figure 5.28** (a) Average particle diameter,  $d_z$ , and (b) dispersity,  $D_w$ , versus monomer conversion,  $X_m$ , of multi-layered particles (HM-505). The dashed line at 360 minutes indicates the shot addition of 0.1 g MPTMS, the dashed line at 420 minutes indicates the beginning of encapsulating feed of styrene and *n*-butyl acrylate and the dashed line at 900 minutes indicates the end of the monomer feed. Monomer was fed at a rate of  $2.5 \text{ mL h}^{-1}$ . On feeding monomer particle size increases with little change to the dispersity.

To more clearly analyze the particle size information the plot was split into two parts; before monomer feed (Figure 5.29) and during monomer feed (Figure 5.30), the former could be plotted against monomer conversion as is conventional, the latter however was plotted against monomer fed into the polymerization. The plot of  $d_z^3$  vs. monomer conversion before the monomer feed showed a linear fit ( $R^2=0.994$ ) suggesting that particle growth is occurring with no secondary particles being formed (Figure 5.29). The plot of  $d_z^3$  vs. volume of monomer fed into the polymerization should also be linear as particle volume should scale linearly to volume of monomer introduced. Indeed the plot of  $d_z^3$  vs. volume of monomer fed into the reaction (mL) is linear ( $R^2=0.998$ ) (Figure 5.30), suggesting polymerization is occurring around the existing particles and no secondary particles are being formed.

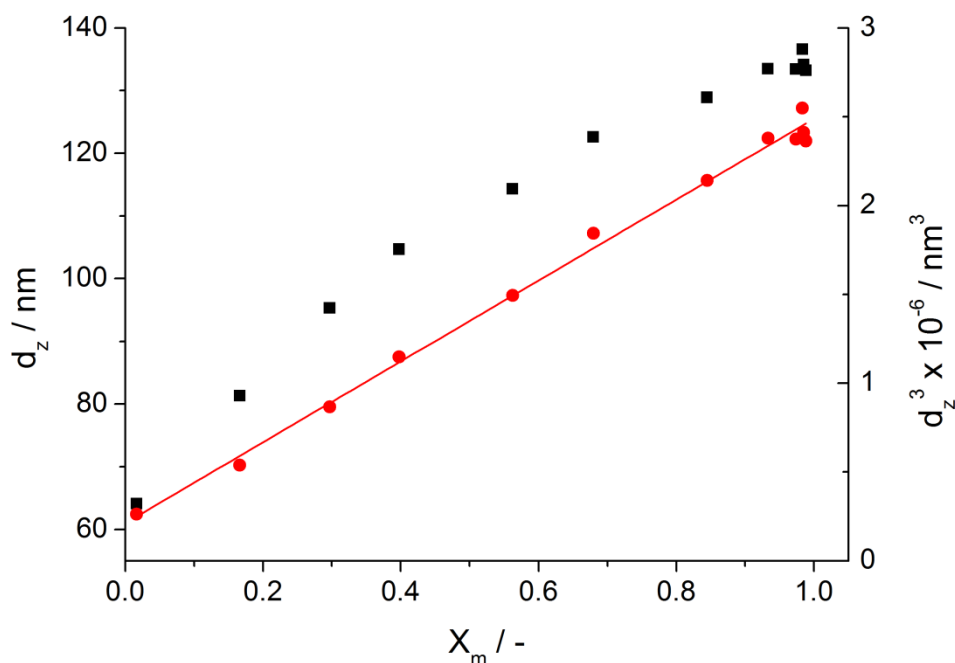


**Figure 5.29** Average particle diameter,  $d_z$  (■) and  $d_z^3$  versus monomer conversion,  $X_m$ , of multi-layered particles before the monomer feed (HM-505).  $R^2$  for linear fit of  $d_z^3$  is 0.994.

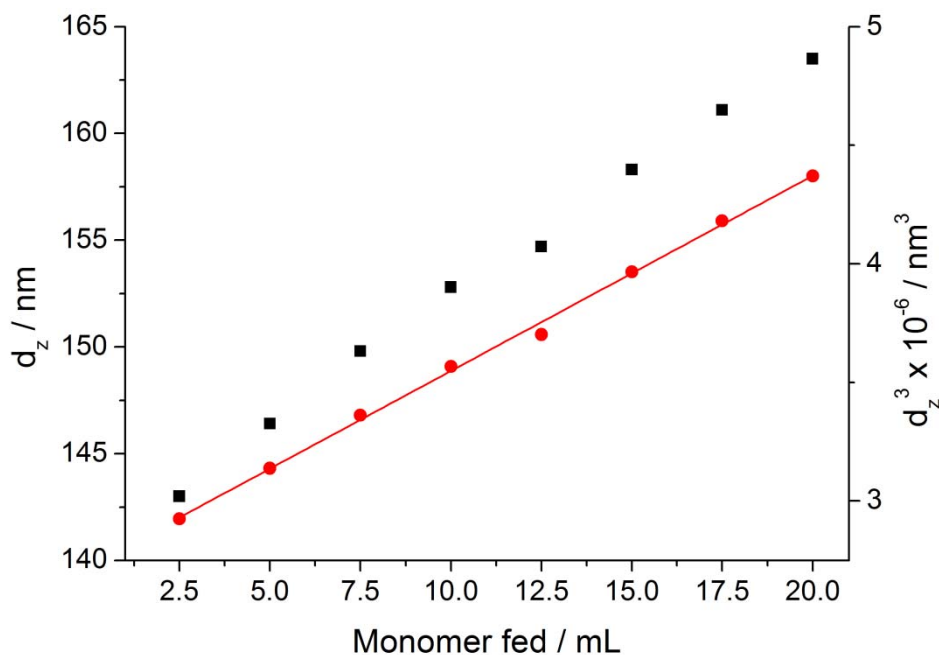


**Figure 5.30** Average particle diameter,  $d_z$  (■) and  $d_z^3$  versus monomer fed in to the reaction (mL) of multi-layered particles during the monomer feed (HM-505).  $R^2$  for linear fit of  $d_z^3$  is 0.998.

Another method to check whether final particle size of 171.0 nm after the encapsulating feed is logical is to compare measured and theoretical particle size. In order to do this we must make a few assumptions; (1) number of particles is calculated using the particle size before the start of the monomer feed (taken from DLS measurement of particles at 420 minutes) and we assume that at this point particles are monodisperse, (2) density of the particle is that of the polymer only, (3) thus we only assume the mass of the polymer.

First we must define the number of particles ( $N$ ) before the monomer feed:

$$N = \frac{\frac{m_1}{\rho}}{\frac{4}{3}\pi r_1^3} \quad (5.10)$$

Where  $m_1$  is the mass of polymer in the batch polymerization,  $\rho$  is density of the polymer and  $r_1$  is the radius of the polymer particle before monomer feed has started. Next the total volume of monomer ( $V_{tot}$ ) is required:

$$V_{tot} = \frac{m_1 + m_2}{\rho} \quad (5.11)$$

Where  $m_2$  is the mass of monomer fed into the polymerization, as monomer composition is the same as in the batch polymerization  $\rho$  is unchanged. The volume of one encapsulated particle ( $V_2$ ) is defined as:

$$V_2 = \frac{4}{3}\pi r_2^3 \quad (5.12)$$

Where  $r_2$  is the radius of the multi-layered particle (after encapsulation). The volume of one encapsulated particle can also be defined as follows:

$$V_2 = \frac{V_{tot}}{N} \quad (5.13)$$

By substituting equations (5.10)-(5.12) into equation (5.13) and rearranging we can define  $r_2$ :

$$r_2 = \sqrt[3]{\frac{(m_1 + m_2)}{m_1} \times r_1^3} \quad (5.14)$$

The following values were used to calculate the theoretical value of the radius of the final multi-layered;  $m_1 = 20.04$  g,  $m_2 = 17.97$  g and  $r_1 = 69.75 \times 10^{-9}$  m.

$$r_2 = 86.0 \times 10^{-9} \text{ m} \quad (5.15)$$

$$D_2 = 172 \times 10^{-9} \text{ m} \quad (5.16)$$

Where  $D_2$  is the diameter of the multi-layered particle. The theoretical diameter of the multi-layered particle (172 nm) is 1 nm off the particle diameter measured by DLS (171 nm), from this we can infer that the polymerization is occurring around the existing particles and no secondary particles are being formed.

SEM analysis was performed to determine morphology of the multi-layered particles (SEM was used as cryo-TEM was unavailable). Location of the soft outer-shell with respect to the core illustrates whether the particles are in-fact encapsulated or have formed other morphologies such as dumbbells. The SEM image indicates an egg-yolk morphology suggesting that the core is in the centre of the particles, in

other words it suggests that the particles have been encapsulated in a soft poly(styrene-*co-n*-butyl acrylate) shell (Figure 5.31 and Appendix V Figure V.1). But this is not perfect data; these particles are soft and therefore film form, thus altering the morphology. Also very low beam energy (keV) was required (below 5.0 keV) to prevent degradation of the beam-labile polymer, it must be noted that low keV is not suitable for imaging very small particles such as these. Thus the morphology gained by SEM is only indicative and cryo-TEM analysis is required to verify the morphology. However the combination of SEM images and DLS data does suggest that the morphology is that of multi-layer particles.

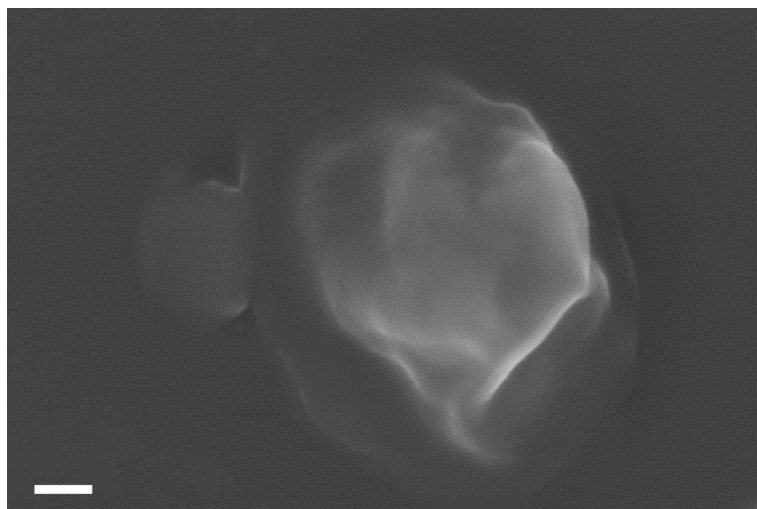


**Figure 5.31** SEM image of multi-layered particle (HM-505) (scale: 100 nm).

Table 5.1 details how the four types of particles synthesized will be described in shorthand from here on in.

**Table 5.1** Table listing all particles synthesized and their abbreviations.

| Exp.   | Abbrev. Name          | Full Description of Particles   |
|--------|-----------------------|---|
| HM-501 | P(Sty- <i>co</i> -BA) | Poly(styrene- <i>co</i> - <i>n</i> -butyl acrylate) particles   |
| HM-502 | Laponite armoured     | Laponite armoured poly(styrene- <i>co</i> - <i>n</i> -butyl acrylate) particles                       |
| HM-503 | Laponite core-shell   | Laponite cross-linked around poly(styrene- <i>co</i> - <i>n</i> -butyl acrylate) particles with MPTMS |
| HM-505 | Multi-layered         | Multi-layered particles prepared by encapsulation of Laponite core-shell particles                    |

### 5.3.2. Thermal and mechanical testing of films prepared from multi-layered particles

Dynamic mechanical thermal analysis (DMTA) was used to determine how these different particles affected the mechanical and thermal properties of their respective films. The films were formed by casting the latexes in a polypropylene dish and evaporating the water at room temperature over 7 days. The films were fully transparent and free of any defects indicating the polymer and clay were well dispersed (Figure 5.32). It was expected HM-501, HM-502 and HM-505 would film form as polymer inter-diffusion is clearly possible, however, HM-503 also film formed and did not crack despite the Laponite/MPTMS shell, suggesting that the shell was permeable to polymer diffusion, which is most-likely because the shell is relatively thin.



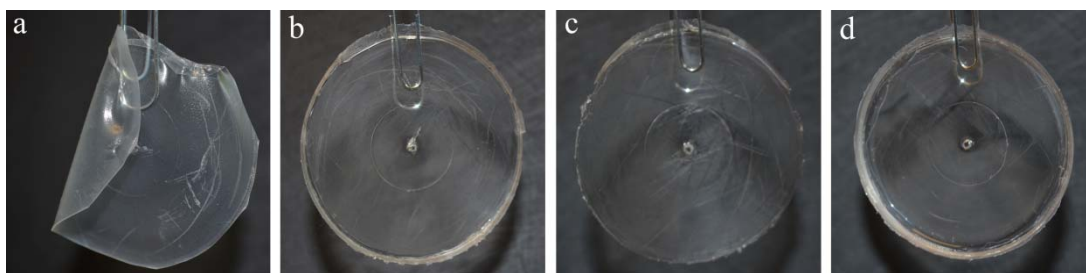


**Figure 5.32** Thin films of (a) poly(styrene-*co*-*n*-butyl acrylate) (HM-501), (b) Laponite armoured particles (HM-502), (c) Laponite core-shell particles (HM-503) and (d) multi-layered particles of 1% cross-linked Laponite armoured poly(styrene-*co*-*n*-butyl acrylate) multi-layered particles (HM-505). Films were prepared by casting 10.0 g of 10 wt.% latexes in a polypropylene pot.

Two types of measurements were conducted to determine the mechanical and thermal properties of the films; stress-strain and temperature sweep experiments. Films for stress-strain measurements were prepared by casting 10.0 g of 10 wt.% latex into polypropylene pots (of dimensions 5.5 cm in diameter and 0.5 cm deep). Stress-strain measurements were performed in tensile mode on films of approximate dimensions of 10 x 2 x 0.3 mm; dimensions were measured using a micrometer, where length was determined by apparatus geometry. Measurements were performed at 25 °C, with a rate of 0.1 N min<sup>-1</sup> and a maximum load of 3 N, with no relaxation. Strain, defined as the change in length with respect to the original length (10 mm) (equation (5.17)), is applied and the stress, unit of force per area (2 x 0.3 mm<sup>2</sup>) (Pa) required to achieve said strain, is measured.

$$\varepsilon = \frac{\Delta l}{l} \quad (5.17)$$

Where  $l$  is the initial length of the material and  $\Delta l$  is the change in length.

The plot of stress vs. strain produces a bell-like curve, the positive gradient describing elastic deformation and the negative gradient describing plastic deformation of the material. The magnitude of the curve is indicative of the toughness of the material, by simply looking at the stress-strain plot (Figure 5.33) it is clear that the toughness of each material is in the order of:

$$P(\text{Sty-}co\text{-BA}) < \text{Multi-layered} < \text{Laponite armoured} < \text{Laponite core-shell}$$

This can be described more quantitatively by interpreting specific points of the graph.

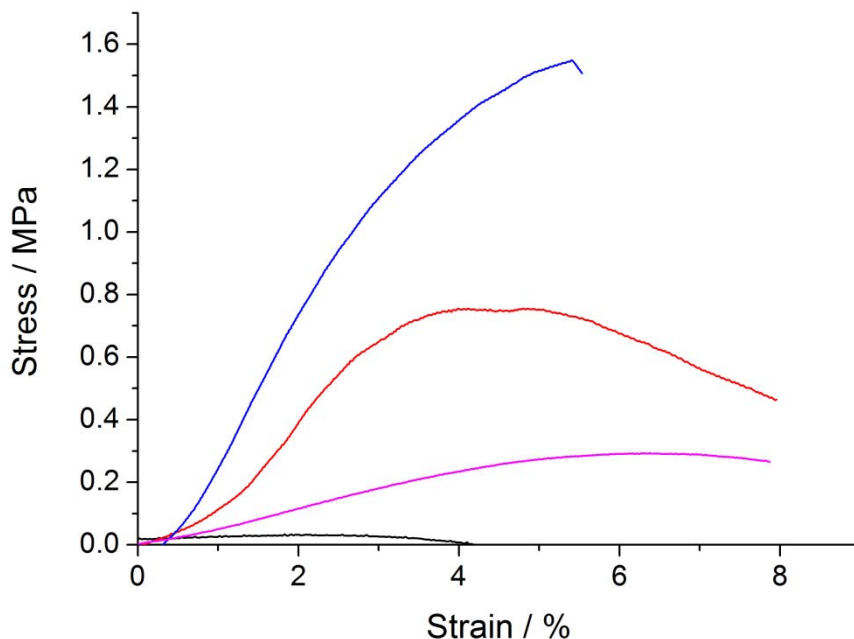


**Figure 5.33** Stress-strain curve of films formed from poly(styrene-*co*-*n*-butyl acrylate) particles (HM-501) (—), Laponite armoured particles (HM-502) (—), Laponite core-shell particles (HM-503) (—) and multi-layered particles (HM-505) (—).

The positive gradient of the stress strain curve provides Young's modulus (equation (5.18)), this is taken from the linear section; the deviation from linearity at low strain is due to the initial load on the sample. The ultimate tensile strength (UTS), the stress a material can withstand before failing, is the maximum point on the stress-strain curve and the strain at this point, the strain at UTS, also provides useful information about the material.

$$E = \frac{\sigma}{\epsilon} \quad (5.18)$$

Where  $E$  is Young's modulus,  $\sigma$  is stress and  $\epsilon$  is strain.

In comparison to the poly(styrene-*co*-*n*-butyl acrylate) film (HM-501), the film formed from Laponite armoured particles (HM-502) show a great increase in Young's modulus, UTS and strain at UTS (Figure 5.33 and Table 5.2). In this case 38-fold increase in Young's modulus was found, this is comparable to similar stress-

strain measurements performed by Bourgeat-Lami and co-workers; films formed from 9 wt.% Laponite RD (with respect to monomer)) armoured poly(styrene-*co-n*-butyl acrylate) particles, prepared by miniemulsion polymerization, showed a 50-fold increase in Young's modulus when compared to pure poly(styrene-*co-n*-butyl acrylate) films, the increased mechanical strength was attributed to the percolating structure of Laponite throughout the film.<sup>5</sup> The different grade of Laponite used and different particle synthesis method combined with the unknown temperature at which these measurements were conducted, means a direct comparison is not possible. The Laponite core-shell particles (HM-503) show a further increase in Young's modulus, UTS and strain at UTS is observed. Young's modulus for HM-503 shows a 55-fold increase when compared to HM-501 and a 1.4-fold increase when compared to HM-502. In this case the negative gradient is not observed as the film has snapped shortly after the UTS, therefore the film is not only tougher but now less viscous; where toughness is defined as the ability of a material to absorb mechanical energy without fracturing or deforming and viscosity is defined as the ability of a material to flow and deform.<sup>81</sup> The multi-layered particles exhibited a substantial decrease in the Young's modulus and UTS, though they remain somewhat greater than the original poly(styrene-*co-n*-butyl acrylate) film (7.2-fold increase in Young's modulus). The strain at UTS for the multi-layered particles is, however, larger than the previous films, suggesting that it is a more elastic material.

**Table 5.2** Table of characteristic properties from Stress-Strain DMTA plots, at 25 °C.

| Exp.   | Film                    | UTS<br>(MPa) | Strain at UTS<br>(%) | Young's<br>Modulus<br>(MPa) |
|--------|-------------------------|--------------|----------------------|-----------------------------|
| HM-501 | P(Sty- <i>co</i> -BA)   | 0.035        | 2.23                 | 0.863                       |
| HM-502 | Laponite<br>armoured    | 0.794        | 5.17                 | 32.8                        |
| HM-503 | Laponite core-<br>shell | 1.40         | 5.30                 | 47.5                        |
| HM-505 | Multi-layered           | 0.282        | 6.33                 | 6.24                        |

The increase in Young's modulus, UTS and strain at UTS has been attributed to the formation of a honey-comb structure on film formation.<sup>5</sup> Thus explaining the increased mechanical strength when this Laponite layer is cross-linked with MPTMS, the excess Laponite is scooped up forming a thicker cross-linked shell (Figure 5.34 c); thus further reinforcing the honey-comb structure increasing the toughness of the material. This also explains how on encapsulation in poly(styrene-*co-n*-butyl acrylate) to form multi-layered particles, mechanical strength is reduced due to loss of the honey-comb structure within the film. The cross-linked Laponite rings regularly dispersed throughout the film (Figure 5.34 d) provides some additional strength to the material in comparison to poly(styrene-*co-n*-butyl acrylate) films, but not to the same extent that the honey-comb structure provides.

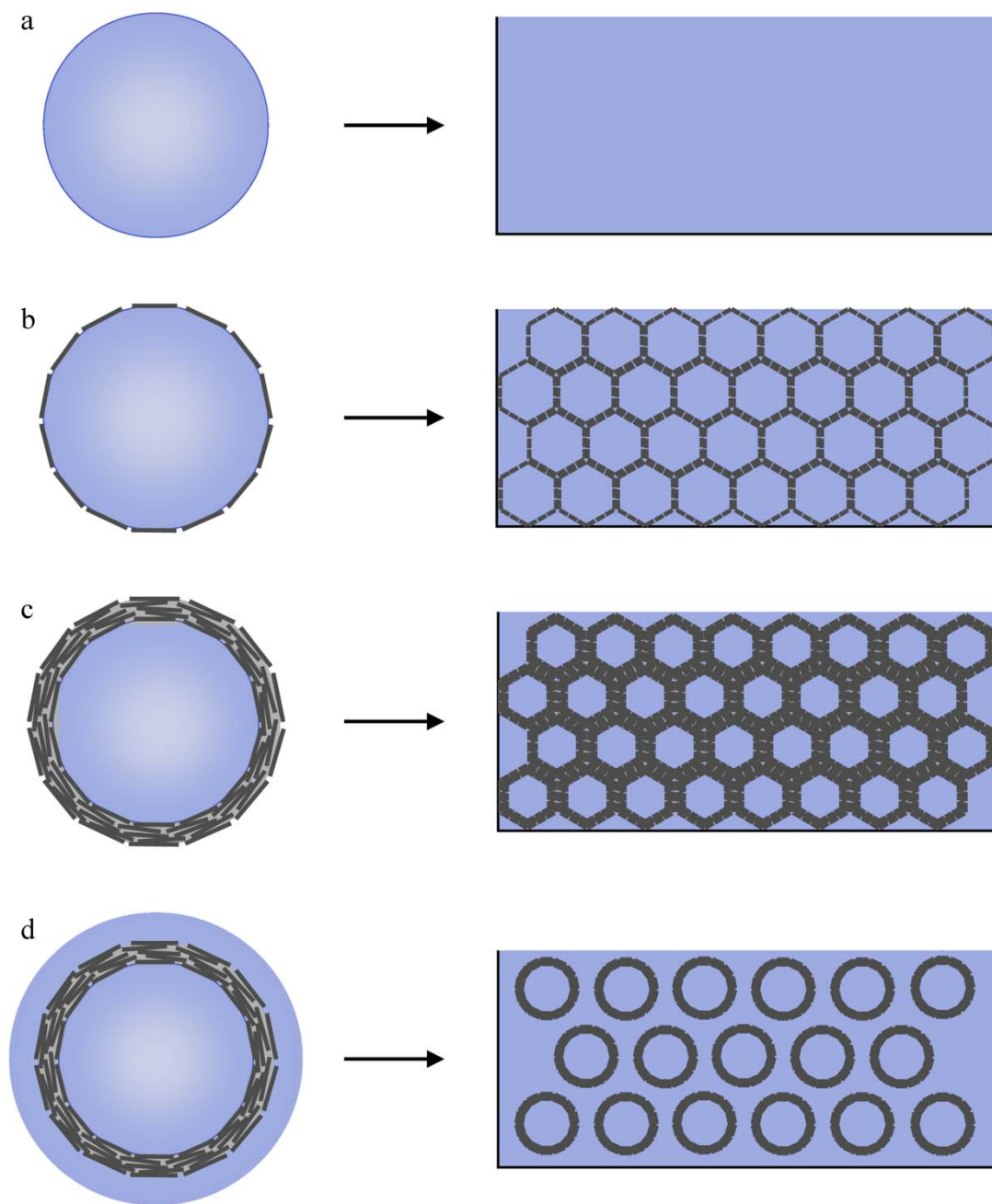


**Figure 5.34** Schematic representation of the multilayer particles and the respective structure of the film they form. (a) poly(Sty-co-BA) latex, (b) Laponite armoured poly(Sty-co-BA) latex, (c) cross-linked Laponite armoured poly(Sty-co-BA) latex and (d) multi-layered particles of encapsulated cross-linked Laponite armoured poly(Sty-co-BA) latex.

Films for Temperature sweep measurements were prepared by casting 50 g of 10 wt.% latex into a Teflon-lined petri-dish (of dimensions 9 cm in diameter and 1.4 cm deep) and were left to dry at room temperature for three weeks. Temperature sweep measurements were performed in three-point bending mode, within the temperature range of -80 to 120 °C with a heating rate of 2 °C min<sup>-1</sup> and with a

displacement of 0.02 mm. The films had approximate dimensions of 10 x 3 x 1 mm, the dimensions were measured using a micrometer, where length was determined by apparatus geometry. The data gained from this experiment is dependent on the frequency of oscillation, the frequency used for the following temperature sweep experiments were at 1 Hz, for the comparative 10 Hz data the reader is referred to V Figures V.2-V.4). A sinusoidal deformation is applied to the sample, with a displacement of 0.02 mm, this stress is described as:

$$\sigma = \sigma_o \sin \omega t \quad (5.19)$$

Where  $\sigma$  is the stress at time  $t$ ,  $\sigma_o$  is the maximum stress and  $\omega$  is the frequency. The resulting shape of the wave is determined by the viscous and elastic properties of the material measured. When the material is subjected to a sinusoidal deformation it can respond in two manners; in-phase the elastic response or out-of-phase the viscous response, viscous elastic materials fall between these two extremes. The in-phase response is described as the storage modulus and the out-of-phase response is described as the loss modulus and the sum of these two components gives the complex modulus.

$$E' = \varepsilon_o \sin(\delta) \quad (5.20)$$

$$E'' = \varepsilon_o \cos(\delta) \quad (5.21)$$

$$E = E' + E'' \quad (5.22)$$

Where  $E'$  is the storage modulus,  $E''$  is the loss modulus,  $E$  is the complex modulus,  $\varepsilon_o$  is the strain at maximum stress and  $\delta$  is the angle of the difference between the applied stress and the resultant strain (also described as the phase angle). It is important to note that though conceptually similar the storage modulus and Young's modulus are different and will not have the same values, they are therefore not comparable.<sup>81</sup> Storage modulus vs. temperature plots (Figure 5.35) show a small increases in  $E'$  in the glassy region in the order of:

$P(\text{Sty-co-BA}) < \text{Multi-layered} < \text{Laponite armoured} \sim \text{Laponite core-shell}$

A more dramatic difference was observed at the rubber plateau in the same order as above (Figure 5.35). The rubber plateau for HM-505 suggests that there is still a Laponite network throughout the film. The measurement for the poly(styrene-*co-n*-butyl acrylate) film (HM-501) was interrupted at approximately 20 °C as the film became too viscous for the DMTA to obtain accurate measurements. Bourgeat-Lami and co-workers also found a small increase in  $E'$  in the glassy region and a large increase in  $E'$  in the rubbery plateau after incorporation of 10 wt.% Laponite (with respect to polymer) into a poly(styrene) matrix by means of Pickering emulsion polymerization.<sup>32</sup> This was also observed in a similar system where 1:1 ratio of methyl methacrylate and *n*-butyl acrylate were used instead of styrene.<sup>82</sup>

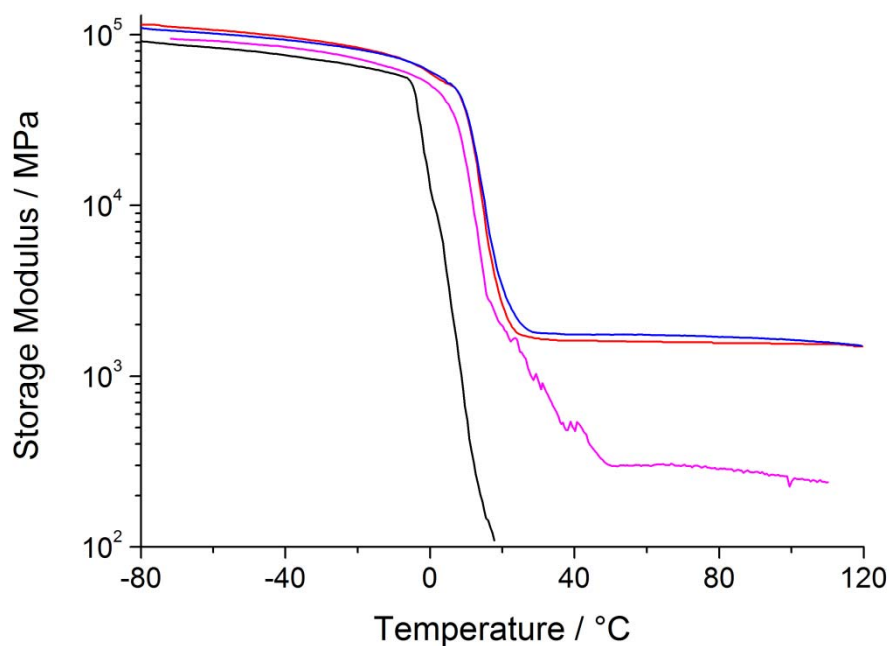


**Figure 5.35** Storage modulus versus temperature of films formed from poly(styrene-*co-n*-butyl acrylate) particles (HM-501) (—), Laponite armoured particles (HM-502) (—), Laponite core-shell particles (HM-503) (—) and multi-layered particles (HM-505) (—).

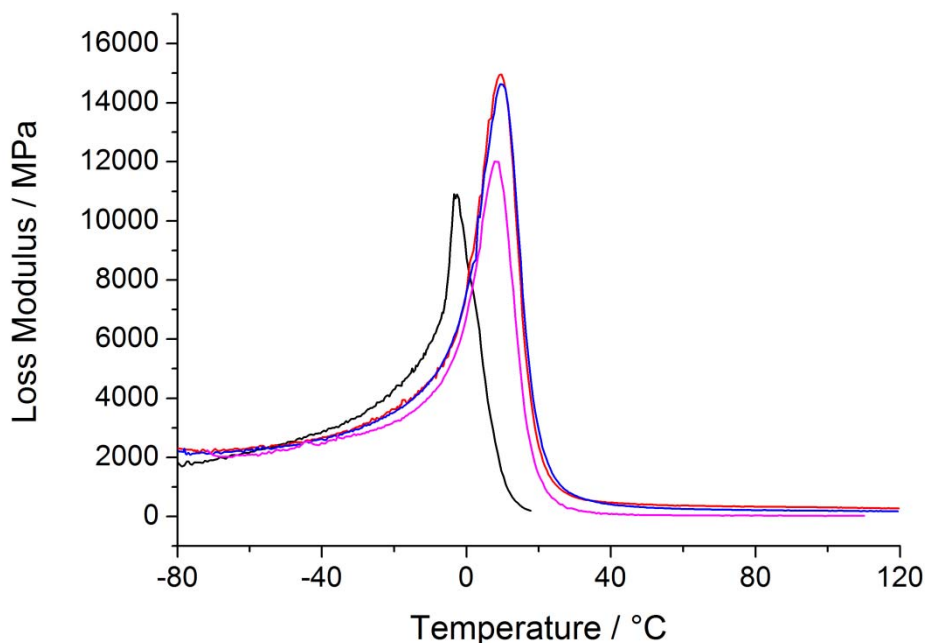


**Figure 5.36** Loss Modulus versus temperature of films formed from poly(styrene-*co*-*n*-butyl acrylate) particles (HM-501) (—), Laponite armoured particles (HM-502) (—), Laponite core-shell particles (HM-503) (—) and multi-layered particles (HM-505) (—).

The loss modulus vs. temperature plot shows typical curves<sup>47, 82</sup> with a shift to higher temperatures in incorporation of Laponite clay. The DMTA results can be understood in more detail by interpreting the Tan  $\delta$  plot.

Tan  $\delta$ , also described as damping, is the ratio of loss to storage modulus (equation (5.23)), in other words it is the dissipation of energy in a material under a cyclic load from which we can gain information such as the  $T_g$  from the peak maxima and comparative viscous behaviour.

$$\text{Tan } \delta = \frac{E''}{E'} \quad (5.23)$$

Only one peak was observed in the Tan  $\delta$  plots (Figure 5.37), indicating that the films and polymer composition were homogeneous; in cases where a copolymer or film is not homogeneous, for example where there is significant composition drift in the copolymer, two or more peaks can be observed illustrating the behaviour in the different regions. The  $T_g$ , taken from the peak maxima, of the poly(styrene-*co*-*n*-butyl acrylate) film (HM-501) measured at 1Hz was found to be 10.91 °C (Figure



5.37 and Table 5.3). The  $T_g$  appears to increase for the Laponite armoured film (HM-502) to 17.8 °C, this increases slightly for the core-shell Laponite film (HM-503) to 18.5 °C. Films formed from the multi-layered particles (HM-505) have a  $T_g$  of 15.5 °C, which is higher than that of the poly(styrene-*co*-*n*-butyl acrylate) film and lower than the Laponite armoured film (HM-502). In reality the  $T_g$  of the polymer has not changed, the mobility of polymer chains in the vicinity of the clay platelets has reduced, resulting in the higher  $T_g$ .<sup>47, 48, 83</sup> The magnitude of the Tan  $\delta$  peak is indicative of the viscous nature of the material, the greater the magnitude the more viscous the material. The film produced from the poly(styrene-*co*-*n*-butyl acrylate) particles (HM-501) displays the greatest magnitude; this magnitude drops dramatically when compared to the multilayer particles (HM-505), it diminishes further still for the Laponite armoured film (HM-502) and very slightly more for the cross-linked Laponite armoured film (HM-503). Thus the order of films in terms of viscous nature are as follows, beginning with the most viscous film:

$$\text{P(Sty-}co\text{-BA)} > \text{Multilayer} > \text{Laponite armoured} > \text{Laponite core shell}$$

The change in magnitude corresponds with the observed  $T_g$  for the films (Figure 5.37 and Table 5.3). These observations are logical when considering the structure of the films (Figure 5.34); as the Laponite armoured (HM-502) and cross-linked Laponite (HM-503) films both have the internal honey-comb Laponite structure throughout the film which is not present in the films prepared from poly(styrene-*co*-*n*-butyl acrylate) (HM-501) particles. The cross-linked Laponite film would display a greater rigidity and would thus be less viscous. On encapsulation (HM-505), and loss of said structure the viscous nature of the film has increased as one might expect (Figure 5.34).

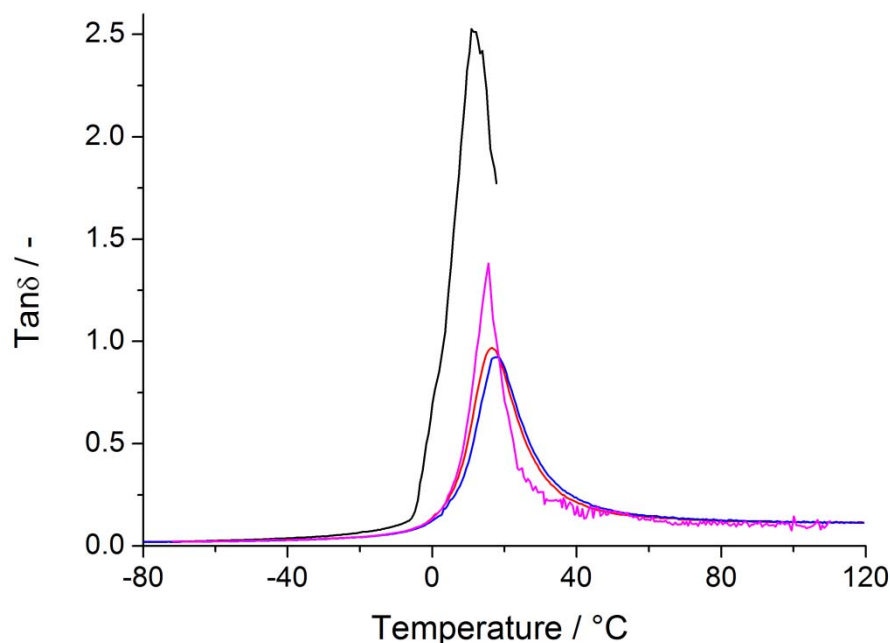


**Figure 5.37** Tan  $\delta$  versus temperature of films formed from poly(styrene-*co*-*n*-butyl acrylate) particles (HM-501) (—), Laponite armoured particles (HM-502) (—), Laponite core-shell particles (HM-503) (—) and multi-layered particles (HM-505) (—).

**Table 5.3** Table of the  $T_g$  measured by DMTA, where the  $T_g$  is taken as the onset and the maximum of the tan  $\delta$  versus temperature plot (Figure 5.37).

| Exp.   | Film                  | $T_g$ (onset)<br>(°C) | $T_g$ (peak maxima)<br>(°C) |
|--------|-----------------------|-----------------------|-----------------------------|
| HM-501 | P(Sty- <i>co</i> -BA) | -3.63                 | 10.91                       |
| HM-502 | Laponite armoured     | -1.28                 | 17.83                       |
| HM-503 | Laponite core-shell   | 2.15                  | 18.45                       |
| HM-505 | Multi-layered         | -0.21                 | 15.53                       |

The  $T_g$  of the composite polymer films were also measured by DSC. It must be stressed that the  $T_g$  values gained from DSC will differ to those gained by DMTA; DSC measures the change in heat capacity and is dependent on heating rate and DMTA measures the change in mechanical response of a polymer film and is dependent on frequency,  $T_g$  values gained from DMTA are generally greater than those obtained from DSC.<sup>81, 84</sup> Three cycles of heating the polymer from -80 to

120 °C and cooling back to -80 °C were performed, the two  $T_g$  measurements were taken, from the onset and the midpoint of the steepest slope. The average of the three  $T_g$  measurements are cited in Table 5.4 (Appendix V Figure V.5). Although direct comparisons of values between  $T_g$  data gained from DMTA and DSC are not possible, the observed trend is the same.

**Table 5.4** Table of  $T_g$  of the polymer films measured by DSC.

| Exp.   | Film                  | $T_g$ (onset)<br>(°C) | $T_g$ (midpoint)<br>(°C) |
|--------|-----------------------|-----------------------|--------------------------|
| HM-501 | P(Sty- <i>co</i> -BA) | -0.34                 | 6.01                     |
| HM-502 | Laponite armoured     | 1.91                  | 7.55                     |
| HM-503 | Laponite core-shell   | 2.35                  | 8.21                     |
| HM-505 | Multi-layered         | 1.89                  | 7.09                     |

Thermogravimetric analysis (TGA) was performed to gain an understanding of the thermal properties of the films (Figure 5.38). Films of an approximate mass of 10 mg were heated from 25.0 °C to 1000 °C at a rate of 10 °C min<sup>-1</sup>, under a flow of air in alumina pans. TGA accurately measures the mass of a sample (g, to 6 d.p.) as a function of temperature; by looking at the loss of mass from a sample as it is heated, thermal properties of the films can be deduced. The total mass loss measured by TGA was found to be within 2 % of the theoretical calculation assuming that complete combustion occurs and thus all polymer is removed and mass loss of Laponite within the film is comparable to the mass loss in its original state (Table 5.7).

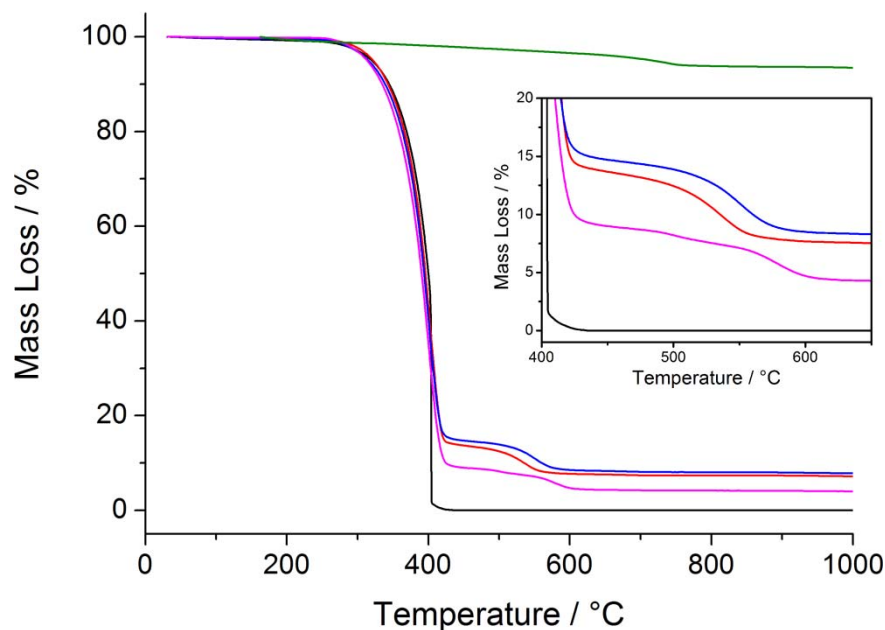


**Figure 5.38** TGA of films formed from poly(styrene-*co*-*n*-butyl acrylate) particles (HM-501) (—), Laponite armoured particles (HM-502) (—), Laponite core-shell particles (HM-503) (—), multi-layered particles (HM-505) (—) and Laponite XLS (—).

In the case of the poly(styrene-*co*-*n*-butyl acrylate) (HM-501) all the polymer is calcined, the sample reaches a mass of 0.0 mg at 427 °C. TGA of Laponite XLS shows that it loses 6.55 % of its mass. Knowing that the polymer loses all its mass and the Laponite loses 6.55 % of its mass when heated up to 1000 °C it is possible to calculate theoretical values of mass loss, which can be compared to the experimental values (Table 5.5 and Table 5.6).

On incorporation of Laponite as a Pickering stabilizer (HM-502), a shoulder after the initial mass loss is observed, where the first drop is at 427 °C and the second is at 537 °C (Figure 5.38 and Table 5.8). Comparing the first mass loss at 427 °C, 85.70 % (Table 5.8), to the theoretical percentage mass loss of polymer in the film, 90.96 % (Table 5.6), it is evident that the Laponite is effectively shielding a small portion of the polymer shifting complete combustion to higher temperature of 537 °C where 92.56 % mass of the original film is lost; this total mass loss is comparable to the theoretical value. This additional thermal stability has been

attributed to the clay hindering diffusion of volatile decomposition materials.<sup>5, 41, 85-88</sup> Similar results are found for the films where the Laponite shell is cross-linked with MPTMS (HM-503). The initial mass loss for these core-shell Laponite particles (HM-503) is at the same temperature as it was for HM-502, 427 °C, the shoulder however is extended by 14 °C to 551 °C (Table 5.8). Again by comparing the first percentage mass loss at 427 °C, 84.62 % (Table 5.8), to the theoretical mass loss of the polymer, 90.57 % (Table 5.6), a shielding effect is once again observed. A value close to the theoretical value is reached at 551 °C where the mass loss is 92.20 %. For the film prepared from the multi-layer particles (HM-505) three drops in mass are observed the first at 427 °C, the same as the previous examples, the second is a small bump at 504 °C and then the final shoulder at 579 °C. The shoulder for the multi-layer particles extends to a higher temperature than the previous two films suggesting a slight increased thermal stability.

**Table 5.5** Table showing final monomer conversion and composition of polymer films.

| Exp.   | Film                  | Laponite:Monomer<br>(g g <sup>-1</sup> ) | X <sub>m</sub><br>(%) |
|--------|-----------------------|--|-----------------------|
| HM-501 | P(Sty- <i>co</i> -BA) | 0.00                                     | 99.8                  |
| HM-502 | Laponite armoured     | 0.10                                     | 100.0                 |
| HM-503 | Laponite core-shell   | 0.10                                     | 100.0                 |
| HM-505 | Multi-layered         | 0.05                                     | 99.0                  |

**Table 5.6** Table showing the theoretical mass loss, calculated from relative masses, of the films broken down into its substituents; % mass loss of film due to complete polymer calcination and % mass loss of film due to Laponite clay.

| Exp.   | Film                  | Mass Loss %<br>Polymer<br>(Theory) | Mass Loss %<br>Laponite<br>(Theory) | Total Mass<br>Loss (%)<br>(Theory) |
|--------|-----------------------|------------------------------------|-------------------------------------|------------------------------------|
| HM-501 | P(Sty- <i>co</i> -BA) | 100                                | —                                   | 100.00                             |
| HM-502 | Laponite armoured     | 90.96                              | 0.60                                | 91.56                              |
| HM-503 | Laponite core-shell   | 90.57                              | 0.62                                | 91.19                              |
| HM-505 | Multi-layered         | 94.78                              | 0.34                                | 95.12                              |

**Table 5.7** Table comparing theoretical and experimental mass loss (%) of films when heated to 1000 °C at a rate of 10 °C min<sup>-1</sup>, where experimental mass loss is measured by TGA.

| Exp.   | Film                  | Mass Loss (Theory)<br>(%) | Mass Loss (TGA)<br>(%) |
|--------|-----------------------|---------------------------|------------------------|
| HM-501 | P(Sty- <i>co</i> -BA) | 100                       | 100.00                 |
| HM-502 | Laponite armoured     | 91.56                     | 92.85                  |
| HM-503 | Laponite core-shell   | 91.19                     | 92.20                  |
| HM-505 | Multi-layered         | 95.12                     | 96.01                  |

**Table 5.8** Table illustrating temperature at points of mass loss and percentage of mass lost at said temperature.

| Exp.   | Film                  | Mass Loss 1 |          | Mass Loss 2 |          | Mass Loss 3 |          |
|--------|-----------------------|-------------|----------|-------------|----------|-------------|----------|
|        |                       | T (°C)      | Mass (%) | T (°C)      | Mass (%) | T (°C)      | Mass (%) |
| HM-501 | P(Sty- <i>co</i> -BA) | 427         | 100.00   | —           | —        | —           | —        |
| HM-502 | Laponite armoured     | 427         | 85.70    | 537         | 7.15     | —           | —        |
| HM-503 | Laponite core-shell   | 427         | 84.62    | 551         | 7.58     | —           | —        |
| HM-505 | Multi-layered         | 427         | 90.28    | 504         | 1.65     | 579         | 4.08     |

The thermal stability of polymer-clay nanocomposite films is thought to derive from a decrease in thermal motion of the polymer when in close contact with the clay; the polymer in close vicinity to the clay is thermally shielded from degradation to a higher temperature.<sup>88-91</sup> This explains the difference in the number of shoulders present in the TGA; no shoulder, one shoulder and two shoulders could be explained by the number of polymer clay interfaces in the sample, ignoring the interstitial polymer from the diffusion step of film formation as the amount is very small so will not be distinct in the TGA plot and can therefore be deemed negligible in comparison (Figure 5.39). In the case where the film is prepared from the poly(styrene-*co*-*n*-butyl acrylate) particles (HM-501) a homogenous film is produced with no polymer-clay interface and no shoulder is observed. In the cases of the Laponite armoured particles (HM-502) and core-shell Laponite particles (HM-503) one type of polymer-clay interface is found, the internal polymer to the honey-comb structured Laponite network, for both these films only one shoulder is observed. For the films prepared from the multi-layer particles (HM-505) there are two polymer-clay interfaces the internal polymer-Laponite and the Laponite-external (interstitial in the film) polymer, in this case two shoulders are observed in the TGA. Additionally having two interfaces drastically increases the polymer-clay surface area, increasing the temperature of complete polymer combustion.

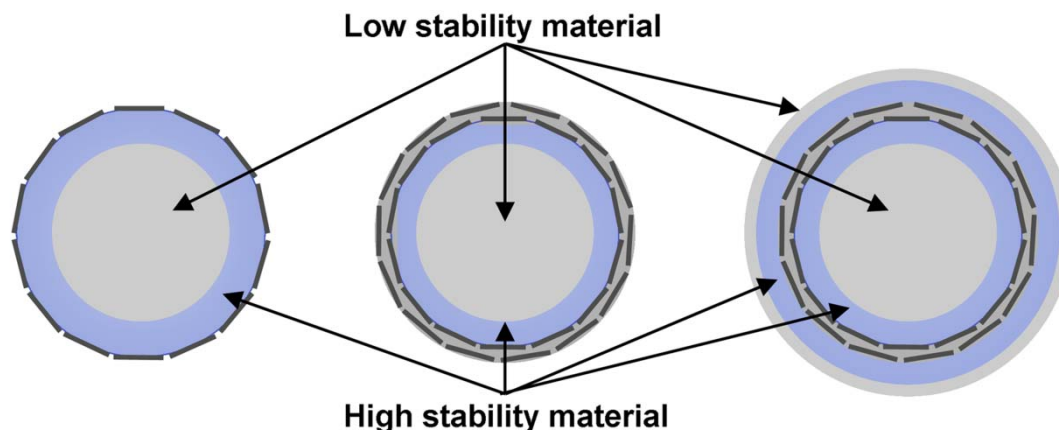


**Figure 5.39** Scheme illustrating the effect of morphology on thermal stability of polymer.

From the TGA of the polymer-composite films we know that complete degradation occurs above 530 °C, therefore we performed an isothermal TGA at 500 °C for two hours to calcine the majority of the polymer (Figure 5.41), leaving some char so that we could image the remaining porous structure by SEM thus illustrate the formation of a the honeycomb structure and obtain structural information on the different films (Figure 5.40). The Laponite armoured poly(styrene-*co-n*-butyl acrylate) (HM-502) film shows a clear porous honey-comb structure where the edges are a combination of Laponite clay and char. It is important to note that Laponite alone cannot be visualised by SEM as it does not have a high enough resolution. The core-shell Laponite particles (HM-503) show a similar internal structure to HM-502. However, qualitatively speaking the Laponite edges appear much thicker in the case of HM-503, this is likely a direct result from the composite Laponite, MPTMS and poly(styrene-*co-n*-butyl acrylate) shell. Comparison of TGA's performed to 1000 °C and the 500 °C isothermal illustrate that this is not an effect of the amount of char remaining as this is small, in fact in terms of % mass HM-502 appears to have retained a greater amount of char (Table 5.9) The multi-layered particles (HM-505) appear to have a less well-defined porous network, this is possibly due to collapse of



the distributed Laponite rings as the interstitial polymer (outer-shell of particle) is calcined.

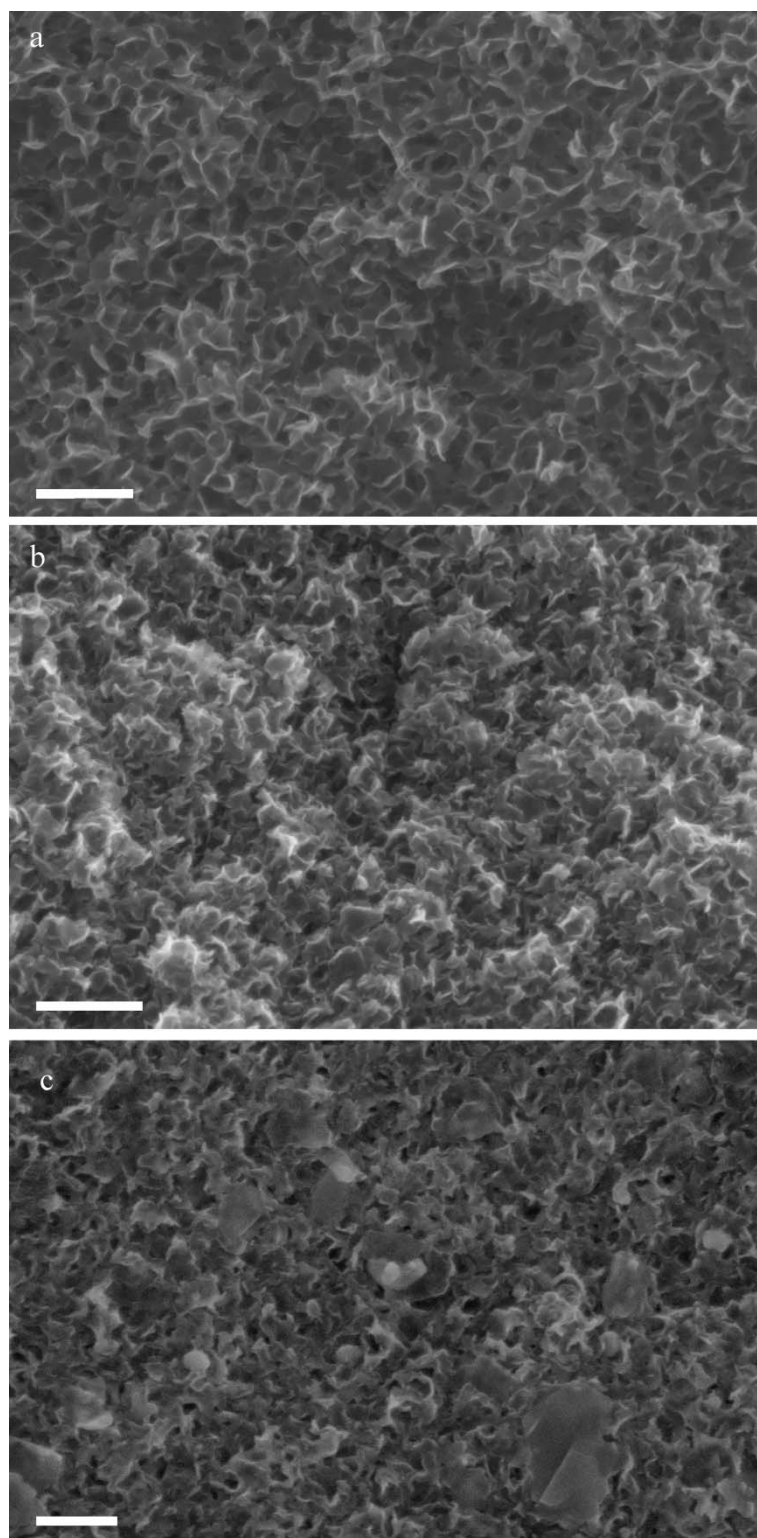


**Figure 5.40** SEM images of films of (a) Laponite armoured particles (HM-502), (b) Laponite core-shell particles (HM-503) and (c) multi-layered particles (HM-505) after being heated to 500 °C for two hours.

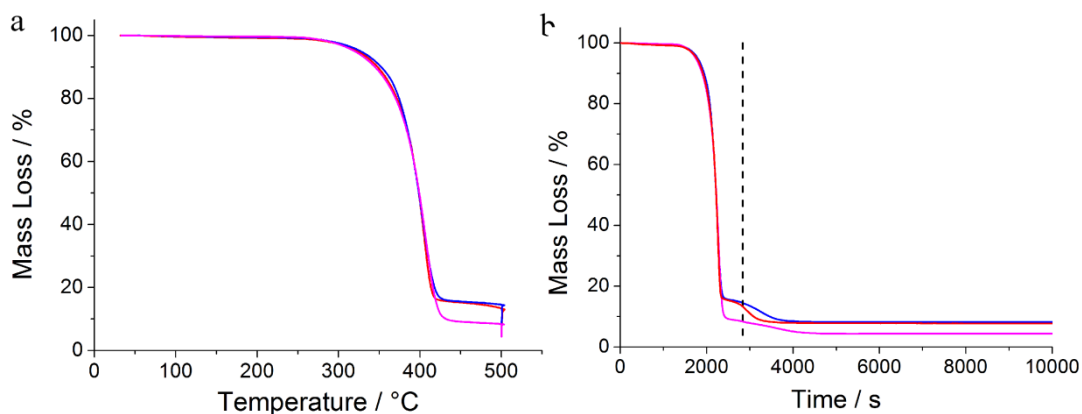


**Figure 5.41** TGA of films formed from Laponite armoured particles (HM-502) (—), Laponite core-shell particles (HM-503) (—) and multi-layered particles (HM-505) (—). Samples were heated to 500 °C at a rate of 10 °C min<sup>-1</sup>, after which the 500 °C temperature was maintained for two hours. The dashed line represents the start of the 500 °C isothermal.

**Table 5.9** Table comparing final mass (%) when sample is heated to 1000 °C and after a two hour isothermal at 500 °C. Char remaining is the difference between mass remaining at 1000 °C and 500 °C.

| Exp.   | Film                   | Mass Remaining<br>@ 1000 °C<br>(%) | Mass Remaining<br>@ 500 °C<br>(%) | Difference in<br>Char Remaining<br>(%) |
|--------|------------------------|------------------------------------|-----------------------------------|--|
| HM-502 | Laponite<br>armoured   | 7.147                              | 7.794                             | 0.647                                  |
| HM-503 | Laponite<br>core-shell | 7.803                              | 8.192                             | 0.389                                  |
| HM-505 | Multi-layered          | 3.987                              | 4.447                             | 0.460                                  |

## 5.4. Conclusions

In conclusion, we have developed a method that we believe produces multi-layered composite particles, wherein the inner shell is composed of Laponite clay platelets. This was achieved by overcoming the desire of the clay platelets to reside at the polymer-water interface through immobilization by cross-linking the clay with a tri-functional silylating agent. We have shown that the morphology of composite particles (bare, armoured, core-shell and multi-layer) greatly affects the thermal and mechanical properties of the subsequent films formed. Increasing polymer-clay surface area, as in the case of multi-layer particles, significantly contributes to the thermal stability of the film. Contrastingly, films formed from these multi-layer particles show a severe decrease in mechanical strength when compared to the armoured and core-shell particle morphologies due to the lack of an inorganic honeycomb structure. We propose that through further work in controlling the outer-shell thickness it may be possible to tune the mechanical and thermal properties thus enabling fine tuning of bulk properties through control of morphology on the nanometre scale.

## 5.5. Experimental

### 5.5.1. Materials

Styrene and *n*-butyl acrylate were purchased from Aldrich at purities  $\geq$  99.0%. The initiator ammonium persulfate (APS) and 3-methacryloxypropyl trimethoxysilane (MPTMS) were purchased from Aldrich. Laponite XLS was kindly donated by Rockwood Additives Ltd. All chemicals were used as received unless otherwise stated. Lacey carbon film 300 mesh copper TEM grids and SEM specimen stubs were purchased from Agar Scientific. Silicon wafers for mounting SEM samples were kindly donated by Wacker Chemie AG.

### 5.5.2. Equipment

Emulsion polymerizations were carried out in 250 mL Radley Reactor-Ready Duo double-walled glass reactors equipped with an external heating bath (Julabo F-25 unit), a Teflon overhead anchor stirrer fitted approximately 2 cm from the bottom of the reactor vessel (Radley) typically running at 250 rpm. Monomer was fed into the reaction mixture with a Harvard Instrument PHD 2000 Infusion syringe pump. Particle sizes and dispersities were measured by dynamic light scattering using a Malvern Zetasizer Nano using a  $173^\circ$  backscattering angle, at 25 °C, with an equilibration time of 120 s and an average of 3 measurements each with a minimum of 12 sub-runs were taken. Cryo-TEM analysis was performed on a Jeol 2010F TEM (200kV FEG) fitted with a Gatan Ultrascan 4000 camera; samples were prepared by adding a drop of diluted latex to a suspended lacey carbon grid, wicking the excess liquid away with filter paper and plunging into liquid ethane. SEM was performed on a Zeiss SUPRA 55-VP FEGSEM; sample were prepared by adding a aqueous drop of diluted sample to a silicon wafer and drying at room temperature for 12 hours, the sample was subsequently carbon coated with a carbon evaporator for 4

seconds. DMTA measurements were performed on a Triton Tritec Dynamic Mechanical Thermal Analyser. Stress-strain measurements were performed in tensile mode on films of approximate dimensions of 10 x 2 x 0.3 mm; dimensions were measured using a micrometer, where length was determined by apparatus geometry. Measurements were performed at 25 °C, with a rate of 0.1 N min<sup>-1</sup> and a maximum load of 3 N, with no relaxation, an average of 3 measurements were taken. Temperature sweep measurements were performed in three-point bending mode, within the temperature range of -80 to 120 °C with a heating rate of 2 °C min<sup>-1</sup>, at 1 and 10 Hz and with a displacement of 0.02 mm. The films had approximate dimensions of 10 x 3 x 1 mm, the dimensions were measured using a micrometer, where length was determined by apparatus geometry. DSC measurements were performed on a Mettler Toledo DSC1-400, within the mass range of 10-25 mg, with a heating rate of 1 °C min<sup>-1</sup>. TGA measurements were performed on a Mettler Toledo DSC1-Star using 70 µL alumina pans, with a heating rate of 10 °C min<sup>-1</sup>.

### 5.5.3. Particle synthesis

#### 5.5.3.1. *Poly(styrene-co-n-butyl acrylate) emulsion (HM-501)*

180.0 g of deionised water was placed under a nitrogen atmosphere in a 250 mL double walled glass reactor by purging for 20 minutes. Styrene (8.00 g) and *n*-butyl acrylate (12.00 g) (total monomer, 10.0 wt.%) was added and the mixture was degassed for a further 5 minutes and then heated to 70 °C whilst stirring at 250 rpm. Emulsion polymerization was initiated upon addition of 0.15 g APS dissolved in 1 g of water. Monomer conversion was monitored *via* gravimetry by taking ~1.5 mL samples by syringe. Conversion: 99.8 %. Particle size ( $d_z$ ): 631.3 nm. PDI: 0.002.

### 5.5.3.2. Typical Laponite stabilized emulsion (HM-502)

2.00 g Laponite clay XLS was dispersed in 179 g of deionized water and placed in under a nitrogen atmosphere in a 250 mL double walled glass reactor by purging for 20 minutes. Styrene (8.00 g) and *n*-butyl acrylate (12.00 g) (total monomer, 10.0 wt.%) was added and the mixture was degassed for a further 5 minutes and then heated to 70 °C whilst stirring at 250 rpm. Emulsion polymerization was initiated upon addition of 0.15 g APS dissolved in 1 g of water. Monomer conversion was monitored *via* gravimetry by taking ~1.5 mL by syringe. Conversion: 100.0 %. Particle size ( $d_z$ ): 131.9 nm. PDI: 0.004. Final pH: 8.41.

### 5.5.3.3. Cross-linking of Laponite

Typical solids stabilized emulsion procedure was followed (above). At 6 hours 0.10 g MPTMS (0.5 wt.% with respect to monomer and 2.83 mM with respect to water) was shot added to the reaction. Monomer conversion was monitored *via* gravimetry by taking ~1.5 mL by syringe. Final pH: 8.32.

**Table 5.10** Table of reagent quantities.

| Exp.     | Laponite<br>(g) | Sty<br>(g) | BA<br>(g) | MPTMS<br>(g) | Water<br>(g) | (APS)<br>(g) |
|----------|-----------------|------------|-----------|--------------|--------------|--------------|
| BL-067   | 2.00            | 7.96       | 11.94     | 0.10         | 181.24       | 0.15         |
| HM-4-503 | 2.00            | 8.00       | 12.02     | 0.10         | 180.21       | 0.15         |

**Table 5.11** Table showing conversion particle size and dispersity of particles.

| Exp.   |              | $X_m$<br>(%) | $d_z$<br>(nm) | $D_I$ |
|--------|--------------|--------------|---------------|-------|
| BL-067 | End          | 99.2         | 127.7         | 0.06  |
| HM-503 | Before MPTMS | 95.39        | 124.7         | 0.049 |
|        | End          | 100.0        | 126.9         | 0.025 |

#### 5.5.3.4. MPTMS introduced at $t_0$

Typical solids stabilized emulsion procedure was followed (above). At  $t_0$  0.10 g MPTMS (0.5 wt.% with respect to monomer and 2.83 mM with respect to water) was shot added to the reaction. Monomer conversion was monitored *via* gravimetry by taking ~1.5 mL by syringe. Final pH: 8.66

**Table 5.12** Table of reagent quantities.

| Exp.   | Laponite<br>(g) | Sty<br>(g) | BA<br>(g) | MPTMS<br>(g) | Water<br>(g) | (APS)<br>(g) |
|--------|-----------------|------------|-----------|--------------|--------------|--------------|
| HM-504 | 2.00            | 8.01       | 12.01     | 0.10         | 180.20       | 0.15         |
| BL-050 | 2.00            | 7.97       | 11.95     | 0.10         | 181.41       | 0.15         |

**Table 5.13** Table showing monomer conversion, particle size and dispersity of particles.

| Exp.   | $X_m$<br>(%) | $d_z$<br>(nm) | $D_I$ |
|--------|--------------|---------------|-------|
| HM-504 | 100          | 160.2         | 0.059 |
| BL-050 | 98.6         | 157.3         | 0.055 |

#### 5.5.3.5. Multi-layer particles prepared by encapsulation of Laponite stabilized latex in poly(styrene-co-*n*-butyl acrylate)

Typical solids stabilized emulsion procedure was followed (above) at 6 hours 0.10 g MPTMS was introduced by shot addition to the reaction, at 7 hours 20 mL of styrene and *n*-butyl acrylate (40:60 wt.%) was fed at 2.5 mL h<sup>-1</sup>. Monomer conversion was monitored *via* gravimetry by taking ~1.5 mL sample by syringe. Final pH: 8.10.

**Table 5.14** Table of encapsulation of Laponite stabilized poly(styrene-*co-n*-butyl acrylate) latex before encapsulating feed.

| Sample | Sty<br>(g) | BA<br>(g) | Laponite<br>(g) | Water<br>(g) | APS<br>(g) | MPTMS<br>(g) |
|--------|------------|-----------|-----------------|--------------|------------|--------------|
| HM-506 | 8.00       | 12.01     | 2.00            | 179.8        | 0.15       | 0.10         |
| HM-505 | 8.02       | 12.02     | 2.00            | 180.0        | 0.15       | 0.10         |
| HM-507 | 8.01       | 12.01     | 2.00            | 180.0        | 0.15       | 0.10         |

**Table 5.15** Table of encapsulation of Laponite stabilized (styrene-*co-n*-butyl acrylate) latex. Amounts of monomer stated are those from the feed.

| Sample | Sty<br>(g) | BA<br>(g) | Feed<br>Rate<br>(mL h <sup>-1</sup> ) | X <sub>m</sub><br>(%) | d <sub>z</sub><br>(nm) | D <sub>I</sub> | Average X <sub>m</sub><br>during feed<br>(%) |
|--------|------------|-----------|---------------------------------------|-----------------------|------------------------|----------------|--|
| HM-506 | 7.19       | 10.78     | 3.33                                  | 1.01                  | 171.9                  | 0.091          | 82.81  |
| HM-505 | 7.19       | 10.78     | 2.5                                   | 0.99                  | 171.0                  | 0.035          | 90.93  |
| HM-507 | 7.19       | 10.78     | 1.5                                   | 0.91                  | 172.6                  | 0.081          | 88.47  |



## 5.6. References

1. Choudalakis, G.; Gotsis, A. D. *Eur. Polym. J.* **2009**, 45, 967-984.
2. Herrera-Alonso, J. M.; Sedláková, Z.; Marand, E. *J. Membr. Sci.* **2010**, 363, 48-56.
3. Lee, D. C.; Jang, L. W. *J. Appl. Polym. Sci.* **1996**, 61, 1117-1122.
4. Giannelis, E. P. *Adv. Mater.* **1996**, 8, 29-35.
5. Negrete-Herrera, N.; Putaux, J.-L.; David, L.; Haas, F. D.; Bourgeat-Lami, E. *Macromol. Rapid Commun.* **2007**, 28, 1567-1573.
6. Wang, T.; Colver, P. J.; Bon, S. A. F.; Keddie, J. L. *Soft Matter* **2009**, 5, 3842-3849.
7. Noh, M. W.; Lee, D. C. *Polym. Bull.* **1999**, 42, 619-626.
8. zu Putlitz, B.; Landfester, K.; Fischer, H.; Antonietti, M. *Adv. Mater.* **2001**, 13, 500-503.
9. Ramsden, W. *Proc. R. Soc. Lond.* **1903**, 72, 156-164.
10. Pickering, S. U. *J. Chem. Soc., Trans.* **1907**, 91, 2001-2021.
11. Binks, B. P.; Lumsdon, S. O. *Langmuir* **2000**, 16, 8622-8631.
12. Schmid, A.; Tonnar, J.; Armes, S. P. *Adv. Mater.* **2008**, 20, 3331-3336.
13. Colard, C. A. L.; Teixeira, R. F. A.; Bon, S. A. F. *Langmuir* **2010**, 26, 7915-7921.
14. Tiarks, F.; Landfester, K.; Antonietti, M. *Langmuir* **2001**, 17, 5775-5780.
15. Fortuna, S.; Colard, C. A. L.; Troisi, A.; Bon, S. A. F. *Langmuir* **2009**, 25, 12399-12403.
16. Skelhon, T. S.; Grossiord, N.; Morgan, A. R.; Bon, S. A. F. *J. Mater. Chem.* **2012**, 22, 19289-19295.
17. González-Matheus, K.; Leal, G. P.; Tollan, C.; Asua, J. M. *Polymer* **2013**, 54, 6314-6320.
18. Chen, T.; Colver, P. J.; Bon, S. A. F. *Adv. Mater.* **2007**, 19, 2286-2289.
19. Liu, Y.; Chen, X.; Wang, R.; Xin, J. H. *Mater. Lett.* **2006**, 60, 3731-3734.

20. Li, X.; Sun, G.; Li, Y.; Yu, J. C.; Wu, J.; Ma, G.-H.; Ngai, T. *Langmuir* **2014**, 30, 2676-2683.
21. Zhou, J.; Qiao, X.; Binks, B. P.; Sun, K.; Bai, M.; Li, Y.; Liu, Y. *Langmuir* **2011**, 27, 3308-3316.
22. de Folter, J. W. J.; Hutter, E. M.; Castillo, S. I. R.; Klop, K. E.; Philipse, A. P.; Kegel, W. K. *Langmuir* **2013**, 30, 955-964.
23. Morgan, A. R.; Ballard, N.; Rochford, L. A.; Nurumbetov, G.; Skelhon, T. S.; Bon, S. A. F. *Soft Matter* **2013**, 9, 487-491.
24. Kim, Y. J.; Liu, Y. D.; Seo, Y.; Choi, H. J. *Langmuir* **2013**, .
25. Thickett, S. C.; Zetterlund, P. B. *ACS Macro Lett.* **2013**, 630-634.
26. Thickett, S. C.; Wood, N.; Ng, Y. H.; Zetterlund, P. B. *Nanoscale* **2014**, 6, 8590-8594.
27. Song, X.; Yang, Y.; Liu, J.; Zhao, H. *Langmuir* **2010**, 27, 1186-1191.
28. Kim, S. D.; Zhang, W. L.; Choi, H. J. *Mater. Chem. C* **2014**, 2, 7541-7546.
29. Ashby, N. P.; Binks, B. P. *PCCP* **2000**, 2, 5640-5646.
30. Bourgeat-Lami, E.; Guimarães, T. R.; Pereira, A. M. C.; Alves, G. M.; Moreira, J. C.; Putaux, J.-L.; dos Santos, A. M. *Macromol. Rapid Commun.* **2010**, 31, 1874-1880.
31. Bourgeat-Lami, E.; Herrera, N. N.; Putaux, J.-L.; Perro, A.; Reculosa, S.; Ravaine, S.; Duguet, E. *Macromol. Symp.* **2007**, 248, 213-226.
32. Ruggerone, R.; Plummer, C. J. G.; Herrera, N. N.; Bourgeat-Lami, E.; Månson, J.-A. E. *Eur. Polym. J.* **2009**, 45, 621-629.
33. Sheibat-Othman, N.; Cenacchi-Pereira, A.-M.; Santos, A. M. D.; Bourgeat-Lami, E. *J. Polym. Sci., Part A: Polym. Chem.* **2011**, 49, 4771-4784.
34. Negrete-Herrera, N.; Putaux, J.-L.; David, L.; Bourgeat-Lami, E. *Macromolecules* **2006**, 39, 9177-9184.
35. Cauvin, S.; Colver, P. J.; Bon, S. A. F. *Macromolecules* **2005**, 38, 7887-7889.
36. Bon, S. A. F.; Colver, P. J. *Langmuir* **2007**, 23, 8316-8322.
37. Kim, Y. J.; Liu, Y. D.; Choi, H. J.; Park, S.-J. *J. Colloid Interface Sci.* **2013**, 394, 108-114.
38. Bon, S. A. F.; Chen, T. *Langmuir* **2007**, 23, 9527-9530.

39. Bon, S. A. F.; Mookhoek, S. D.; Colver, P. J.; Fischer, H. R.; van der Zwaag, S. *Eur. Polym. J.* **2007**, 43, 4839-4842.
40. van den Dungen, E. T. A.; Galineau, J.; Hartmann, P. C. *Macromol. Symp.* **2012**, 313-314, 128-134.
41. Voorn, D. J.; Ming, W.; van Herk, A. M. *Macromolecules* **2006**, 39, 2137-2143.
42. Abdolbaghi, S.; Pourmahdian, S.; Saadat, Y. *Colloid. Polym. Sci.* **2014**, 292, 1091-1097.
43. Teixeira, R. F. A.; McKenzie, H. S.; Boyd, A. A.; Bon, S. A. F. *Macromolecules* **2011**, 44, 7415-7422.
44. Schmid, A.; Scherl, P.; Armes, S. P.; Leite, C. A. P.; Galembeck, F. *Macromolecules* **2009**, 42, 3721-3728.
45. Teixeira, R. *Multi-layered nanocomposite polymer latexes and films* Ph.D. University of Warwick.Chemistry Department. U.K. 2011.
46. Chevalier, Y.; Pichot, C.; Graillat, C.; Joanicot, M.; Wong, K.; Maquet, J.; Lindner, P.; Cabane, B. *Colloid. Polym. Sci.* **1992**, 270, 806-821.
47. Faucheu, J.; Gauthier, C.; Chazeau, L.; Cavaillé, J.-Y.; Mellon, V.; Pardal, F.; Lami, E. B. *Polymer* **2010**, 51, 4462-4471.
48. Becker, O.; Varley, R.; Simon, G. *Polymer* **2002**, 43, 4365-4373.
49. Wakiya, T.; Morisaki, T.; Ishibashi, N.; Nishimura, S.; Takafuji, M.; Nagaoka, S.; Yamada, Y.; Nozato, S.; Ihara, H. *Mater. Lett.* **2011**, 65, 1407-1409.
50. Caruso, R. A.; Susha, A.; Caruso, F. *Chem. Mater.* **2001**, 13, 400-409.
51. Caruso, F.; Möhwald, H. *Langmuir* **1999**, 15, 8276-8281.
52. Furusawa, K.; Nagashima, K.; Anzai, C. *Colloid. Polym. Sci.* **1994**, 272, 1104-1110.
53. Zhang, J.; Coombs, N.; Kumacheva, E. *J. Am. Chem. Soc.* **2002**, 124, 14512-14513.
54. Li, J.; Stöver, H. D. H. *Langmuir* **2010**, 26, 15554-15560.
55. Li, J.; Hitchcock, A. P.; Stöver, H. D. H. *Langmuir* **2010**, 26, 17926-17935.
56. Sacanna, S.; Philipse, A. P. *Adv. Mater.* **2007**, 19, 3824-3826.

57. Colver, P. J.; Colard, C. A. L.; Bon, S. A. F. *J. Am. Chem. Soc.* **2008**, 130, 16850-16851.
58. Voorn, D. J.; Ming, W.; Herk, A. M. v.; Bomans, P. H. H.; Frederik, P. M.; Gasemjit, P.; Johanssmann, D. *Langmuir* **2005**, 21, 6950-6956.
59. Herrera, N. N.; Letoffe, J.-M.; Putaux, J.-L.; David, L.; Bourgeat-Lami, E. *Langmuir* **2004**, 20, 1564-1571.
60. Mballa, M. M.; Heuts, J. A.; Herk, A. *Colloid. Polym. Sci.* **2013**, 291, 501-513.
61. Herk, A. M. v.; Voorn, D. J.; Ming, W. *Macromolecules* **2006**, 39, 4654-4656.
62. Alexandre, M.; Dubois, P. *Mater. Sci. Eng. R-Rep* **2000**, 28, 1-63.
63. Prado, L. A. S. d. A.; Karthikeyan, C. S.; Schulte, K.; Nunes, S. P.; de Torriani, I. L. *J. Non-Cryst. Solids* **2005**, 351, 970-975.
64. Technical Information B-RI 2 1 Laponite Performance Additives. BYK Additives and Instruments. 2013. Germany.
65. Fitch, R. *Polymer Colloids: A Comprehensive Introduction* Academic Press, London, 1997.
66. Gilbert, R. G. *Emulsion Polymerization: A Mechanistic Approach* Academic Press, London, 1995.
67. Mballa Mballa, M.; Heuts, J. A.; van Herk, A. *Colloid. Polym. Sci.* **2013**, 291, 1419-1427.
68. Herrera, N. N.; Letoffe, J.-M.; Reymond, J.-P.; Bourgeat-Lami, E. *J. Mater. Chem.* **2005**, 15, 863-871.
69. Daniel, L. M.; Frost, R. L.; Zhu, H. Y. *J. Colloid Interface Sci.* **2008**, 321, 302-309.
70. Savard, S.; Blanchard, L. P.; Léonard, J.; Prud'homme, R. E. *Polym. Compos.* **1984**, 5, 242-249.
71. Altmann, S.; Pfeiffer, J. *Monatsh. Chem.* **2003**, 134, 1081-1092.
72. Brinker, C. J.; Scherer, G. W. *Sol-Gel Science: the Physics and Chemistry of Sol-Gel Processing* Academic Press, New York, 1990.
73. Liles, D. T.; Murray, D. L.; D. C. Corporation. Silicone/Organic Copolymer Emulsions US5932651 A **1999**.

74. Bourgeat-Lami, E.; Tissot, I.; Lefebvre, F. *Macromolecules* **2002**, 35, 6185-6191.
75. Tissot, I.; Reymond, J. P.; Lefebvre, F.; Bourgeat-Lami, E. *Chem. Mater.* **2002**, 14, 1325-1331.
76. Coltrain, B. K.; Landry, C. J. T.; O'Reilly, J. M.; Chamberlain, A. M.; Rakes, G. A.; Sedita, J. S.; Kelts, L. W.; Landry, M. R.; Long, V. K. *Chem. Mater.* **1993**, 5, 1445-1455.
77. Rao, V. L.; Babu, G. N. *Eur. Polym. J.* **1989**, 25, 605-609.
78. Varma, I. K.; Tomar, A. K.; Anand, R. C. *J. Appl. Polym. Sci.* **1987**, 33, 1377-1388.
79. Wei, Y.; Yang, D.; Tang, L.; Hutchins, M. K. *J. Mater. Res.* **1993**, 8, 1143-1152.
80. Slomkowski, S.; Alemán José, V.; Gilbert Robert, G.; Hess, M.; Horie, K.; Jones Richard, G.; Kubisa, P.; Meisel, I.; Mormann, W.; Penczek, S.; Stepto Robert, F. T. *Pure Appl. Chem.* **2011**, 83, 2229-2259.
81. Dynamic Mechanical Analysis (DMA). PerkinElmer. 2008. USA.
82. Plummer, C. J. G.; Ruggerone, R.; Bourgeat-Lami, E.; Månson, J.-A. E. *Polymer* **2011**, 52, 2009-2015.
83. van der Vegt, A. K. *From Polymers to Plastics* VSSD, The Netherlands, 2002.
84. Scheirs, J. *Compositional and Failure Analysis of Polymers: A Practical Approach* John Wiley & Sons, U.K., 2000.
85. Mittal, V. *Polymer Nanocomposites by Emulsion and Suspension Polymerization* RSC Publishing, Cambridge, 2011.
86. Zhu, J.; Wilkie, C. A. *Polym. Int.* **2000**, 49, 1158-1163.
87. Burnside, S. D.; Giannelis, E. P. *Chem. Mater.* **1995**, 7, 1597-1600.
88. Chirowodza, H.; Weber, W.; Hartmann, P.; Pasch, H. *Macromol. Symp.* **2012**, 313-314, 135-145.
89. Blumstein, A. *J. Polym. Sci. A Gen.* **1965**, 3, 2665-2672.
90. Gilman, J. W. *Applied Clay Science* **1999**, 15, 31-49.

91. Colver, P. J. *Using Pickering Stabilisation as a Tool for the Fabrication of Supra-Colloidal Structures* Ph.D. University of Warwick.Chemistry Department. U.K. 2008.

## Chapter 6: Conclusions and Outlook

---

In this thesis we have explored two areas particle encapsulation and modification and responsive microgels. In this Chapter we discuss the conclusions of the work presented in this thesis and discuss future work and potential applications.

**Chapter 2** investigated the encapsulation of non-spherical, sub-micron calcium carbonate particles, from which we produced hollow non-spherical particles. We also touched upon the potential to use this encapsulation method to prepare nano-rattles. *Further investigation into the versatility of the encapsulating polymerization by encapsulating other pigment particles such as titanium dioxide or phthalocyanine blue would be of great interest. Further analysis is needed of the morphology of the silica-CaCO<sub>3</sub> particles (cross-sections prepared by FIB-SEM) and nano-rattle structure by TEM and EDX.*

**Chapter 3** described modification by thiol-ene Michael addition of the polymer encapsulated calcium carbonate particles synthesized in Chapter 2. We determined, by Raman spectroscopy and quantitative analysis of pendant vinyl groups by bromination titrations, that small hydrophilic (2-mercaptoethanol) and hydrophobic (1-dodecanethiol) molecules were found to not only react with the surface vinyl groups but penetrated the polymer shell to consume all pendant vinyl groups. Contrastingly  $\omega$ -thiol functionalized poly(styrene) only reacted with 22 % of the pendant vinyl groups. *Further investigations to determine whether surface modification does in-fact alter the dispersibility of these composite particles. This could be achieved by dispersing poly(styrene) modified poly(PETA) within a poly(styrene) polymer melt followed by investigation of polymer melt rheology and mechanical analysis to determine the effect of the modification.*

**Chapter 4** explored the polymerization of DEGDA and MAA in the absence of calcium carbonate; it was found that stable microgel particles were formed, which exhibited pH responsive behaviour, wherein poly(DEGDA-co-MAA) particles swelled to 49 times their volume when the pH was adjusted to 8. We utilized this pH responsiveness to investigate gelling of the microgels; gels formed at 0.036 polymer volume fraction. We also investigated their performance as Pickering stabilizers for dodecane-in-water emulsions, from which highly concentrated emulsions were formed which gelled at high pH. *Further investigation into gelling behaviour of the microgels at various pHs is required. Cryo-SEM analysis of emulsions stabilized with these microgel particles would provide invaluable information on their structure and would provide insight into their wettability at various pHs.*

**Chapter 5** investigated the synthesis and analysis of multi-layered composite particles where the inner-shell is composed of a layer of immobilized Laponite clay. We explored the effect of particle morphology on the bulk properties of films through mechanical and thermal analysis. *Cryo-TEM of the multi-layered particles is required to determine the particles morphology. Analysis of film structure by analysing cross-sections (prepared by FIB-SEM) using cryo-TEM would provide much needed information to fully justify findings from mechanical and thermal analysis.*



# Appendix I: Characterization of Colloids

---

## I.1. Gravimetry

Polymer conversion was measured by gravimetry, where samples were taken during and at the end of the reaction. Samples were weighed immediately as they were taken from the reaction vessel ( $M_{Wet}$ ), and after drying they were weighed again ( $M_{Dry}$ ). During drying we assume that all water and unreacted monomer evaporates. Monomer conversion  $X_m$  is calculated using the following equation:

$$X_m = \left( \frac{M_{Dry}}{M_{Wet}} - \frac{M_{0,Solid}}{M_{0,Total}} \right) \times \left( \frac{M_{0,Total}}{M_{0,Monomer}} \right) \quad (I.1)$$

Where  $M_{0,Solid}$  is the mass of any solid added into the reaction, such as surfactant or pigment,  $M_{0, Total}$  is the total mass of the system and  $M_{0,Monomer}$  is the mass of monomer added to the reaction.

## I.2. Electrophoretic Light Scattering

Electrophoretic light scattering measures the electrophoretic mobility of charged particles relative to the liquid they are suspended in. Electrophoretic mobility is the velocity of a particle in a unit electric field; in addition to Brownian motion, charged particles in an electric field move to the oppositely charged electrode. A liquid layer in two parts around the particle, the Stern (inner) layer where ions are strongly bound to the particles surface and the diffuse (outer) layer where the ions are more loosely associated; the potential measured at the boundary of the diffuse layer (known as the slipping plane) is the zeta potential (Figure I.1). The zeta potential ( $Z$ ) is related to the electrophoretic mobility by the Henry equation:

$$U_E = \frac{2\varepsilon Z f(\kappa a)}{3\eta} \quad (\text{I.2})$$

Where  $U_E$  is the electrophoretic mobility,  $\varepsilon$  is the dielectric constant,  $\eta$  is the viscosity and  $f(\kappa a)$  is Henry's function where  $\kappa$  is the Debye length and  $a$  is the radius of the particle ( $\kappa a$  is the ratio of the particles radius to the electrical double layer).

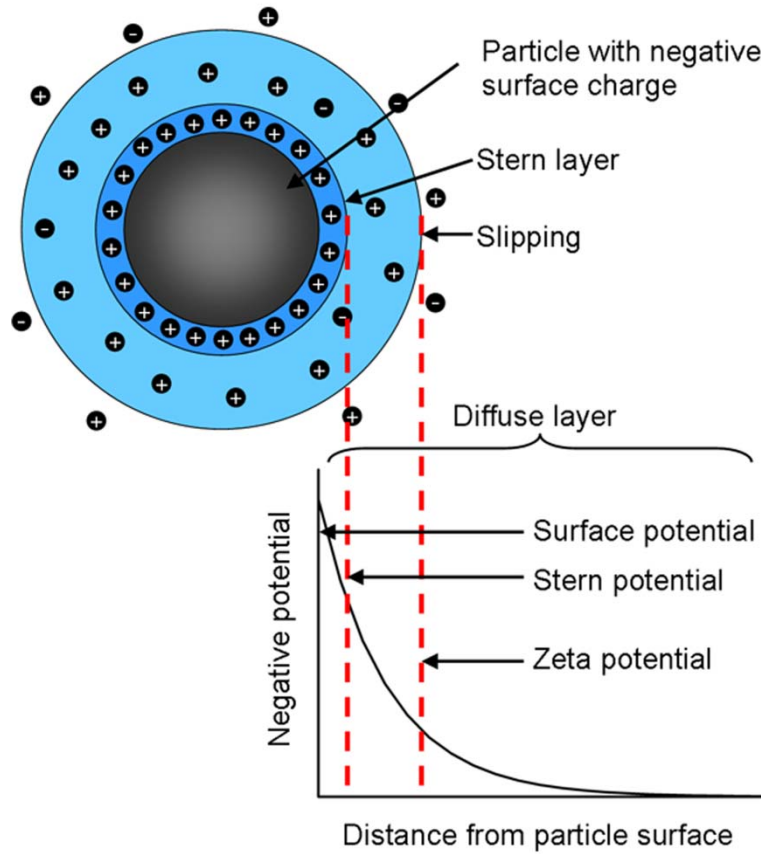


**Figure I.1** Schematic representation of the slipping plane and the corresponding zeta potential.

The Smoluchowski approximation is applied, this assumes the thickness of the double layer is negligible in comparison to the particle size;  $f(\kappa a)$  is taken to be 1.5. This approximation holds for particles greater than 200 nm in diameter and for aqueous media of moderate electrolyte concentration ( $>10^{-1}$  M).

Electrophoretic mobility is measured using a combination of Laser Doppler Velocimetry and phase analysis light scattering. Two laser beams cross in the sample

cell to form interference fringes, when the electric field is applied the particles move and scatter the light. The intensity of scattered light fluctuates with a frequency which is related to the particle velocity, thus electrophoretic mobility. Zeta potential is not a measure of surface potential, however, the magnitude of the zeta potential provides an indication of the stability of the colloidal system.

## I.3. Particle Size Measurements

### I.3.1. Dynamic light scattering

Dynamic light scattering (DLS) measures the Brownian motion of particles, their random movement as they are bombarded by solvent molecules, and relates this to their size; the smaller the particle the faster their Brownian motion. The velocity of Brownian motion, known as the translational diffusion coefficient is measured and the hydrodynamic diameter calculated using the Stokes-Einstein equation:

$$d(H) = \frac{kT}{3\pi\eta D} \quad (\text{I.3})$$

Where  $d(H)$  is the hydrodynamic diameter,  $D$  the translational diffusion coefficient,  $k$  the Boltzmann's constant,  $T$  the absolute temperature and  $\eta$  the viscosity. Hydrodynamic diameter notes that it is related to the movement through a fluid.

The light of the incident beam is scattered by the dispersed particles. A detector at  $173^\circ$  records the scattered light, a speckled pattern, and measures the intensity fluctuations over time as this pattern changes due to the movement of particles; smaller particles having faster fluctuations than (Figure I.2).

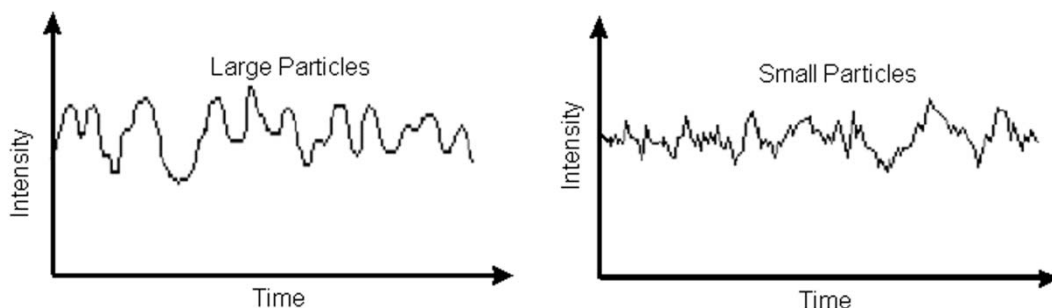


**Figure I.2** Scheme representing typical intensity fluctuations for large and small particles.

A correlator compares the signals over time. The correlation function is an exponential decay; the smaller the particles the quicker the decay function due to faster Brownian motion and thus more rapid fluctuation of light intensity (Figure I.3).

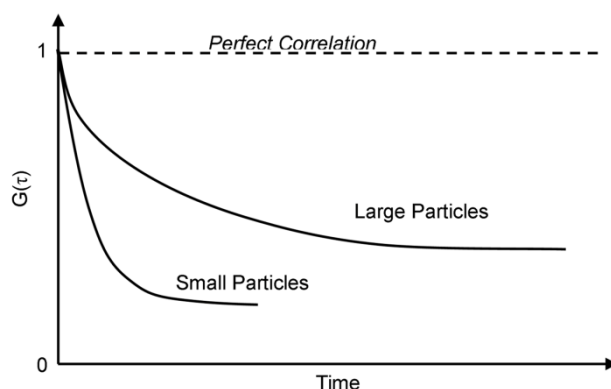


**Figure I.3** Graph of the correlation function as a function of time for small or large particles in dynamic light scattering measurements.

### I.3.2. Laser diffraction

Dispersed colloidal particles will scatter a laser beam with an angle that is particle size dependent; the angle increases with decreasing particle size. Particle size also affects the intensity of scattered light with smaller particles exhibiting a decreased intensity. Mie theory is applied to the scattering pattern. Mie scattering takes the following assumptions: the particles are spherical, the sample is dilute and the optical properties of the sample and dispersant are known. Although the theory

assumes the particles to be spherical non-spherical particles can be measured, in this case an equivalent spherical diameter is given.

## **I.4. Electron Microscopy**

Electron microscopy is similar in principle to optical microscopy, but light is replaced by an electron beam. High vacuum is required for propagation of the electron beam. The electrons are accelerated by an electrical potential and are focussed by a series of electromagnetic lenses. The resolution of the image is question is determined by the wavelength of the beam, light has a wavelength of approximately 400 nm, the wavelength of an electron beam is proportional to the accelerating voltage, for example at 20 keV the equivalent wavelength is 0.01 nm.

### **I.4.1. Scanning electron microscopy**

SEM produces topographical images of the sample by detecting the intensity of backscattered and escaping secondary electrons. Electron potentials in the range of 1-30 keV can be used, higher electron potentials provide greater resolution, though can be damaging to softer materials (i.e. low  $T_g$  polymers). If not conducting, the sample must be coated in a thin layer of conductive material, either carbon by carbon evaporation or a metallic layer of Au, AuPd or Pt by sputter coating. The conductive surface prevents the accumulation of negative charge and deflection of the imaging beam. The conductive layer can cause artefacts in the image.

### **I.4.2. Transmission electron microscopy**

TEM uses a higher electron potential than SEM, in the range of 80 kV to 1 MV, resulting in a much higher resolution. Transmission relays that the electron beam passes through the sample, thus only very thin samples can be analysed. Contrast is obtained from partial scattering of the electron beam passing through the

sample; the higher the electron density of the material the stronger the electron scattering resulting in a darker contrast of the image.

Cryo-TEM is where the water-borne sample is frozen and is used for very soft materials (such as polymers with low  $T_g$ ) or to image in solution; this is achieved by plunging the grid with a thin layer of water containing the particles into liquid ethane, this rapidly freezes the sample resulting in amorphous ice (crystalline ice yields artefacts and reduces resolution, trapped ethane can also produce artefacts in the image).

## I.5. Rheology

Rheology describes the flow of materials. Viscosity describes the resistance or stress (Pa) of a material with respect to an applied force, in this case shear rate ( $s^{-1}$ ).

$$Viscosity = \frac{Shear\ Stress}{Shear\ Rate}$$

The profile of the plot of viscosity vs. shear strain indicates whether the material is Newtonian (i.e. viscosity is unaffected by shear rate), shear thinning (i.e. on increasing shear rate viscosity decreases) or shear thickening (i.e. on increasing shear rate viscosity increases). The plot of shear stress vs. shear rate also elucidates on the type of material (Figure I.4). The majority of colloidal systems are shear thinning. Some materials have a yield stress, an increasing viscosity as shear rate tends to zero, indicating solid like behaviour when at rest. Alternatively a material may exhibit a Newtonian plateau, which describes liquid like behaviour as shear rate tends to zero. These are observed in the Log plot of shear viscosity vs. shear rate (Figure I.5).

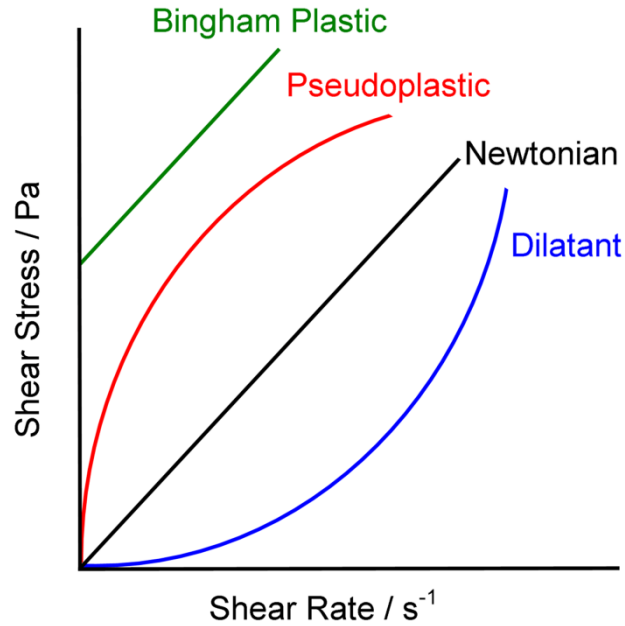


**Figure I.4** Scheme of shear stress vs. shear rate, illustrating changes in plot for Newtonian and non-Newtonian materials.

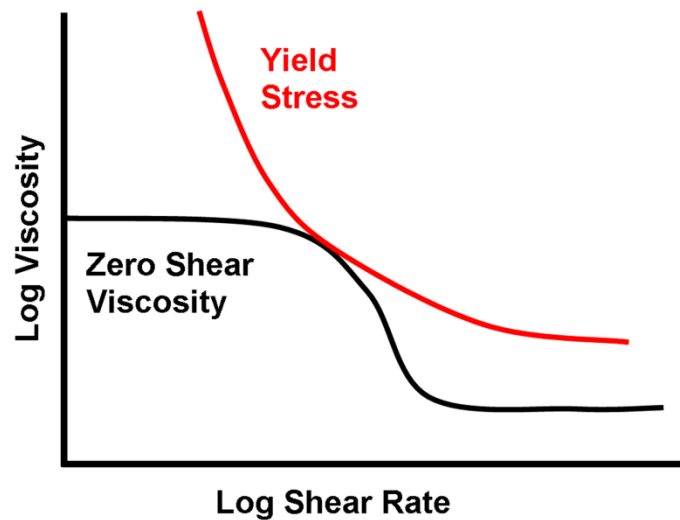


**Figure I.5** Scheme illustrating the appearance of a yield stress and zero shear viscosity on a log plot of viscosity vs. shear rate.

We can also define a materials viscoelastic behaviour by probing the response to oscillatory deformation and frequency sweep. Oscillatory analysis characterizes viscoelastic behaviour by applying a sinusoidal force (shear stress) and measuring the displacement (strain) (Figure I.6). The modulus, or stiffness, of the material is defined by shear stress divided by shear strain.

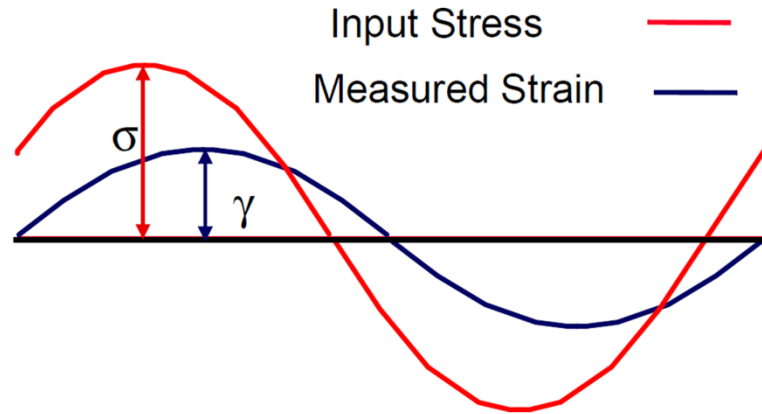


**Figure I.6** Scheme indicating relationship between applied stress and measure strain for viscoelastic materials.

The phase angle is the lag between the applied and measured sinusoidal signal and describes the ratio of viscous and elastic properties (Figure I.7).

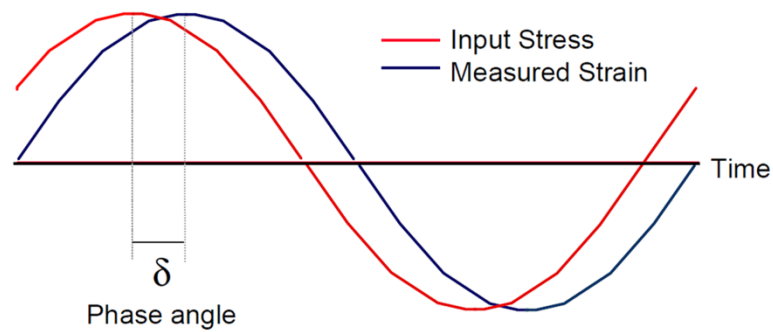


**Figure I.7** Illustration of the phase angle as a result the lag between applied and measured sinusoidal signals.

For a purely elastic material (solid-like behaviour) the sinusoidal curve of applied stress and measured strain are in phase as it exhibits instantaneous deformation on applied force, thus  $\delta = 0^\circ$ . For a purely viscous material (liquid-like behaviour) the sinusoidal curve of applied stress and measured strain are a quarter of a cycle out of phase, thus  $\delta = 90^\circ$  (Figure I.8).



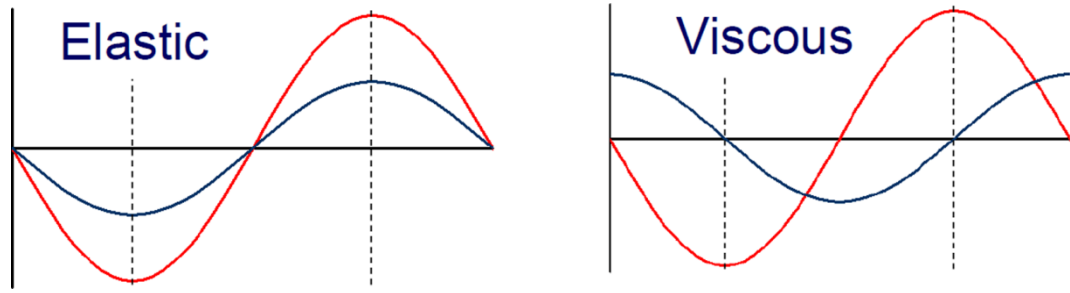


**Figure I.8** Illustration of the phase angle of purely elastic and purely viscous materials.

From this we can define the storage (elastic) modulus ( $G'$ ) and the loss (viscous) modulus ( $G''$ ):

$$G' = \frac{\text{Stress}}{\text{Strain}} \times \sin \delta$$

$$G'' = \frac{\text{Stress}}{\text{Strain}} \times \cos \delta$$

If  $G' > G''$ ,  $\delta < 45^\circ$ , thus the material is solid-like. If  $G' < G''$ ,  $\delta > 45^\circ$ , thus the material is liquid-like. Amplitude sweep oscillatory measurements illustrate the stability of a material; it is used to determine the linear viscoelastic region (LVR), ensuring subsequent measurements are under conditions that will not destroy the material. A frequency sweep is used to classify a material (Figure I.9).

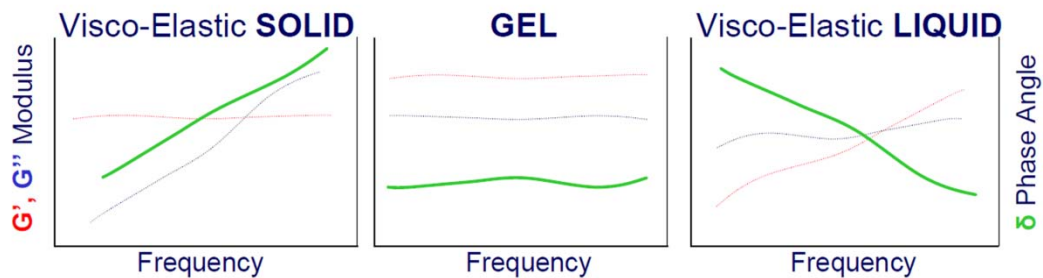


**Figure I.9** Illustration of plots produced from a frequency sweep for viscoelastic solids, viscoelastic liquids and gels.

## Appendix II: Complement to Chapter 2

### II.1. Raw Zeta Potential Data

**Table II.1** Raw data for zeta potential measurements as a function of [NaCl] for calcium carbonate (SOCAL P3) (Figure 2.14).

| [NaCl]<br>(mol dm <sup>-3</sup> ) | Zeta Potential<br>(mV ± S.D.) | Mobility<br>(μmcm/Vs ± S.D.) | Conductivity<br>(mS/cm ± S.D.) |
|-----------------------------------|-------------------------------|------------------------------|--------------------------------|
| 0                                 | 10.7 ± 0.500                  | 0.8402 ± 0.03931             | 0.0477 ± 0.00182               |
| 0.001                             | 11.7 ± 0.268                  | 0.9167 ± 0.02152             | 0.164 ± 0.00378                |
| 0.005                             | 10.2 ± 0.750                  | 0.8009 ± 0.05924             | 0.621 ± 0.0185                 |
| 0.01                              | 9.01 ± 0.479                  | 0.7065 ± 0.03755             | 1.28 ± 0.0622                  |
| 0.05                              | 7.42 ± 0.786                  | 0.5816 ± 0.06160             | 5.49 ± 0.117                   |
| 0.1                               | 5.23 ± 0.807                  | 0.4102 ± 0.06322             | 10.7 ± 0.446                   |
| 0.5                               | 3.23 ± 0.907                  | 0.3735 ± 0.07109             | 45.6 ± 1.56                    |
| 1                                 | 0.055 ± 0.200                 | 0.04501 ± 0.06288            | 86.8 ± 1.20                    |

**Table II.2** Raw data for zeta potential measurements as a function of pH for calcium carbonate (SOCAL P3) (Figure 2.15).

| pH    | Zeta Potential<br>(mV $\pm$ S.D.) | Mobility<br>( $\mu\text{mcm/Vs}$ $\pm$ S.D.) | Conductivity<br>(mS/cm $\pm$ S.D.) |
|-------|-----------------------------------|--|------------------------------------|
| 8.56  | 16.03 $\pm$ 0.472                 | 1.257 $\pm$ 0.03721                          | 0.161 $\pm$ 0.00197                |
| 9.10  | 16.03 $\pm$ 0.520                 | 1.256 $\pm$ 0.04202                          | 0.0835 $\pm$ 0.00132               |
| 9.33  | 12.25 $\pm$ 0.967                 | 0.9612 $\pm$ 0.07584                         | 0.0459 $\pm$ 0.00127               |
| 9.51  | 14.37 $\pm$ 0.952                 | 1.125 $\pm$ 0.07427                          | 0.135 $\pm$ 0.00216                |
| 10.00 | 12.97 $\pm$ 0.403                 | 1.016 $\pm$ 0.03062                          | 0.0515 $\pm$ 0.000774              |
| 10.62 | 3.07 $\pm$ 0.511                  | 0.2404 $\pm$ 0.04077                         | 0.106 $\pm$ 0.00114                |
| 10.97 | 1.01 $\pm$ 0.530                  | 0.07956 $\pm$ 0.04167                        | 0.184 $\pm$ 0.00274                |
| 11.27 | 0.614 $\pm$ 0.490                 | 0.04819 $\pm$ 0.03852                        | 0.342 $\pm$ 0.00515                |
| 11.32 | -4.89 $\pm$ 0.721                 | -0.3834 $\pm$ 0.05652                        | 0.423 $\pm$ 0.00882                |
| 11.75 | -5.72 $\pm$ 1.08                  | -0.4482 $\pm$ 0.08482                        | 1.04 $\pm$ 0.0386                  |
| 11.88 | -41.22 $\pm$ 1.39                 | -3.230 $\pm$ 0.1104                          | 1.35 $\pm$ 0.0528                  |
| 11.98 | -13.00 $\pm$ 1.61                 | -1.023 $\pm$ 0.1298                          | 1.84 $\pm$ 0.0872                  |
| 12.28 | -13.28 $\pm$ 2.11                 | -1.039 $\pm$ 0.1664                          | 1.04 $\pm$ 0.0386                  |
| 12.36 | -16.7 $\pm$ 1.35                  | -1.311 $\pm$ 0.1055                          | 5.11 $\pm$ 0.402                   |

**Table II.3** Raw data for zeta potential measurements as a function of [NaCl] for calcium carbonate particles encapsulated in a poly(MAA-*co*-DEGDA) shell (Figure 2.22).

| [NaCl]<br>(mol dm <sup>-3</sup> ) | Zeta Potential<br>(mV ± S.D.) | Mobility<br>(μmcm/Vs ± S.D.) | Conductivity<br>(mS/cm ± S.D.) |
|-----------------------------------|-------------------------------|------------------------------|--------------------------------|
| 0.001                             | -29.1 ± 0.542                 | -2.280 ± 0.04358             | 0.187 ± 0.00264                |
| 0.005                             | -34.4 ± 0.953                 | -2.696 ± 0.07418             | 0.705 ± 0.0285                 |
| 0.01                              | -35.7 ± 1.59                  | -2.799 ± 0.1248              | 1.29 ± 0.0776                  |
| 0.05                              | -28.2 ± 1.07                  | -2.210 ± 0.08258             | 5.38 ± 0.127                   |
| 0.1                               | -26.4 ± 1.61                  | -2.064 ± 0.1265              | 11.5 ± 0.440                   |
| 0.5                               | -20.8 ± 1.43                  | -1.628 ± 0.1137              | 46.6 ± 0.972                   |
| 1                                 | -13.8 ± 1.50                  | -1.085 ± 0.115               | 86.5 ± 2.43                    |

**Table II.4** Raw data for zeta potential measurements as a function of [NaCl] for calcium carbonate encapsulated in poly(MAA-*co*-DEGDA) primer followed by a poly(MMA) shell (HM-4-136) (Figure 2.30).

| [NaCl]<br>(mol dm <sup>-3</sup> ) | Zeta Potential<br>(mV ± S.D.) | Mobility<br>(μmcm/Vs ± S.D.) | Conductivity<br>(mS/cm ± S.D.) |
|-----------------------------------|-------------------------------|------------------------------|--------------------------------|
| 0.001                             | -29.5 ± 0.378                 | -2.309 ± 0.03058             | 0.179 ± 0.00472                |
| 0.005                             | -33.6 ± 1.14                  | -2.637 ± 0.08805             | 0.704 ± 0.0293                 |
| 0.01                              | -34.8 ± 1.65                  | -2.727 ± 0.1297              | 1.33 ± 0.0760                  |
| 0.05                              | -28.6 ± 1.56                  | -2.238 ± 0.1214              | 5.75 ± 0.137                   |
| 0.1                               | -26.8 ± 1.57                  | -2.101 ± 0.1252              | 11.1 ± 0.397                   |
| 0.5                               | -17.6 ± 1.15                  | -1.382 ± 0.08954             | 46.8 ± 0.969                   |
| 1                                 | -11.7 ± 0.920                 | -0.9194 ± 0.07290            | 86.5 ± 2.55                    |

**Table II.5** Raw data for zeta potential measurements as a function of pH for amorphous calcium carbonate (Figure 2.40).

| pH    | Zeta Potential<br>(mV $\pm$ S.D.) | Mobility<br>( $\mu\text{mcm/Vs}$ $\pm$ S.D.) | Conductivity<br>(mS/cm $\pm$ S.D.) |
|-------|-----------------------------------|--|------------------------------------|
| 7.50  | -21.4 $\pm$ 1.12                  | -1.675 $\pm$ 0.08710                         | 0.224 $\pm$ 0.00273                |
| 8.04  | -15.3 $\pm$ 1.65                  | -1.201 $\pm$ 0.1304                          | 0.167 $\pm$ 0.00240                |
| 8.43  | -12.5 $\pm$ 1.47                  | -0.9837 $\pm$ 0.1144                         | 0.201 $\pm$ 0.0033                 |
| 8.51  | -6.18 $\pm$ 1.82                  | -0.4841 $\pm$ 0.1427                         | 0.174 $\pm$ 0.00179                |
| 9.02  | -2.04 $\pm$ 1.64                  | -0.1596 $\pm$ 0.1282                         | 0.117 $\pm$ 0.000894               |
| 9.49  | -0.0353 $\pm$ 0.149               | -0.002762 $\pm$ 0.0165                       | 0.00444 $\pm$ 0.0062               |
| 10.08 | -12.9 $\pm$ 0.737                 | -1.016 $\pm$ 0.05752                         | 0.109 $\pm$ 0.0012                 |
| 10.95 | -16.0 $\pm$ 1.11                  | -1.255 $\pm$ 0.08709                         | 0.309 $\pm$ 0.00417                |

**Table II.6** Raw data for zeta potential measurements as a function of pH for amorphous calcium carbonate-silica composite particles (Figure 2.40).

| pH    | Zeta Potential<br>(mV $\pm$ S.D.) | Mobility<br>( $\mu\text{mcm/Vs}$ $\pm$ S.D.) | Conductivity<br>(mS/cm $\pm$ S.D.) |
|-------|-----------------------------------|--|------------------------------------|
| 7.65  | -19.1 $\pm$ 0.924                 | -1.498 $\pm$ 0.07157                         | 0.662 $\pm$ 0.0243                 |
| 8.14  | -22.8 $\pm$ 0.869                 | -1.782 $\pm$ 0.06888                         | 0.550 $\pm$ 0.0177                 |
| 8.47  | -23.5 $\pm$ 1.07                  | -1.839 $\pm$ 0.08290                         | 0.343 $\pm$ 0.00824                |
| 8.97  | -25.6 $\pm$ 0.599                 | -2.003 $\pm$ 0.04646                         | 0.204 $\pm$ 0.00378                |
| 9.54  | -27.5 $\pm$ 0.717                 | -2.003 $\pm$ 0.04646                         | 0.123 $\pm$ 0.00216                |
| 9.88  | -32.3 $\pm$ 0.483                 | -2.535 $\pm$ 0.03835                         | 0.0814 $\pm$ 0.00133               |
| 10.00 | -32.5 $\pm$ 0.522                 | -2.547 $\pm$ 0.04182                         | 0.0876 $\pm$ 0.00129               |
| 10.59 | -43.3 $\pm$ 1.01                  | -3.398 $\pm$ 0.8005                          | 0.221 $\pm$ 0.0048                 |
| 10.91 | -46.6 $\pm$ 0.607                 | -3.651 $\pm$ 0.04741                         | 0.288 $\pm$ 0.00565                |

## II.2. Repeated Conversion Plots for $\text{CaCO}_3$ Encapsulation

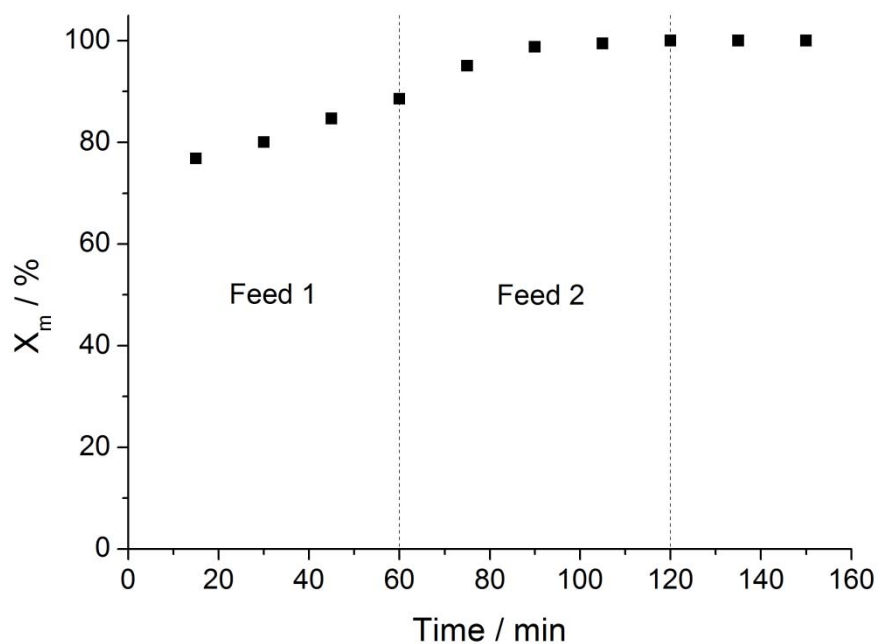


**Figure II.1** Overall monomer conversion,  $X_m$ , versus time for the encapsulation of calcium carbonate (HM-4-120, repeat of HM-3-014). Feed 1; MAA and DEGDA mixture. Feed 2; DEGDA. Monomer was fed at a rate of  $0.5 \text{ mL h}^{-1}$ .

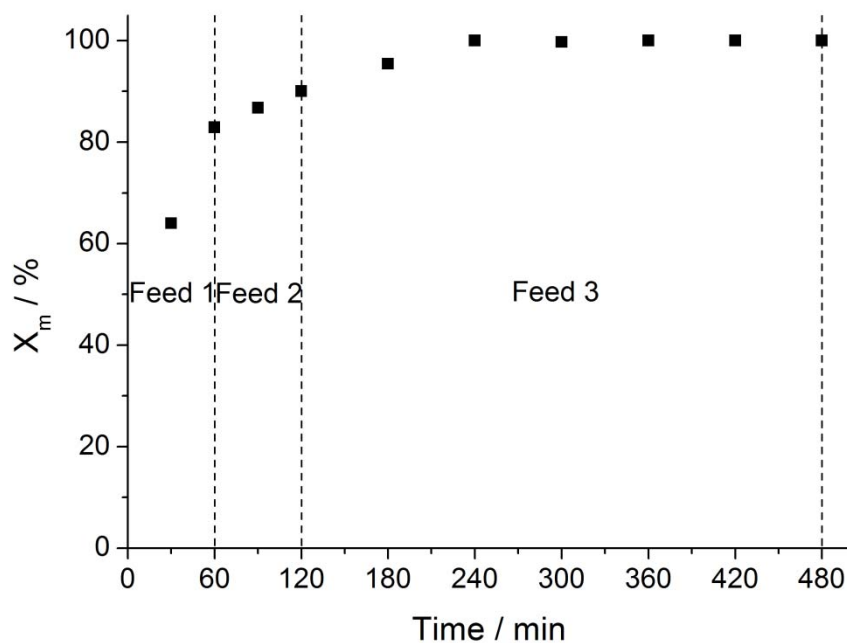


**Figure II.2** Overall monomer conversion;  $X_m$  vs. time of encapsulation of calcium carbonate (HM-4-136, repeat of HM-3-006). Feed 1; MAA and DEGDA mixture. Feed 2; DEGDA. Feed 3; MMA feed. The first two feeds were fed at a rate of  $0.5 \text{ mL h}^{-1}$  and MMA was fed at a rate of  $1 \text{ mL h}^{-1}$ .

## II.3. EDAX Analysis of Calcium Carbonate-Silica Composite Particles

**Table II.7** Table of wt.% of silica in amorphous  $\text{CaCO}_3$  particles formed in the presence of Ludox calculated from EDAX measurements.

| Number  | Wt.% Silica |
|---------|-------------|
| 1       | 4.595       |
| 2       | 4.920       |
| 3       | 4.915       |
| 4       | 4.055       |
| 5       | 4.491       |
| 6       | 3.762       |
| Average | 4.456       |

## Appendix III: Complement to Chapter 3

### III.1. Additional Images of Composite Particles

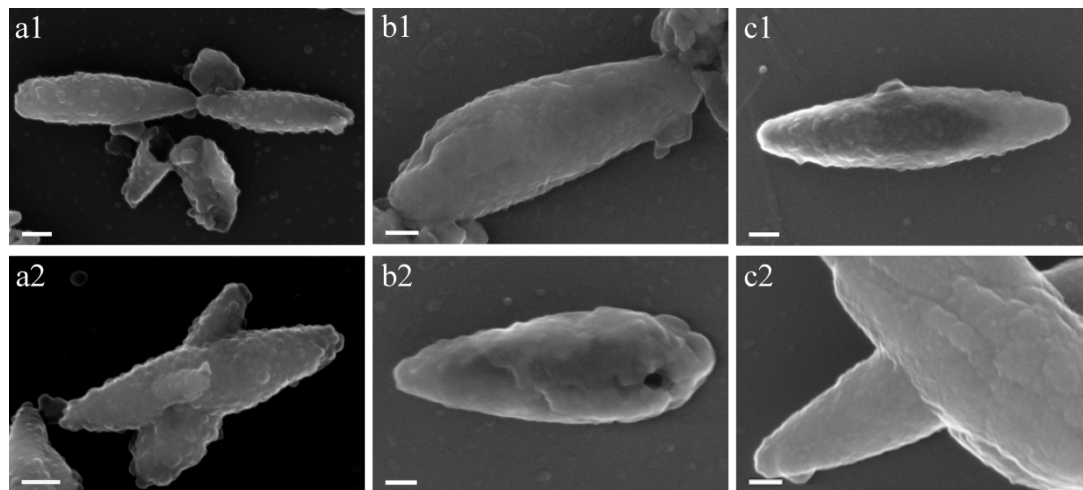


**Figure III.1** SEM images of (a) poly(DEGDA)-C particles (HM-301), (b) poly(PETA)-C and (c) poly(DPEPHA)-C particles ((a) scale bar: 200 nm. (b-c) scale bar: 100 nm).

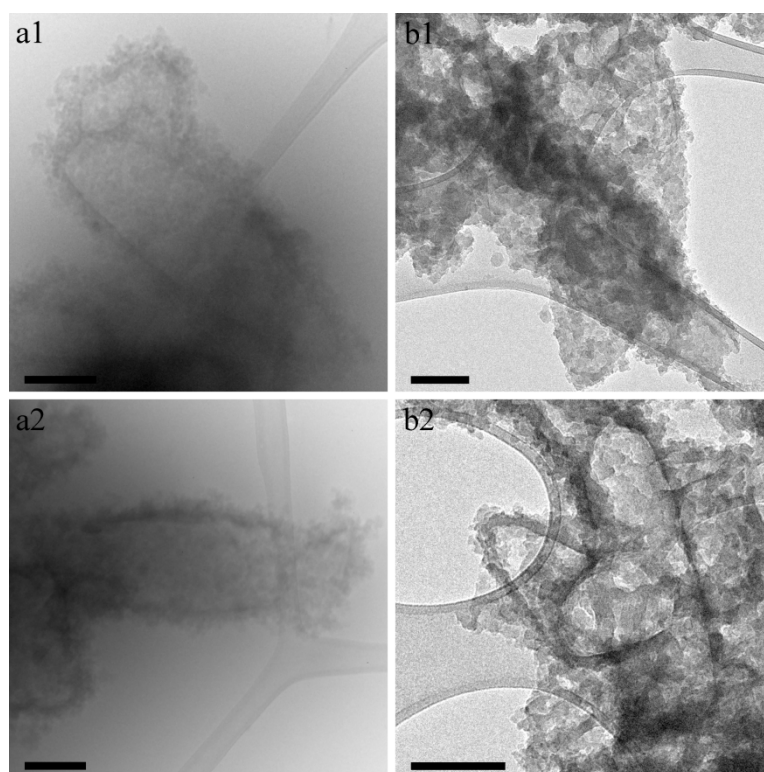


**Figure III.2** Cryo-TEM images of (a) hollowed poly(DEGDA)-C particles (HM-304) and (b) hollowed poly(DPEPHA)-C particles (scale bar: 200 nm).



### III.2. Zeta Potential Data

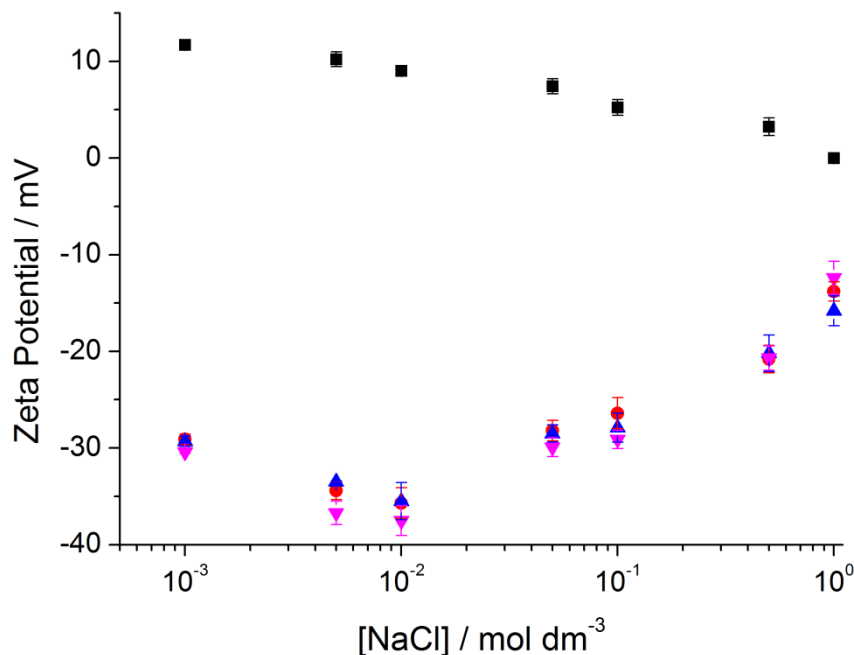


**Figure III.3** Graph of zeta potential of bare  $\text{CaCO}_3$  particles (Socal P3) (■), poly(DEGDA)-C particles (HM-301) (●), poly(PETA)-C particles (HM-302) (▲) and poly(DPEPHA)-C particles (HM-303) (▼) as a function of salt (NaCl) concentration. Zeta potential measurements were performed at pH 9.3 and an average of 6 measurements was recorded.

**Table III.1** Raw data for zeta potential measurements as a function of [NaCl] for calcium carbonate (SOCAL P3).

| [NaCl]<br>(mol dm <sup>-3</sup> ) | Zeta Potential<br>(mV ± S.D.) | Mobility<br>(μmcm/Vs ± S.D.) | Conductivity<br>(mS/cm ± S.D.) |
|-----------------------------------|-------------------------------|------------------------------|--------------------------------|
| 0                                 | 10.7 ± 0.500                  | 0.8402 ± 0.03931             | 0.0477 ± 0.00182               |
| 0.001                             | 11.7 ± 0.268                  | 0.9167 ± 0.02152             | 0.164 ± 0.00378                |
| 0.005                             | 10.2 ± 0.750                  | 0.8009 ± 0.05924             | 0.621 ± 0.0185                 |
| 0.01                              | 9.01 ± 0.479                  | 0.7065 ± 0.03755             | 1.28 ± 0.0622                  |
| 0.05                              | 7.42 ± 0.786                  | 0.5816 ± 0.06160             | 5.49 ± 0.117                   |
| 0.1                               | 5.23 ± 0.807                  | 0.4102 ± 0.06322             | 10.7 ± 0.446                   |
| 0.5                               | 3.23 ± 0.907                  | 0.3735 ± 0.07109             | 45.6 ± 1.56                    |
| 1                                 | 0.055 ± 0.200                 | 0.04501 ± 0.06288            | 86.8 ± 1.20                    |

**Table III.2** Raw data for zeta potential measurements as a function of [NaCl] for calcium carbonate encapsulated in poly(MAA-*co*-DEGDA).

| [NaCl]<br>(mol dm <sup>-3</sup> ) | Zeta Potential<br>(mV ± S.D.) | Mobility<br>(μmcm/Vs ± S.D.) | Conductivity<br>(mS/cm ± S.D.) |
|-----------------------------------|-------------------------------|------------------------------|--------------------------------|
| 0.001                             | -29.1 ± 0.542                 | -2.280 ± 0.04358             | 0.187 ± 0.00264                |
| 0.005                             | -34.4 ± 0.953                 | -2.696 ± 0.07418             | 0.705 ± 0.0285                 |
| 0.01                              | -35.7 ± 1.59                  | -2.799 ± 0.1248              | 1.29 ± 0.0776                  |
| 0.05                              | -28.2 ± 1.07                  | -2.21 ± 0.08258              | 5.38 ± 0.127                   |
| 0.1                               | -26.4 ± 1.61                  | -2.064 ± 0.1265              | 11.5 ± 0.440                   |
| 0.5                               | -20.8 ± 1.43                  | -1.628 ± 0.1137              | 46.6 ± 0.972                   |
| 1                                 | -13.8 ± 1.50                  | -1.085 ± 0.115               | 86.5 ± 2.43                    |

**Table III.3** Raw data for zeta potential measurements as a function of [NaCl] for calcium carbonate encapsulated in poly(MAA-*co*-DEGDA-*co*-PETA).

| [NaCl]<br>(mol dm <sup>-3</sup> ) | Zeta Potential<br>(mV ± S.D.) | Mobility<br>(μmcm/Vs ± S.D.) | Conductivity<br>(mS/cm ± S.D.) |
|-----------------------------------|-------------------------------|------------------------------|--------------------------------|
| 0.001                             | -29.3 ± 0.537                 | -2.297 ± 0.4116              | 0.178 ± 0.00147                |
| 0.005                             | -33.5 ± 0.0961                | -2.624 ± 0.07578             | 0.666 ± 0.0241                 |
| 0.01                              | -35.5 ± 0.0961                | -2.781 ± 0.1518              | 1.28 ± 0.0740                  |
| 0.05                              | -28.5 ± 0.909                 | -2.237 ± 0.06950             | 5.46 ± 0.120                   |
| 0.1                               | -27.9 ± 1.50                  | -2.189 ± 0.1180              | 11.1 ± 0.306                   |
| 0.5                               | -20.1 ± 1.88                  | -1.584 ± 0.1488              | 48.0 ± 1.22                    |
| 1                                 | -15.8 ± 1.54                  | -1.242 ± 0.1215              | 87.9 ± 2.06                    |

**Table III.4** Raw data for zeta potential measurements as a function of [NaCl] for calcium carbonate encapsulated in poly(MAA-*co*-DEGDA-*co*-DPEPHA).

| [NaCl]<br>(mol dm <sup>-3</sup> ) | Zeta Potential<br>(mV ± S.D.) | Mobility<br>(μmcm/Vs ± S.D.) | Conductivity<br>(mS/cm ± S.D.) |
|-----------------------------------|-------------------------------|------------------------------|--------------------------------|
| 0.001                             | -30.4 ± 0.167                 | -2.382 ± 0.01127             | 0.173 ± 0.00351                |
| 0.005                             | -36.7 ± 1.21                  | -2.874 ± 0.09410             | 0.699 ± 0.0284                 |
| 0.01                              | -37.5 ± 1.53                  | -2.937 ± 0.1185              | 1.37 ± 0.0826                  |
| 0.05                              | -29.9 ± 0.985                 | -2.342 ± 0.07564             | 5.64 ± 0.137                   |
| 0.1                               | -29.1 ± 0.945                 | -2.280 ± 0.07432             | 11.1 ± 0.423                   |
| 0.5                               | -20.7 ± 1.25                  | -1.625 ± 0.09847             | 46.9 ± 0.920                   |
| 1                                 | -12.4 ± 1.71                  | -0.9762 ± 0.1340             | 87.5 ± 2.51                    |

## Appendix IV: Complement to Chapter 4

### IV.1. Pycnometry Data

**Table IV.1** Pycnometry of poly(DEGDA-*co*-MAA); sample weight was 0.3226 g and experiment was performed at 28.6 °C.

| Run     | Volume<br>(cm <sup>3</sup> ± S.D.) | Density<br>(g cm <sup>-3</sup> ± S.D.) |
|---------|------------------------------------|--|
| 1       | 0.2268 ± 0.0004                    | 1.4227 ± 0.0025                        |
| 2       | 0.2267 ± 0.0003                    | 1.4232 ± 0.0021                        |
| 3       | 0.2260 ± 0.0003                    | 1.4272 ± 0.0020                        |
| 4       | 0.2261 ± 0.0002                    | 1.4265 ± 0.0013                        |
| 5       | 0.2261 ± 0.0002                    | 1.4267 ± 0.0014                        |
| Average | 0.2263 ± 0.0003                    | 1.4252 ± 0.0021                        |

## IV.2. Rheology of Gels

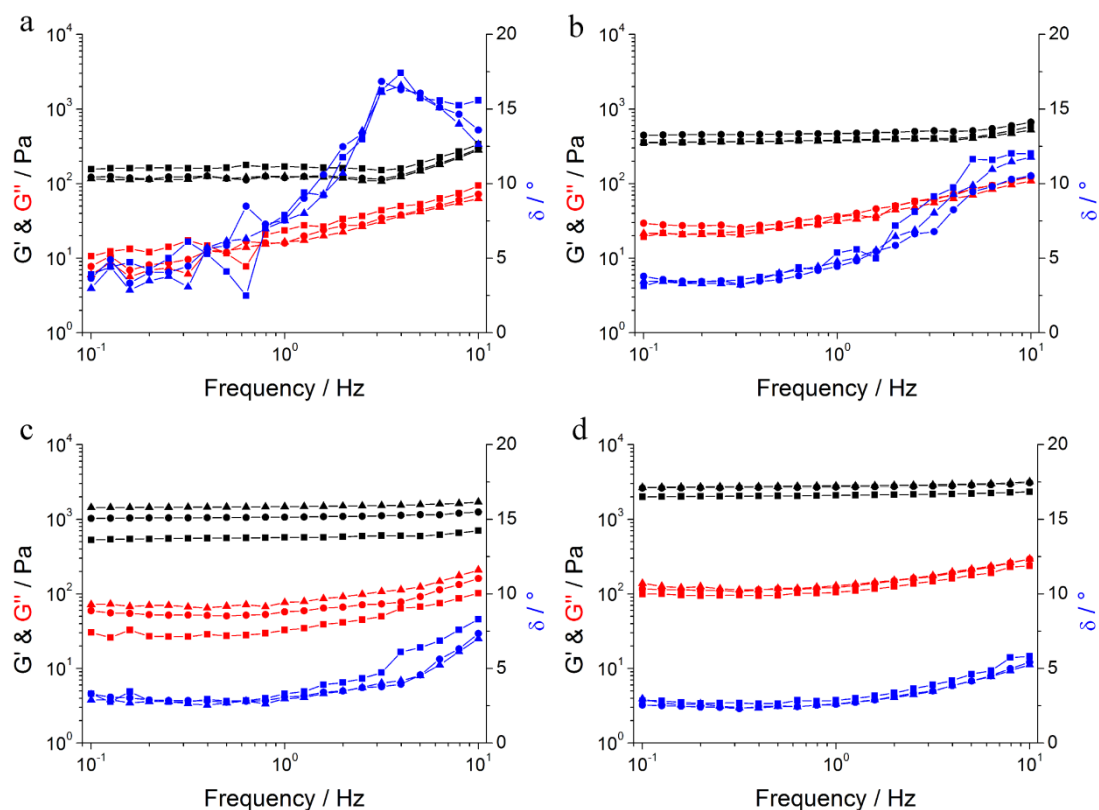


**Figure IV.1** Frequency sweeps of (a) 5, (b) 6, (c) 7.5 and (d) 10 wt.% poly(DEGDA-co-MAA) microgels; storage modulus,  $G'$ , (■), loss modulus,  $G''$ , (■) and phase angle,  $\delta$ , (■). Each frequency sweep was repeated for three different microgels represented by a different shaped symbol; HM-409 (■), HM-410 (●) and HM-411 (▲).

## Appendix V: Complement to Chapter 5

### V.1. Additional SEM Images

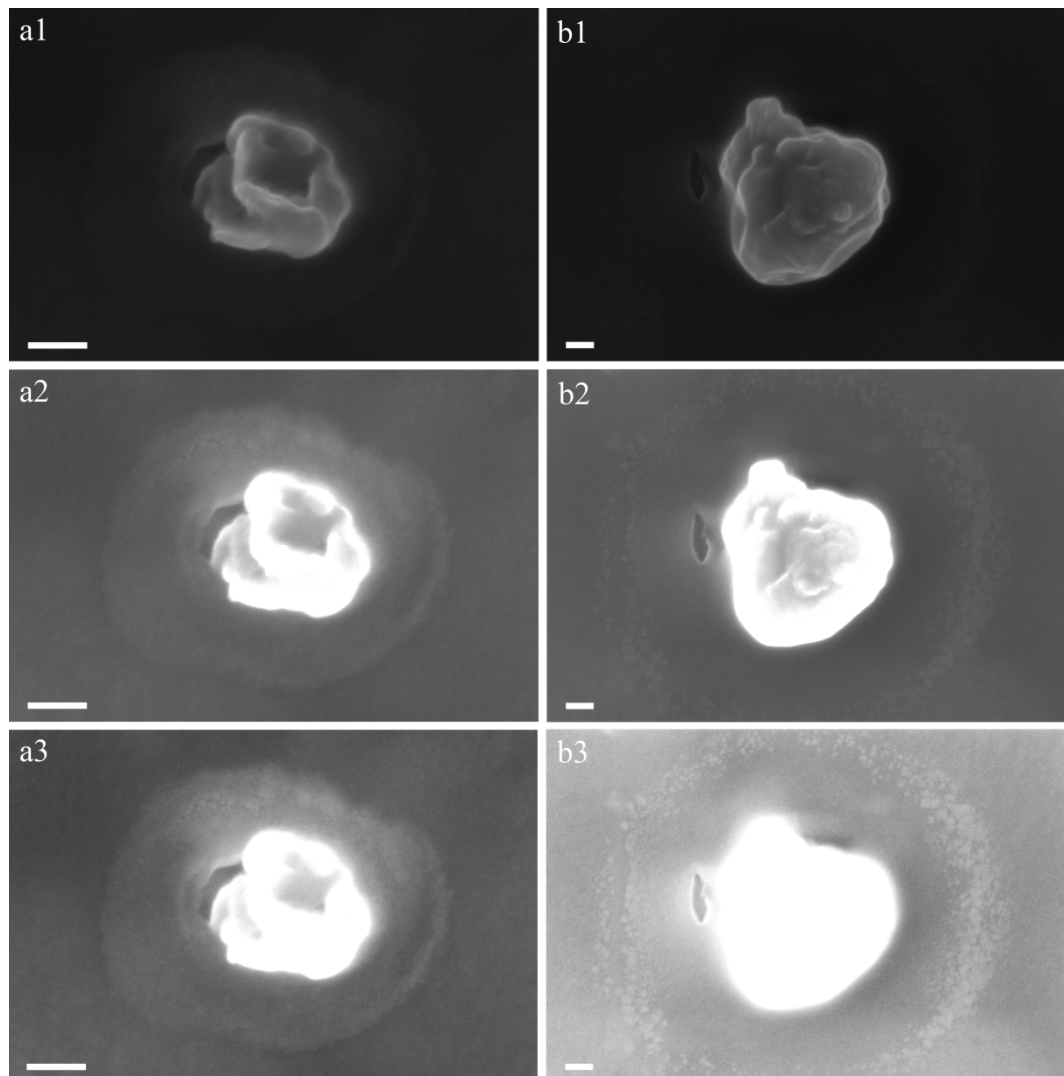


**Figure V.1** Additional SEM images of 1 % cross-linked Laponite Pickering poly(styrene-*co*-*n*-butyl acrylate) encapsulated in film poly(styrene-*co*-*n*-butyl acrylate) (HM-504) (scale: 100 nm). Where a and b are different particles and 1 denotes the original SEM image and 2 and 3 are the image with increased contrast to elucidate the film formed polymer shell. The apparent hole in the images is from sublimed polymer as a result of high magnification (required to accurately focus the image).

## V.2. Temperature Sweep Plots

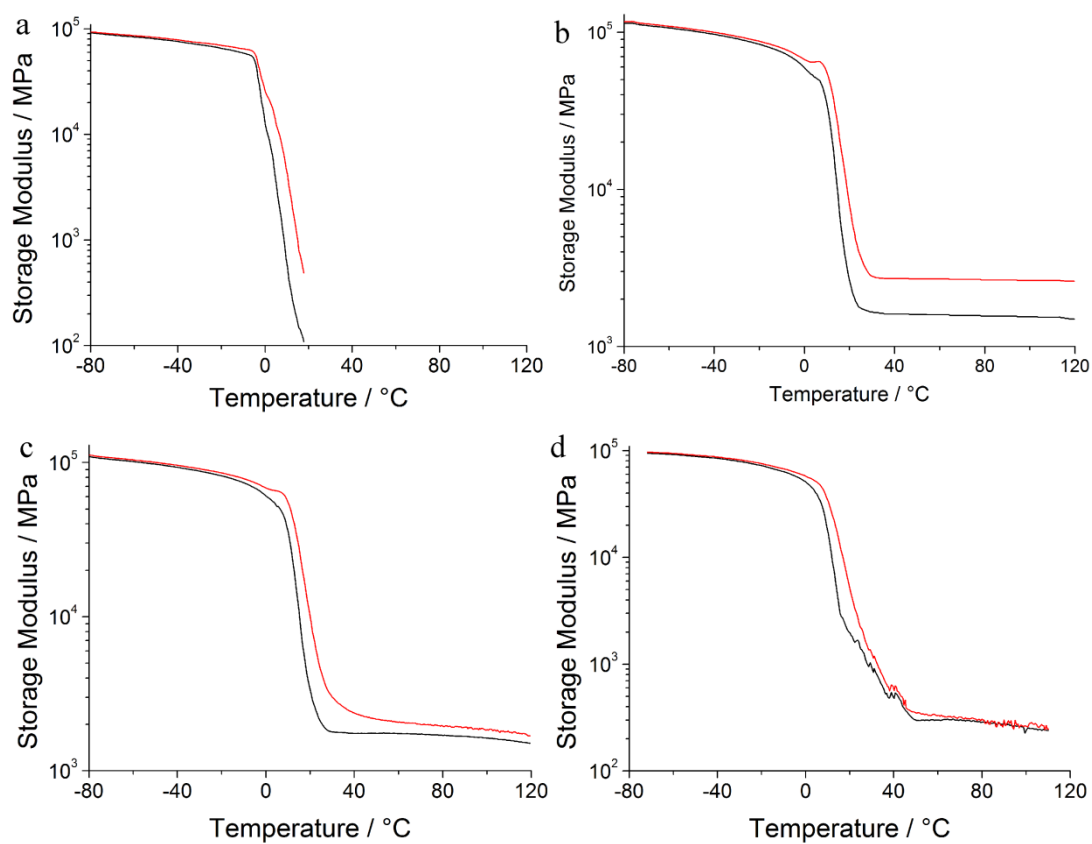


**Figure V.2** Storage modulus vs. temperature for (a) poly(Sty-co-BA) (HM-501), (b) Laponite armoured poly(Sty-co-BA) (HM-502), (c) Laponite core-shell (HM-503) and (d) multi-layered particles (HM-505), conducted at frequencies of 1 Hz (—) and 10 Hz (—).

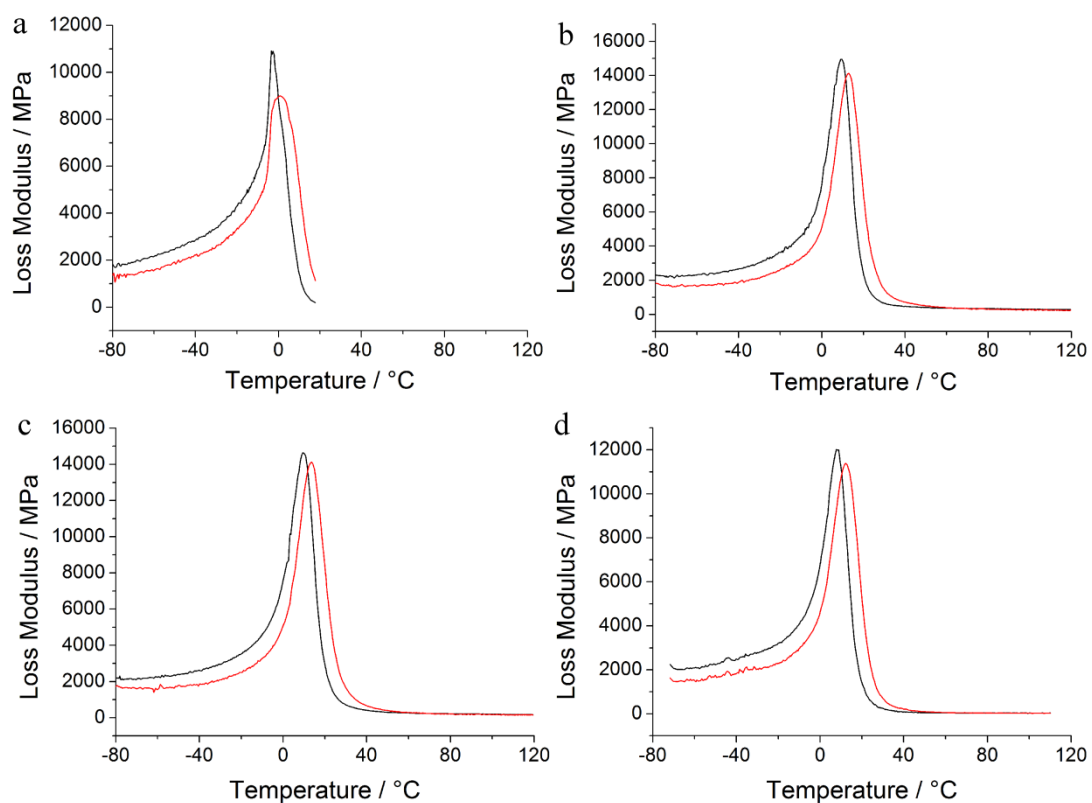


**Figure V.3** Loss modulus vs. temperature for (a) poly(Sty-co-BA) (HM-501), (b) Laponite armoured poly(Sty-co-BA) (HM-502), (c) Laponite core-shell (HM-503) and (d) multi-layered particles (HM-505), conducted at frequencies of 1 Hz (—) and 10 Hz (—).



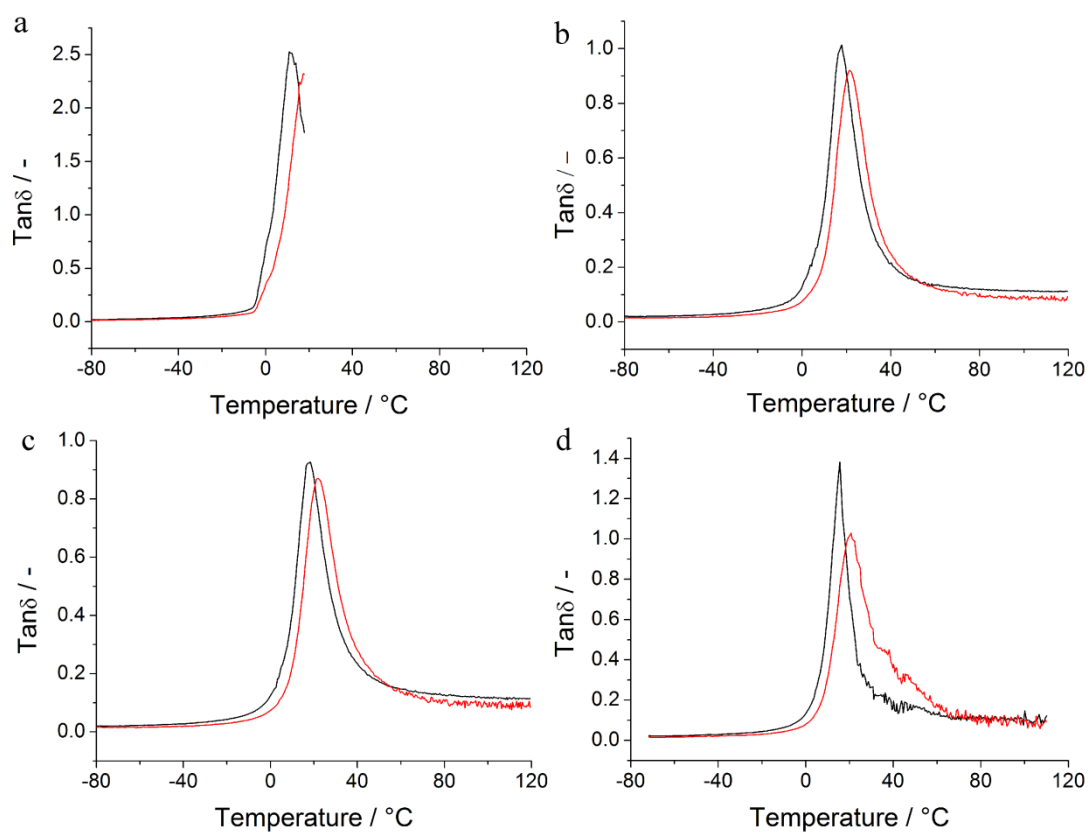


**Figure V.4**  $\text{Tan}\delta$  vs. temperature for (a) poly(Sty-co-BA) (HM-501), (b) Laponite armoured poly(Sty-co-BA) (HM-502), (c) Laponite core-shell (HM-503) and (d) multi-layered particles (HM-505), conducted at frequencies of 1 Hz (—) and 10 Hz (—).

### V.3. Additional DSC Data

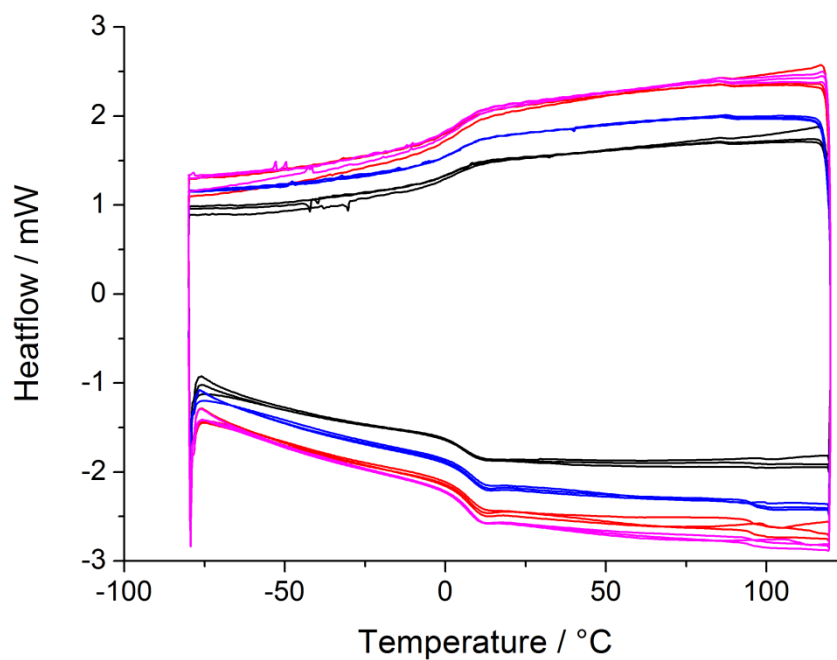


**Figure V.5** DSC of poly(styrene-*co*-*n*-butyl acrylate) film (HM-4-085) (—), 1% Laponite Pickering poly(styrene-*co*-*n*-butyl acrylate) film (HM-4-074) (—), 1% cross-linked Laponite Pickering poly(styrene-*co*-*n*-butyl acrylate) (—) and 1 % cross-linked Laponite Pickering poly(styrene-*co*-*n*-butyl acrylate) encapsulated in film poly(styrene-*co*-*n*-butyl acrylate) (HM-4-095) (—).

**Table V.1** Table of  $T_g$  of the polymer films measured by DSC.

| Exp.     | Film                   | Cycle | $T_g$ (onset)<br>(°C) | $T_g$ (midpoint)<br>(°C) | Average<br>$T_g$ (onset)<br>(°C) | Average<br>$T_g$ (midpoint)<br>(°C) |
|----------|------------------------|-------|-----------------------|--------------------------|----------------------------------|-------------------------------------|
| HM-4-085 | P(Sty- <i>co</i> -BA)  | 1     | -0.34                 | 6.03                     | -0.34                            | 6.01                                |
|          |                        | 2     | -0.37                 | 6.02                     |                                  |                                     |
|          |                        | 3     | -0.32                 | 5.99                     |                                  |                                     |
| HM-4-074 | Laponite<br>armoured   | 1     | 1.91                  | 7.55                     | 1.91                             | 7.55                                |
|          |                        | 2     | 1.90                  | 7.56                     |                                  |                                     |
|          |                        | 3     | 1.91                  | 7.55                     |                                  |                                     |
| HM-4-113 | Laponite<br>core-shell | 1     | 2.38                  | 8.23                     | 2.35                             | 8.21                                |
|          |                        | 2     | 2.32                  | 8.19                     |                                  |                                     |
|          |                        | 3     | 2.35                  | 8.20                     |                                  |                                     |
| HM-4-095 | Multi-layered          | 1     | 1.82                  | 7.10                     | 1.89                             | 7.09                                |
|          |                        | 2     | 1.98                  | 7.10                     |                                  |                                     |
|          |                        | 3     | 1.88                  | 7.07                     |                                  |                                     |

## V.4. TGA vs. Heatflow Plots

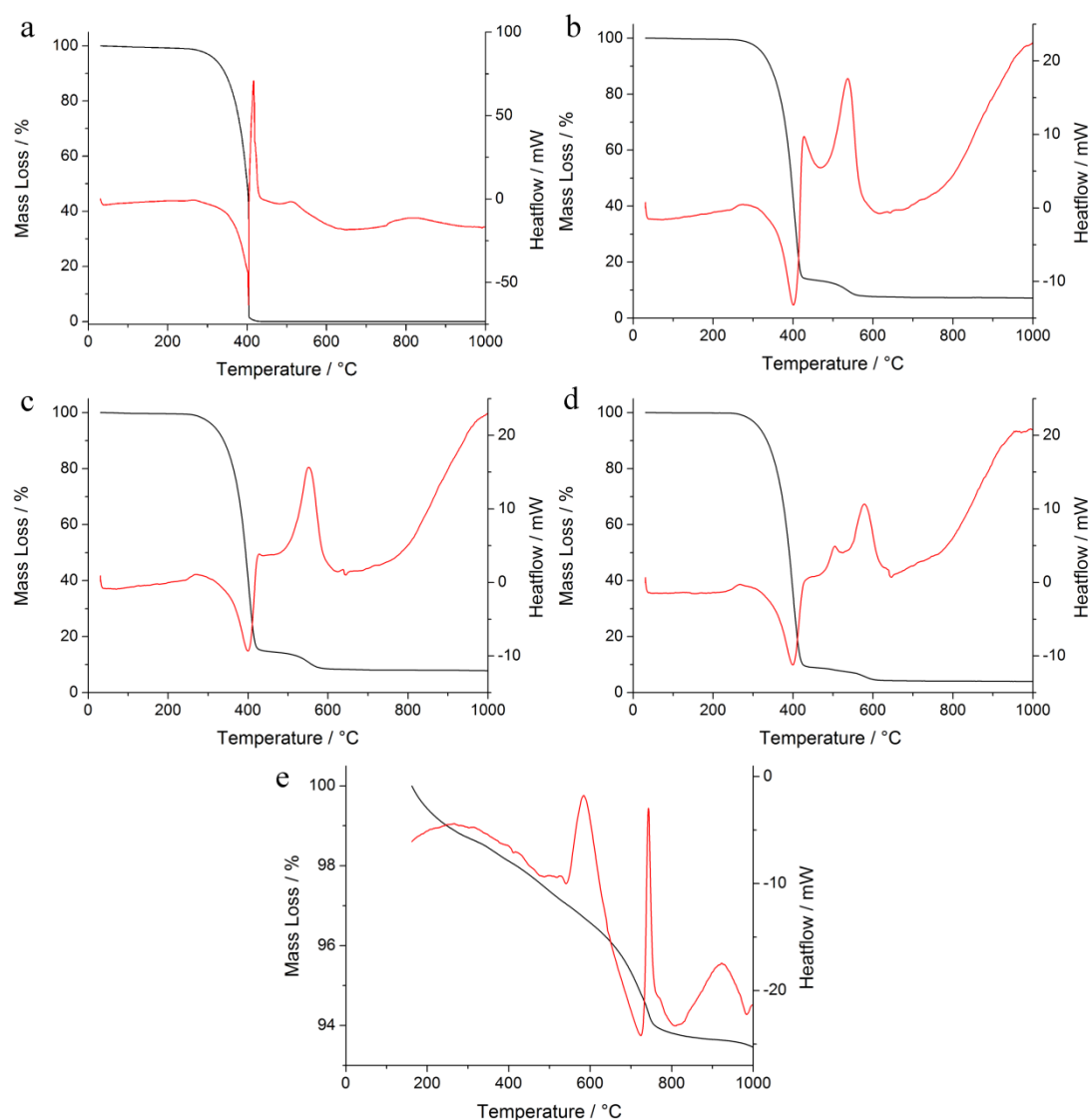


**Figure V.6** TGA of (a) poly(Sty-co-BA) film (HM-501), Laponite armoured poly(Sty-co-BA) film (HM-502), (c) Laponite core-shell particles (HM-503), (d) multi-layered particles (HM-505) and (e) Laponite XLS; mass loss (—) and heatflow (—).